The Development of an In-Silico Model of the Human Head for the Simulation of Traumatic Brain Injury

A thesis submitted in fulfilment of the requirements for the degree of Master of Biomechanical Engineering in the University of Canterbury

By Frederick David Allan Wright

University of Canterbury

2021

Acknowledgements

I would like to express my deepest thanks to my supervisor, Paul Docherty for all the support and guidance he has provided me throughout this project. The odds were stacked against us from the beginning and COVID-19 threw yet another spanner in the works, but we made it. I would also like to acknowledge by amazing family, friends, and fiancé for all the love and support they have given me over this year. I truly could not have done it without you. Lastly, thanks to Gavin for keeping me company while I worked from home.

Abstract

The anatomy of the human head is highly complex, consisting of several different layers of biological material. The layers in the brain are both solid and liquid. The tissues and fluids which are present in the head have been shown to exhibit non-linear material parameters including hyper elasticity, viscoelasticity and anisotropy. As result modelling of the human head is a complex challenge.

Traumatic brain injury (TBI) classification methods are somewhat arbitrary and stochastic in nature. Currently, the accuracy of head injury diagnosis is often dependent on the past experiences and knowledge of the individual practitioner. For this reason, the development of a human head model is beneficial. Due to the inherent complexity of human anatomy, an accurate representation of head geometry is computationally expensive.

A proposed head model was developed in ANSYS and consists of a skull, the cerebrospinal fluid (CSF) and the brain. The final geometry of the model was established via conversion of magnetic resonance imaging (MRI) and computed tomography (CT) scans into .stl files. The brain was represented as a 12 term Ogden Hyperelastic solid with a 12 term Prony series approximation of viscoelastic damping. The skull was represented as a 3 term Prony viscoelastic damped solid. The CSF was represented as a fluid-like solid material with a large Youngs modulus and small shear modulus. Simulation was run using ANSYS transient mechanical solver.

Simulated results showed similar patterns of stress distribution, implying that the CSF has a major effect on the way stress is propagated throughout the brain. This was hypothesized to be a function of both the material parameters of the CSF and the geometry of the head. The final model was able to converge to a 10s simulated impact after approximately 2 hours of computational time. The model developed for this thesis enables further insights into the inner mechanics of TBI and will benefit from further development.

A secondary analysis considered the effects of soft tissue artefact on measurements collected by skin mounted acceleration sensors. The skin, skull, sensor system was modelled as a non-linear spring mass damper system. Comparison of simulated results to acceleration results collect via mouthguard mounted

sensors showed accurate representation of the skin, outlining the need to include the dynamic response of the skin when performing analysis on results collected from skin mounted sensors.

Contents

Introduction

Traumatic brain injury (TBI) is the defined as dysfunction of the brain due to some external force. The symptoms of TBI can range from asymptomatic and mild, moderate, severe up to death. Such injuries are common for athletes participating in sports such as American football, soccer, boxing, and rugby. The specific outcomes of TBI are established and identifiable. However, the likelihood of TBI as a result of a specific impact is often based on the past experience of physicians or the current gold standard of the Head Injury Criterion (HIC). Such definitions are inherently stochastic and can fail to account for secondary modes of injury such as rotational acceleration of the head and subdural haematoma. The development of a computational simulation for head injuries will allow further insight into the internal pressures, forces and other factors which may be relevant to judging the severity of a TBI due to a head injury.

Chapter 1

Anatomy of the Human Head

Outline of Structure

The anatomy of the human head is highly complex, comprising of several distinct regions of tissue, fluid and bone. The skull of an adult is comprised of 22 bones, 8 of which are cranial bones. In children and infants, the skull exhibits a high elasticity as the bones are still forming, but following maturation it becomes much less elastic and more brittle as age increase (Netter & Colacino, 1989; Schulte-Geers et al., 2011).

Within the intracranial cavity, dura mater adheres to the skull separating into two distinct layers, the endocranial and meningeal. These layers separate at various points throughout the cavity to form sinuses, in which cerebral spinal fluid (CSF) can re-enter the bloodstream. The CSF layer has many functions, most prominently it provides a medium for the brain to exhibit buoyancy. Without this buoyancy the tissue of the brain would collapse under its own weight (Prosser, Vender, & Solares, 2011). The CSF also provides a layer of cushioning between the sub-arachnoid layer and pia mater on the exterior of the brain (Panzer, Myers, Capehart, & Bass, 2012). CSF is produced in the ventricles, similarly to blood plasma it is blood with

red and white blood cells removed. CSF can flow around the brain, through the ventricles via the cerebral aqueduct and down the spine via apertures at the base of the head. Figure 1 outlines a sagittal cross section of the head with key anatomical features labelled.

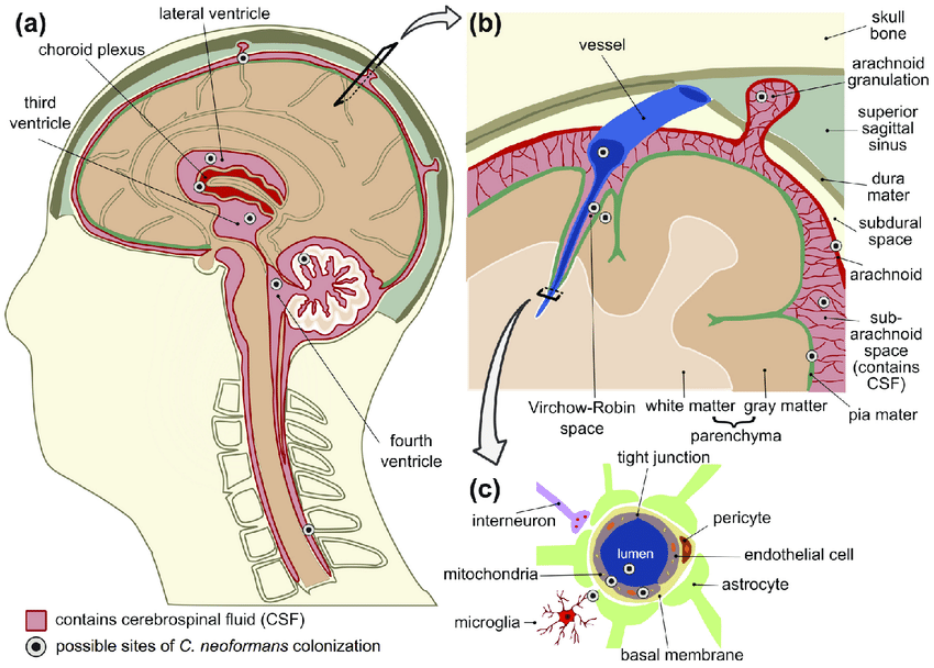

Figure 1: Sagittal cross section of the head with labelled anatomy (Colombo & Rodrigues, 2015).

The tissue of the brain in not uniformly homogeneous, exhibiting unique structural properties in separate regions (Hrapko, Van Dommelen, Peters, & Wismans, 2006). The brain also exhibits a level of anisotropy, meaning that it will display varying geometric deformation properties according to the direction of force application (Giordano, Cloots, Van Dommelen, & Kleiven, 2014). The intricate nature of the head's anatomy must be simplified for accurate and efficient simulation to be performed.

Material Properties

Not only is the geometry of the human body complex, so too are the material properties. This is due not only to its composition being comprised of several interacting materials, but also to the complexity of each individual material in it-self. To simplify the description, biological materials can be described with three main sub-categories: Soft tissue (skin, muscle, brain), hard tissue (bone, cartilage) and fluids (blood, CSF, plasma) (R. Narayan & ebrary, 2009; Ratner, Hoffman, Schoen, Lemons, & Schoen, 2012). It is often

not possible to model these materials using standard linear methods and as such, more complex models must be employed. Both soft and hard tissue have been found to be hyper-elastic, visco-elastic, anisotropic and non-homogeneous properties (Butler et al., 2015; El Sayed, Mota, Fraternali, & Ortiz, 2008; Giordano et al., 2014; Goldsmith & Plunkett, 2004; Inglese et al., 2005; R. Narayan & ebrary, 2009; Post et al., 2015; Ratner et al., 2012; Smith, 2019; Zhou, Li, & Kleiven, 2019). Biological fluids can also exhibit non-Newtonian properties, though CSF and blood plasma are often modelled as water due to their similar densities (Panzer et al., 2012).

The transverse anisotropy within the soft tissue of the brain is attributed to the presence of axonal fibers. These fibers, which are rigid tubular structures and water molecules are able to diffuse more freely while moving axially along them but are constrained from moving across the walls of the axons. As a result, the direction of mechanical loads applied to the brain will affect the resultant elastic modulus which is exhibited by the tissue. Thus, the appropriate value of elastic modulus for brain tissue models can be ambiguous. To combat this ambiguity a diffusion tensor which includes measured values of diffusivity can be introduced to the material model. Depending on the size of this tensor, the resultant model can have a dramatically increased level of mathematical complexity (De Erausquin & Alba-Ferrara, 2013; Feng, Okamoto, Namani, Genin, & Bayly, 2013; Giordano et al., 2014).

CSF is produced in the ventricles. CSF is effectively blood which has the red and white blood cells removed. The resultant fluid flows throughout the ventricular system and the spinal canal. The fluid has been shown to have a similar density to water (Jin et al., 2015; Sweetman & Linninger, 2011), and shares many similarities to blood plasma, which is produced in a similar fashion. CSF is generally considered to be a Newtonian, water-like fluid, the high concentration of proteins, glucose and residual blood cells has been hypothesized to cause variations in its viscosity (Bloomfield, Johnston, & Bilston, 1998). The authors concluded that for low shear rates and at 37 °C CSF exhibits clearly Newtonian behavior. In several head models, CSF has also been represented as a fluid-like solid material with a high elastic modulus and low shear modulus (Chafi, Dirisala, Karami, & Ziejewski, 2009; Jin et al., 2015).

Traumatic Brain Injury

Classification of TBI

In general, the classification of TBI is somewhat arbitrary and relies heavily on the past experiences and knowledge of the individual performing diagnosis and treatment. One of the common classification methods is the use of the Glasgow Coma Scale (GCS) which is a standardized method of evaluating the level of consciousness of a patient (McNett, 2007). There are three main scoring sections, eye opening (e), motor skills (m) and verbal score (v). each of these three scores are recorded and used to evaluate the severity of injury. Baalen et al. (2003) discusses the GCS and several other scoring methods such as the Galveston amnesia and orientation test (GOAT), a similarly symptom based assessment, and the mechanism of injury assessment, where the cause of the injury is accounted for in the assessment. The authors discuss how these assessments paired with evaluation of computed tomography (CT) scans can be used to predict severity and assess potential outcomes for the patient. The authors reviewed literature with valid and reliable measurements of initial severity and final outcome of injury and concluded that both CT-parameters and symptom based classification systems are valid (Changaris et al., 1987; Choi et al., 1994; Healey et al., 2003; McNett, 2007; R. K. Narayan et al., 1981; Rovlias & Kotsou, 2004).

Saatman et al. (2008) further discusses the classification of TBI for the implementation of targeted therapy using combined databases from the National Institute of Neurological Disorders and Stroke, Brain Injury Association of America, the Defense Veterans Brain Injury Center and the National Institute of Disability and Rehabilitation Research. Specific methods of symptom-based assessment such as the GOAT and GCS are discussed alongside several other methods including pathoanatomic and pathophysiological methods. Such methods account for the injury mode and location within the brain and the information related the injury to the expected outcomes, providing specific treatment to overcome chronic symptoms. The use of a physical medium assessment is also discussed, whereby the forces involved are examined to enable identification of common injury patterns. This enables a somewhat standard assessment and establishment of treatment plans. However, almost all these methods still rely on experience and empirical evidence for validation. While they examine the causes and consequences of TBI, they overlook what the underlying mechanics might be and how this can affect patient outcomes.

When shifting from typical medical methods to methods which incorporate biomechanics, the common gold standard in TBI classification is the head injury criterion (HIC). This method was proposed by McHenry (2004) as a way to categorize the nature and severity of head injury based on the observed magnitudes and direction of forces involved. Specifically, it introduces a scalar function of the translational acceleration of the head during impact. The HIC was established using experimental data in which anterior and posterior impacts were applied to human cadavers during crash tests and virtual load (Szabo & Welcher, 1996). Because the HIC does not distinguish between the injury mode or account for the torque of the impact, it is not a perfect representation of the real system. Furthermore, because the precise real loading values during TBI are not accurately recorded, it is somewhat stochastic in nature. It also does not account for various factors such as the observed rotational acceleration and the anisotropic nature of brain tissue, These factors have been shown to play a significant role during injury (Goriely et al., 2015). Hence, the HIC is stochastic in nature and predicts a broad range of outcomes for most impacts.

Biomechanics of TBI

The symptomatic outcomes of TBI are largely understood by physicians, however the biomechanics that lead to these outcomes are still an active area of research. It is understood that there are two main modes of TBI, blunt force trauma and exposure to pressure waves (Moss, King, & Blackman, 2009). Each of these modes has different causes and can lead to different biomechanical loading within the head.

Computational models of the human head have been developed since as early as 1975 as discussed by Shugar and Katona (1975). But the continued development of more powerful computational resources has allowed more complex models to be developed. Panzer et al. (2012) investigated how a shockwave from an explosion might cause damage. Using FEA simulation it was found that the wave front can cause a ripple of the skull, applying potentially harmful loads to the brain all around the head. Raul, Baumgartner, Willinger, and Ludes (2006) discusses the effects which the falx cerebelli and tentorium might have on the internal mechanics of brain injury. The significant difference in mechanical properties at the boundaries in contact with these two regions means there is likely to be strain induced.

Zhou et al. (2019) discussed the brain – CSF interface and how the CSF layer is theorized to act as a damper during TBI. It is possible that due to the head essentially being a closed container, the CSF layer could be modelled as a solid with a high elasticity, or as a hydrostatic material. In doing this fluid dynamics could be disregarded, allowing a substantially less complex model to be established.

Due to the inherent complexity of the anatomy of the head, many models simplify the geometry, material models and loading scenarios in order to allow effective simulation to be performed. A common method of simplification is the representation of CSF as a fluid like solid material. Chafi et al. (2009) discusses the outcomes of modelling CSF as a nearly incompressible elastic solid with a low shear modulus and a viscoelastic solid with low shear modulus. The study showed that varying the material properties did not have a major effect on the experienced intracranial pressure.

Short and Long-Term Effect of Traumatic Brain Injury

TBI has been known to occur in individuals from a variety of different causes. While it generally occurs following some blunt force trauma, it is possible to receive TBI following an indirect application of force such as whiplash or pressure waves (Chen & Huang, 2011; Findling, Schuster, Sellner, Ettlin, & Allum, 2011). TBI is commonly observed in athletes who participate in contact sports such as rugby (Hollis et al., 2011), ice hockey, American football (Bachynski & Goldberg, 2014) and boxing (Lijuan Zhang et al., 2003). However, it is also common in non-contact sports such as soccer (Levy et al., 2012) and as a result of accidents such as falls and car crashes (Hardman & Manoukian, 2002).

The effects of TBI have both short and long-term effects. In the short term those effected can lose consciousness, experience dizziness, amnesia, blurred vision, fatigue and impaired cognitive function (NZMOH, 2019). These symptoms have been long established and observed following the occurrence of injury. However the long term effects of TBI are still an active area of research. DeKosky and Ikonomovic (2010) discusses long term the effects of mild, mild repetitive and severe TBI. The paper states that even mild TBI can result in long term cognitive impairment and post-traumatic stress disorder (PTSD), mild repetitive trauma is linked to dementia and severe TBI can cause to Alzheimer's disease later in life. It is

also reported that in the United States of America alone more than 1.5 million citizens have sustained mild head injuries below the threshold for hospitalization.

Dean and Sterr (2013) discusses the long-term effects of TBI on cognitive function. It was found that those who had suffered from mild TBI (mTBI) exhibited consistently lower scores on the n-back continuous performance task and Paced Serial Visual Addition Test (PSVAT), which is a test commonly used in neuroscience to assess cognitive and neuropathological function (Forns et al., 2014). These symptoms were observed not only in individuals who displayed consistent Post-Concussion Disorder (PCD) symptoms, but all who had experienced mTBI. The lack of correlation between the levels of initially observed symptoms and performance scores lead the researchers to hypothesize that the initial symptom report should not be a major consideration when predicting the long-term cognitive effect of an injury. It has also been discussed that mTBI can lead to psychological complications for patients later in life. Such complications include depression and PTSD (Gomez-Hernandez, Max, Kosier, Paradiso, & Robinson, 1997; Rapoport, McCullagh, Streiner, & Feinstein, 2003).

Taylor et al. (2008) discussed the effects of TBI in young children, specifically relating to their readiness for schooling. It was observed that in children who experienced TBI between ages 3-6, the severity of injury as well as their home environment influenced their readiness for school. It is also discussed that there are many consequences for children who experience TBI at a young age, such as impaired academic performance relative to age expectations, behavioural issues, lack of social understanding, and adaptive functioning. All these symptoms are testament to the importance of further understanding the mechanics of TBI in order to enable more effective treatment and prevention.

Past Methods and Studies in Head Modelling

Physical studies

Both biomechanicians and physicians have long studied the causes and effects of TBI. A study by (Pierce, Smith, Trojanowski, & McIntosh, 1998) followed a group of rats which were systematically exposed to various modes of head trauma and tested over the following year to establish the initial and lingering symptoms they exhibited. Similarly, a study by (Miller, Chinzei, Orssengo, & Bednarz, 2000) involved

performing similar tests on pigs, Figure 2 shows the live animal testing device used in this study. The study involved the removal of the scalp and brain to allow an indenter to directly interface with the animal's brain.

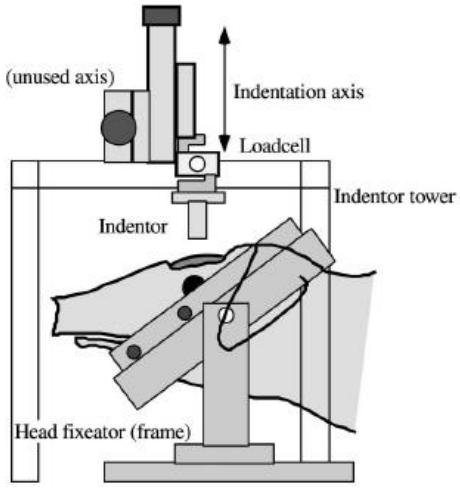

Figure 2: Depiction of brain impactor used in a study of TBI by (Miller et al., 2000)

Further animal experimentation has been performed to investigate the pathophysiological outcomes of direct missile impact to the brain. This study used anesthetized mongrel cats, which were placed briefly into a stereo axial frame, which removed the sloping wall of the right frontal sinus, allowing the missile to penetrate the intact posterior sinus wall. Steel spheres of varying sizes were then fired at the animals, allowing a missile wound track to be established and analysed. (Carey, Sarna, Farrell, & Happel, 1989)

Cernak (2005) further discusses several animal models and experiments in which fluid percussion, static loading, direct dynamic and indirect dynamic loading cases were investigated on sheep, rabbits, cats, dogs, mice and rats. In all experiments conducted the subjects were exposed to immediately or long-term fatal injury. The study concluded that animal experimentation for the study of TBI was uncommon but vital to further develop the complex mechanisms at play during head injury and that more complex experiments are necessary to fully develop such an understanding. The ethical implications of such studies are questionable and would not be feasible for continuation into human studies. Compounded with this, the unique physiology and anatomy of all species means it is difficult to scale such experiments to a human comparison.

In general, head models are developed using physiological scans of humans and tissue parameters established via ex-vivo experimentation or from similar tissue studies on animals. Alternatively, anthropomorphic human dummies and human cadavers have been reported as being used for the validation of head models (Raul et al., 2006; Shen et al., 2006; Shugar & Katona, 1975; Takhounts et al., 2003; Yan & Pangestu, 2011; Liying Zhang et al., 2001). In some cases, live human subjects are used to investigate the kinematics of impacts which could cause injury. Szabo and Welcher (1996) outlined an experiment in which human subjects were exposed to four rear end car impacts over four days. The subjects were instrumented to record the movements and accelerations experienced as a result of the impacts. Studies have also been performed using professional athletes and military personnel who are expected to experience some form of trauma throughout their careers (Hollis et al., 2011; D. King, P. Hume, C. Gissane, & T. Clark, 2017a, 2017b; D. A. King, P. Hume, C. Gissane, & T. Clark, 2017). In such studies, instrumentation is embedded into equipment which would otherwise be worn by the subjects regardless of experimentation. Due to the de-coupling which is often present between where instrumentation is mounted and the head during trauma, such studies often provide results which are not immediately relevant without spatial transform and the inclusion of complex dynamic systems. In most cases, no immediately or long-term fatal forces are applied during the studies due to the ethical concerns of performing such experiments (A. J. Bartsch et al., 2019; Birzer & Hamilton, 2019; G. Fife, O'Sullivan, & Pieter, 2013; G. P. Fife, O'Sullivan, Pieter, Cook, & Kaminski, 2013; Goldsmith, 2001; Montgomery, Fenton, McClelland, MacFlynn, & Rutherford, 1991; B. Rowson & Duma, 2020; S. Rowson et al., 2012).

In-Silico Studies

To avoid injury to subjects and ethical limitations, biomechanicians have been attempted to use computer simulation to examine the internal mechanics of head injury since as early as the 1970s (Shugar & Katona, 1975). Such simulations involve initially establishing tissue parameters and mechanical properties of the various materials in the head before establishing a model which can be used to run a finite element analysis (FEA) which evaluates the effects of an external application of force. A leading contemporary model is the Royal Institute of Technology (KTH) of Stockholm's model (Kleiven, 2002). This model is based

in 3D scans of the human head and incorporates three distinct layers: the skull, CSF and brain. It also incorporates several other detailed models (Giordano et al., 2014). Figure 3 shows the KTH model. This model accurately represents the basic anatomy of the head.

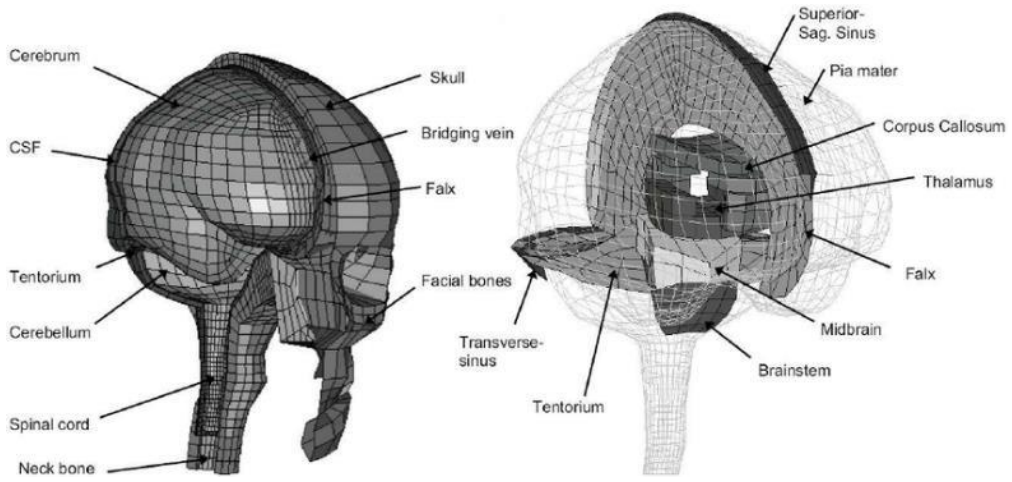

Figure 3: Outline of the KTH head model as outlined in (Kleiven, 2002).

With continuous advancement of computational tools, the ability to perform accurate simulations of human anatomy and physiology is becoming more achievable. Not only does computer simulation provide a consistent and stable environment for repeated testing, but it also removes the need to endanger test subjects for the sake of experimentation. To perform computational analysis a FEA is performed. This can be implemented using several applications such as MATLAB, COMSOL and ANSYS.

It has been established that intracranial pressure (ICP) can be modelled to capture injury location within the brain tissue (Ward, Chan, & Nahum, 1980). Using known tissue parameters and wave theory to model the propagation of pressure waves, areas of high strain within the brain can be determined. Thus, the locality and extent of damage can be estimated.

In order to simulate real world conditions, Giordano et al. (2014) imposed kinematics based on the concussive sports accidents from the North American National Football League (NANFL). Alternatively Gilchrist and O'Donoghue (2000) and Rezaei, Sarvghad-Moghaddam, Eslaminejad, Ziejewski, and Karami

(2016) both simulated simple applications of force to a specific part of the head. These studies outline the relevance of both real world and basic simulated input forces when performing in-silico experimentation.

Smith (2019) used a simplified model of the human brain to analyze the movement of pressure waves throughout the intracranial medium. This method enabled a more efficient and timely simulation of the injury and allowed initial observations to be made regarding the nature of such waves and how they move through the head. This model provided a solid foundation to enable further development and analysis of the problem through refinement of the model. In particular, the model lacked true head tissue definition. Hence, measures such as the addition of a skull and CSF could be beneficial.

There are contradictory publications which discuss the relevance of skull elasticity when modelling ICP for the purpose of studying TBI. Rezaei et al. (2016) discusses the lack of effect that skull elasticity has on ICP. The analysis considered an adult head model, to investigate the effect of skull elasticity, the material was first simulated as a deformable solid, then as a rigid body. It was found that initially there was a small difference in the experienced ICP, however over time, the effect disappeared. Moss et al. (2009) discuss the effects that skull flexure has on ICP when acted on by a blast wave. It is shown that a ripple through the skull causes several areas of high pressure which can cause subdural hematoma and TBI. This lack of consensus regarding the validity of rigid bone modelling implies ambiguity and that benefit could arise from further investigation into the subject.

Finite Element Analysis

Outline of FEA

Finite Element Analysis (FEA) is the process of discretizing a model down into a finite number of smaller elements to allow the discrete analysis of loading cases, usually via partial differential methods, which would otherwise require difficult or impossible differentiation to solve. This process has long been employed by engineers to solve many complex problems computationally including the analysis of linear static structural systems, dynamic structural systems, buckling, fatigue analysis, heat transfer and thermal analysis, crash simulation and optimization analysis (Gokhale, 2008). In its simplest form, static structures can be broken into single dimensional elements which are attached at nodes. This formulation can be

scaled up dimensionally and further developed to account for more complex geometry and modelling. This process is known as meshing.

This discretization of geometry of objects allows simplified mathematical analysis to be performed iteratively on each individual element and in turn find their interaction with other elements which are connected via nodes. The element behaviors that conform to the governing equations is achieved using simultaneous equations and enables prediction of the behavior of complex shapes which would otherwise not be possible using closed form calculations. By decreasing the size of elements, FEA can improve mesh quality and provide more accurate results to the real-world system which it is representing. However, this accuracy comes at a computational cost.

There are several different solvers/methods which can be employed when performing FEA such as transient, static, iterative, direct and explicit solver engines. Each solver has some benefits and drawbacks which should be weighed against one another to select the most appropriate solver based on the specific case being solved. For example, an explicit solver is always stable, but this has a massive computational cost. A transient solver is able to provide long term solutions but will always take longer than an equivalent static solutions, and direct solvers tend to be more stable than iterative solvers, however they have a larger hardware requirement due to the increased size of the involved matrices and tensors used during solution. There are also many different software packages that are designed to simplify the process of performing FEA (Hutton, 2004).

FEA is used to perform both explicit and implicit analysis. These correspond to time dependent and time independent analysis respectively. For cases where the effects of acceleration are prominent, time-dependent analysis is required, cases where acceleration effects are negligible can be referred to as ‘quasi-static’ and this allows for time-independent (implicit) analysis. In general, problems which have large deformations, geometric non-linearity and boundary non-linearity require explicit analysis to be performed for accurate results. Performing explicit analysis is substantially more computationally expensive than implicit. Therefore, wherever possible, FEA models are simplified to allow for implicit analysis.

Outline of Computational Fluid Dynamics (CFD)

CFD is a category of FEA specifically for the computational analysis of fluid systems. Since fluids are able to flow in such a way that there would be massive distortion of elements when meshed traditionally, they require specialized meshing and computational techniques. Most CFD software is based on the Navier-Stokes equations for the conservation of mass, momentum, and energy. These are outlined in Equations 1 a through f.

$$\rho\left(\frac{\partial \vec{u}}{\partial t} + \vec{u}.\nabla\vec{u}\right) = -\nabla p + v\Delta\vec{u}$$

$$\nabla.\vec{u} = 0 \qquad \text{(Eq. 1(a))}$$

Expanded continuity: $\frac{\partial(\rho v)}{\partial t} + \frac{\partial(\rho u)}{\partial x} + \frac{\partial(\rho v)}{\partial y} + \frac{\partial(\rho w)}{\partial z} = 0$ (Eq. 1(b))

X-Momentum: $\frac{\partial(\rho v)}{\partial t} + \frac{\partial(\rho u^2)}{\partial x} + \frac{\partial(\rho uv)}{\partial y} + \frac{\partial(\rho uw)}{\partial z} = -\frac{\partial \rho}{\partial x} + \frac{1}{Re_f}\left[\frac{\partial \tau_{xx}}{\partial x} + \frac{\partial \tau_{xy}}{\partial y} + \frac{\partial \tau_{xz}}{\partial z}\right]$ (Eq. 1(c))

Y-Momentum: $\frac{\partial(\rho v)}{\partial t} + \frac{\partial(\rho u^2)}{\partial x} + \frac{\partial(\rho uv)}{\partial y} + \frac{\partial(\rho uw)}{\partial z} = -\frac{\partial \rho}{\partial y} + \frac{1}{Re_f}\left[\frac{\partial \tau_{xy}}{\partial x} + \frac{\partial \tau_{yy}}{\partial y} + \frac{\partial \tau_{yz}}{\partial z}\right]$ (Eq. 1(d))

Z-Momentum: $\frac{\partial(\rho v)}{\partial t} + \frac{\partial(\rho u^2)}{\partial x} + \frac{\partial(\rho uv)}{\partial y} + \frac{\partial(\rho uw)}{\partial z} = -\frac{\partial \rho}{\partial z} + \frac{1}{Re_f}\left[\frac{\partial \tau_{zx}}{\partial x} + \frac{\partial \tau_{zy}}{\partial y} + \frac{\partial \tau_{zz}}{\partial z}\right]$ (Eq. 1(e))

Energy: $\frac{\partial(E_r)}{\partial t} + \frac{\partial(uE_r)}{\partial x} + \frac{\partial(vE_r)}{\partial y} + \frac{\partial(wE_r)}{\partial z} = -\frac{\partial(\rho u)}{\partial x} - \frac{\partial(\rho v)}{\partial y} - \frac{\partial(\rho w)}{\partial z} - \frac{1}{Re_f Pr_f}\left[\frac{\partial q_x}{\partial x} + \frac{\partial q_y}{\partial y} + \frac{\partial q_z}{\partial z}\right] + \frac{1}{Re_f}\left[\frac{\partial \tau_{zx}}{\partial x} + \frac{\partial \tau_{zy}}{\partial y} + \frac{\partial \tau_{zz}}{\partial z} + \frac{\partial \tau_{xy}}{\partial x} + \frac{\partial \tau_{yy}}{\partial y} + \frac{\partial \tau_{yz}}{\partial z} + \frac{\partial \tau_{xx}}{\partial x} + \frac{\partial \tau_{xy}}{\partial y} + \frac{\partial \tau_{xz}}{\partial z}\right]$ (Eq. 1(f))

Where u, v, and w are the velocity in the x, y and z directions, respectively. ρ is pressure, r is density, T is temperature, R_e is the Reynolds number, τ is stress, q is heat flux and P_r is the Prandtl number.

These equations are formulated by applying Newton's second law to fluid motion. In particular changes in fluid momentum are linked to the velocity, pressure, shear stress and density of a flowing fluid are related. Depending on the applied boundary conditions and requirements of the specific problem, these equations are simplified in the interest of computational efficiency. Fluid elements are generally represented in a Eulerian domain, while solid elements are represented as Newtonian. In simple terms, this means the overall fluid domain is meshed, but specific cells are then 'filled' with fluid which can flow through to adjacent cells (Donea, Giuliani, & Halleux, 1982). Alternatively, a Lagrangian domain which is used for solid objects does not allow flow between cells, rather the cells themselves deform with applied external forces.

In general, CFD is used to simulate the interactions of fluids within a rigid domain and between one another. However, it is possible for fluids to interact with solid objects. This leads to the requirement of fluid-solid interaction (FSI) simulations (Génevaux, Habibi, & Dischler, 2003).

FSI

FSI is the coupling of fluid simulation with solid simulation. This allows the analysis of systems where solid objects effect or are affected by the flow of fluids. The process is often undertaken in an iterative manner, in particular the individual systems are solved sequentially with their results fed into one-another, or in an explicit way, in which a large system of equations representing both the solid and fluid domains is solved simultaneously. Explicit analysis has the benefit of more consistent convergence when non-linear systems are modelled. However, it is more computationally expensive than its iterative counterpart (Madhukar & Ostoja-Starzewski, 2019).

Currently, simulation of FSI is a rare and difficult task, in most software packages it is included via a basic and limited module. In particular, FSI modules will often only include one way coupling between the fluid and solid domains, limit the solid domain to being rigid or not include transient solvers. However, the inclusion of the CSF in the head means that FSI is necessary when construction an accurate model.

Chapter 2: Geometry

Initial geometry for model development

The precursor to this study was performed in Smith (2019). This analysis used a homogeneous model of a human brain, based on MRI scans. This same geometry was initially used in the development of the new head model and is outlined in Figure 4. In the interest of increased accuracy, the model was expanded to include the ventricles, CSF and brain.

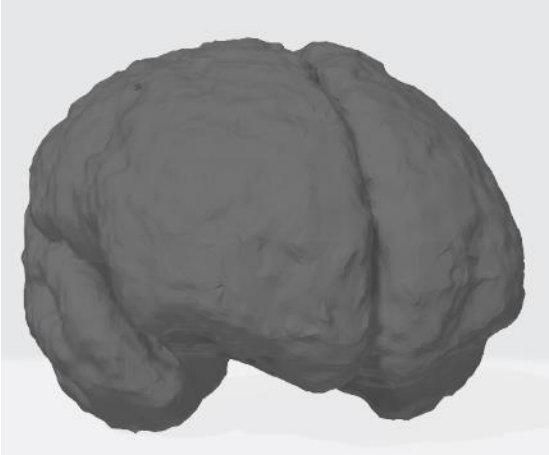

Figure 4: Original brain geometry used in (Smith, 2019)

The expansion of this geometry to include the skull, CSF and ventricles will effect the simulation results in several ways. On a computational level, the added geometric complexity will increase the computational load for both the meshing and load simulation steps. The addition of the skull in particular will increase the spatial distribution of loads experienced in the brain and may also decrease the magnitude of induced deformation for similar loading cases to the simulated brain tissue. The CSF will act as somewhat of a viscous damper between the skull and brain, while also allowing more distribution of stress waves throughout the intracranial medium. The ventricles will allow regions of internal fluid where pressure will propagate differently to the homogenous brain, resulting in differing internal stress distributions.

Before constructing a model based on human anatomy it was important to verify the feasibility of the modelling method, and in doing so learn more about the intricacies of performing such FEA. Performing

initial tests on more simplified geometry means that calculation times are shorter, allowing for more efficient observations of convergence criteria and material model performance. The shortened computational time also lowered the likelihood of hardware faults causing issues during simulation. In the interest of simplicity, the model was initially broken into its most basic form of three rectangular layers stacked atop one another with fixed ends. This geometry is shown in Figure 5.

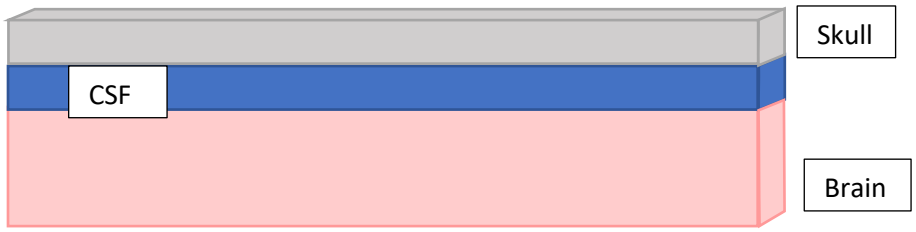

Figure 5: Outline of the simplest geometry used for proof of concept modelling.

Haeussinger et al. (2011) measured the thickness of the skull scalp and CSF layers for 24 subjects, the study found the average skull thickness of 5.242mm and average CSF thickness of 4.175mm. These values were used as the basis for layer thickness selection when generating basic geometry. To generate this basic rectangular geometry, ANSYS SpaceClaim was used to draw a 20mm by 100mm rectangle, which was extruded to the appropriate width according to whether it represented skull or CSF layer. A third rectangle was then extruded with a depth of 20mm to represent the brain. This depth was arbitrarily selected to be larger than the skull and CSF layers combined.

This simple geometry allowed adjustment of contact methods, boundary conditions, initial insight into the interaction of materials and selection of appropriate material models for each layer. Following this, the next iteration was a slightly more complex cylindrical model. The radius of the skull cylinders was based on the measurements of Li, Ruan, Xie, Wang, and Liu (2007), which reported the measurements of 3000 subjects' skulls. The mean length of a male skull was selected as 175.81 mm. The thickness of the skull and CSF were also based on the values reported in Haeussinger et al. (2011). This cylindrical geometry is shown in Figure 6.

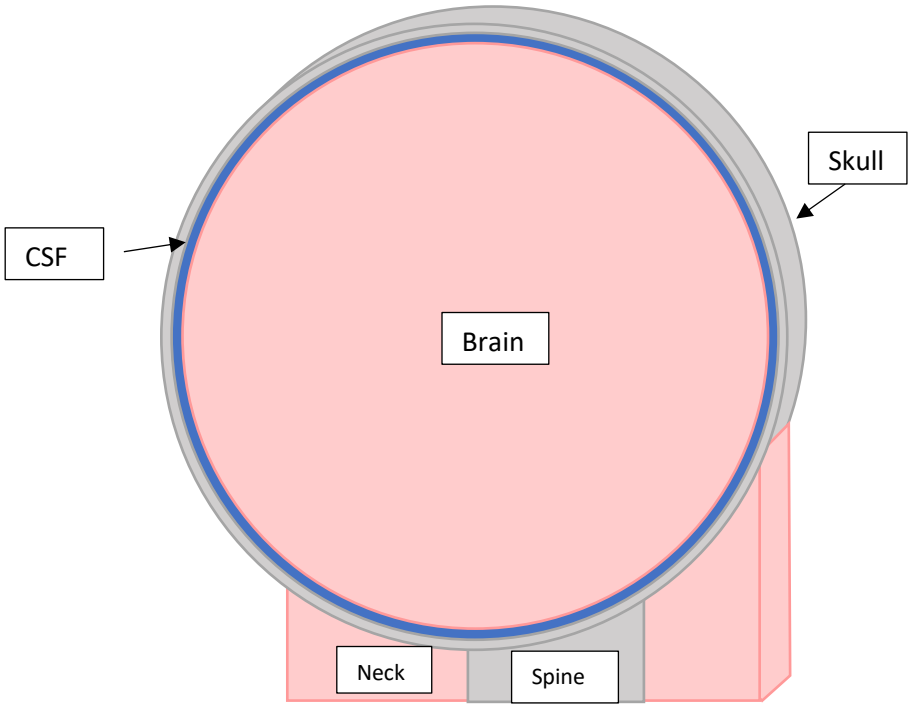

Figure 6: The cylindrical geometry used for development of the model.

The cylindrical geometry allowed more physiological representation to be tested. Notably this involved varying the general method of support at the base of the 'skull', selection of impact zone and boundary conditions in the CSF region. The areas labelled 'Neck' and 'Spine' are a representation of where the skull attaches to the spine and neck. This region was initially treated as a fixed boundary condition but following convergence issues it was adjusted to have a spring support with an arbitrarily large spring constant to allow some movement of the skull without introducing rigid body motion.

(Smith, 2019) used an individual node to introduce a point load into the brain. In order to more accurately represent a real world system, a distributed load was selected. To test loading options, the impact zone was modelled using distribution only across faces, on whole elements, on mesh elements, or on nodes, with a geometric ark depth varying from 1 mm to 3 mm. After trialing simulation with several datasets used for the material properties of the skull, brain and CSF regions a final material characteristic was selected. This involved reviewing several existing studies and including various combinations of viscoelastic damping and hyper elasticity. Because the specific form of material models varied across studies, the process of adjusting materials was iterative in nature. Based on the expected convergence times, mesh deformation metrics and realism of resultant stress concentrations the appropriate boundary conditions were varied until the most appropriate method for the purposes of this study was established. This was dependent on the material models used for the skull, CSF and brain. Several solver methods and software packages were compared before the geometry was next scaled to a spherical model.

This model allowed further refinement of the most appropriate meshing techniques, material models, boundary conditions, workflow, and solvers before implementing the model on a full human head geometry. It was established that for the most realistic and efficient simulation to be performed, surface meshing should initially be performed on the exterior of the CSF layer, this should then be inflated to ensure the CSF mesh was at least 2 elements thick, decreasing the likelihood of inverted mesh elements and excessive distortion. The skull and brain regions were adequately meshed using a basic tetrahedral method. The most time efficient boundary conditions were found to be either a no separation or bonded contact between the skull, CSF and brain.

Anatomical Scanning

The final head model geometry was based on anatomical scans. Due to the need for three distinct layers of different material, this required a combination of multiple scans. There are several methods of scanning live subjects which are employed by medical professionals. Some common internal scanning methods are Xray, Computed Tomography (CT) and Magnetic Resonance Imaging (MRI) (Bell, Fernandes, & Andersen, 2018).

CT scanning is a form of computerized x-ray scanning, in which a narrow x-ray beam is rotated around a subject to produce a multi-layered scan. Stacking the resultant scans allows for a 3d representation of the subject to be achieved (Buzug, 2011). Since CT scanning gives high definition of bones, a dataset produced using this method was used to produce a skull geometry. MRI on the other hand is a relatively non-invasive method of scanning which produces a high-definition image of soft tissues using a similar stacked-slice method (Morris & Slesnick, 2018; Vlaardingerbroek & Boer, 2013). As such, a dataset produced using MRI was used to produce the brain and ventricle geometries.

Both these datasets were taken from the same live subject and are part of the open-source database used by 3D slicer. 3D Slicer is an opensource medical image processing package which allows the visualization and procession of medical images (Fedorov et al., 2012; Pieper, Halle, & Kikinis, 2004) (BWH, 2021).

Tissue Identification and Mapping

The skull, brain and ventricle geometries were all separately produced by initially running the inbuilt functions of 3D Slicer. This ran an edge finding and classification algorithm on each layer, which was then used as a basis to add to and subtract from manually. The basic functionality of the algorithm is to identify regions of different tissue. Figure 7 shows an initial output of the function on a slice of an MRI.

Figure 7: Initially classified MRI slice.

Because the CSF, bone and brain all exhibit different material properties, they are identifiable by their varying colors and tones. Such variation is relatively clear for a computational algorithm, but before manually adjusting the layers it was important to adjust the contrast and brightness of each image to

make more visible to the human eye. This is particularly important in MRI scans as the dura and arachnoid layers are difficult to distinguish from brain tissue in noisy areas. Figure 8 shows the difference made by adjusting the image.

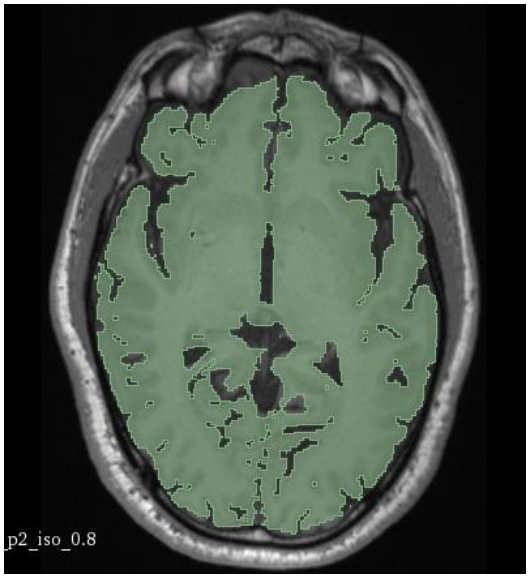

Figure 8: Refined MRI slice.

By manually parsing each layer and hand painting regions the edge finder had missed, or erasing noisy areas, the geometries for brain, ventricles and skull were all roughed out based on the data sets. It became apparent during this process that the MRI scan slices had been recorded with a slight rotation along the craniocaudal and anteroposterior axes. This meant it was not possible to paint and erase identified regions of tissue on the exact same plane which the slices had been recorded on. This could have been corrected by manually transforming the image vectors. In particular, this would mean performing vector transforms for each image layer which corrected the rotation of the scans, but ultimately this was deemed unnecessary as the exported geometry required substantial post processing regardless of this correctional step. These geometries where then individually exported to an .stl format for further processing. Figure 9 shows these initial representations of the geometries.

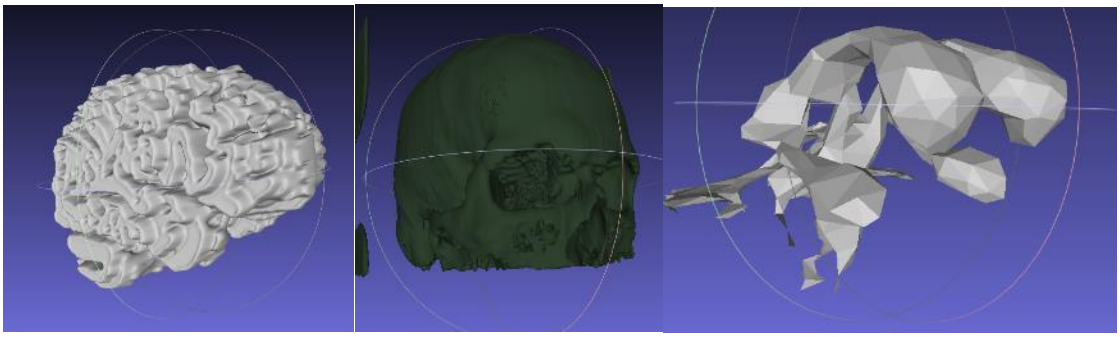

Figure 9: Initial .stl files for the brain (left), skull (middle) and ventricles (right).

Key features and overlapping regions were noted in each geometry set. This enabled an accurate merge of all the final geometries for the head model.

Post Processing of STL

As illustrated in Figure 9, the sliced .stl files required some post-processing before they could be used. With each file having a different layer resolution and thickness requirements, this required a substantial amount of manual adjustment before a final geometry was produced. Initially the whole model was imported into meshlab where it was simplified to a more manageable size. For the brain .stl this meant decreasing the element count from 352,760 Vertices and 705,812 faces to, the skull from 2,504 vertices and 5000 faces. With a smaller file size, the mesh could then be imported into blender, where satellite objects where removed and the geometry was manually smoothed in 3d space. This involved the use of the inflate, smooth, flatten and fill tools. For the brain geometry this was a relatively basic procedure as there were no thin sections and most tissue had been correctly labelled in slicer. Figure 10 shows the result of the processing.

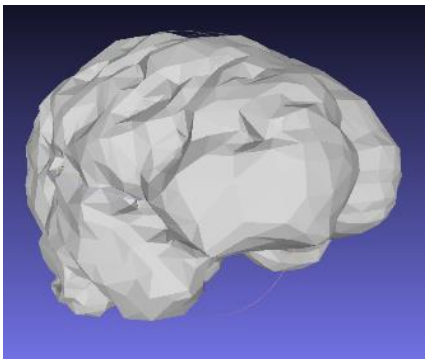

Figure 10: the processed brain geometry.

This new .stl file was then initially imported into mesh mixer, where a repair algorithm was run to remove any overlapping, inverted or disconnected elements. The geometry was then solidified and exported for use in ANSYS Spaceclaim. Since the geometry was still relatively large and complex, it was imported as a faceted solid then finally converted to a solid object for modelling.

While the skull and ventricles underwent a similar procedure, they required some extra processing. In particular, because of the low layer resolution of the MRI scan used to produce the ventricle geometry, some regions were disconnected from one another, and some tissue regions had been incorrectly labelled. Similar to the brain geometry, smaller objects were removed in Meshlab, before the disconnected regions were grown and merged to achieve a cohesive geometry. This geometry was then filled, smoothed, simplified and solidified in a similar way to that of the brain before being imported as a facetted body into ANSYS SpaceClaim for final conversion and assembly.

Some regions of the skull are very thin and exhibit variation in tissue density, and it is not safe for high dosages of radiation to be experience in the head on live subjects. Hence, the CT scan resulted in some major disconnection between some regions and had several areas of noise which had been selected. After initial decimation, filling, smoothing and flattening the skull geometry still had several areas of disconnection, where there were voids in the geometry which needed to be filled in.

The geometry was simplified and solidified before being imported into Space Claim, where the shrink-wrap function was used. By outlining a boundary condition around the base of the skull where the spinal

cord enters the skull, all other regions could be filled and solidified using this function. It also meant that major features such as the eye sockets, cheek bones and nasal cavity could be preserved.

Model Synthesis

With the three skull CSF and brain geometries, an assembly and final geometry could be produced. This involved first aligning all the separate geometries appropriately before mating the parts. The brain and ventricles were the first stage of this. Since the brain had been produced as filled and homogeneous object for simplicity of processing, the ventricle geometry initially needed to be aligned then used to create an internal void in the brain. The ventricles are arranged in such a way that the first and second are situated in the top of the brain inside the frontal lobe and relatively symmetric about the sagittal plane, while the third and fourth are situated behind and below them, running towards the spine. Since the two geometries had been produced based on the same MRI scan, they had reference planes which could be aligned to allow for accurate placement of the ventricles inside the brain geometry. However, in the process of being imported and exported between several software packages, these planes required some adjustment to correctly align the geometries.

Both the brain and ventricle geometries were imported into ANSYS SpaceClaim as faceted bodies. This allowed manipulation of the geometry at a lower computational cost than importing and working with the full stl mesh. It also allowed specific facetted body tools to be used. The brain and ventricle bodies were by creating mates between the top and front planes of each object. Once aligned, the ventricles were used as a cutting tool to create an internal void within the brain. To open the ventricles at the base of the brain where the spine attaches, a 7mm extruded cut was performed. The resultant geometry was then saved as a new object.

The skull required a high level of post processing to form a coherent final geometry. Consequently, some adjustment was required to ensure a stable assembly was achieved for FEA simulation. Similarly to the ventricles and brain, the skull was imported and converted to a facetted body in ANSYS Spaceclaim. The original brain body was then aligned via mating the principal planes of each object, then manually rotated to minimize any internal overlap. To ensure no overlap occurred, the brain geometry was completely

smoothed using the shrink-wrap function in ANSYS SpaceClaim, then inflated to increase its total diameter by 4.175 mm. This value corresponded to the average thickness of CSF as reported in Haeussinger et al. (2011). The centers of this new geometry and the skull were then re-aligned, and the rotation about the craniocaudal and anteroposterior axes was manually adjusted to minimize the total volume of overlap between the two objects. With overlap minimized, the modified brain geometry was used as a cutter to remove excess material from the skull's interior. This created an appropriately sized internal cranial cavity in the skull. The brain with ventricle geometry was then imported and aligned via the principal planes within the cranial cavity, ensuring there was no overlap or contact between the two geometries.

Because the CSF is thin and difficult to distinguish in the MRI and CT scans used in producing the head geometry, all attempts resulted in incomplete CSF geometry which would have required substantial post processing in order to be made coherent for use. It was also observed that since there was like some slight shift of the brain internally to the skull between the MRI and CT scans being performed, it would not be appropriate to use a CSF geometry produced from either dataset. Contrastingly to the processes used in producing brain, skull, and ventricles, the CSF geometry was produced by filling the void between the skull and brain once the two final object geometries were aligned. This was achieved by initially capping the spinal cord entry hole at the base of the skull, then using a Boolean difference tool to generate a new object which represented the CSF and ventricles. This method ensured that there was no overlap between objects and all three layers contacted one another perfectly, simplifying the meshing and contact generation process required for FEA.

Chapter 3: FEA Software

With FEA being so widely used throughout industry there are several different software packages available to simplify the process for specialized applications. In general packages are sold as an overall system with specific modules for specific applications such as harmonic analysis, fluid solid interaction, fluid dynamics, transient and static structural analysis, heat transfer and electrical dynamics. Given the requirements for the head model are relatively bespoke, no one software package was perfectly suited to this application. The software needed to be capable of performing FSI, include definitions of the specific material models

used and be available to the University of Canterbury. The following is an overview of the various packages which were investigated.

MATLAB

MATLAB is not a specific FEA package, but an internal development environment for the M coding language. Because the environment is so widely used in the research and academia field, there are several pre-developed code libraries available for the specific applications of FEA. The Partial Differential Equation Toolbox™ can be used as a basis for the modelling of brain tissue as shown in Smith (2019). The base equation for this toolbox is shown in Equation 2.

$$\mathbf{M\ddot{u}} + \mathbf{D} + \boldsymbol{\nabla} \cdot (\mathbf{C} \otimes \boldsymbol{\nabla}\mathbf{u}) + \mathbf{Au} = \mathbf{f} \qquad \text{(Eq 2)}$$

Where M is the mass matrix, a diagonal matrix with density values (ρ) shown in Equation X. D is a damping matrix which is modified based on the solver type and material models used. C represents a tensor element which is a function of Poisson's Ratio (υ) and Young's Modulus (E).

Developing the model using MATLAB would have the benefit of being able to produce all elements of the system based on the essential principals of the specific material models and solvers used. However, this was assumed to require a significant and prohibitive time investment. Another disadvantage in building the application in MATLAB was the limited graphical interface. For such complex geometry advanced imaging codes would be required to properly observe simulated behavior. However, the most prevalent shortcoming of MATLAB for this specific application was the lack of body interaction available in existing libraries. This meant without the development or modification of an existing FEA library, it was not possible to simulate the interaction of different materials and geometries in a single model.

Consequently, MATLAB alone would not be appropriate in the context of this project. In order to simplify workflow the software used needs more advanced graphical interface tools for the visualization and manipulation of the complex physiological geometries of the head. In addition, MATLAB's inability to

account for body interactions would imply the need to use a homogenous geometry, which would not produce results that are realistic to the real world. Thus, it can be concluded that MATLAB is not the most appropriate software package to use for this project.

COMSOL

COMSOL is a specific FEA package which is widely used for both research and industrial applications. It has a well-polished interface and wide breadth of features. Most notably, for this application, there are several proprietary direct solvers built in such as MUMPS, PARADISO, SPOOLES and Dense matrix solvers(BR & Venkateswaran, 2012). Hence it is suitable for transient analysis of unstable and dynamic systems and can solve such systems more efficiently than many other FEA packages. When compared to ANSYS, which has only one direct solver available, COMSOL is typically able to perform complex analysis in a shorter time in many cases, or with a lower hardware requirement.

COMSOL also has powerful FSI capabilities which are preconfigured for complex models. However, the specific modules required for such capabilities are spread throughout multiple different packages which were not available at the University of Canterbury.

The graphical interface of COMSOL allows low level generation of geometries, but also includes complex manipulation of imported geometry. Hence, for the complex geometry requirements of head modelling it is suitable. The direct solver capabilities of COMSOL allow efficient simulation of unstable problems with typically lower hardware requirements than alternative FEA packages. With the correct software modules included in the specific COMSOL license, it is an appropriate tool to produce a head model. However, in the context of this project, a more appropriate tool was found.

ABAQUS

ABAQUS is an FEA software suite currently targeted more directly at industry over academia. Its close integration to DS Solidworks means it is common choice for design analysis commercially. The FEA community held the fluid simulation capabilities of ABAQUS in high regard, however training resources for ABAQUS were not as readily available when compared to both COMSOL and ANSYS.

While ABAQUS is able to provide the requisite FSI, FEA and graphical capabilities to produce a complex head model, the unfamiliar interface and lack of accessible documentation meant it was assumed that it would take a prohibitive amount of time to develop the skills required to efficiently and effectively use ABAQUS in the context of this project. In addition to this, more appropriate and familiar software packages were available at the time of development.

ANSYS

Much like COMSOL, ANSYS is a specialized FEA package with specific modules available for use. The workflow and system layout used in ANSYS varies when compared to COMSOL. There is a large range of iterative mechanical solvers available in ANSYS. The AUTODYN dynamic solver is also very well known throughout industry. In general, ANSYS allows a lower level interface when configuring simulations and models. Ansys has built in FSI capabilities for FSI, and a wide range of available material models. For the development of a head model, it can provide complex graphical interfaces during the production and refinement of geometry through the use of SpaceClaim.

Ansys mechanical provides a logical interface for mechanical solvers which simplifies the workflow when meshing and configuring complex models and includes comprehensive post processing tools. The only direct solver available for use is the SPARSE Direct solver, which has a higher hardware requirement than those available in COMSOL. Given the appropriate hardware is available, ANSYS is an appropriate software package for the purposes and requirements of this project. Ultimately, the reason ANSYS was selected for this model was that its fluid solid interaction system coupling module was available within the University of Canterbury, unlike the FSI module of COMSOL.

Chapter 4: Material Models

The physical properties of biological materials do not typically conform to simple Newtonian models. Materials in the human body can be separated into the categories of soft tissue, hard tissue and fluids. For the context of a head model, one of each of these categories is required. The CSF is a fluid, the brain is soft tissue, and the skull is hard tissue. In general, simple solids can be described by their shear and

elastic behavior. However, the brain and skull do not conform to standard linear shear or elastic behavior. Thus, more complex models are required for the simulation of these tissues.

Elasticity

Elasticity can be defined as a material's ability to return to its normal shape following stretching or compression. The elasticity of a material can be described by its elastic moduli (Pawlik & Reisman, 1980). In perfectly elastic materials, this is enough to define its elastic behavior. However, in the physical world all material also has a limit to the magnitude of deformation from which it can recover. This limit quantifies the point at which some given material stops behaving elastically. Before this point, known as the elastic limit or yield point, a linearly elastic material can be modelled via Hooke's law (Mihai, Chin, Janmey, & Goriely, 2015). To simplify simulation, it is beneficial to only expose a model to external forces which will result in lower deformation than the elastic limit of a material.

Hyperelasticity

Biological material elasticity is often more accurately described by hyper elastic models, which are a further development of basic linear elasticity. In hyperelastic material models, the elastic response is non-linear to the extent that a linear approximation of such a material would be highly inaccurate. The elastic modulus changes as the material experiences different values of stress and strain. Such materials are able to undergo larger than expected deformation before plastic deformation or failure occurs. A common feature of these materials is near or total incompressibility (Weiss, Maker, & Govindjee, 1996). Figure 11 outlines a comparison between a linear and a hyper elastic material model as illustrated in (PALS Martins, RM Natal Jorge, & AJM Ferreira, 2006b).

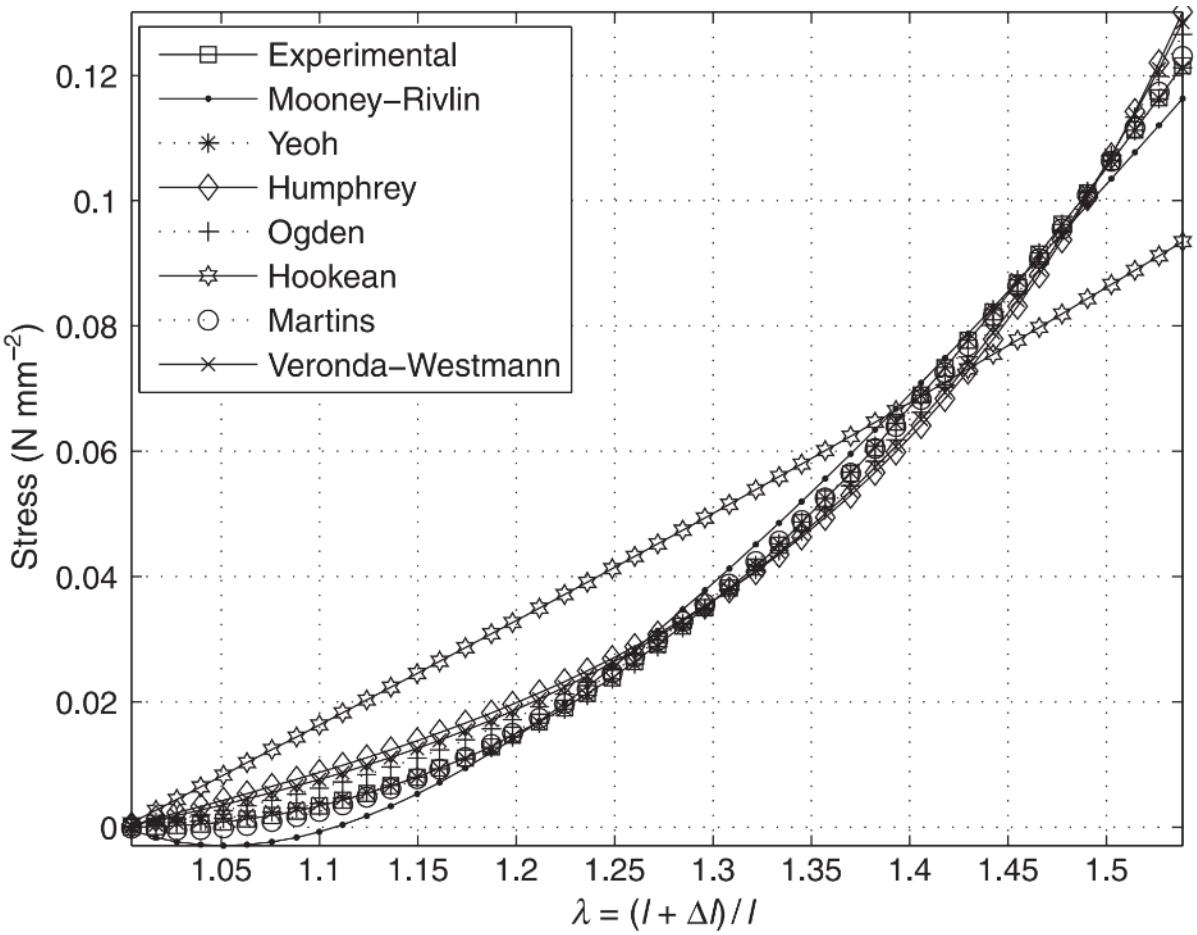

Figure 11: Comparison of the stress/strain response of linearly elastic and hyper elastic materials courtesy of (Martins et al., 2006b).

Because it is no longer possible to model hyper elastic materials via only their elastic moduli, the area under the curve shown in Figure 11 is used. This is equivalent to the stored energy of the material while undergoing stretching and can be generally represented via the strain energy Ψ function outlined in equation 3.

$$\Psi \quad = \Psi_{dev} + \Psi_{vol} \qquad \text{(Eq 3)}$$

Where Ψ_{dev} and Ψ_{vol} are the deviatoric and volumetric strain energy's, respectively. There are several common forms of hyper elastic model representation such as the Neo-Hookean, Mooney-Rivlin and

Ogden models (Marckmann & Verron, 2006). Three of these common forms are built into ANSYS, though it should be noted they are represented with a modified standard form (ANSYS, 2021).

Neo-Hookean

The Neo-Hookean model is the simplest form of hyper elastic material model and is outlined in Equation 4a,b (Marckmann & Verron, 2006).

$$\Psi = \frac{\mu}{2}(I_1 - 3) + \frac{1}{d}(J-1)^2 \qquad \text{(Eq 4(a))}$$

$$d = \frac{2}{K_0} \qquad \text{(Eq 4(b))}$$

Where μ is the initial shear modulus of the material, d is the incompressibility constant and K_0 is the initial bulk modulus I is the first invariant of the right Cauchy-Green tensor and J is the determinant of the deformation gradient tensor. This function uses a linear relation between the strain energy potential and the first strain invariant. Note that while the equation is in a linear form, the invariant itself is a non-linear function of strain.

Mooney-Rivlin

The Mooney-Rivlin model is a commonly used for of the strain energy potential function of hyper elastic materials. It is more complex than the Neo-Hookean model and is therefore used to represent more non-linear materials. Equation 5 outlines this model.

$$\Psi = C_{10}(I_1 - 3) + C_{01}(I_2 - 3) + \frac{1}{d}(J-1)^2 \qquad \text{(Eq 5)}$$

Where the initial shear modulus is:

$$u_0 = 2(C_{10} + C_{01}) \quad \text{(Eq 5(b))}$$

And the initial bulk modulus is:

$$K_0 = 2/d \quad \text{(Eq 5(c))}$$

Equation 5 can be expanded to contain more polynomial terms to capture non-linear behavior more accurately.

Ogden

Unlike the previous two models the Ogden model is derived from principal strains functions (ANSYS, 2021). Equation 6 shows the Ogden model.

$$\Psi = \sum_{i=1}^{N} \frac{u_i}{a_i}\left(\lambda_1^{a_i} + \lambda_2^{a_i} + \lambda_3^{a_i} - 3\right) + \sum_{k=1}^{N} \frac{1}{d}(J-1)^{2k} \quad \text{(Eq 6)}$$

Where the initial shear modulus is:

$$u_0 = \frac{1}{2}\sum_{i=1}^{N}(u_i a_i) \quad \text{(Eq 6(a))}$$

The initial bulk modulus is:

$$K_0 = \frac{1}{2}\sum_{k=1}^{N}\frac{2}{d_k} \qquad \text{(Eq 6(b))}$$

a is a dimensionless non-linearlity constant and $\lambda_1^{a_i}, \lambda_2^{a_i}, \lambda_3^{a_i}$ are the principal strains in the xx ,yy and zz directions respectively. Like the Mooney-Rivlin model, the Ogden model can be expanded with more terms to capture material non-linearity more accurately.

There have been several studies into hyperelastic properties of brain tissue. Mihai et al. (2015) specifically outline a comparison between the accuracy of various hyper elastic models when simulating the deformation of brain tissue and fat. It was found that the most consistently low error for the brain tissue model when compared to a physical experiment was achieved using a higher order Ogden model. As such, the Ogden model of Hyperelasticity was selected for the development of this head model. Due to the limitations of the inbuilt material models in ANSYS, the highest order model which could be used was a third order Ogden model. Table 1 outlines these material properties courtesy of Mihai et al. (2015).

Table 1: Ogden model parameters used for this model.

u_1	a_i	u_2	a_i	u_3	a_i
-3543 pa	1	-2723 pa	-1	654 pa	2

It should be noted that (Mihai et al., 2015) assumed a fully incompressible material model, and the incompressibility factors where therefore set to one. Figure 12 outlines a graph of the elasticity characteristics of the model.

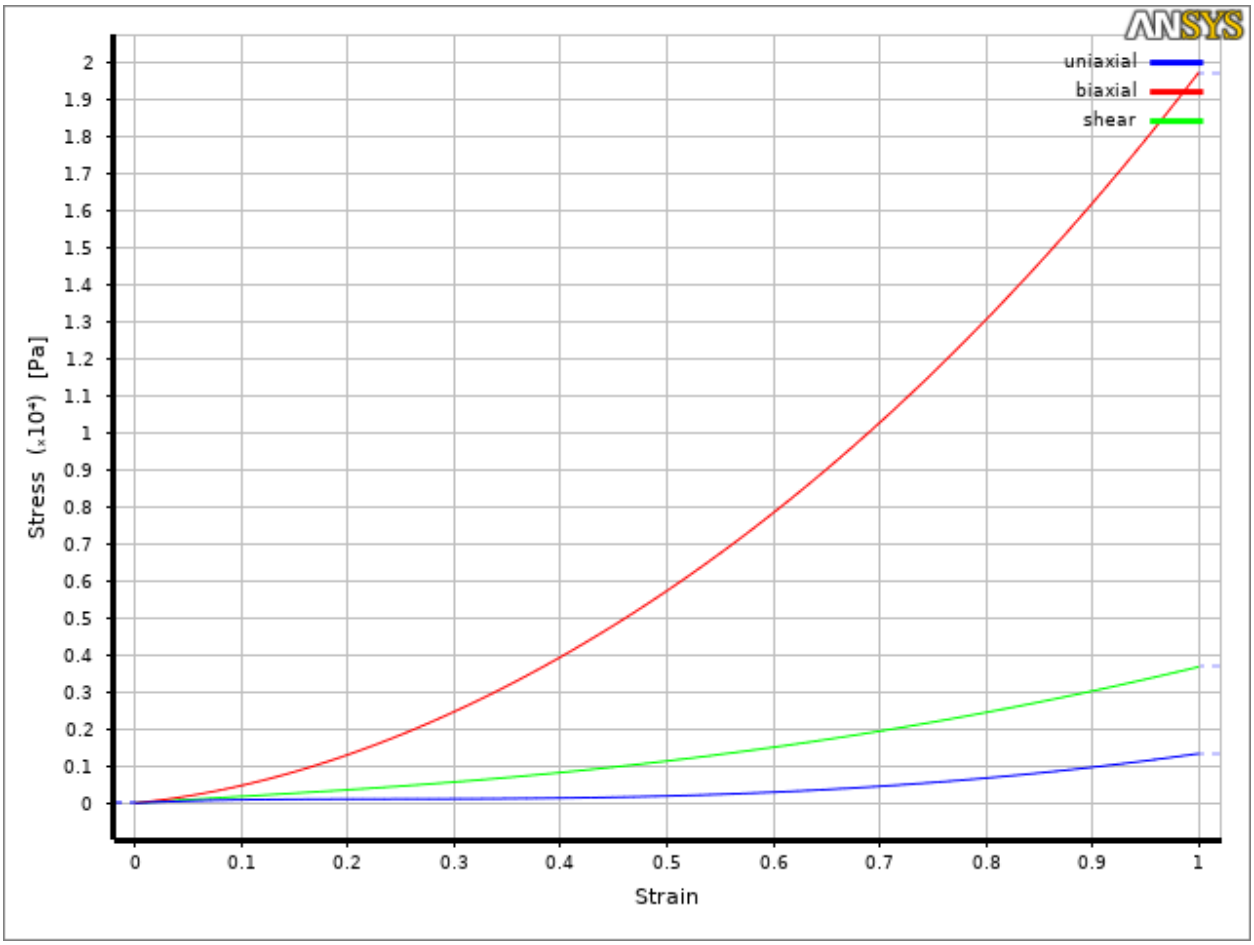

Figure 12: 3rd order Ogden material model used for simulation of brain tissue based on the parameters outlined in Table 2.

Damping/ Viscoelasticity

Damping can be defined as a physical systems ability to restrain relative motion through dissipation of energy. In simple viscous damping, the rate of dissipation is relative to the velocity of movement. Without external input, dampers will not tend toward their original state. In contrast, oscillatory systems must exhibit a level of elasticity in addition to damping.

The behavior of many biomechanical materials can be approximated as complex oscillatory systems that include both viscous damping and elastic restorative forces. Such models are referred to as viscoelastic. Many soft tissues have been found to exhibit viscoelastic behavior. These include the scalp, brain and dura Galford and McElhaney (1970), the skin (Khatyr, Imberdis, Vescovo, Varchon, & Lagarde, 2004), and specific regions of brain tissue (Van Dommelen, Hrapko, & Peters, 2010).

Maxwell Model

A simple viscoelastic model is the Maxwell model. In this model a spring and dashpot are placed in series as outlined in Figure 13.

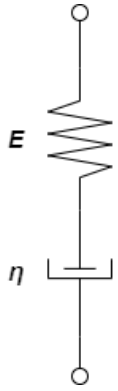

Figure 13: The Maxwell model of viscoelasticity.

In a Maxwell model the spring and dashpot experience the same stress, while the system's strain is distributed between the two. The Maxwell model can be represented in the form of Equation 7.

$$\frac{d\epsilon}{dt} = \frac{d\epsilon_D}{dt} + \frac{d\epsilon_S}{dt} = \frac{\sigma}{\eta} + \frac{1}{E}\frac{d\sigma}{dt} \qquad \text{(Eq 7)}$$

Where ϵ_D is the strain of the damper, ϵ_s is the strain of the spring, η is the equivalent damping constant, E is the equivalent spring constant and σ is the stress (ANSYS, 2021). When a material is put under a constant strain, the Maxwell, stresses will relax over time. If the material is put under a constant stress, there will be an instantaneous elastic strain response from the spring, which relaxes instantly after the release of stress. There is also a viscous component from the damper, which increases with time while stress is applied. As a result, after step strain input the Maxwell model predicts exponential decay of stress over time and is inaccurate for representing creep. Thus, it is not appropriate to model the behavior of the brain, which has been shown to exhibit creep characteristics.

Kelvin-Voigt (parallel)

The Kelvin-Voigt viscoelasticity model is similar to the Maxwell model, but the spring and damper elements are represented in parallel to one another. As a result, they experience the same strain while

stress is distributed between them. This model is often used to describe the creep behavior of materials. Figure 14 outlines the Kelvin-Voigt viscoelastic model.

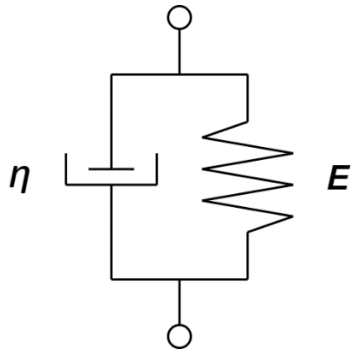

Figure 14: The Kelvin-Voigt model of viscoelasticity.

The Kelvin Voigt model is represented mathematically in Equation 8.

$$\sigma(t) = E\epsilon(t) + \eta\frac{d\epsilon(t)}{dt} \qquad \text{(Eq 8)}$$

This model represents a material which is able to undergo reversible viscoelastic strain. Under application of a constant stress, the material will deform at a decreasing rate until a steady state strain is reached. Upon the release of stress, the material will return gradually to its undeformed state. The Kelvin-Voigt model very accurately models creep. However the model had been experimentally determined to be imprecise when modelling relaxation (Handbook & Fundamental, 2011). Thus, a more complex model is required to accurately model the material behaviour of the brain.

Standard Linear Solid (SLS) Model

The standard linear model of viscoelasticity expands the Maxwell model by adding a Hookean spring in parallel. This model is depicted in Figure 15.

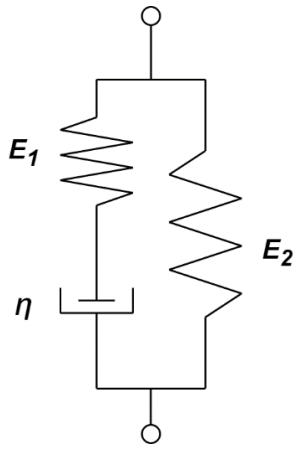

Figure 15: The standard linear solid model (SLS).

Mathematically, this model is represented in Equation 9.

$$\frac{d\varepsilon}{dt} = \frac{\frac{E_2}{\eta}\left(\frac{\eta}{E_2}\frac{d\sigma}{dt} + \sigma - E_1\varepsilon\right)}{E_1 + E_2} \quad \text{(Eq 9)}$$

This model more accurately represents biological tissue than both the Maxwell and Kelvin-Voigt by incorporating aspects of both. However, it is mathematically prone to error under specific loading cases and more complex to calculate (Lakes & Lakes, 2009). Therefore, a more stable material model would be appropriate in the context of this head model.

Prony Series

The SLS model can be further expanded with the addition of several Maxwell systems being added in parallel, this is referred to as a Prony series (ANSYS, 2021; Lakes & Lakes, 2009) Figure 16 depicts this model.

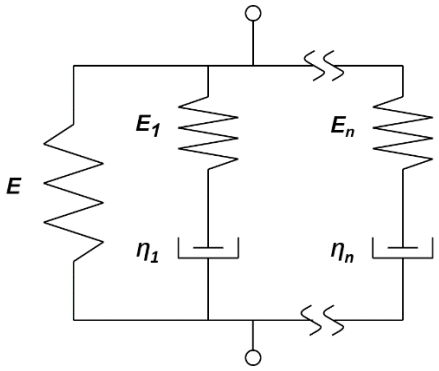

Figure 16: Prony Series model of viscoelasticity.

The resultant shear modulus with respect to time of this model is mathematically represented in Equation 10.

$$G(t) = G_0\left(1 - \sum_{i=1}^{n} G_i\left(1 - e^{-\frac{t}{\tau_i}}\right)\right) \qquad \text{(Eq 10)}$$

Where all G terms are:

$$G = \frac{E}{2(1+\eta)} \qquad \text{(Eq 10(a))}$$

Where G_0 is the instantaneous initial shear modulus, G_i is the shear material constant and τ_i the time constant. This model can be expanded to n = ∞ to capture the behavior of specific materials more accurately. The performance of higher order Prony Series was shown to be accurate in modelling the behavior of both the brain and skull. Thus, A 12-term series and 3 term series where selected for the material models of the brain and skull tissue respectively. Table 2 outlines the parameters used for these models as reported from (Panzer et al., 2012; Shen et al., 2006; Yan & Pangestu, 2011).

Table 2: Prony series parameters used for this model.

Brain Model		Skull Model	
Parameter	Value	Parameter	Value
τ_1	0.0001 s	τ_1	3000 s
η_1	0.2 Pa s	η_1	2e10 Pa s
τ_2	0.001 s	τ_2	0.3333 s
η_2	0.36 Pa s	η_2	2.290e12 Pa s
τ_3	0.01 s	τ_3	3.636e-6 s
η_3	3.83 Pa s	η_3	4.709e12 Pa s
τ_4	0.1 s		
η_4	5.46 Pa s		
τ_5	0.5 s		
η_5	39.2 Pa s		
τ_6	1 s		
η_6	11.57 Pa s		
τ_7	5 s		
η_7	19.16 Pa s		
τ_8	10 s		
η_8	604.2 Pa s		
τ_9	50 s		
η_9	25.47 Pa s		
τ_{10}	100 s		
η_{10}	3268 Pa s		
τ_{11}	500 s		
η_{11}	0.02 Pa s		
τ_{12}	1000 s		
η_{12}	587.8 Pa s		

Anisotropy

The existence of anisotropic material properties in human white matter due to the arrangement of axonal fibers has been observed in several studies (Giordano et al., 2014; Giordano & Kleiven, 2014; Inglese et al., 2005). Madhukar and Ostoja-Starzewski (2019) specifically investigated the effects this may have on the mechanical modelling of the brain. This presence of densely packed axonal fiber tracts can be approximated as transverse isotropy, meaning the fibers tend to be perpendicular to planes of isotropy throughout the brain (Feng et al., 2013). Transverse isotropy can be modelled using the strain energy function in Equation 11:

$$W = W(\tilde{I}_1, \tilde{I}_2, \tilde{I}_3, \tilde{I}_4, \tilde{I}_5) = W_{iso}(\tilde{I}_1, \tilde{I}_2, \tilde{I}_3) + W_{aniso}(\tilde{I}_4, \tilde{I}_5) \quad \text{(Eq 11)}$$

Where $W_{iso}(\tilde{I}_1, \tilde{I}_2, \tilde{I}_3)$ is the response of the isotropic strain matrix, while $W_{aniso}(\tilde{I}_4, \tilde{I}_5)$ describes the behavior due to directional fiber reinforcement. $\tilde{I}_1, \tilde{I}_2, \tilde{I}_3$ are standard invariants of the isochoric right Cauchy green deformation tensor, while $\tilde{I}_4, \tilde{I}_5$ are two pseudo invariants which account for the fiber reinforcement (Destrade, Mac Donald, Murphy, & Saccomandi, 2013; Feng et al., 2013). However, as discussed in PALS Martins, RM Natal Jorge, and AJM Ferreira (2006a) the effect of anisotropy has a negligible effect on simulation outcomes and it was therefore excluded from the model proposed in this thesis.

Fluid Models

The development of this model focused primarily on solid material properties. However, the necessity of modelling CSF meant it was also necessary to investigate fluid material models. In general, Computational Fluid Dynamic (CFD) analysis is based on the Navier-Stokes equations which describe the motion of viscous fluid substances (Constantin & Foias, 1988).

The Navier-Stokes equations are formulated by applying Newton's second law to the motion of fluid. Specifically, changes in fluid momentum are related to velocity, pressure, shear stress, and density of the

fluid. These equations are outlined in Equation 1. The Navier Stokes equations can be simplified with the application of boundary conditions. For the purposes of this model temperature of the fluid was neglected during calculation and where true fluid models were used, two open flow boundaries were included to represent where the CSF could flow between the intracranial cavity and the spinal canal.

Fluid regions are typically represented via Eulerian domains. Thus, the full region in which the fluid is expected to reside is meshed. Individual cells are then 'filled' with fluid, the fluid is and allowed to flow between adjacent cells. Because fluid is able to flow to adjacent cells, it is important to ensure the mesh resolution is finer than that of any thin solid features the fluid can interact with (Donea et al., 1982).

A review of several studies which detailed the development and use of head models and the mechanical properties of CSF showed that it is common practice to either represent the CSF as a standard fluid with similar viscous properties to water, as a fluid like solid, or to entirely exclude the CSF layer (Chafi et al., 2009; G. P. Fife et al., 2013; Gilchrist & O'Donoghue, 2000; Goldsmith, 2001; Hardman & Manoukian, 2002; Jin et al., 2015; Kleiven, 2002; Madhukar & Ostoja-Starzewski, 2019; Panzer et al., 2012; Prosser et al., 2011; Raul et al., 2006; Shen et al., 2006; Shugar & Katona, 1975; Sweetman & Linninger, 2011; Takhounts et al., 2003; Yan & Pangestu, 2011; Liying Zhang et al., 2001). In this thesis project, several simulations failed to converge while using viscous fluid material models for CSF. Furthermore, prohibitively long convergence times for explicit material models, a fluid like orthotropic solid model was selected for use. The material constants were selected based on the values reported in Chafi et al. (2009). The density was set as 1007kgm^{-3}, a damping ratio of 0.8, Young's modulus of 2200MPa and shear modulus of 2.2Pa. This resulted in a Poisson's ratio of 0.49.

Element and Solver Types

Ansys selects element types based on analysis configuration by the user, the specific mesh geometry for a given domain and the input material models. Typically, there are two different types of element per material. The contact elements and the internal elements. The specific type of element is highly dependent of material models and can be manually overridden when specialized elements are required.

Fluid Solver

The ANSYS Workbench interface allows coupling of fluid and solid solvers. Both the fluid and solid solver take advantage of the mechanical meshing interface. When producing a mesh for the fluid solver, the geometry is initially imported into the mechanical meshing module. This allows geometry to be meshed and adjusted before the resultant elements are converted to a fluid mesh via proprietary engine for use in a fluid solver. The conversion categorizes elements based on named selections, which are defined in the mechanical meshing module. Elements are separated into three general categories of walls, inlets/outlets and internal elements. For FSI simulations, the wall elements are defined as deforming. This accounts for any movement of the solids during simulation. However, for typical fluid simulations wall elements are treated as rigid.

Solid Solver

For basic solid models there are typically two types of elements used. These are contact elements and body elements. The body element types are dependent on the specific material models for a given geometry, and the contact element types are dependent on the boundary conditions of the model. In most cases, the inbuilt meshing system is proficient in appropriately identifying which elements are necessary. However, in special cases, the use of uncommon element types is required.

In certain simulations, it is possible to simplify fluid simulation substantially using specialized elements. When the behavior of solid bodies enclosing fluids that can be approximated as having no net flow, it is possible to hydrostatically model the system. Ansys has several specialized element types available for this process which were investigated for the purposes of this model.

Hydrostatic modelling of the system means there is no need to include system coupling between fluid and solid solvers. In such a solution, the flow of fluid is treated as irrelevant. This allows a single mechanical solver to be used for calculation of the domain deformation, internal pressure, and propagation of stress. For the head model developed in this thesis, a hydrostatic model allowed substantial reduction in simulation time and hardware requirement while still providing realistic results. It also means

convergence of the model could be achieved for more loading cases. CSF is introduced and removed from the body only in the head. Thus, it is reasonable to assume that a hydrostatic model is theoretically valid.

Explicit Solver

Explicit solvers allow the direct solution of nodal accelerations. This removes the requirement of iterative solutions as used in implicit solver. Thus, explicit solvers are more stable and able to converge to solutions for non-linear systems more consistently than implicit solvers. However, the time step of an explicit solver is required to be less than the Courant time step, which is the time it takes a sound wave to travel across a single element. This results in the requirement of explicit solvers to have timesteps which are several orders of magnitude smaller than equivalent implicit solvers. In general, the direct solution method of explicit solvers requires a much higher computational cost and has a heavier hardware requirement.

Fluid 80

Historically the fluid 80 element type was used by ANSYS mechanical's ADPL solver when simulating problems that included fluids with no net flow rate contained in vessels. The applications of the Fluid 80 element were somewhat limited, most notably by its inherent geometric restrictions. Fluid 80 elements are defined by eight nodes, each with three degrees of freedom. Thus, they require a higher order tetrahedral mesh. The fundamental fluid 80 element has since been superseded by several separate fluid elements including FLUID29, FLUID30, FLUID220 and FLUID221 (ANSYS, 2021). Each of these element types has a more specialized use case, typically based on the mesh shape requirements of specific geometries and the system boundary conditions. Though it should be noted that these elements are only accessible via ADPL code input, and their usage is inconsistently documented. The elements are typically used when relatively large fluid domains are enclosed by thin solids. The requirement of a head model is such that the fluid domain is thin relative to the solid domain. Following investigation into each of these elements, they were experimentally determined to be unsuitable for this model due to convergence issues during simulation.

HSFLD242

Much like other FLUID elements, the HSFLD242 element is possible via the assumption of a hydrostatic system. These elements are well suited to modelling systems where it can be assumed that there is no sloshing of fluids, meaning there is a uniform pressure throughout the entire fluid domain. As such the elements are overlaid on the faces of enclosing solid elements using a surface mapping command. An extra node which is common to all the faces is then added to complete the fluid domain, this is a common pressure node. Due to the use of a single node to represent the pressure of all elements in the fluid domain, it is necessary to identify areas internal to the fluid domain which overlap with other solid bodies. These regions are assigned a negative volume.

At the time of investigation, all documentation on these elements was specifically for basic geometry. The HSFLD implementation required individual nodes and elements to be identified and mapped manually. Given that the final head geometry in this model had more than 300,000 nodes it was not realistic to employ the use of these elements. This compounded with a general lack of training material and documentation with these specialized elements ultimately meant they were not used in the final head model.

FSI within the Head (Solver Types)

The presence of CSF means it is necessary to include some form of fluid solid interaction. Several methods of simulating FSI were investigated during the development of this model.

Transient FSI System Coupling

In the context of ANSYS, the process of FSI is most commonly achieved by first creating two separate systems. One system for the fluid domain and one system for the solid domain. These systems are coupled to allow data transfer during simulation. The process involves defining geometry for both the fluid and solid domains, separately meshing them and identifying the geometric regions that will interact with one another. These regions are treated as system coupling regions.

During calculation, data transfer is performed by a coupling engine in an iterative process. The solid system finds a solution for a given time increment, then provides an incremental displacement output to

the fluid domain. Calculations for pressure and flow are then performed in the fluid system, and incremental pressure is output to the solid system. At the beginning of each solution step the output of the previous solver step is used to initialize the new calculation phase. This data transfer can be gradually introduced to each system via interpolative ramping. It can also be adjusted with an included damping parameter to decrease the risk of excessive distortion of elements. However, the inclusion of damping during transfer decreases the potential accuracy of the simulation. This process repeats until the desired simulation time is reached.

Convergence of complex systems using this method can lead to erratic, incorrect simulation. To combat this the boundaries of system coupling are defined as dynamic mesh zones, which iteratively update as the solid domain deforms. The system coupling method has the main benefit of providing a true representation of fluid flow, but has a high complexity, meaning it is difficult to get the solver to converge to a solution, and a relatively high computational cost for a non-explicit solver.

Explicit FSI

As with purely solid explicit dynamic analysis, FSI using explicit solvers is very computationally expensive. The benefit of using an explicit simulation is the stability of the solver, and the ability to simulate dynamic systems such as rigid body motion. FSI is introduced to this system using Arbitrary-Lagrange Eulerian (ALE) coupling. This method differentiates regions of geometry into Lagrangian and virtual Eulerian domains. Because a Eulerian domain is comprised of filled 'void' cells between which fluids are able to flow, it is important to ensure the mesh resolution of the Eulerian domain is finer than that of the Langrangian. Specifically, the Eulerian cell size must be smaller than the thinnest section of solid domain with which it will interact. Failing this, the fluid will be allowed to flow to cells in the Eulerian domain which are outside of the solids meant to contain them.

In the context of a head model, this means the cell size of the Euler domain must be less than 5mm. As such, the model's resolution is significantly increased when compared to other methods. Consequently, the computational cost of such simulations is huge. A 5s long simulation using a basic cylindrical geometry was estimated to need between 5500 and 9000 hours to complete using a 32 core 2.1 GHz system. This

estimate was following substantial simplification of the model, including the use of symmetry and mesh refinement.

Pseudo FSI

Due to the extreme computational loads which were required for successful simulation using the Explicit method, and difficulty in achieving successful convergence via the system coupling method, it was elected to use a method in which the fluid domain of the CSF was represented as an orthotropic solid material with a large Young's modulus, meaning it experiences little to no compression under load, and a low shear modulus, meaning the elements could exhibit high shear strain. This is an acceptable approximation for nearly incompressible Newtonian fluids. However, for compressible non-Newtonian fluids a pseudo fluid model would not be accurate.

The main disadvantage of this method is that is unable to capture flow dynamics of fluids. However, assuming a hydrostatic system where the net flow in and out is negligible this factor can be somewhat discounted. To achieve this, the spinal opening at the base of the skull was closed, meaning the CSF was no longer able to flow in or out of the head. Initially, standard elements were used for the CSF region. To account for the inability of these elements to flow the CSF was split into 16 different regions, all of which had frictionless contacts between other CSF regions as well as the skull and brain. This allowed more movement of individual CSF regions and was able to partially capture what effect internal flow of CSF might have on stress propagation. However, these elements did not account for pressure experienced in fluids, and specific mechanical fluid elements were found to be more appropriate in the context of modelling a hydrostatic head. Specialized 'Fluid 30' elements were then used during meshing of the CSF. This meant that first order tetrahedral elements were required for the CSF mesh. Using the pseudo fluid method, the boundary conditions were set to bonded between the brain, CSF and skull. This allowed successful convergence to a solution of a 10s impact response simulation for the full head geometry in 127 minutes.

Meshing

Meshing is the cornerstone of a successful simulation. The type, size and shape of elements used when generating mesh are highly dependent on the specific geometry and material models being used for FEA. It is important to strike a balance between producing a high enough resolution mesh without imposing excessive computational load for any given analysis. During development of the head model several methods of meshing were tested.

During initial model development, meshing could be heavily optimized due to the existence of symmetry within geometries, constraints to two dimensions and regions of uniform thickness. This meant face meshing, sweep and inflation methods worked efficiently while also enabling a numerically simplified model. The increased complexity of the final head geometry meant that the final meshing stage was not only more complex, but also lead to a more numerically complex model.

As discussed in the ALE section, further consideration was appropriate when preparing the mesh in a fluid domain which was interacting with solids. It was also necessary to enable dynamic mesh adjustment when performing fluid solid interaction via system coupling. This is due to the need for the fluid domain to adjust its boundary shapes and conditions based on the deforming solid domain. Dynamic Mesh adjustment or re-meshing is a feature available in some FEA packages for use in models which are expected to have large deformation. It is available to the static structural solver in ANSYS mechanical but not the transient solver. This is due to the potentially major increase in computational load which it can cause when enabled for transient solutions.

An .stl geometry of the head comprising of the brain, CSF and skull was produced using 3D Slicer to analyze CT and MRI scans of an adult male human head. These were processed and imported to ANSYS SpaceClaim. The skull and brain of the final head geometry were meshed using standard tetrahedral elements. Because the geometry had been imported as an .stl file, there already existed accurate surface meshing on both the skull and brain. Mesh refinement was included in areas where the geometry had fine details, such as around the ventricular opening and between the cerebellum and occipital lobe. The mesh resolution and sizing was left to the default setting in the ANSYS mechanical meshing module.

The CSF required specific mesh optimization and employed the use of a patch conforming mesh method. This meant that finer details were captured with tetrahedral elements as required using FLUID30 elements to represent the CSF. This meant fewer complex regions which did not require finer meshing were not excluded as with default patch independent methods, however because the CSF was consistently thin and likely to experience higher relative deformation than the skull and brain this was deemed appropriate. The skull, CSF and brain meshes were all left with default element sizing, as adjustment of this variable caused failure to successfully mesh the model.

Chapter 5: Results

The geometry of the head model which was developed for this thesis project was initially very basic, then was iteratively increased to represent human anatomy more accurately. The first iteration of the model was based on a simple rectangular geometry, which is shown in Figure 17.

Basic Geometry

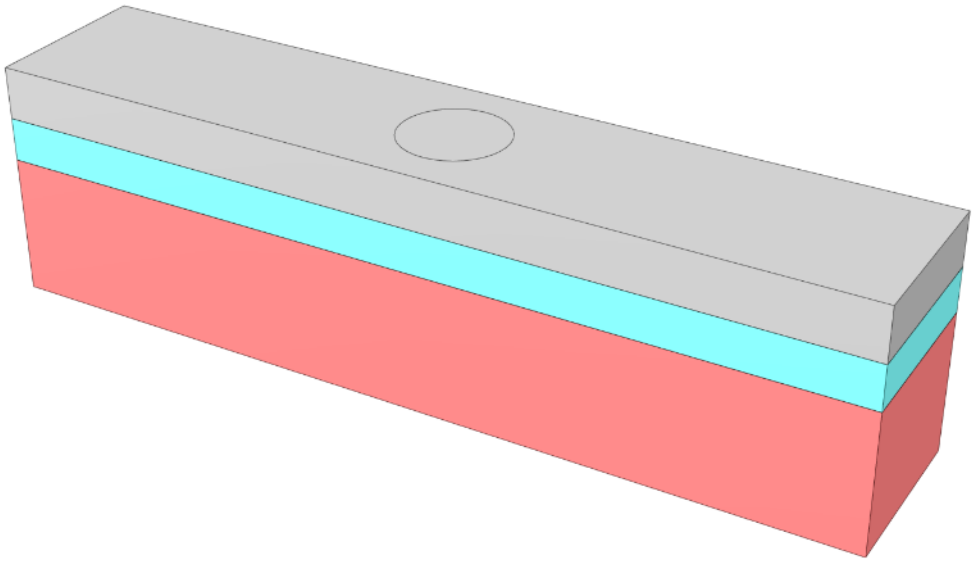

Figure 17: Basic rectangular geometry initially used for simplicity.

The model consists of three distinct layers for the skull, CSF and brain. This model allowed different material models and boundary conditions to tested. The geometric simplicity allowed fast convergence of simulations, which was essential during the first phase of adjusting variables and learning about ANSYS' interface and capabilities. The layer thickness of the skull was set to 5.242mm and CSF thickness was 4.175mm as reported in Haeussinger et al. (2011). This was repeated for all subsequent simplified geometries. Figure 18 shows a basic mesh of the initial rectangular geometry.

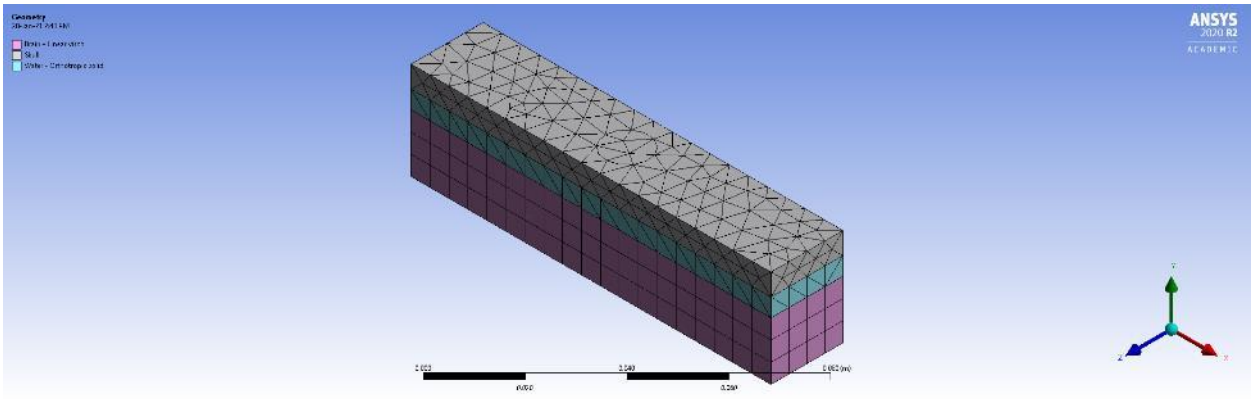

Figure 18: Meshed basic rectangular geometry.

Each geometric layer was an independent body, which was meshed individually. The mesh consisted of 3263 elements and 706 nodes.

This geometry was used for initial comparison of solver types and was able to fully converge for all trialed solver methods. As such it was used as a baseline for comparison of solver performance.

Extended Basic Geometry

Following initial proof of concept testing with the basic rectangular geometry, the model was iterated to a more complex cylindrical geometry to closer represent a head. The cylindrical geometry included three concentric layers, one for the brain, the CSF and the skull. For all simulations, no movement in the z direction was allowed. This condition was imposed by a zero displacement boundary on all capping faces. Figure 19 shows this cylindrical geometry. Figure 20 outlines the meshed geometry used for FEA analysis.

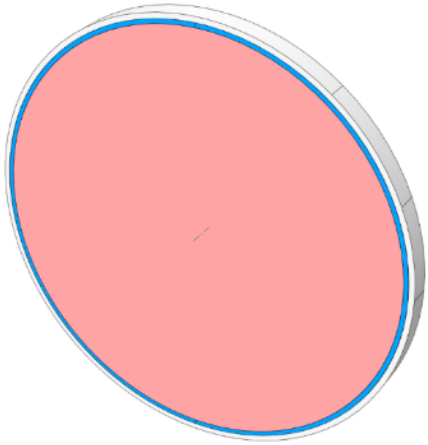

Figure 19: Basic cylindrical geometry.

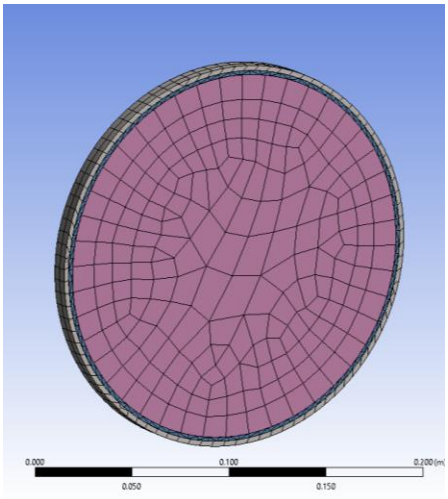

Figure 20: Meshed cylindrical geometry.

The basic cylindrical geometry was further extended to a sphere for the next iteration of the head model. As with previous geometries, the spherical geometry had three distinct layers to represent the skull, CSF and brain. A cross section of the spherical geometry is shown in Figure 21, with the generated mesh shown in Figure 22.

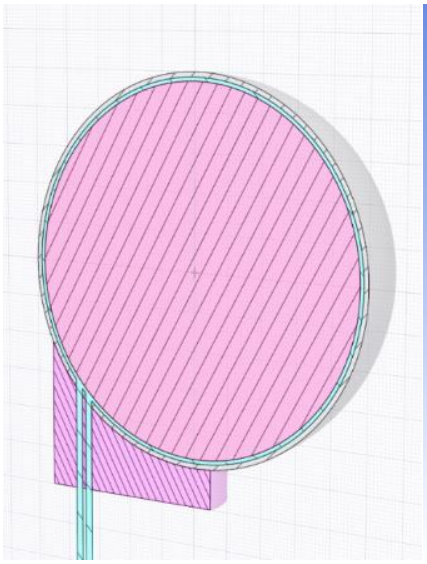

Figure 21: Basic spherical geometry.

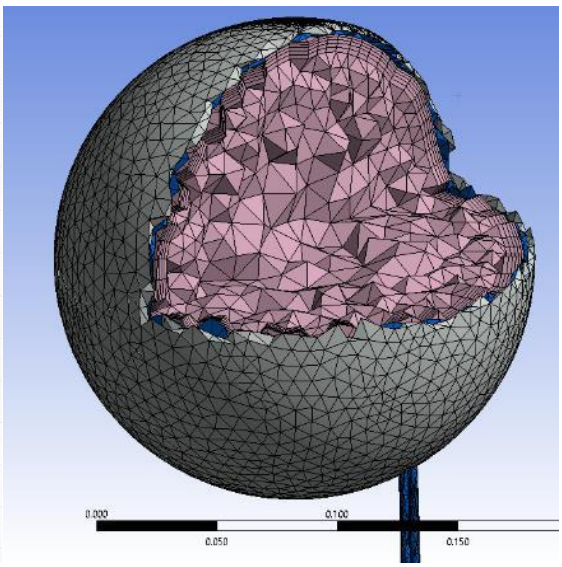

Figure 22: Meshed basic spherical geometry.

The spherical geometry was the final simplified representation of the head which was used before the geometry generated from MRI and CT scans was implemented.

Table 3 outlines the performance of the different geometries for different solvers. Each solution was for a 5 second transient simulation following a 100N impact over 0.01s at the top of the anterior of the representative skull layer. The equivalent attachment points of the neck were set to a stiff boundary with spring constant of 10kN/m. For the rectangular model, this boundary condition was applied on the ends parallel to the ZY plane. Table 3 outlines the solution metrics for each simulation as run on the three basic geometry's.

Table 3: Performance outline for different solvers.

Element type	Geometry								
	Rectangular			Cylindrical			Spherical		
FSI	Solution time	Memory used	Total I/O written	Solution time	Memory used	Total I/O written	Solution time	Memory used	Total I/O written
	2hrs 20m	9280 MB	246.9 GB	No Convergence	-	-	No Convergence	-	-
Explicit	47hrs 32m	26.4 GB	-	9987hrs (est.)	36.54 GB	-	Too large for estimate	-	-
Pseudo Fluid	54.3s	1071 MB	7.6 GB	67.1s	1109.0 MB	14.8 GB	23.8m	19.7 GB	37.9 GB

Final Geometry

Following processing of human CT and MRI scans each geometric layer was produced to be an accurate representation of human physiology. The final skull geometry following acquisition, STL processing and cling wrapping is shown in Figure 23. Figure 24 shows the CSF and ventricular geometry used in the final head model. Figure 25 outlines the final brain geometry used for the head model

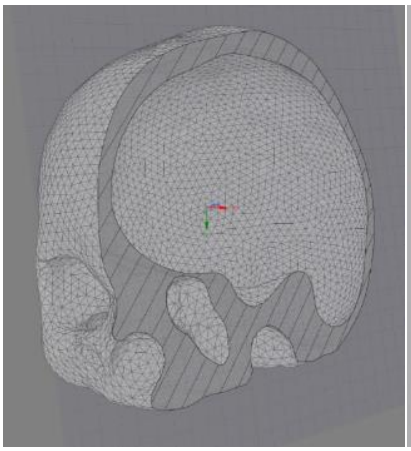

Figure 23: Final skull geometry as imported to SpaceClaim.

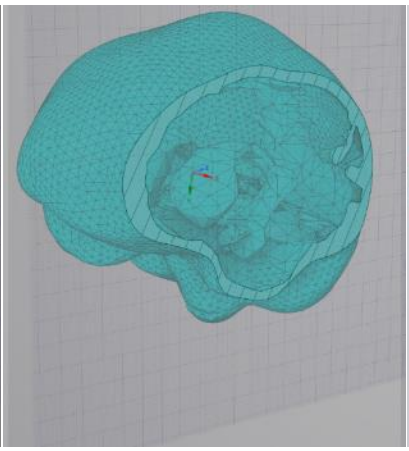

Figure 24: Final CSF and ventricle geometry.

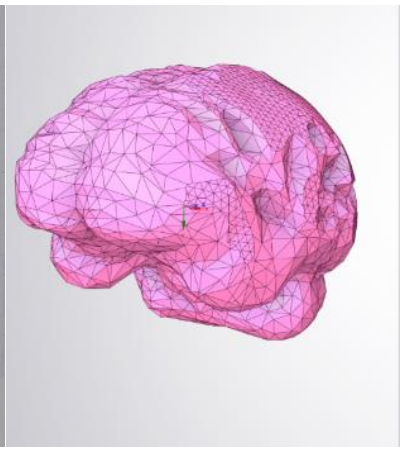

Figure 25: Final brain geometry.

A cross section of the assembly of the skull, CSF and brain is shown in Figure 26.

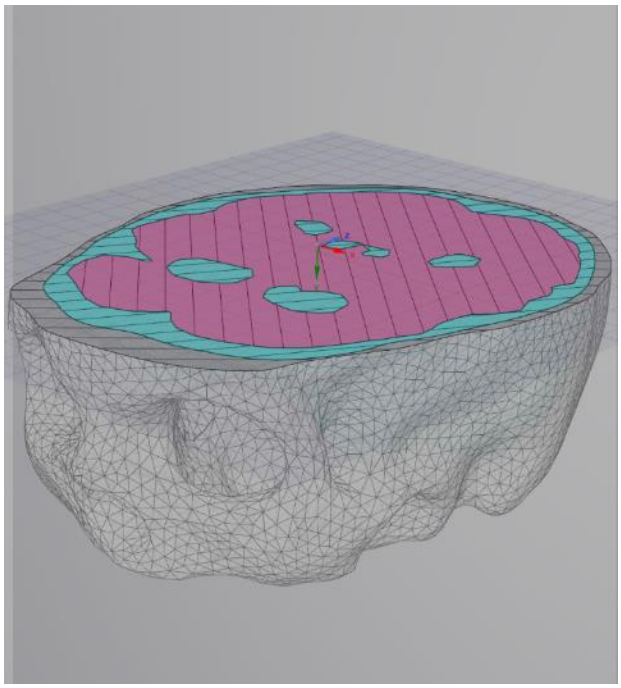

Figure 26: Final assembled head geometry.

Figure 27 shows the meshed brain gemoetry used in the final head model. Figure 28 shows the final CSF mesh used in the head model. Figure 39 shows the final skull mesh used in the head model.

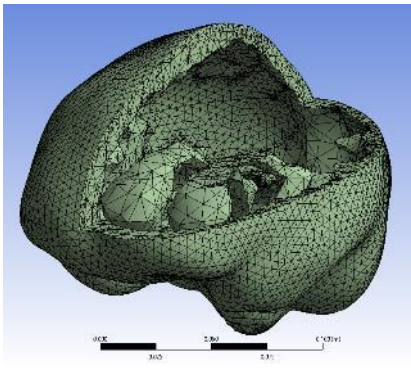

Figure 27: Meshed final brain geometry.

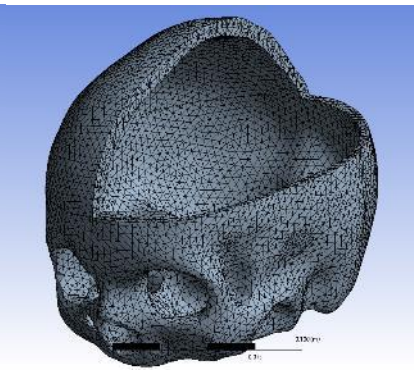

Figure 28: Meshed final CSF geometry.

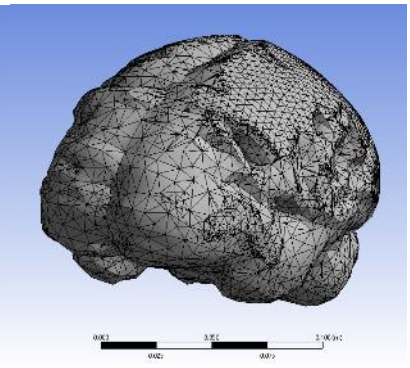

Figure 29: Meshed final skull geometry.

Figure 30 shows a cross sectional view of the final mesh used for simulations run with the head model.

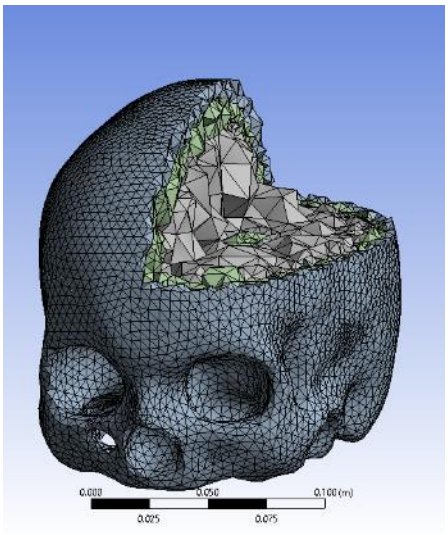

Figure 30: Meshed and assembled head geometry.

Once fully assembled and meshed, the final head geometry consisted of 220760 nodes and 191222 elements.

Impact Simulations

Impacts were simulated for several load locations. All impact zones were identically loaded with the remote force signal outlined in Table 4.

Table 4: Remote input force configuration.

Time (s)	X	Y	Z
0	0	0	0
1e-4	0	0	0
2e-4	1000N	1000N	0
3e-4	0	0	0

Figure 31 shows the location of impact zone 1. The resultant Von-Mises stress over time for a 10s simulation with a remote force at impact zone 1 is shown in Figure 32. The simulation took 7818s to complete, had a maximum total memory allocation of 49.6 GB and wrote a total of 1359.5 GB of data to the hard drive during solution.

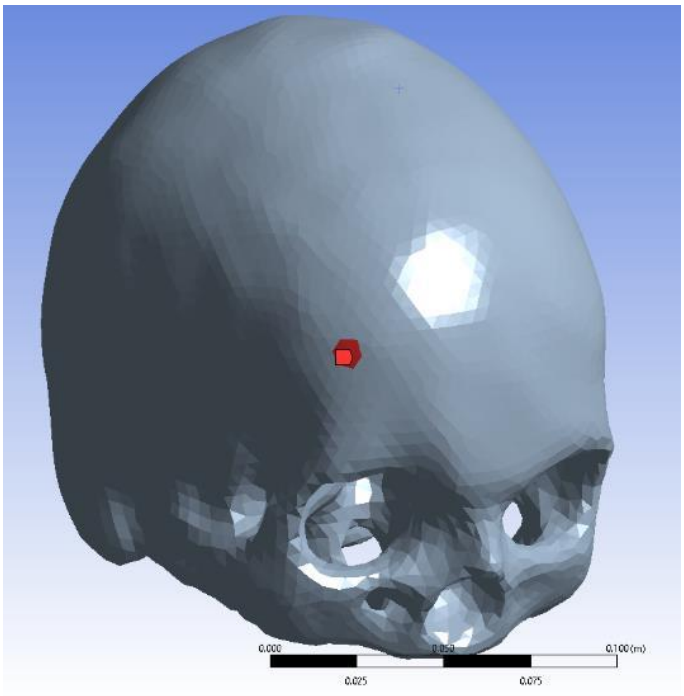

Figure 31: Impact zone 1 location.

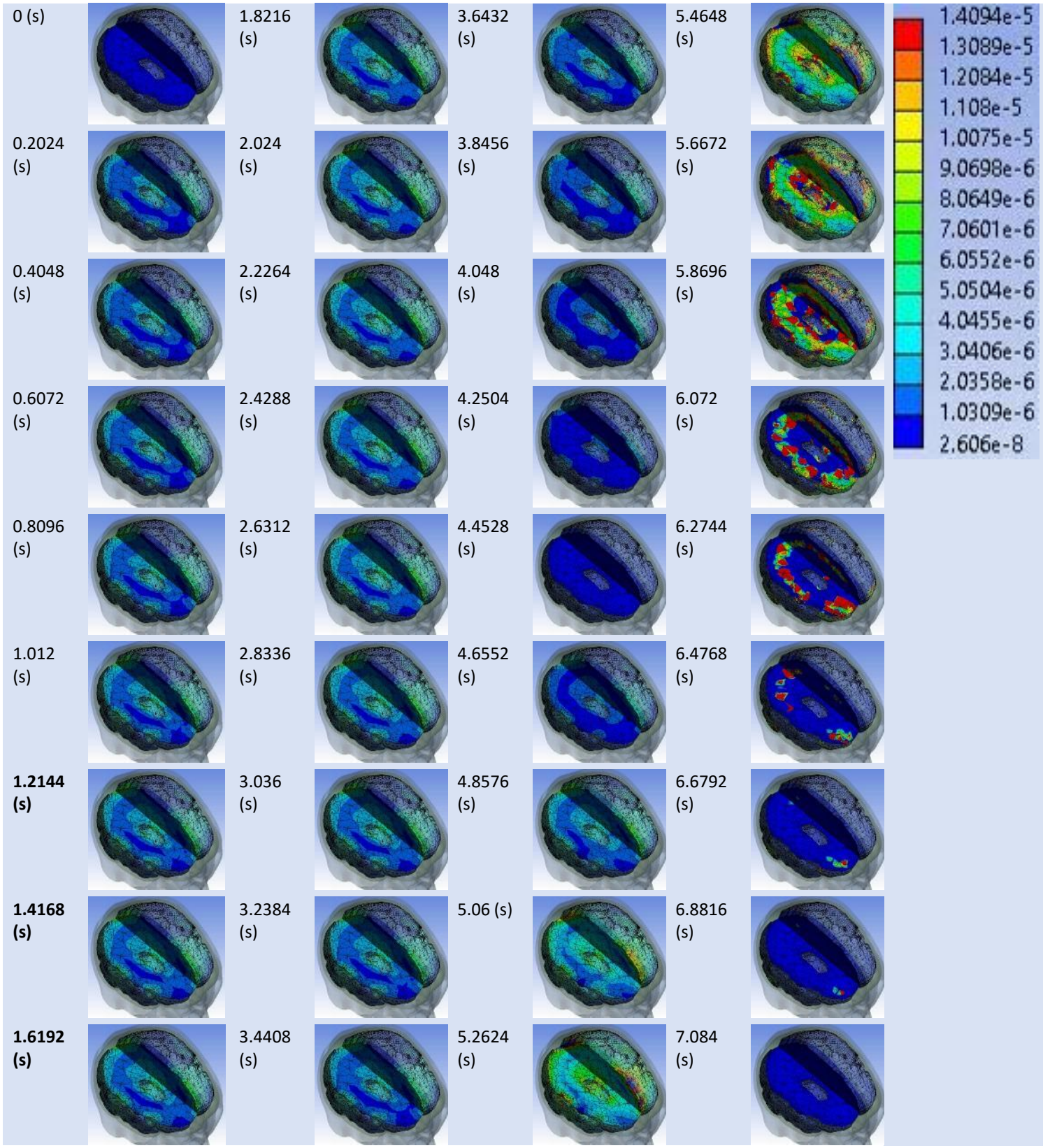

Figure 32:Von-Mises Stress over time for full simulation with impact Zone

Simulation showed similar behaviour for all impact zones initially, with more variation shown after penetration of a second pressure wave. In the interest of a clearer visualisation of results, all subsequent result sets are shown from the beginning of the second pressure wave's penetration, until visible dissipation of the wave. Full result sets including initial wave propagation are included in Appendix A.

The location of impact zone 2 is shown in Figure 33.

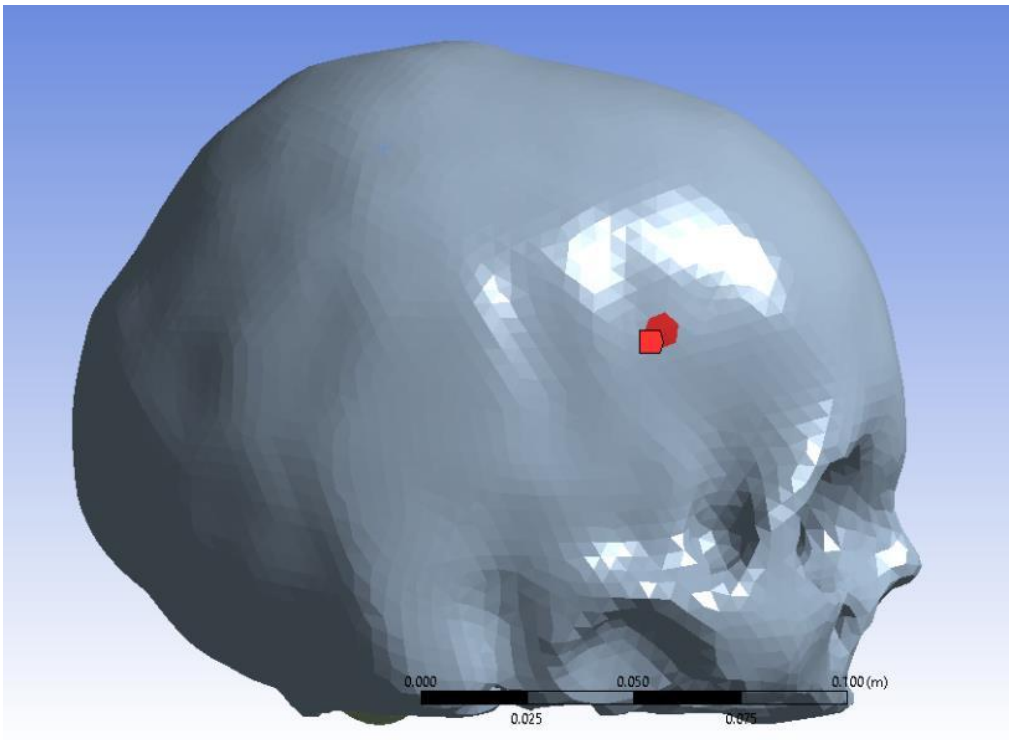

Figure 33: Location of impact zone 2.

The von-mises stress over time for a 10s simulation with a remote force at impact zone 2 is shown in Figure 34. The simulation took 1.9hrs to complete, had a maximum total memory allocation of 49.6 GB and wrote a total of 1359.5 GB of data to the hard drive during solution.

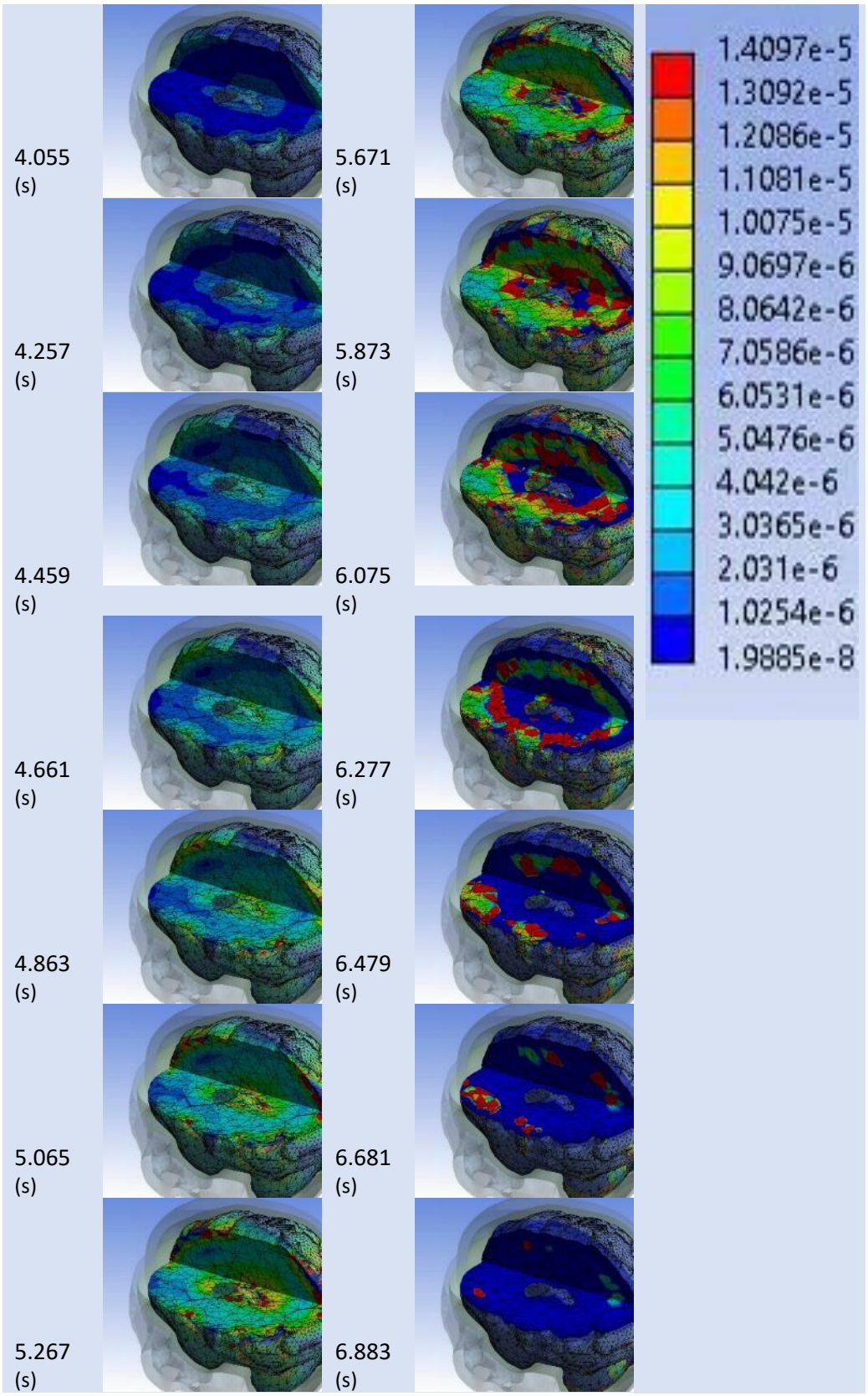

Figure 34: Von-Misses Stress over time for impact zone 2.

Figure 35 outlines the location of impact zone 3.

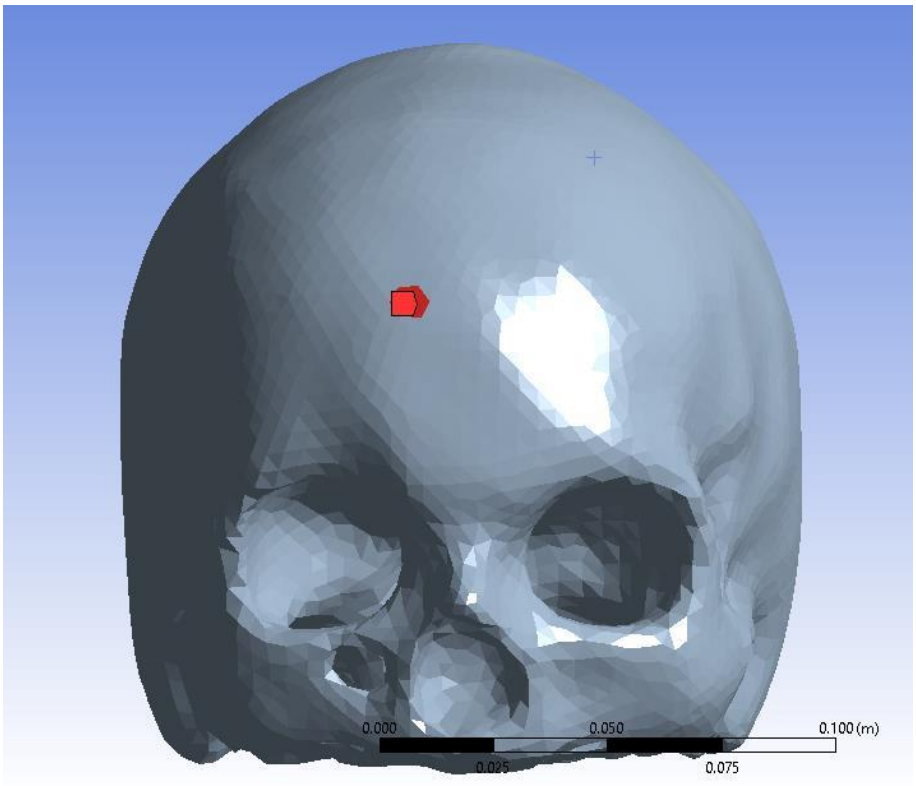

Figure 35: Location of impact zone 3.

The von-mises stress over time for a 10s simulation with a remote force at impact zone 3 is shown in Figure 36. The simulation took 1.7hrs to complete, had a maximum total memory allocation of 57.7 GB and wrote a total of 924.9.5 GB of data to the hard drive during solution.

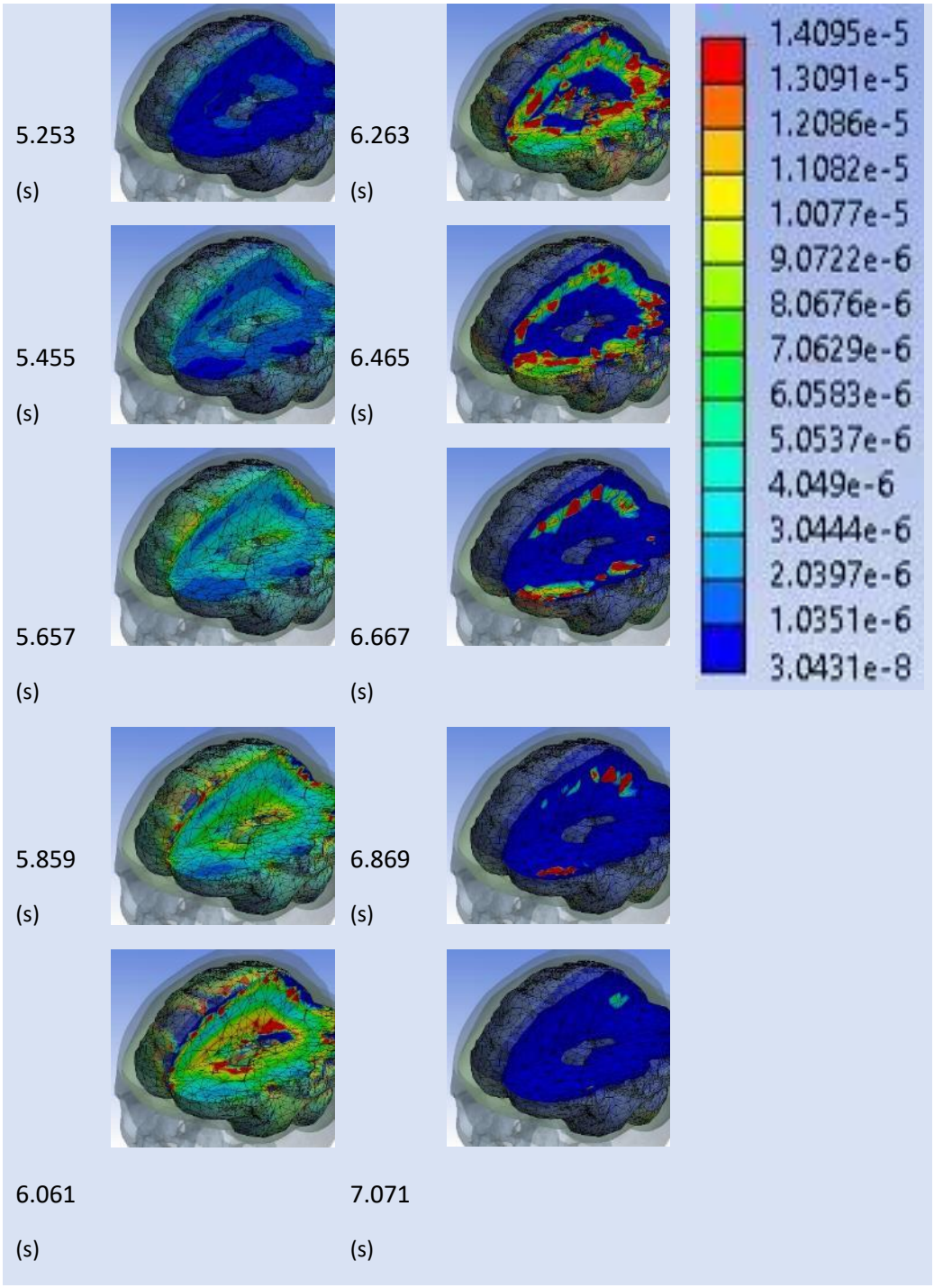

Figure 36 : Von-Misses Stress over time for impact zone 3

Figure 37 shows the location of impact zone 4.

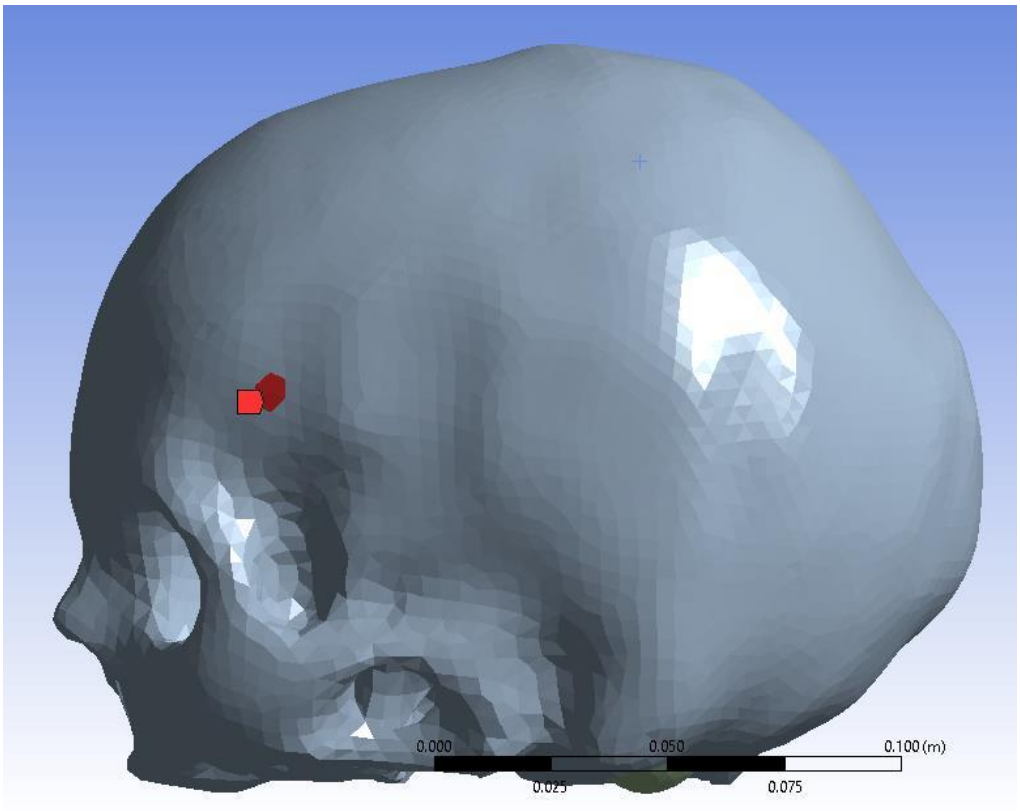

Figure 37: Location of impact zone 4.

Figure 38 outlines the von-mises stress over time for a 10s simulation with a remote force at impact zone 4. The simulation took 1.5hrs to complete, had a maximum total memory allocation of 52.5 GB and wrote a total of 1150.1GB of data to the hard drive during solution.

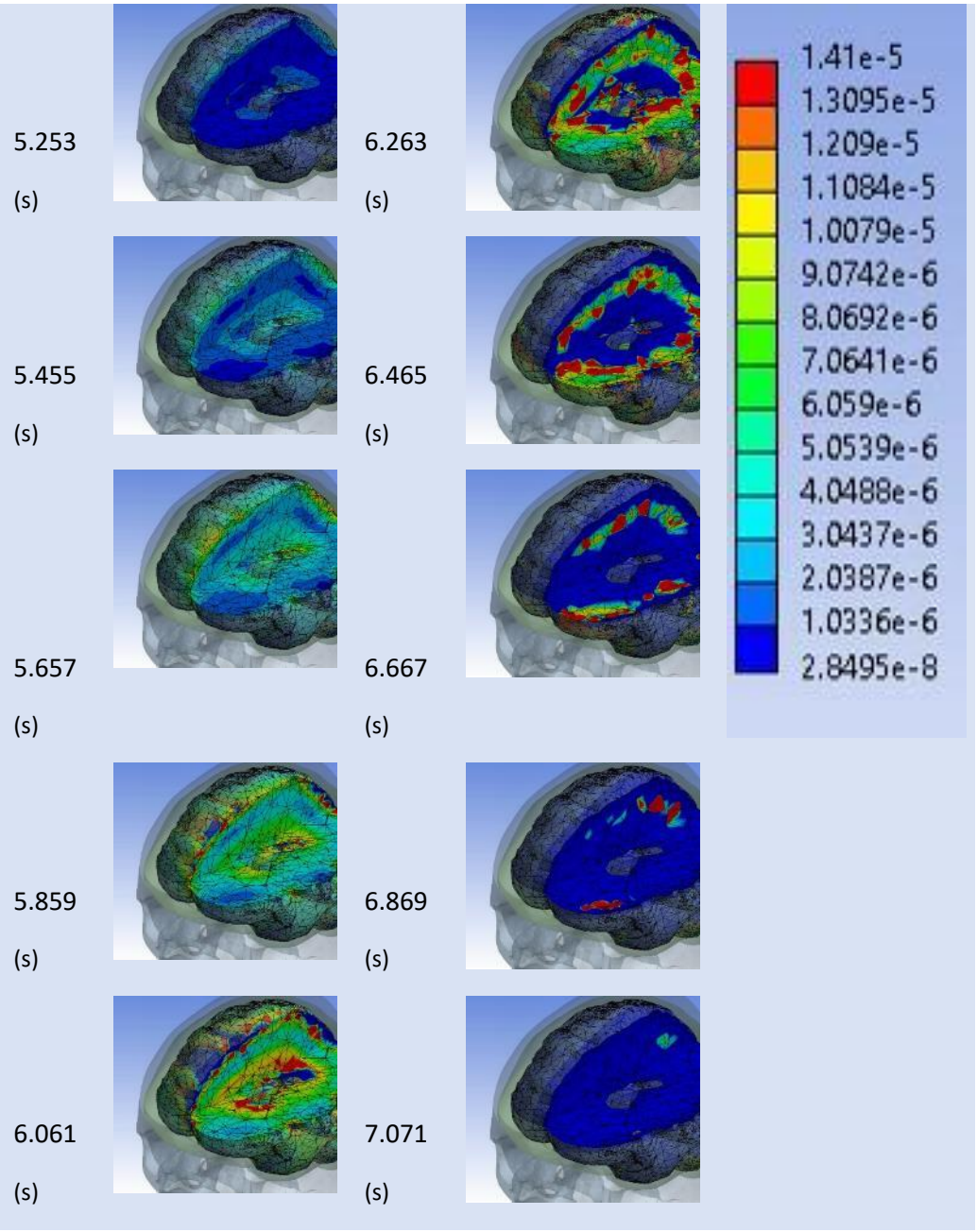

Figure 38: Von-Misses Stress over time for impact zone 4

Figure 39 shows the location of impact zone 5.

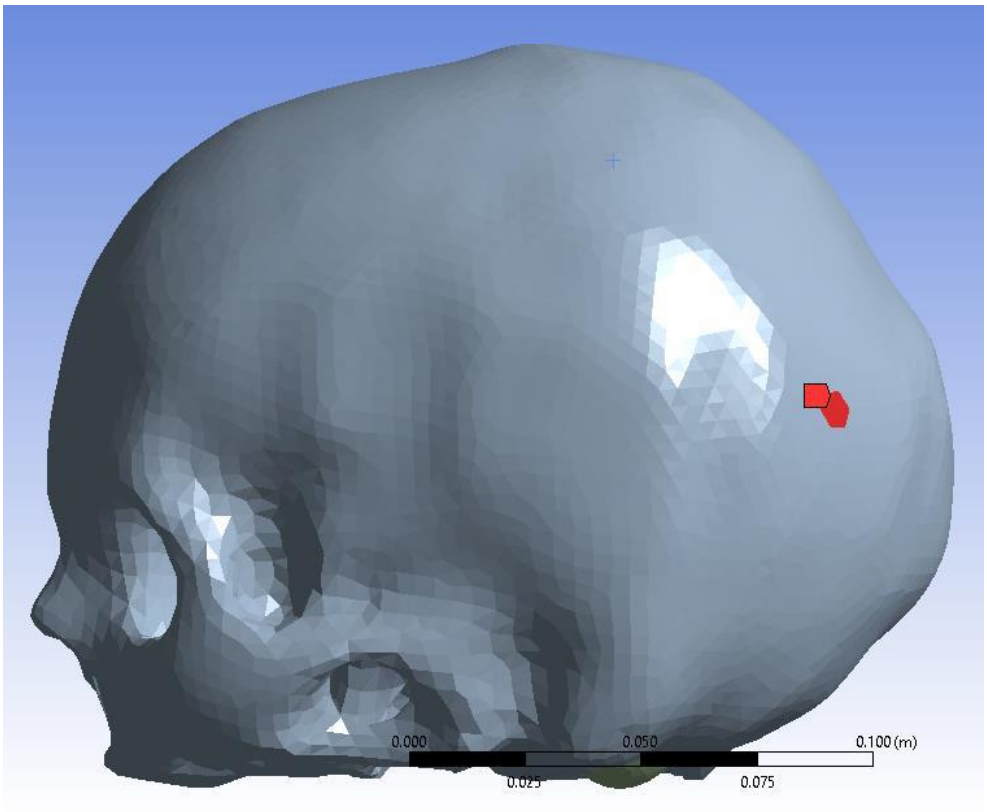

Figure 39: Location of impact zone 5.

Figure 40 outlines the von-mises stress over time for a 10s simulation with a remote force at impact zone 5. The simulation took 1.5hrs to complete, had a maximum total memory allocation of 52.9 GB and wrote a total of 900.6GB of data to the hard drive during solution.

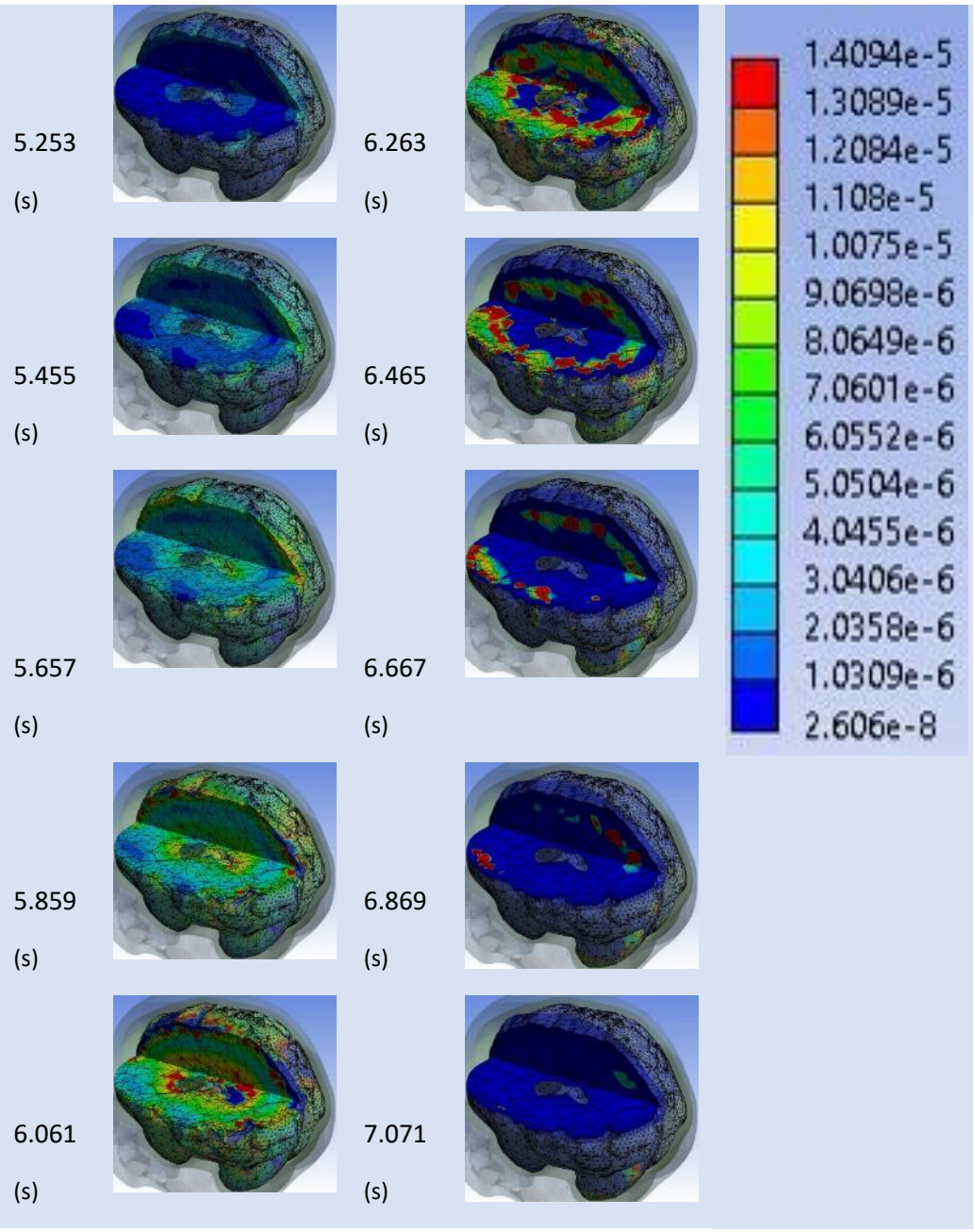

Figure 40: Von-Misses Stress over time for impact zone 5

Figure 41 shows the location of impact zone 8 on the skull.

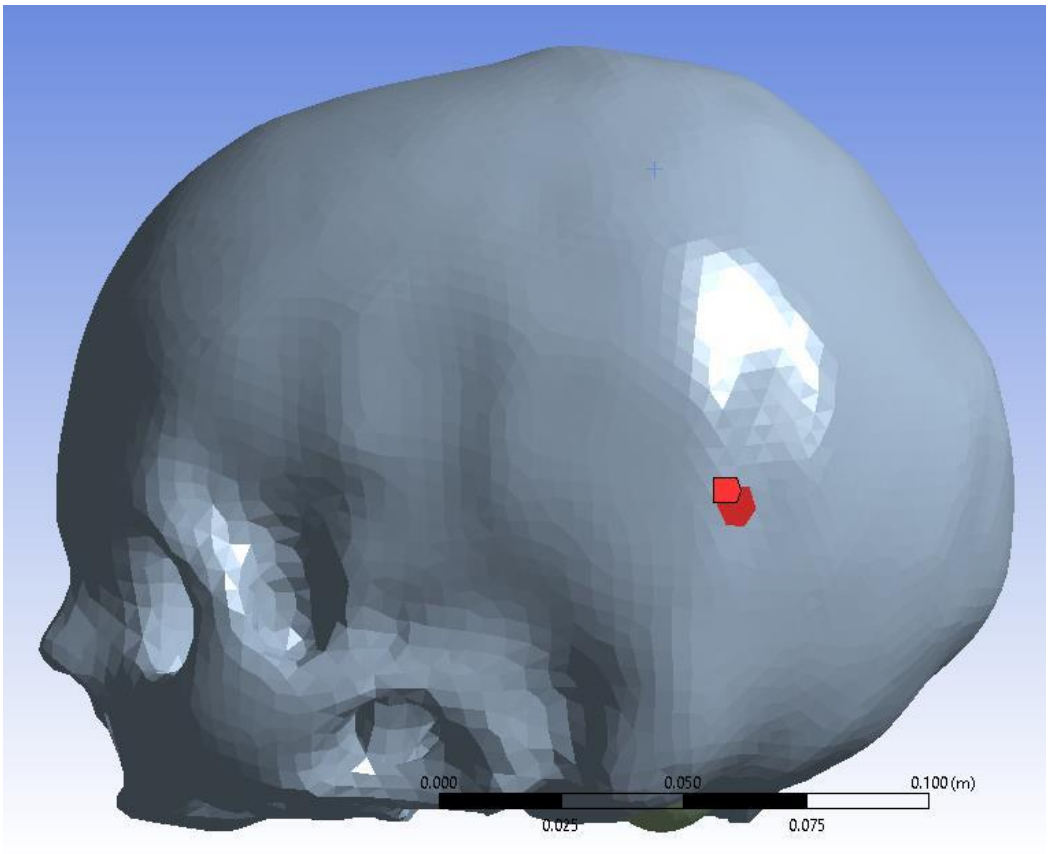

Figure 41: Location of impact zone 8.

Figure 42 outlines the von-mises stress over time for a 10s simulation with a remote force at impact zone 6. The simulation took 1.4s to complete, had a maximum total memory allocation of 49.6 GB and wrote a total of 919GB of data to the hard drive during solution.

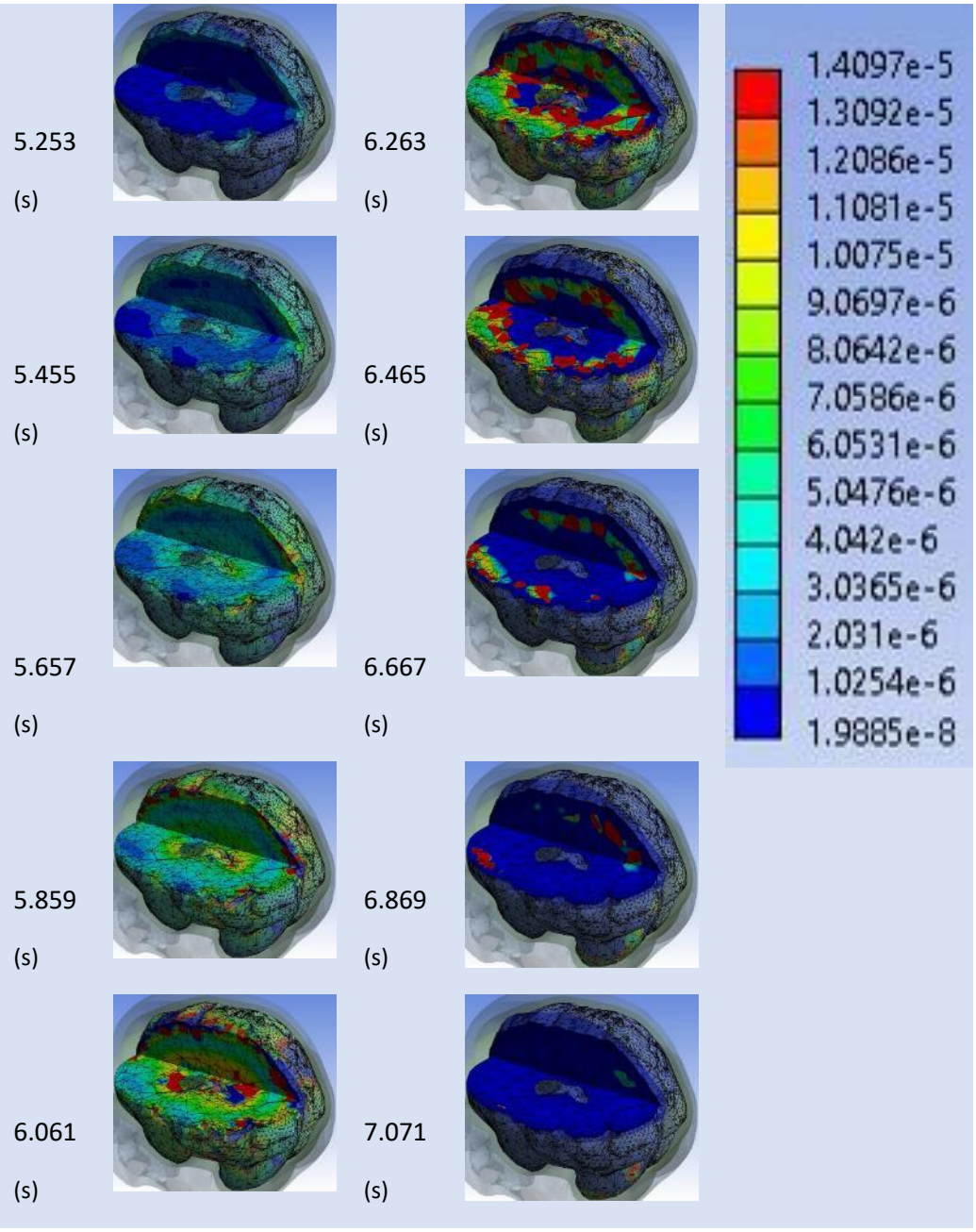

Figure 42: Von-Misses Stress over time for impact zone 6

Figure 43 shows the location of impact zone 7.

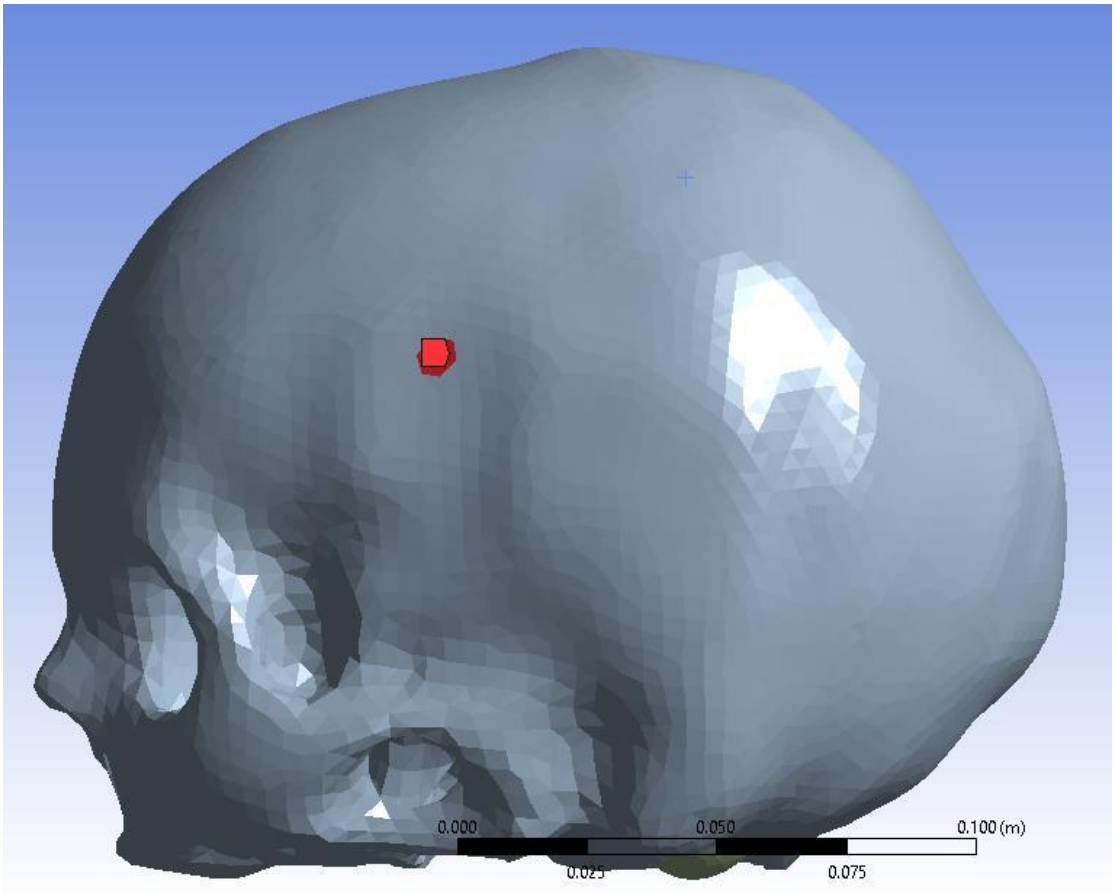

Figure 43: Location of impact zone 7.

Figure 44 outlines the von-mises stress over time for a 10s simulation with a remote force at impact zone 7. The simulation took 3.2s to complete, had a maximum total memory allocation of 52.7 GB and wrote a total of 2221.5GB of data to the hard drive during solution.

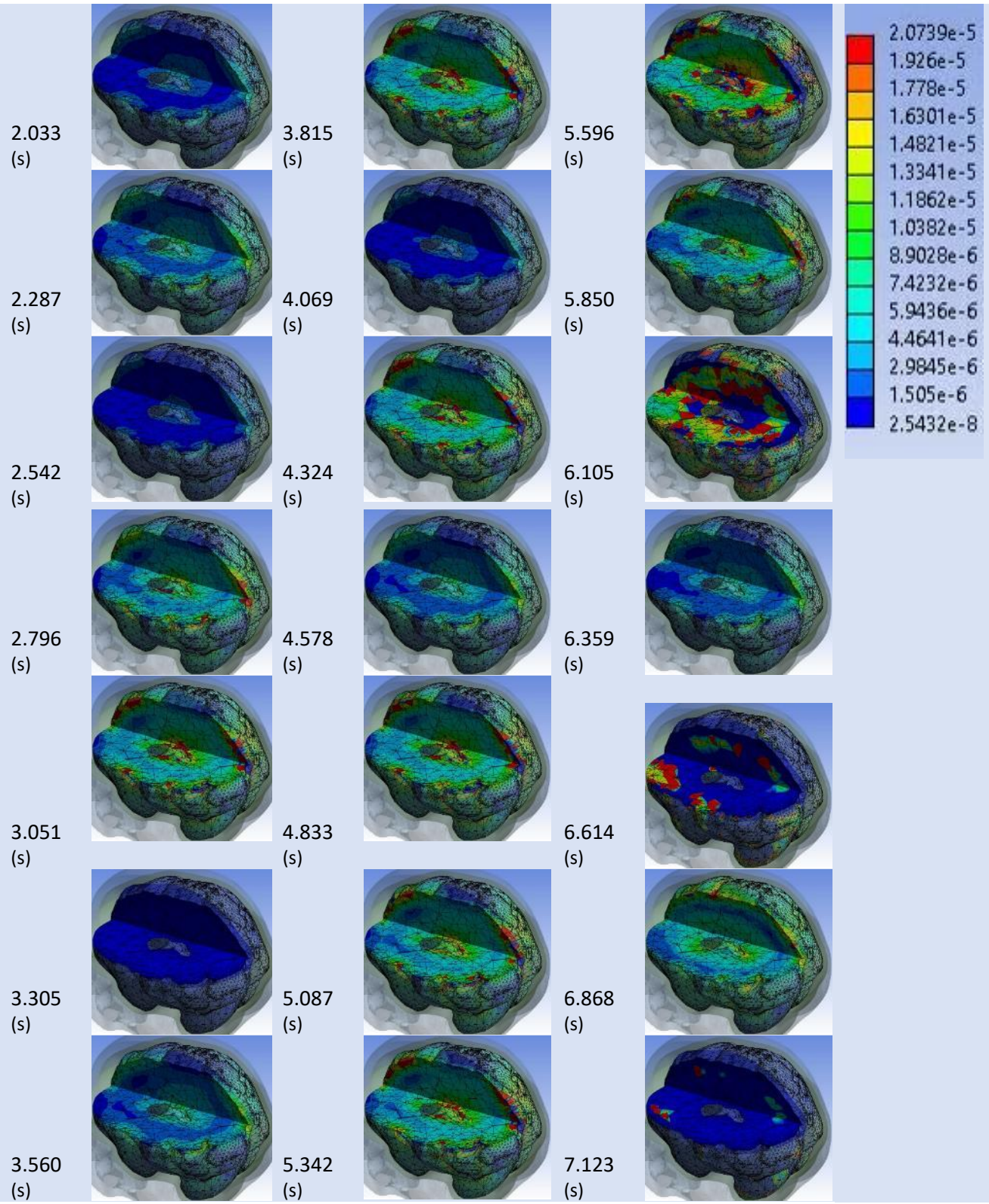

Figure 44: Von-Misses Stress over time for impact zone 7

Figure 45 shows the location of impact zone 8.

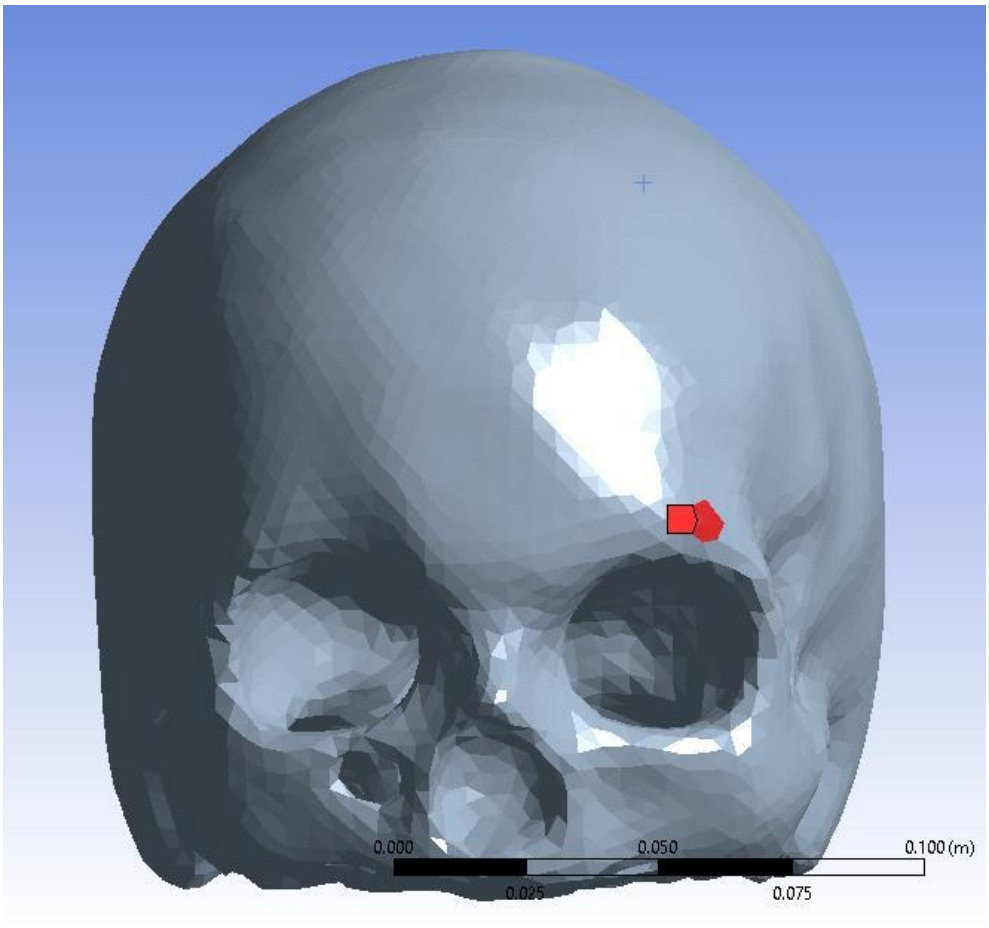

Figure 45: Location of impact zone 8.

Figure 46 outlines the von-mises stress over time for a 10s simulation with a remote force at impact zone 8. The simulation took 2.3hrs to complete, had a maximum total memory allocation of 55.4 GB and wrote a total of 1332.2GB of data to the hard drive during solution.

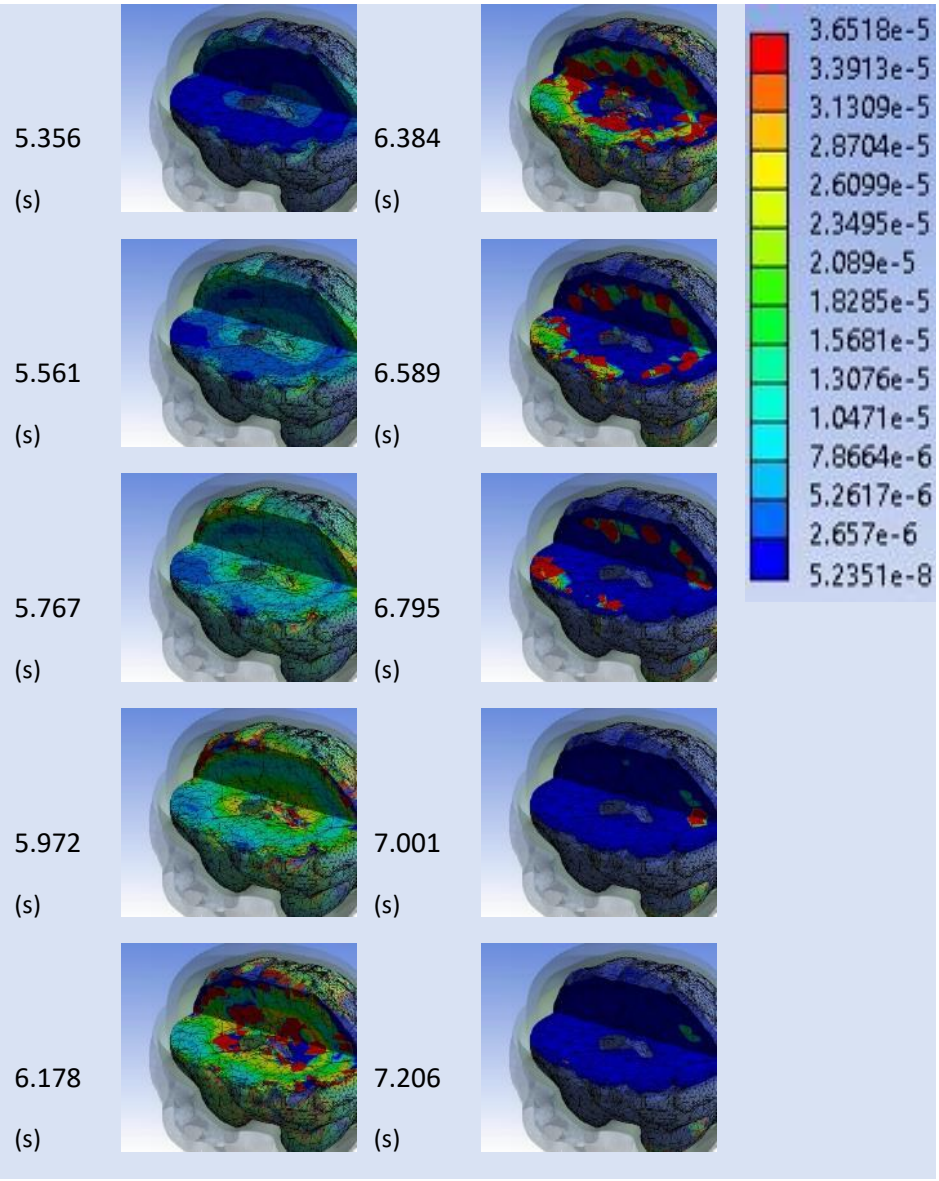

Figure 46: Von-Misses Stress over time for impact zone 8

Figure 47 shows the location of impact zone 9.

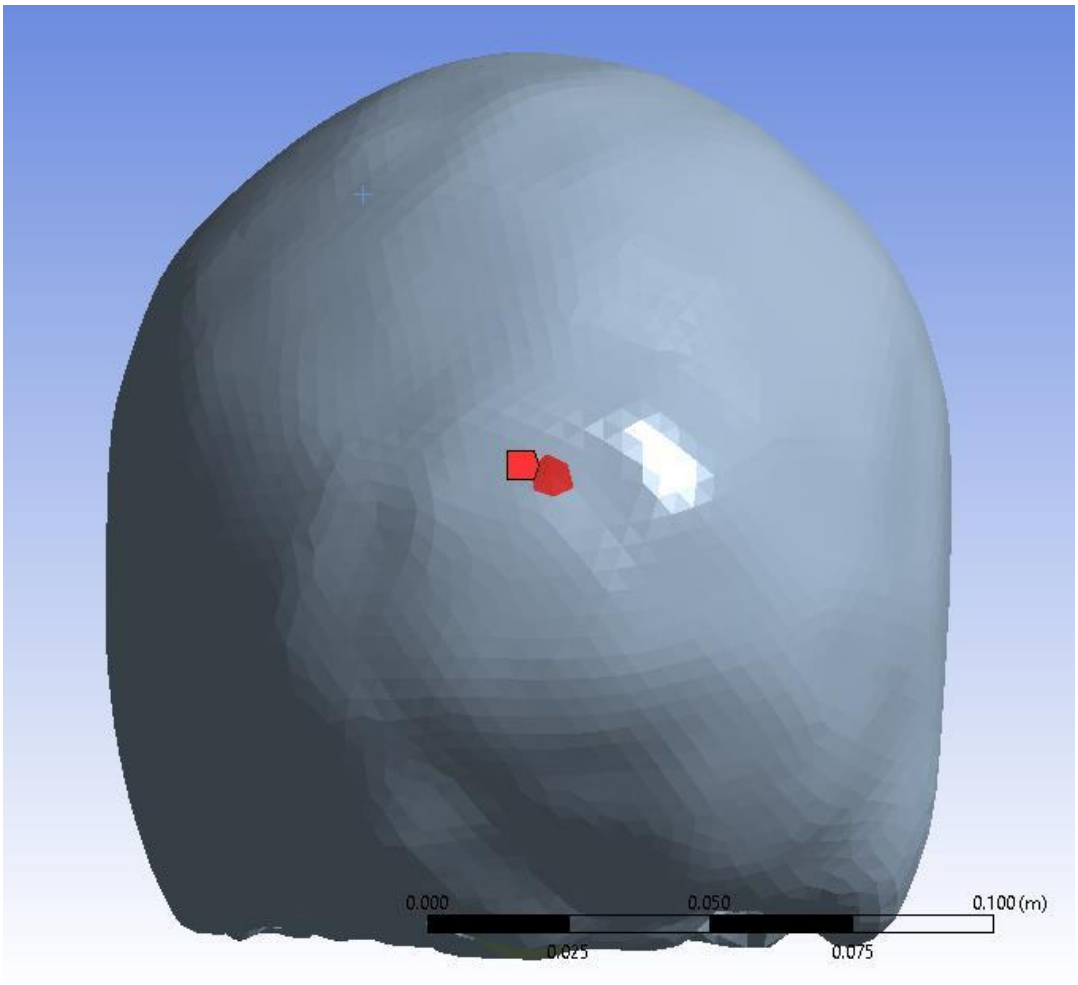

Figure 47: Location of impact zone 9.

Figure 48 outlines the von-mises stress over time for a 10s simulation with a remote force at impact zone 9. The simulation took 2.33s to complete, had a maximum total memory allocation of 54.5 GB and wrote a total of 1332.2GB of data to the hard drive during solution.

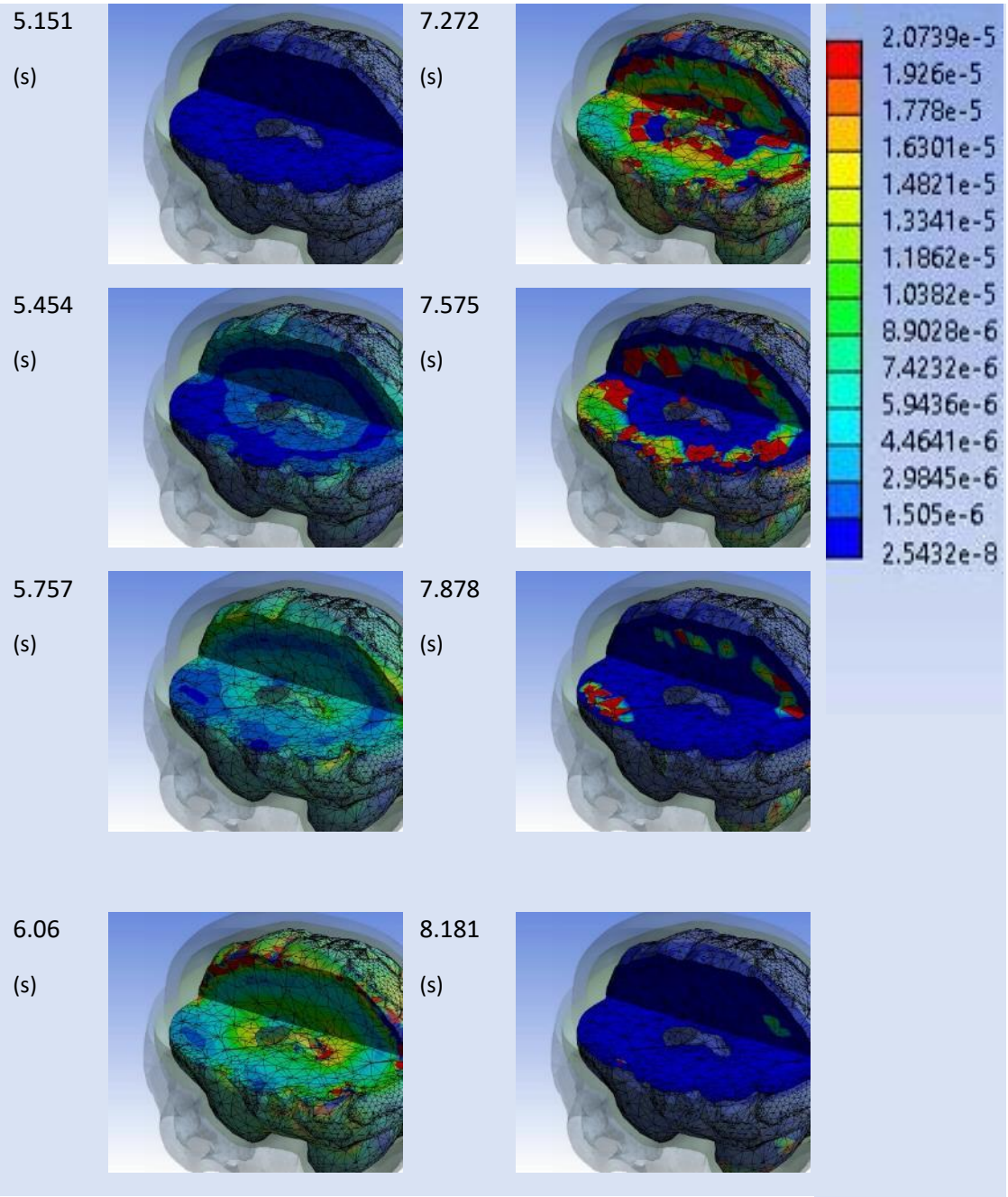

Figure 48: Von-Misses Stress over time for impact zone 9

Chapter 6: Discussion

The only geometry which successfully converged for all solver methods was the most basic rectangular model. This model had the added benefit of being substantially less complex than the other geometries, which resulted in much shorter solution times. Table 3 shows that for the pseudo fluid model, this geometry was able to converge to a solution for a 5 second transient simulation after 54.3s. The final head geometry varied for different impact locations but averaged a simulation time of 7204 seconds. These increases illustrate the importance of ensuring the simulation is as simplified as possible, while still providing a reasonable level of accuracy.

The explicit solution method is likely to be the most versatile in terms of input forces and accelerations, and the most stable in terms of convergence. However, even for the simplified rectangular geometry the computational time for a 5 second transient simulation was 47 hours and 32 minutes. This is a 1965.22% increase over the fluid solver method, and a 5177.78% increase over the pseudo fluid method. Extrapolation from the average solution time for a 10s simulation of from the final head geometry is estimated to require 105.61hrs of computational time. However, this assumes a linearly scaling relationship of simulation time. In reality, the explicit solver's estimated solution time exceeded 10,000 hours. Because of this, using the current technology and resources available, an explicit solution of this head model is not feasible in a PC environment. As computational resources continue to develop over time, this method may eventually be appropriate and feasible.

The fluid solver FSI method failed to converge for all geometries more complex than the initial rectangular geometry. This was despite continued attempts to simplify the simulation and provide more relaxed coupling. This included ramped data transfers (where the force and displacement outputs were ramped over several iterations at the beginning of each simulation step), increased damping and relaxation factors, reduction in input force magnitude and time, ramping of input force over time, implementation of nonlinear and direct solution methods, non-linear adaptive meshing methods, adjustment of material parameters, adjustment of geometry and variation of boundary conditions. Despite these attempts,

sometimes with multiple adaptations to viable influential settings, convergence was ultimately never achieved.

The pseudo-fluid and fluid30 models have the disadvantage of being unable to represent fluid flow throughout the CSF domains. Rather, they both assume a closed system with no net flow. For many applications, this method would be inappropriate. In the context of a head impact, the CSF layer's most important mechanical contribution can be assumed to be providing a medium which acts as a damper between the skull and the brain. As such it is reasonable to assume the system is closed, that is no (or a negligible volume) of CSF can flow out of its cavity in the head during impact. Given that the only paths out of this system are via small openings into the spinal canal and absorption in the ventricles it is likely that the net flow out is negligible.

When compared to other studies on brain impacts where the CSF or skull are both excluded a notable difference is the decreased transfer of stress into the brain at the initial impact zone. It should be noted that this assumes the impact is not of a high enough magnitude to cause material failure of the skull. It can be observed that following initial impact and deformation of the skull, a pressure wave is introduced into the CSF layer, where it is dispersed throughout the full volume, including the ventricles this is illustrated between 0 and 4.250s in Figure 29. For all impact zones a common feature was an initial, smaller magnitude stress wave traveling around the head. To better illustrate the second phase of pressure propagation, this initial wave was excluded from all impacts following impact zone 1. The full simulation data sets are shown in Appendix AAA. A secondary wave then forms, this pressure then 'squeezes' the brain from all directions in a somewhat uniform pattern, causing a ring wave of pressure to enter the brain tissue and eventually diffuse. This phenomenon was common to all simulations and is illustrated in Figures 29, 31, 33, 35, 37, 39, 41, 43 and 45. There is a significant time delay observed in this transfer, with some simulated impacts not showing significant stress propagation in the brain from the CSF for up to 6 seconds following the initial impact. Examples of this phenomenon are shown in Figures 33, 35, 37 and 45 which correspond to impact zones 3 as shown in 32, impact zone 4 as shown in 34, impact zone 5 as shown in Figure 36 and impact zone 9 as shown in Figure 44.

It can be observed that the CSF layer seems to cause an increased surface area of deformation in the brain, thus decreasing the observed peak magnitude of the resultant forces exerted on the brain when compared to simulation of direct impact to the brain. This may mean there is less concentrated regional damage during some impacts than predicted in models which do not include the CSF as outlined in (Smith, 2019). However, the wider distribution of damage may lead to more non-localized harm.

When comparing the propagation of stress waves throughout the brain between all impact zones some similarities appear. It can be observed that there are two stages of propagation, initially a lower magnitude wave 'squeezes' inward in a somewhat uniform fashion at the interface between the CSF and the brain This phase is illustrated in Figure 33. After a short delay, a higher magnitude wave then travels through the brain. This second wave grows quickly then travels inward and eventually dissipates. This second wave is shown to appear after 4.6552 in Figure 29, which corresponds to impact zone 1 as shown in Figure 28. Both waves seem to appear somewhat uniformly around the brain's geometry as illustrated in Figures 31, 33, 35, 37, 39, 41, 43 and 45, implying that they have been distributed throughout the CSF before reaching the brain. Some concentrated regions of stress develop as the wave dissipates, as can be observed in Figures 29, 31, 33, 35, 37, 39, 41, 43 and 45. These tended to appear at the front of the head regardless of the initial impact location. This observation was most prominently shown in Figure 31, which corresponded to simulated impact zone 2 as outlined in Figure 30. This impact zone was located on the countercoup of the head, but its relative proximity to impact zone 9 (shown in Figure 44) which showed similar anterior stress concentration to the rest of the group.

Most impact zones showed consistent delay between initial impact and the second wave beginning to propagate throughout the brain. For impact zones 2, 3, 4, 5, 6, 8 and 9 the second wave began propagating around 5 seconds after the initial impact. While impact zones 1, 7 and 10 showed some variation. Impact zone 7 showed the initial stress in the brain after impact being of a higher magnitude than other impacts. There was also no delay between the first and second waves reaching the brain. Despite this variation in propagation time, the distribution of the stress appeared to follow a similar pattern to other impacts. The quicker appearance of the second wave and higher initial magnitude of the first wave may be due to the CSF, skull or both layers being thinner in the region of impact zone 7.

Impacts at zones 1, 2, 3, 4, 5 and 6 all showed similar magnitude of stress throughout the brain, while zones 7, 8 and 9 all showed regions of higher magnitude, with the largest stress values being seen in the simulation for impact zone 8. Considering the proximity that these zones had to others and the simulation was run using identical input forces, it is surprising that there is significant variation between simulations. This may imply some randomness exists in the way in which stress is propagated throughout the CSF and brain.

All impacts simulated in this study assumed that there was no contact between the skull and the brain. It can be assumed that for larger impacts, there might be enough deflection of the skull to cause contact to occur with the brain. In such a case, the CSF would not be able to disperse the force as effectively as simulated. Thus, it can be hypothesized that such impacts may lead to more localized concentrations of stress around the initial impact zone. The inclusion of forces this significant could be beneficial for future simulations, however in such a case it is likely that the flow of CSF will need to be included.

With the exception of impact zone 9 as shown Figures 45 Figure 44, all simulations showed dissipation of the pressure waves within approximately 7 seconds. Zone 9 showed dissipation after approximately 8 seconds. This is could be due to a thinner layer of CSF between impact zone 9 and the brain. This may have caused the initial impact force to reach the brain in a shorter period of time than other simulations, meaning the CSF did not contribute much dissipation of stress. Based on the proximity between impact zones 9 and 10, it is unlikely that only the location on the skull had a significant contribution to the observed difference in dissipation time.

The variation in solution time for different impact zones implies that the complexity of pressure wave propagation may have some dependency on the impact location. This, in turn, implies that there may be some correlation between the location of the initial impact and the severity of injury received. This head model has the potential to allow further insight into how the initial impact location may lead to varying severity of injury, allowing more effective diagnosis and treatment of subjects experiencing TBI.

All simulations showed the stress wave traveled inward from the exterior of the brain, and outward into the brain from the ventricles before meeting within the brain tissue and dissipating. This highlights the

importance of including the ventricles in head simulation. Modelling the brain as homogenous with filled ventricles would likely result in a lower penetration depth of stress. The model presented in this thesis is therefore more suitable for performing analysis of TBI and head injury than other homogenous brain models.

On average, the final head model was capable of converging to a solution for a 10s simulation after 7204 seconds, or approximately 2 hours. With such low solution times, it is possible to run several simulations per day, enabling efficient workflow while studying different loading cases. Thus, the potential for advancing understanding of the internal mechanics of head injury using this model is huge. Compounding with this the model has been developed in such a way that it is relatively simple for someone with the appropriate knowledge to adjust and continue development.

The final geometry was based on true anatomical scans of a human head. Despite initially being of a low slice resolution and misalignment of the working planes and scanned features, the final processed geometries are a realistic representation of a human head. Several existing models use basic approximations of the head such as slices, sphere's, and basic geometric representations of human anatomy. The inclusion of geometry which was established from true human physiology propels this model to a higher level than these alternatives. As such, it is likely that this model can more realistically simulate TBI than some available alternatives.

The full head model proposed in this thesis lacks strong validation. However, the inclusion of material models which have been individually validated provides a lower level of validation to the fidelity of the model. In addition, the geometry used in this model was generated from physical scans of human head, with minimal modification made. Overall, this results in a model which is valid in the respect that each of the individual components has been validated before assembly. However, further validation of the model via comparison to physical experimentation would be beneficial. Undertaking such a validation in an ethical and exhaustive manner would be highly complex and is beyond the scope of this project.

A significant difficulty surrounding in-vivo research into the internal mechanisms of head injury is the sporadic nature of their occurrence. It is difficult to predict when an injury might occur and unethical to

reproduce one for the purpose of research. Compounded with this is the difficulty of recording reliable and accurate in-vivo data on healthy tissue during an impact. The development of this model allows an environment in which specific variables can be kept constant, allowing experimentation to be performed which allows observation of the internal behavior of the head during impact. The model also removes the ethical concerns surrounding physical studies of a similar nature by entirely removing the risk of harm to live subjects.

When reviewing the current state of head injury categorization, it can be observed that many commonly used systems, such as the HIC (ref), are stochastic in nature. This is often a result of categorization being dependent on the experience and knowledge of the individual diagnosing or treating such injuries. By allowing further insight into the specific mechanisms involved following an impact, this model has the potential to allow the development of more specialized and reliable methods of head injury characterization. In addition to this, with input of forces based on observed head injury events, it could be possible to repeat such events in-silico. This would allow further insights into where specific localized damage may have occurred, and how this might manifest as certain symptoms experienced by subjects following injury. Thus, allowing more targeted therapy to be provided to subjects who have experienced head injury, potentially leading to more positive patient outcomes.

The variation in observed maximum magnitude of stress outlined in Figure 45 from impact zone 7 when compared to results for the alternative impact zones implies that there may be some relationship between the locality of initial impact and the severity of injury received. By running an analysis using this model which maps the maximum observed internal stress in the brain tissue to the location of impact on the skull, it could be possible to locate areas of high risk. This could be used as a basis for a new method of head injury categorization, or for the design of protective equipment.

There was a common tendency to disperse pressure and relatively uniformly apply it throughout the head across simulations of different impact zones. This tendency is likely to be a function of the brain, CSF and skull's geometry. This somewhat uniform stress distribution is preferable to a stress distribution with high peak stresses. Hence, it could be claimed that the head seems to have some inherent dissipative

properties, which means that human anatomy is optimized to minimize the potential damage which arises as a result of head impacts. This observation is in line with several studies such as Pérez García and Gómez Martínez (2010) and Pérez García and Gómez Martínez (2010) which have found that naturally occurring structures have a tendency to occur in optimized ways. Further investigation into whether this phenomenon is observed for alternative physiologies could provide insight into the significance of geometric anatomy of the human brain in avoiding injury.

CSF and the ventricular cavities have been established as structurally important within the head as they are known to allow the brain tissue to display buoyancy (Schwab et al., 1998). The results simulated results outlined in this thesis project imply that the CSF plays a key role in the minimization of harm as a result of head impact. Not only does the CSF provide a damping effect internal to the head, but the natural shape of the ventricles appears to also influence the level of potential harm following impact. These observations highlight the biomechanical importance of CSF in the head, and in turn how important it is to include the CSF and ventricles in models used for simulation of head impacts.

A notable shortcoming of the model developed in this thesis project was the representation of the CSF as a 'fluid-like' solid, rather than a true fluid. This was as a result of difficulties encountered during attempted convergence of true fluid solid structure interaction models. It is possible that further code development may enable a true FSI model to be established. However, the benefit of this very large time investment are unclear. For the purposes of this project such development was not feasible. The decision to develop the model without the use of true fluid flow simulation has inherent inaccuracy, but significant computational efficiency gains. As such, the net loss suffered as a result of modelling the CSF as a solid was at least partially accounted for.

Since the model developed in this thesis project made use of an implicit transient solver, it is unable to represent cases of high deformation and rigid body motion. As such the model is limited to smaller magnitude impacts, and is unable to simulate acceleration based loading cases. In particular the accelerations recorded through the use of the mouthguard sensors outlined in chapter 6 would have involved modelling of rigid body motion. With more powerful computational resources, it is possible that

an explicit solver which uses ALE methods to represent FSI could be possible, but this was not achievable within the scope of this project. Despite this, an efficient and function model was developed. In addition, the conditions required for successful simulation using implicit solutions meant the neck was treated as a stiff boundary. In reality, the Neck is not rigid, and it is possible that it introduces dynamic behavior to the system which has the potential to modify observed internal stress. However, it can be assumed that it is most likely to decrease observed stress and in the context of designing for injury minimization it is not detrimental to over-estimate the potential inflicted damage.

Chapter 6 – Additional Work.

Soft Tissue Artifact in Head Injury Accelerometer Measurements

The following is an abridged version of the submitted paper "An in-silico study of the effect of non-linear skin dynamics on skin-mounted accelerometer inference of skull motion" which was submitted to the journal of Biomedical Signal Processing & Control.

INTRODUCTION

Traumatic brain injuries can lead to serious morbidity and mortality (El Sayed et al., 2008; Goldsmith & Plunkett, 2004; Mark W. Greve, 2009; Meaney, Morrison, & Dale Bass, 2014; Pierce et al., 1998). The sudden and unexpected nature of most head injuries coupled with the inability to palpitate the brain has led to a paucity of research in traumatic brain injury. However, recent research in high contact sports has led to an emergence of data relating to head impact kinematics and their cognitive effects (Gilchrist & O'Donoghue, 2000; S. Rowson et al., 2012; Liying Zhang, Yang, & King, 2004). A 2020 systematic review suggested that over two-thirds of the 168 head impact telemetry papers published in the previous decade may be imprecise due to the methods employed to record, verify and process the impact data (Patton et al., 2020). Patton et al. (2020) emphasise concerns over the reliance of many researchers on invalidated filtering algorithms to remove false positive impacts without corresponding video verification.

A common problem in biomechanics is soft tissue artefact (STA), where skin deforms relative to the underlying bone. This relative motion results in discrepancy between skin-mounted sensor acceleration readings and the acceleration of the underlying physical structure (Lucchetti, Cappozzo, Cappello, & Della Croce, 1998; Shultz, Kedgley, & Jenkyn, 2011). Often due to marker inertia (Shultz et al., 2011), the effects of skin deformation can become exaggerated during short-duration, high-magnitude events measured by head impact telemetry systems (Patton, 2016; Wu et al., 2016). Specifically, telemetry systems adhered to the head via the mastoid process have been reported to substantially over-estimate head acceleration on impact due to STA (Wu et al., 2016). Significant measurement error has also been observed for helmet-

and headband-based telemetry systems due to insufficient sensor-skull system coupling, producing excess sensor movement relative to the skull (Cummiskey et al., 2017) (Jadischke, Viano, Dau, King, & McCarthy, 2013). Consequently, there is ongoing reporting of unrealistic head impact telemetry data (Jadischke et al., 2013; Doug King et al., 2017a; Patton, 2016; S. Rowson et al., 2012; Wu et al., 2016).

Accurate reporting of head impact telemetry data is crucial to enable the development of valid injury severity criteria and finite element brain modelling of potentially injurious events (Post et al., 2015). More accurate data could provide a basis for the development of training methodologies and suggest changes to improve athlete brain health and wellbeing. More recent evolutions of head impact telemetry systems include inertial measurement unit (IMU) sensors embedded in mouthguards to improve coupling of skull-sensor systems (A. Bartsch, Samorezov, Benzel, Miele, & Brett, 2014; A. J. Bartsch et al., 2019; Greybe et al., 2020; Wu et al., 2016; Wu, Zarnescu, Nangia, Cam, & Camarillo, 2014). A model of the coupled skull and skin to sensor unit system would be beneficial to investigate how similar the motion of skin mounted sensors is to the measurements produced by more closely coupled mouthguard sensors during head impacts or acceleration. The process of modelling skin deformation has been investigated in depth by (Jor, Parker, Taberner, Nash, & Nielsen, 2013; Parker, 2016) and this can be used as a basis of model development.

METHOD

The skin was modelled based on a modified first order underdamped mass spring damper system as defined by Equation 1.

$$\ddot{u}_S = \frac{1}{m}(-k(u_R)\dot{u}_R - c(u_R)u_R) \quad (1)$$

$$u_R = u_S - u_C \quad (1a)$$

Where u_R is the relative displacement between skin (u_S) and the skull (u_C) [m], $\ddot{u}$ is the resultant acceleration [m·s^{-2}], $\dot{u}$ is the velocity [m·s^{-1}], and m the combined mass of a sensor adhered to the skin and effective mass of the moving skin section. In this equation the variables $k(u_R)$ and $c(u_R)$ are the nonlinear functions representing the skin's effective spring constant and damping respectively, which are a non-linear function of displacement. Figure 1 outlines the model visually.

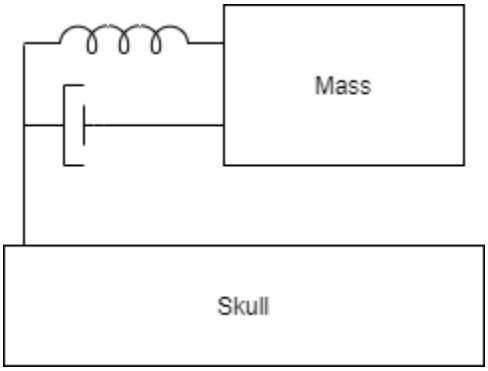

Figure 49: Visual representation of the modelled spring mass damper system.

In this model, the spring and damper contributions were represented by non-linear functions. These were established using MATLAB's least squared curve fitting function (lsqcurvefit) to parameterize data which was collected by Parker (2016). The spring relationship was observed with a least squares analysis of candidate models to have an exponential shape (equation 2).

$$k(u_R) = \theta_1 e^{\theta_2 u_R} \quad (2)$$

The damping relationship was determined to be a power function (equation 3).

$$c(u_R) = \theta_3 u_R^{\theta_4} + \theta_5 \quad (3)$$

Substituting Equations 2 and 3 into Equation 1 results in Equation 1b.

$$\ddot{u}_S = \frac{1}{m}\left(-\theta_1 e^{\theta_2|u_R|}\dot{u}_R - \left(\theta_3|u_R|^{\theta_4} + \theta_5\right)u_R\right) \quad (1b)$$

Where θ_1 through θ_4 are equation constants established via the aforementioned curve fitting. It should be noted that the values obtained by Parker (2016) were adjusted due to a suspected error in reported units. When compared to the values reported in Wu et al. (2016), those reported by Parker (2016) were 1000x higher than expected. This disparity was accounted for by correcting the units of spring constant reported in Parker (2016) from $N \cdot mm^{-1}$ to the SI unit of $N \cdot m^{-1}$.

MATLAB was then used to simulate the skin's response to the acceleration of the skull. Head acceleration data was collected by the head impact research team, (ASTEM, Swansea University, UK), during a collegiate men's rugby game via IMUsinstrumented mouthguards. Institutional ethical approval for the data collection was provided in accordance with the 2013 Helsinki Declaration (SU 2016-059). Before using the data, it was analysed using both frequency decomposition (Shenoi, 2006) and visual verification of impact. A low pass filter (LPF) was implemented via MATLAB's digital filtering toolbox to ensure that high frequency effects did not produce impossible acceleration profiles.

Because the data had been collected via mouthguard sensor, it was multiplied by an affine transform matrix to initially shift the accelerations to the approximate centre of mass of the head, then to the equivalent location of a sensor placed behind the ear. Figure 2 outlines these locations. The simulation was repeated with four datasets corresponding to separate measured impacts throughout the game.

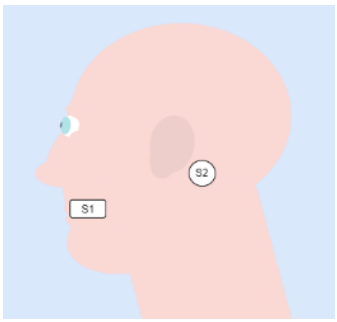

Figure 50: Sagittal view of the relative locations of the mouthguard sensor (S1) and a sensor adhered to the skin behind the ear (S2).

The transformed and filtered data was then used to forward simulate the skin response according to Equation 1b, with the spring and damping constants re-calculated at each time step. The displacement and velocity of the skull was determined using simple time-stepping numerical integration of the acceleration profiles. Initial conditions were set to rest for all displacements and velocities. After simulation, the absolute values of acceleration were considered.

The simulation was then repeated with constant k and c values (Equation 1c). For the linear model, the constants were set based on the values at 1 mm ($k_{linear} = k(0.001), c_{linear} = k(0.001)$). This was used to find the disparity between predicted motion of the skin based on a linear and non-linear model.

$$\ddot{u}_S = \frac{1}{m}(-\theta_1 e^{0.001\theta_2}\dot{u}_R - (\theta_3 0.001^B + \theta_4)u_R)$$

(1c)

To investigate the generalisable differences in responses from the linear and nonlinear model, a dual parametric sweep study was performed. This involved running the forward simulation using a single period sine acceleration input. The period of the sine curve was assessed on the range of 8 to 12 ms, and the magnitude range was assessed from 0 to 1000 $m \cdot s^{-2}$. The peak absolute acceleration of the skin was measured for each model and input condition. This enabled a relationship to be determined between variation of output for the linear and non-linear models' and the magnitude of acceleration at a given period.

RESULTS

The identified non-linear relationship between displacement and effective damping between the skin and skull motion is shown in Figure 3 (left). The fitted non-linear relationship between relative displacement of the skin and skull and Hooke's coefficient is shown in Figure 3 (right). Table 1 provides the established equation parameters according to Equation 2 and 3. Figure 4 compares the movement of the skull and the simulated response of the skin using both the linear and non-linear models for relatively large impact. Figure 5 shows the same comparison for a lower magnitude impact.

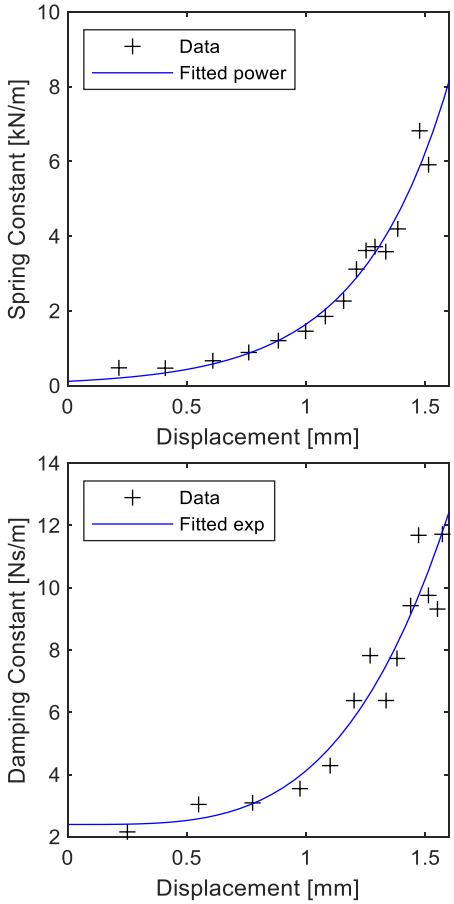

Figure 3: Identified exponential relationship between displacement and effective damping (left) and identified exponential relationship between displacement and effective spring constant of the skin (right).

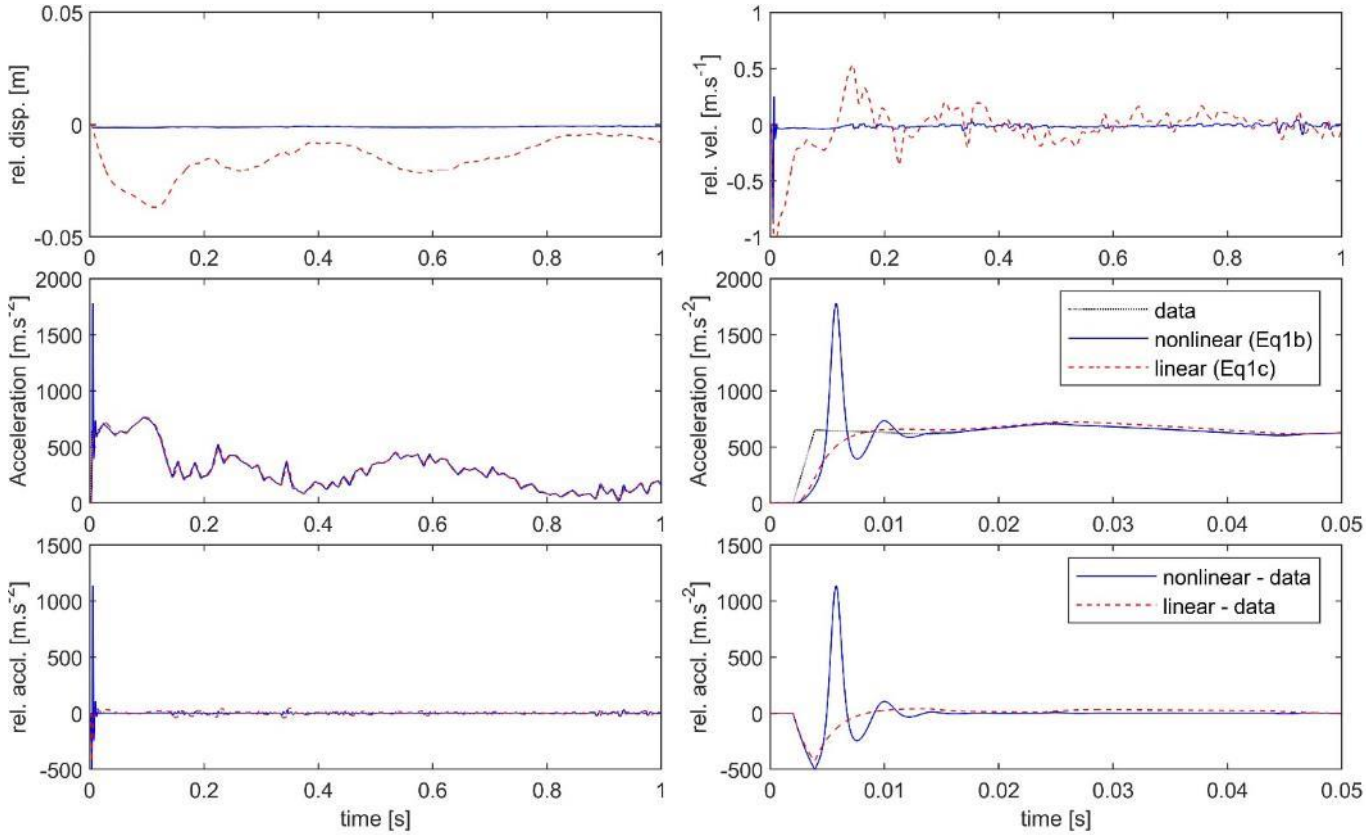

Figure 4: Comparison between the linear and non-linear models and the measured kinematic data for a large magnitude impact.

Note the different x-axis scales of the bottom right and middle right plots.

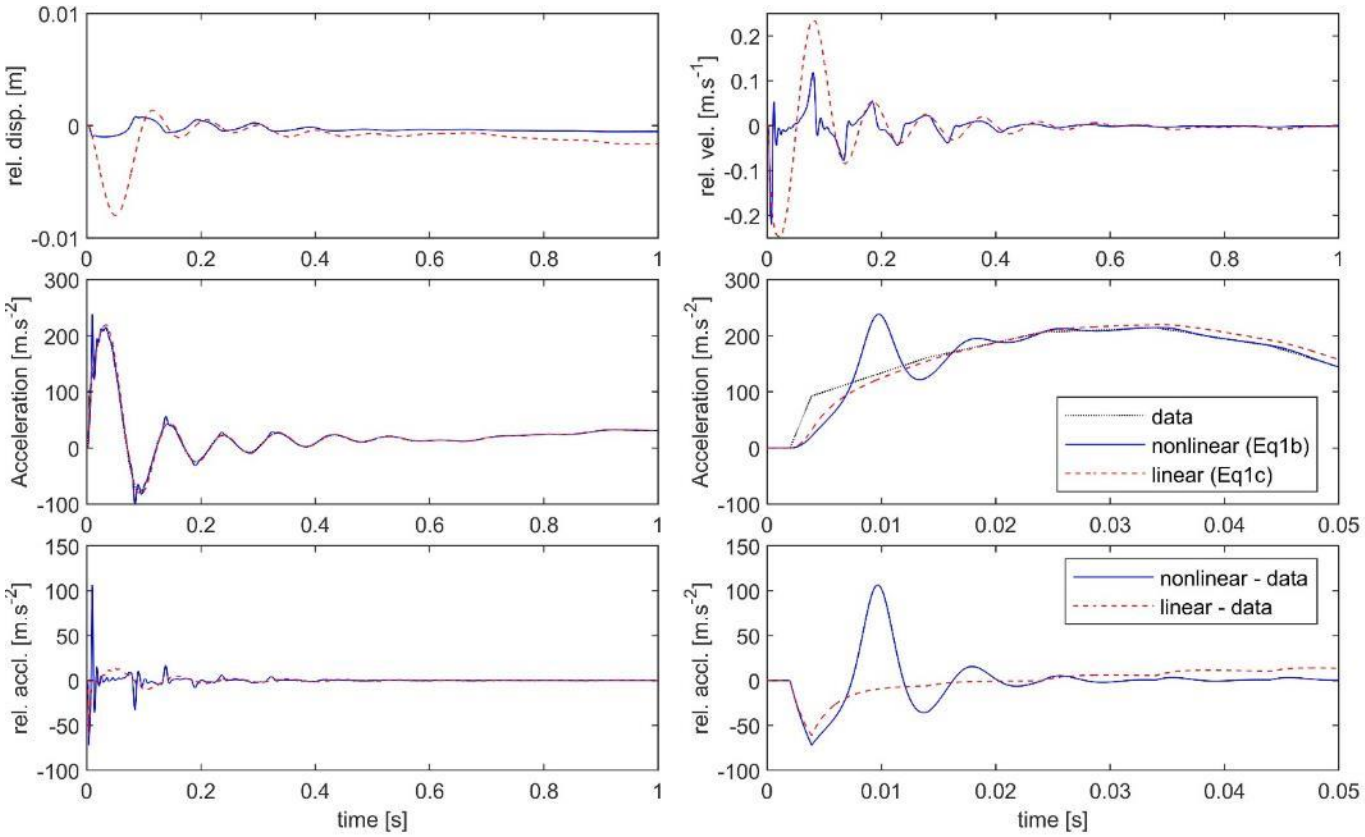

Figure 5: Comparison between the linear and non-linear models and the measured kinematic data for a low magnitude impact.

Table 5: The established parameters for the non-linear spring and damping relationships.

Equation	**Parameter**	**Value**
2	θ_1	1.139 x10^5
(Spring)	θ_2	2.669 x10^3
3	θ_3	3.000 x10^{11}
(Damper)	θ_4	3.7467
	θ_5	2.396

Table 2 presents a comparison between the peak accelerations of the measured data, the non-linear model and the linear model. Figure 6 shows an example of the difference in response of the linear and non-linear systems over a varying magnitude of acceleration input. The resultant peak accelerations for both the linear and non-linear systems are subsequently plotted according to input signals.

Table 6: Overview of simulation results for four measured impacts. Note the peak recorded acceleration is considered after the affine transformation.

Impact number	*Peak recorded acceleration (measured)*	*Peak simulated acceleration (non-linear)*	*Peak simulated acceleration (linear)*
1	*735.7 $m \cdot s^{-2}$*	*1738.8 $m \cdot s^{-2}$*	*740.5 $m \cdot s^{-2}$*
2	*360.5 $m \cdot s^{-2}$*	*360.6 $m \cdot s^{-2}$*	*366.6 $m \cdot s^{-2}$*
3	*214.1 $m \cdot s^{-2}$*	*238.1 $m \cdot s^{-2}$*	*219.8 $m \cdot s^{-2}$*
4	*763.3 $m \cdot s^{-2}$*	*1780.1 $m \cdot s^{-2}$*	*765.6 $m \cdot s^{-2}$*

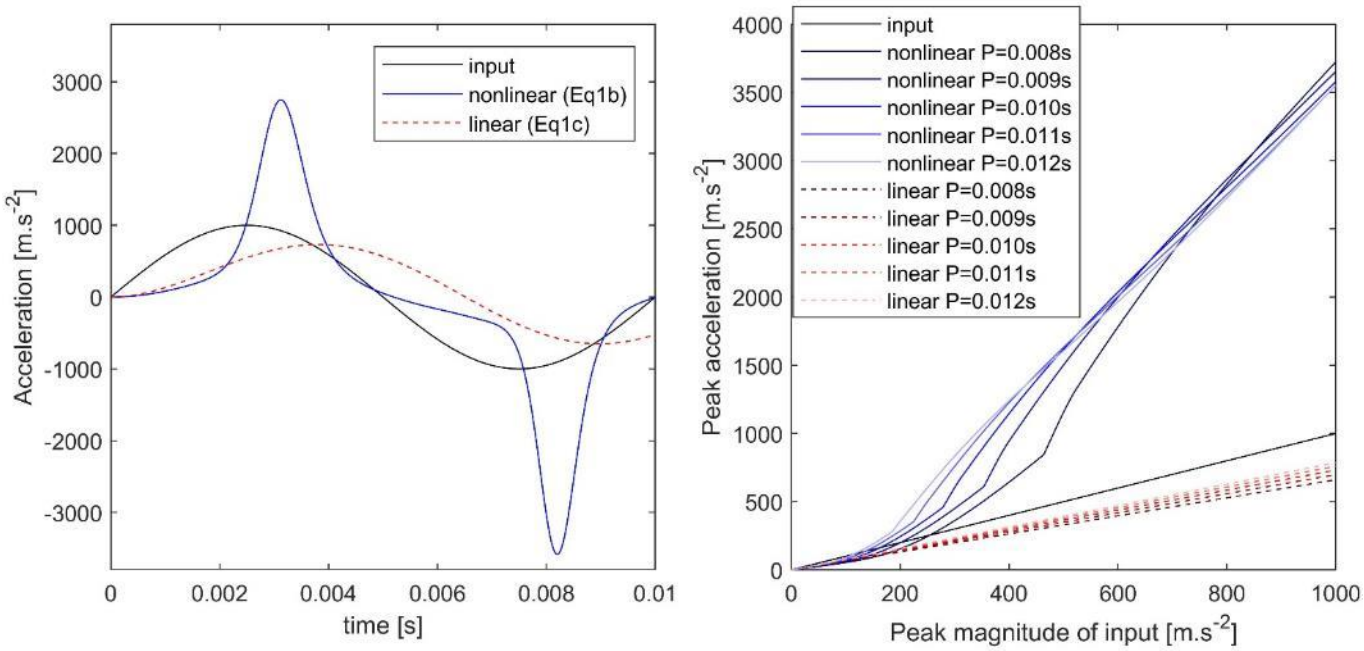

Figure 6: Comparison of the outputs for the linear and non-linear systems to sine wave input (top). Peak simulated accelerations for both the linear and non-linear systems according to the input signal conditions (bottom).

DISCUSSION

Figure 4 shows that a sudden, large acceleration of the head is likely to produce a large increase in acceleration of the skin, compared to the skull. This effect was not present in the linear model. Hence, the increased acceleration observed in this simulation may be due to the non-linear nature of the skin's effective spring and damping properties with respect to relative displacement. If repeated in physical experiments, this implies that in order to get data which closely represents the head's acceleration, a sensor should be attached in such a way that the results do not include STA. This result is in agreement with (Wu et al., 2016). Furthermore, this research has shown that, despite the non-linearity of the skin physiology, for smaller displacements the effects of this non-linearity of the skull-skin-sensor response is negligible. This implies the existence of an inflection point beneath which it may be realistic to model the skin as a linear mass damper system and to assume skull acceleration from skin mounted sensors.

To simplify this analysis, the effects of rotational acceleration on the skin-skull system response were excluded. Rotation was considered in the affine transformation of the acceleration data. If the rotational spring and damping relationship is similarly non-linear, it is possible that this analysis has underestimated the expected accelerations observed on the skin. However, since the accelerometer's centre of mass is very close to the centre of the adhesion area, the rotations of the accelerometer are unlikely to cause significant differences to assumed skull acceleration.

Both the linear and non-linear models resulted in a similar lag time to peak acceleration, when compared to the mouthguard data. This is expected for any second order underdamped spring mass damper system. It can be observed that higher impulse leads to higher expected acceleration of the skin (Figure 6 and Table 2) . This highlights the importance of removing any high-frequency interference from measured data. Overlooking this would likely lead to much larger simulated peaks in acceleration of the skin, and possibly even lead to a numerical divergence that must be accounted for in forward simulations. In this case, the filtered acceleration data had sufficient fidelity to allow precise evaluation of velocity and displacement with no apparent numerical instability.

The relative velocity in Figure 4 shows some unusual behaviour. However, this is explained by the behaviour of the damping equation (Equation 3). In particular, as the relative displacement begins to exceed 1 mm, the damping increases drastically, causing a sudden and strong restoring force. This explains the relative speed spikes at approximately 0.08 and 0.13 s. Repeating the simulation over different cases further illustrated the presence of a non-linear response in the skin and the implied existence of an inflection point below which it may be reasonable to model the skin as linear. Since the relative displacement shown in Figure (weaker hit) does not exceed 1 mm, no such spike in relative velocity was observed and the non-linear model effectively matched the linear model.

The parametric sweep study showed that there is a clear point of inflection at which the non-linear model begins to diverge significantly from the linear model. For the t = 0.01 case (Figure 6), this point occurred at an input magnitude of 272 $m \cdot s^{-2}$ (Figure 6). Below this magnitude, the non-linear model's peak acceleration output followed a somewhat linear path, similar to the linear model. Figure 6 also shows that for smaller duration impacts, the inflection occurs at larger acceleration magnitudes. However, when inflection occurs, divergence from the linear model was more pronounced. It is therefore reasonable to accept that, for accelerations below the inflection points, it may be valid to use a linear model when simulating this STA. However, even in these cases, a degree of bias will affect the results due to the non-linear nature of the physical system. This is illustrated by the already diverging values at accelerations lower than the point of inflection.

This model for the skin does not account for tensile or compressive failure of the skin, though it is unlikely that this would have a major effect on the outcome at such small displacements. It would also be exceedingly difficult to collect such data from *in-vivo* skin in an ethical way. In contrast, the mechanical behaviour of skin *ex vivo* has commanded considerable study (Joodaki & Panzer, 2018), including the high strain rate behaviour (Butler et al., 2015; Shergold, Fleck, & Radford, 2006) and the local composition and directionality effects (Khatyr et al., 2004). Although there are known degradative effects on mechanical properties of *ex vivo* biomaterials (with experimental methods to minimise such effects continually improving), strain-rate effects are still widely acknowledged in skin. Therefore, viscoelastic properties of skin need to be considered during a dynamic event such as those outlined here.

The simulation did not account for relative motion between the skull and the accelerometer components within the mouthguard. However, the coupling between the mouthguard and the player's teeth was tight and unlikely to significantly affect the results, when compared to the dominating non-linearity of the skin. The use of skin-mounted inertial sensors is common in sport-related head impact research (Chrisman et al., 2016; Hecimovich, King, Dempsey, Gittins, & Murphy, 2018; King, Hecimovich, Clark, & Gissane, 2017; Doug King et al., 2017a, 2017b; D. A. King et al., 2017; Lynall et al., 2016). Previous in-vivo experiments have shown that skin-mounted inertial sensors can over-estimate head accelerations by 120% (Wu et al., 2016). The model presented in Equation 1 predicts that a skin-sensor system yields a much greater over-estimation in the peak acceleration of the head during a harsh sporting head impact. The discrepancy in over-prediction between this model and the experiments of Wu et al. can be explained by the relatively low magnitude impacts (~15 g) used in their *in vivo* study, due to the ethical concerns surrounding intentional impacts. Figure 6 shows that 15 g (147 $m \cdot s^{-1}$) impact is below the inflection points of the non-linear model. The present simulations demonstrate that the errors do not diminish with larger magnitude impacts. Rather it implies the discrepancies due to STA may increase with impact magnitude.

This discrepancy has important implications for the interpretation of existing sport-related head impact data. In general, the median (or mean) head impact accelerations reported across a variety of sports are consistent and relatively low, ranging from 13 – 22 g research (Chrisman et al., 2016; Hecimovich et al., 2018; D King et al., 2017; Doug King et al., 2017a, 2017b; D. A. King et al., 2017; Lynall et al., 2016). That is only marginally higher than the 10 g threshold usually employed to prevent sensors from recording motion associated with daily activities like running (King, Hume, Gissane, Brughelli, & Clark, 2016; Liying Zhang et al., 2004). However, the maximum impact magnitudes reported in these studies are high, ranging from 66 – 153 g. Based on the simulation results, it is likely that these values are over-estimated by approximately 160%. Similarly, existing brain injury thresholds may substantially overestimate the head accelerations associated with sport-related concussion (Campolettano et al., 2020; Mihalik, Lynall, Wasserman, Guskiewicz, & Marshall, 2017; Liying Zhang et al., 2004). These thresholds have been determined based on head accelerations recorded using instrumented helmets, which are subject to even greater errors than skin-mounted patches (Wu et al., 2016). Therefore, they should be used with caution

when monitoring the limits of impact tolerance regarding player health. Head accelerations recorded with instrumented patches and helmets are unlikely to provide realistic input to finite element simulations of brain injury (Beckwith et al., 2018). Significant discrepancies can occur when using differing sensor systems that have variable coupling tolerances with the skull. To get the best estimates of skull motion, data should be collected using the most tightly coupled inertial sensors.

CONCLUSIONS

In this study, a model of the coupled skull-skin-sensor unit system was developed to investigate impact of STA on the overestimation of head acceleration inferred by skin mounted sensors during large impacts. It was observed that when modelled as a physiological, non-linear system, a sensor mounted on the skin can substantially overestimate skull accelerations. These findings are in agreement with results published in existing literature and may explain the discrepancy between skin- and mouthguard-mounted accelerometer measurements. Future head impact telemetry studies should ensure secure sensor-skull coupling of skull motion measurement devices to minimise the effects of soft tissue artefact, ensuring data integrity.

Presentation and Re-simulation of Homogenous Brain Model

During this thesis project, a presentation outlining the conference paper submitted by (Smith, 2019). The presentation was given at the 2020 World Conference for Automation and Controls, and is shown in Appendix B. In conjunction to this, Several more simulations were run using the model proposed by (Smith, 2019).

Future Work

While this model provides a relatively complex model of a human head, in the interest of computational efficiency specific aspects of human physiology were omitted. It may be beneficial to include more detailed geometries in the future. These could include bridging veins, dura layer, scalp, sinuses and axonal fibers. The inclusion of such features would allow comparison to the current model and allow

determination of how effective a simpler geometry is when weighed against the added computational cost.

It could be beneficial to gain successful convergence for this model using a true FSI method, such as system coupling or ALE. The results from such simulation should then be used for comparison to determine the net variation in simulated outcomes and thus the overall validity of modelling using a pseudo fluid method. The variation in results should be weighed against the computational cost of performing the simulation via alternative methods, this will allow an overall observation to be made.

The model developed during this thesis project used fixed and stiff boundary conditions to represent the points at which the neck and spinal cord attached to the head. In the future it could be beneficial to include a simulated neck, and the damping effects which tenses neck muscles might have. It is likely that this would result in rigid body motion of the head geometry. Thus, it may require the use of an explicit solution method. The use of explicit solver methods to allow rigid body motion would enable input of collected data sets from instrumentation methods such as mouthguard sensors. This could in turn allow full in-silico re-simulation of real-world events, allowing a significantly more in-depth analysis of the internal mechanics which occurred during an impact. This information could then be used to identify regions of concentrated stress internal to the brain and allow clinicians to investigate specific symptomatic outcomes. More targeted therapy could then be provided to head impact patients.

While the individual components of this model have been validated in the various studies which produced them, the sum of all components could benefit from physical validation. This would involve the construction of some physical medium which allows real world analysis of the model and can produce a dataset which is able to be compared to a simulated case. The significant time investment which the construction of such a physical model would require meant it was outside of the scope of this project.

As more advanced methods of material identification continue to advance it will be important to ensure the head model developed in this thesis project is continually updated to include relevant materials. The model could also be used as a baseline comparison to establish how significant any changes in simulated outcomes may be as a result of modeling biological materials differently.

Now that this head model has been established, there is a large opportunity for several investigations into the biomechanics of head injury to be made. This will involve simulating several impact cases to experimentally establish injury patterns which may occur, any existing correlation between localized damage and the location or magnitude of impacts, Investigation into the true damage which occurs during micro TBI and investigation into the nature of pressure wave propagation throughout the intracranial medium.

Conclusions

This head model is able to provide high resolution datasets in a three-dimensional space which outline the internal mechanics of head injury as a result of some arbitrary impact. It is able to do so in a way which poses no risk of morbidity or mortality to subjects, and has the potential to enable the development of a less stochastic head injury characterization method. In addition to this it was developed in way that will allow further development, thus allowing higher resolution and more accurate result sets to be produced. This will allow even more insight to be made into the internal mechanisms of head injury. When compared to similar alternatives, it is a more accurate representation of the human head, thus allowing more realistic simulation. Though it would benefit from further development, this model provides a solid basis for future projects moving forward.

References

ANSYS. (2021). Mechanical APDL 2021 R1 Theory Reference.

Baalen, B. V., Odding, E., Maas, A. I., Ribbers, G. M., Bergen, M. P., & Stam, H. J. (2003). Traumatic brain injury: classification of initial severity and determination of functional outcome. *25*(1), 9-18.

Bachynski, K. E., & Goldberg, D. S. (2014). Youth sports & public health: framing risks of mild traumatic brain injury in American football and ice hockey. *The Journal of Law, Medicine & Ethics, 42*(3), 323-333.

Bartsch, A., Samorezov, S., Benzel, E., Miele, V., & Brett, D. (2014). *Validation of an "intelligent mouthguard" single event head impact dosimeter*. Retrieved from

Bartsch, A. J., Hedin, D. S., Gibson, P. L., Miele, V. J., Benzel, E. C., Alberts, J. L., . . . McCrea, M. M. (2019). *Laboratory and on-field data collected by a head impact monitoring mouthguard.* Paper presented at the 2019 41st Annual International Conference of the IEEE Engineering in Medicine and Biology Society (EMBC).

Beckwith, J. G., Zhao, W., Ji, S., Ajamil, A. G., Bolander, R. P., Chu, J. J., . . . Rowson, S. (2018). Estimated brain tissue response following impacts associated with and without diagnosed concussion. *Annals of biomedical engineering, 46*(6), 819-830.

Bell, R. B., Fernandes, R., & Andersen, P. E. (2018). *Oral, head and neck oncology and reconstructive surgery*: Elsevier London.

Birzer, C. H., & Hamilton, J. (2019). Humanitarian engineering education fieldwork and the risk of doing more harm than good. *Australasian Journal of Engineering Education, 24*(2), 51-60.

Bloomfield, I., Johnston, I., & Bilston, L. (1998). Effects of proteins, blood cells and glucose on the viscosity of cerebrospinal fluid. *Pediatric neurosurgery, 28*(5), 246-251.

BR, C. R., & Venkateswaran, P. (2012). COMSOL MULTIPHYSICS®.

Butler, B. J., Boddy, R. L., Bo, C., Arora, H., Williams, A., Proud, W. G., & Brown, K. A. (2015). Composite nature of fresh skin revealed during compression. *Bioinspired, Biomimetic and Nanobiomaterials, 4*(2), 133-139.

Buzug, T. M. (2011). Computed tomography. In *Springer handbook of medical technology* (pp. 311-342): Springer.

BWH. (2021). 3D Slicer. Retrieved from https://www.slicer.org/

Campolettano, E. T., Gellner, R. A., Smith, E. P., Bellamkonda, S., Tierney, C. T., Crisco, J. J., . . . Stitzel, J. D. (2020). Development of a Concussion Risk Function for a Youth Population Using Head Linear and Rotational Acceleration. *Annals of biomedical engineering, 48*(1), 92-103.

Carey, M. E., Sarna, G. S., Farrell, J. B., & Happel, L. T. (1989). Experimental missile wound to the brain. *71*(5), 754-764.

Cernak, I. (2005). Animal models of head trauma. *2*(3), 410-422.

Chafi, M. S., Dirisala, V., Karami, G., & Ziejewski, M. (2009). A finite element method parametric study of the dynamic response of the human brain with different cerebrospinal fluid constitutive properties. *Proceedings of the Institution of Mechanical Engineers, Part H: Journal of Engineering in Medicine, 223*(8), 1003-1019.

Changaris, D. G., McGRAW, C. P., Richardson, J. D., Garretson, H. D., Arpin, E., & Shields, C. B. (1987). Correlation of cerebral perfusion pressure and Glasgow Coma Scale to outcome. *The Journal of trauma, 27*(9), 1007-1013.

Chen, Y., & Huang, W. (2011). Non-impact, blast-induced mild TBI and PTSD: concepts and caveats. *Brain injury, 25*(7-8), 641-650.

Choi, S. C., Barnes, T. Y., Bullock, R., Germanson, T. A., Marmarou, A., & Young, H. F. (1994). Temporal profile of outcomes in severe head injury. *81*(2), 169-173.

Chrisman, S. P., Mac Donald, C. L., Friedman, S., Andre, J., Rowhani-Rahbar, A., Drescher, S., . . . Poliakov, A. V. (2016). Head impact exposure during a weekend youth soccer tournament. *Journal of child neurology, 31*(8), 971-978.

Colombo, A. C., & Rodrigues, M. L. (2015). Fungal colonization of the brain: anatomopathological aspects of neurological cryptococcosis. *Anais da Academia Brasileira de Ciências, 87*(2), 1293-1309.

Constantin, P., & Foias, C. (1988). *Navier-stokes equations*: University of Chicago Press.

Cummiskey, B., Schiffmiller, D., Talavage, T. M., Leverenz, L., Meyer, J. J., Adams, D., & Nauman, E. A. (2017). Reliability and accuracy of helmet-mounted and head-mounted devices used to measure head accelerations. *Proceedings of the Institution of Mechanical Engineers, Part P: Journal of Sports Engineering and Technology, 231*(2), 144-153.

De Erausquin, G. A., & Alba-Ferrara, L. (2013). What does anisotropy measure? Insights from increased and decreased anisotropy in selective fiber tracts in schizophrenia. *Frontiers in integrative neuroscience, 7*, 9.

Dean, P. J. A., & Sterr, A. (2013). Long-term effects of mild traumatic brain injury on cognitive performance. *7*, 30.

DeKosky, S. T., & Ikonomovic, M. D. (2010). Traumatic brain injury--football, warfare, and long-term effects. *The New England journal of medicine, 363*(14), 1293.

Destrade, M., Mac Donald, B., Murphy, J., & Saccomandi, G. (2013). At least three invariants are necessary to model the mechanical response of incompressible, transversely isotropic materials. *Computational Mechanics, 52*(4), 959-969.

Donea, J., Giuliani, S., & Halleux, J.-P. (1982). An arbitrary Lagrangian-Eulerian finite element method for transient dynamic fluid-structure interactions. *Computer Methods in Applied Mechanics and Engineering, 33*(1-3), 689-723.

El Sayed, T., Mota, A., Fraternali, F., & Ortiz, M. (2008). Biomechanics of traumatic brain injury. *Computer Methods in Applied Mechanics and Engineering, 197*(51-52), 4692-4701.

Fedorov, A., Beichel, R., Kalpathy-Cramer, J., Finet, J., Fillion-Robin, J.-C., Pujol, S., . . . Sonka, M. (2012). 3D Slicer as an image computing platform for the Quantitative Imaging Network. *Magnetic resonance imaging, 30*(9), 1323-1341.

Feng, Y., Okamoto, R. J., Namani, R., Genin, G. M., & Bayly, P. V. (2013). Measurements of mechanical anisotropy in brain tissue and implications for transversely isotropic material models of white matter. *Journal of the mechanical behavior of biomedical materials, 23*, 117-132.

Fife, G., O'Sullivan, D., & Pieter, W. (2013). Biomechanics of head injury in olympic taekwondo and boxing. *30*(4), 263.

Fife, G. P., O'Sullivan, D. M., Pieter, W., Cook, D. P., & Kaminski, T. W. (2013). Effects of Olympic-style taekwondo kicks on an instrumented head-form and resultant injury measures. *British journal of sports medicine, 47*(18), 1161-1165.

Findling, O., Schuster, C., Sellner, J., Ettlin, T., & Allum, J. H. (2011). Trunk sway in patients with and without, mild traumatic brain injury after whiplash injury. *Gait & posture, 34*(4), 473-478.

Forns, J., Esnaola, M., López-Vicente, M., Suades-González, E., Alvarez-Pedrerol, M., Julvez, J., . . . Sunyer, J. (2014). The n-back Test and the Attentional Network Task as measures of child neuropsychological development in epidemiological studies. *28*(4), 519.

Galford, J. E., & McElhaney, J. H. (1970). A viscoelastic study of scalp, brain, and dura. *Journal of biomechanics, 3*(2), 211-221.

Génevaux, O., Habibi, A., & Dischler, J.-M. (2003). *Simulating Fluid-Solid Interaction.* Paper presented at the Graphics Interface.

Gilchrist, M., & O'Donoghue, D. (2000). Simulation of the development of frontal head impact injury. *Computational Mechanics, 26*(3), 229-235.

Giordano, C., Cloots, R., Van Dommelen, J., & Kleiven, S. (2014). The influence of anisotropy on brain injury prediction. *Journal of biomechanics, 47*(5), 1052-1059.

Giordano, C., & Kleiven, S. (2014). *Evaluation of axonal strain as a predictor for mild traumatic brain injuries using finite element modeling*. Retrieved from

Gokhale, N. S. (2008). *Practical finite element analysis*: Finite to infinite.

Goldsmith, W. (2001). The state of head injury biomechanics: past, present, and future: part 1. *29*(5&6).

Goldsmith, W., & Plunkett, J. (2004). A biomechanical analysis of the causes of traumatic brain injury in infants and children. *The American journal of forensic medicine and pathology, 25*(2), 89-100.

Gomez-Hernandez, R., Max, J. E., Kosier, T., Paradiso, S., & Robinson, R. G. (1997). Social impairment and depression after traumatic brain injury. *Archives of physical medicine and rehabilitation, 78*(12), 1321-1326.

Goriely, A., Geers, M. G., Holzapfel, G. A., Jayamohan, J., Jérusalem, A., Sivaloganathan, S., . . . Kuhl, E. (2015). Mechanics of the brain: perspectives, challenges, and opportunities. *14*(5), 931-965.

Greybe, D. G., Jones, C. M., Williams, E. M., de Grau, S., Post, A., Gilchrist, M. D., . . . Turner, J. (2020). Comparison of head impact measurements via an instrumented mouthguard and an anthropometric testing device. *Sports Engineering, 23*, 12.

Haeussinger, F. B., Heinzel, S., Hahn, T., Schecklmann, M., Ehlis, A.-C., & Fallgatter, A. J. (2011). Simulation of near-infrared light absorption considering individual head and prefrontal cortex anatomy: implications for optical neuroimaging. *PloS one, 6*(10), e26377.

Handbook, A., & Fundamental, F. (2011). Concepts and Applications. *Ansys Inc., Canonsbyrg, USA*.

Hardman, J. M., & Manoukian, A. (2002). Pathology of head trauma. *Neuroimaging Clinics of North America, 12*(2), 175-187, vii.

Healey, C., Osler, T. M., Rogers, F. B., Healey, M. A., Glance, L. G., Kilgo, P. D., . . . Meredith, J. W. (2003). Improving the Glasgow Coma Scale score: motor score alone is a better predictor. *Journal of Trauma*

Acute Care Surgery

54(4), 671-680.

Hecimovich, M., King, D., Dempsey, A., Gittins, M., & Murphy, M. (2018). Youth Australian footballers experience similar impact forces to the head as Junior-and Senior-League players: a prospective study of kinematic measurements. *Journal of sports science & medicine, 17*(4), 547.

Hollis, S. J., Stevenson, M. R., McIntosh, A. S., Li, L., Heritier, S., Shores, E. A., . . . Finch, C. F. (2011). Mild traumatic brain injury among a cohort of rugby union players: predictors of time to injury. *British journal of sports medicine, 45*(12), 997-999.

Hrapko, M., Van Dommelen, J., Peters, G., & Wismans, J. (2006). The mechanical behaviour of brain tissue: large strain response and constitutive modelling. *Biorheology, 43*(5), 623-636.

Hutton, D. V. (2004). *Fundamentals of finite element analysis*: McGraw-hill.

Inglese, M., Makani, S., Johnson, G., Cohen, B. A., Silver, J. A., Gonen, O., & Grossman, R. I. (2005). Diffuse axonal injury in mild traumatic brain injury: a diffusion tensor imaging study. *Journal of neurosurgery, 103*(2), 298-303.

Jadischke, R., Viano, D. C., Dau, N., King, A. I., & McCarthy, J. (2013). On the accuracy of the Head Impact Telemetry (HIT) System used in football helmets. *Journal of biomechanics, 46*(13), 2310-2315.

Jin, J.-X., Zhang, J.-Y., Song, X.-W., Hu, H., Sun, X.-Y., & Gao, Z.-H. (2015). Effect of cerebrospinal fluid modeled with different material properties on a human finite element head model. *Journal of Mechanics in Medicine Biology*

15(03), 1550027.

Joodaki, H., & Panzer, M. B. (2018). Skin mechanical properties and modeling: A review. *Proceedings of the Institution of Mechanical Engineers, Part H: Journal of Engineering in Medicine, 232*(4), 323-343.

Jor, J. W., Parker, M. D., Taberner, A. J., Nash, M. P., & Nielsen, P. M. (2013). Computational and experimental characterization of skin mechanics: identifying current challenges and future directions. *Wiley Interdisciplinary Reviews: Systems Biology and Medicine, 5*(5), 539-556.

Khatyr, F., Imberdis, C., Vescovo, P., Varchon, D., & Lagarde, J. M. (2004). Model of the viscoelastic behaviour of skin in vivo and study of anisotropy. *Skin research and technology, 10*(2), 96-103.

King, D., Hecimovich, M., Clark, T., & Gissane, C. (2017). Measurement of the head impacts in a sub-elite Australian rules football team with an instrumented patch: an exploratory analysis. *International Journal of Sports Science & Coaching, 12*(3), 359-370.

King, D., Hume, P., Gissane, C., Brughelli, M., & Clark, T. (2016). The influence of head impact threshold for reporting data in contact and collision sports: systematic review and original data analysis. *Sports medicine, 46*(2), 151-169.

King, D., Hume, P., Gissane, C., & Clark, T. (2017a). Head impacts in a junior rugby league team measured with a wireless head impact sensor: an exploratory analysis. *Journal of Neurosurgery: Pediatrics, 19*(1), 13-23.

King, D., Hume, P., Gissane, C., & Clark, T. (2017b). Semi-professional rugby league players have higher concussion risk than professional or amateur participants: a pooled analysis. *Sports medicine, 47*(2), 197-205.

King, D. A., Hume, P., Gissane, C., & Clark, T. (2017). Measurement of Head Impacts in a Senior Amateur Rugby League Team with an Instrumented Patch: Exploratory Analysis. *ARC Journal of Research in Sports Medicine, 2*(1), 9-20.

Kleiven, S. (2002). *Finite element modeling of the human head.* KTH,

Lakes, R., & Lakes, R. S. (2009). *Viscoelastic materials*: Cambridge university press.

Levy, M. L., Kasasbeh, A. S., Baird, L. C., Amene, C., Skeen, J., & Marshall, L. (2012). Concussions in soccer: a current understanding. *World neurosurgery, 78*(5), 535-544.

Li, H., Ruan, J., Xie, Z., Wang, H., & Liu, W. (2007). Investigation of the critical geometric characteristics of living human skulls utilising medical image analysis techniques. *International Journal of Vehicle Safety, 2*(4), 345-367.

Lucchetti, L., Cappozzo, A., Cappello, A., & Della Croce, U. (1998). Skin movement artefact assessment and compensation in the estimation of knee-joint kinematics. *Journal of biomechanics, 31*(11), 977-984.

Lynall, R. C., Clark, M. D., Grand, E. E., Stucker, J. C., Littleton, A. C., Aguilar, A. J., . . . Mihalik, J. P. (2016). Head impact biomechanics in women's college soccer. *Medicine and science in sports and exercise, 48*(9), 1772-1778.

Madhukar, A., & Ostoja-Starzewski, M. (2019). Finite element methods in human head impact simulations: a review. *Annals of biomedical engineering, 47*(9), 1832-1854.

Marckmann, G., & Verron, E. (2006). Comparison of hyperelastic models for rubber-like materials. *Rubber chemistry and technology, 79*(5), 835-858.

Mark W. Greve, M. a. B. J. Z., MD. (2009). Pathophysiology of Traumatic Brain Injury. *MOUNT SINAI JOURNAL OF MEDICINE, 76*, 8.

Martins, P., Natal Jorge, R., & Ferreira, A. (2006a). A comparative study of several material models for prediction of hyperelastic properties: Application to silicone-rubber and soft tissues. *Strain, 42*(3), 135-147.

Martins, P., Natal Jorge, R., & Ferreira, A. (2006b). A comparative study of several material models for prediction of hyperelastic properties: Application to silicone-rubber and soft tissues. *J Strain, 42*(3), 135-147.

McHenry, B. G. (2004). Head injury criterion and the ATB. *ATB Users' group, 29*, 5-8.

McNett, M. (2007). A review of the predictive ability of Glasgow Coma Scale scores in head-injured patients. *Journal of Neuroscience Nursing, 39*(2), 68-75.

Meaney, D. F., Morrison, B., & Dale Bass, C. (2014). The mechanics of traumatic brain injury: a review of what we know and what we need to know for reducing its societal burden. *Journal of biomechanical engineering, 136*(2).

Mihai, L. A., Chin, L., Janmey, P. A., & Goriely, A. (2015). A comparison of hyperelastic constitutive models applicable to brain and fat tissues. *Journal of The Royal Society Interface, 12*(110), 20150486.

Mihalik, J. P., Lynall, R. C., Wasserman, E. B., Guskiewicz, K. M., & Marshall, S. W. (2017). Evaluating the" threshold theory": can head impact indicators help? *Medicine and science in sports and exercise, 49*(2), 247-253.

Miller, K., Chinzei, K., Orssengo, G., & Bednarz, P. (2000). Mechanical properties of brain tissue in-vivo: experiment and computer simulation. *Journal of biomechanics, 33*(11), 1369-1376.

Montgomery, E., Fenton, G., McClelland, R., MacFlynn, G., & Rutherford, W. (1991). The psychobiology of minor head injury. *Psychological medicine, 21*(2), 375-384.

Morris, S. A., & Slesnick, T. C. (2018). Magnetic resonance imaging. *Visual Guide to Neonatal Cardiology*, 104-108.

Moss, W. C., King, M. J., & Blackman, E. G. (2009). Skull flexure from blast waves: a mechanism for brain injury with implications for helmet design. *Physical review letters, 103*(10), 108702.

Narayan, R., & ebrary, I. (2009). *Biomedical materials* (1. Aufl. ed.). New York: Springer.

Narayan, R. K., Greenberg, R. P., Miller, J. D., Enas, G. G., Choi, S. C., Kishore, P. R., . . . Becker, D. P. (1981). Improved confidence of outcome prediction in severe head injury: a comparative analysis of the clinical examination, multimodality evoked potentials, CT scanning, and intracranial pressure. *Journal of neurosurgery, 54*(6), 751-762.

Netter, F. H., & Colacino, S. (1989). *Atlas of human anatomy*: Ciba-Geigy Corporation.

NZMOH. (2019). *Head injury and concussion*. Retrieved from https://www.health.govt.nz/your-health/conditions-and-treatments/accidents-and-injuries/head-injury-and-concussion

Panzer, M. B., Myers, B. S., Capehart, B. P., & Bass, C. R. (2012). Development of a finite element model for blast brain injury and the effects of CSF cavitation. *Annals of biomedical engineering, 40*(7), 1530-1544.

Parker, M. (2016). *Identification of the mechanical properties of living skin: an instrumentation and modelling study.* ResearchSpace@ Auckland,

Patton, D. A. (2016). A review of instrumented equipment to investigate head impacts in sport. *Applied bionics and biomechanics, 2016*.

Patton, D. A., Huber, C. M., Jain, D., Myers, R. K., McDonald, C. C., Margulies, S. S., . . . Arbogast, K. B. (2020). Head Impact Sensor Studies In Sports: A Systematic Review Of Exposure Confirmation Methods. *Annals of biomedical engineering*, 1-11.

Pawlik, P. S., & Reisman, H. (1980). *Elasticity: theory and applications*: Wiley.

Pérez García, A. J., & Gómez Martínez, F. (2010). *Natural structures: strategies for geometric and morphological optimization.* Paper presented at the Symposium of the International Association for Shell and Spatial Structures (50th. 2009. Valencia). Evolution and Trends in Design, Analysis and Construction of Shell and Spatial Structures: Proceedings.

Pieper, S., Halle, M., & Kikinis, R. (2004). *3D Slicer.* Paper presented at the 2004 2nd IEEE international symposium on biomedical imaging: nano to macro (IEEE Cat No. 04EX821).

Pierce, J., Smith, D., Trojanowski, J., & McIntosh, T. (1998). Enduring cognitive, neurobehavioral and histopathological changes persist for up to one year following severe experimental brain injury in rats. *Neuroscience, 87*(2), 359-369.

Post, A., Kendall, M., Koncan, D., Cournoyer, J., Hoshizaki, T. B., Gilchrist, M. D., . . . Marshall, S. (2015). Characterization of persistent concussive syndrome using injury reconstruction and finite element modelling. *Journal of the mechanical behavior of biomedical materials, 41*, 325-335.

Prosser, J. D., Vender, J. R., & Solares, C. A. (2011). Traumatic cerebrospinal fluid leaks. *Otolaryngologic Clinics of North America, 44*(4), 857-873.

Rapoport, M. J., McCullagh, S., Streiner, D., & Feinstein, A. (2003). Age and major depression after mild traumatic brain injury. *The American Journal of Geriatric Psychiatry, 11*(3), 365-369.

Ratner, B. D., Hoffman, A. S., Schoen, F. J., Lemons, J. E., & Schoen, F. J. (2012). *Biomaterials Science : An Introduction to Materials in Medicine*. San Diego, UNITED STATES: Elsevier Science & Technology.

Raul, J.-S., Baumgartner, D., Willinger, R., & Ludes, B. (2006). Finite element modelling of human head injuries caused by a fall. *International journal of legal medicine, 120*(4), 212-218.

Rezaei, A., Sarvghad-Moghaddam, H., Eslaminejad, A., Ziejewski, M., & Karami, G. (2016). *Skull Deformation Has No Impact on the Variation of Brain Intracranial Pressure.* Paper presented at the ASME 2016 International Mechanical Engineering Congress and Exposition.

Rovlias, A., & Kotsou, S. (2004). Classification and regression tree for prediction of outcome after severe head injury using simple clinical and laboratory variables. *Journal of neurotrauma, 21*(7), 886-893.

Rowson, B., & Duma, S. M. (2020). A review of on-field investigations into the biomechanics of concussion in football and translation to head injury mitigation strategies. *Annals of biomedical engineering*, 1-17.

Rowson, S., Duma, S. M., Beckwith, J. G., Chu, J. J., Greenwald, R. M., Crisco, J. J., . . . Maerlender, A. C. (2012). Rotational head kinematics in football impacts: an injury risk function for concussion. *Annals of biomedical engineering, 40*(1), 1-13.

Saatman, K. E., Duhaime, A.-C., Bullock, R., Maas, A. I., Valadka, A., & Manley, G. T. (2008). Classification of traumatic brain injury for targeted therapies. *Journal of neurotrauma, 25*(7), 719-738.

Schulte-Geers, C., Obert, M., Schilling, R. L., Harth, S., Traupe, H., Gizewski, E. R., & Verhoff, M. A. (2011). Age and gender-dependent bone density changes of the human skull disclosed by high-resolution flat-panel computed tomography. *International journal of legal medicine, 125*(3), 417-425.

Schwab, S., Erbguth, F., Aschoff, A., Orberk, E., Spranger, M., & Hacke, W. (1998). " Paradoxical" herniation after decompressive trephining. *Der Nervenarzt, 69*(10), 896-900.

Shen, F., Tay, T., Li, J., Nigen, S., Lee, P., & Chan, H. (2006). Modified Bilston nonlinear viscoelastic model for finite element head injury studies.

Shenoi, B. A. (2006). *Introduction to digital signal: Processing and filter design*: Wiley Online Library.

Shergold, O. A., Fleck, N. A., & Radford, D. (2006). The uniaxial stress versus strain response of pig skin and silicone rubber at low and high strain rates. *International Journal of Impact Engineering, 32*(9), 1384-1402.

Shugar, T. A., & Katona, M. G. (1975). Development of finite element head injury model. *Journal of the Engineering Mechanics Division, 101*(3), 223-239.

Shultz, R., Kedgley, A., & Jenkyn, T. (2011). Quantifying skin motion artifact error of the hindfoot and forefoot marker clusters with the optical tracking of a multi-segment foot model using single-plane fluoroscopy. *Gait & posture, 34*(1), 44-48.

Smith, N. (2019). *An In-Silico Simulation of Pressure Wave Excursions after*

Impact to the Frontal Lobe of a Homogenous Model of the

Brain.

Sweetman, B., & Linninger, A. A. (2011). Cerebrospinal fluid flow dynamics in the central nervous system. *Annals of biomedical engineering, 39*(1), 484-496.

Szabo, T. J., & Welcher, J. B. (1996). Human subject kinematics and electromyographic activity during low speed rear impacts. *SAE Transactions*, 1924-1944.

Takhounts, E. G., Eppinger, R. H., Campbell, J. Q., Tannous, R. E., Power, E. D., & Shook, L. S. (2003). *On the development of the SIMon finite element head model*. Retrieved from

Taylor, H. G., Swartwout, M. D., Yeates, K. O., Walz, N. C., Stancin, T., & Wade, S. L. (2008). Traumatic brain injury in young children: postacute effects on cognitive and school readiness skills. *Journal of the International Neuropsychological Society, 14*(5), 734-745.

Van Dommelen, J., Hrapko, M., & Peters, G. (2010). Constitutive modelling of brain tissue for prediction of traumatic brain injury. In *Neural Tissue Biomechanics* (pp. 41-67): Springer.

Vlaardingerbroek, M. T., & Boer, J. A. (2013). *Magnetic resonance imaging: theory and practice*: Springer Science & Business Media.

Ward, C., Chan, M., & Nahum, A. (1980). Intracranial pressure—a brain injury criterion. *SAE Transactions*, 3867-3880.

Weiss, J. A., Maker, B. N., & Govindjee, S. (1996). Finite element implementation of incompressible, transversely isotropic hyperelasticity. *Computer Methods in Applied Mechanics and Engineering, 135*(1-2), 107-128.

Wu, L. C., Nangia, V., Bui, K., Hammoor, B., Kurt, M., Hernandez, F., . . . Camarillo, D. B. (2016). In vivo evaluation of wearable head impact sensors. *Annals of biomedical engineering, 44*(4), 1234-1245.

Wu, L. C., Zarnescu, L., Nangia, V., Cam, B., & Camarillo, D. B. (2014). A head impact detection system using SVM classification and proximity sensing in an instrumented mouthguard. *IEEE Transactions on Biomedical Engineering, 61*(11), 2659-2668.

Yan, W., & Pangestu, O. D. (2011). A modified human head model for the study of impact head injury. *Computer methods in biomechanics and biomedical engineering, 14*(12), 1049-1057.

Zhang, L., Ravdin, L. D., Relkin, N., Zimmerman, R. D., Jordan, B., Lathan, W. E., & Uluğ, A. M. (2003). Increased diffusion in the brain of professional boxers: a preclinical sign of traumatic brain injury? *American journal of neuroradiology, 24*(1), 52-57.

Zhang, L., Yang, K. H., Dwarampudi, R., Omori, K., Li, T., Chang, K., . . . King, A. I. (2001). Recent advances in brain injury research: a new human head model development and validation.

Zhang, L., Yang, K. H., & King, A. I. (2004). A proposed injury threshold for mild traumatic brain injury. *J. Biomech. Eng., 126*(2), 226-236.

Zhou, Z., Li, X., & Kleiven, S. (2019). Fluid–structure interaction simulation of the brain–skull interface for acute subdural haematoma prediction. *Biomechanics and modeling in mechanobiology, 18*(1), 155-173.

Appendix A: Full Simulation Figures

Impact Zone 1

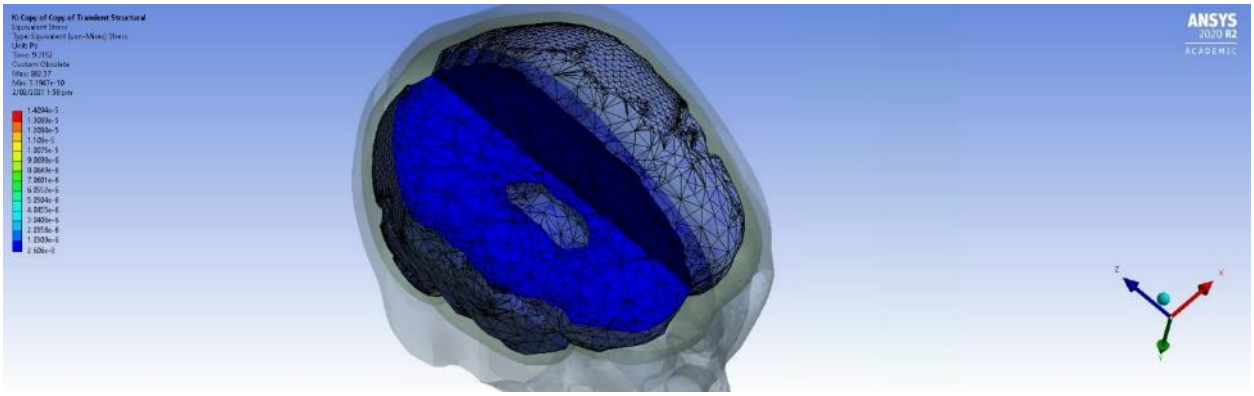

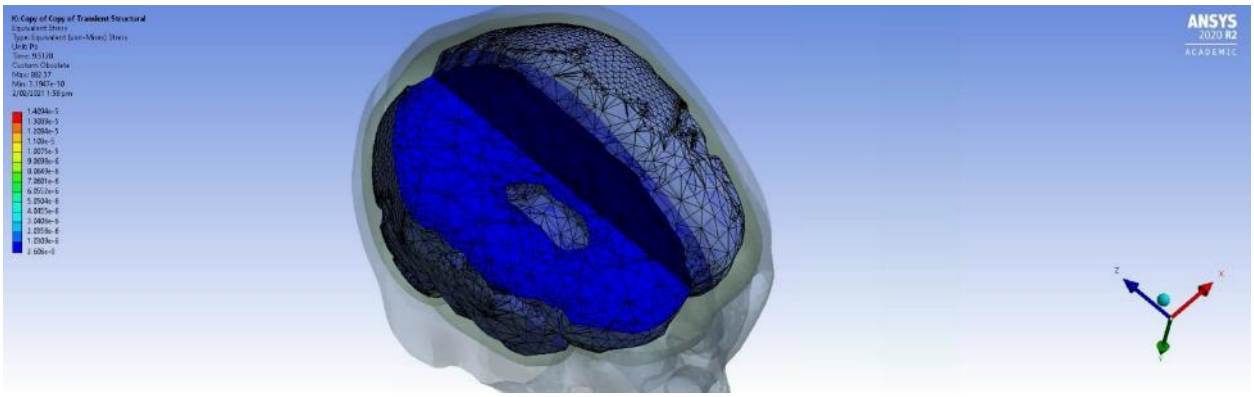

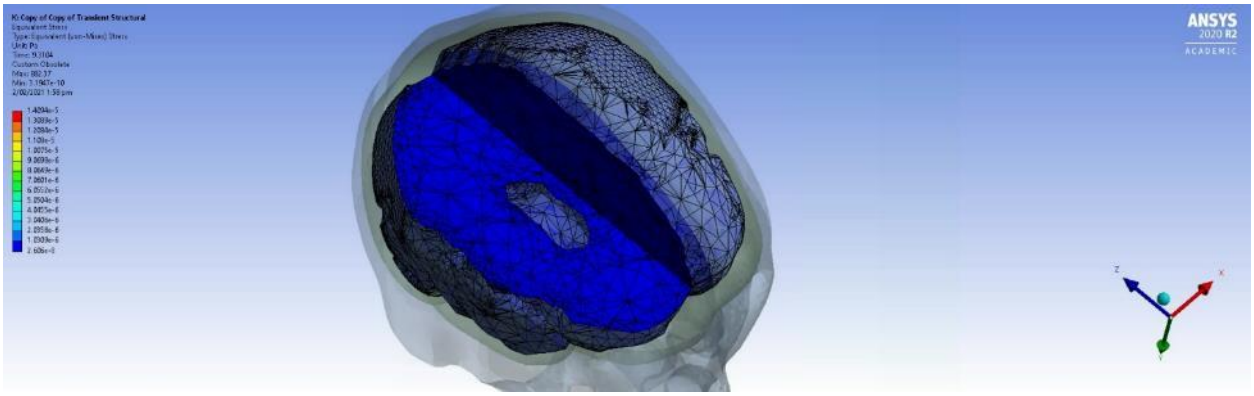

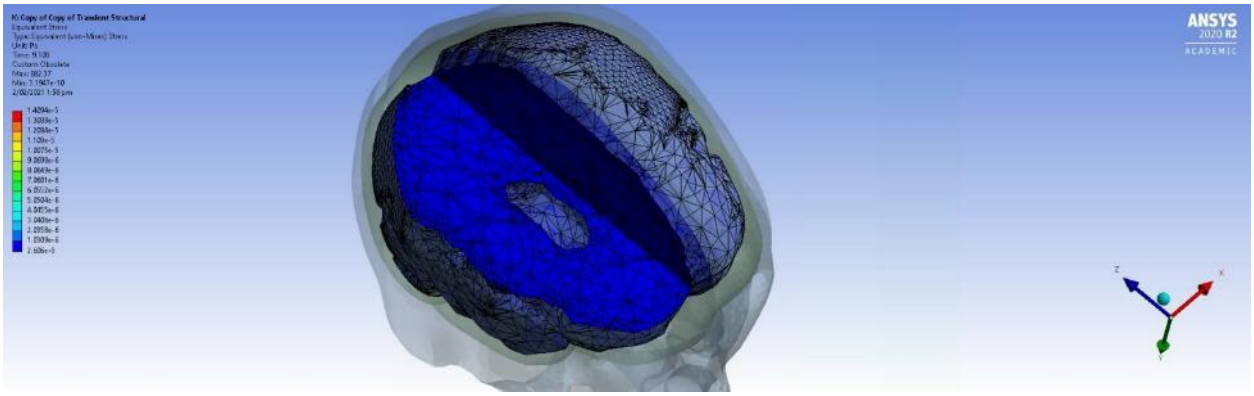
ANSYS
2020 R2
ACADEMIC

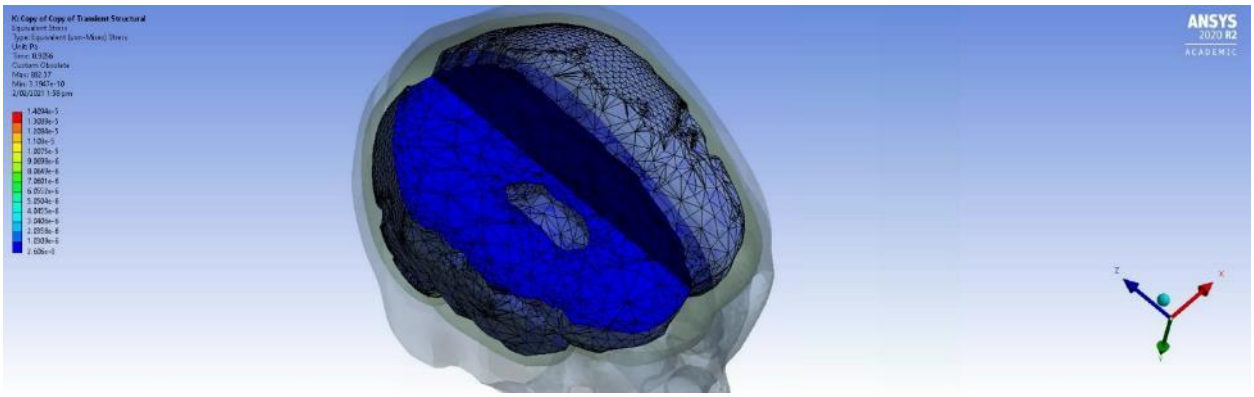
ANSYS
2020 R2
ACADEMIC

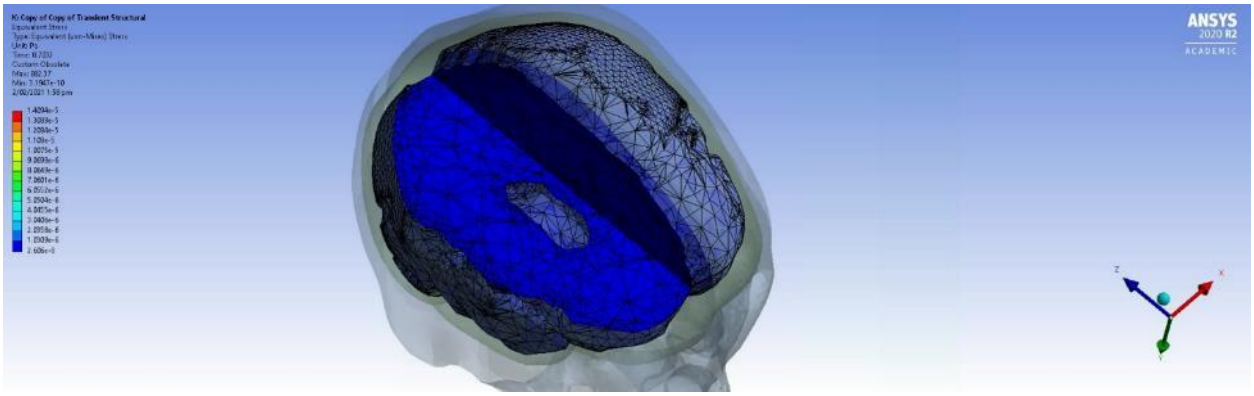
ANSYS
2020 R2
ACADEMIC

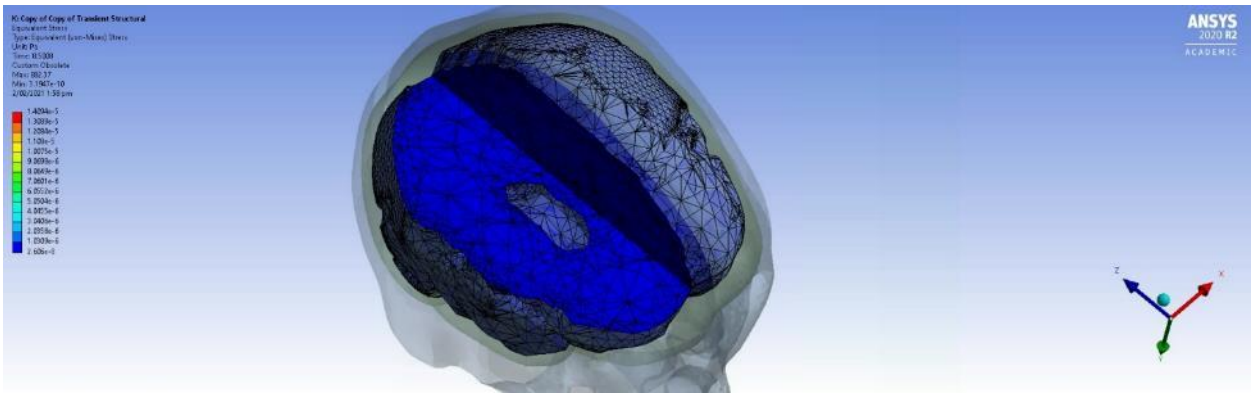
ANSYS
2020 R2
ACADEMIC

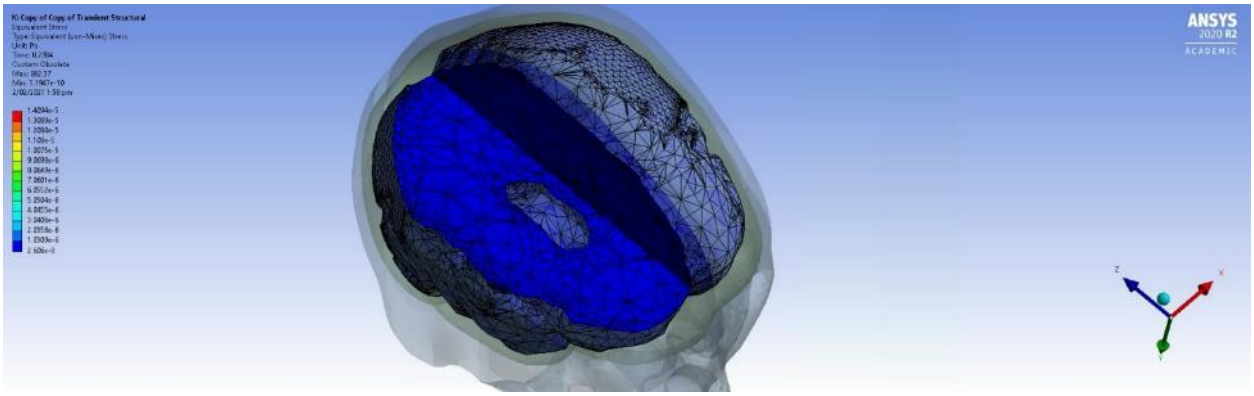
ANSYS
2020 R2
ACADEMIC

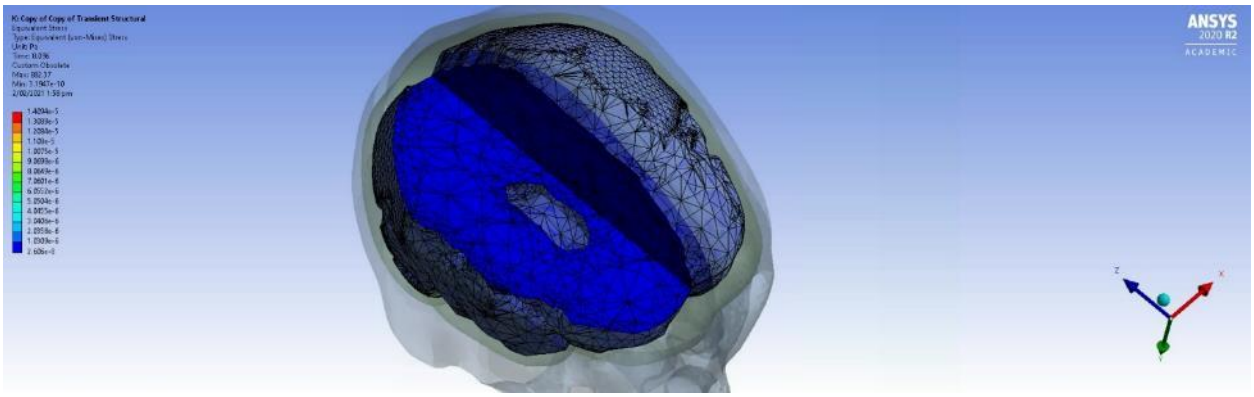
ANSYS
2020 R2
ACADEMIC

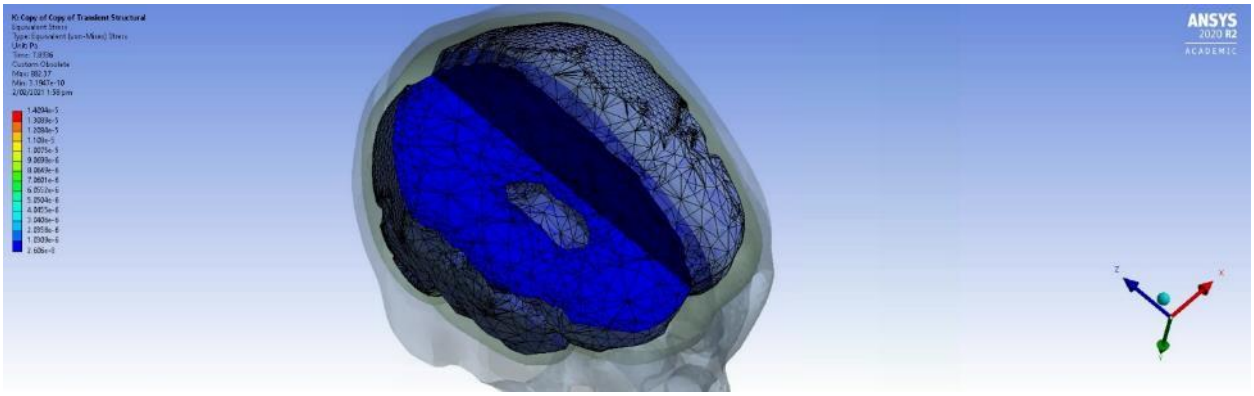
ANSYS
2020 R2
ACADEMIC

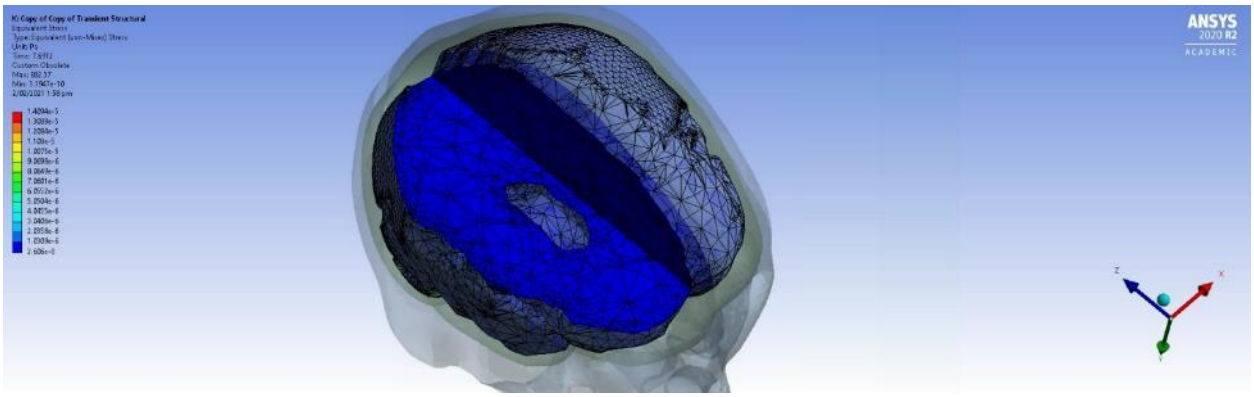
ANSYS
2020 R2
ACADEMIC

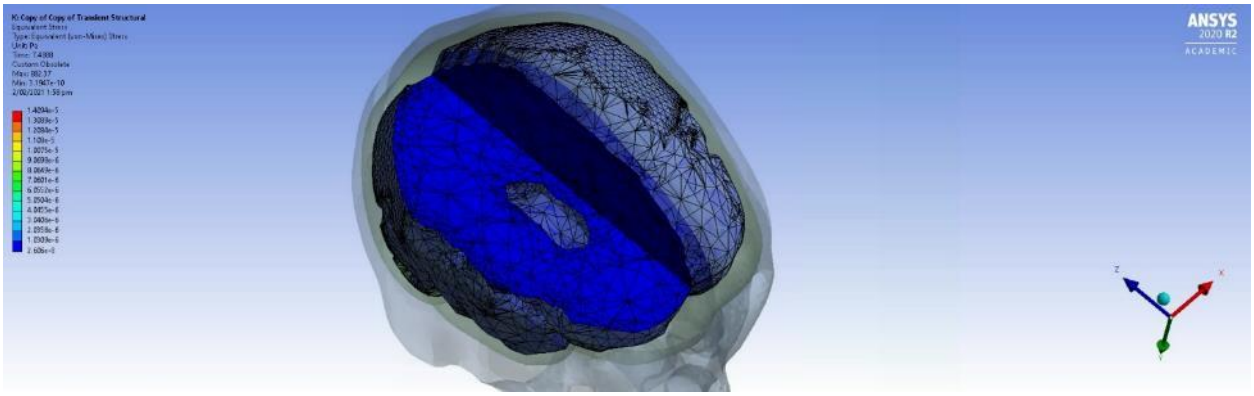
K: Copy of Copy of Transient Structural
Equivalent Stress
Type: Equivalent (von-Mises) Stress
Unit: Pa
Time: 7.4388
Custom Obsolete
Max: 882.37
Min: 3.1947e-10
2/02/2021 1:58 pm
1.4094e-5
1.3089e-5
1.2084e-5
1.108e-5
1.0075e-5
9.0699e-6
8.0649e-6
7.0601e-6
6.0552e-6
5.0504e-6
4.0455e-6
3.0406e-6
2.0358e-6
1.0309e-6
2.606e-8
ANSYS
2020 R2
ACADEMIC

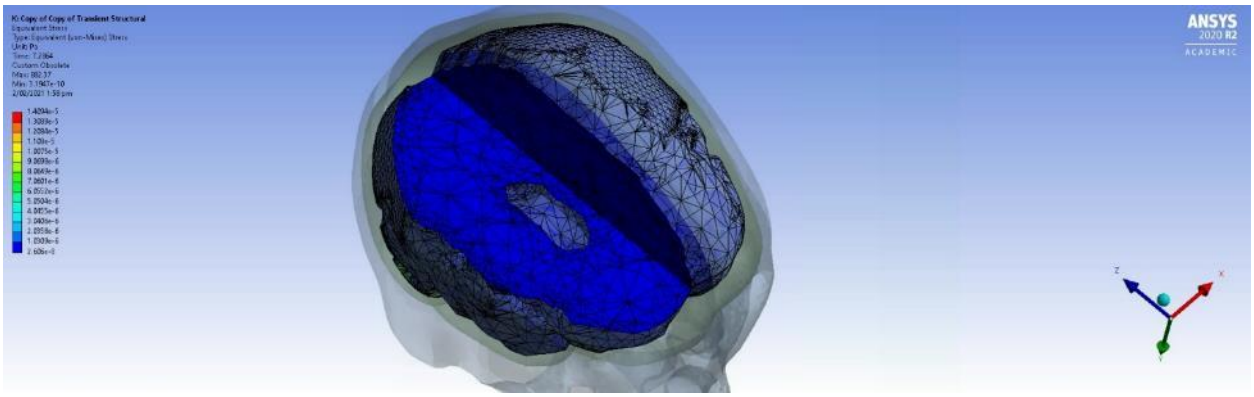
K: Copy of Copy of Transient Structural
Equivalent Stress
Type: Equivalent (von-Mises) Stress
Unit: Pa
Time: 7.2864
Custom Obsolete
Max: 882.37
Min: 3.1947e-10
2/02/2021 1:58 pm
1.4094e-5
1.3089e-5
1.2084e-5
1.108e-5
1.0075e-5
9.0699e-6
8.0649e-6
7.0601e-6
6.0552e-6
5.0504e-6
4.0455e-6
3.0406e-6
2.0358e-6
1.0309e-6
2.606e-8
ANSYS
2020 R2
ACADEMIC

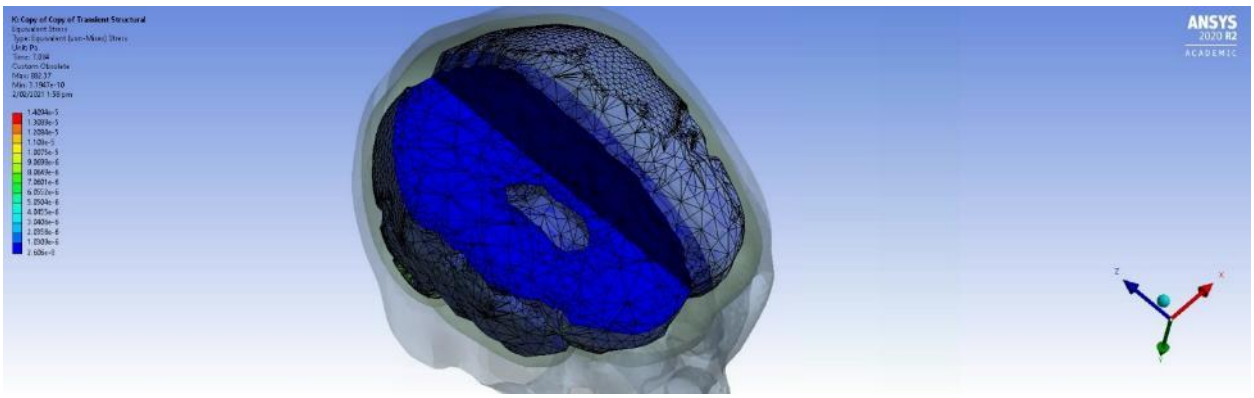
K: Copy of Copy of Transient Structural
Equivalent Stress
Type: Equivalent (von-Mises) Stress
Unit: Pa
Time: 7.894
Custom Obsolete
Max: 882.37
Min: 3.1947e-10
2/02/2021 1:58 pm
1.4094e-5
1.3089e-5
1.2084e-5
1.108e-5
1.0075e-5
9.0699e-6
8.0649e-6
7.0601e-6
6.0552e-6
5.0504e-6
4.0455e-6
3.0406e-6
2.0358e-6
1.0309e-6
2.606e-8
ANSYS
2020 R2
ACADEMIC

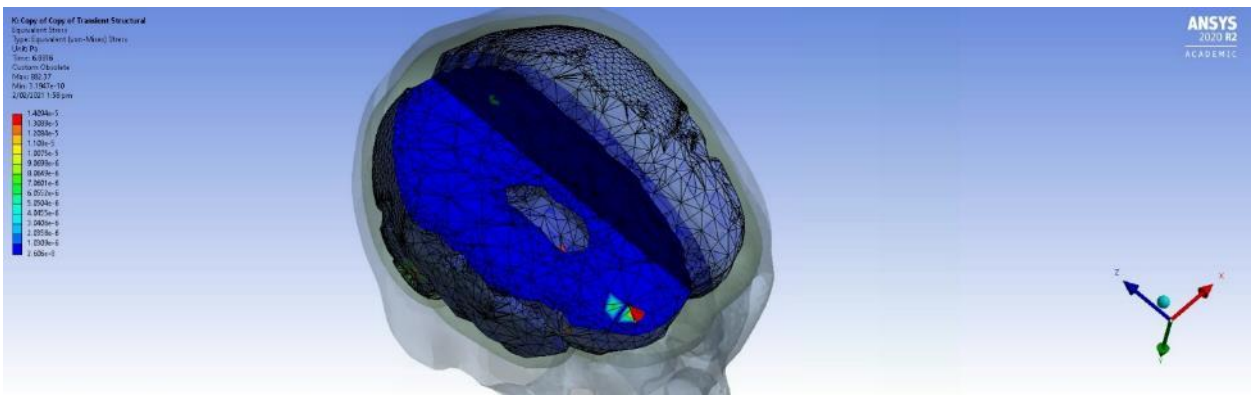
K: Copy of Copy of Transient Structural
Equivalent Stress
Type: Equivalent (von-Mises) Stress
Unit: Pa
Time: 6.9316
Custom Obsolete
Max: 882.37
Min: 3.1947e-10
2/02/2021 1:58 pm
1.4094e-5
1.3089e-5
1.2084e-5
1.108e-5
1.0075e-5
9.0699e-6
8.0649e-6
7.0601e-6
6.0552e-6
5.0504e-6
4.0455e-6
3.0406e-6
2.0358e-6
1.0309e-6
2.606e-8
ANSYS
2020 R2
ACADEMIC

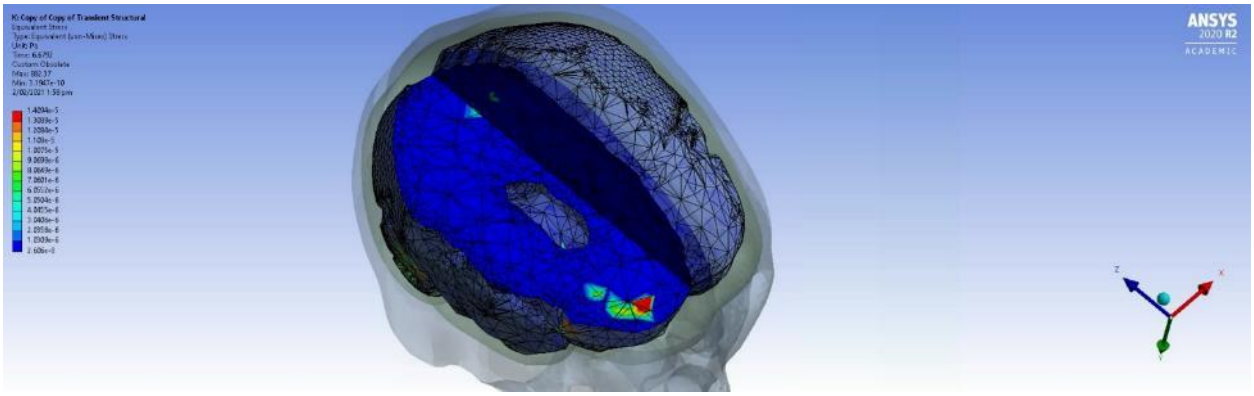
ANSYS
2020 R2
ACADEMIC

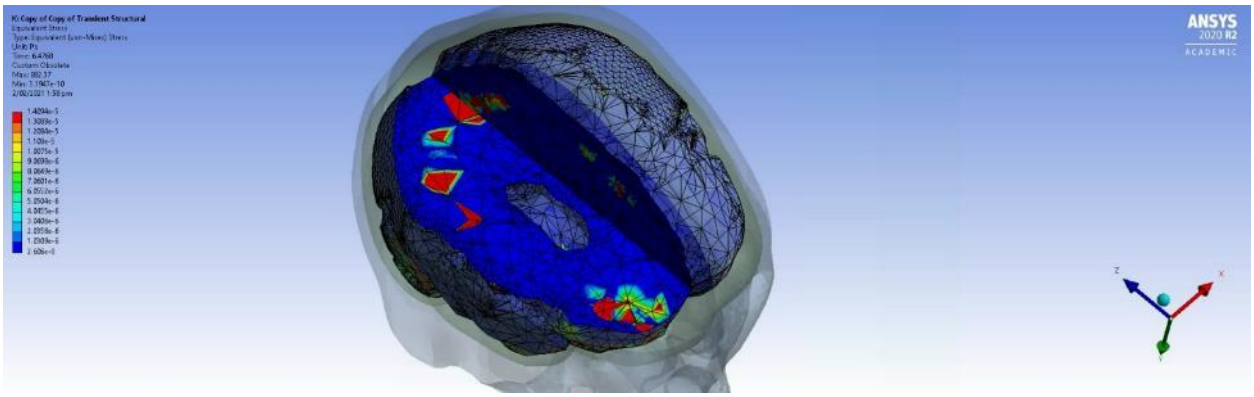
ANSYS
2020 R2
ACADEMIC

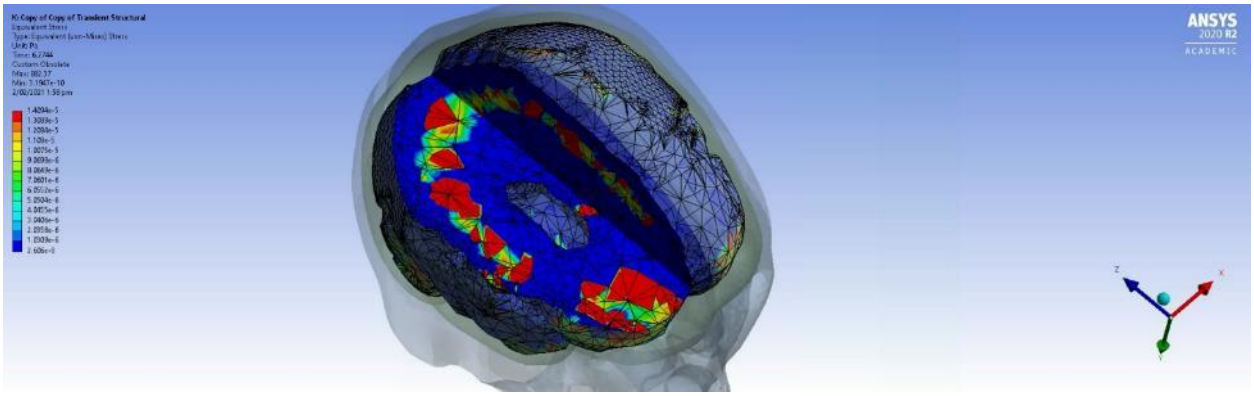
ANSYS
2020 R2
ACADEMIC

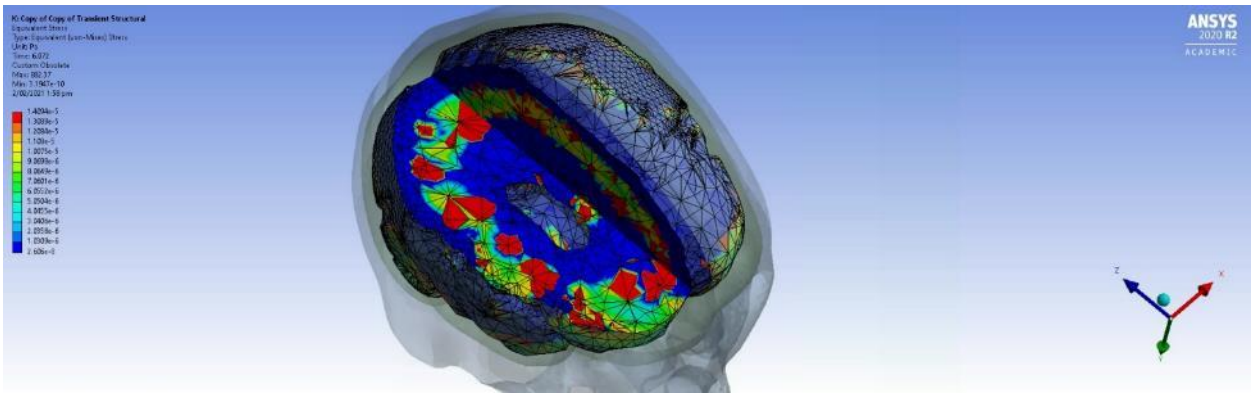
ANSYS
2020 R2
ACADEMIC

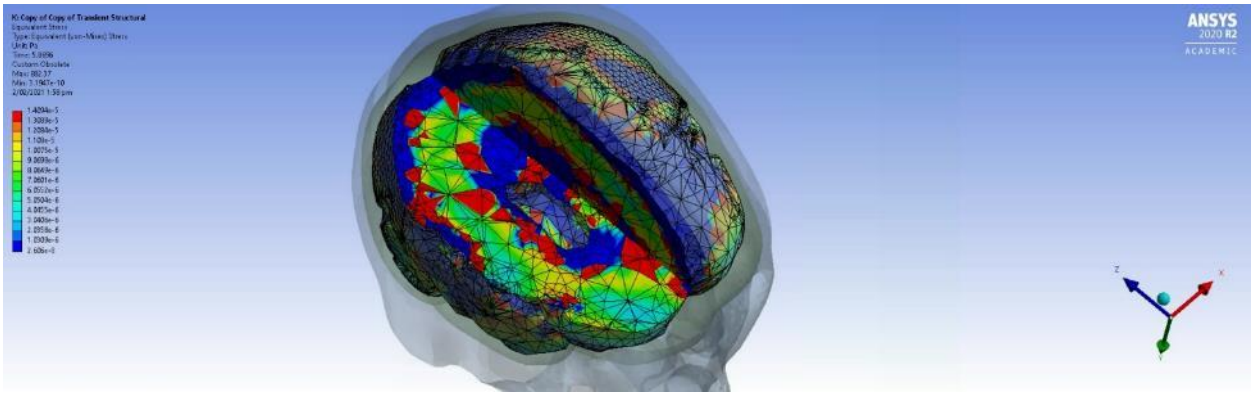
ANSYS
2020 R2
ACADEMIC

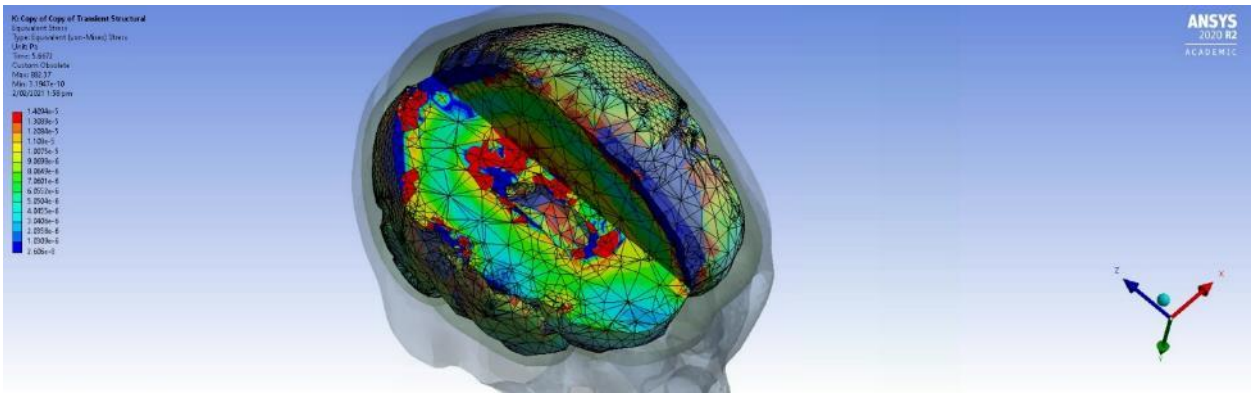
ANSYS
2020 R2
ACADEMIC

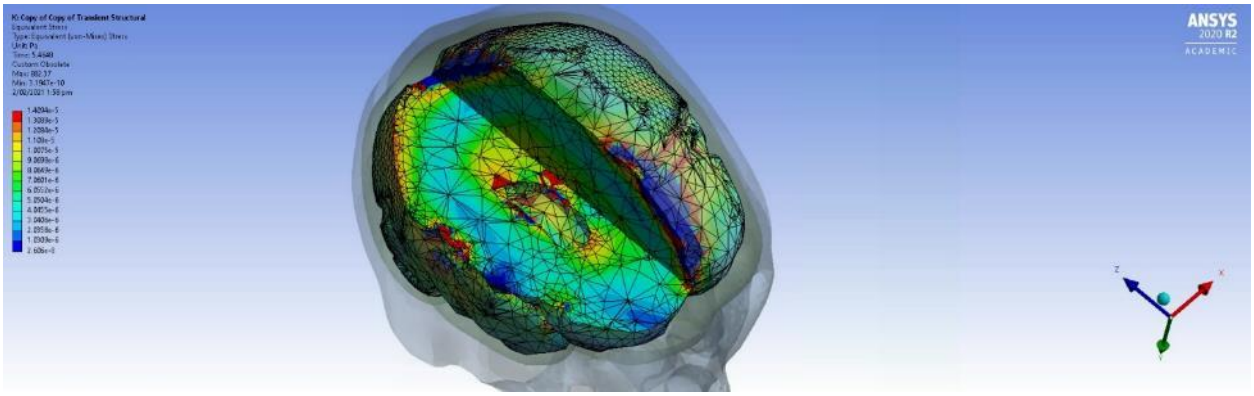
ANSYS
2020 R2
ACADEMIC

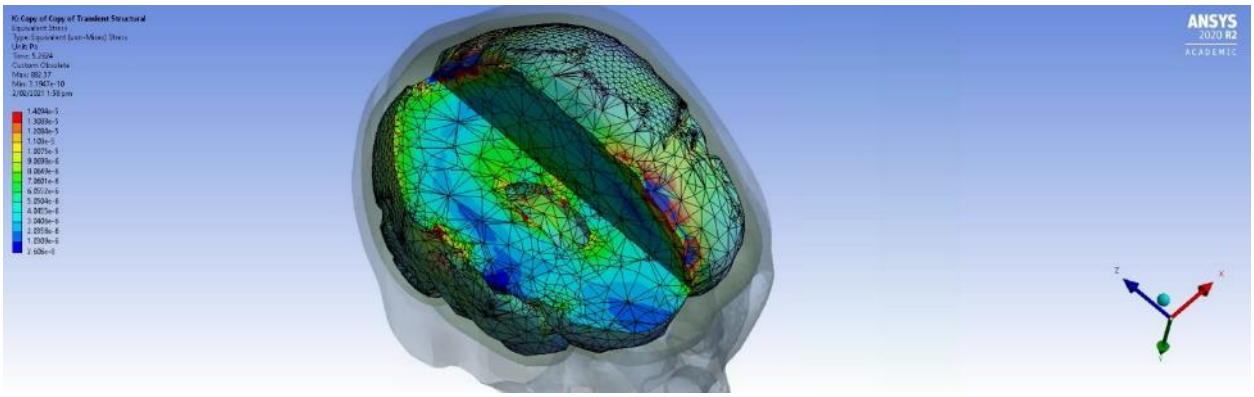
ANSYS
2020 R2
ACADEMIC

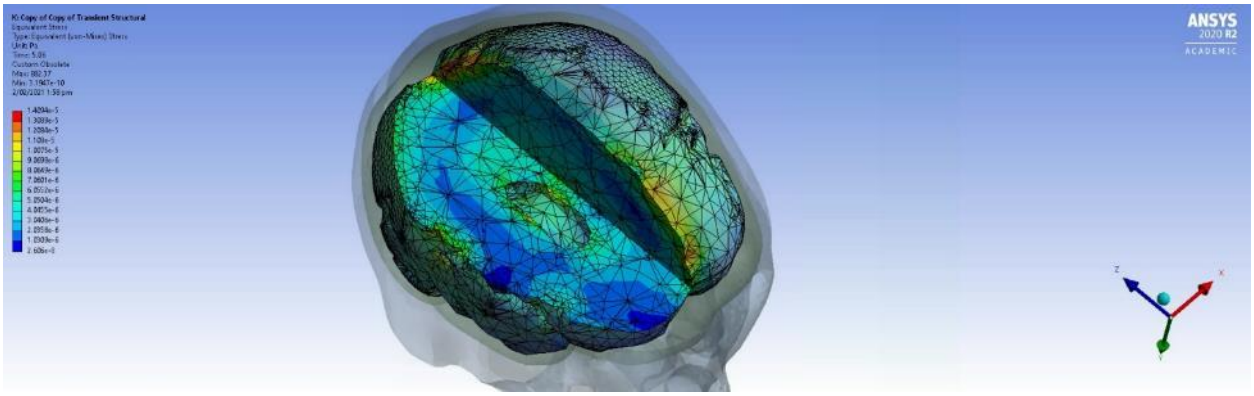
K: Copy of Copy of Transient Structural
Equivalent Stress
Type: Equivalent (von-Mises) Stress
Unit: Pa
Time: 5.08
Custom Obsolete
Max: 882.37
Min: 3.1947e-10
2/02/2021 1:58 pm
1.4094e-5
1.3089e-5
1.2084e-5
1.108e-5
1.0075e-5
9.0699e-6
8.0649e-6
7.0601e-6
6.0552e-6
5.0504e-6
4.0455e-6
3.0406e-6
2.0358e-6
1.0309e-6
2.606e-8
ANSYS
2020 R2
ACADEMIC

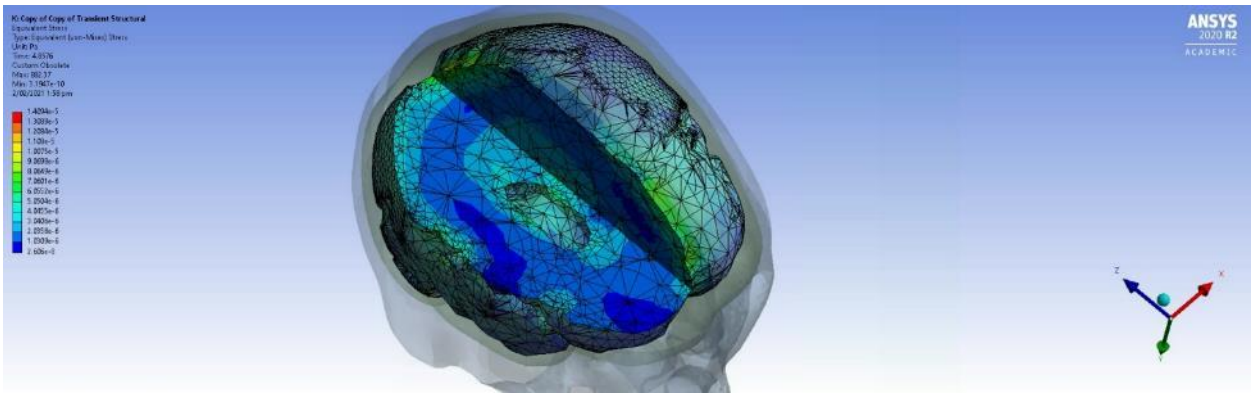
K: Copy of Copy of Transient Structural
Equivalent Stress
Type: Equivalent (von-Mises) Stress
Unit: Pa
Time: 4.8576
Custom Obsolete
Max: 882.37
Min: 3.1947e-10
2/02/2021 1:58 pm
1.4094e-5
1.3089e-5
1.2084e-5
1.108e-5
1.0075e-5
9.0699e-6
8.0649e-6
7.0601e-6
6.0552e-6
5.0504e-6
4.0455e-6
3.0406e-6
2.0358e-6
1.0309e-6
2.606e-8
ANSYS
2020 R2
ACADEMIC

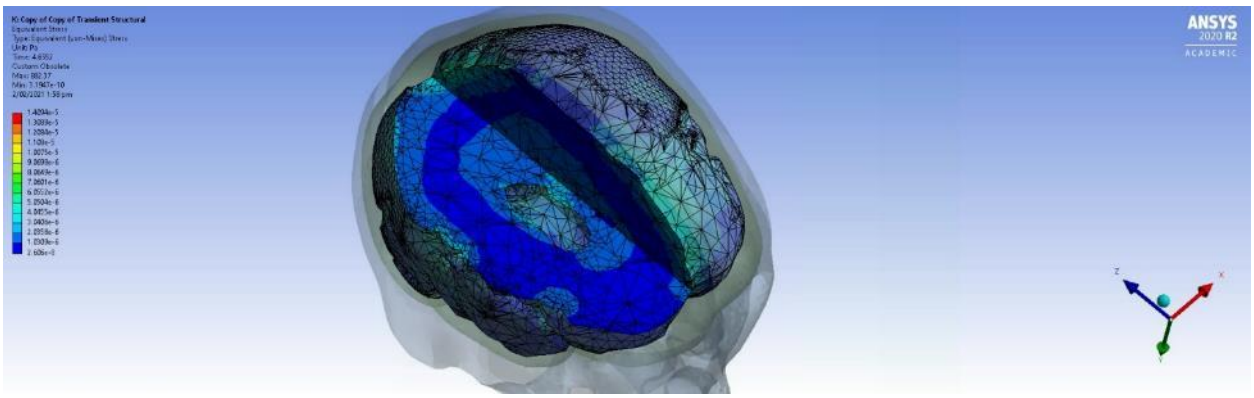
K: Copy of Copy of Transient Structural
Equivalent Stress
Type: Equivalent (von-Mises) Stress
Unit: Pa
Time: 4.8352
Custom Obsolete
Max: 882.37
Min: 3.1947e-10
2/02/2021 1:58 pm
1.4094e-5
1.3089e-5
1.2084e-5
1.108e-5
1.0075e-5
9.0699e-6
8.0649e-6
7.0601e-6
6.0552e-6
5.0504e-6
4.0455e-6
3.0406e-6
2.0358e-6
1.0309e-6
2.606e-8
ANSYS
2020 R2
ACADEMIC

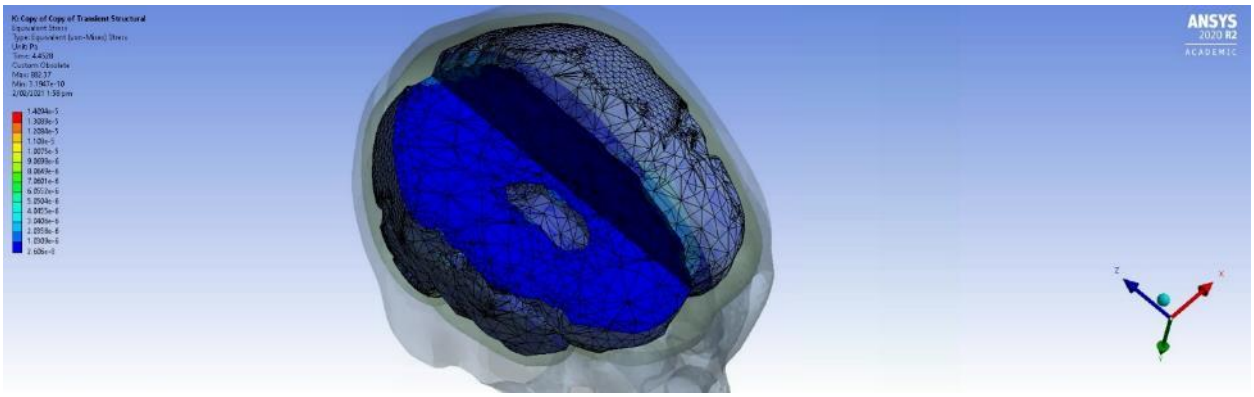
K: Copy of Copy of Transient Structural
Equivalent Stress
Type: Equivalent (von-Mises) Stress
Unit: Pa
Time: 4.4928
Custom Obsolete
Max: 882.37
Min: 3.1947e-10
2/02/2021 1:58 pm
1.4094e-5
1.3089e-5
1.2084e-5
1.108e-5
1.0075e-5
9.0699e-6
8.0649e-6
7.0601e-6
6.0552e-6
5.0504e-6
4.0455e-6
3.0406e-6
2.0358e-6
1.0309e-6
2.606e-8
ANSYS
2020 R2
ACADEMIC

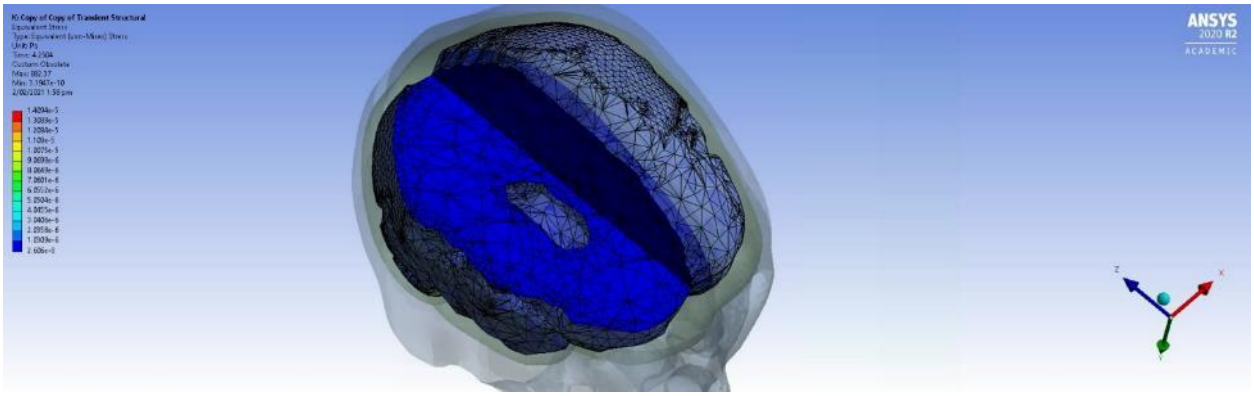
ANSYS
2020 R2
ACADEMIC

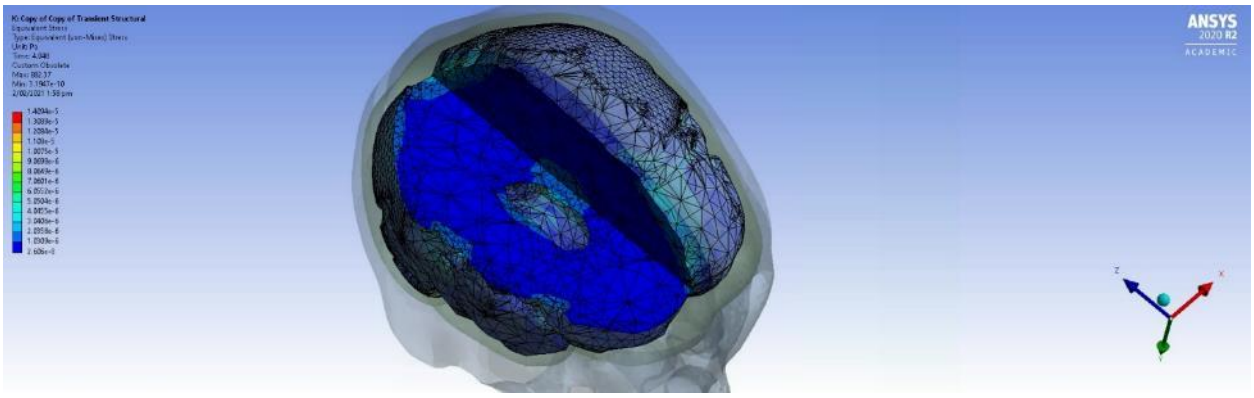
ANSYS
2020 R2
ACADEMIC

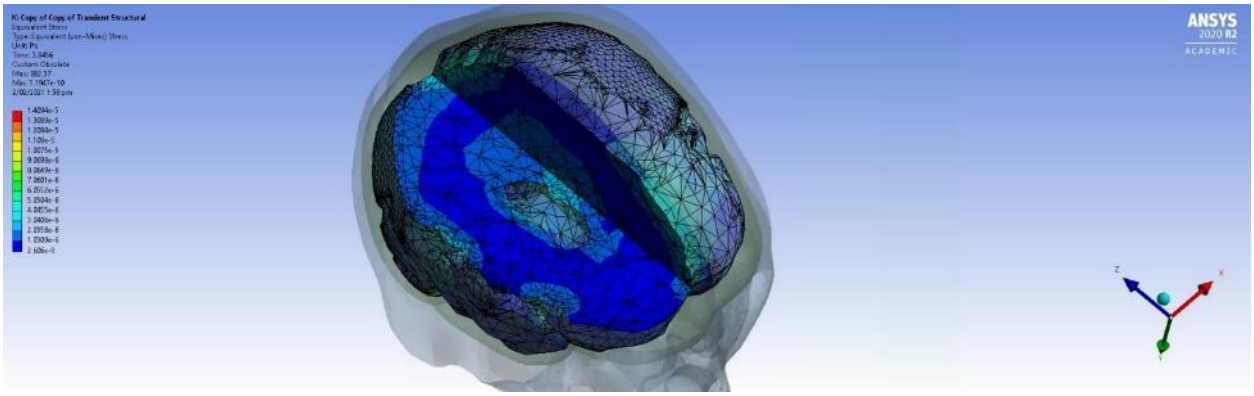
ANSYS
2020 R2
ACADEMIC

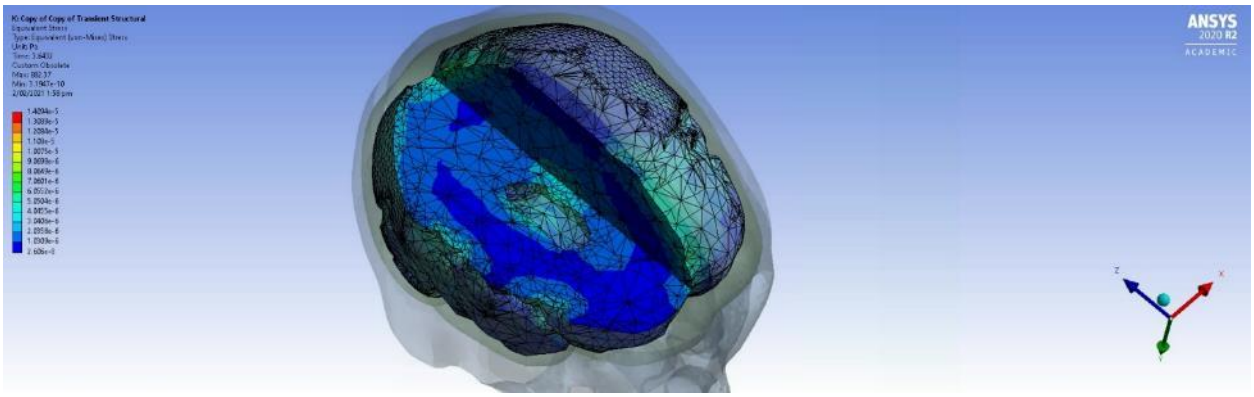
ANSYS
2020 R2
ACADEMIC

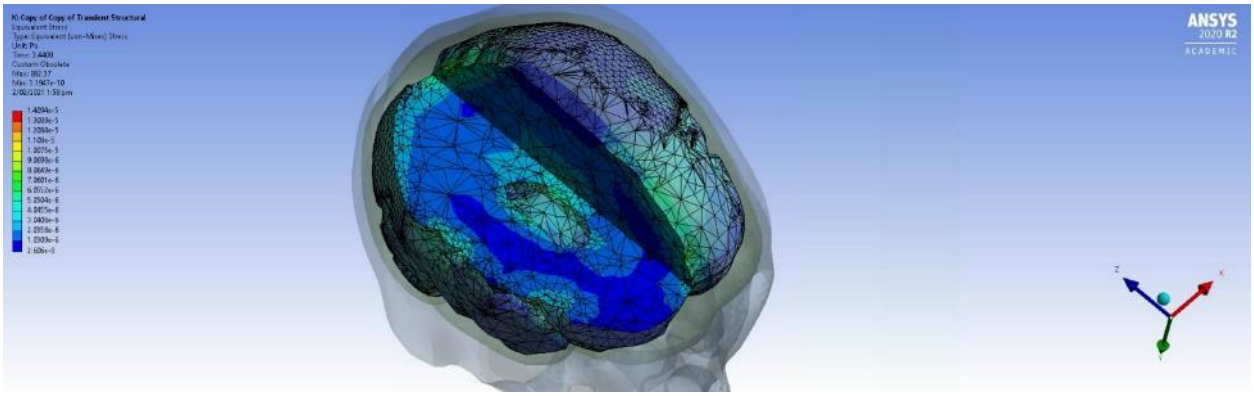
ANSYS
2020 R2
ACADEMIC

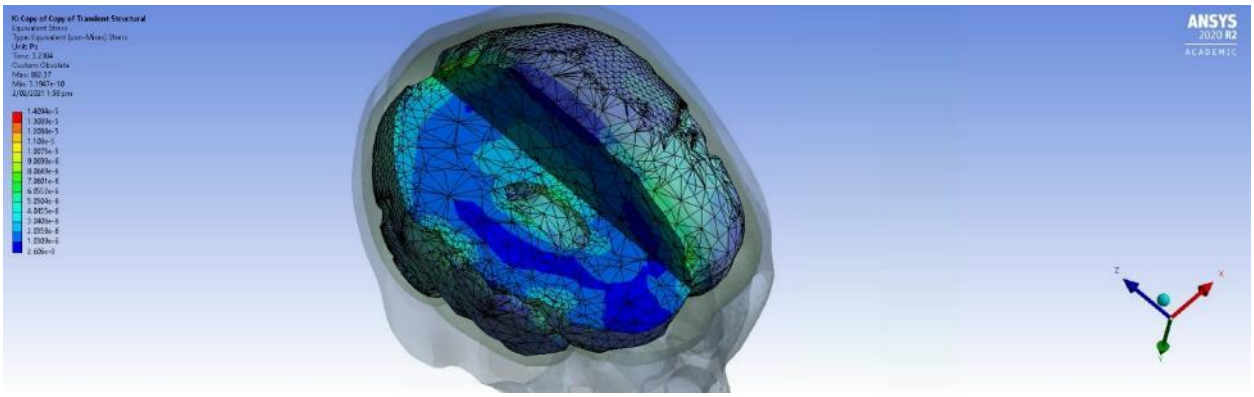
ANSYS
2020 R2
ACADEMIC

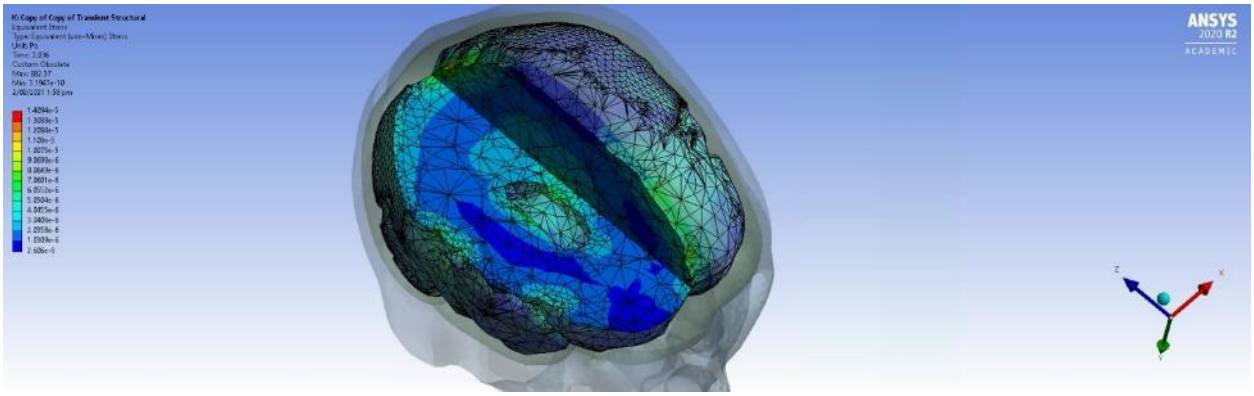
ANSYS
2020 R2
ACADEMIC

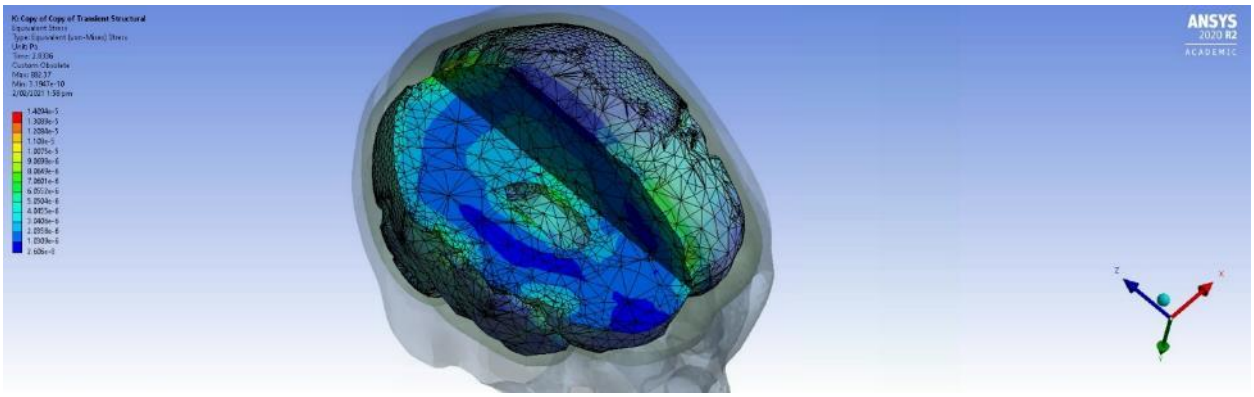
ANSYS
2020 R2
ACADEMIC

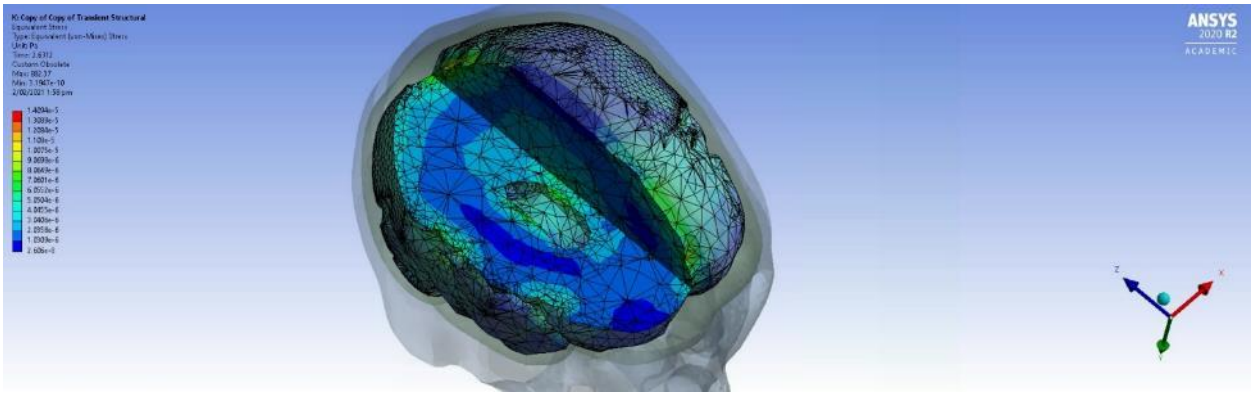
ANSYS
2020 R2
ACADEMIC

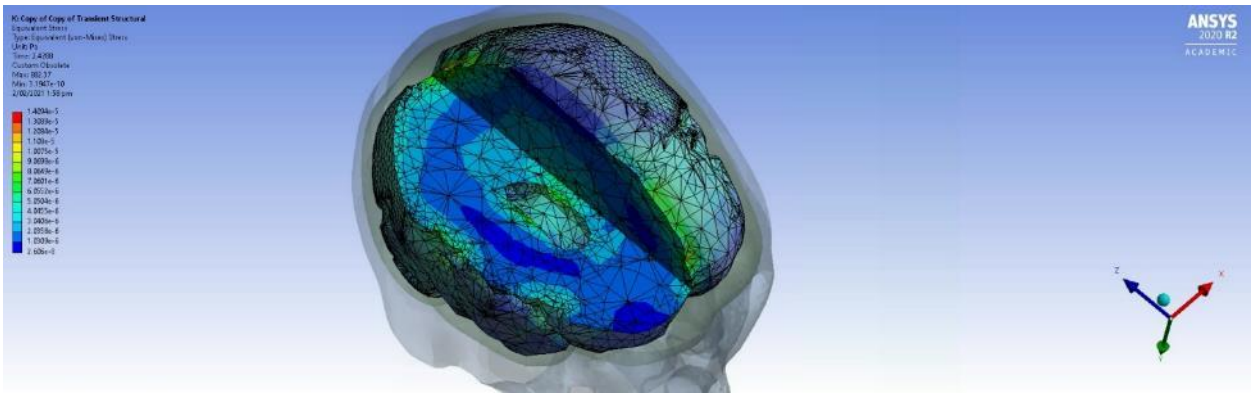
ANSYS
2020 R2
ACADEMIC

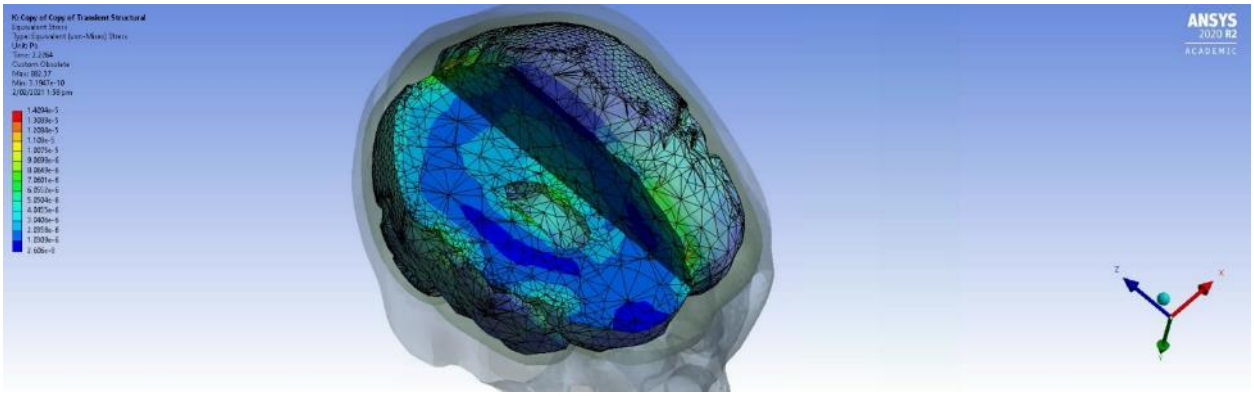
ANSYS
2020 R2
ACADEMIC

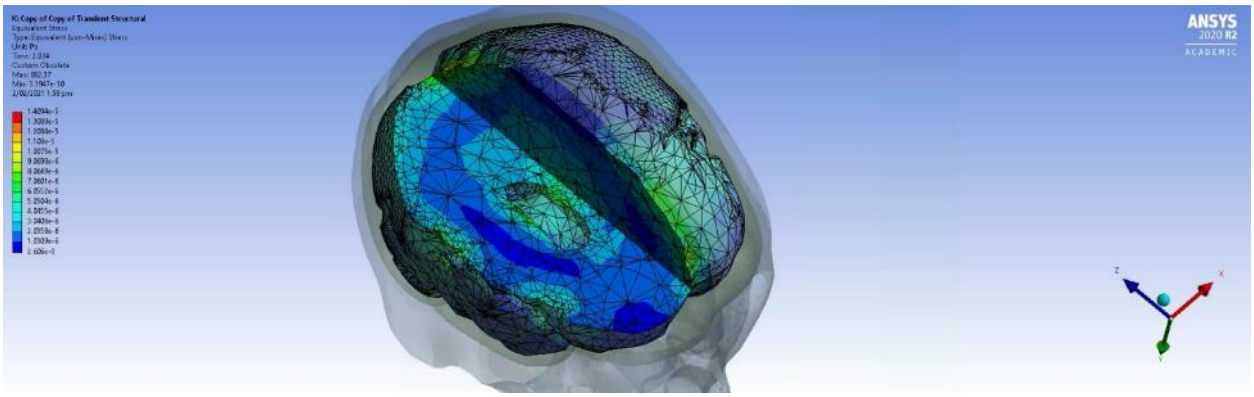
ANSYS
2020 R2
ACADEMIC

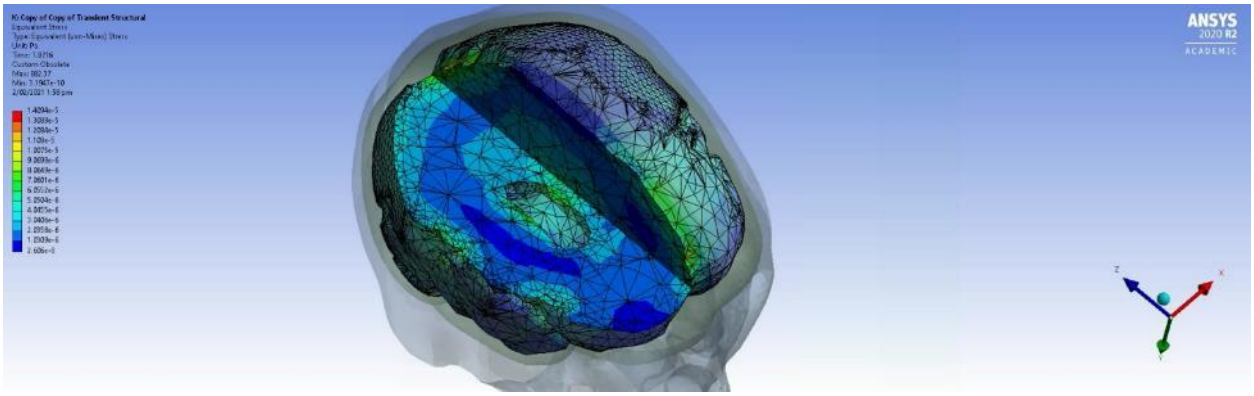
ANSYS
2020 R2
ACADEMIC

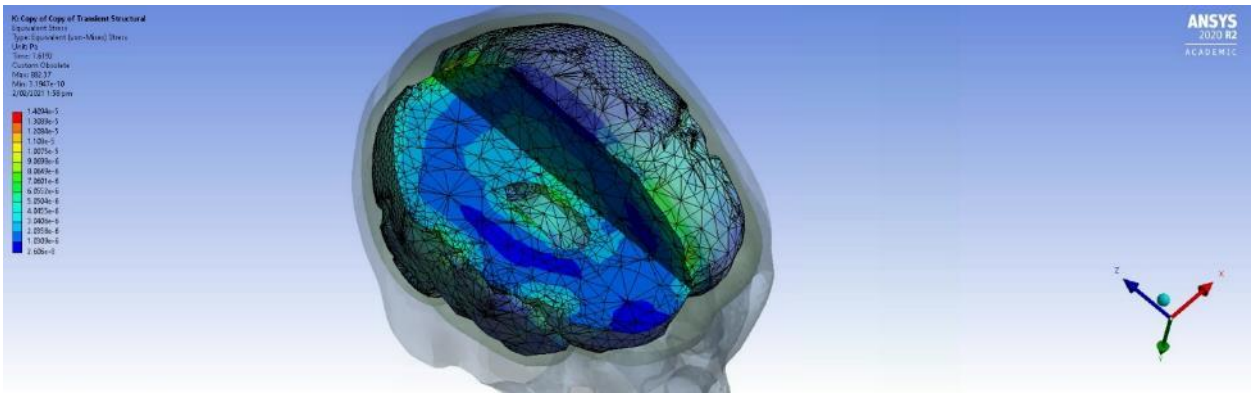
ANSYS
2020 R2
ACADEMIC

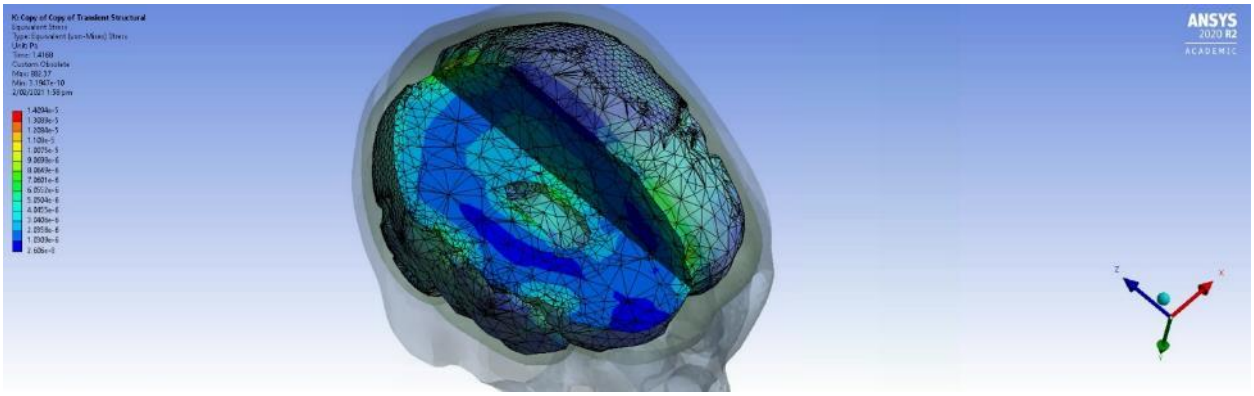
ANSYS
2020 R2
ACADEMIC

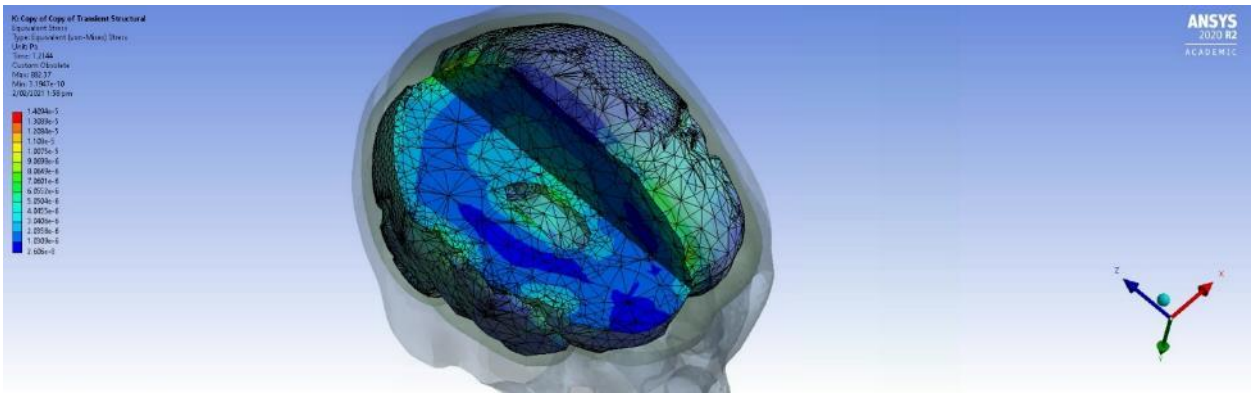
ANSYS
2020 R2
ACADEMIC

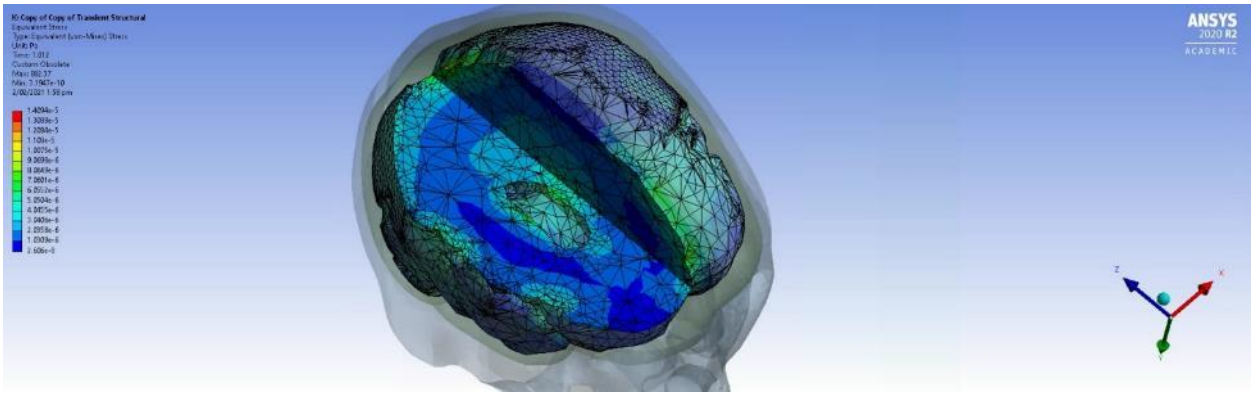
ANSYS
2020 R2
ACADEMIC

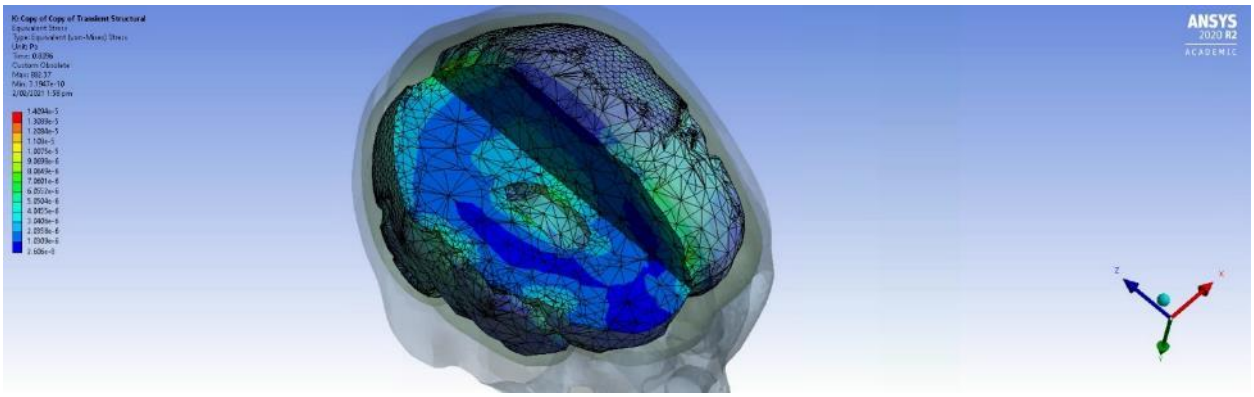
ANSYS
2020 R2
ACADEMIC

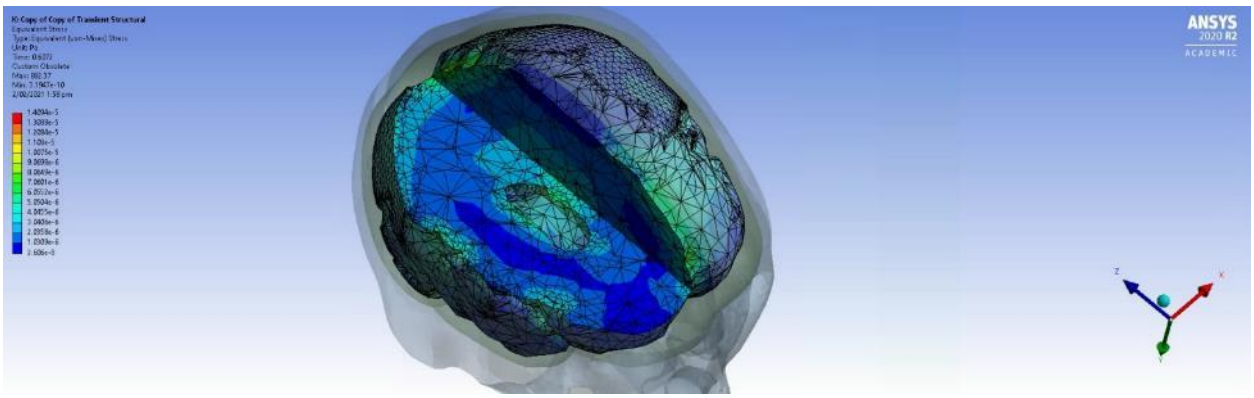
ANSYS
2020 R2
ACADEMIC

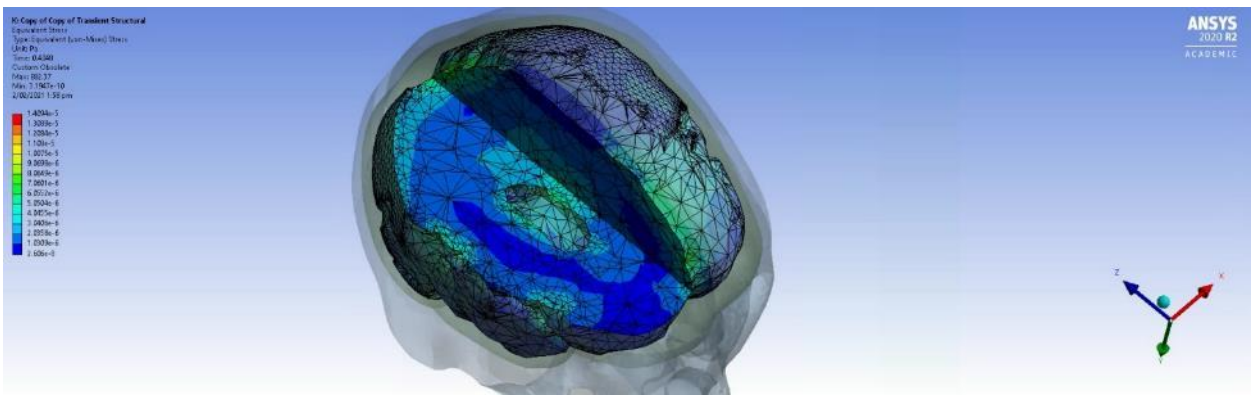
ANSYS
2020 R2
ACADEMIC

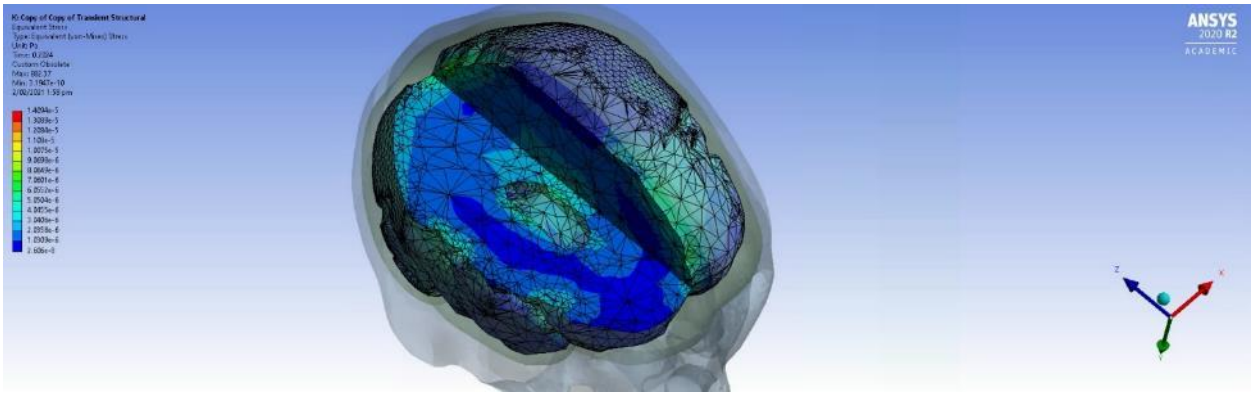
ANSYS
2020 R2
ACADEMIC

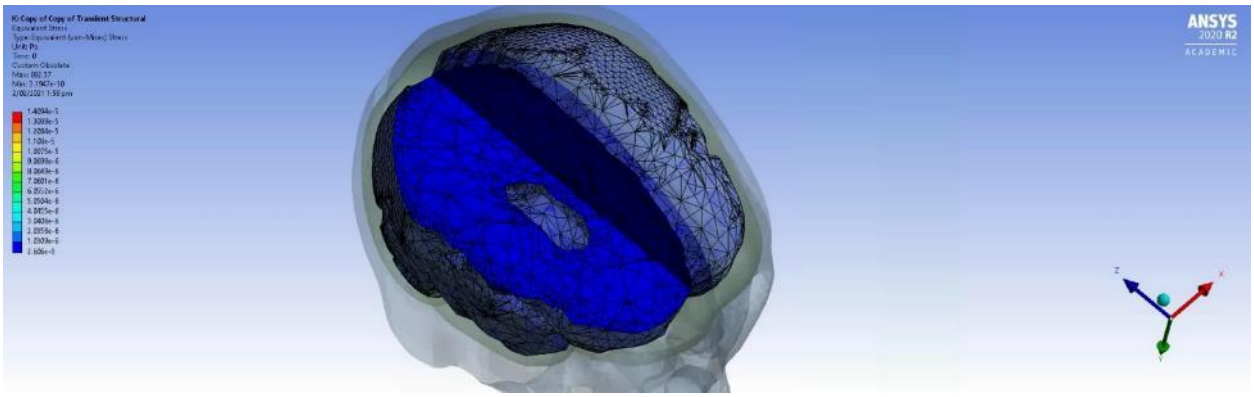
ANSYS
2020 R2
ACADEMIC

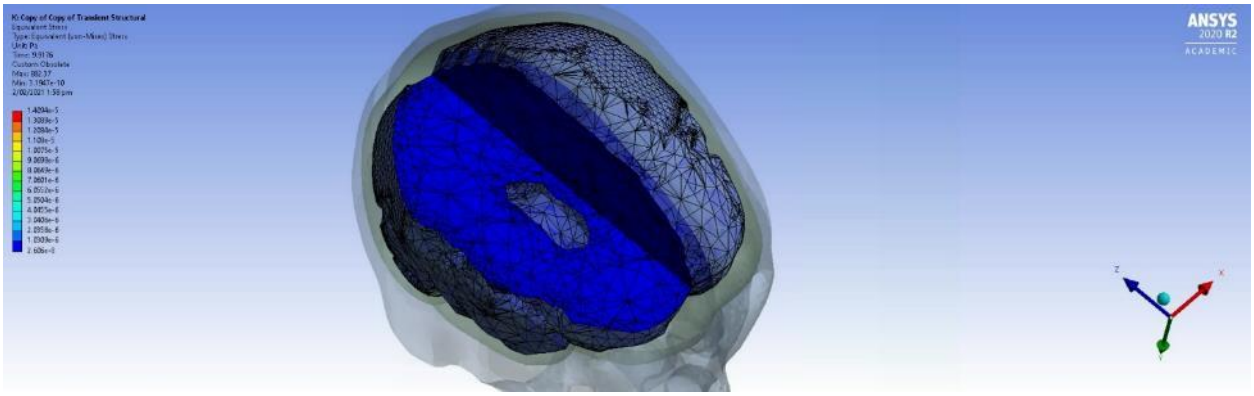
ANSYS
2020 R2
ACADEMIC

Impact Zone 2

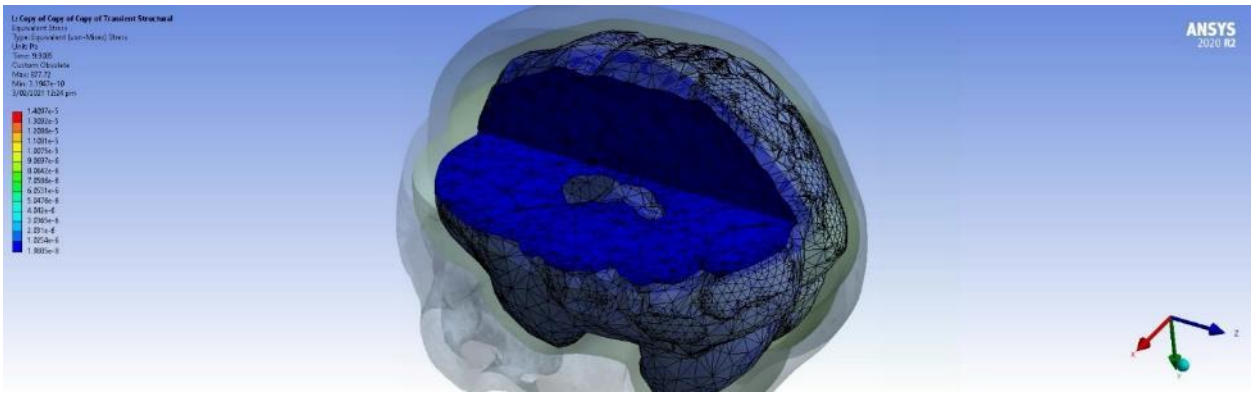

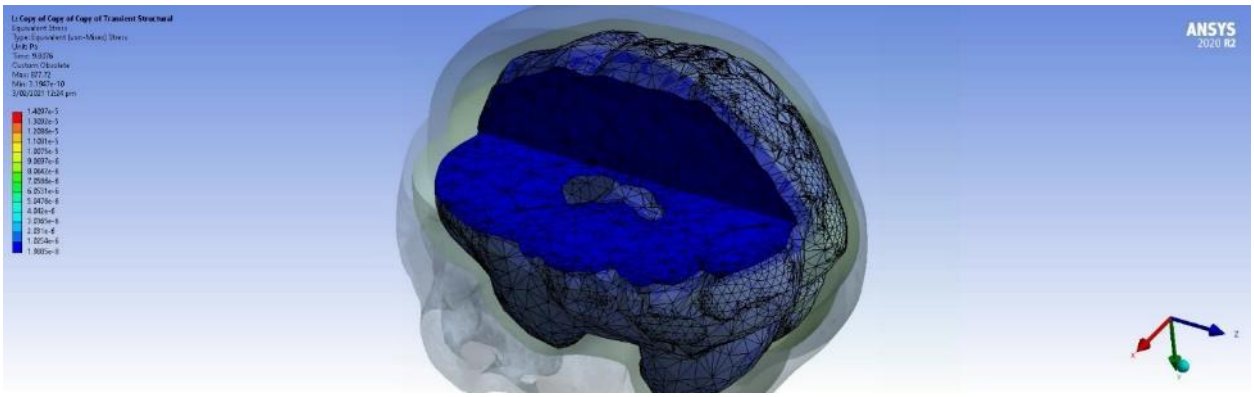

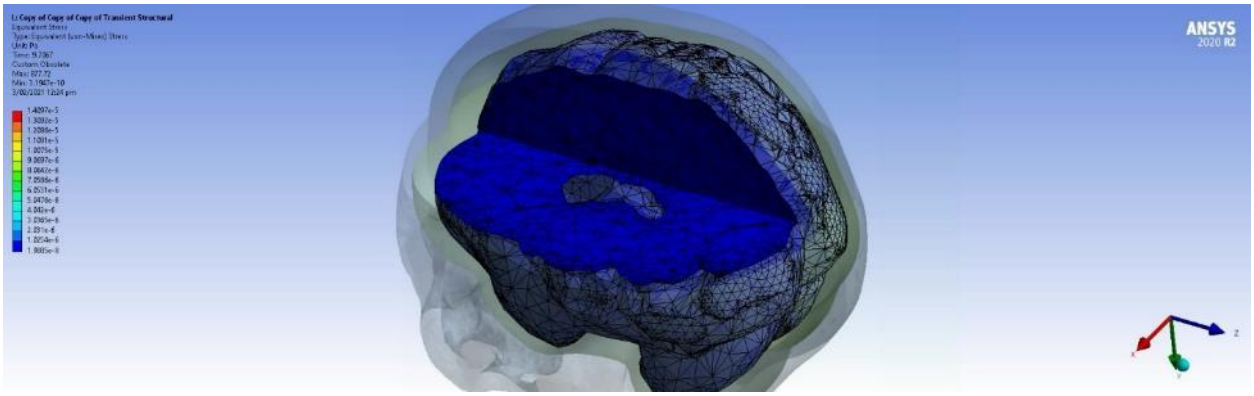

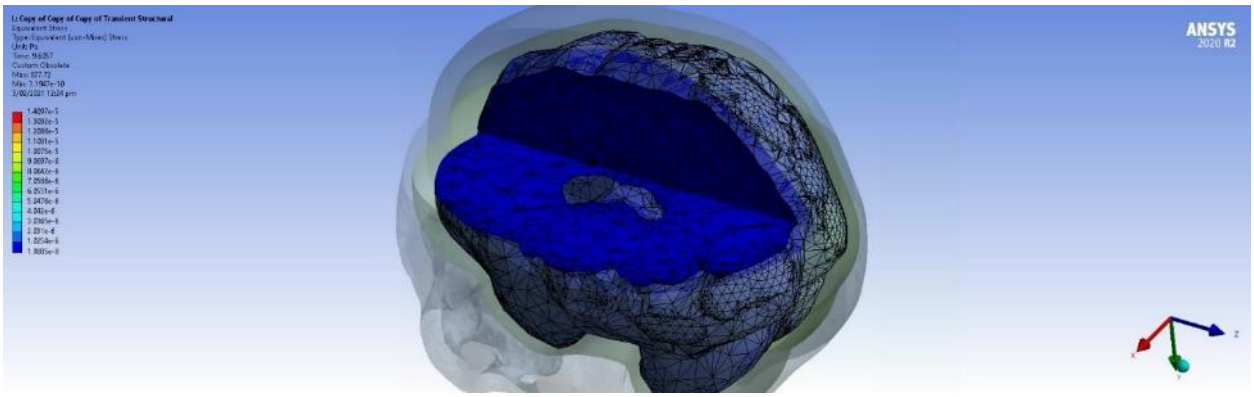

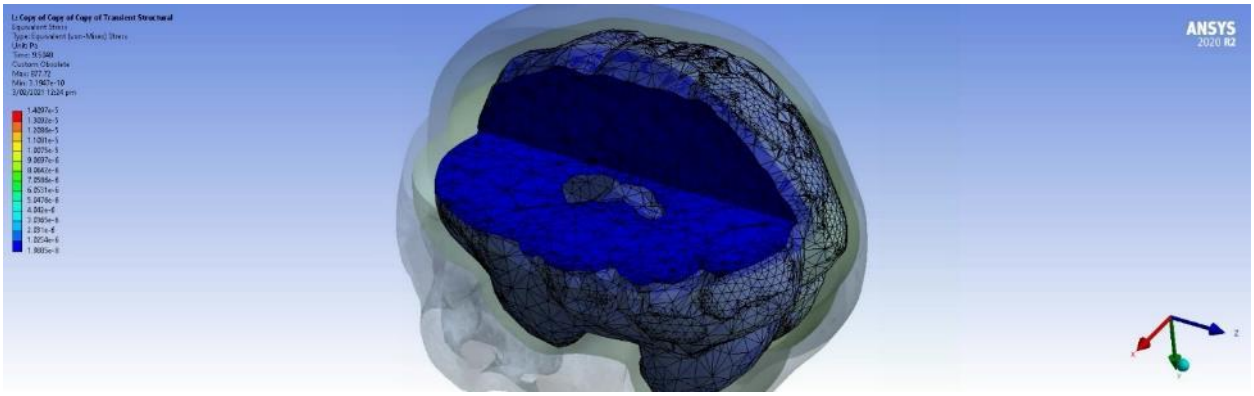
ANSYS
2020 R2

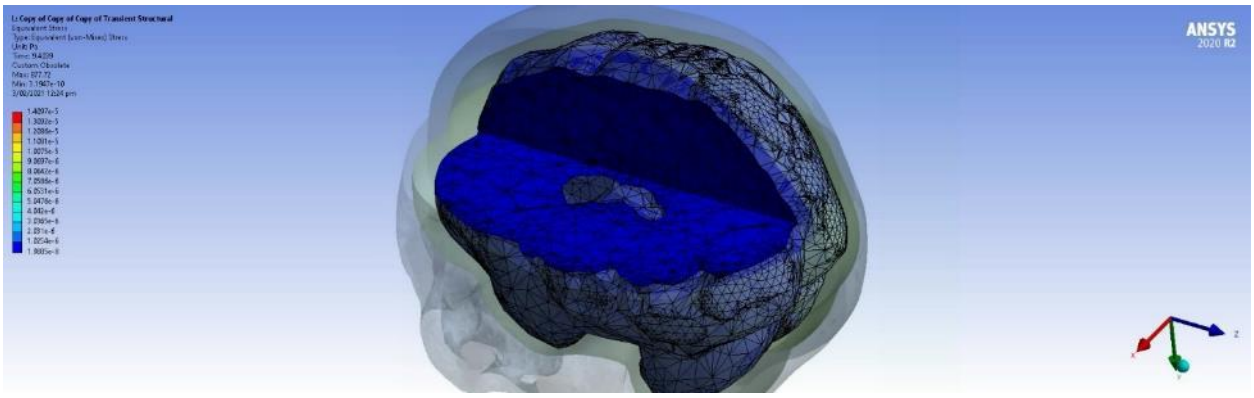
ANSYS
2020 R2

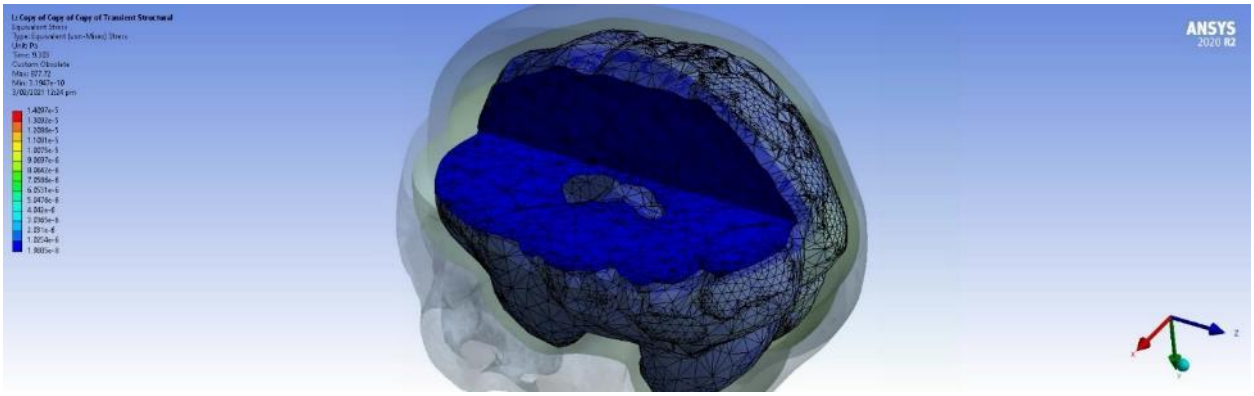
ANSYS
2020 R2

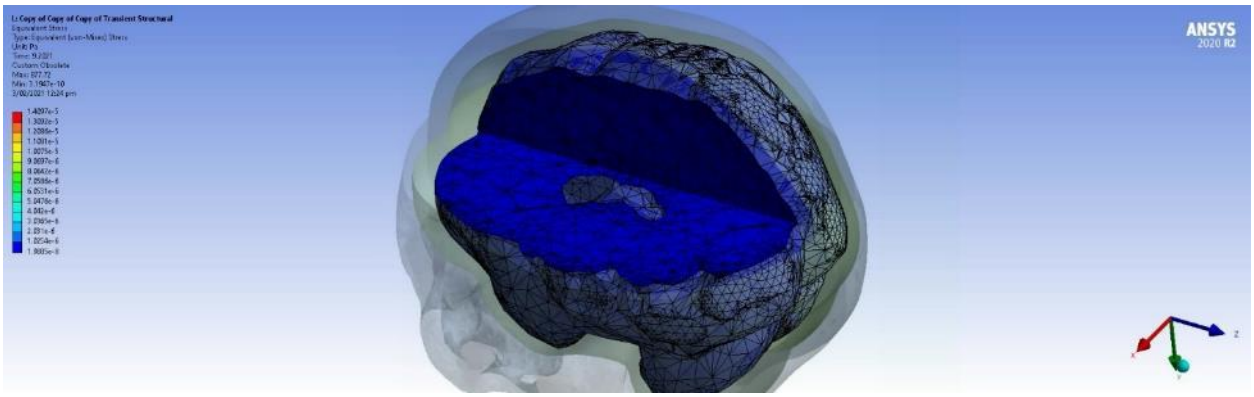
ANSYS
2020 R2

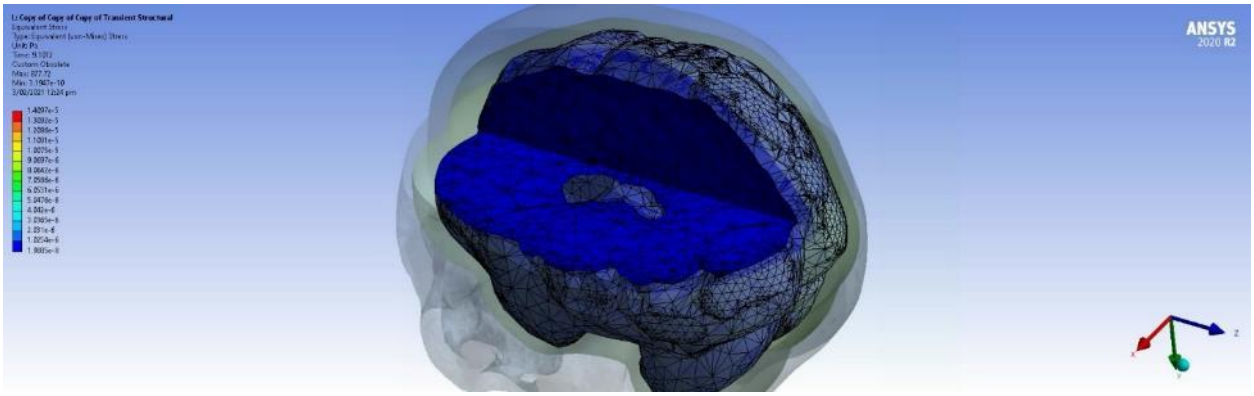
ANSYS
2020 R2

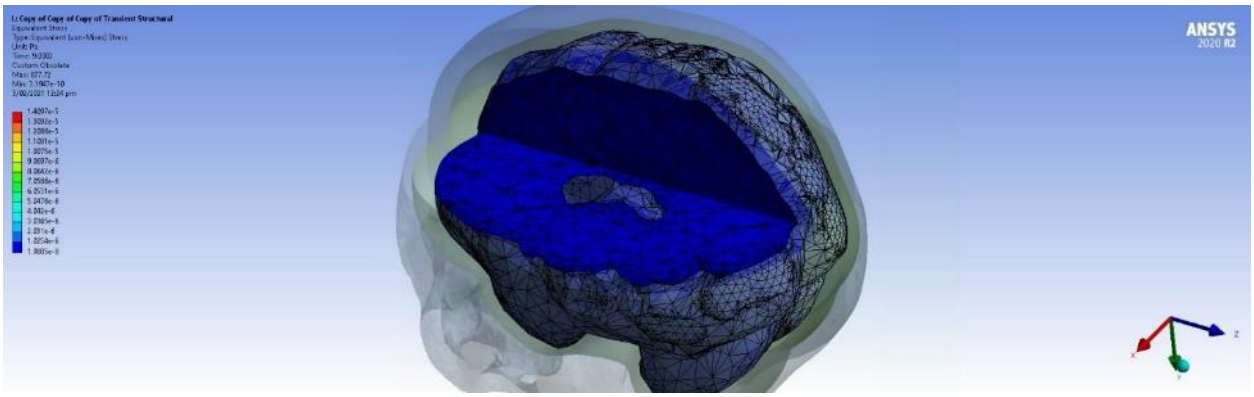
ANSYS
2020 R2

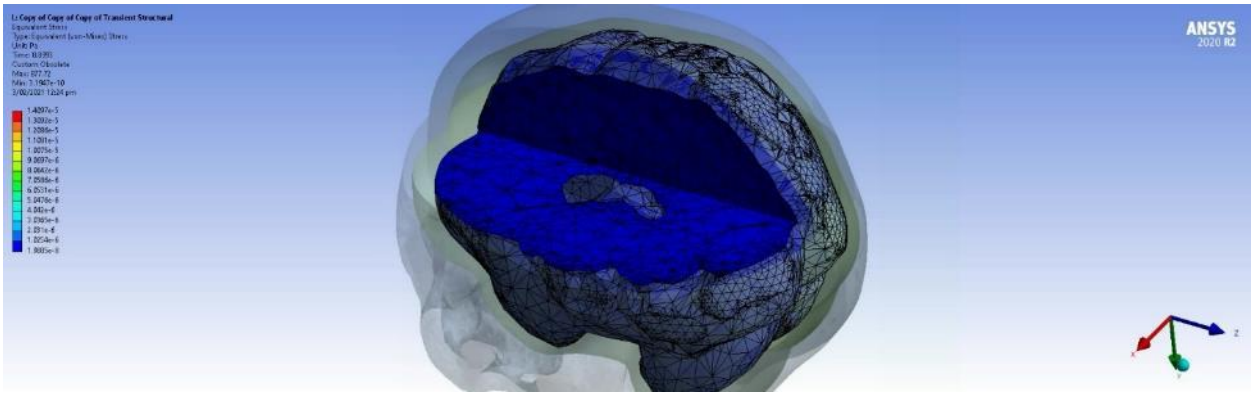
ANSYS
2020 R2

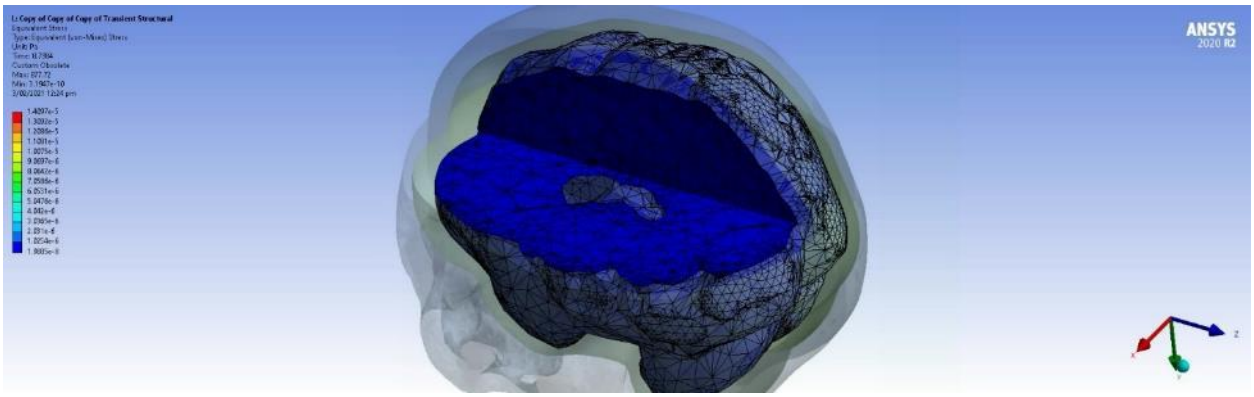
ANSYS
2020 R2

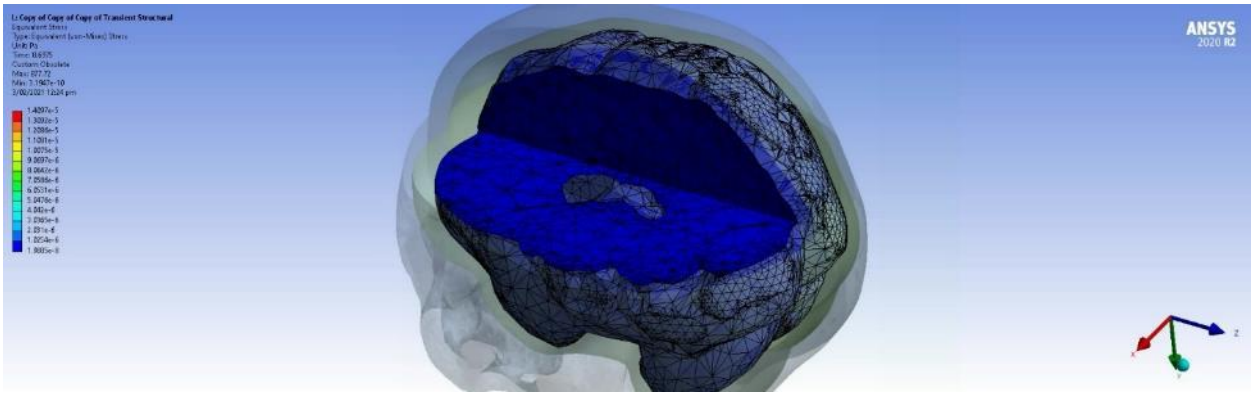
ANSYS
2020 R2

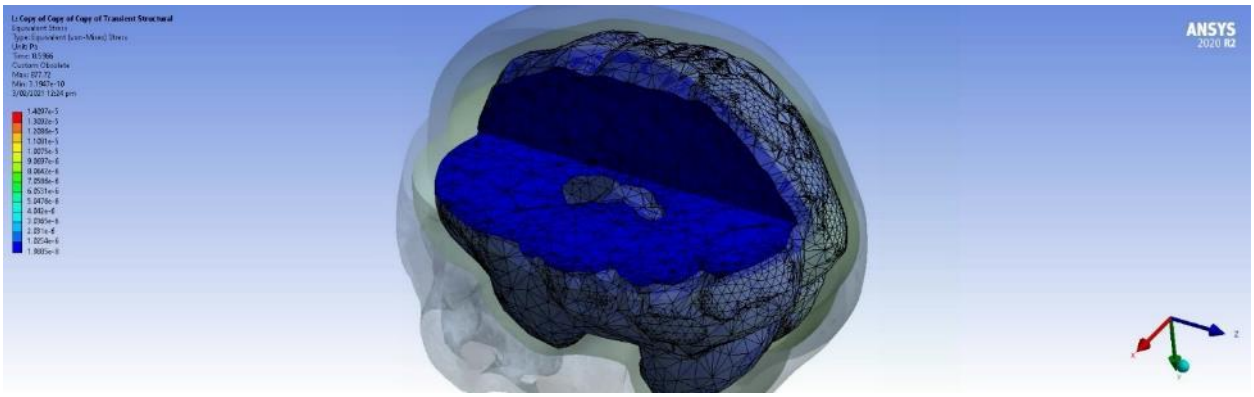
ANSYS
2020 R2

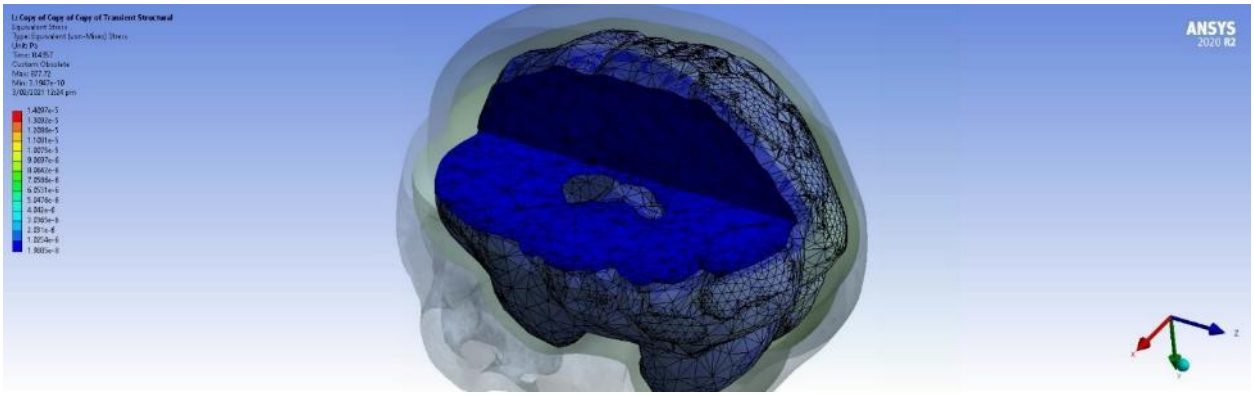
ANSYS
2020 R2

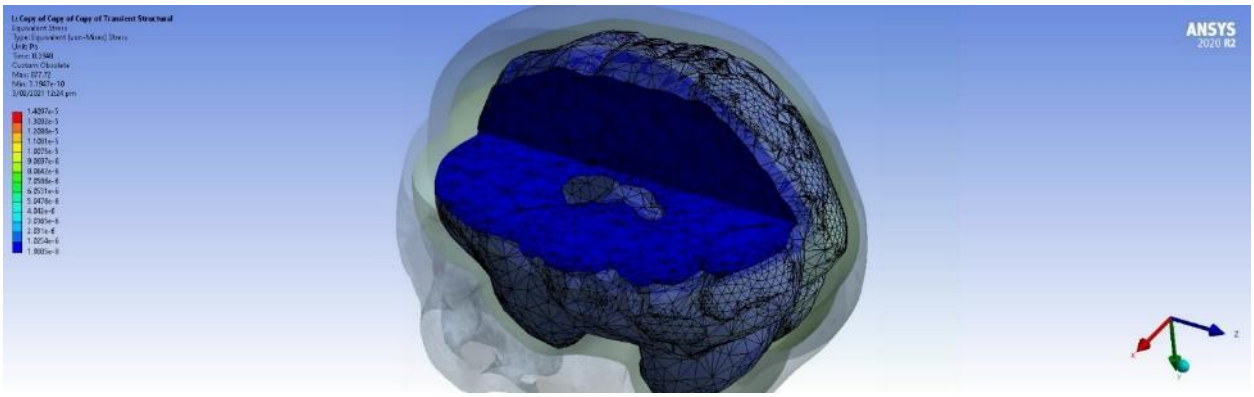
ANSYS
2020 R2

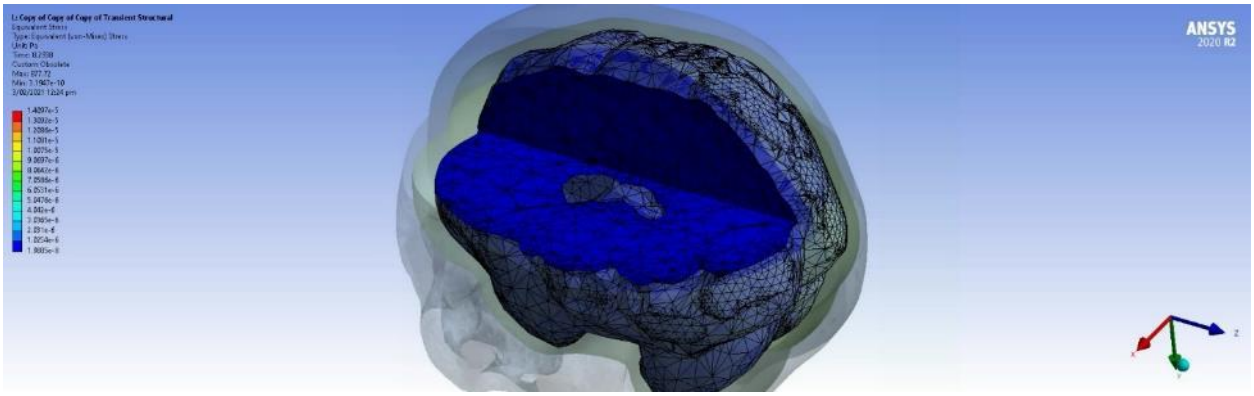
ANSYS
2020 R2

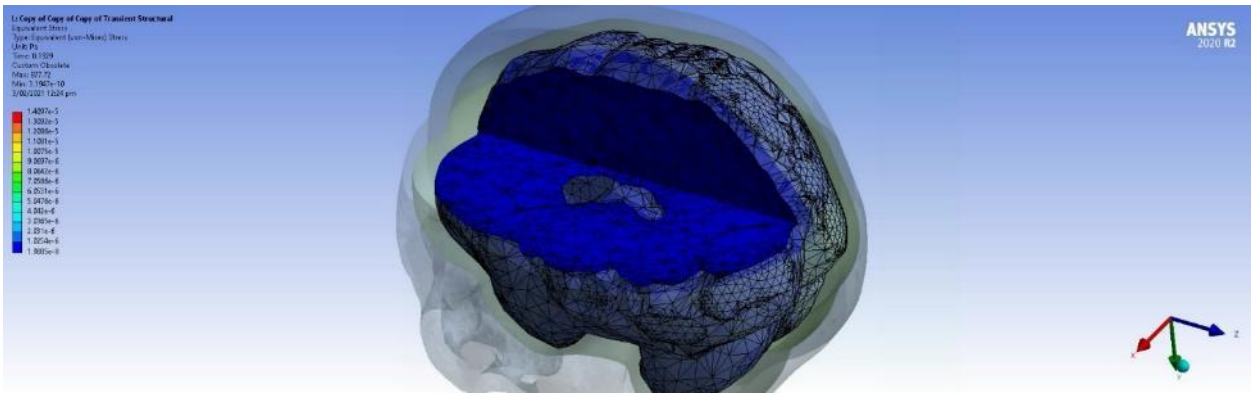
ANSYS
2020 R2

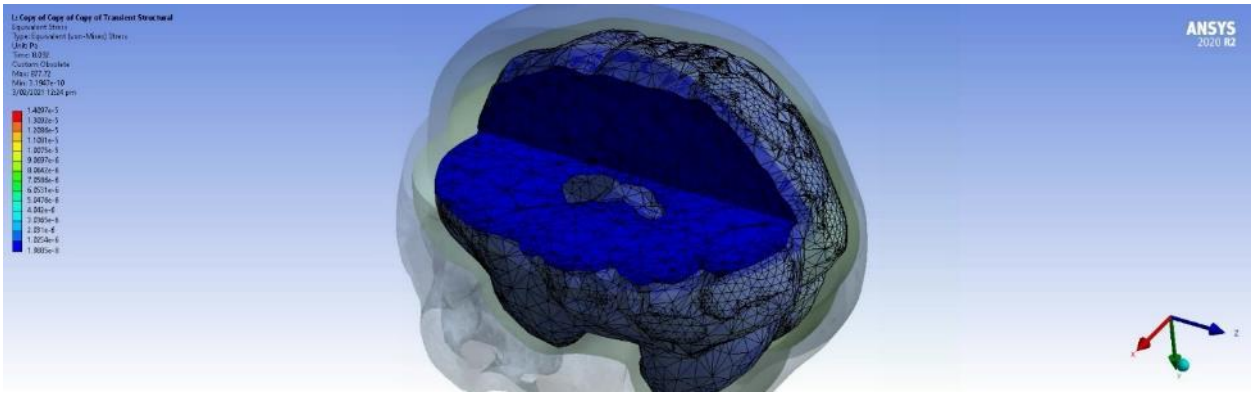
ANSYS
2020 R2

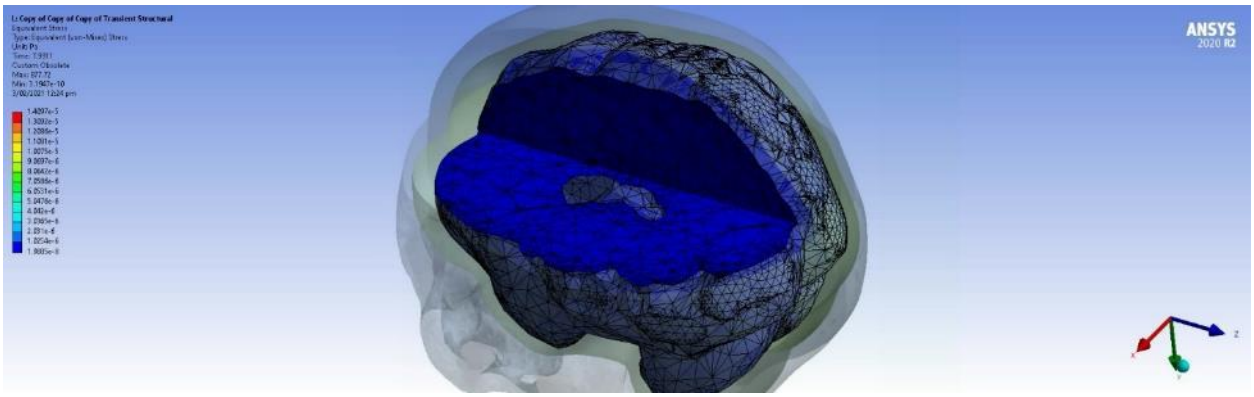
ANSYS
2020 R2

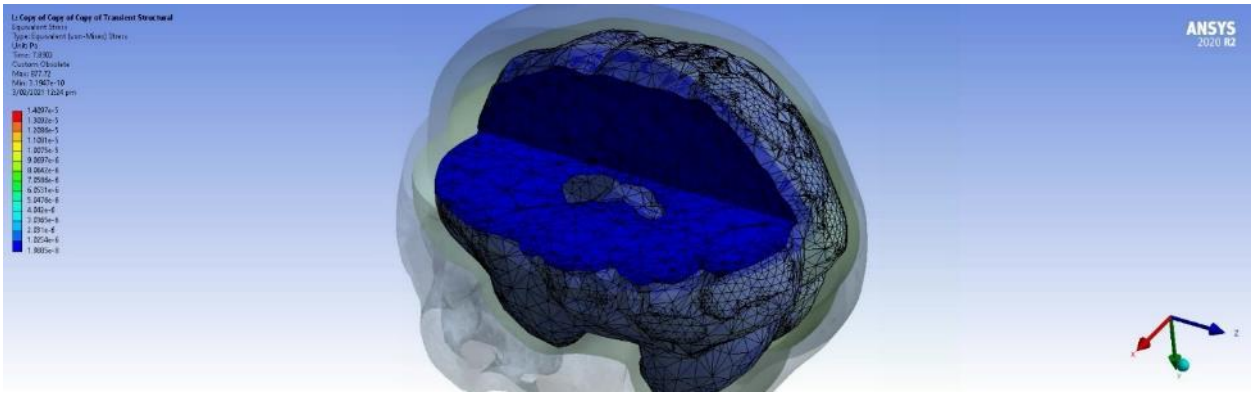
ANSYS
2020 R2

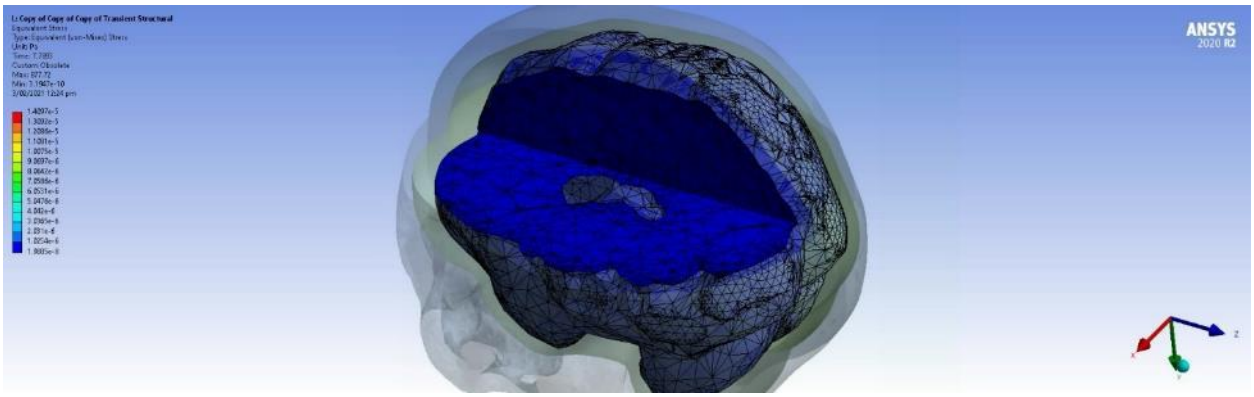
ANSYS
2020 R2

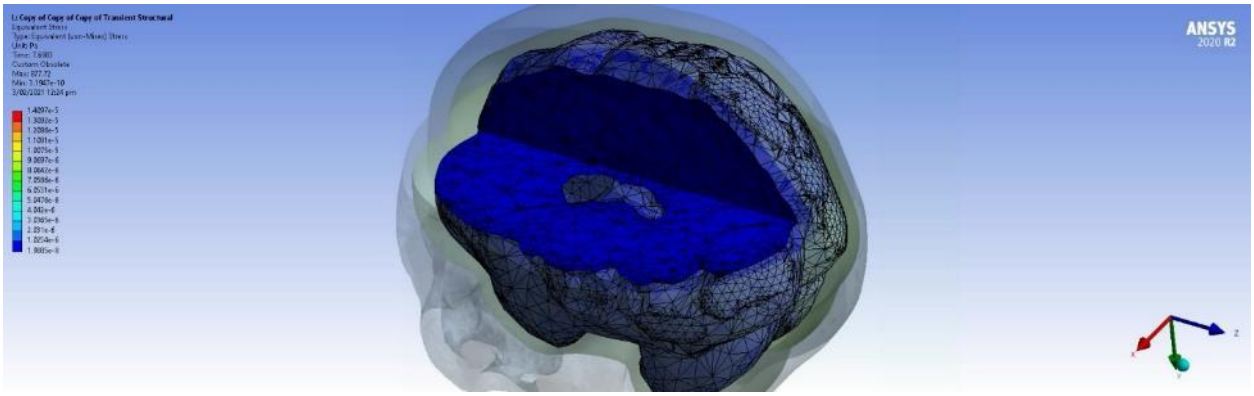
ANSYS
2020 R2

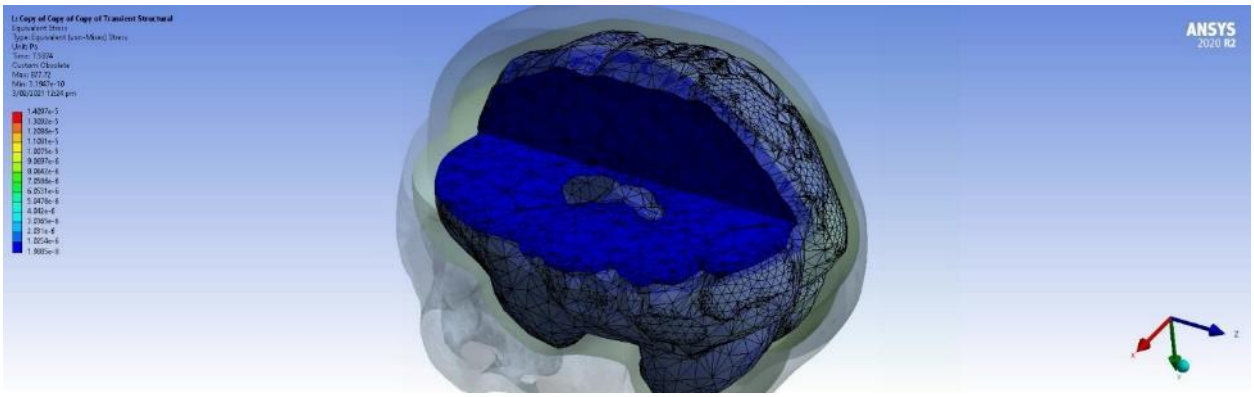
ANSYS
2020 R2

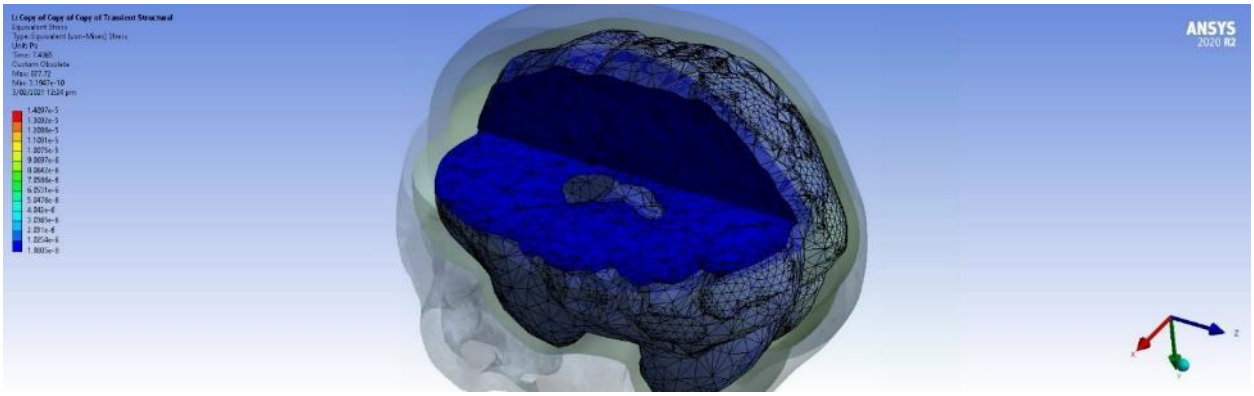
ANSYS
2020 R2

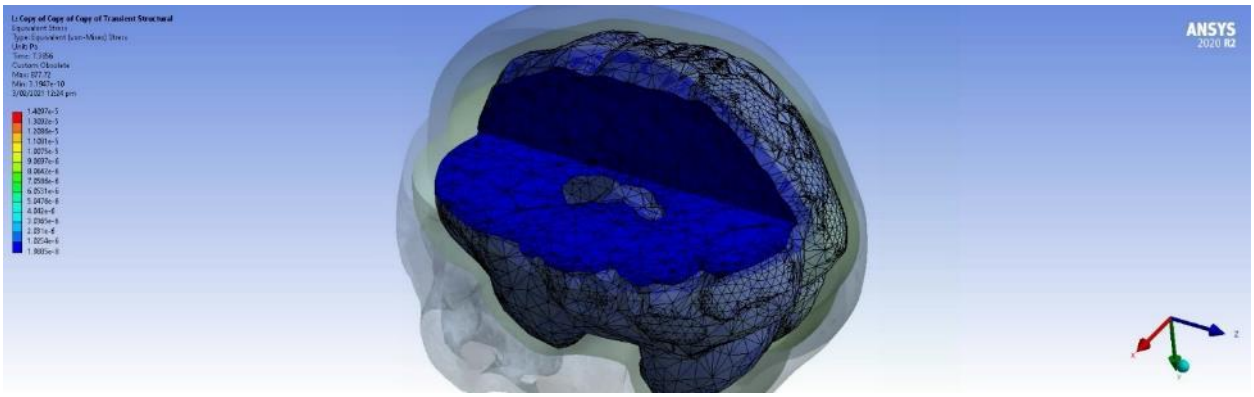
ANSYS
2020 R2

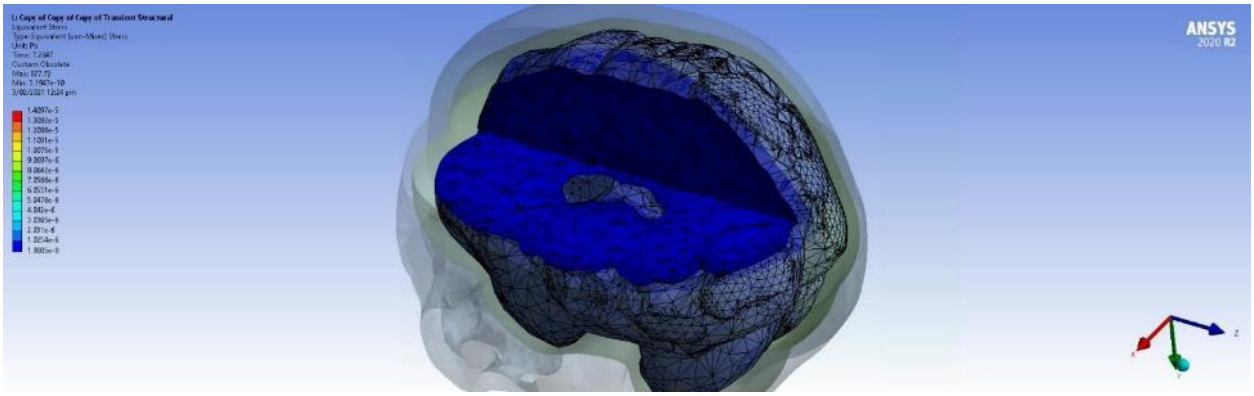
ANSYS
2020 R2

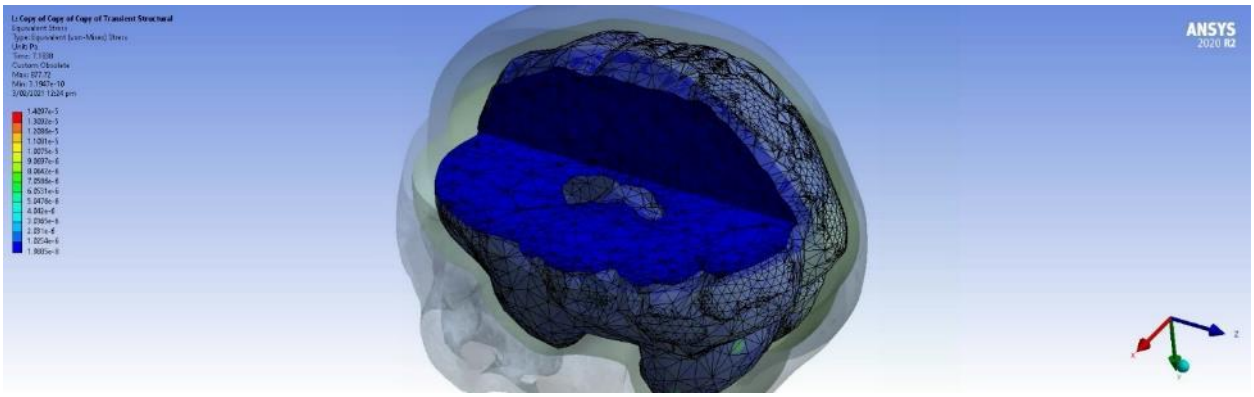
ANSYS
2020 R2

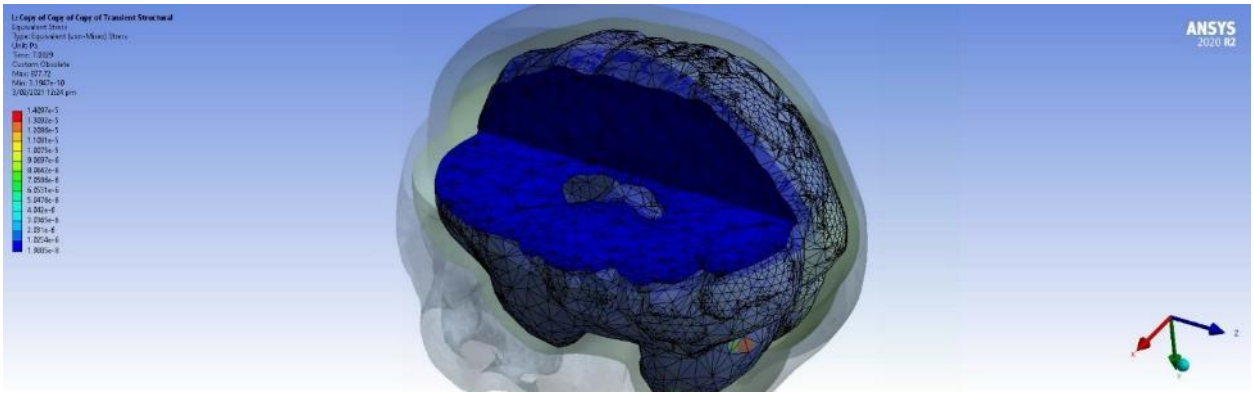
ANSYS
2020 R2

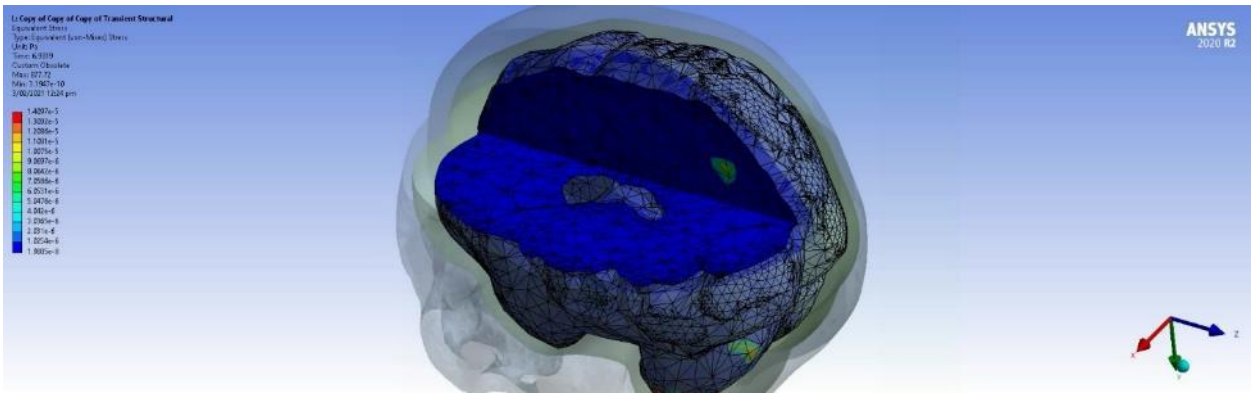
ANSYS
2020 R2

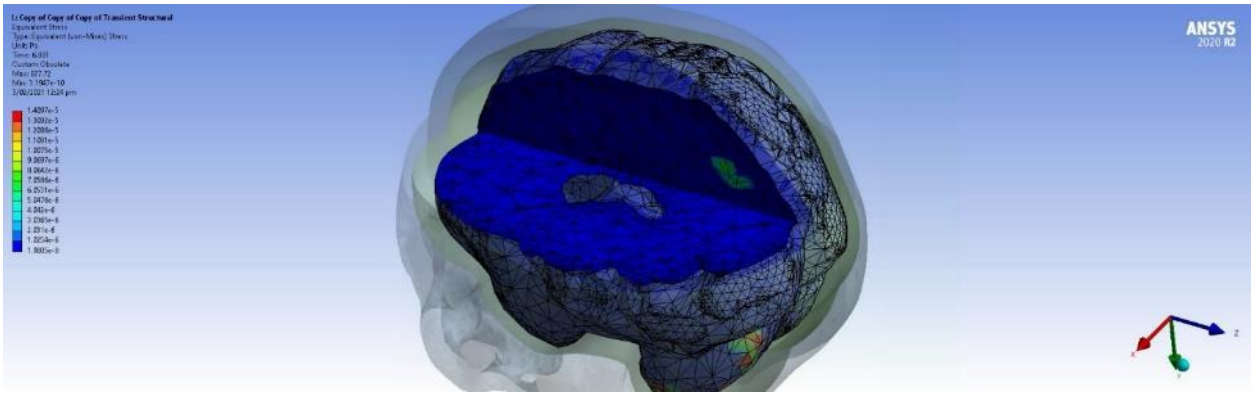
ANSYS
2020 R2

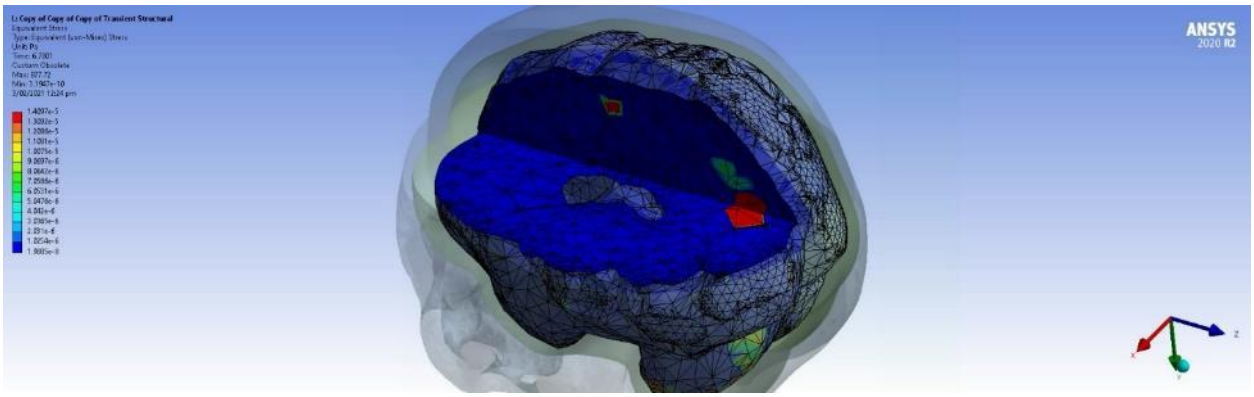
ANSYS
2020 R2

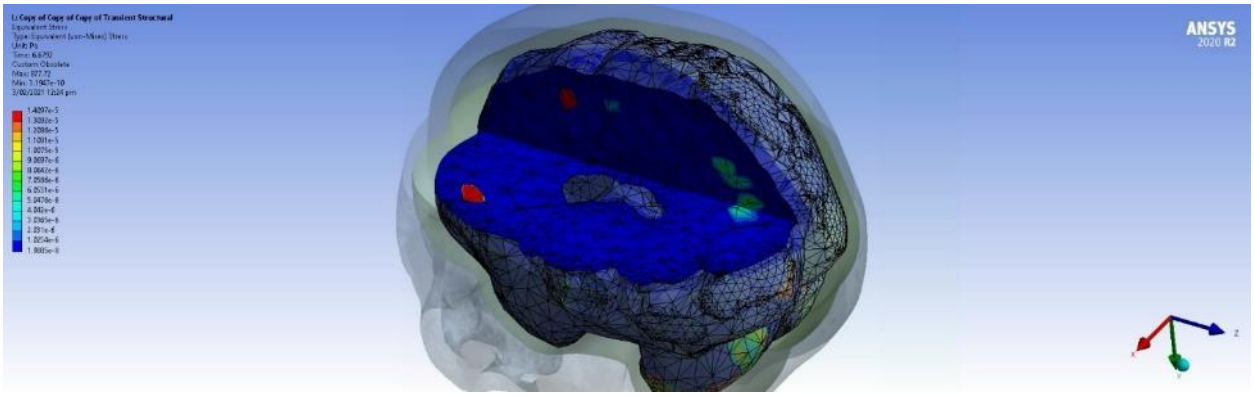
ANSYS
2020 R2

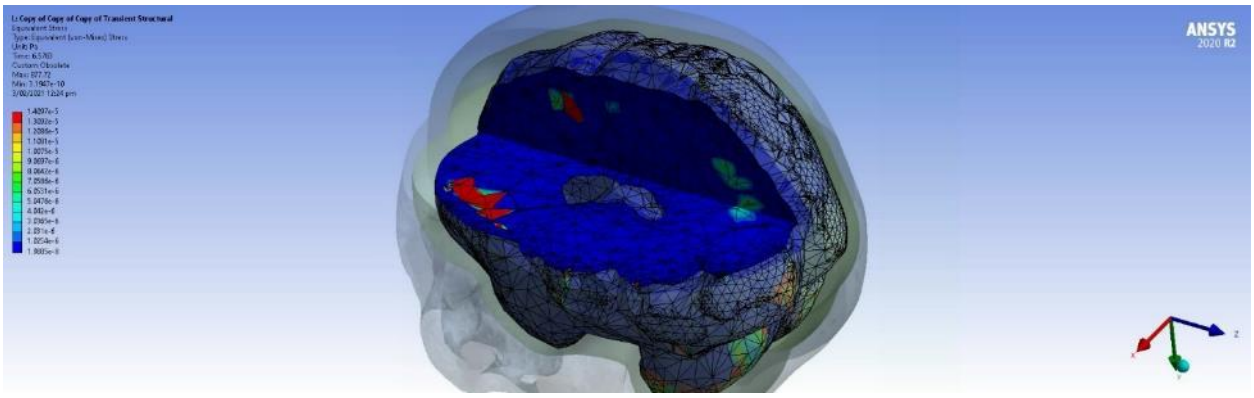
ANSYS
2020 R2

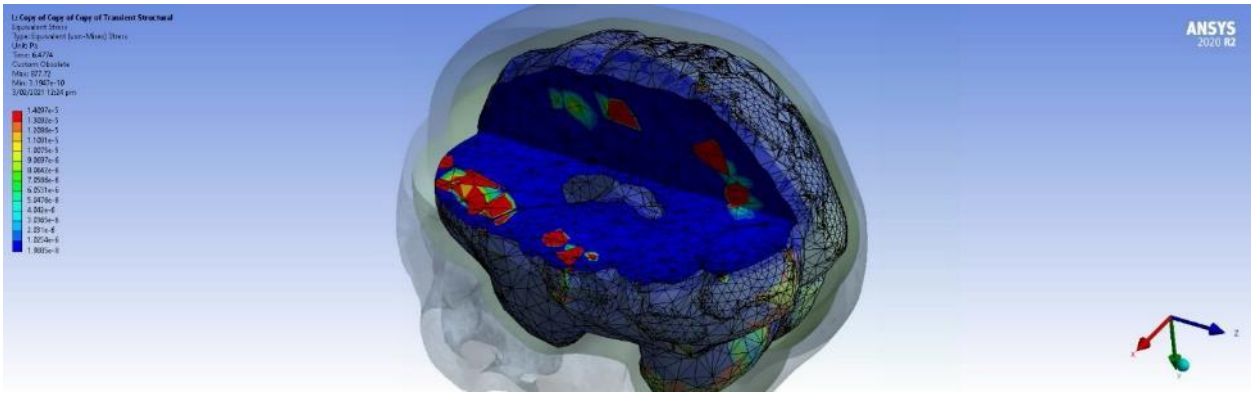
ANSYS
2020 R2

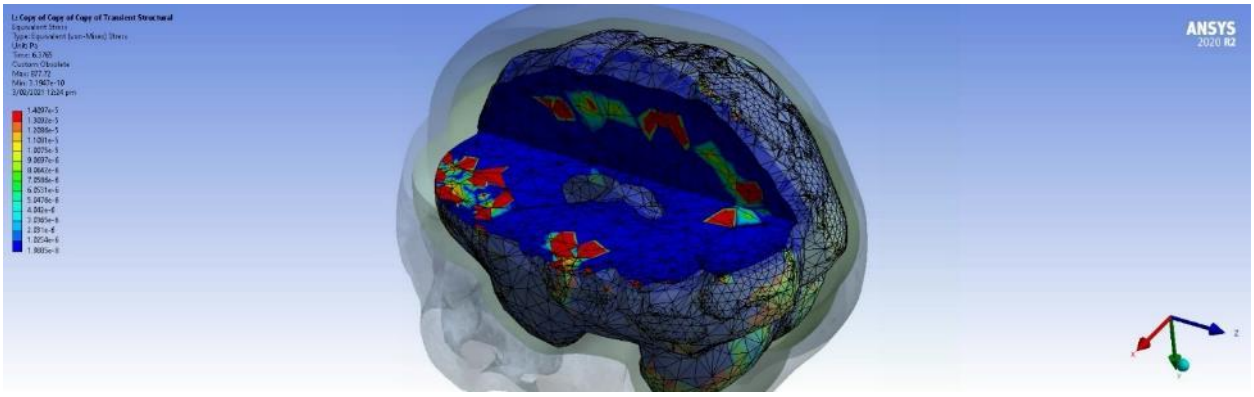
ANSYS
2020 R2

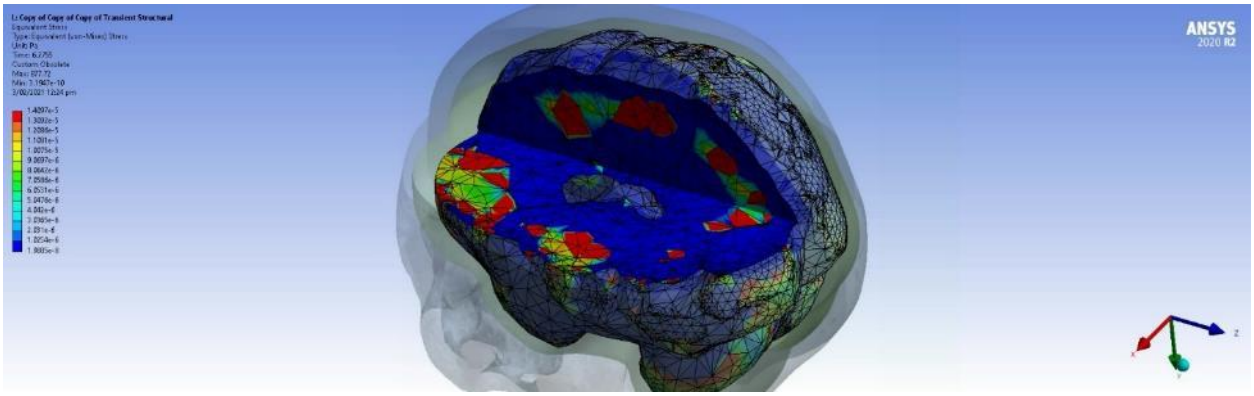
ANSYS
2020 R2

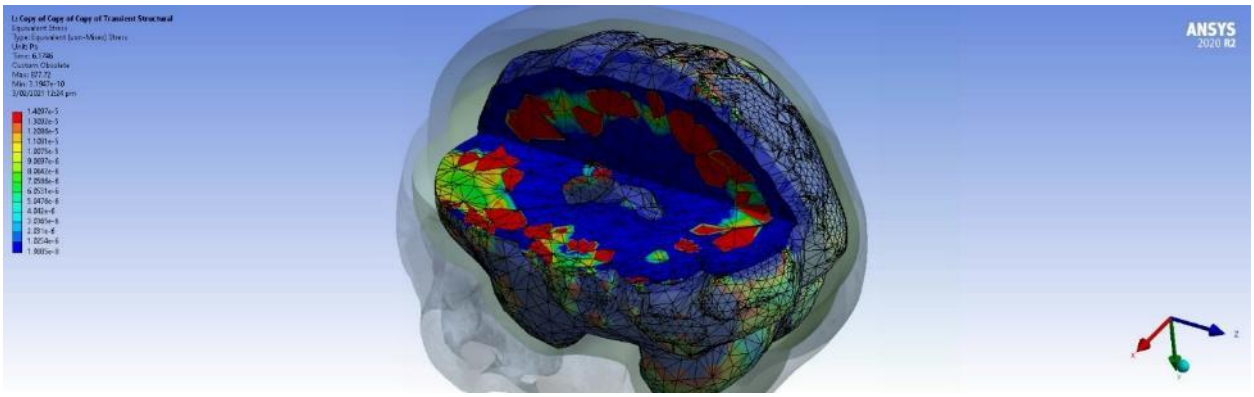
ANSYS
2020 R2

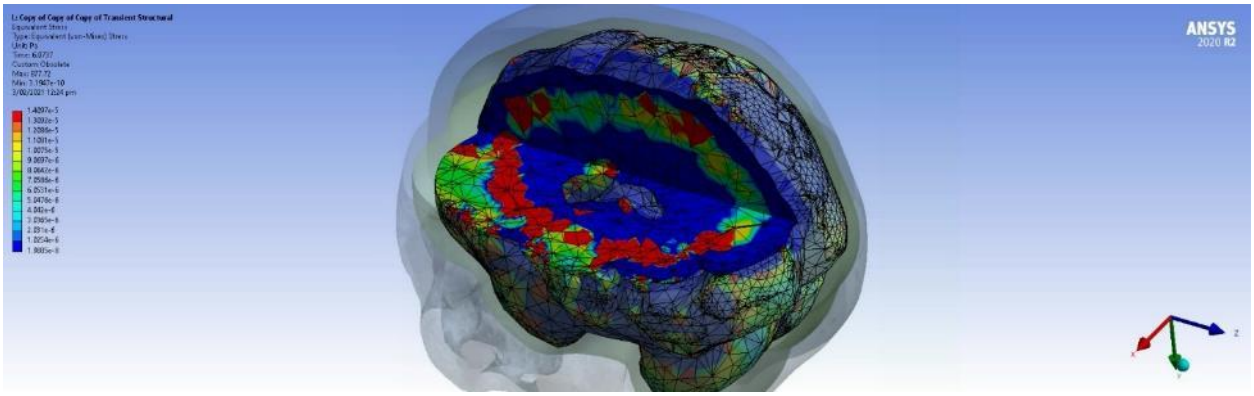
ANSYS
2020 R2

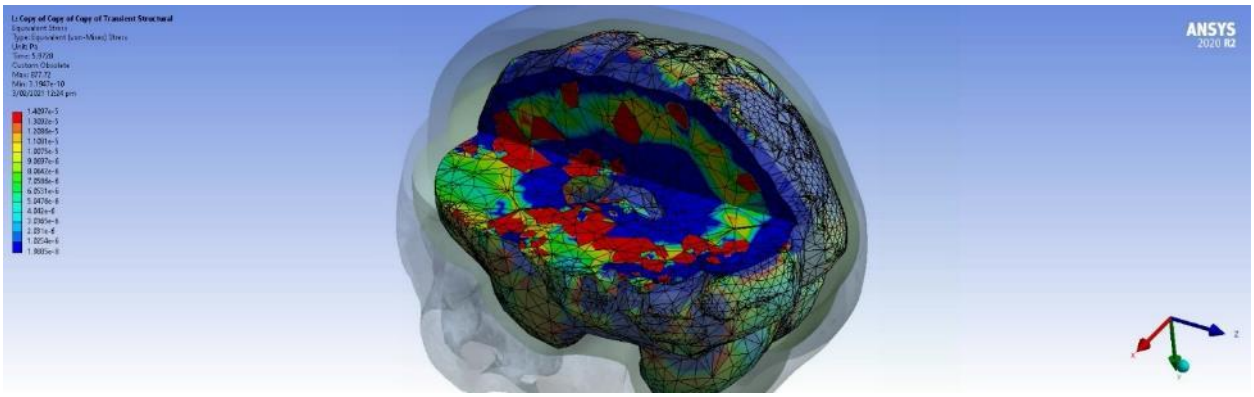
ANSYS
2020 R2

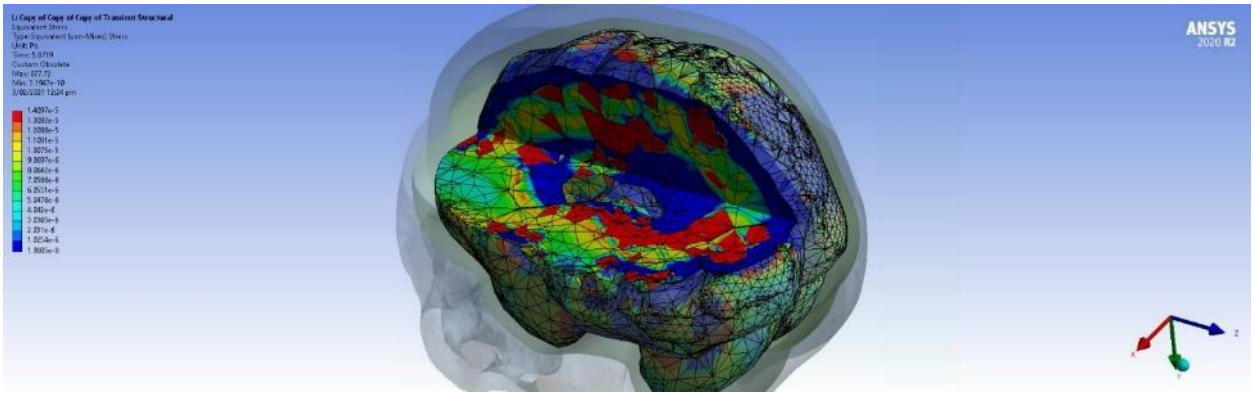
ANSYS
2020 R2

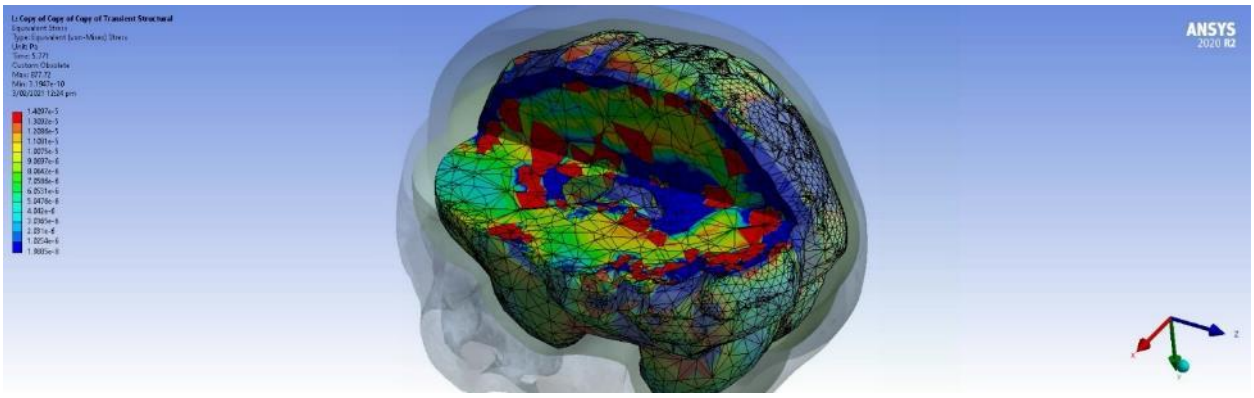
ANSYS
2020 R2

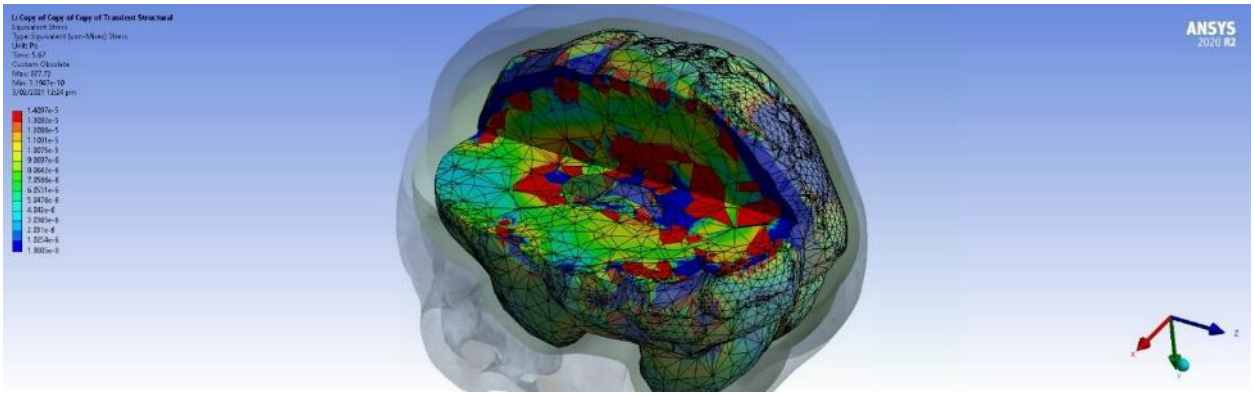
ANSYS
2020 R2

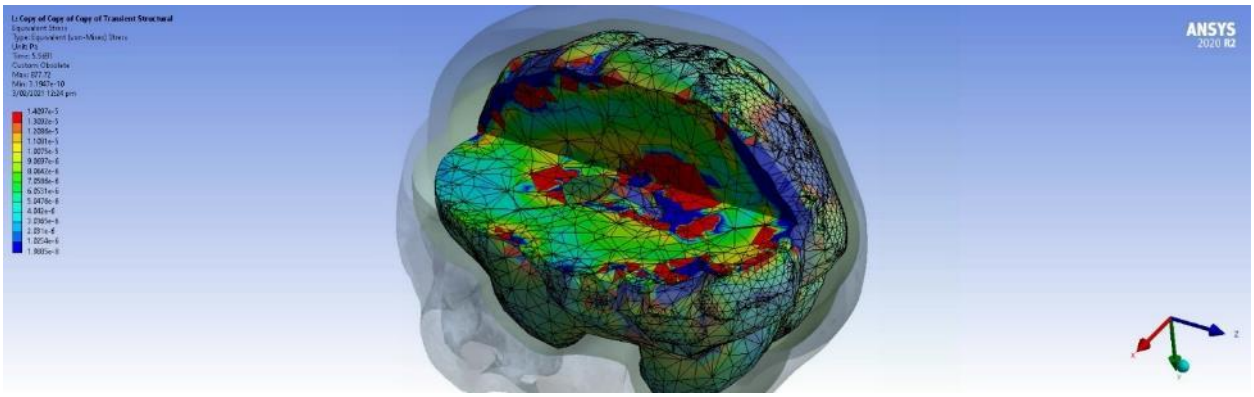
ANSYS
2020 R2

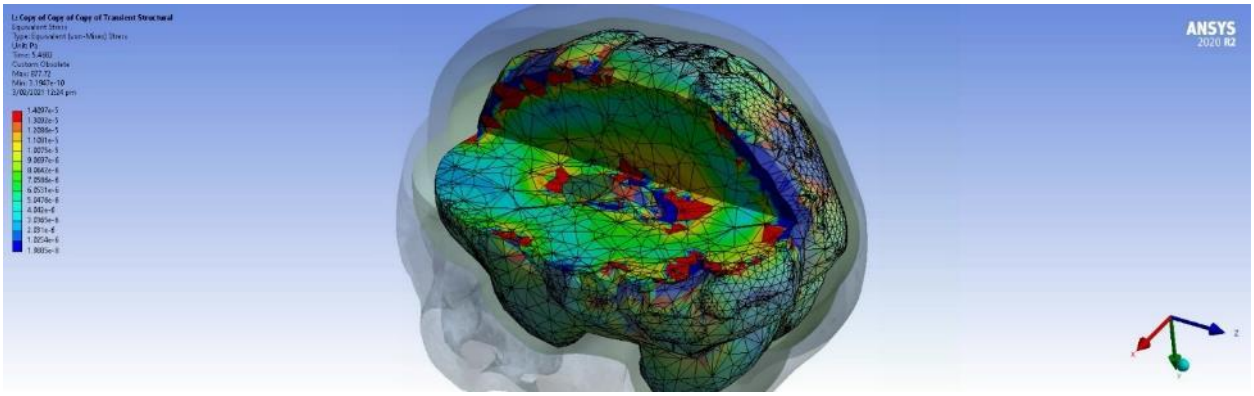
ANSYS
2020 R2

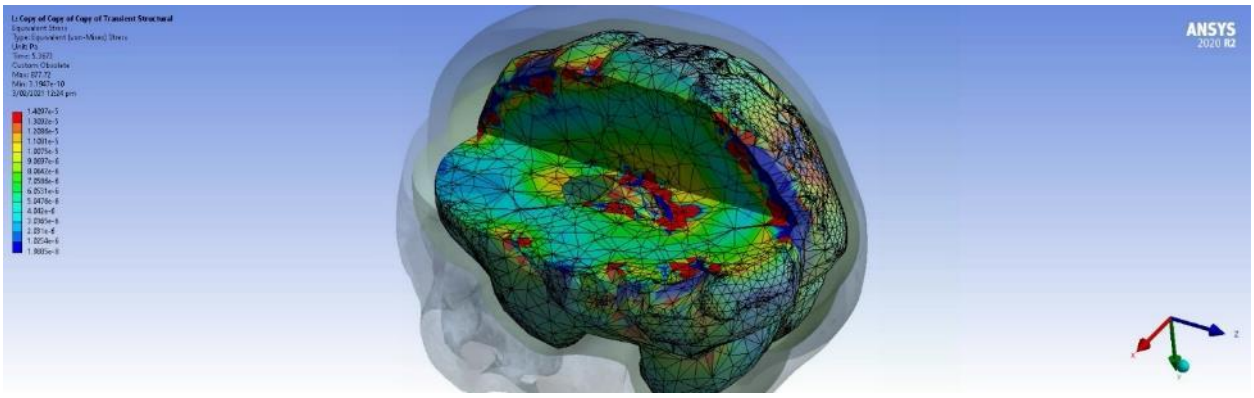
ANSYS
2020 R2

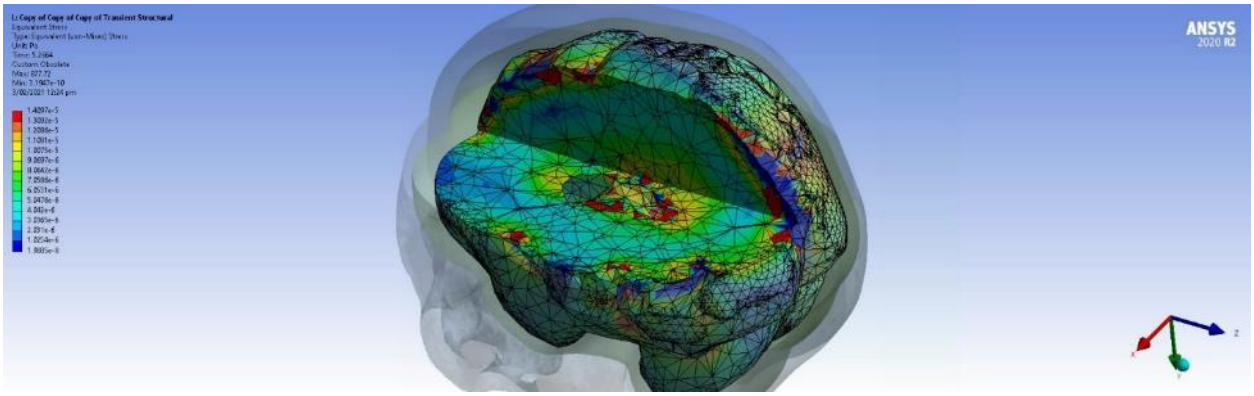
ANSYS
2020 R2

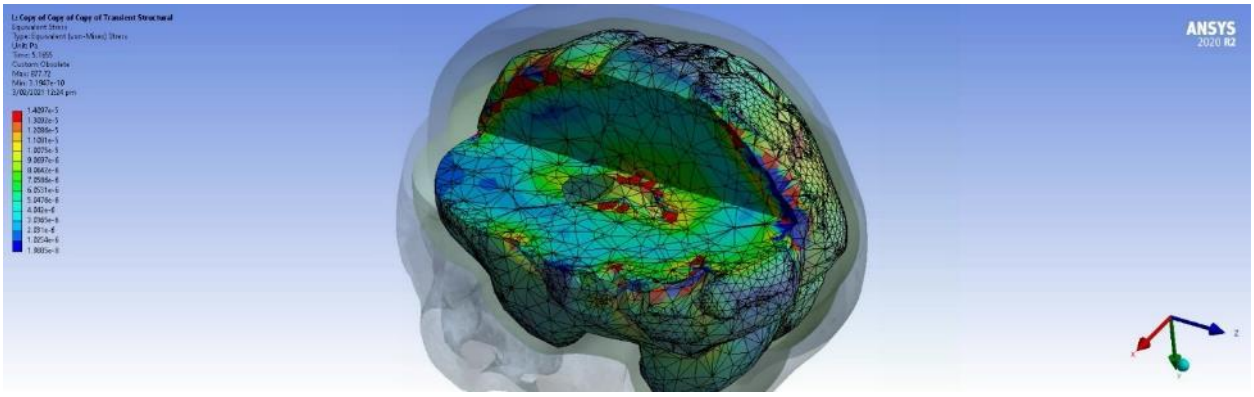
ANSYS
2020 R2

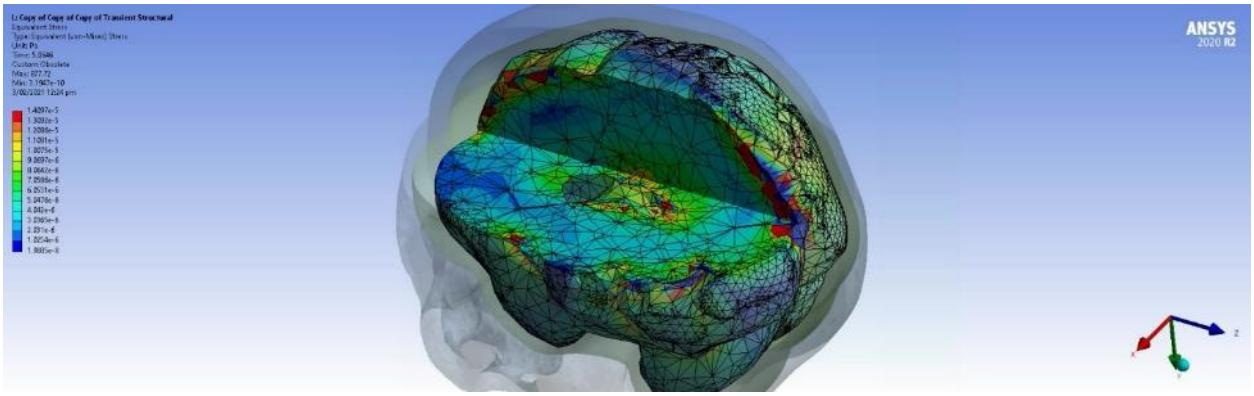
ANSYS
2020 R2

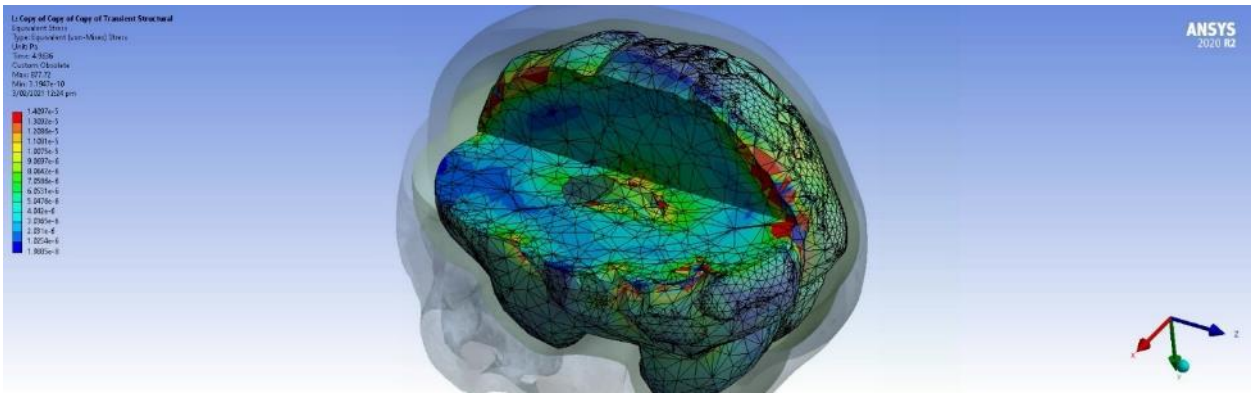
ANSYS
2020 R2

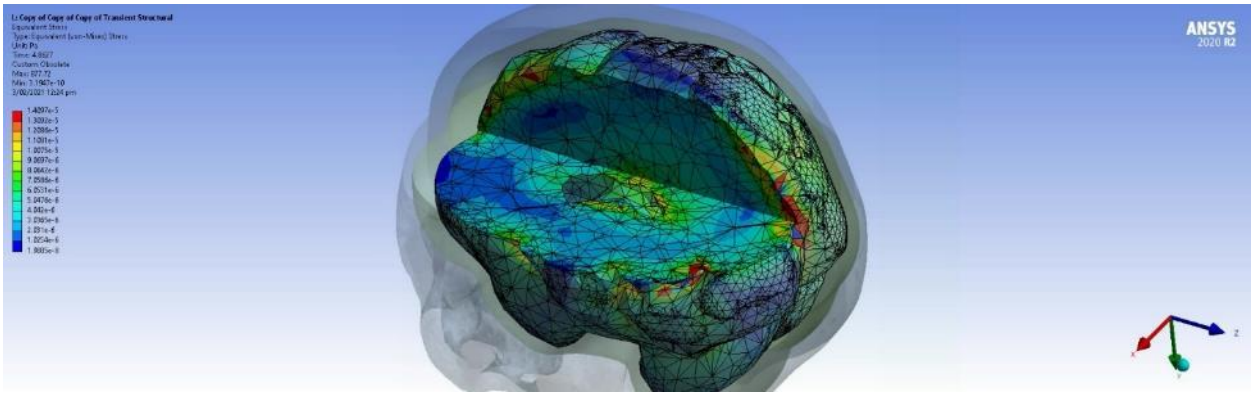
ANSYS
2020 R2

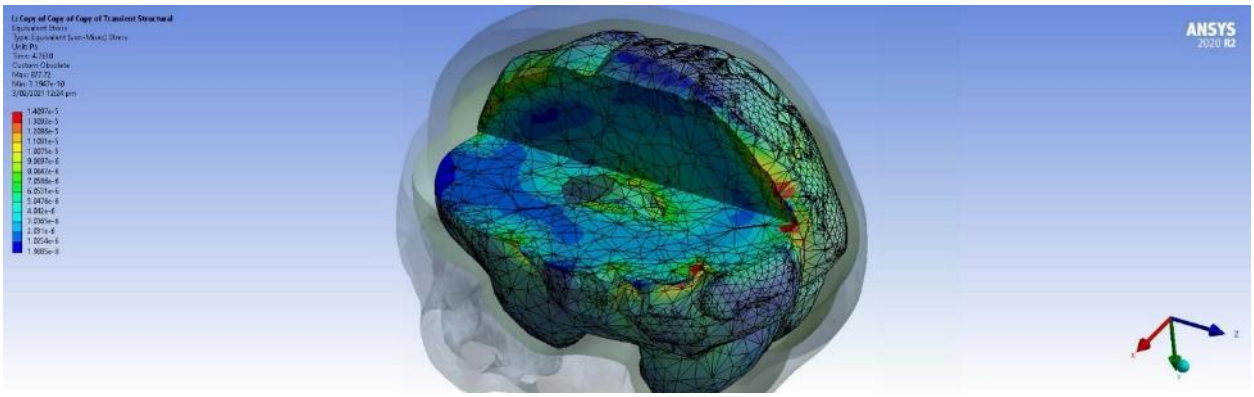
ANSYS
2020 R2

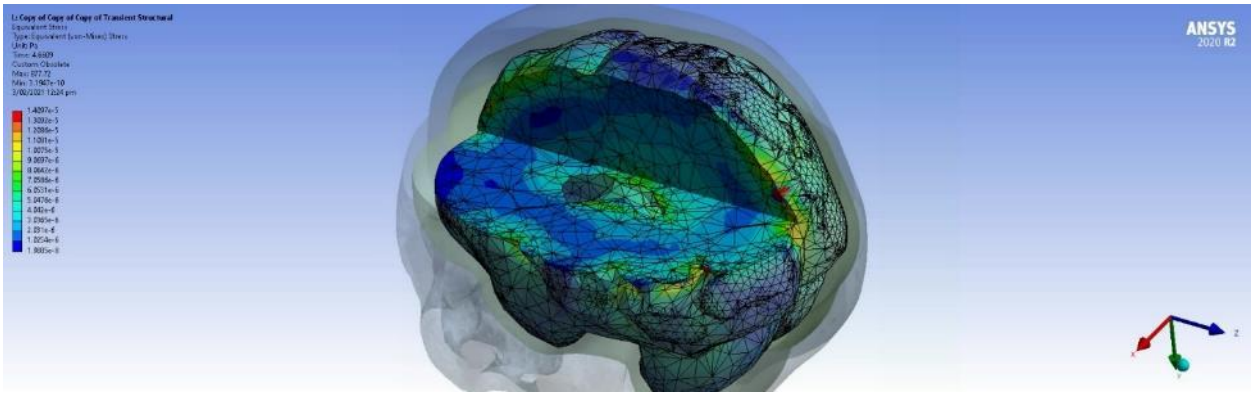
ANSYS
2020 R2

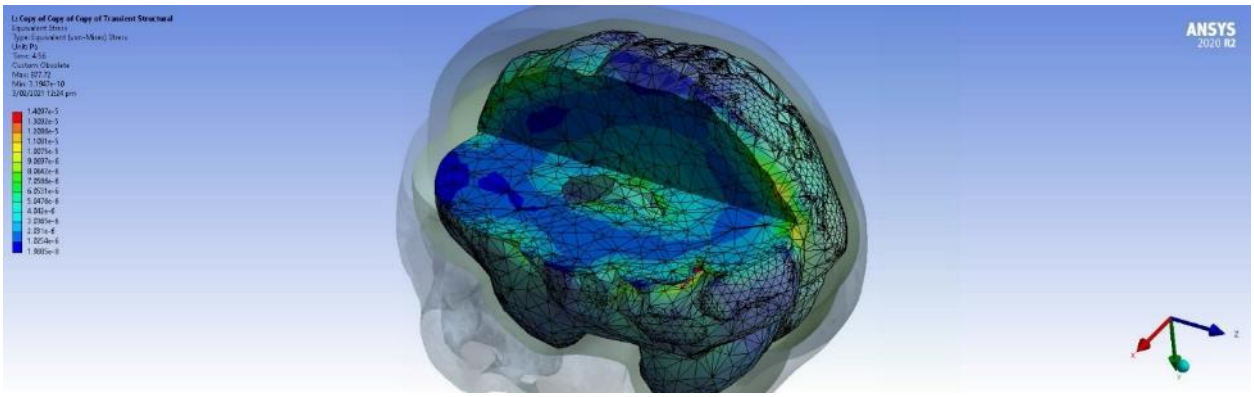
ANSYS
2020 R2

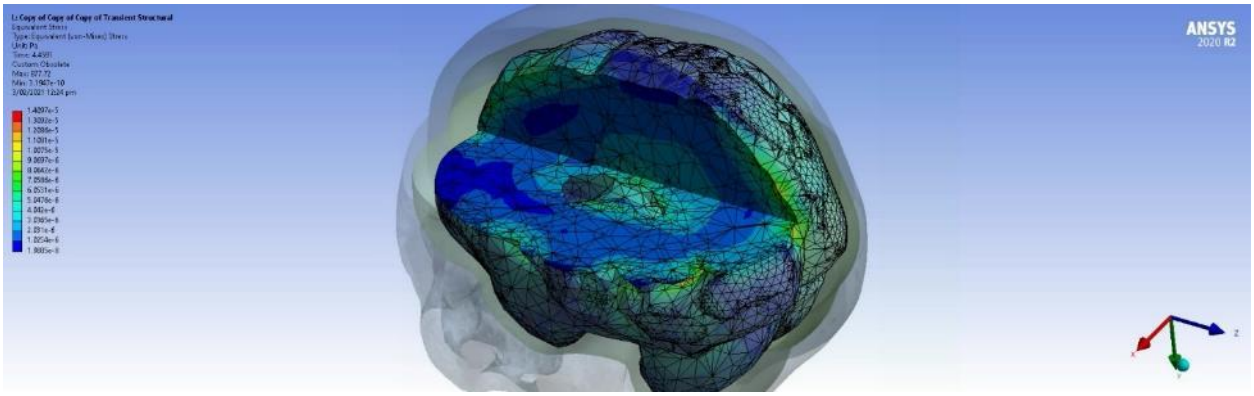
ANSYS
2020 R2

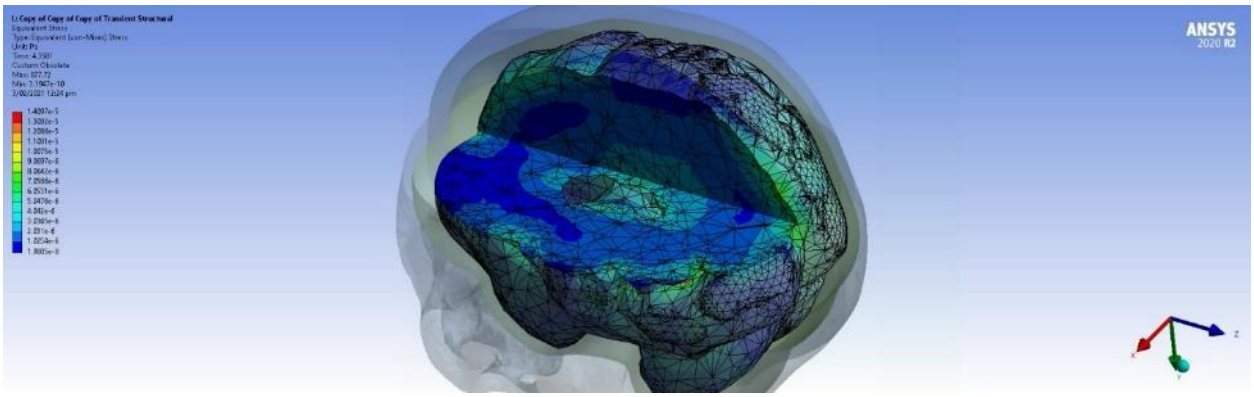
ANSYS
2020 R2

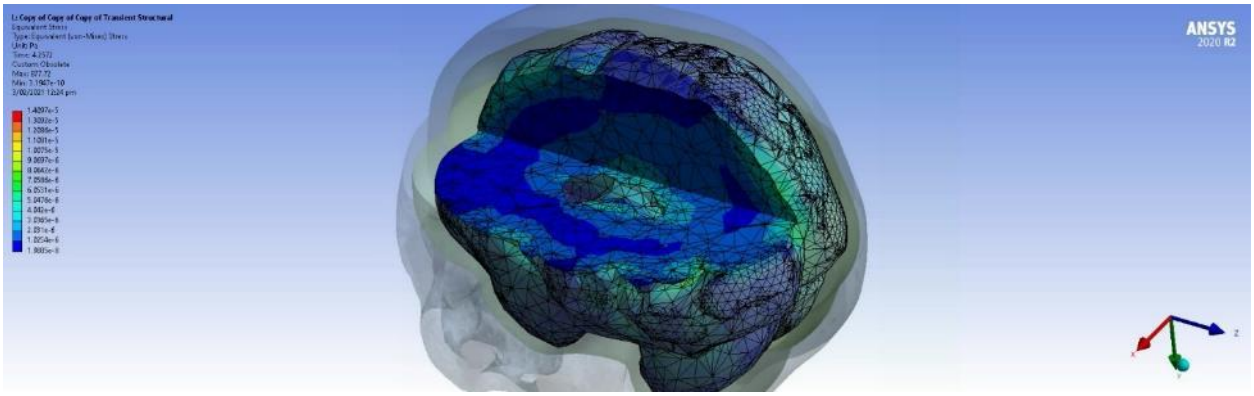
ANSYS
2020 R2

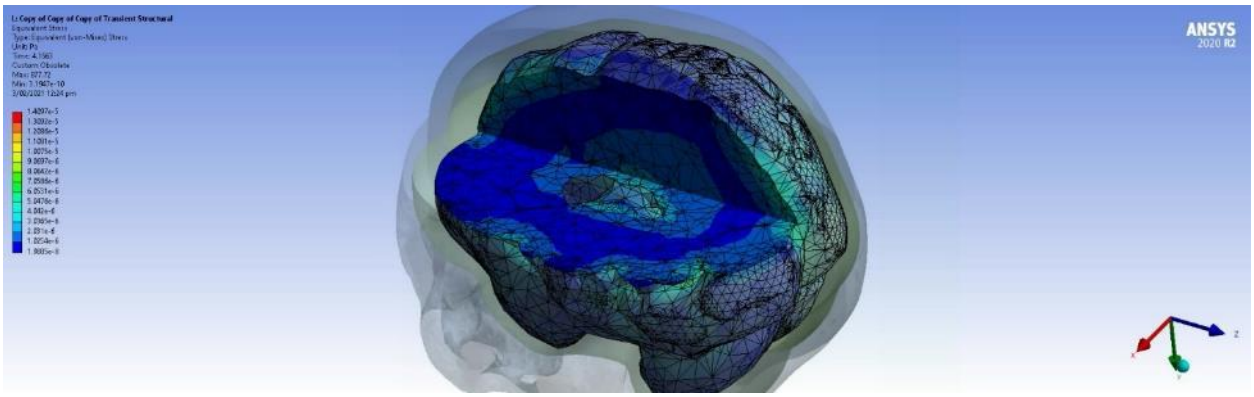
ANSYS
2020 R2

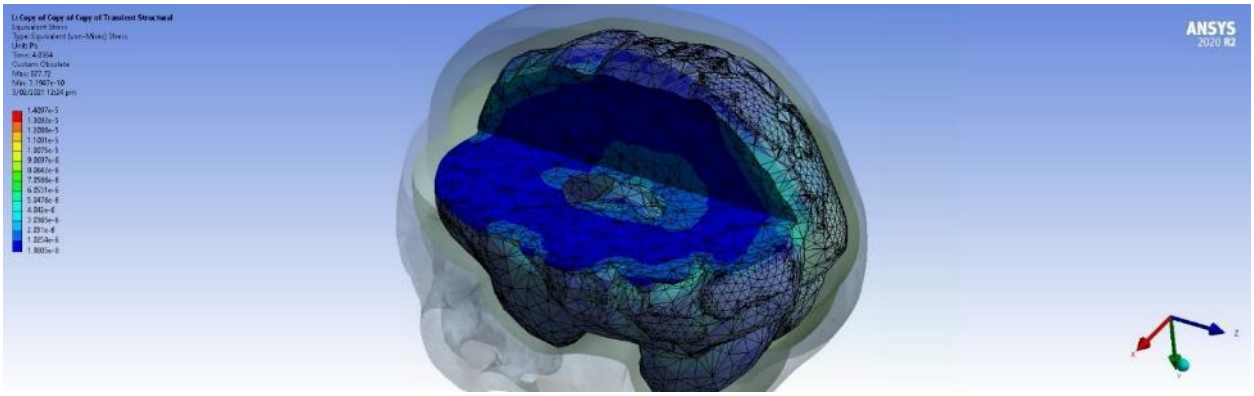
ANSYS
2020 R2

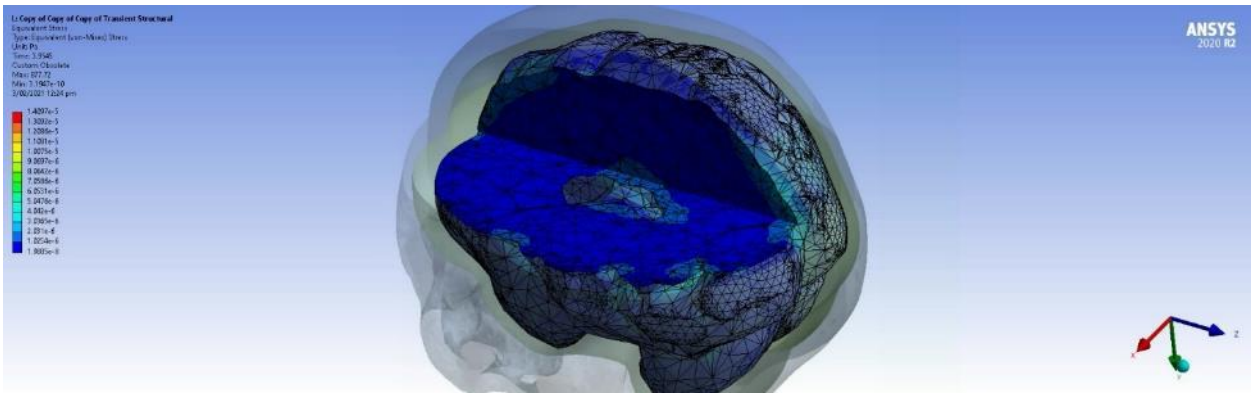
ANSYS
2020 R2

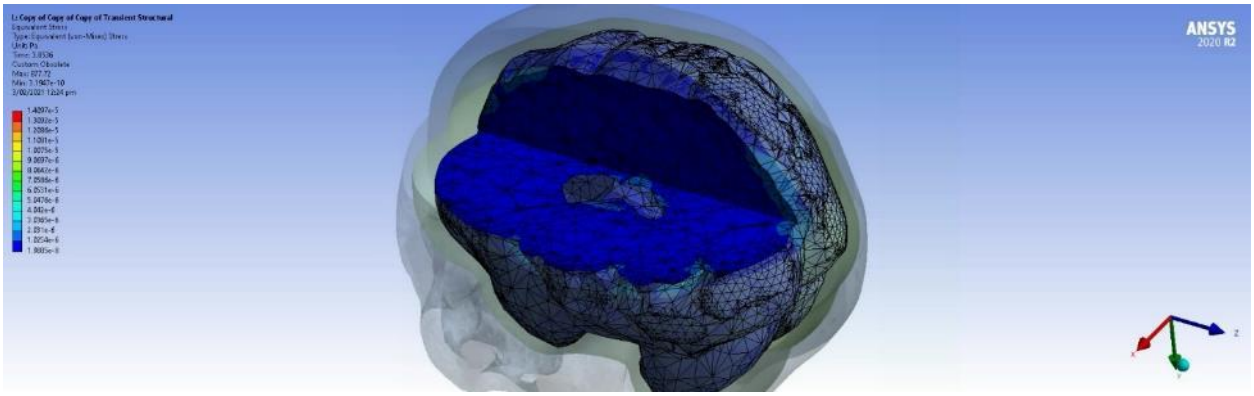
ANSYS
2020 R2

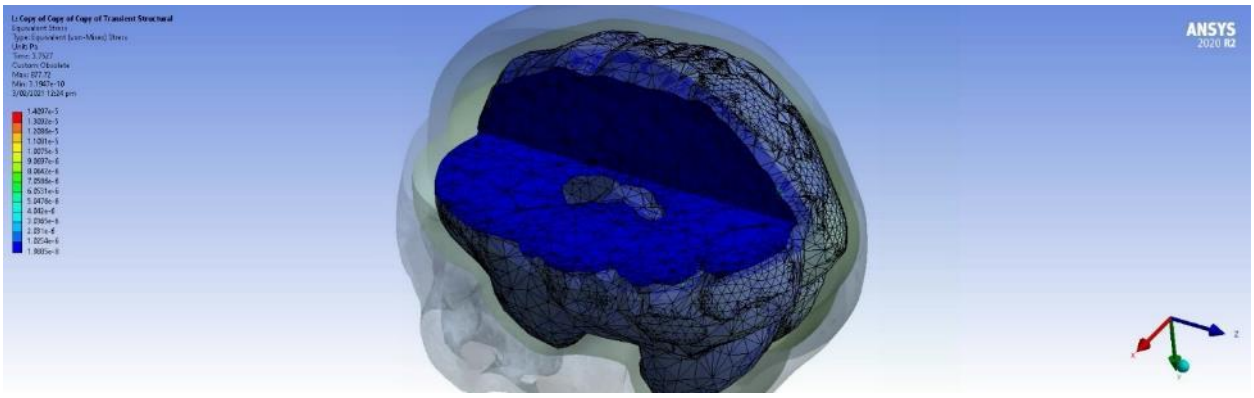
ANSYS
2020 R2

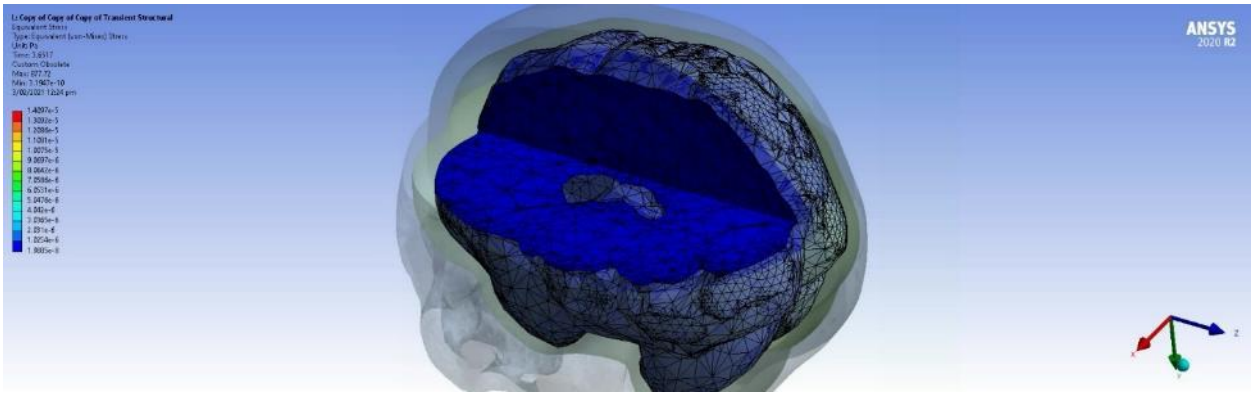
ANSYS
2020 R2

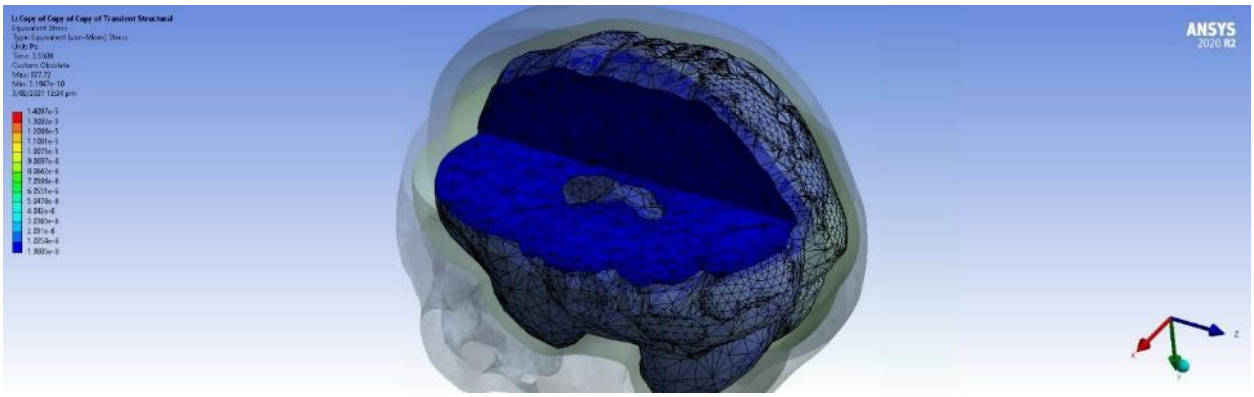
ANSYS
2020 R2

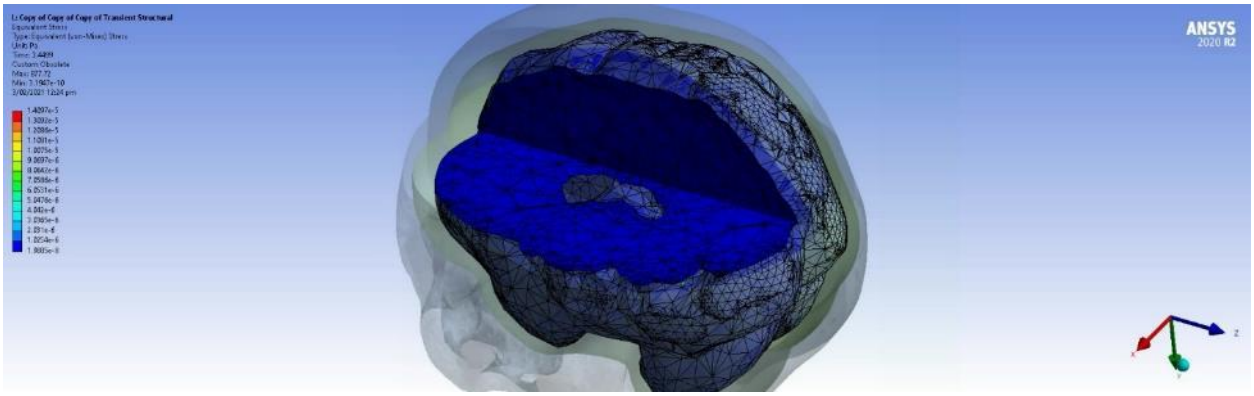
ANSYS
2020 R2

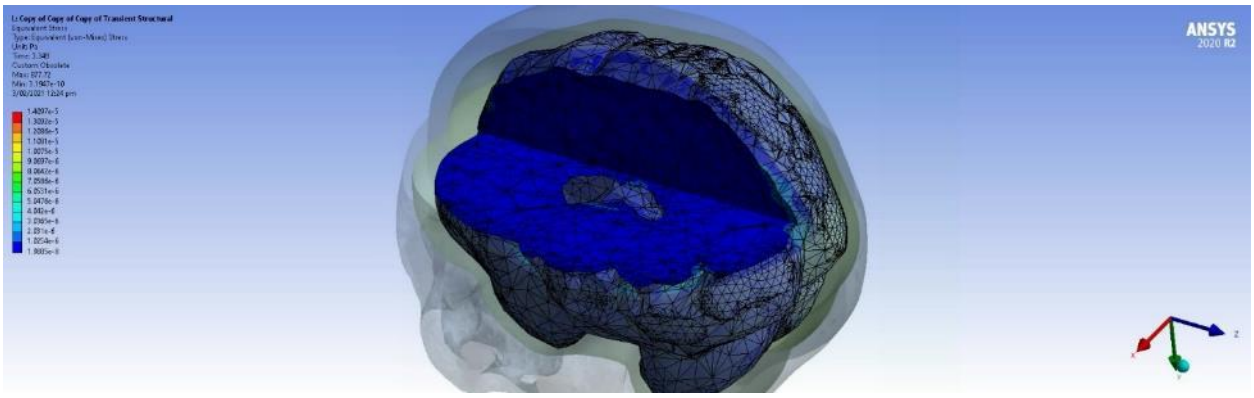
ANSYS
2020 R2

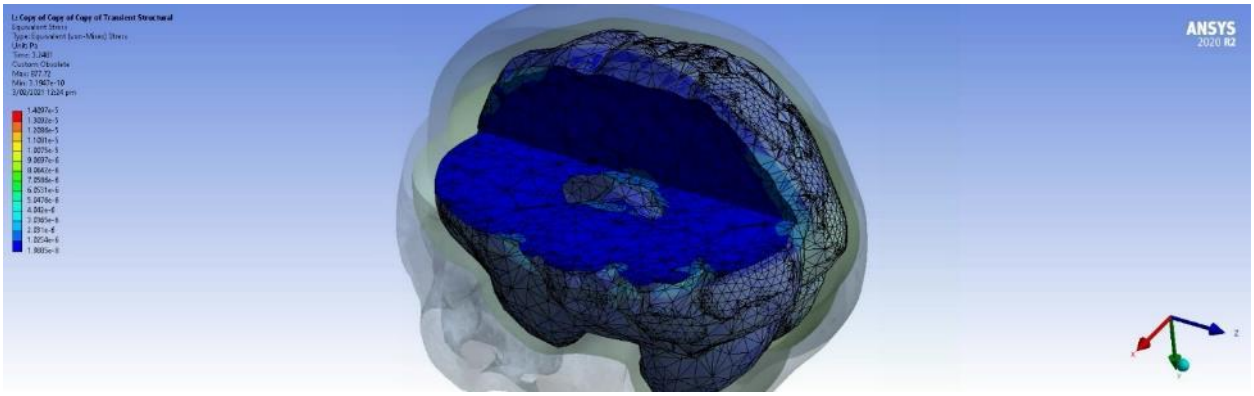
ANSYS
2020 R2

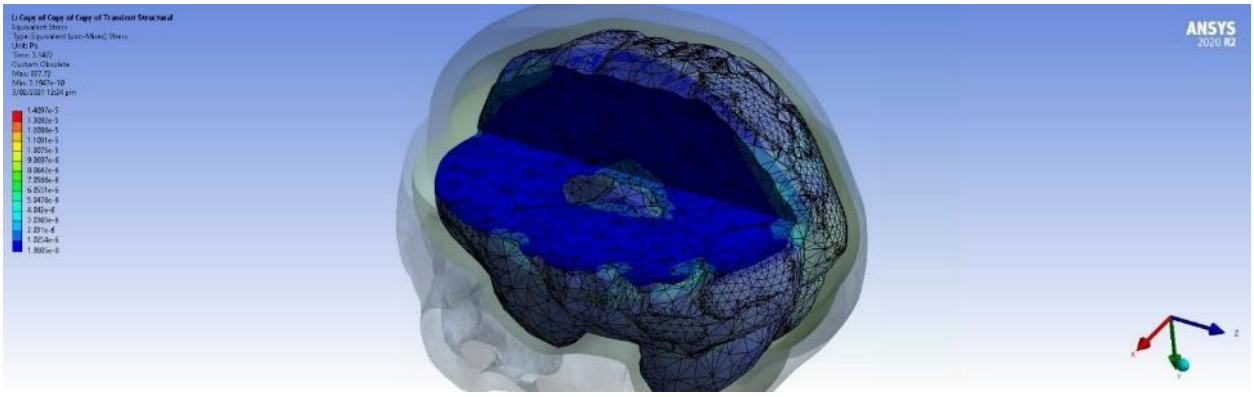
ANSYS
2020 R2

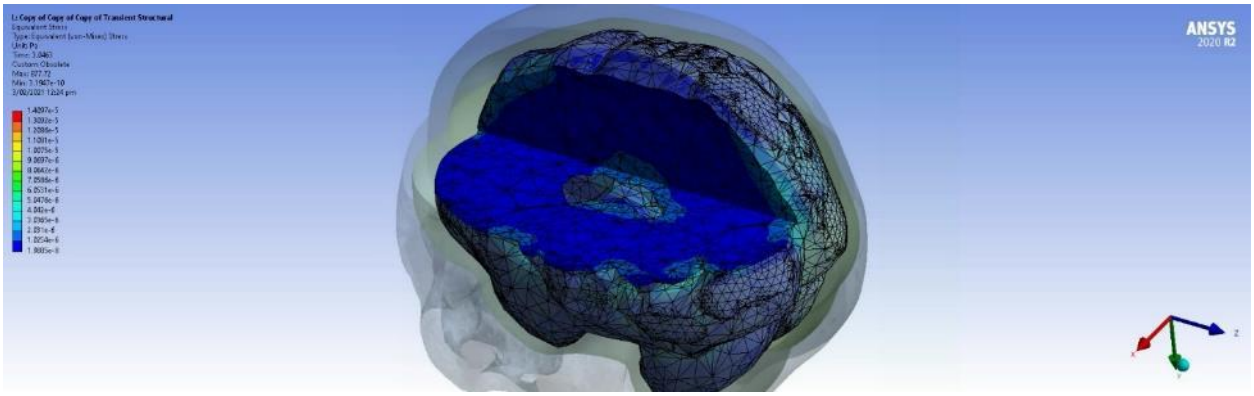
ANSYS
2020 R2

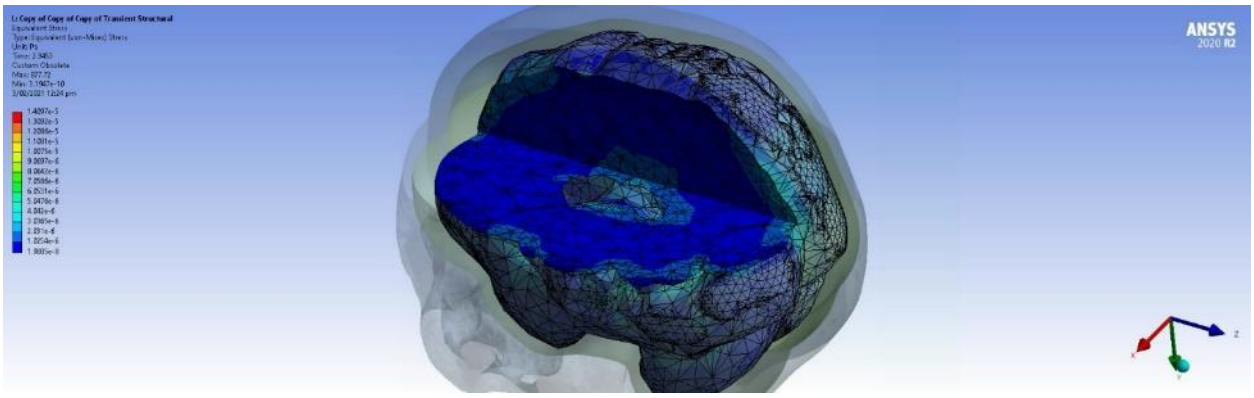
ANSYS
2020 R2

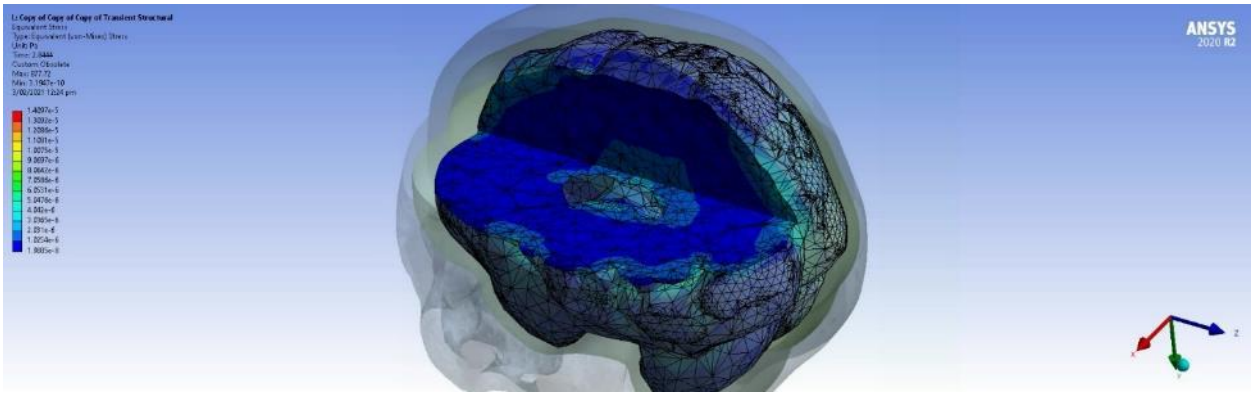
ANSYS
2020 R2

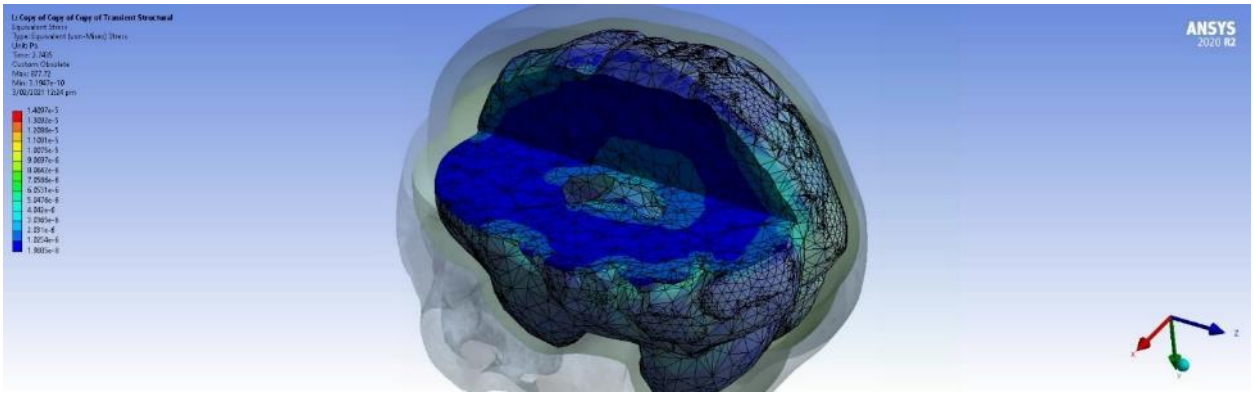
ANSYS
2020 R2

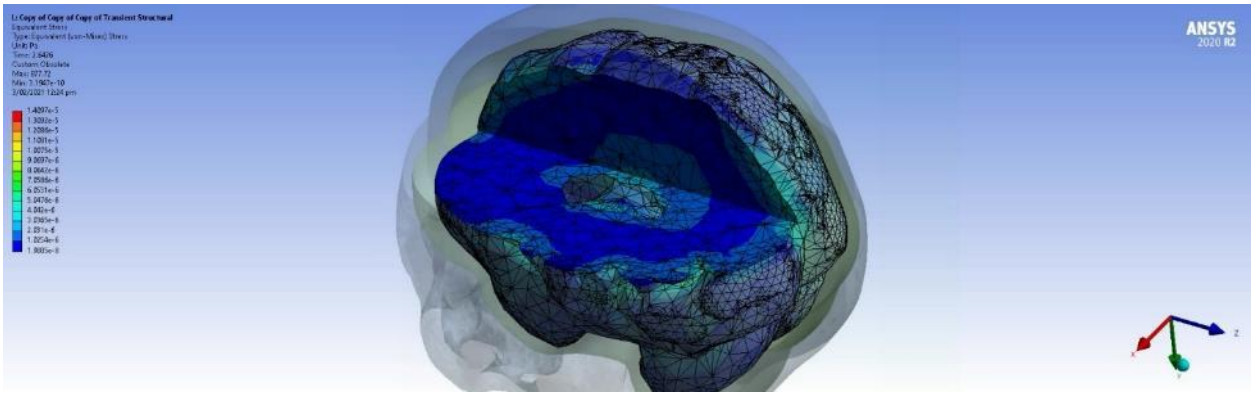
ANSYS
2020 R2

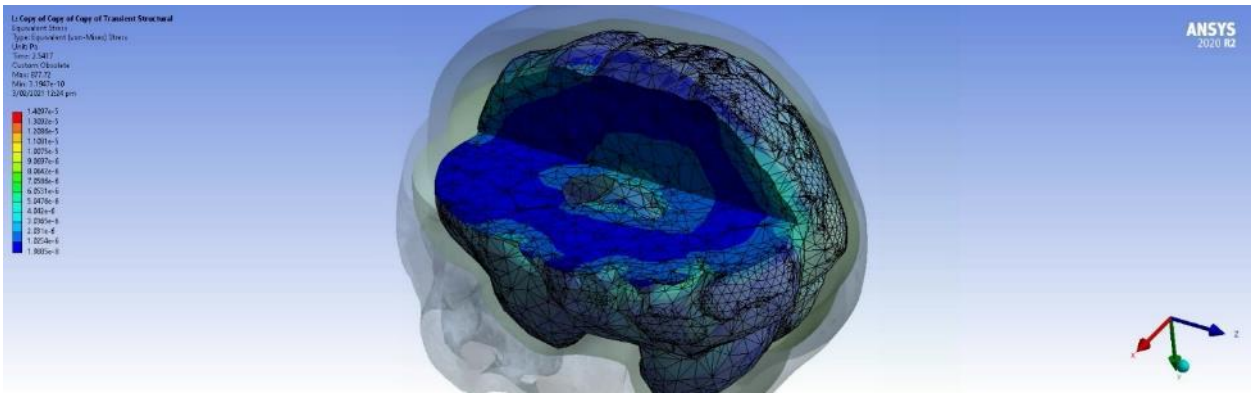
ANSYS
2020 R2

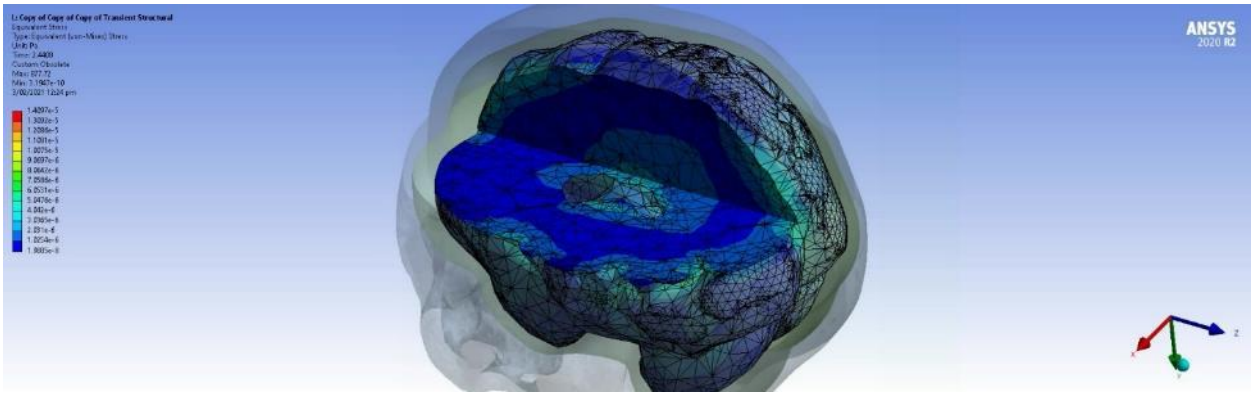
ANSYS
2020 R2

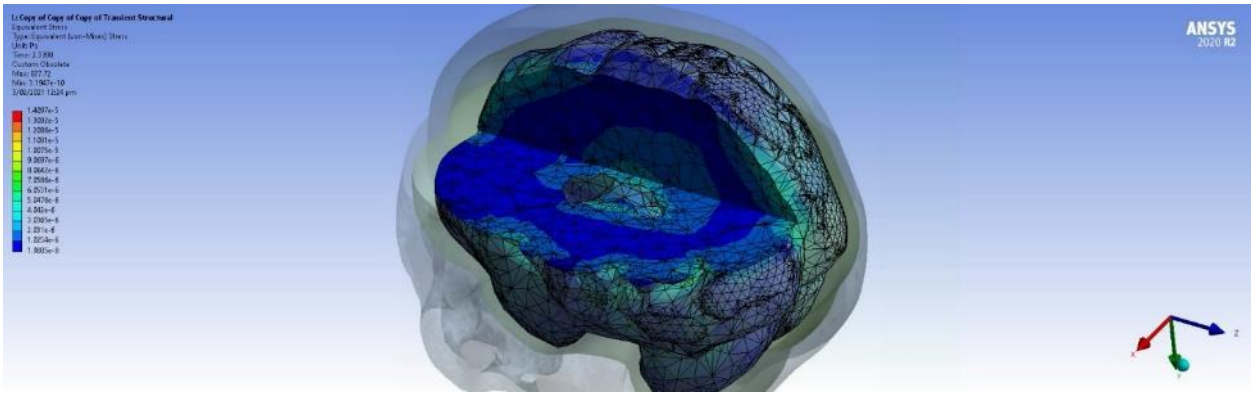
ANSYS
2020 R2

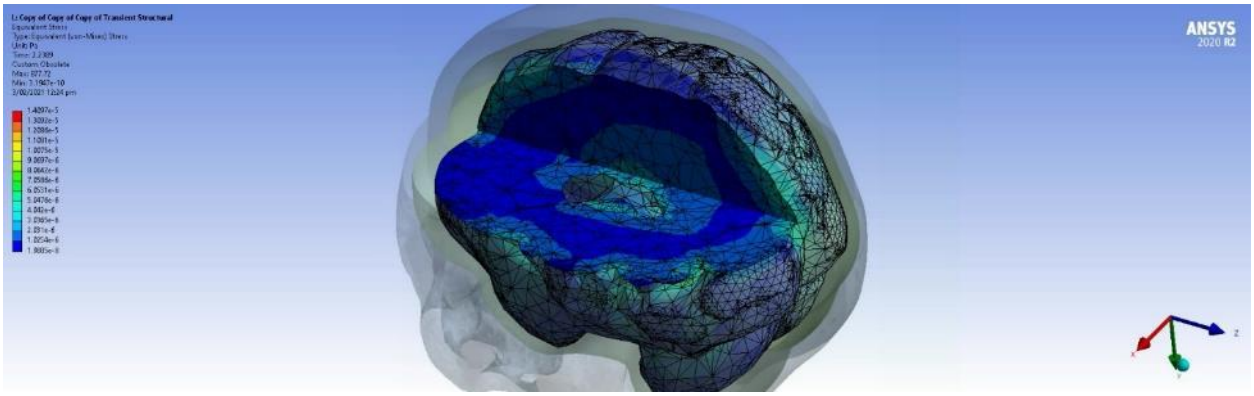
ANSYS
2020 R2

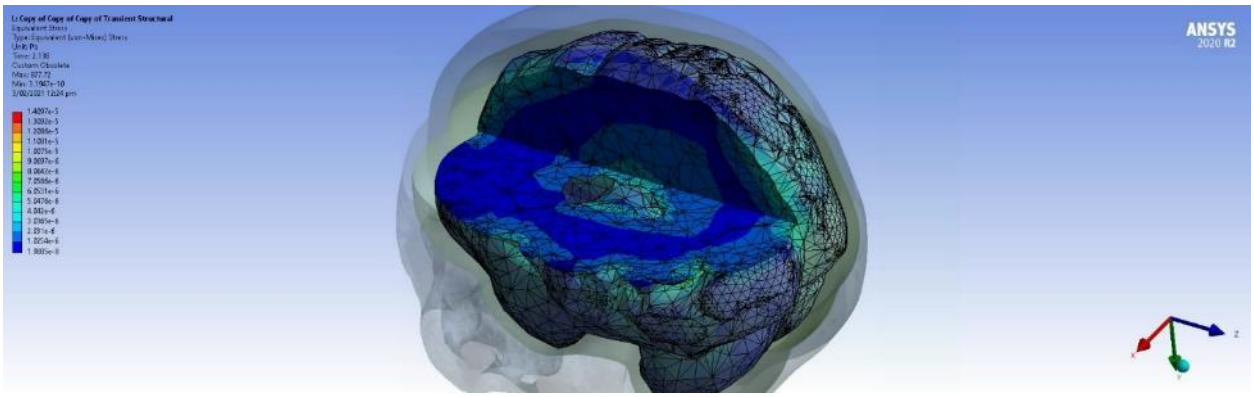
ANSYS
2020 R2

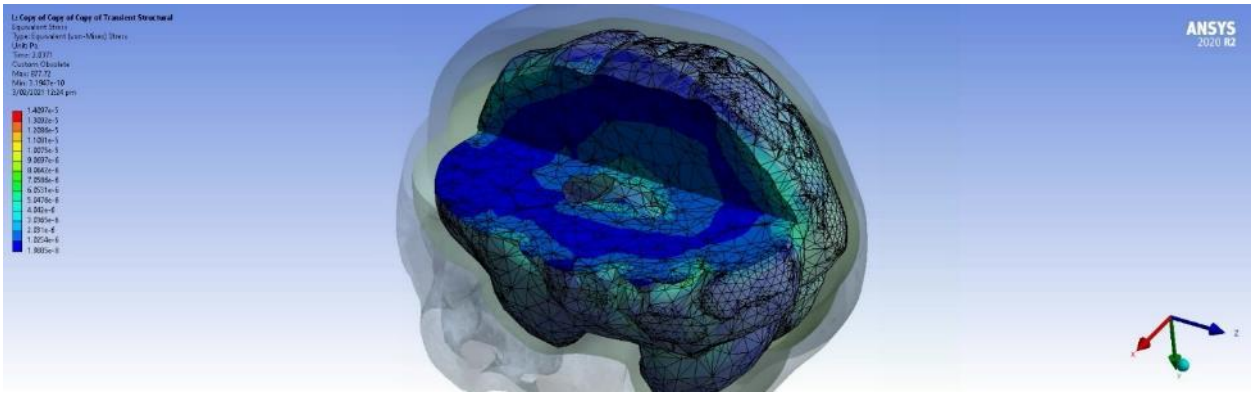
ANSYS
2020 R2

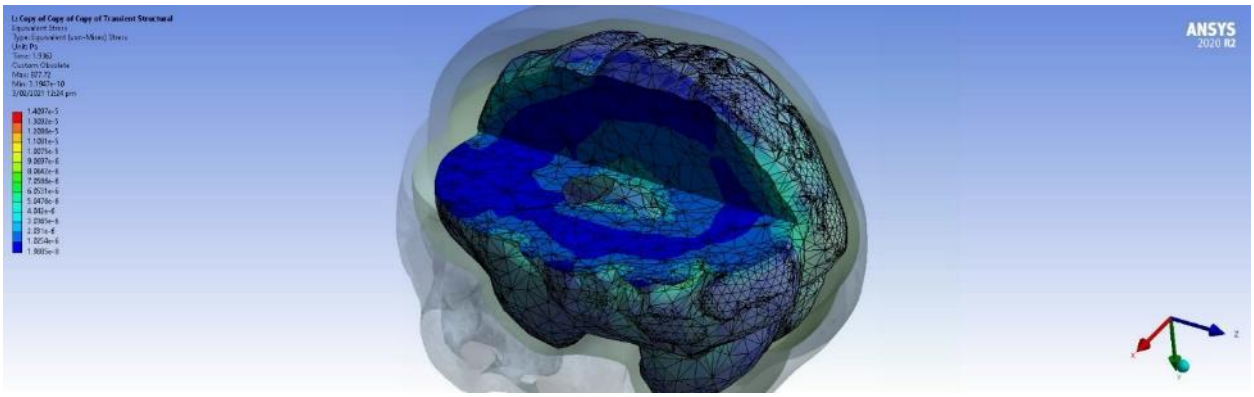
ANSYS
2020 R2

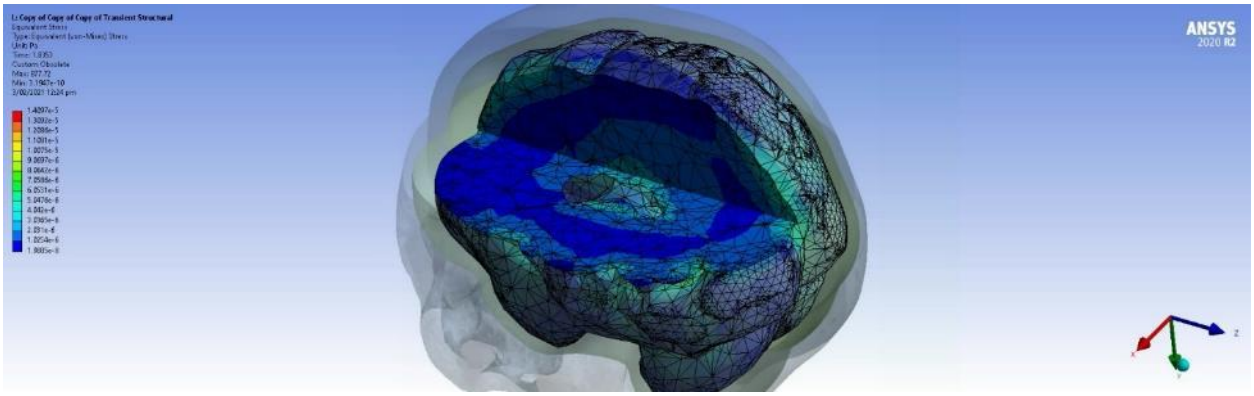
ANSYS
2020 R2

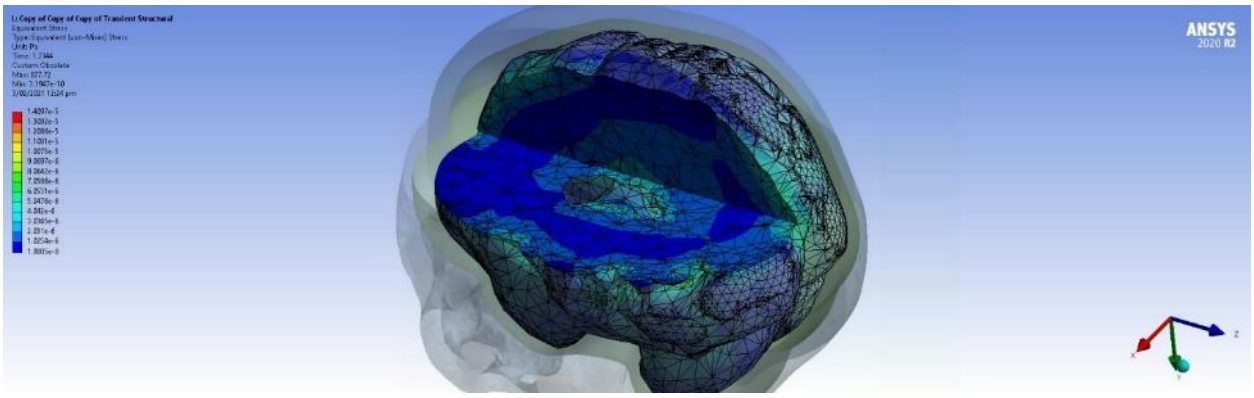
ANSYS
2020 R2

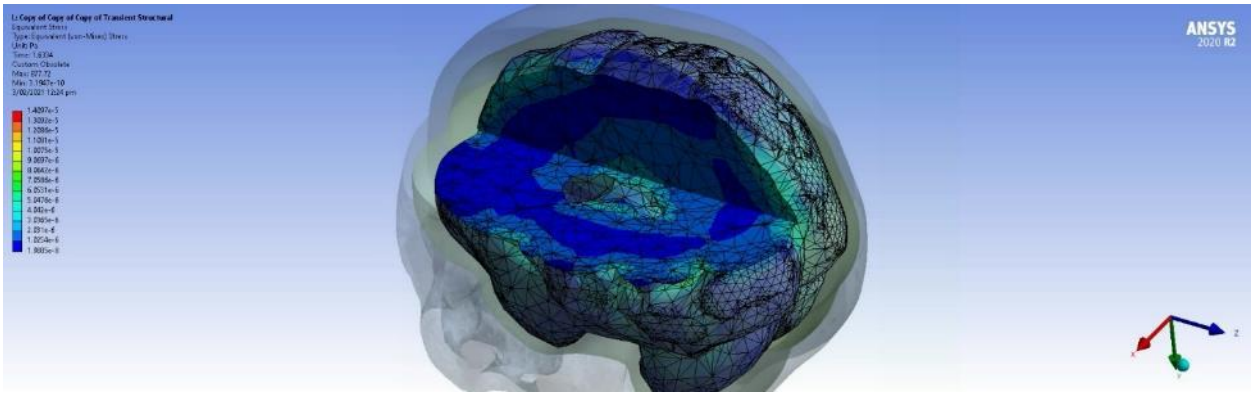
ANSYS
2020 R2

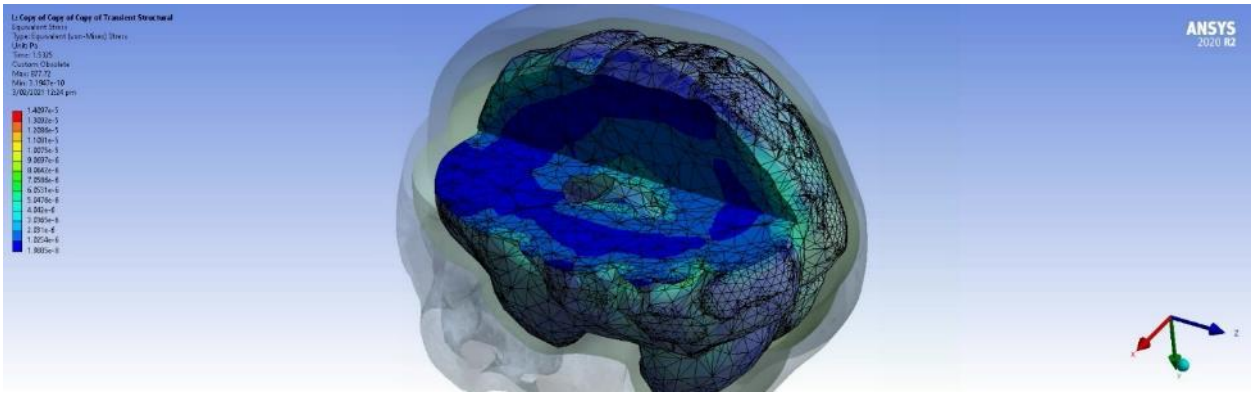
ANSYS
2020 R2

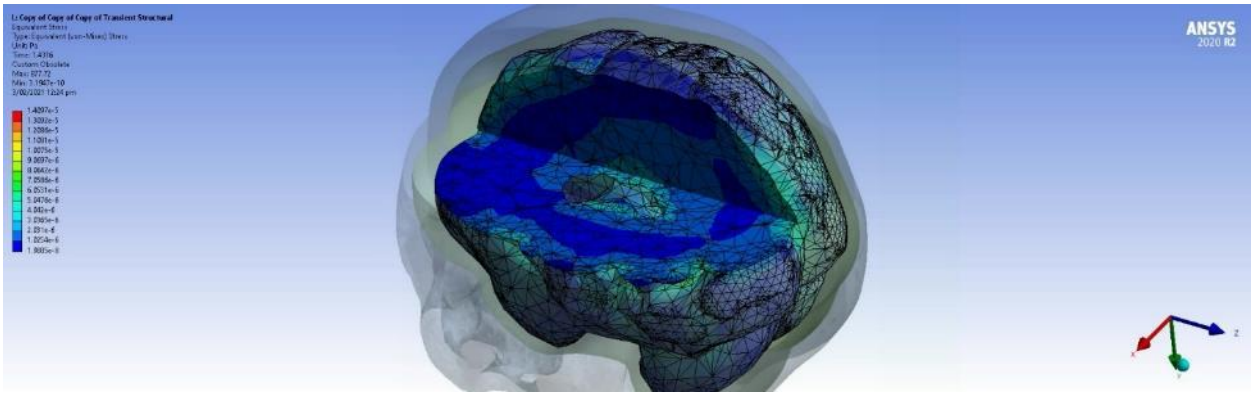
ANSYS
2020 R2

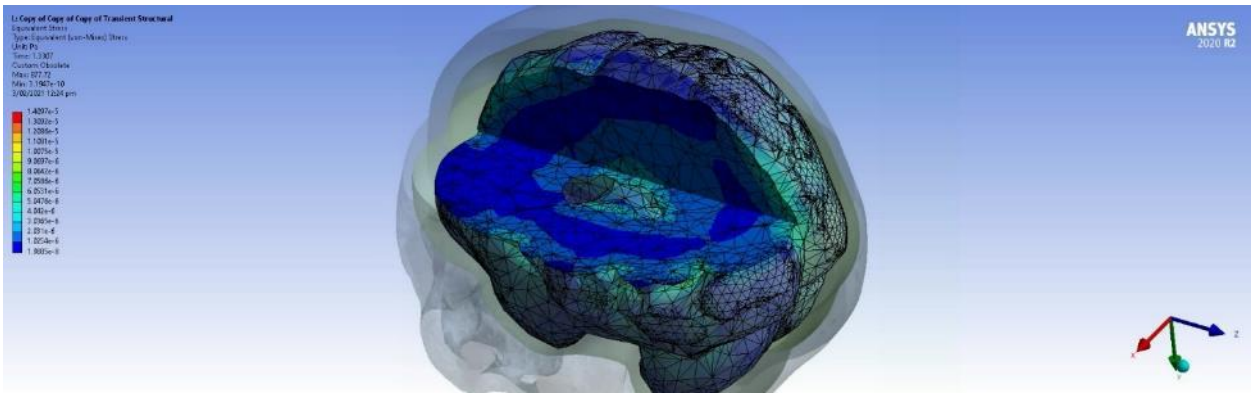
ANSYS
2020 R2

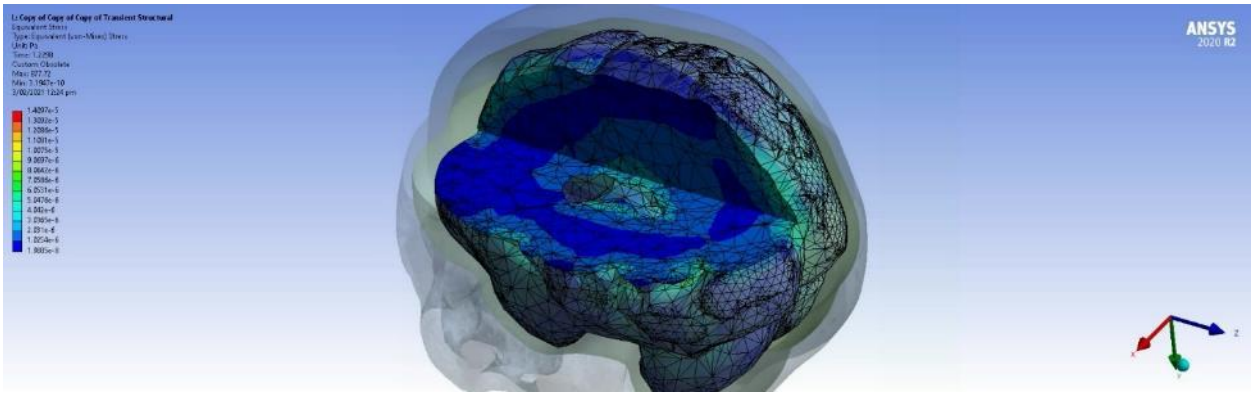
ANSYS
2020 R2

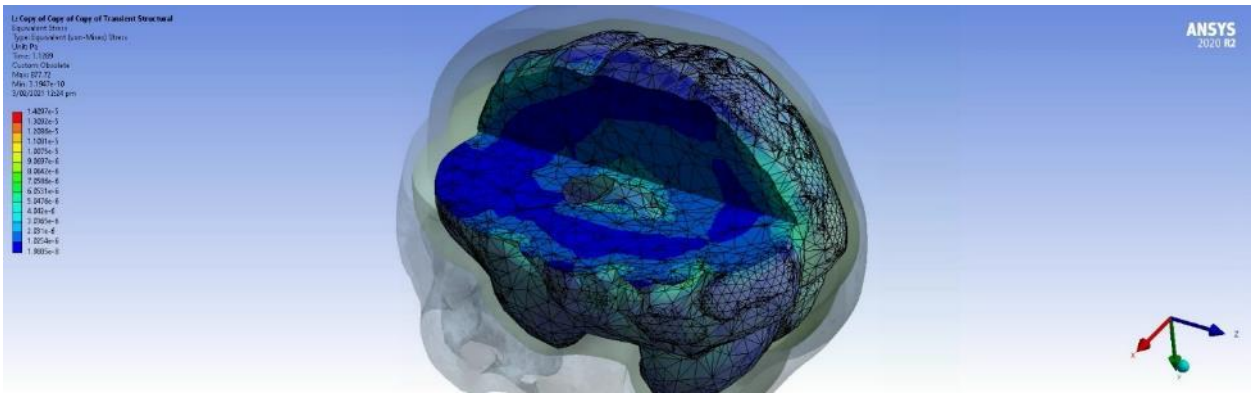
ANSYS
2020 R2

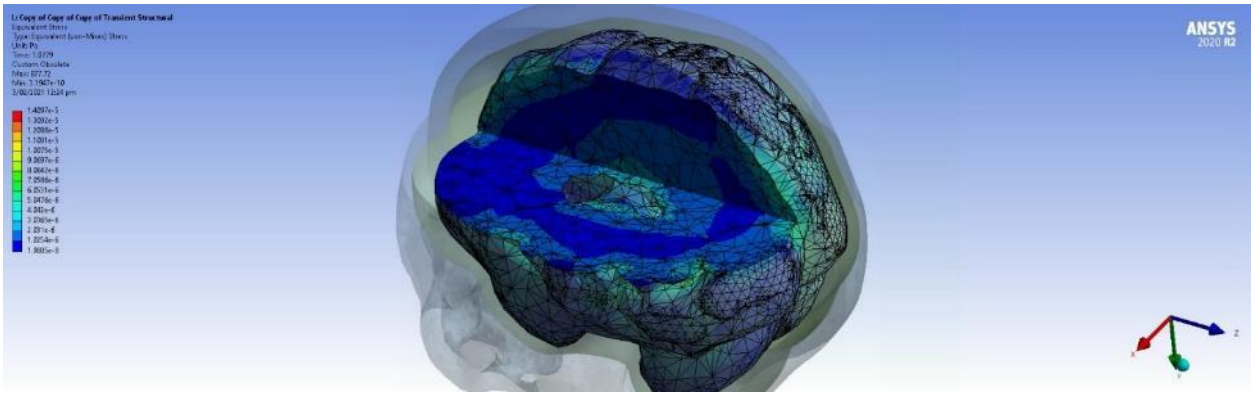
ANSYS
2020 R2

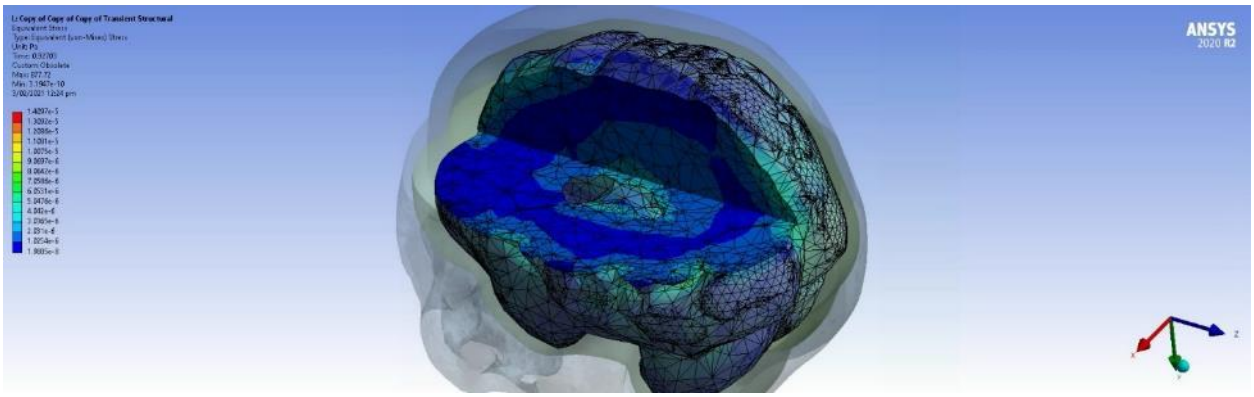
ANSYS
2020 R2

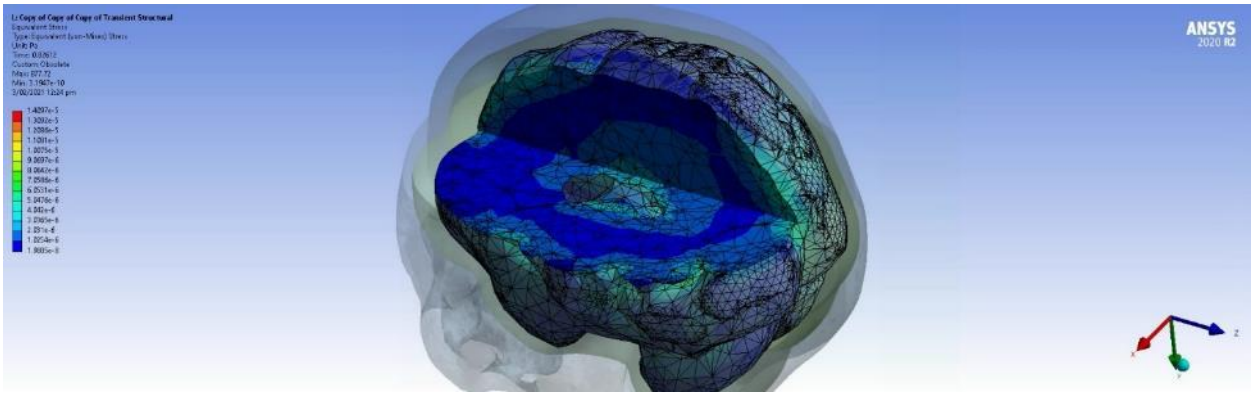
ANSYS
2020 R2

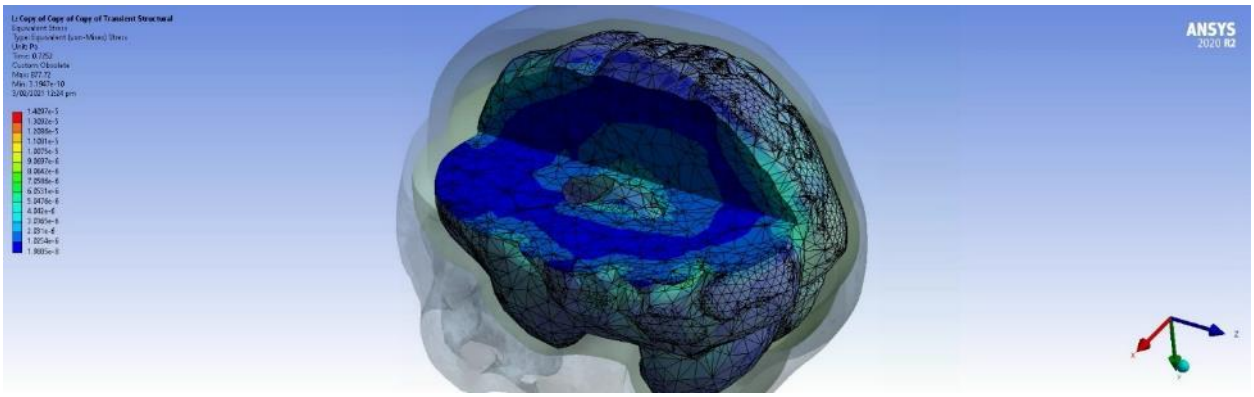
ANSYS
2020 R2

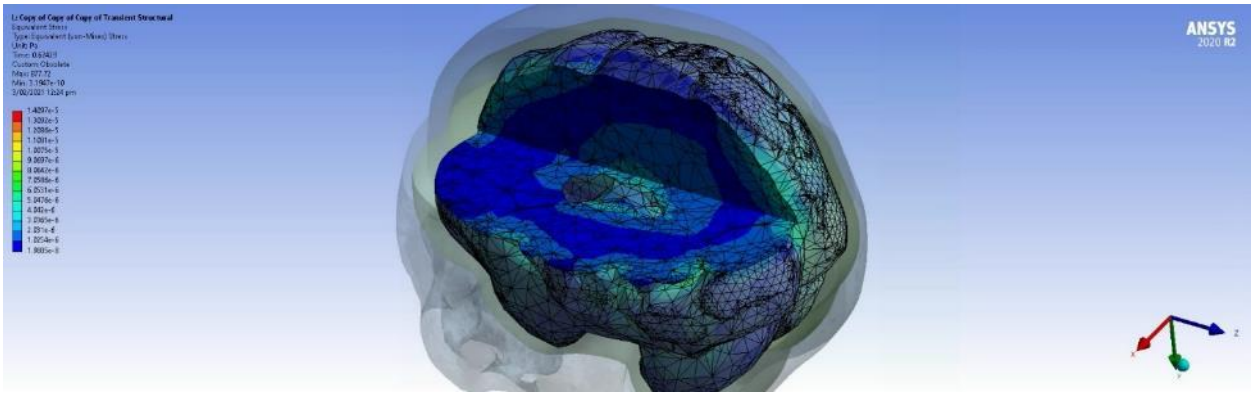
ANSYS
2020 R2

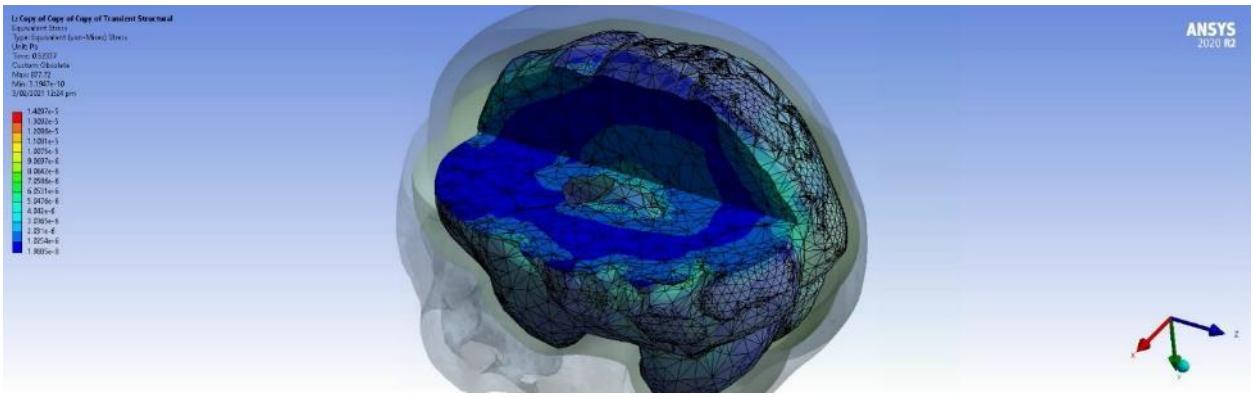
ANSYS
2020 R2

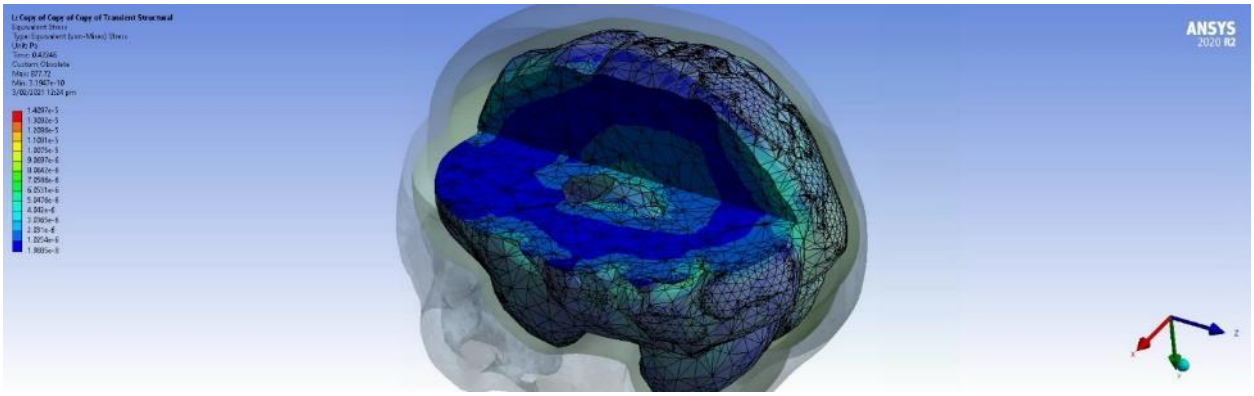
ANSYS
2020 R2

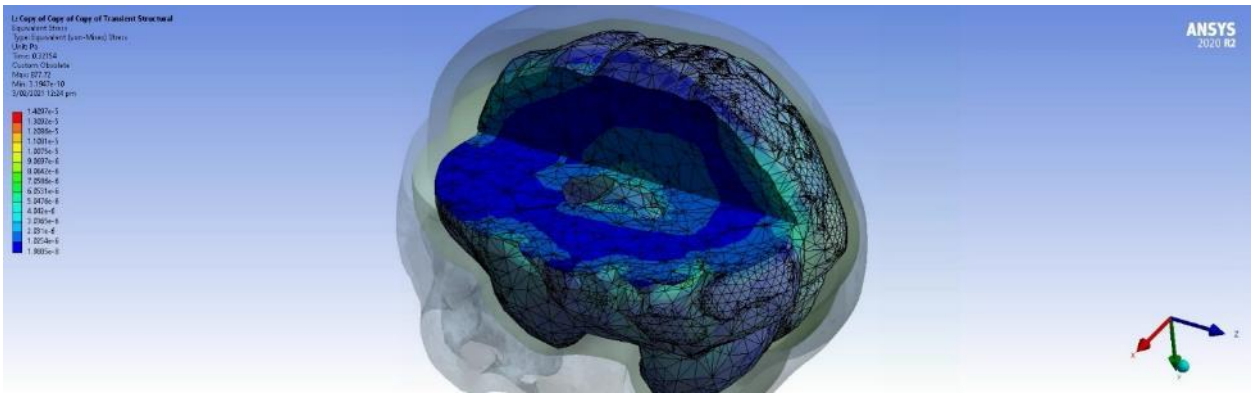
ANSYS
2020 R2

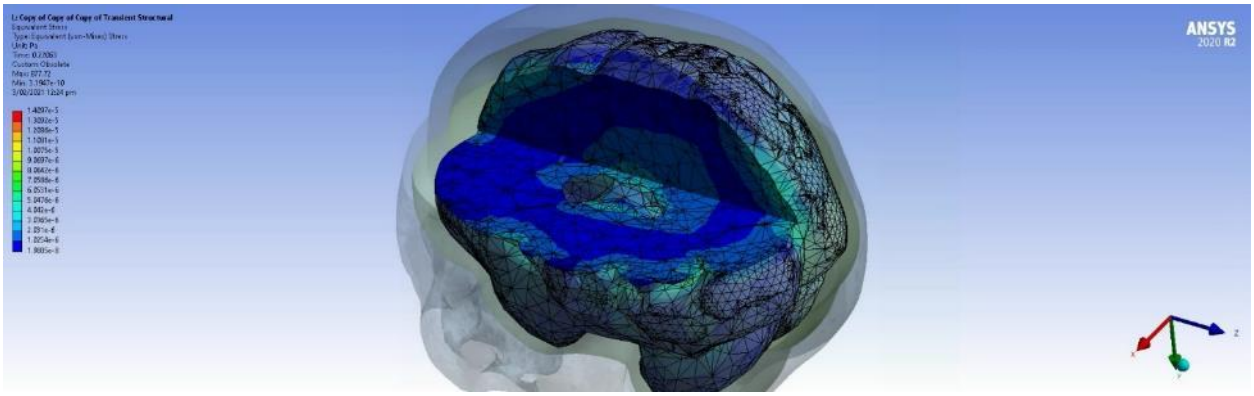
ANSYS
2020 R2

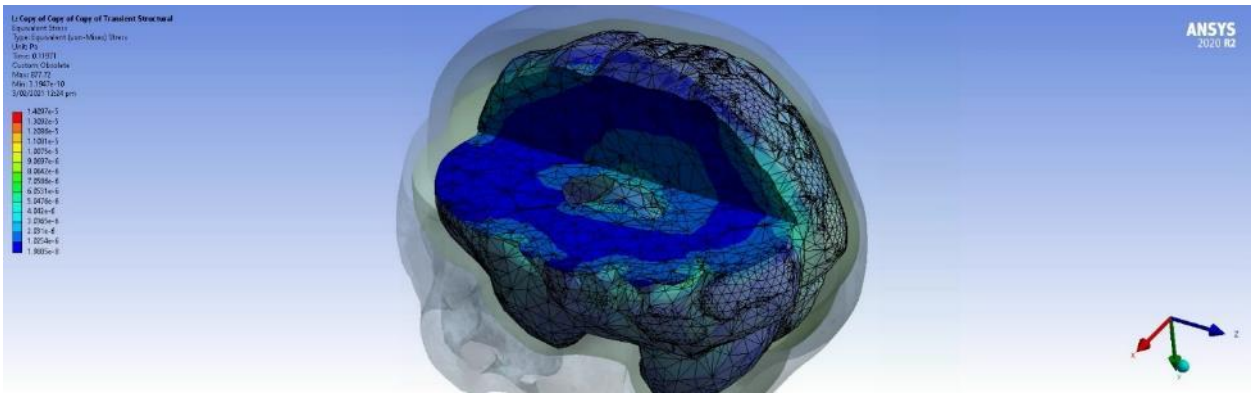
ANSYS
2020 R2

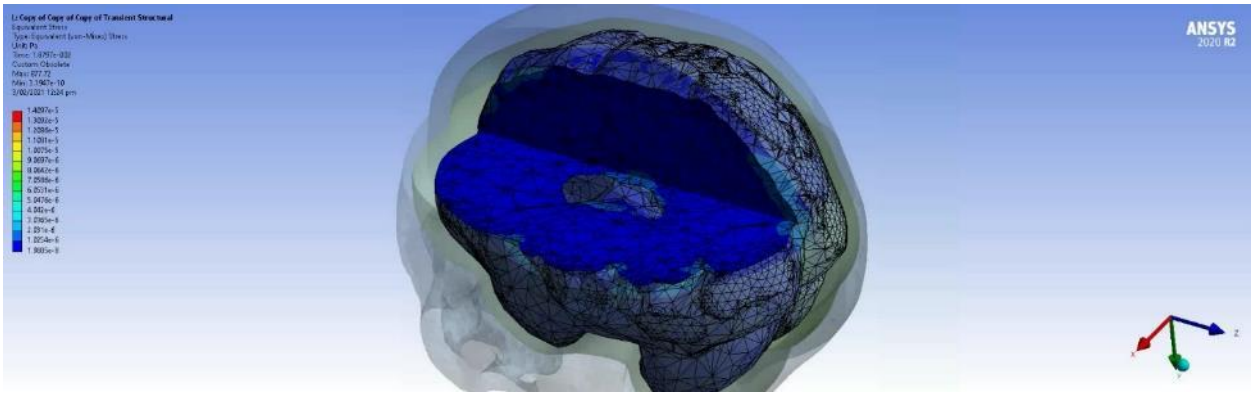
ANSYS
2020 R2

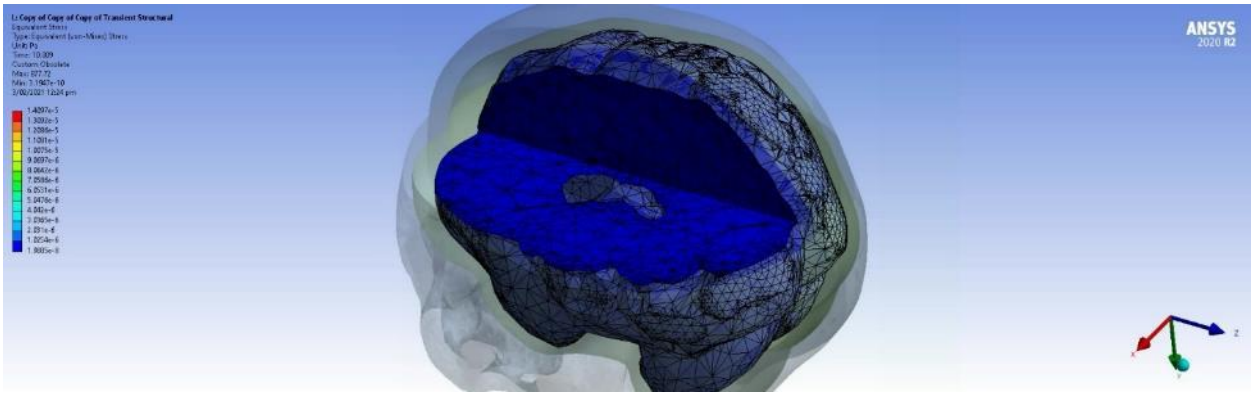
ANSYS
2020 R2

Impact Zone 3

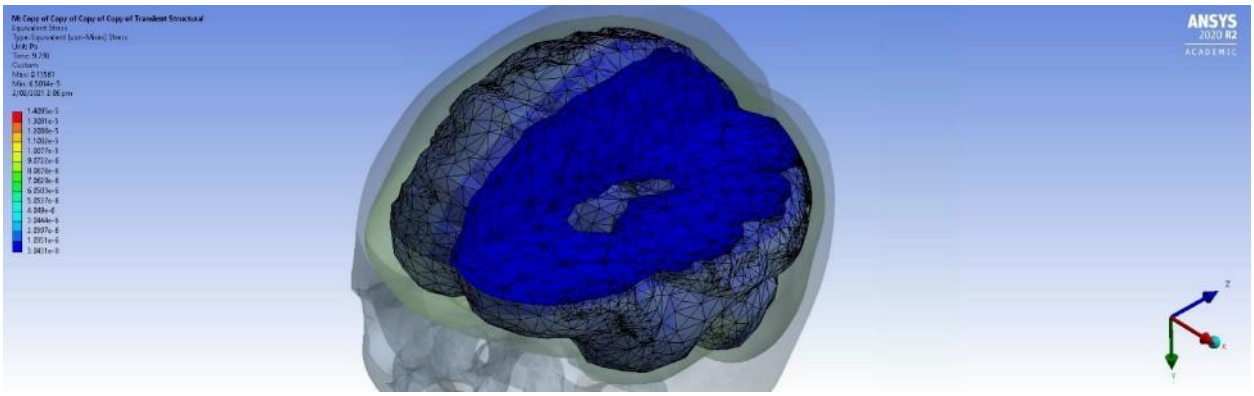

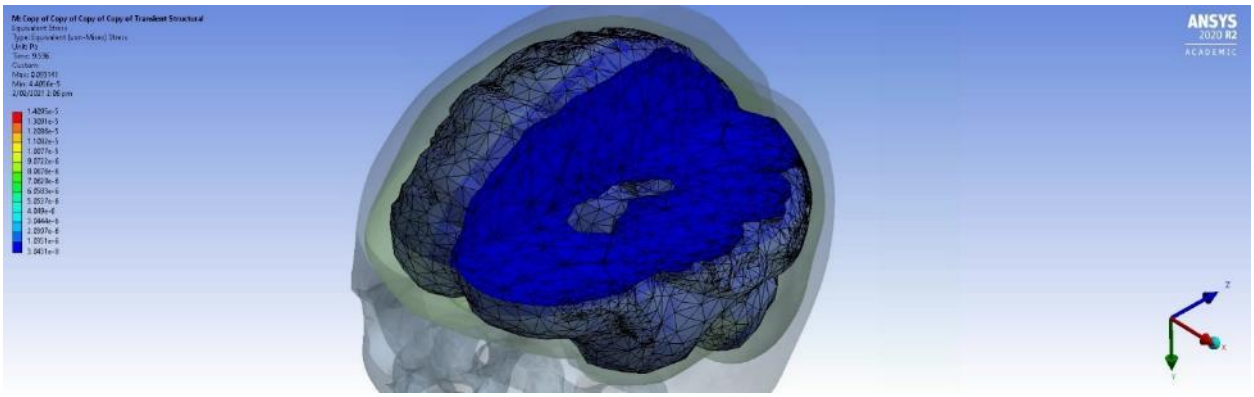

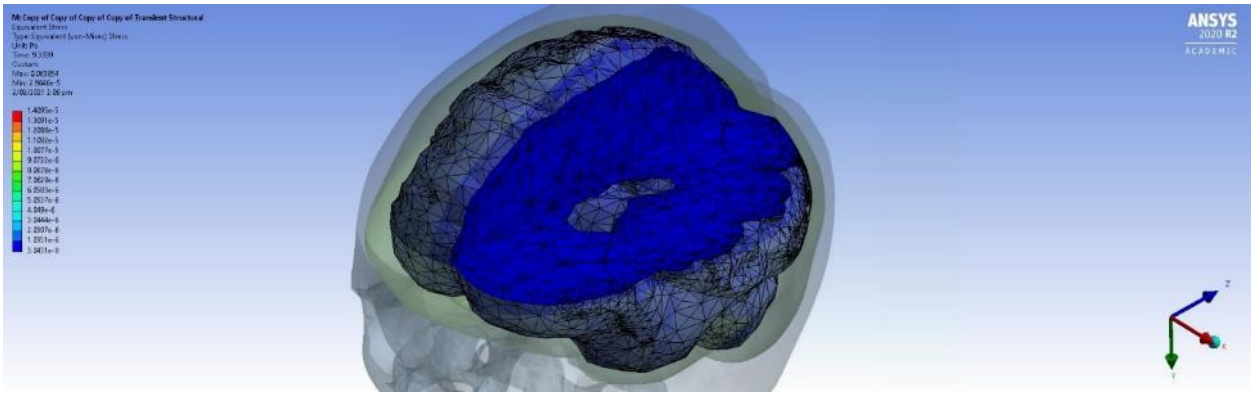

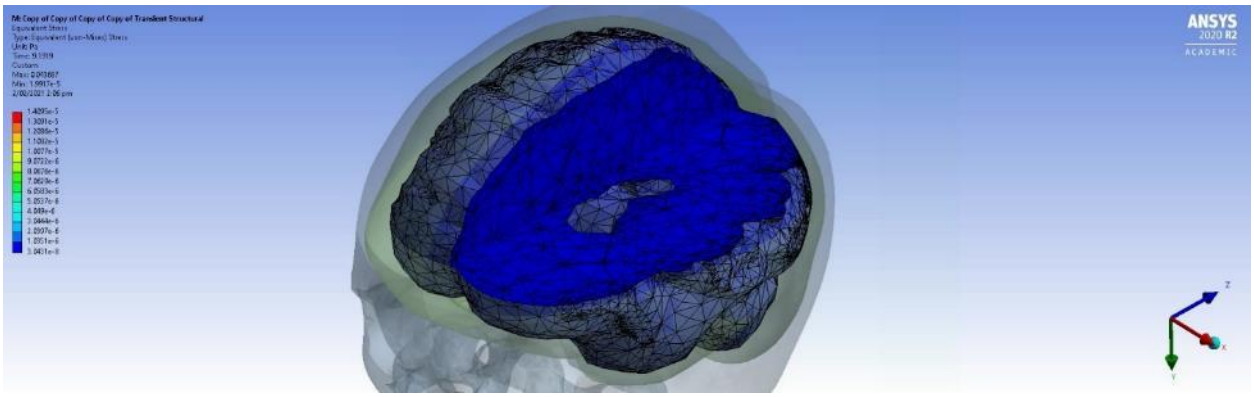

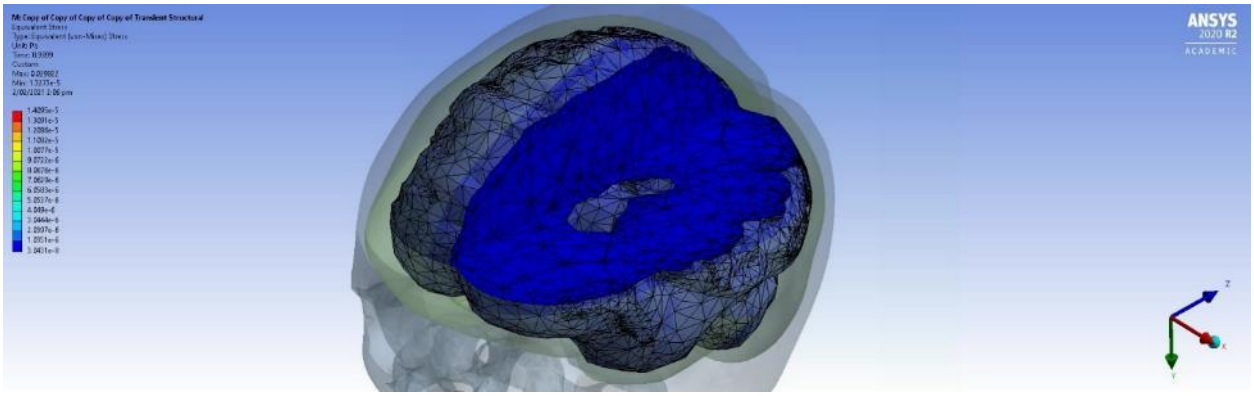
ANSYS
2020 R2
ACADEMIC

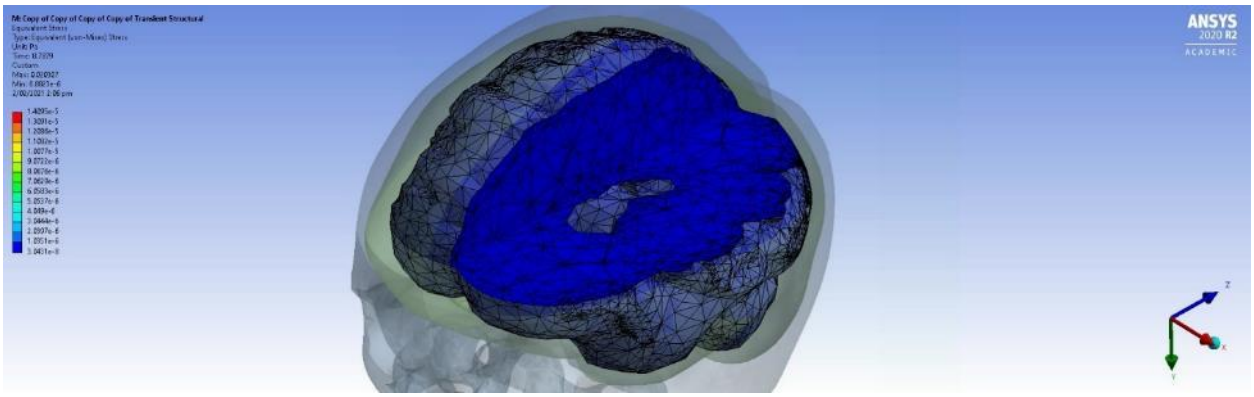
ANSYS
2020 R2
ACADEMIC

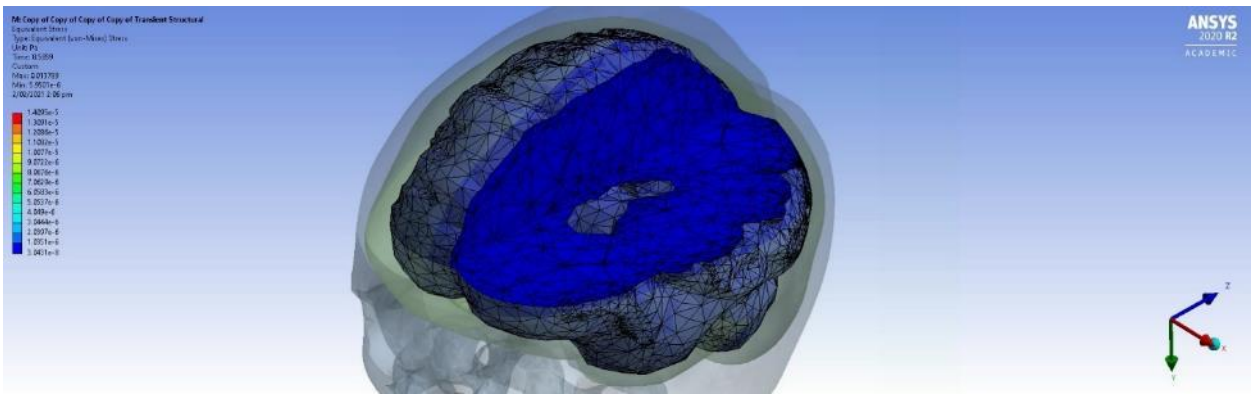
ANSYS
2020 R2
ACADEMIC

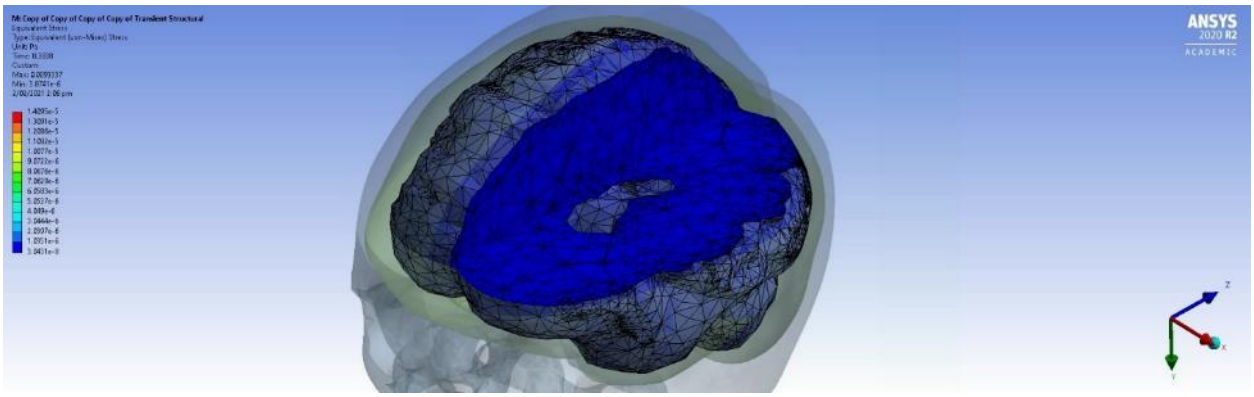
ANSYS
2020 R2
ACADEMIC

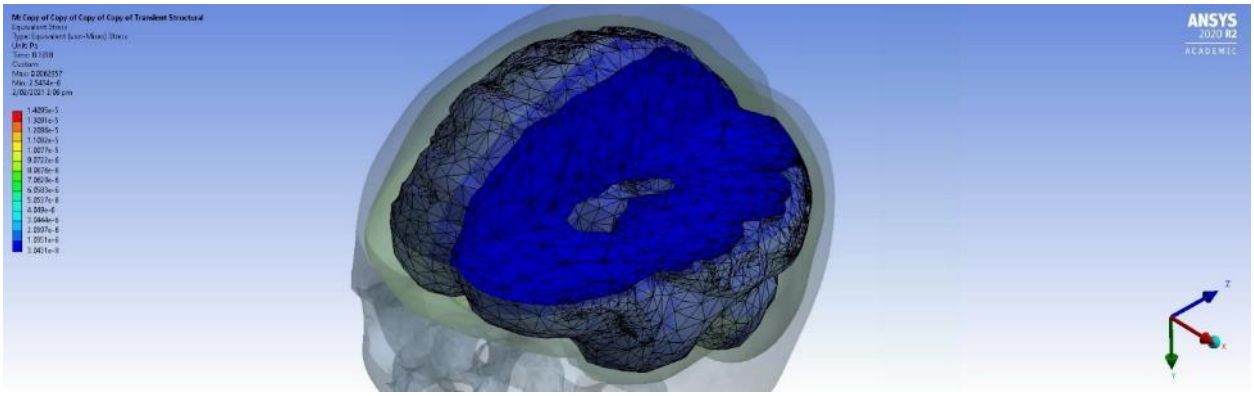
ANSYS
2020 R2
ACADEMIC

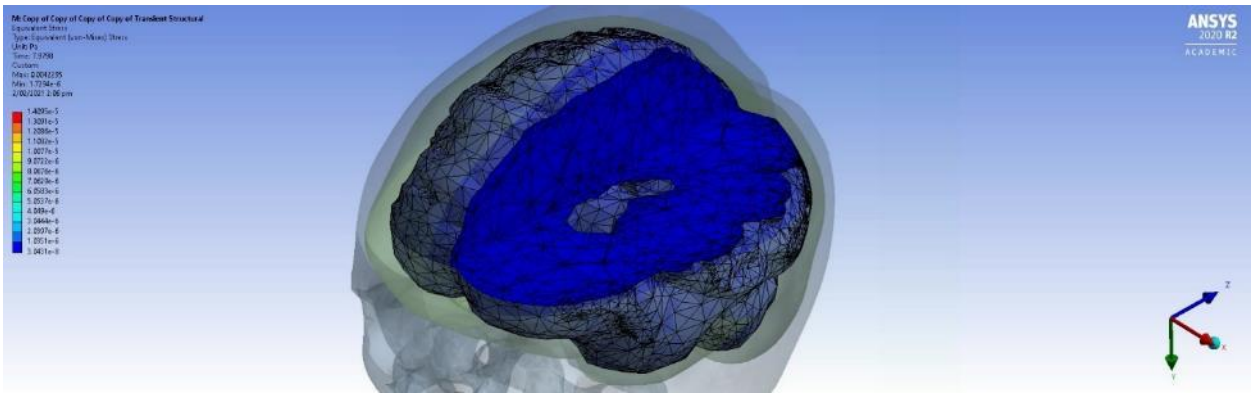
ANSYS
2020 R2
ACADEMIC

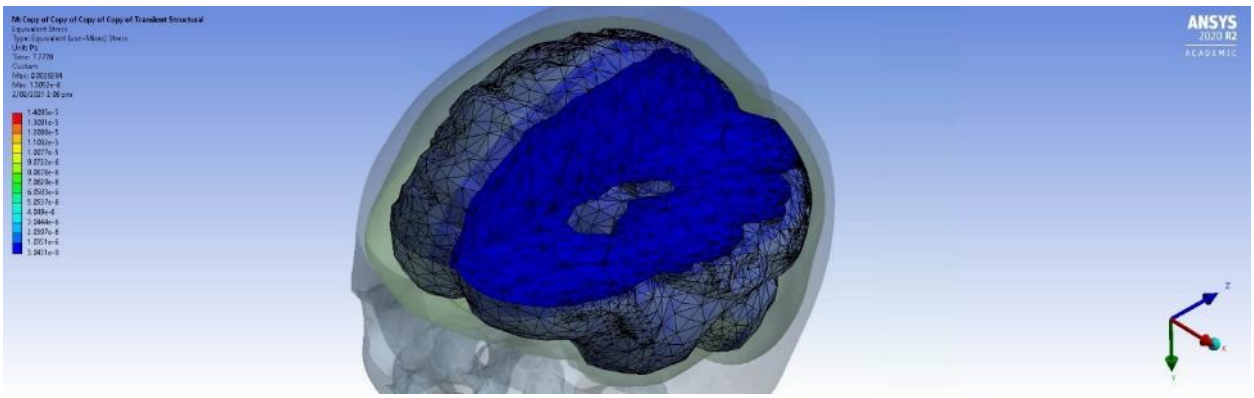
ANSYS
2020 R2
ACADEMIC

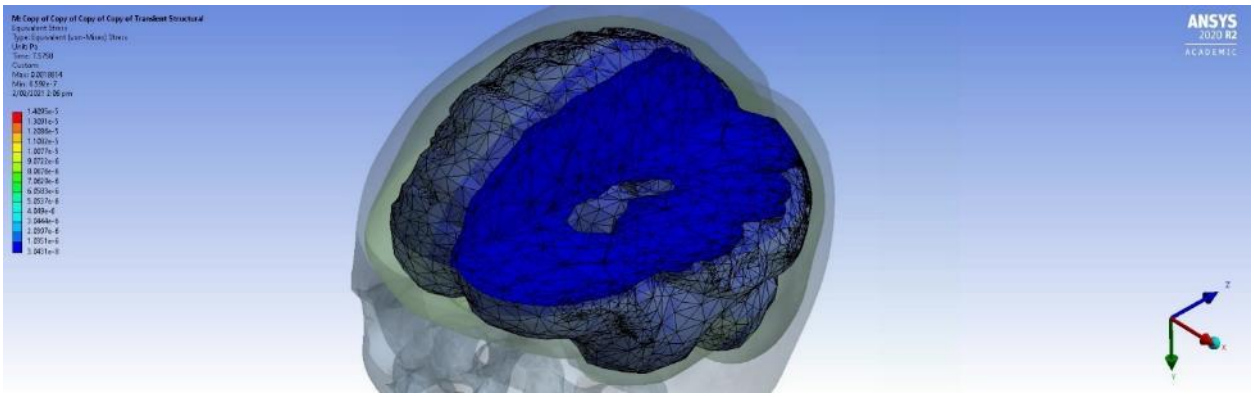
ANSYS
2020 R2
ACADEMIC

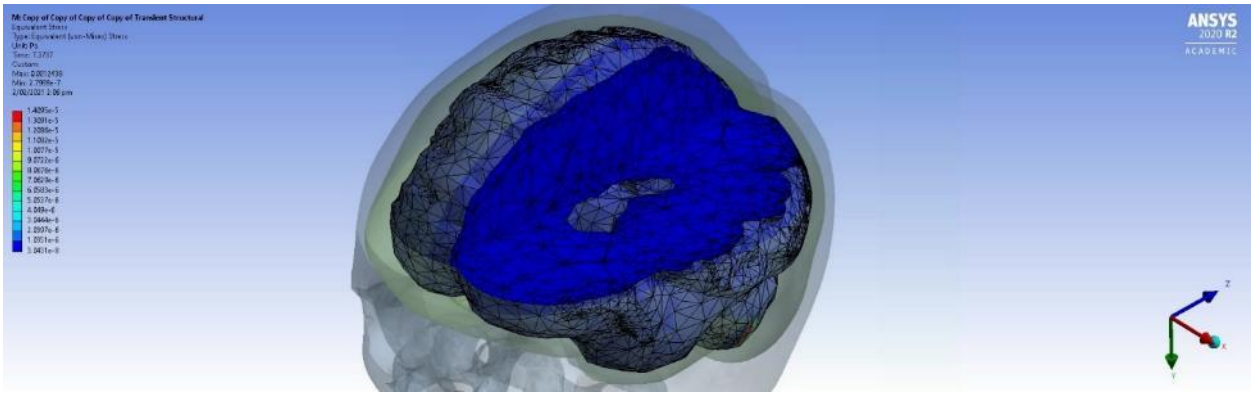
ANSYS
2020 R2
ACADEMIC

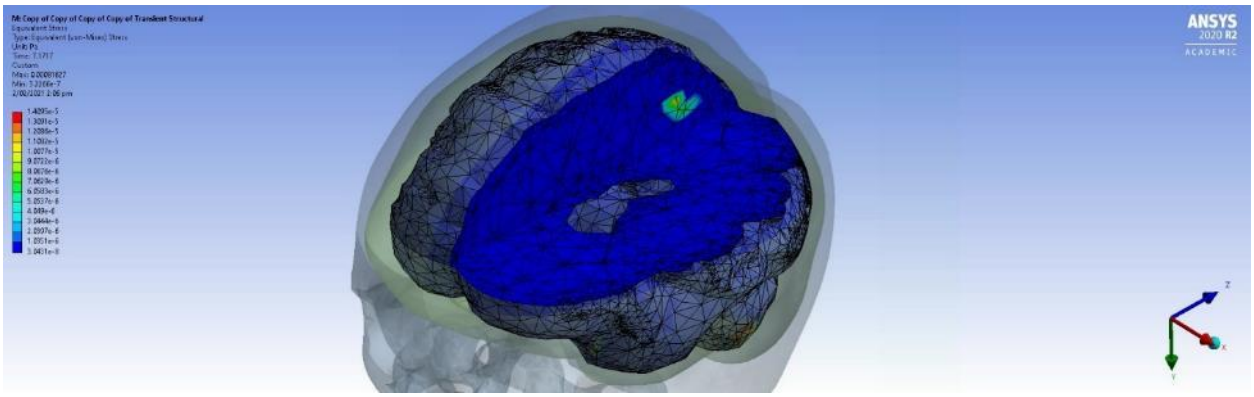
ANSYS
2020 R2
ACADEMIC

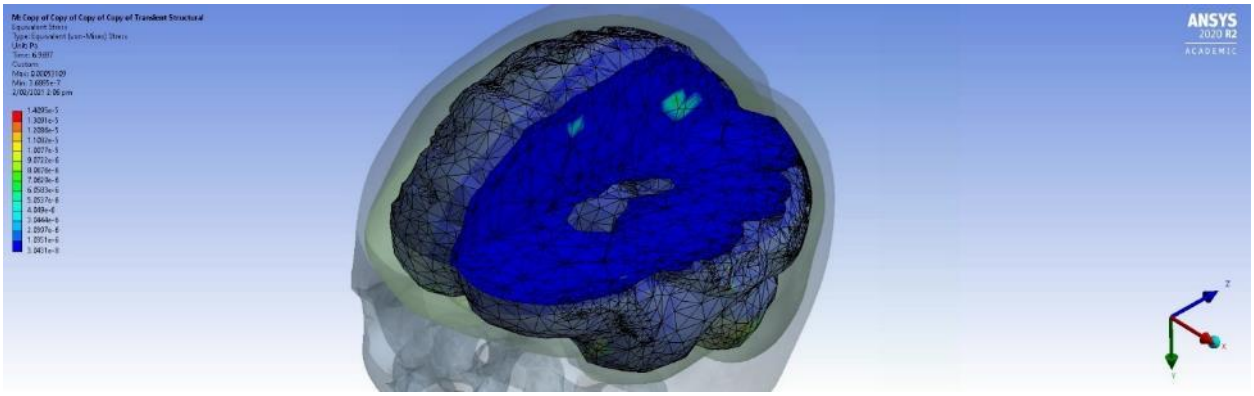
ANSYS
2020 R2
ACADEMIC

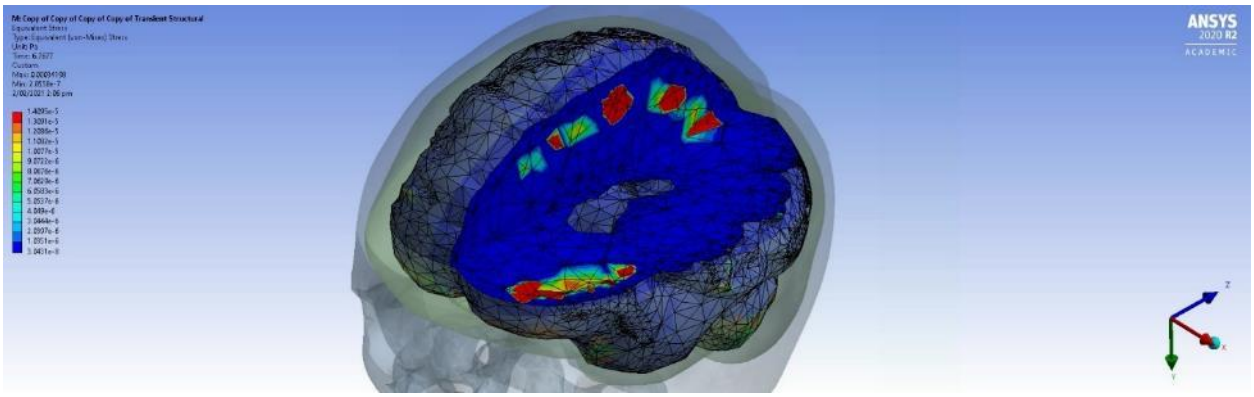
ANSYS
2020 R2
ACADEMIC

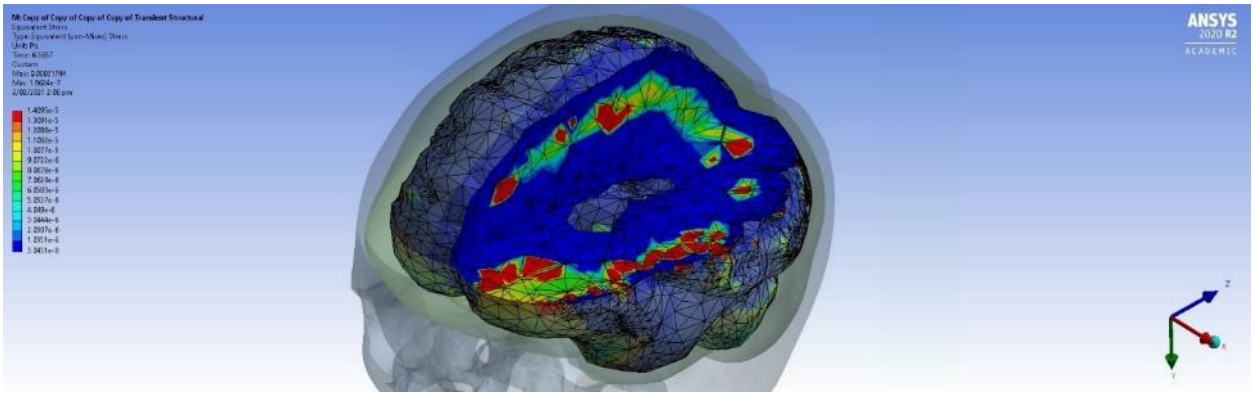
ANSYS
2020 R2
ACADEMIC

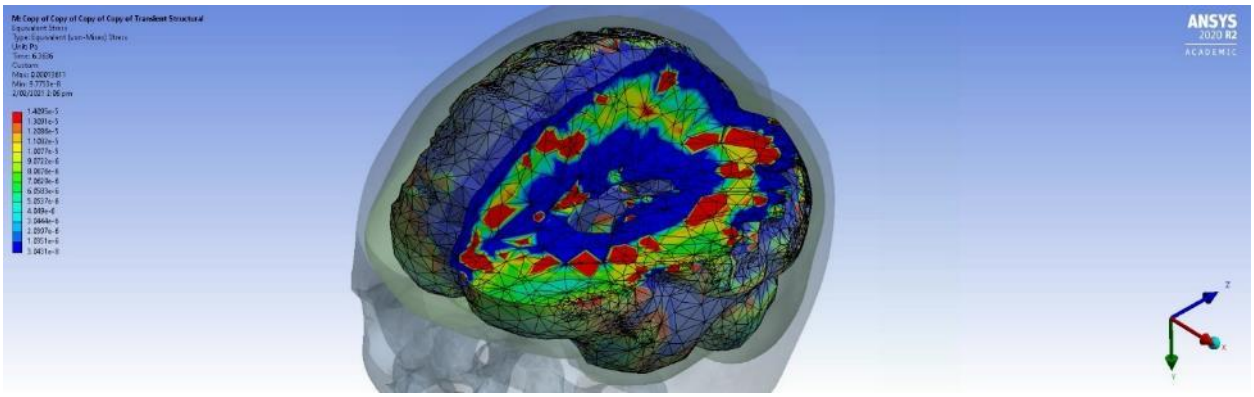
ANSYS
2020 R2
ACADEMIC

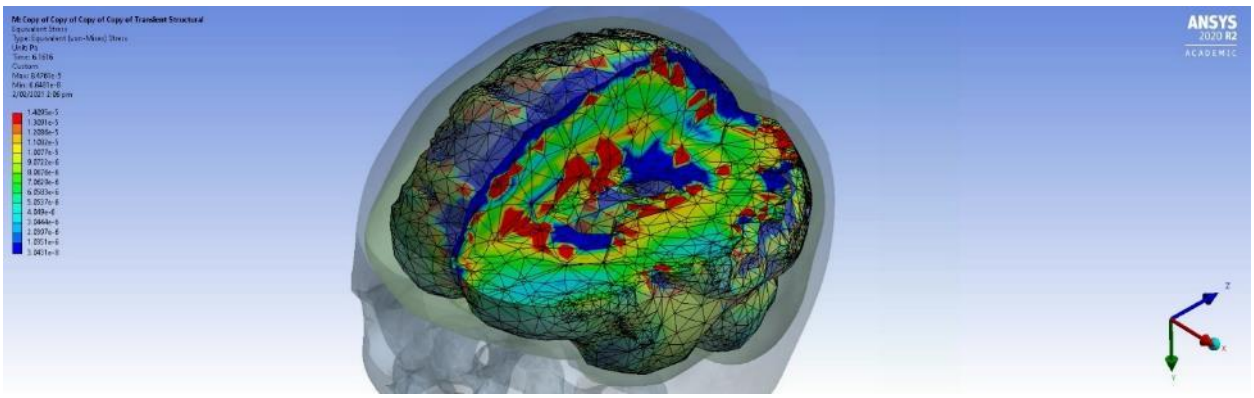
ANSYS
2020 R2
ACADEMIC

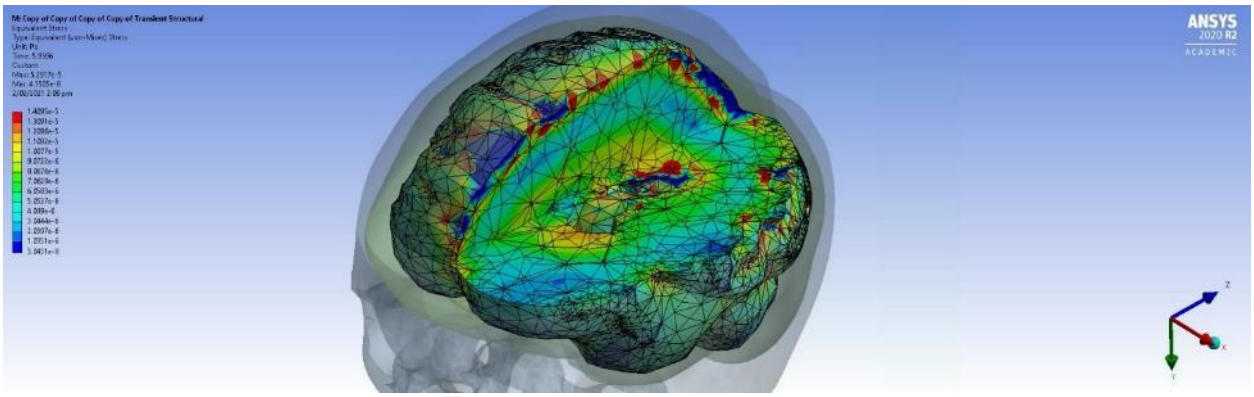
ANSYS
2020 R2
ACADEMIC

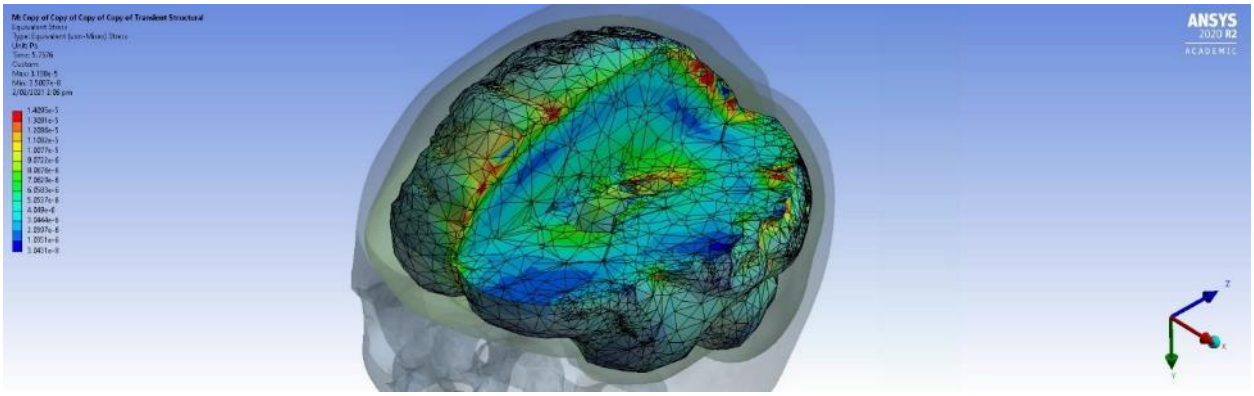
ANSYS
2020 R2
ACADEMIC

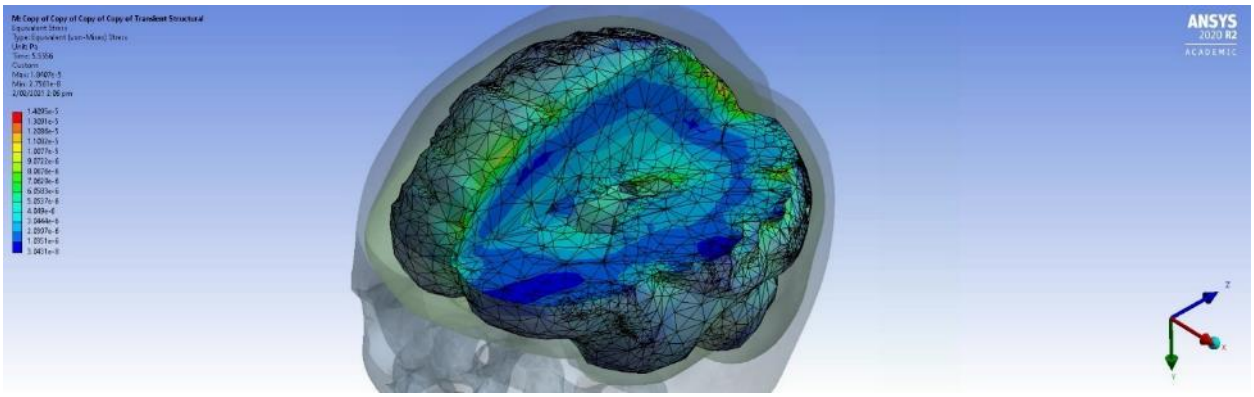
ANSYS
2020 R2
ACADEMIC

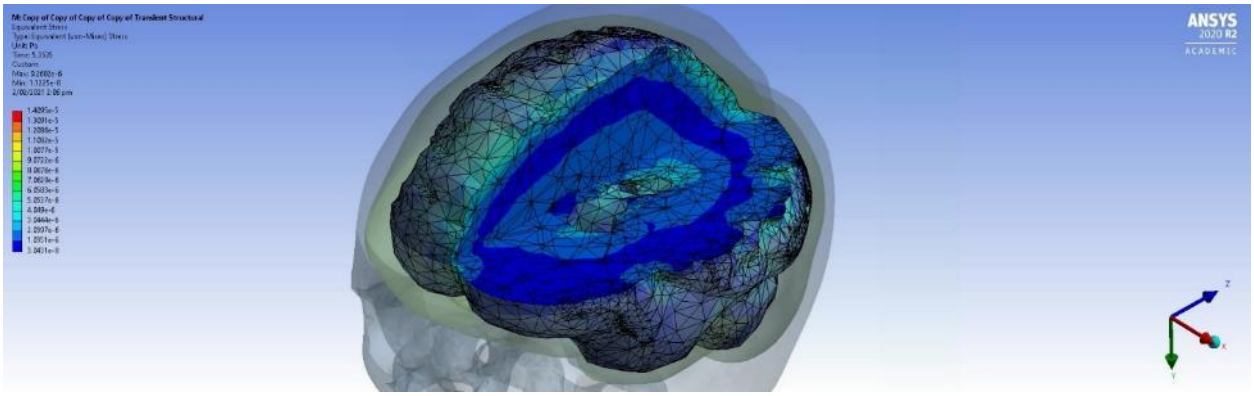
ANSYS
2020 R2
ACADEMIC

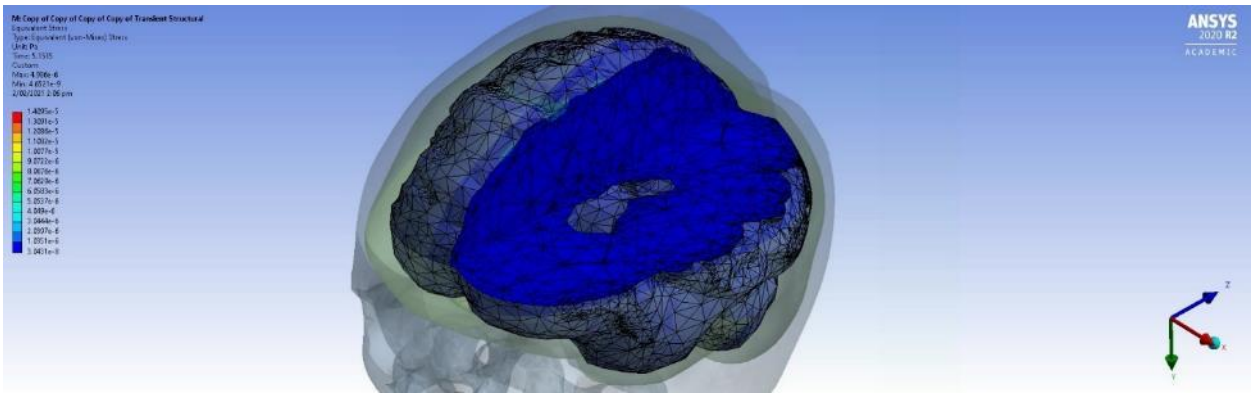
ANSYS
2020 R2
ACADEMIC

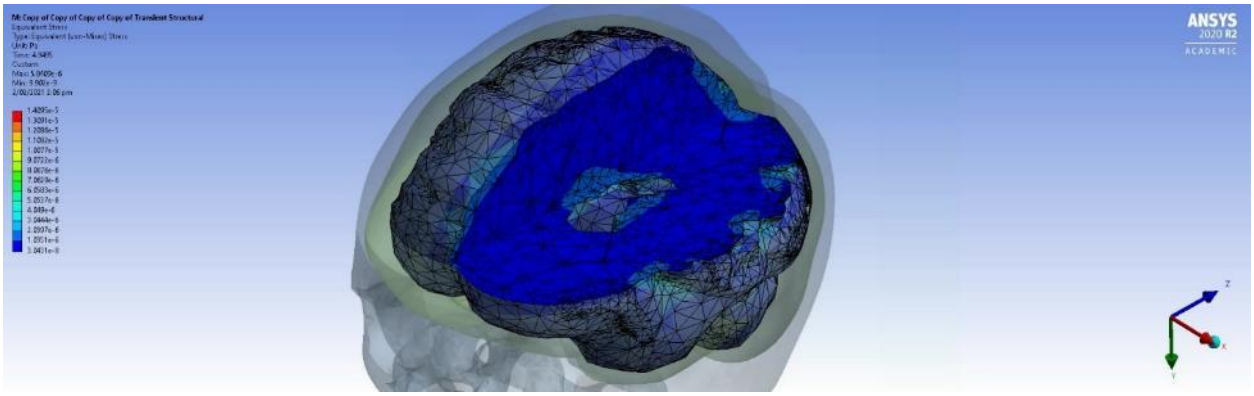
ANSYS
2020 R2
ACADEMIC

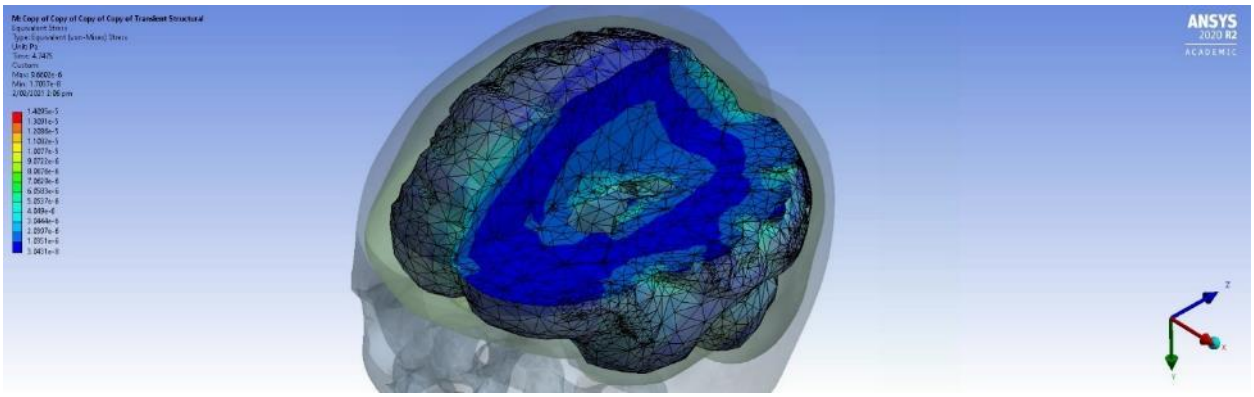
ANSYS
2020 R2
ACADEMIC

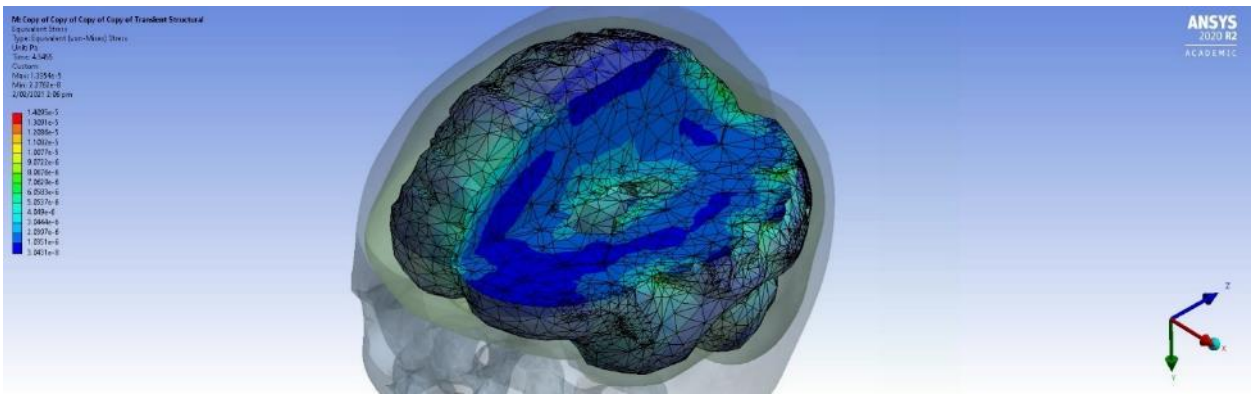
ANSYS
2020 R2
ACADEMIC

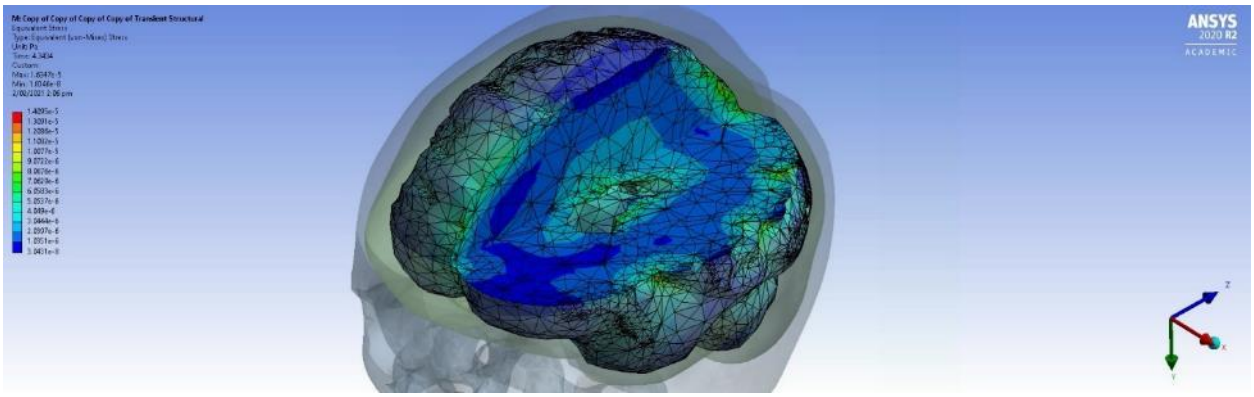
ANSYS
2020 R2
ACADEMIC

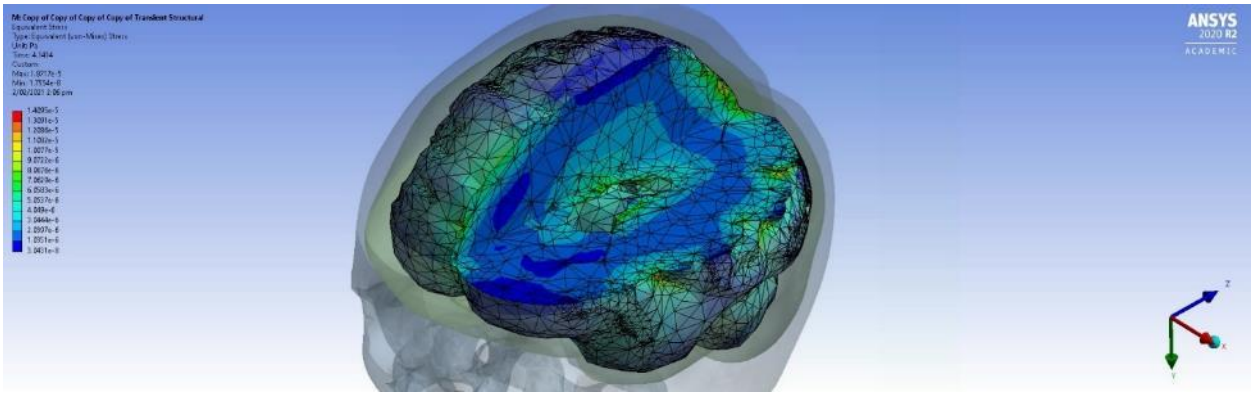
ANSYS
2020 R2
ACADEMIC

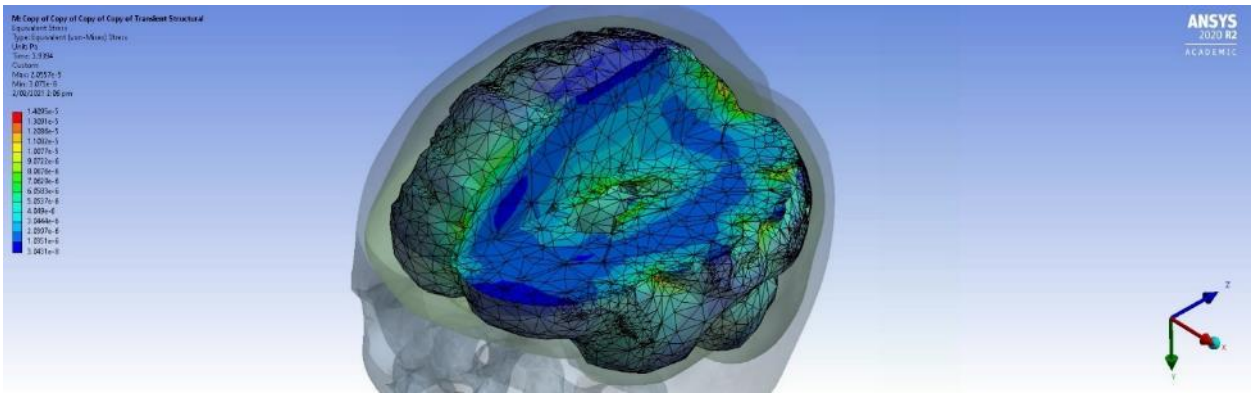
ANSYS
2020 R2
ACADEMIC

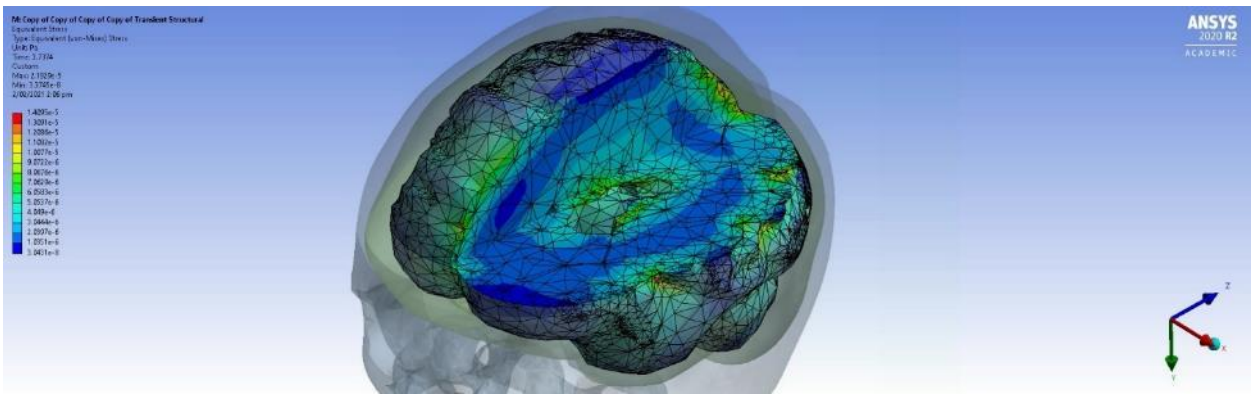
ANSYS
2020 R2
ACADEMIC

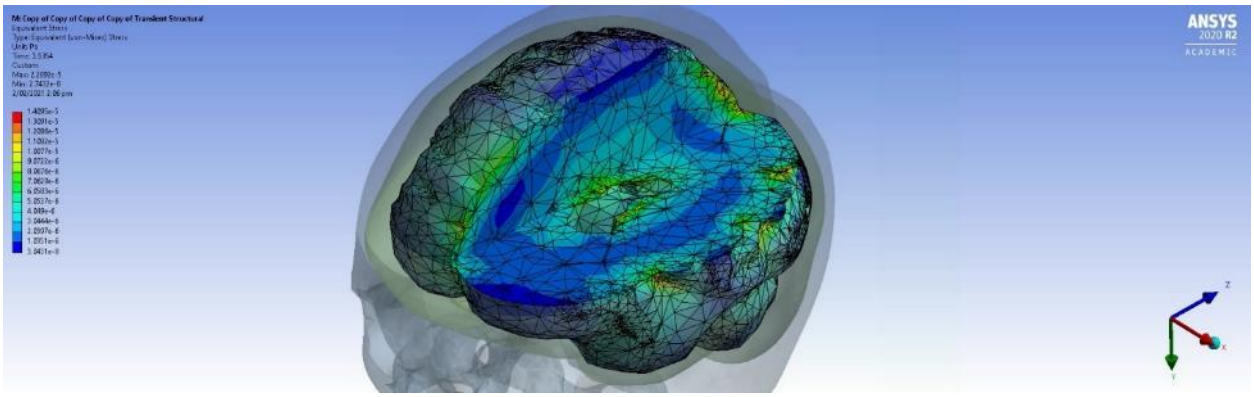
ANSYS
2020 R2
ACADEMIC

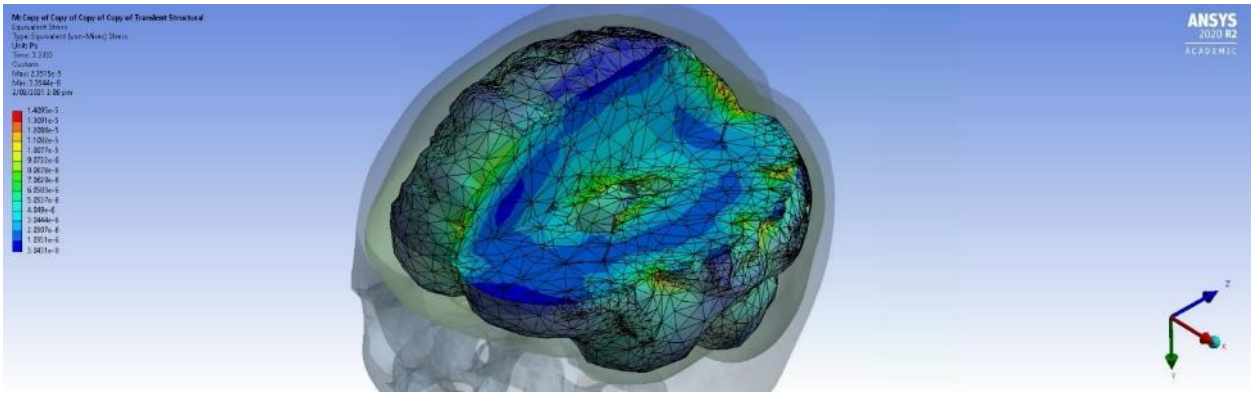
ANSYS
2020 R2
ACADEMIC

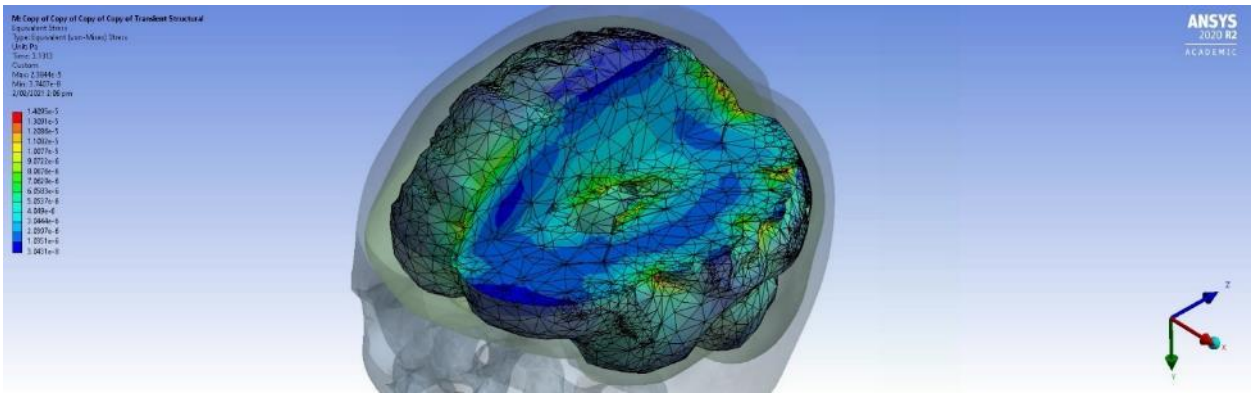
ANSYS
2020 R2
ACADEMIC

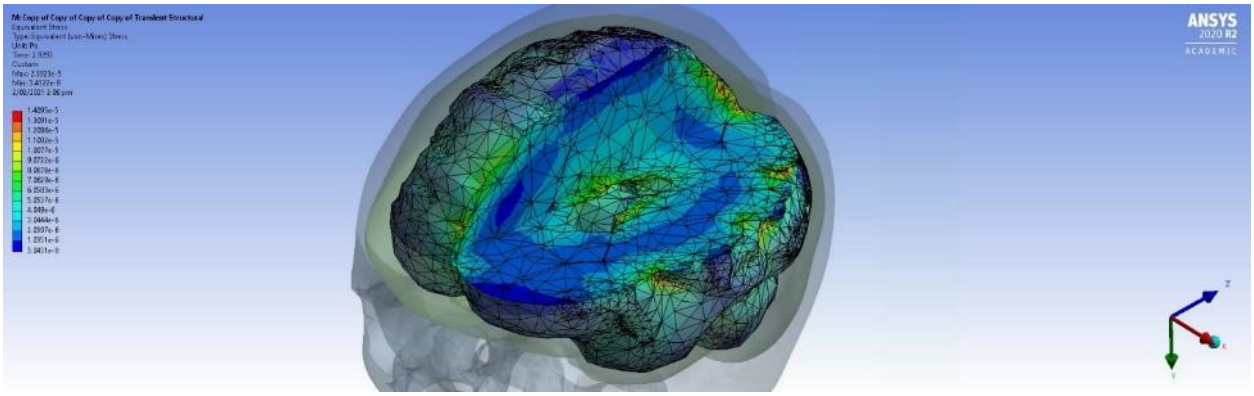
ANSYS
2020 R2
ACADEMIC

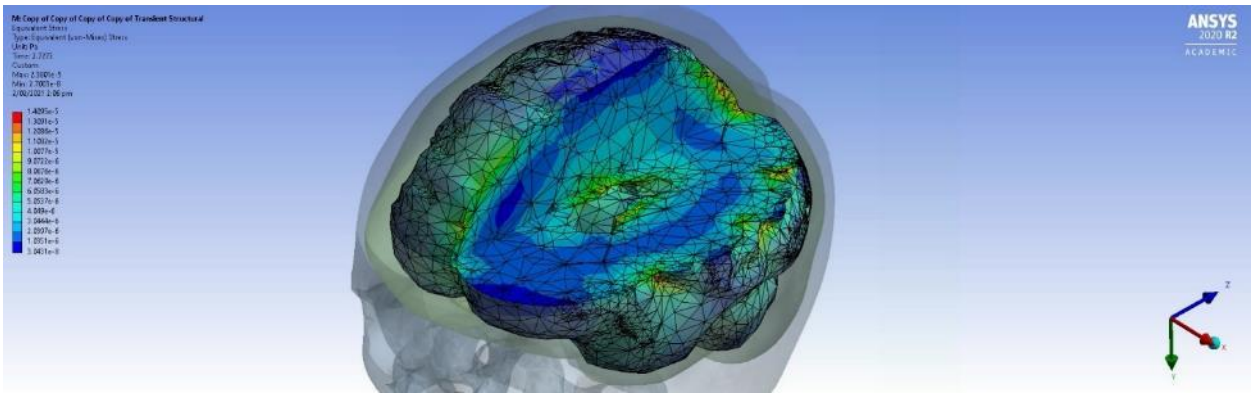
ANSYS
2020 R2
ACADEMIC

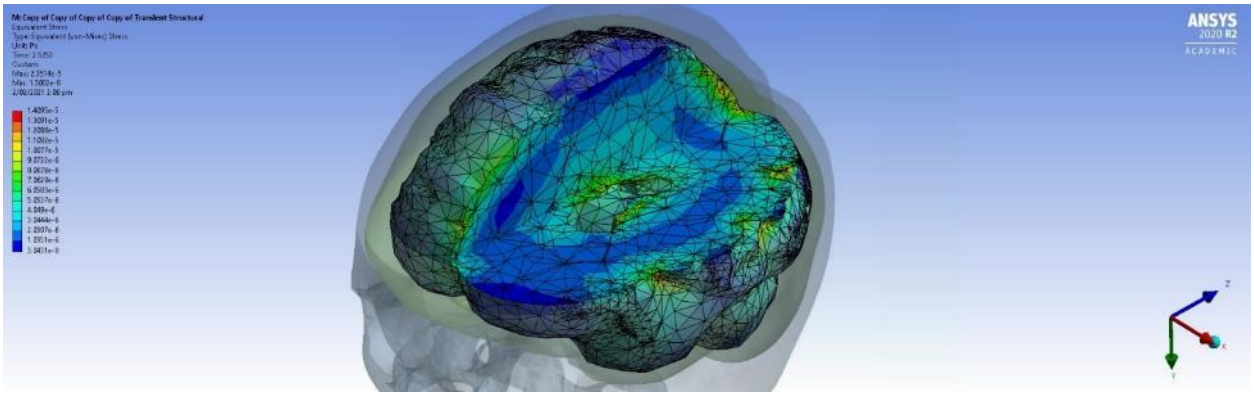
ANSYS
2020 R2
ACADEMIC

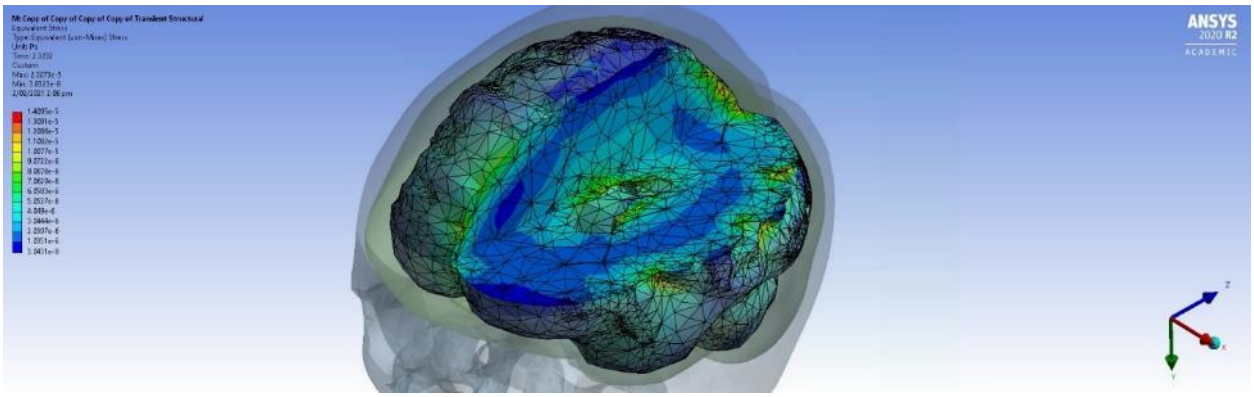
ANSYS
2020 R2
ACADEMIC

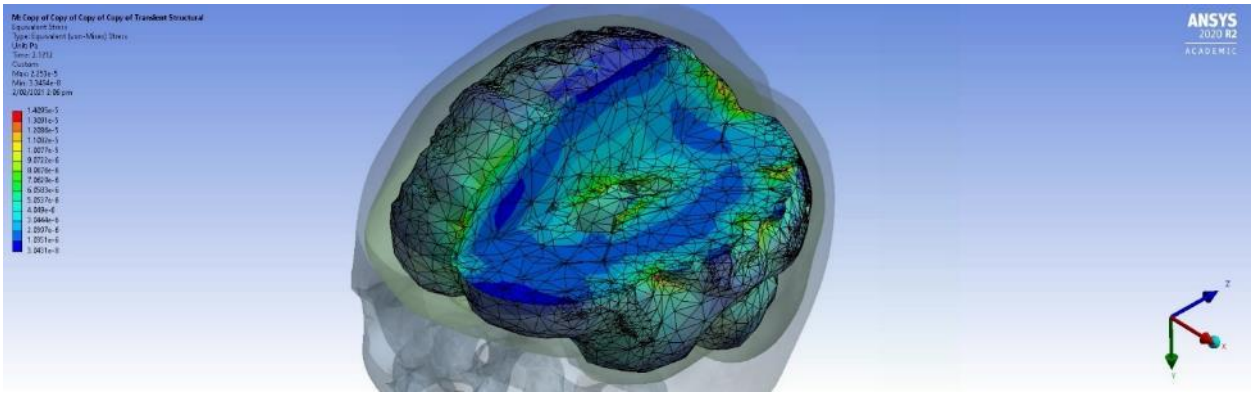
ANSYS
2020 R2
ACADEMIC

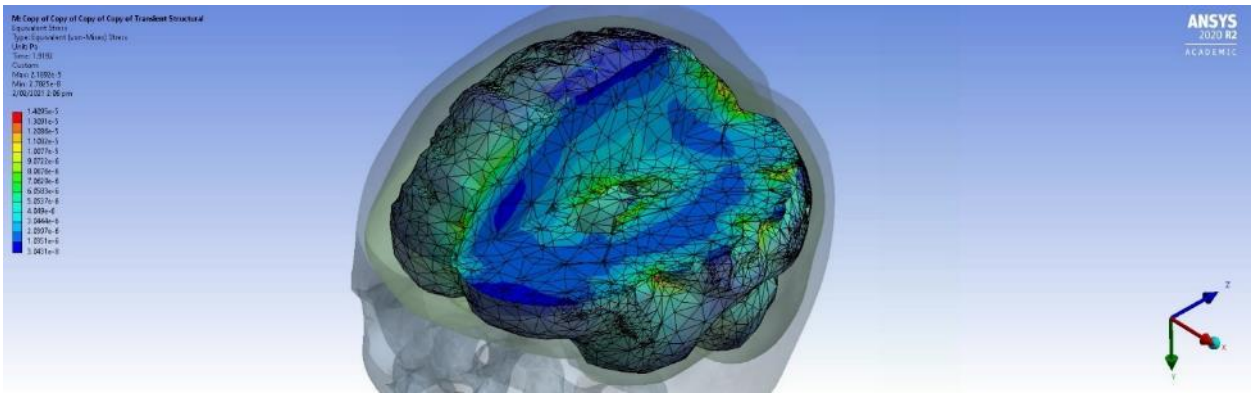
ANSYS
2020 R2
ACADEMIC

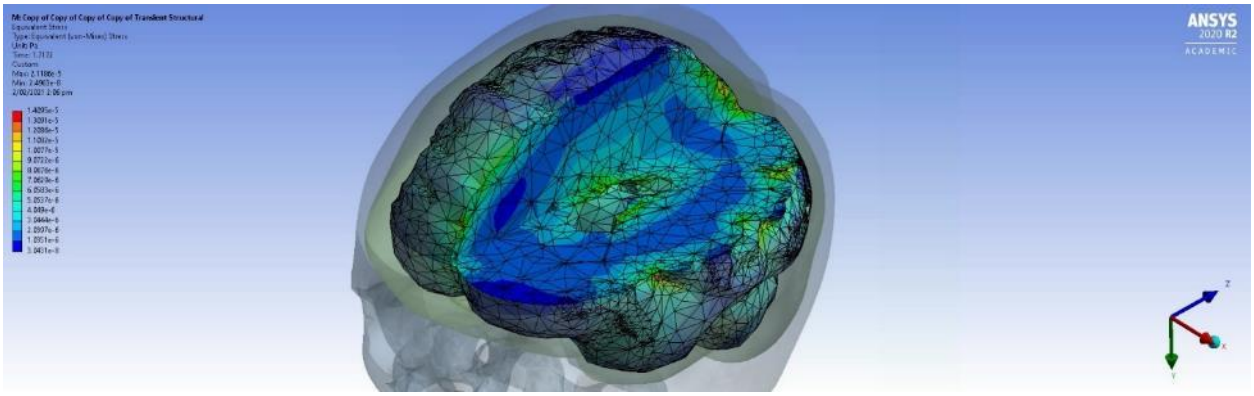
ANSYS
2020 R2
ACADEMIC

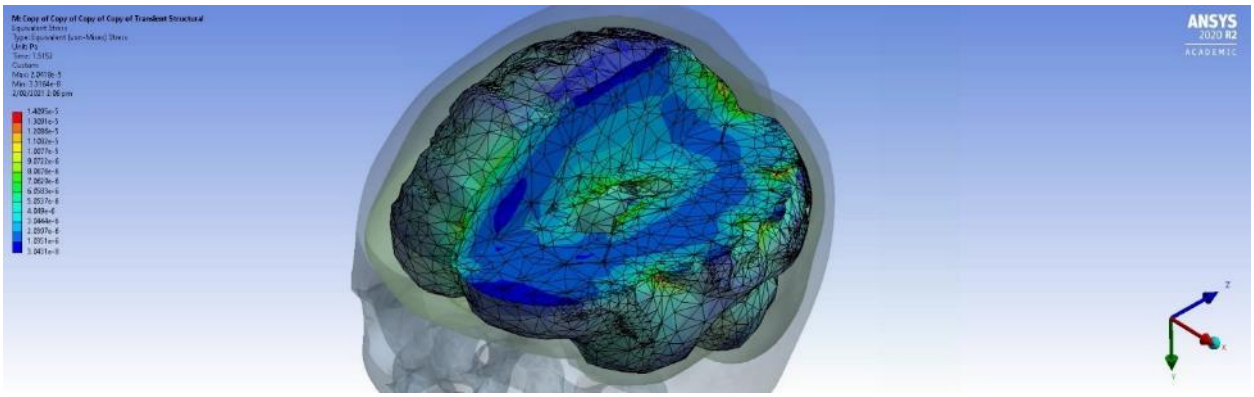
ANSYS
2020 R2
ACADEMIC

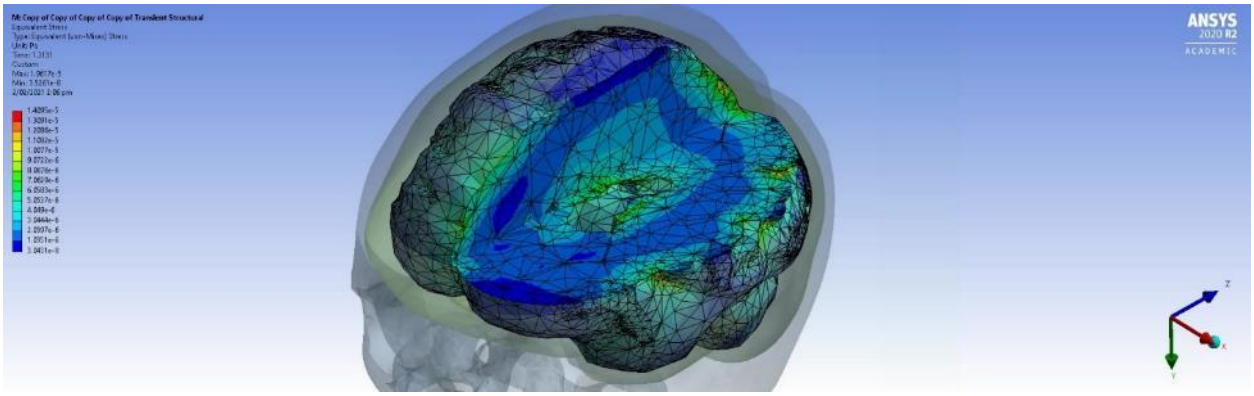
ANSYS
2020 R2
ACADEMIC

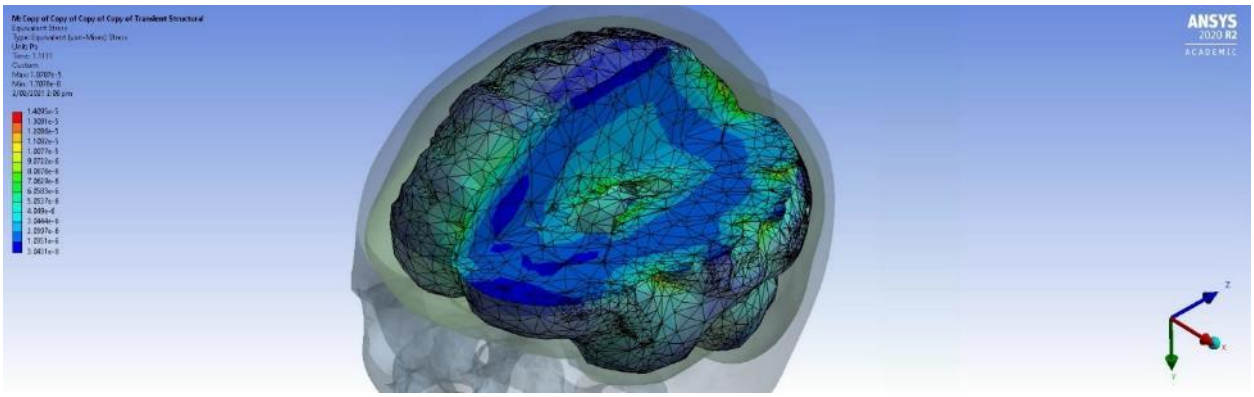
ANSYS
2020 R2
ACADEMIC

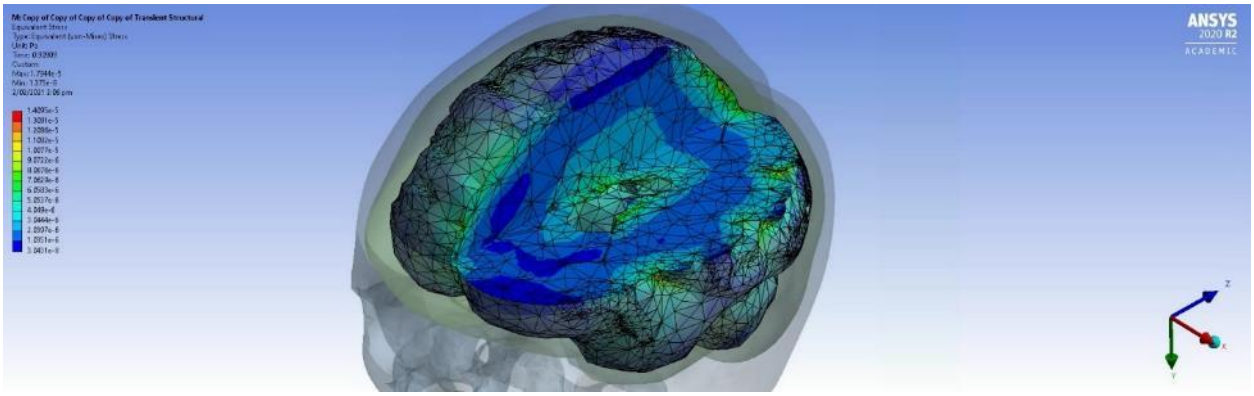
ANSYS
2020 R2
ACADEMIC

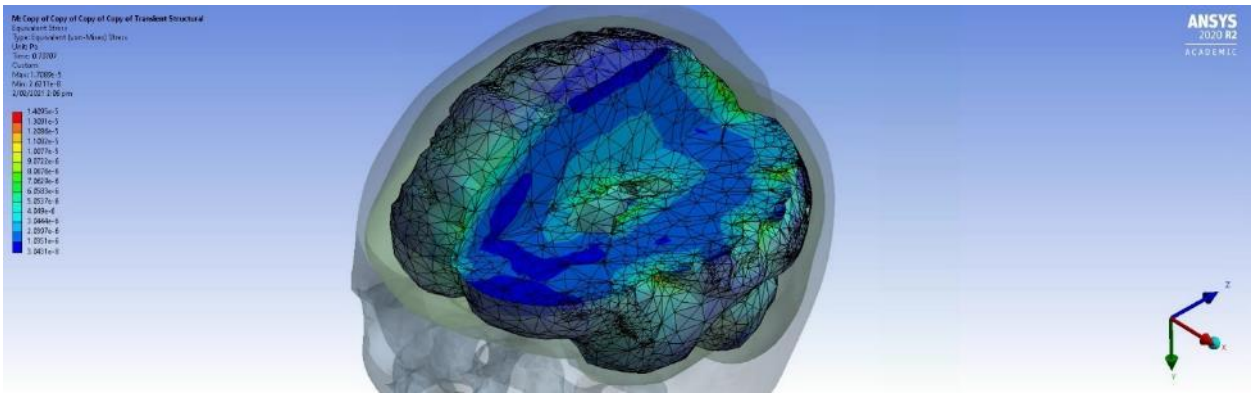
ANSYS
2020 R2
ACADEMIC

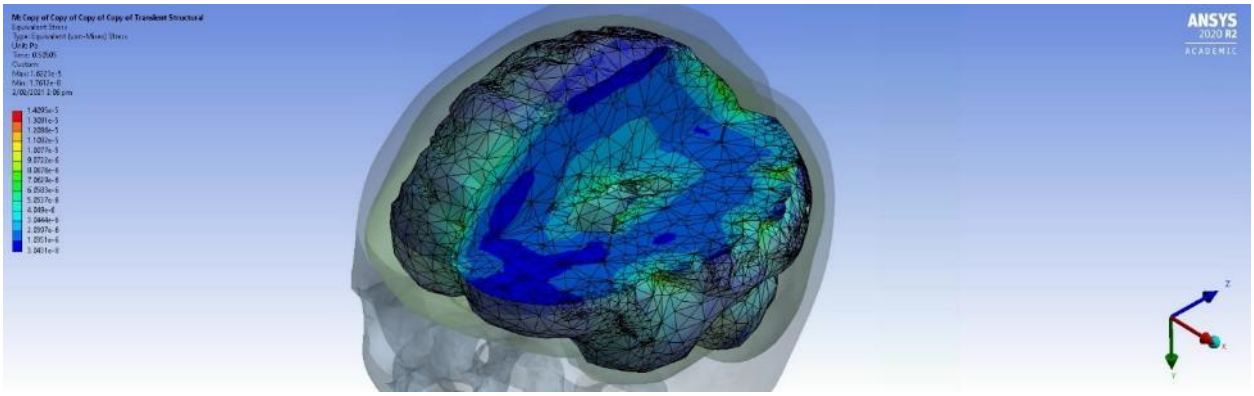
ANSYS
2020 R2
ACADEMIC

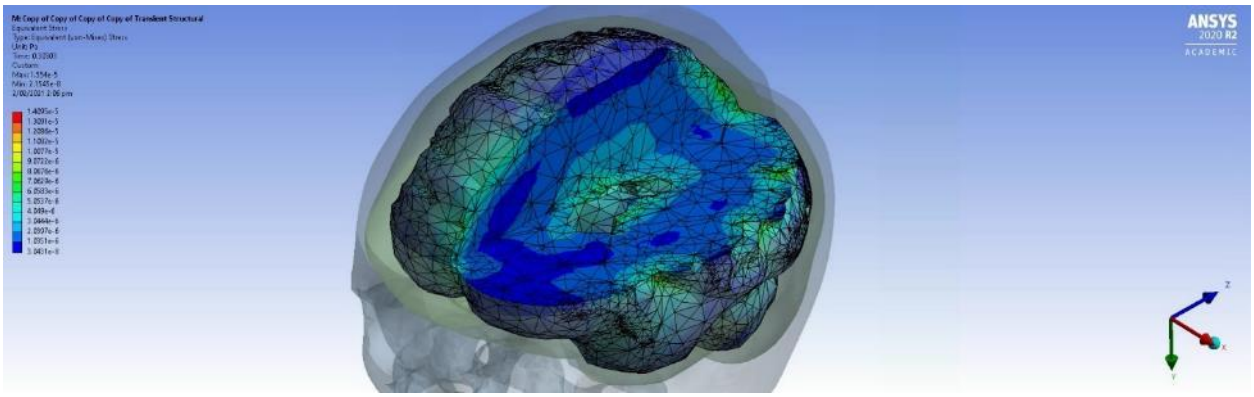
ANSYS
2020 R2
ACADEMIC

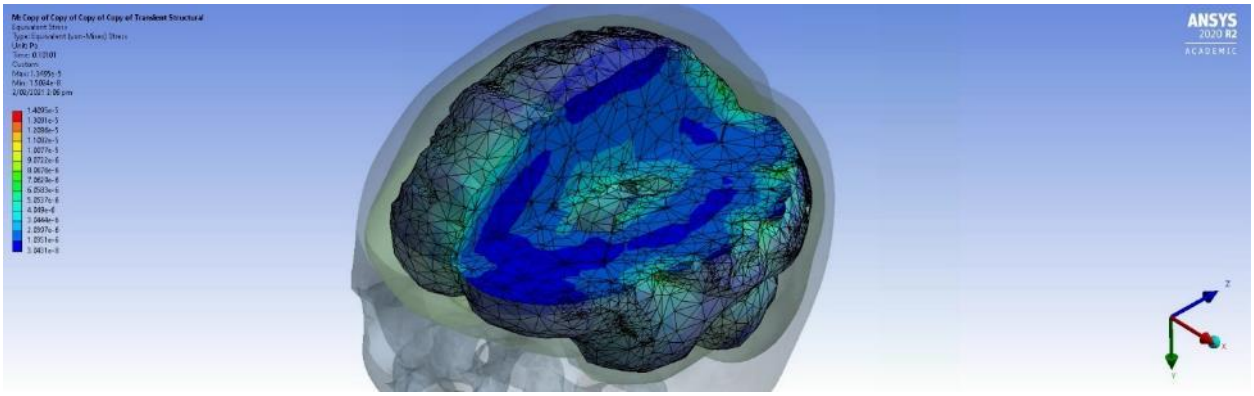

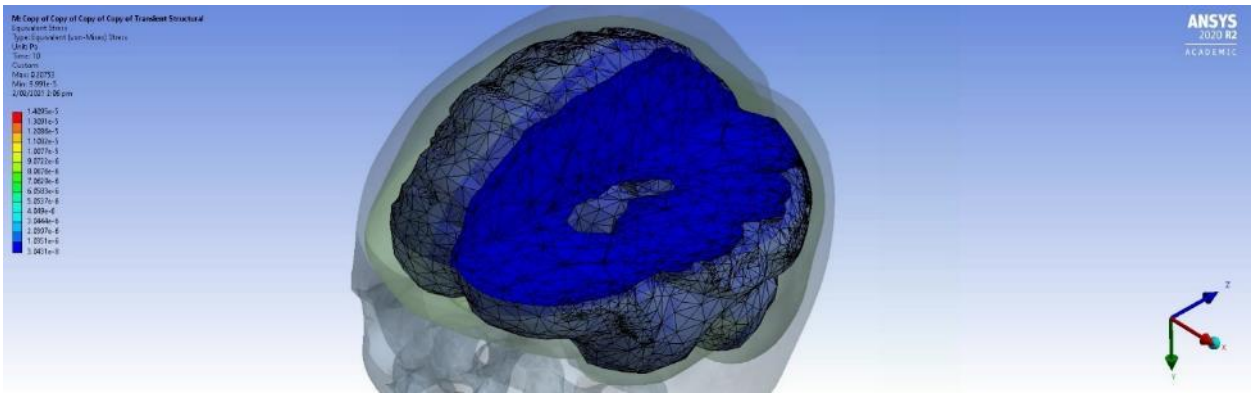

Impact Zone 3

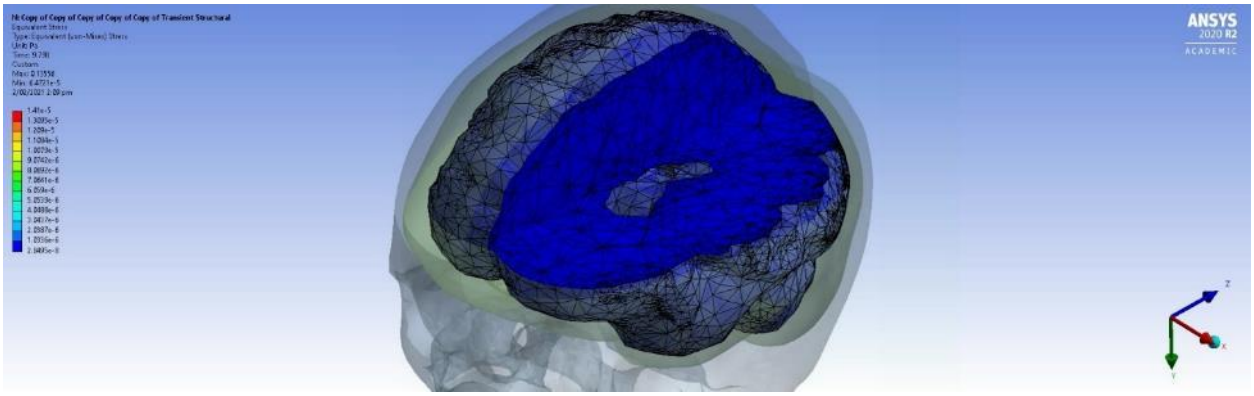

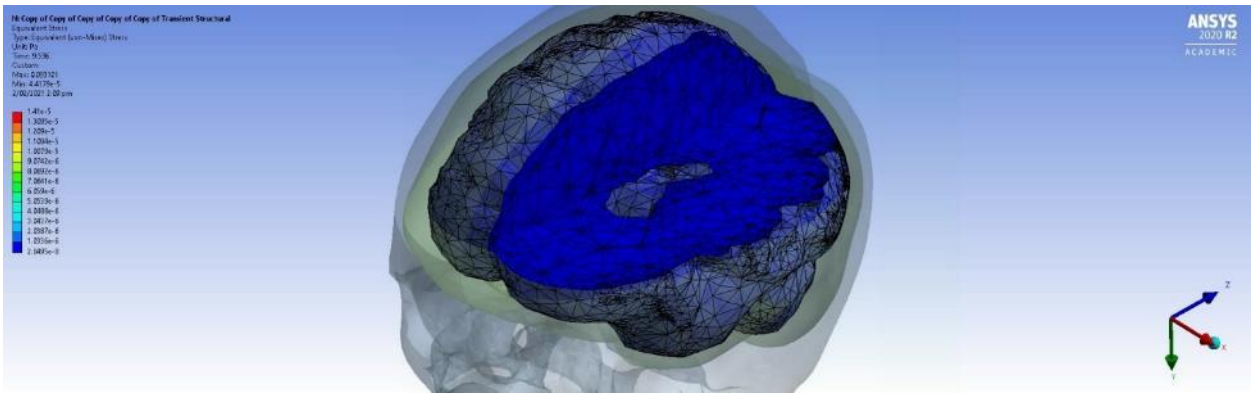

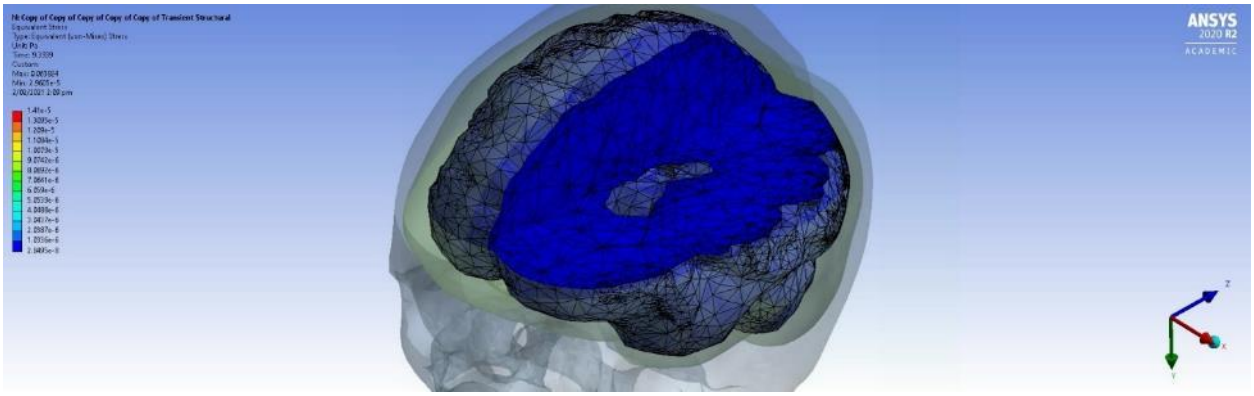
ANSYS
2020 R2
ACADEMIC

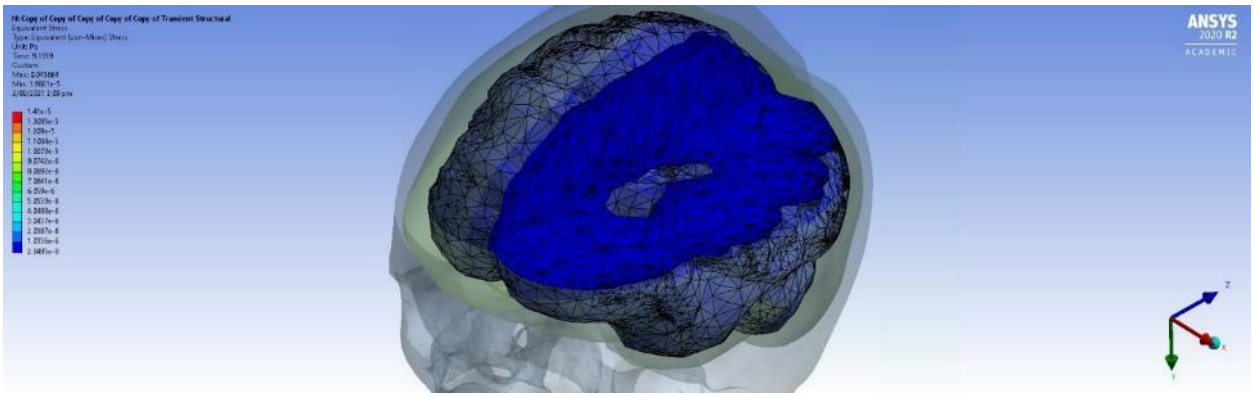
ANSYS
2020 R2
ACADEMIC

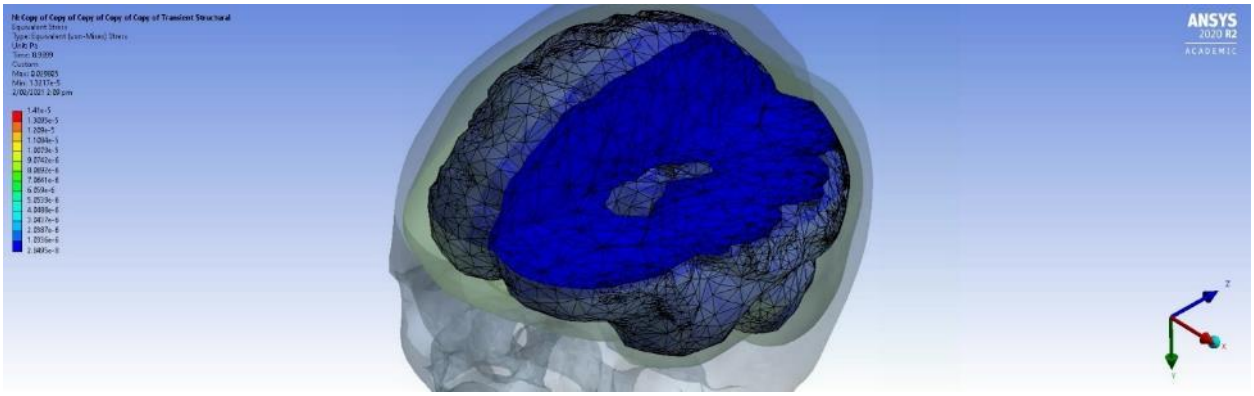
ANSYS
2020 R2
ACADEMIC

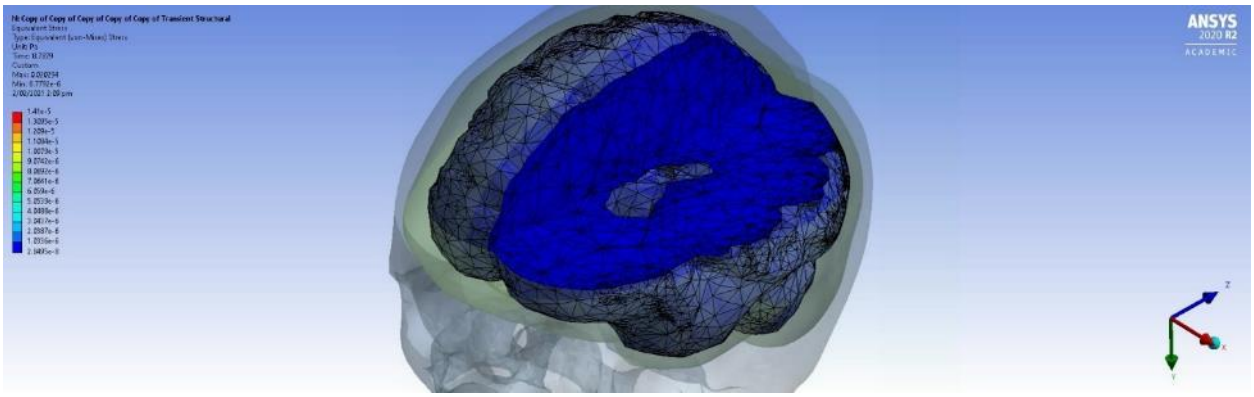
ANSYS
2020 R2
ACADEMIC

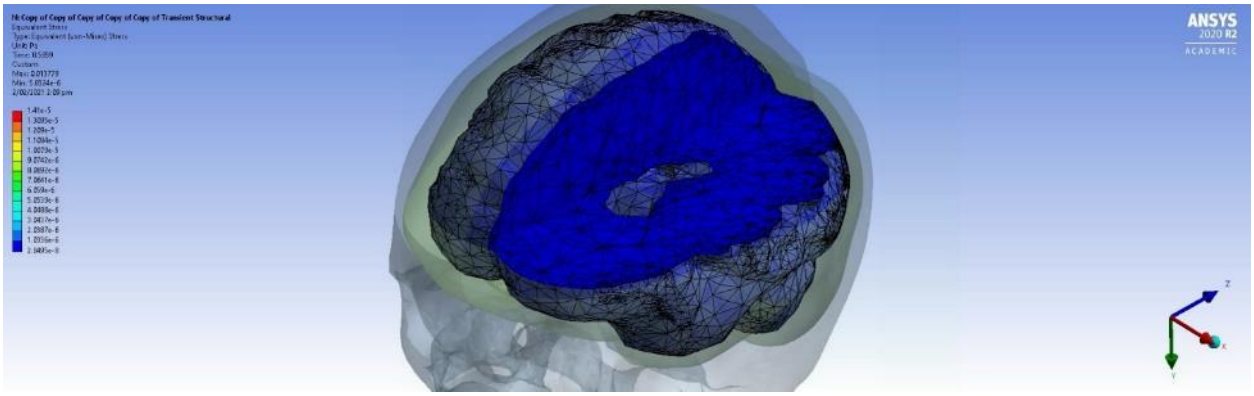
ANSYS
2020 R2
ACADEMIC

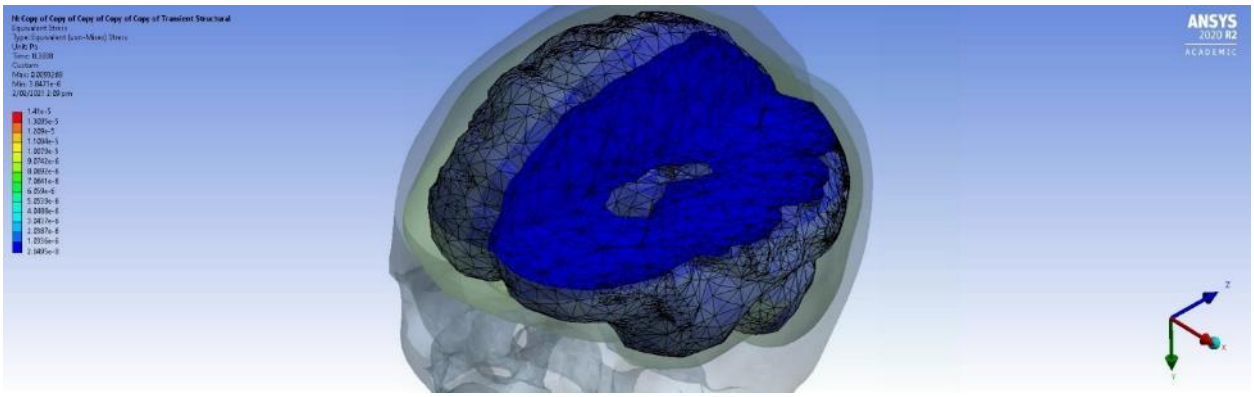
ANSYS
2020 R2
ACADEMIC

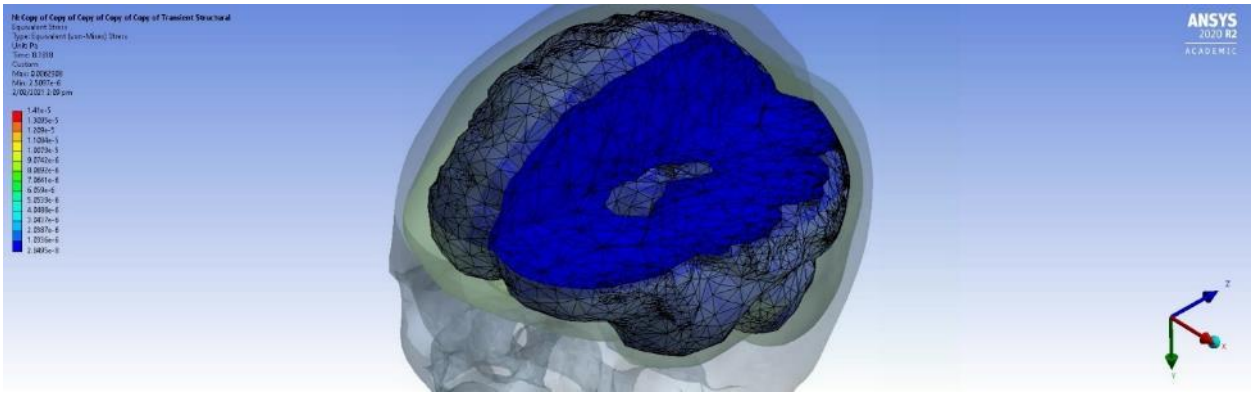
ANSYS
2020 R2
ACADEMIC

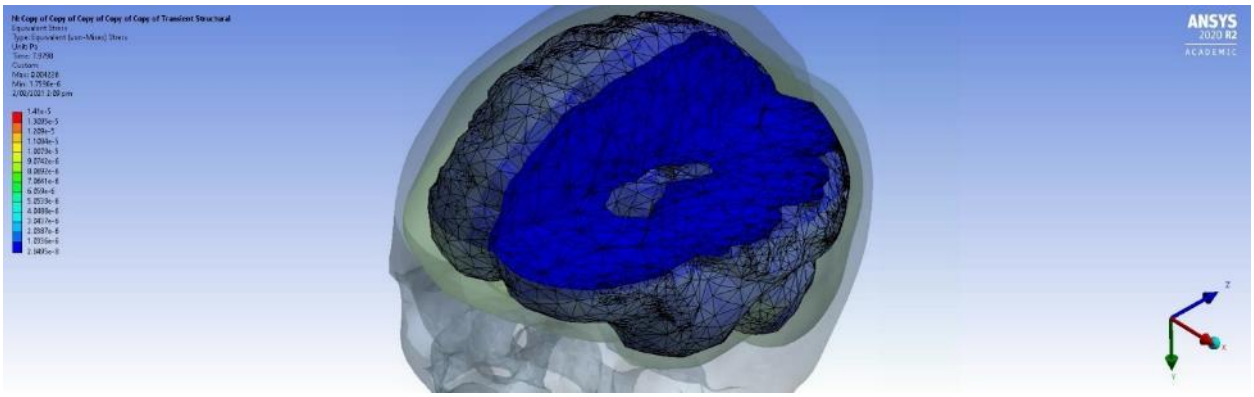
ANSYS
2020 R2
ACADEMIC

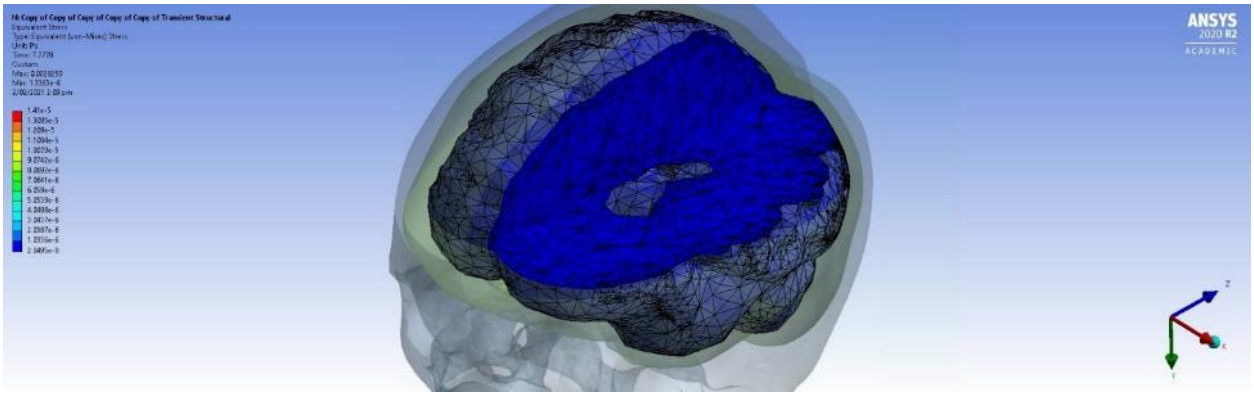
ANSYS
2020 R2
ACADEMIC

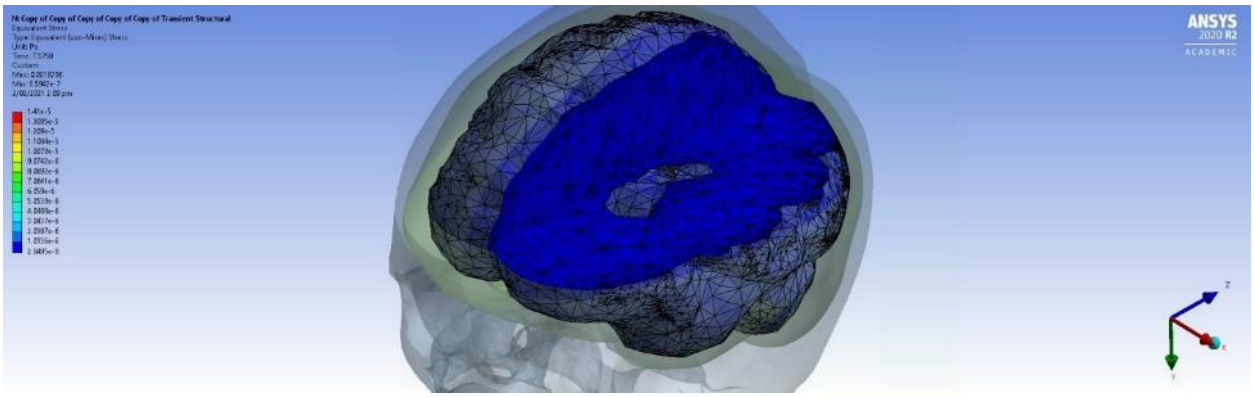
ANSYS
2020 R2
ACADEMIC

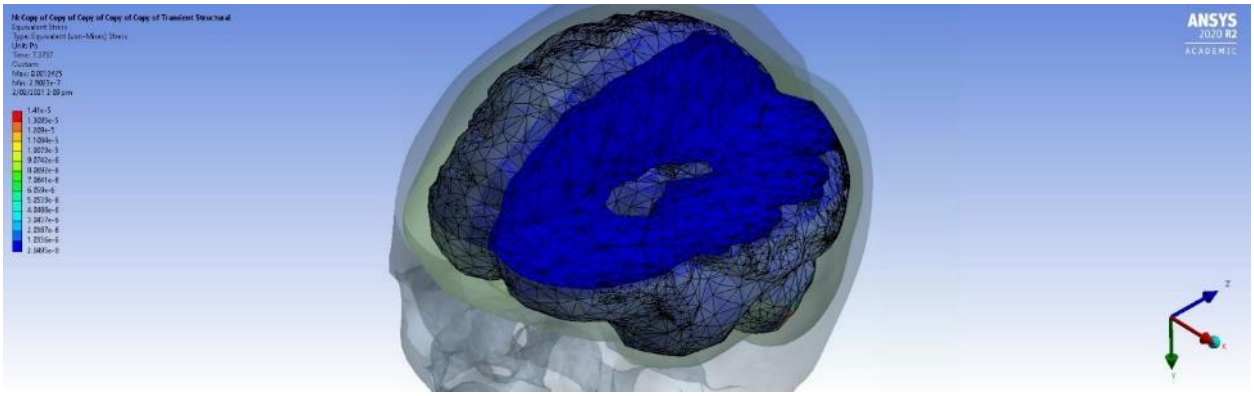
ANSYS
2020 R2
ACADEMIC

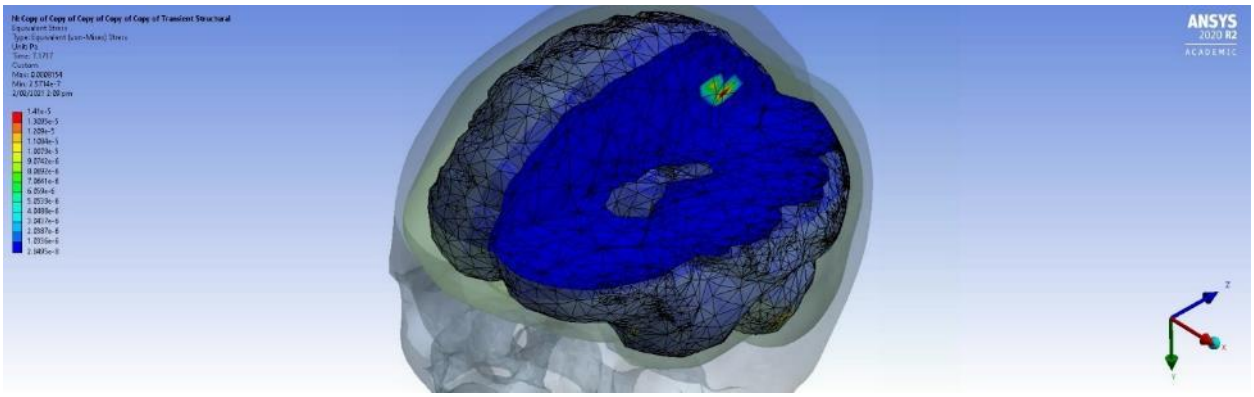
ANSYS
2020 R2
ACADEMIC

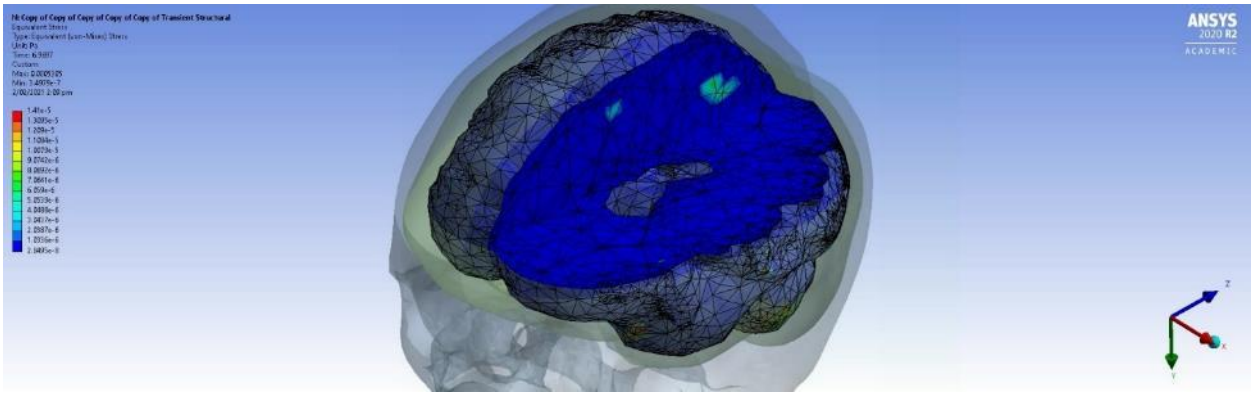
ANSYS
2020 R2
ACADEMIC

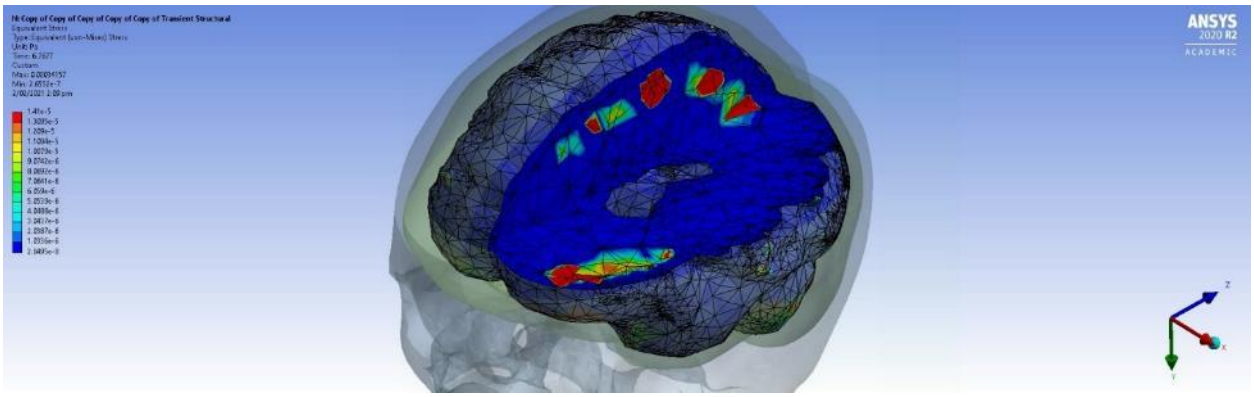
ANSYS
2020 R2
ACADEMIC

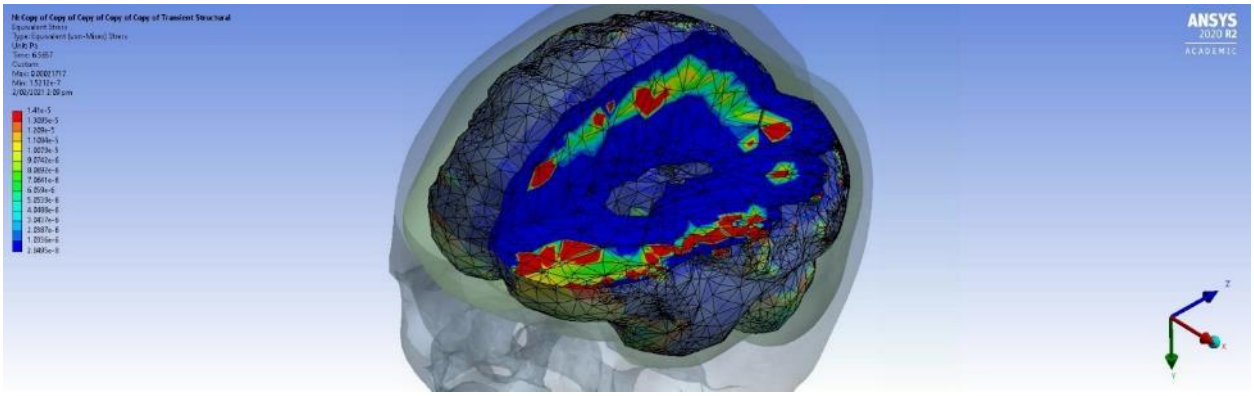
ANSYS
2020 R2
ACADEMIC

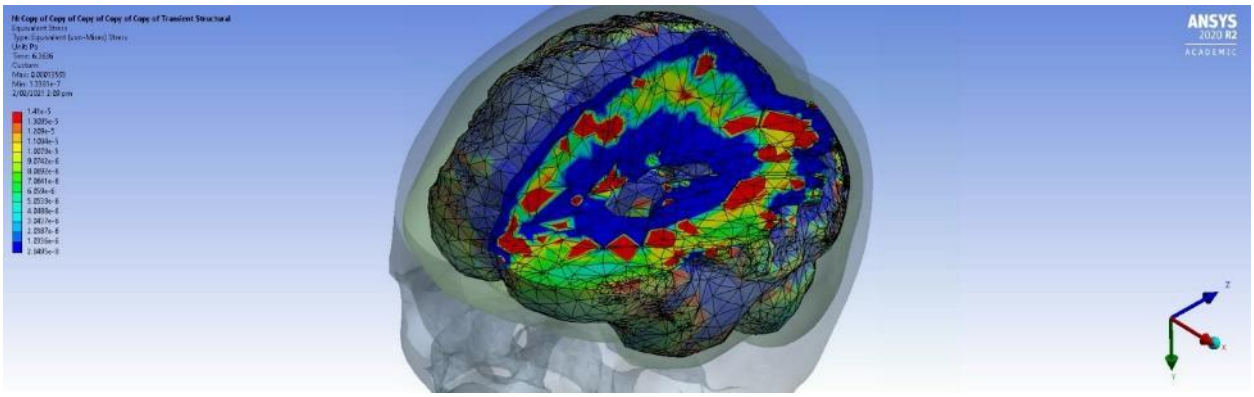
ANSYS
2020 R2
ACADEMIC

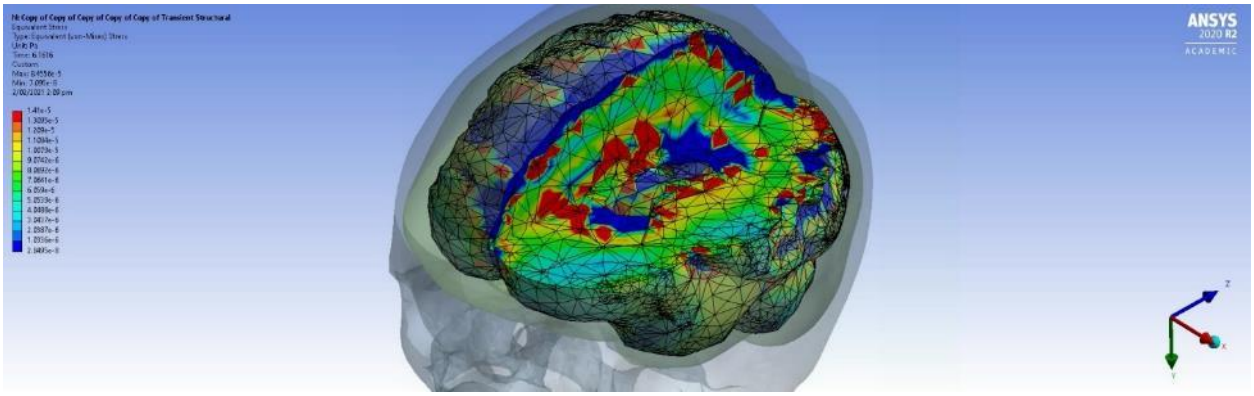
ANSYS
2020 R2
ACADEMIC

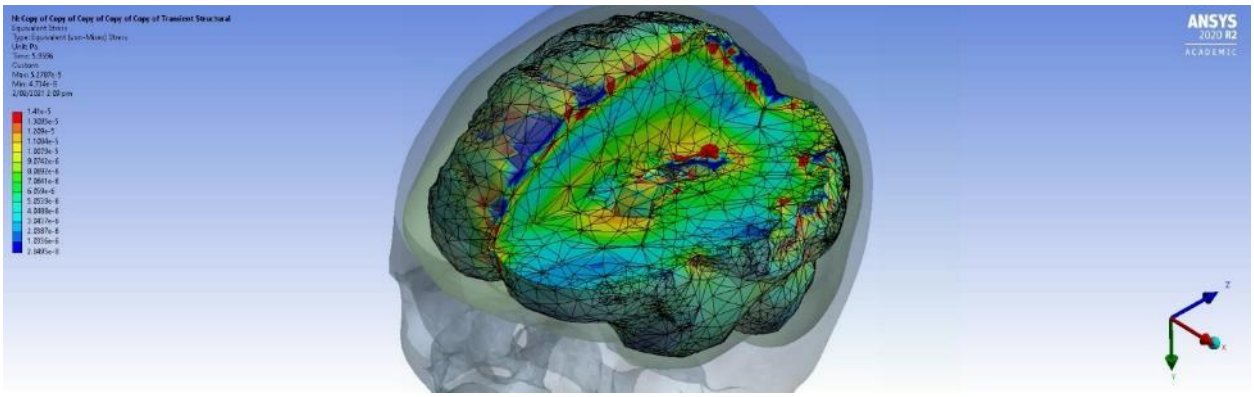
ANSYS
2020 R2
ACADEMIC

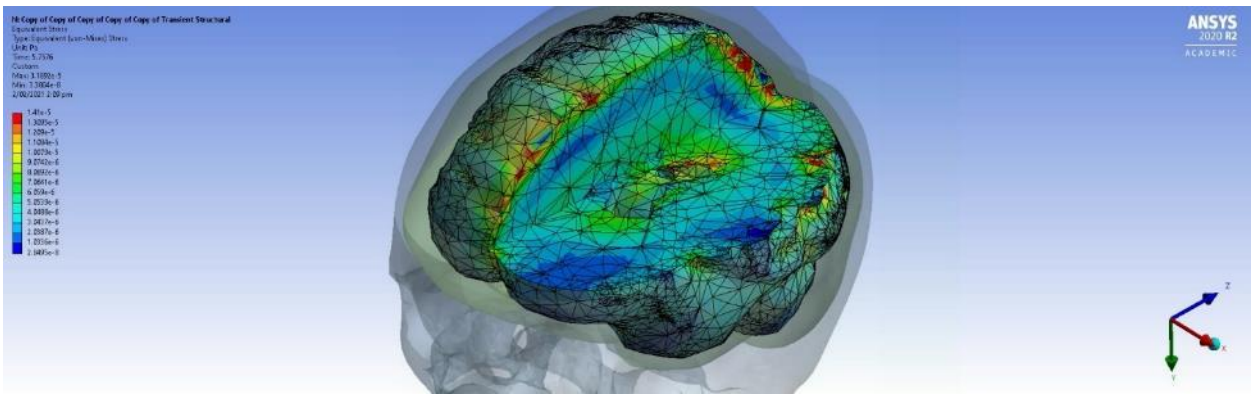
ANSYS
2020 R2
ACADEMIC

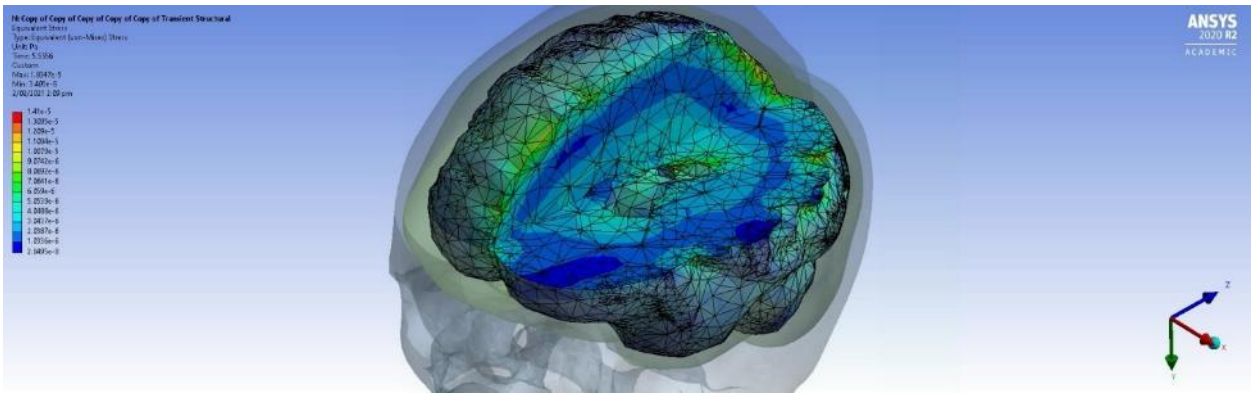
ANSYS
2020 R2
ACADEMIC

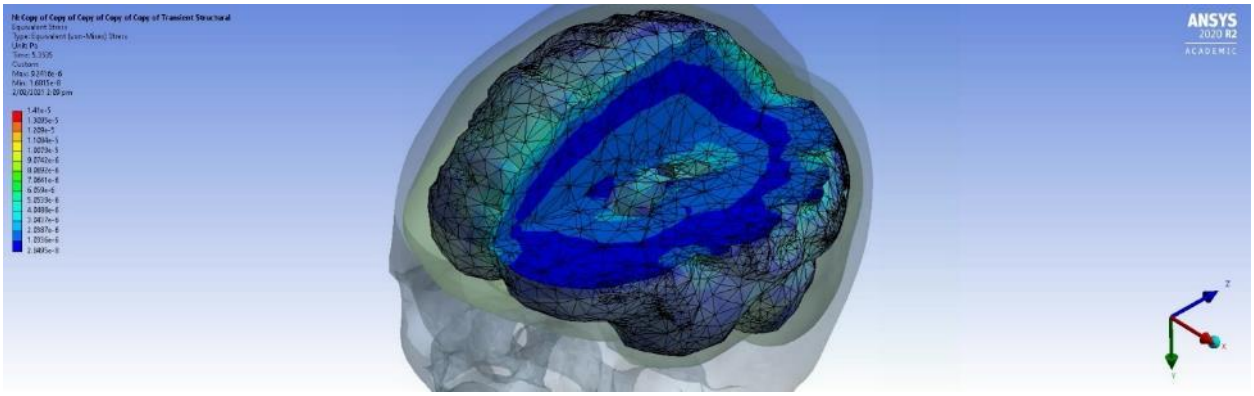
ANSYS
2020 R2
ACADEMIC

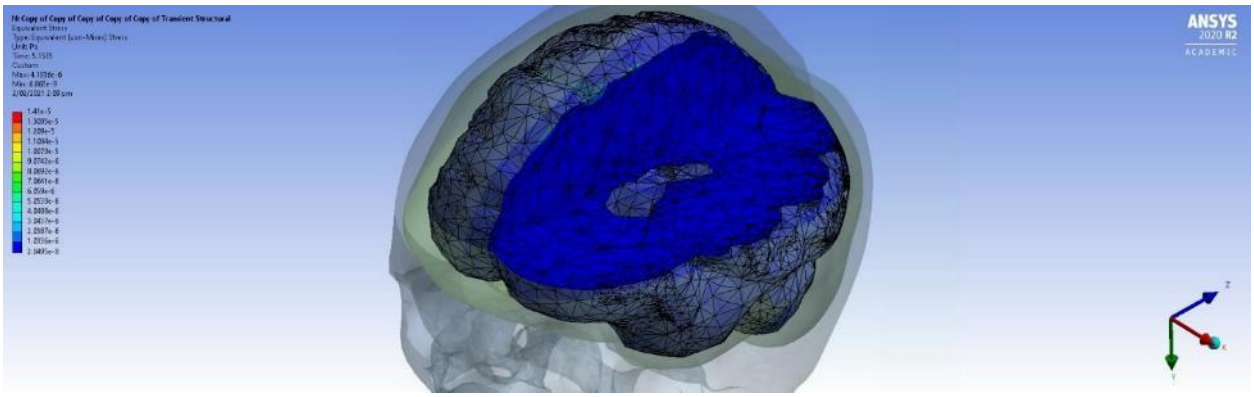
ANSYS
2020 R2
ACADEMIC

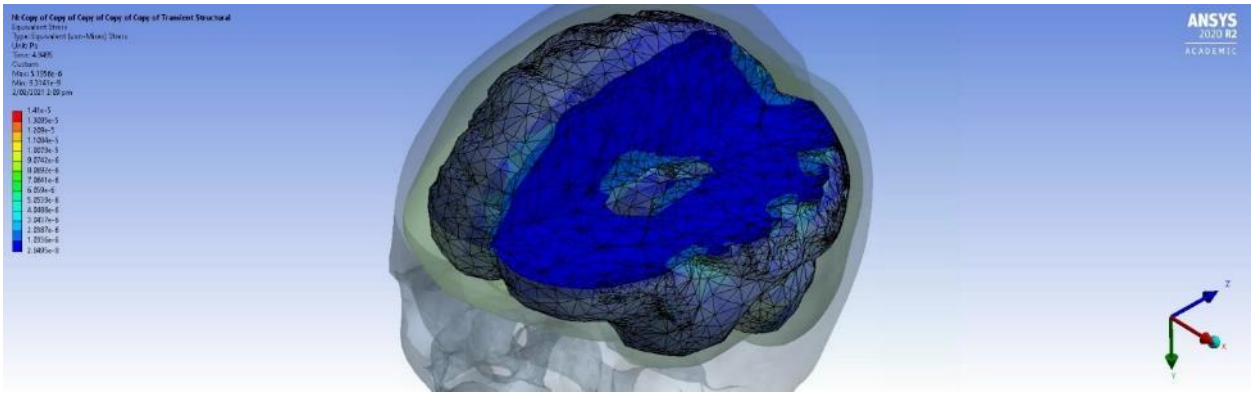
ANSYS
2020 R2
ACADEMIC

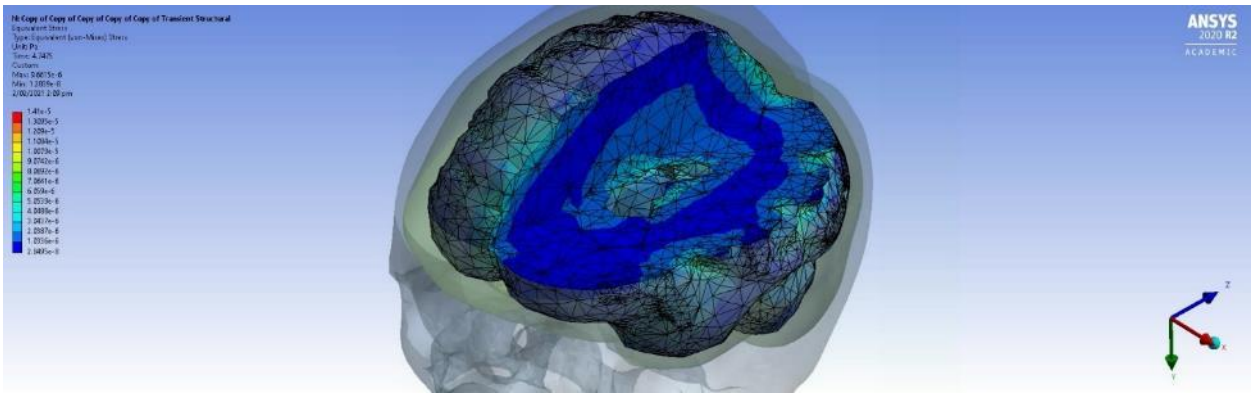
ANSYS
2020 R2
ACADEMIC

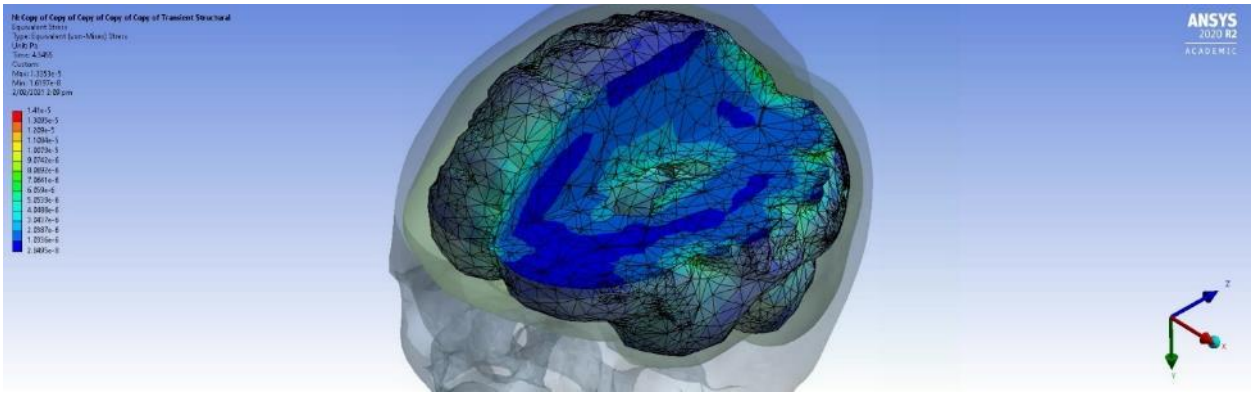
ANSYS
2020 R2
ACADEMIC

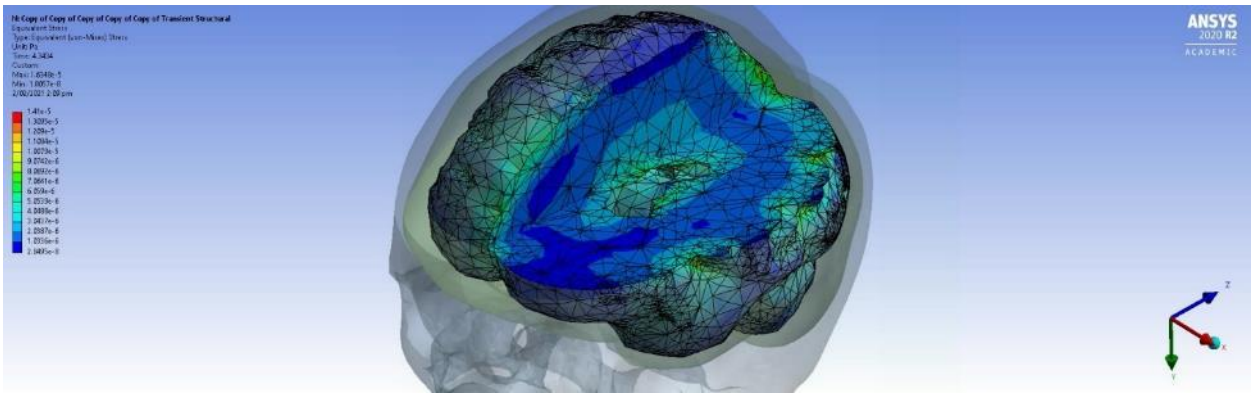
ANSYS
2020 R2
ACADEMIC

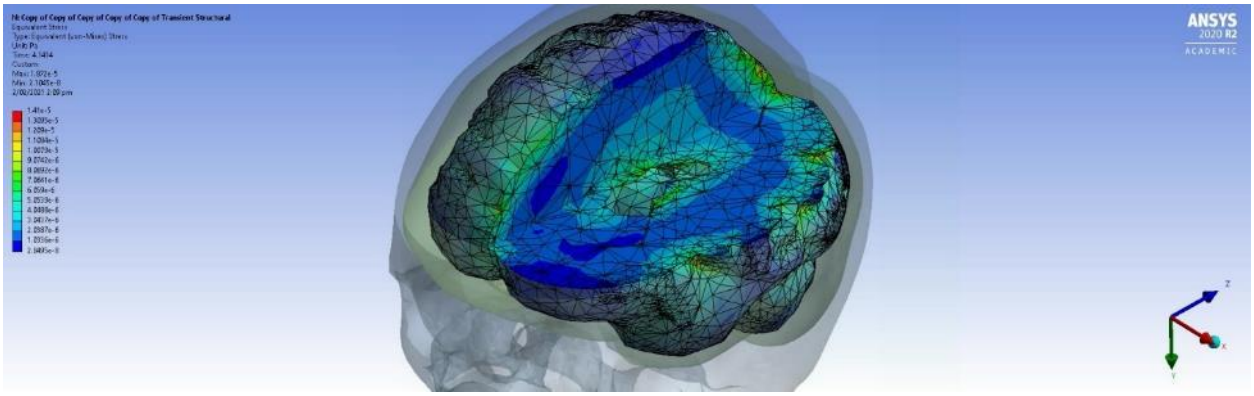
ANSYS
2020 R2
ACADEMIC

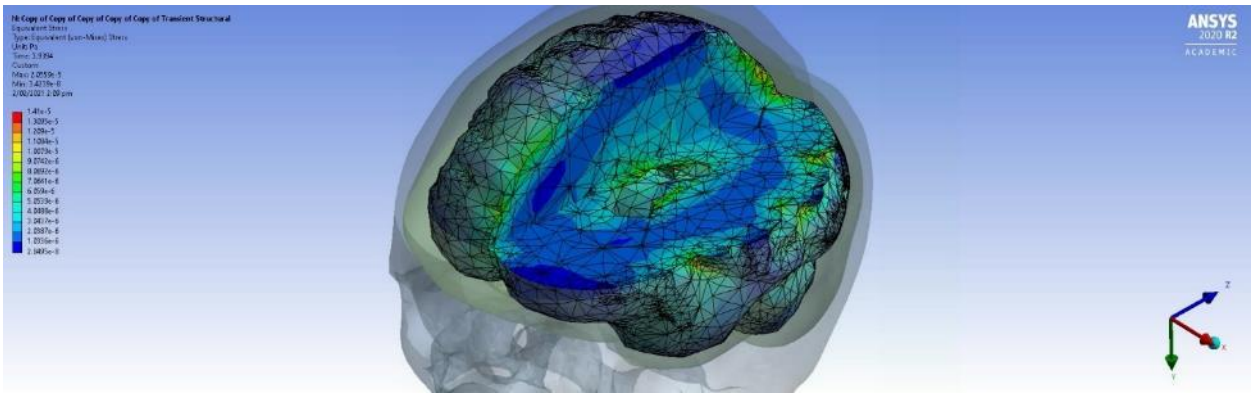
ANSYS
2020 R2
ACADEMIC

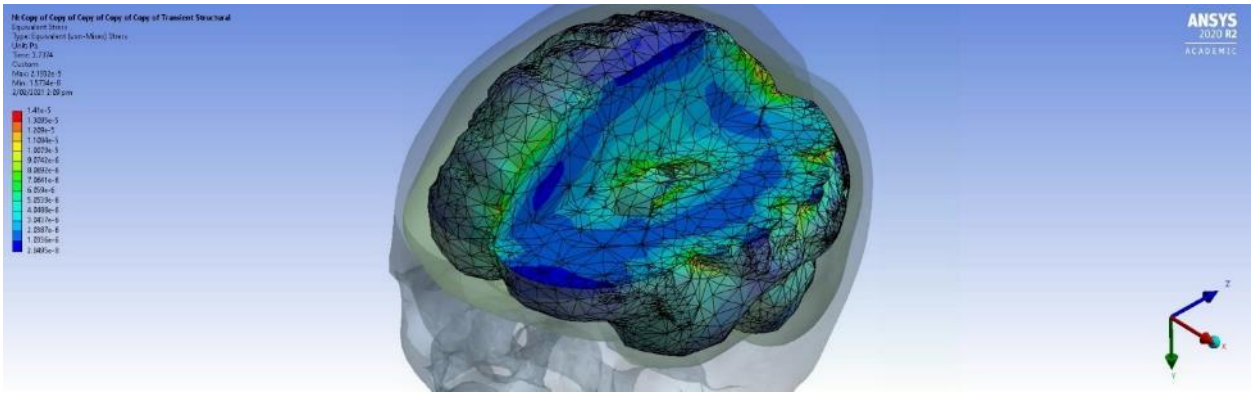
ANSYS
2020 R2
ACADEMIC

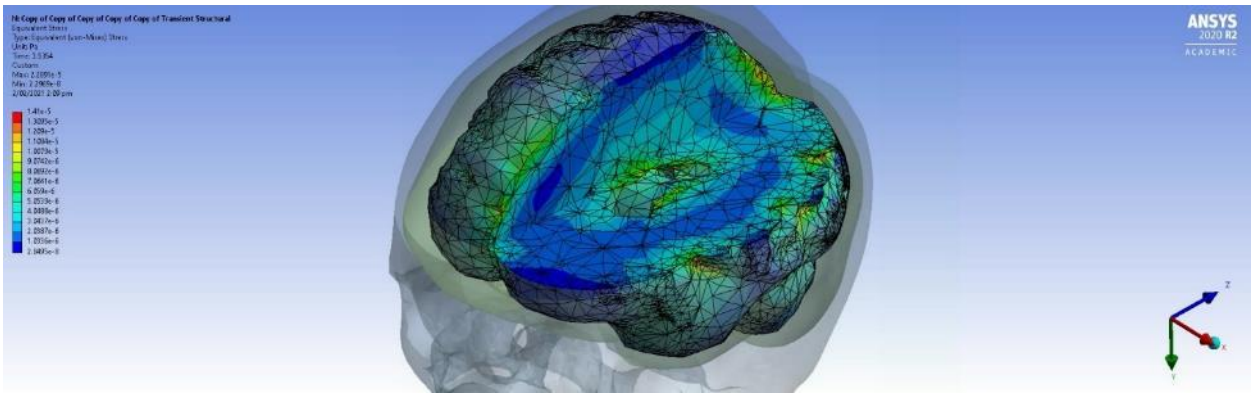
ANSYS
2020 R2
ACADEMIC

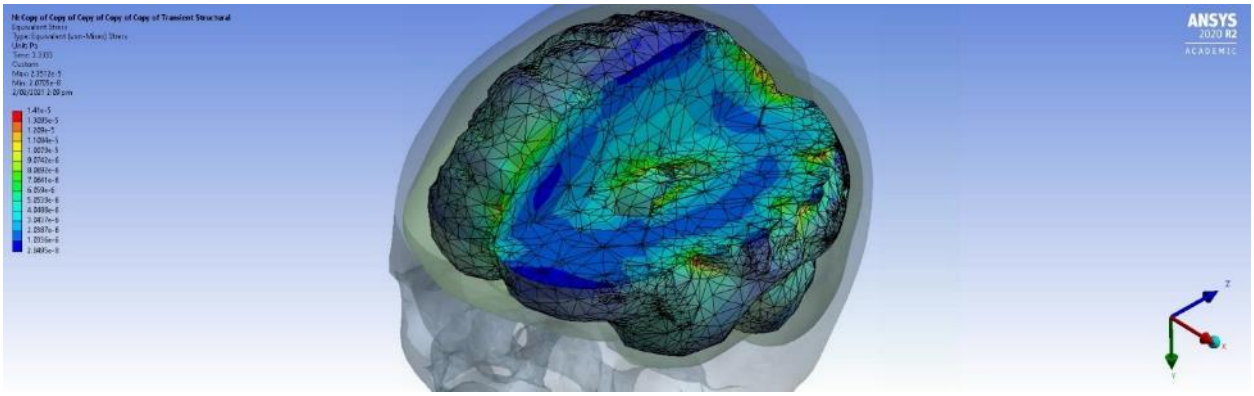
ANSYS
2020 R2
ACADEMIC

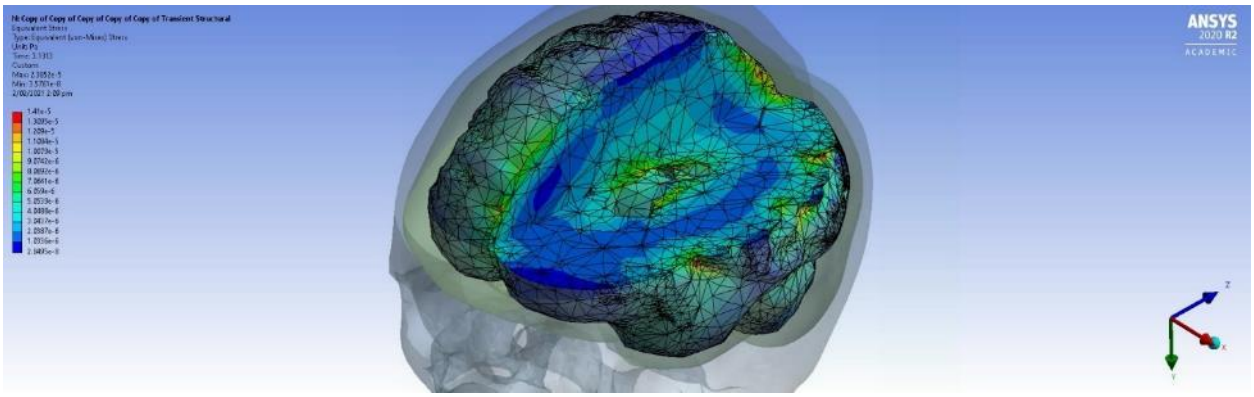
ANSYS
2020 R2
ACADEMIC

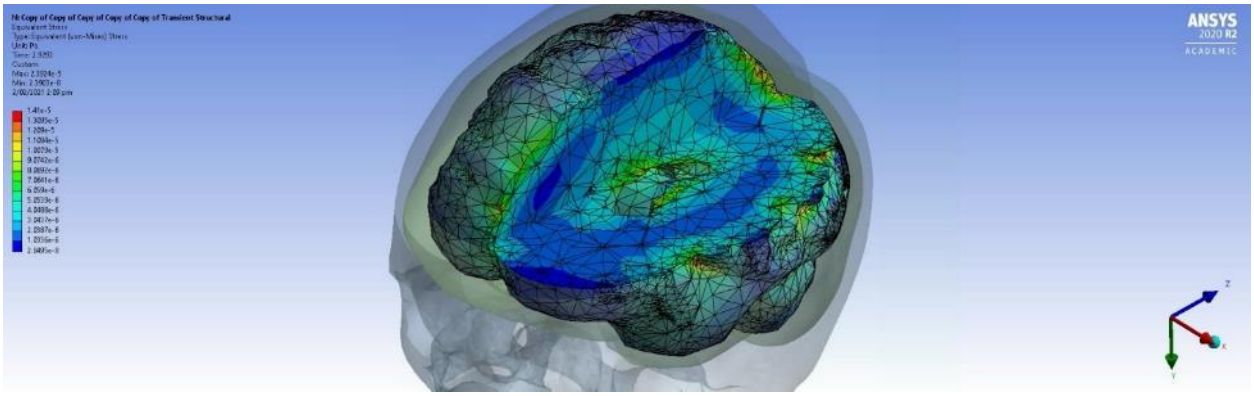
ANSYS
2020 R2
ACADEMIC

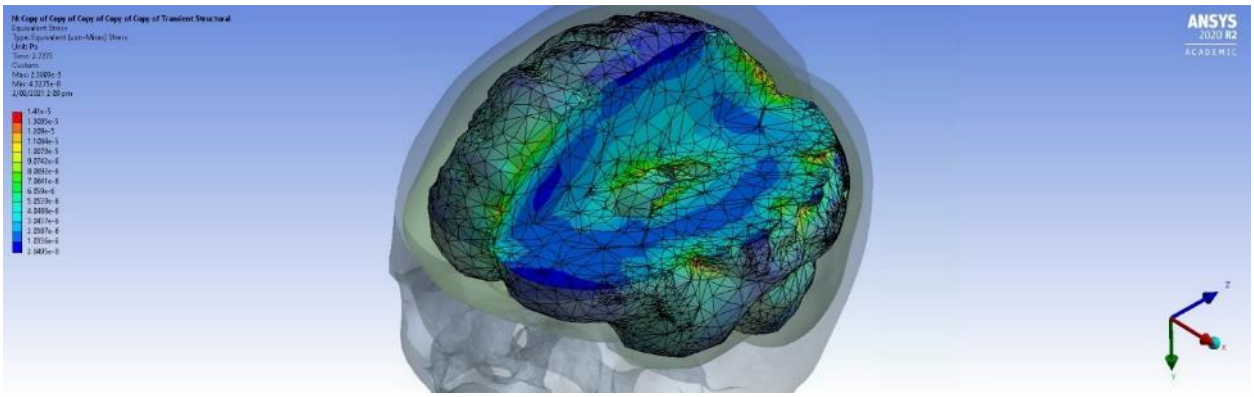
ANSYS
2020 R2
ACADEMIC

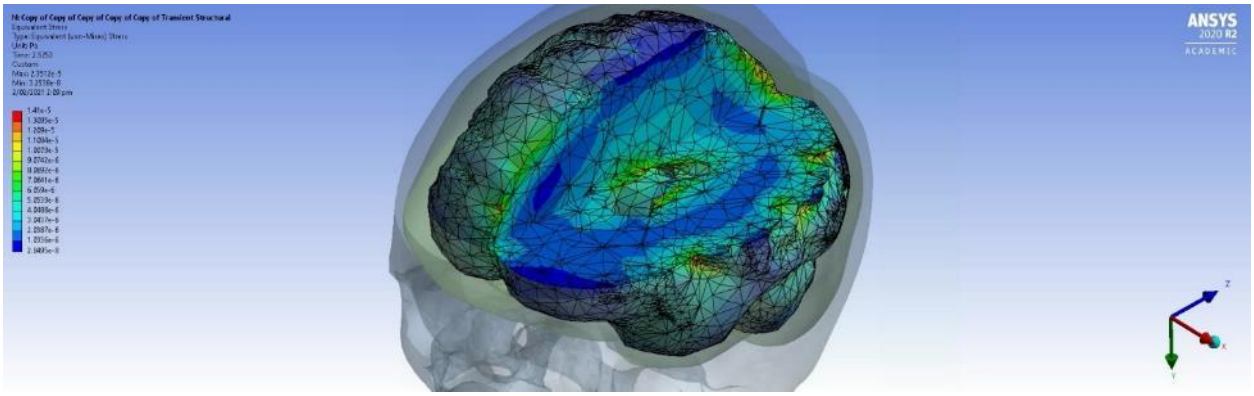
ANSYS
2020 R2
ACADEMIC

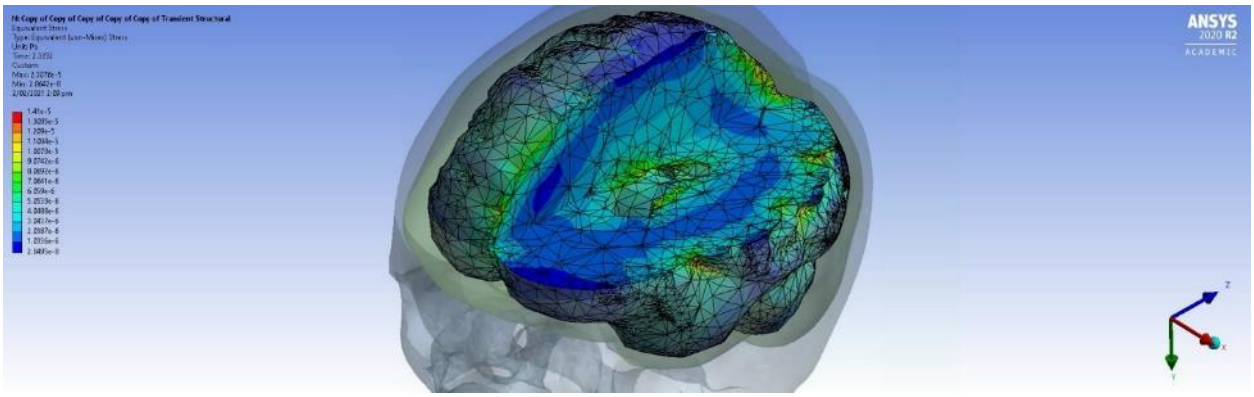
ANSYS
2020 R2
ACADEMIC

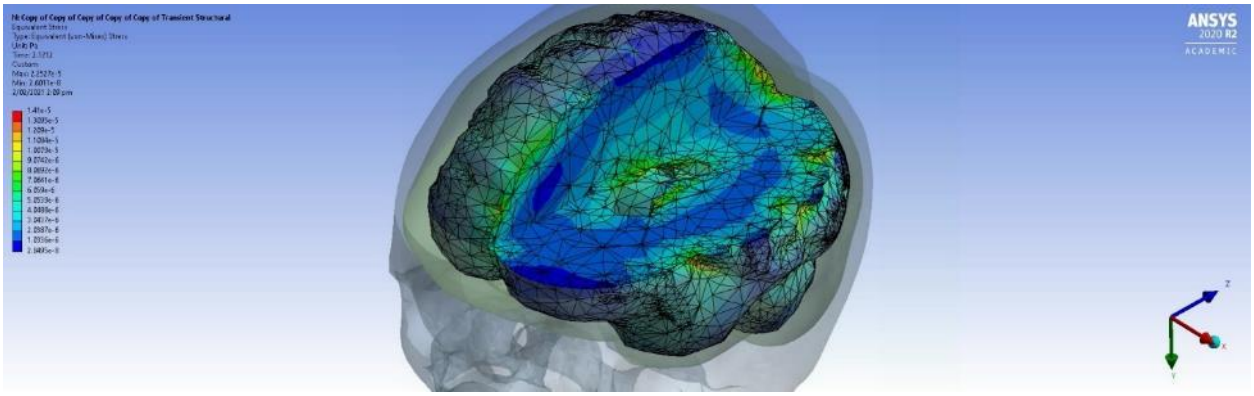
ANSYS
2020 R2
ACADEMIC

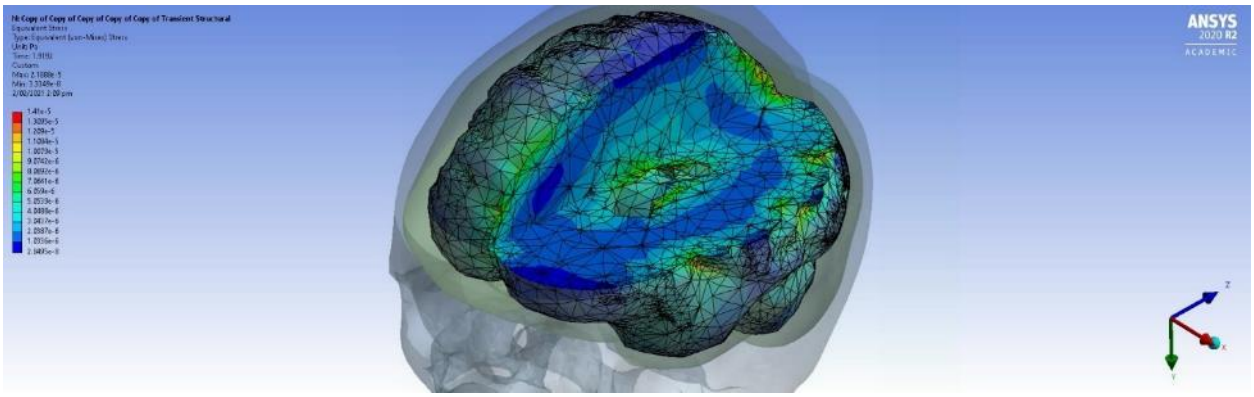
ANSYS
2020 R2
ACADEMIC

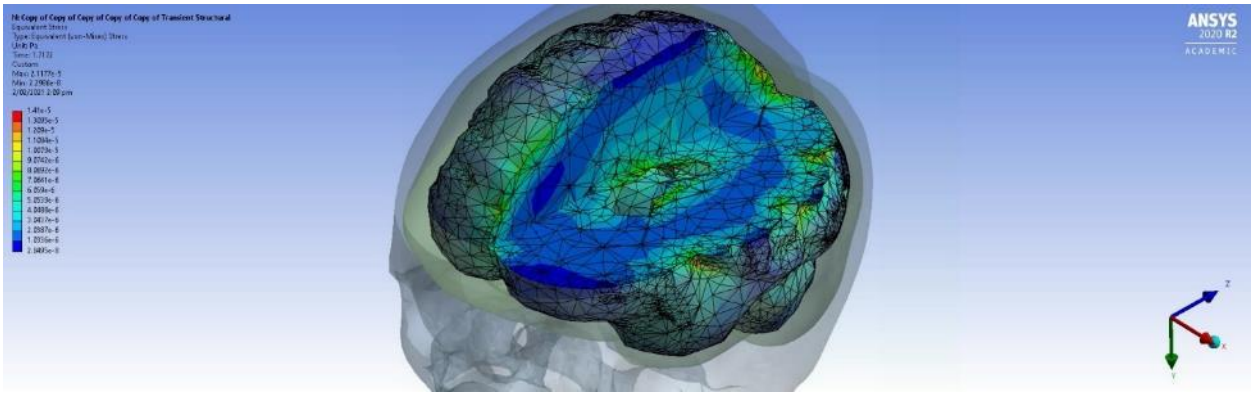
ANSYS
2020 R2
ACADEMIC

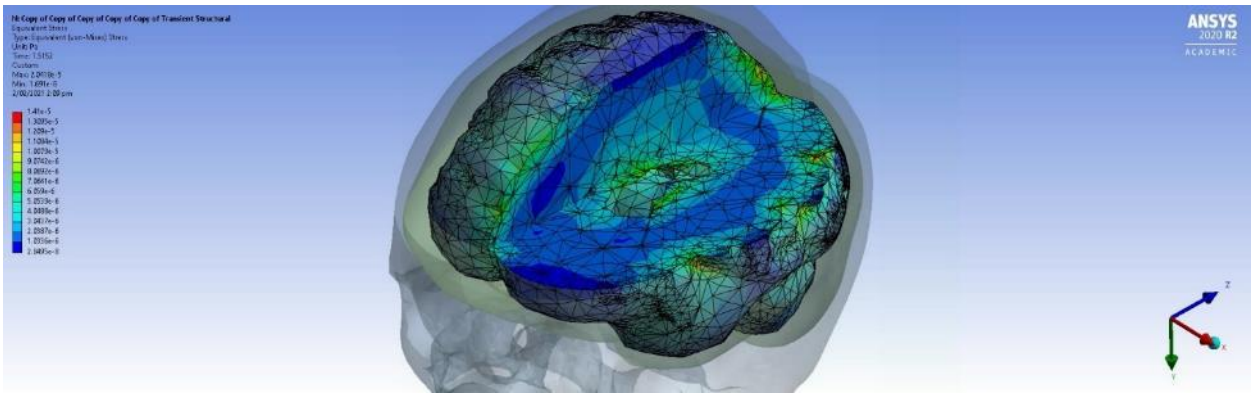
ANSYS
2020 R2
ACADEMIC

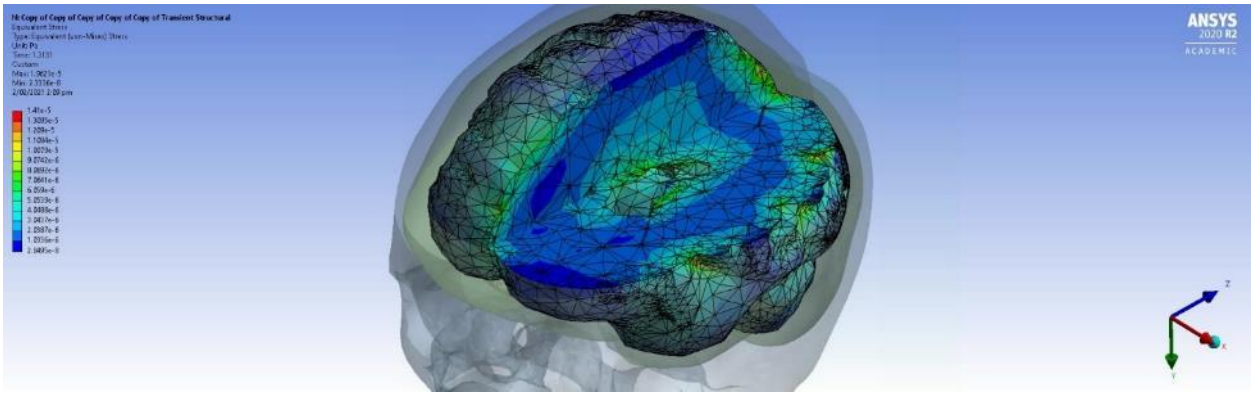
ANSYS
2020 R2
ACADEMIC

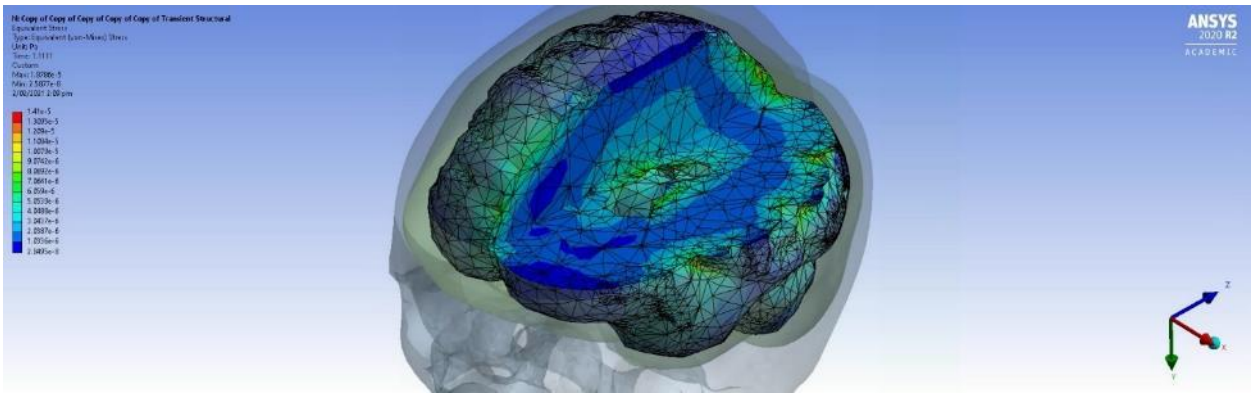
ANSYS
2020 R2
ACADEMIC

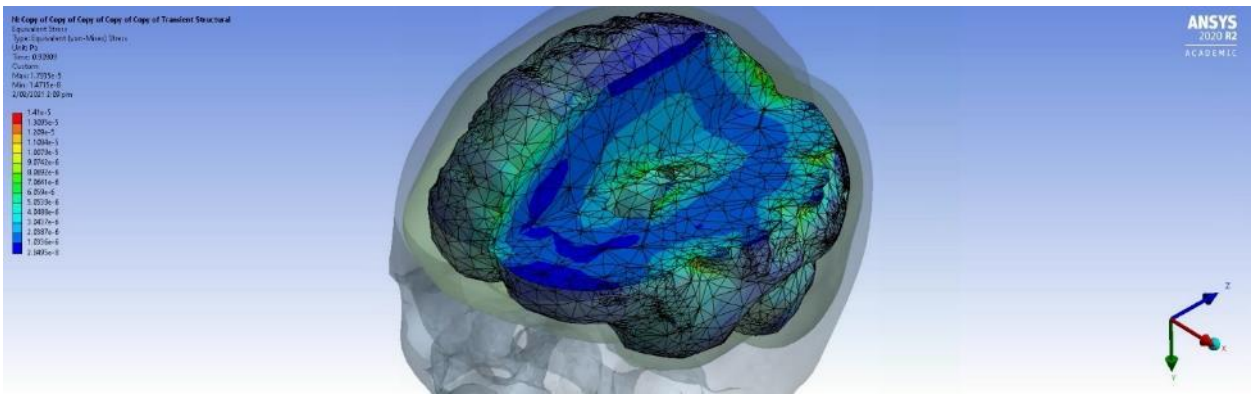
ANSYS
2020 R2
ACADEMIC

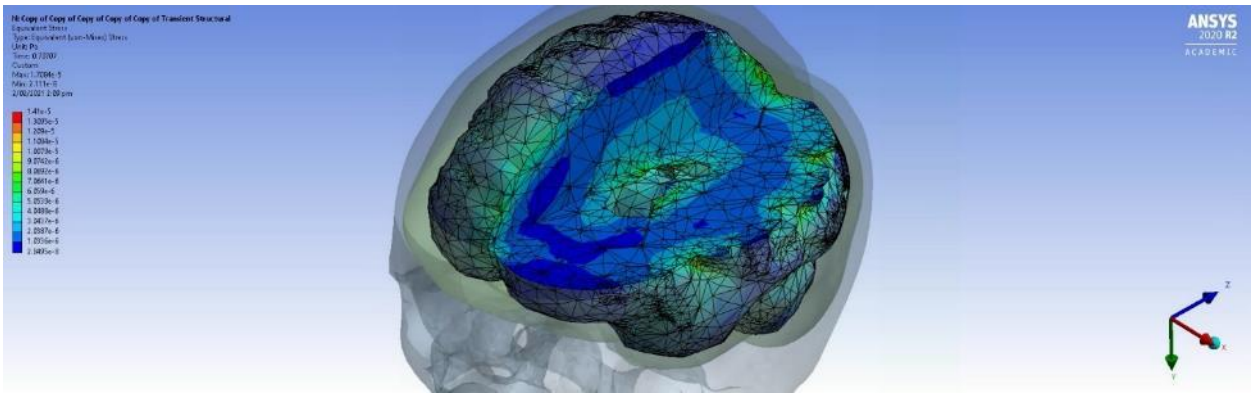
ANSYS
2020 R2
ACADEMIC

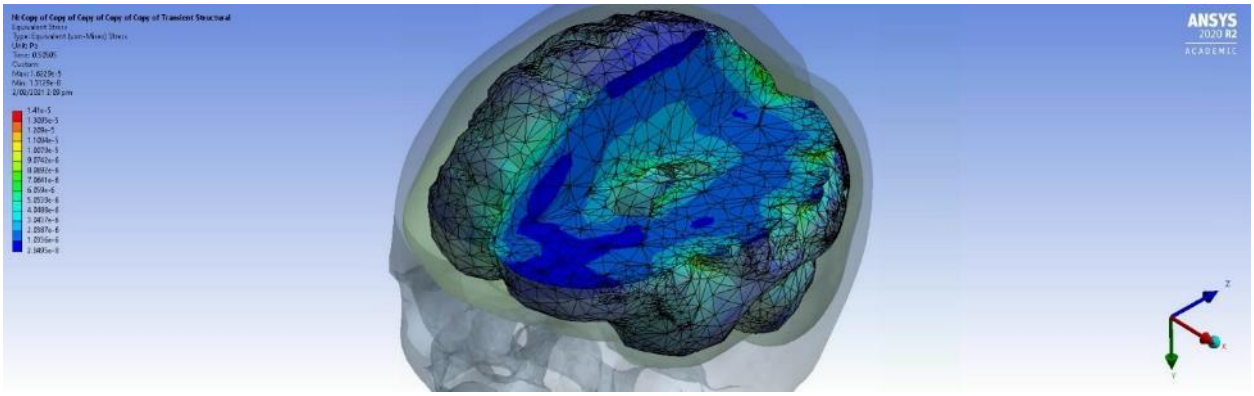
ANSYS
2020 R2
ACADEMIC

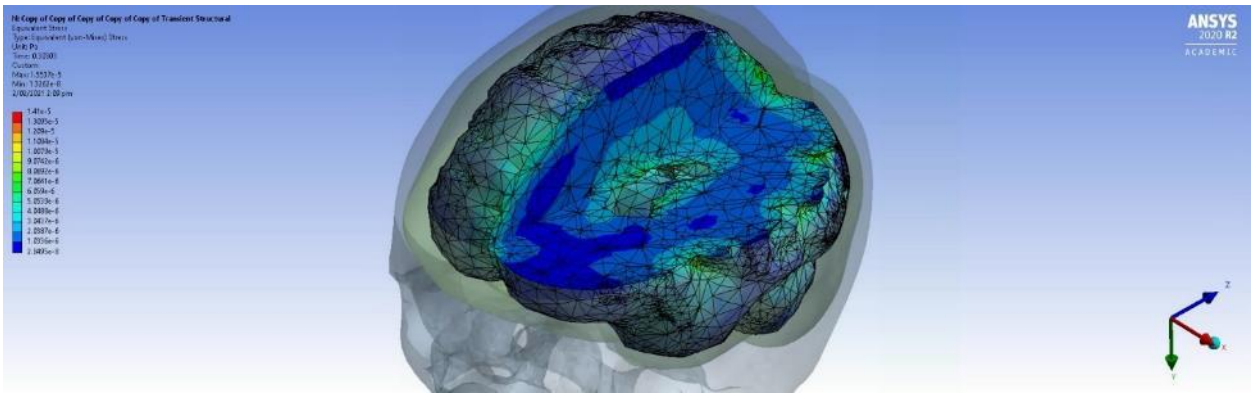
ANSYS
2020 R2
ACADEMIC

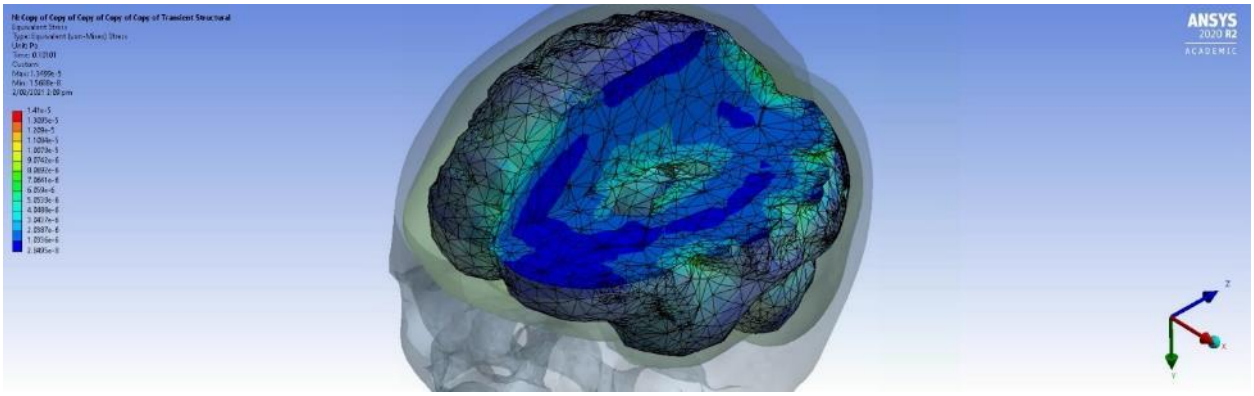
ANSYS
2020 R2
ACADEMIC

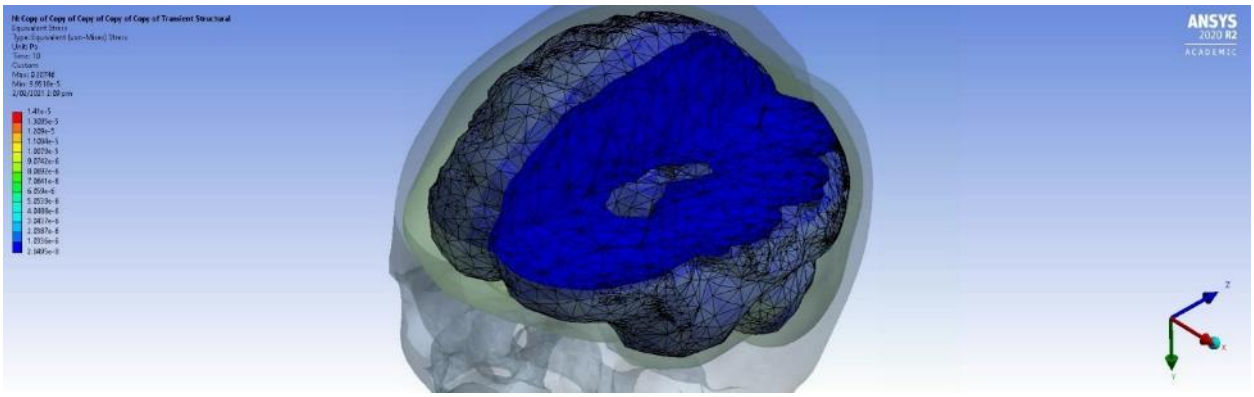
ANSYS
2020 R2
ACADEMIC

Impact Zone 5

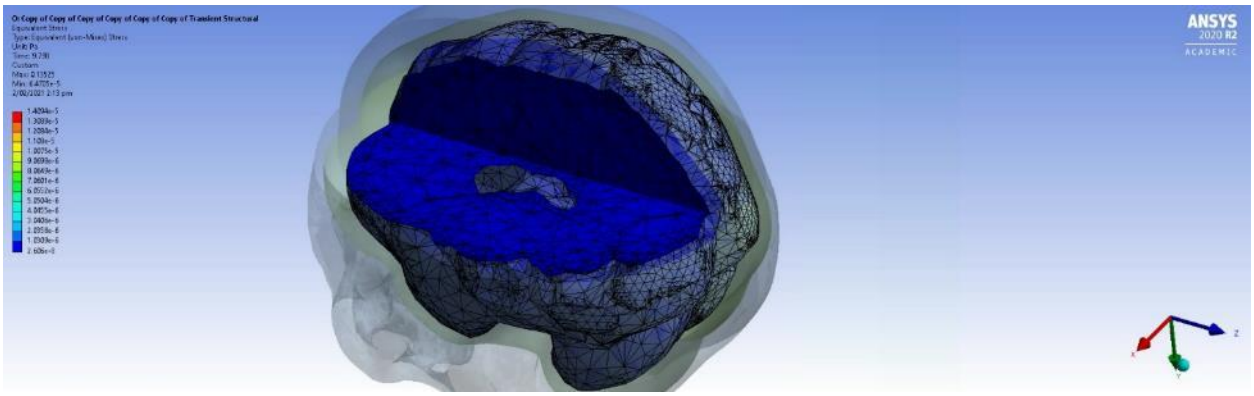

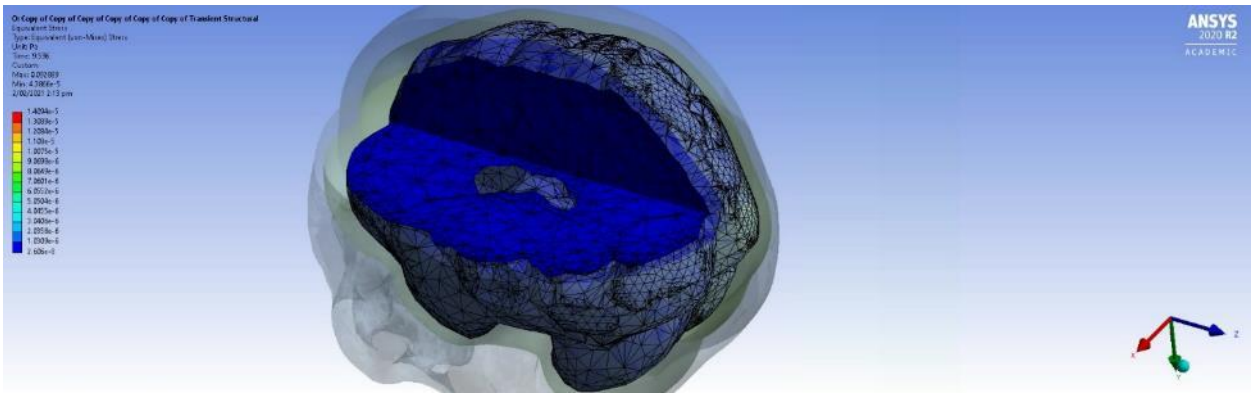

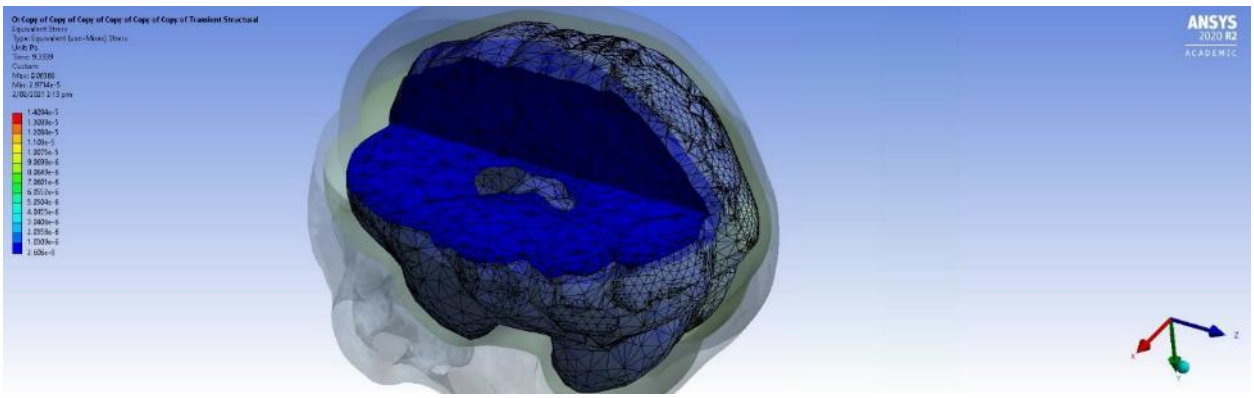

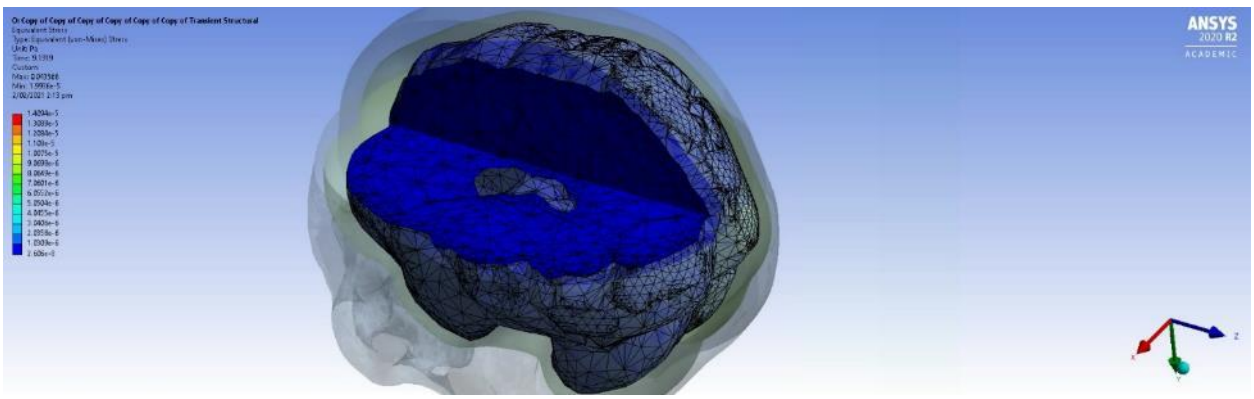

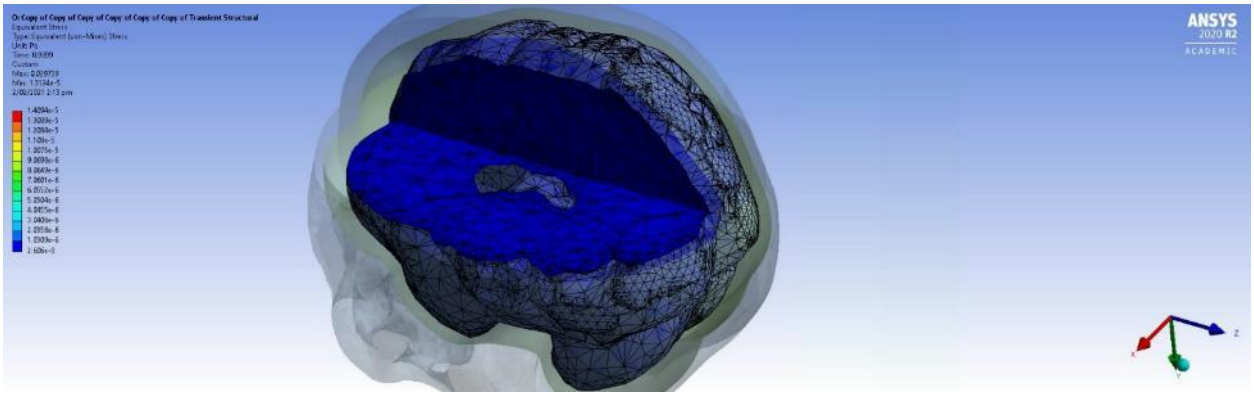
ANSYS
2020 R2
ACADEMIC

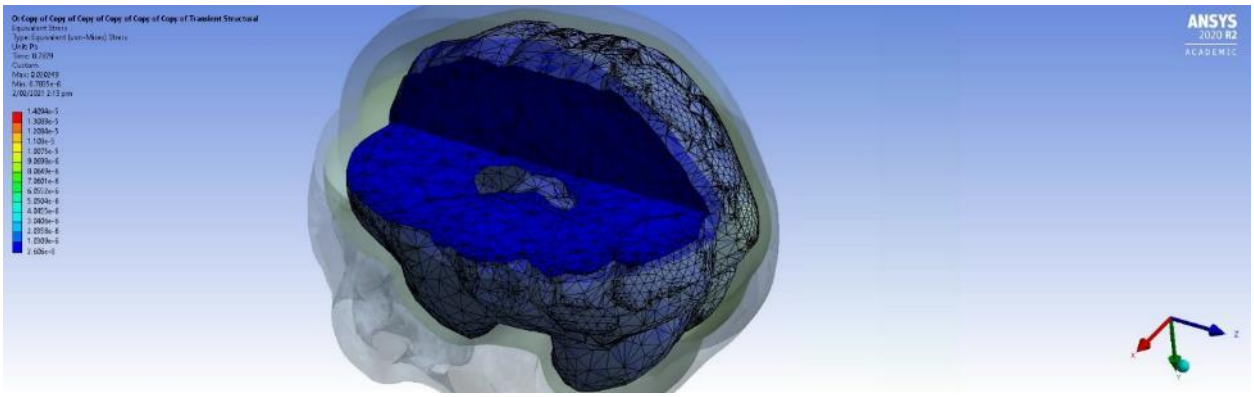
ANSYS
2020 R2
ACADEMIC

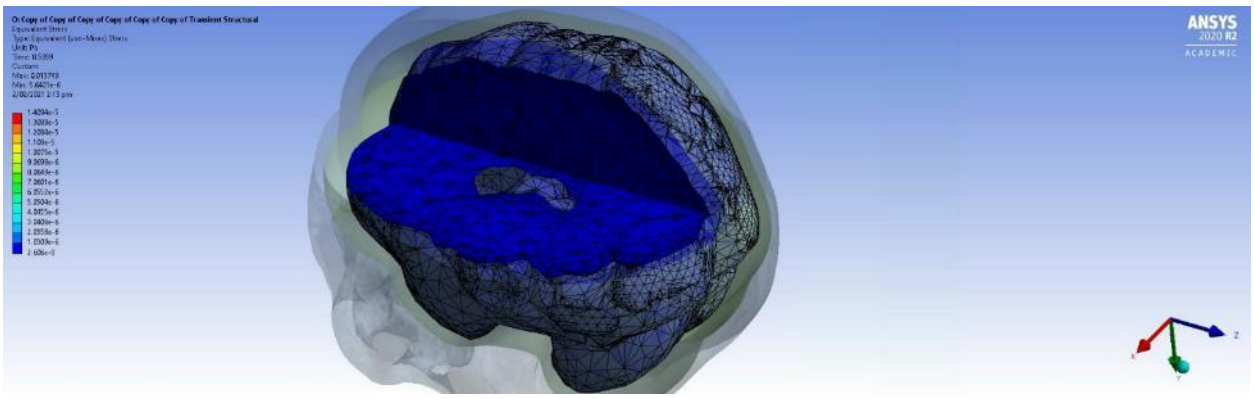
ANSYS
2020 R2
ACADEMIC

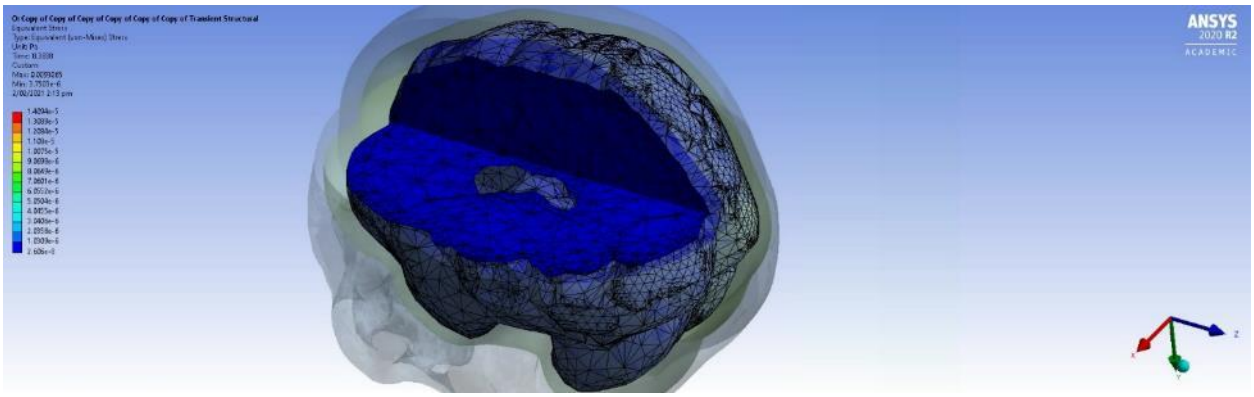
ANSYS
2020 R2
ACADEMIC

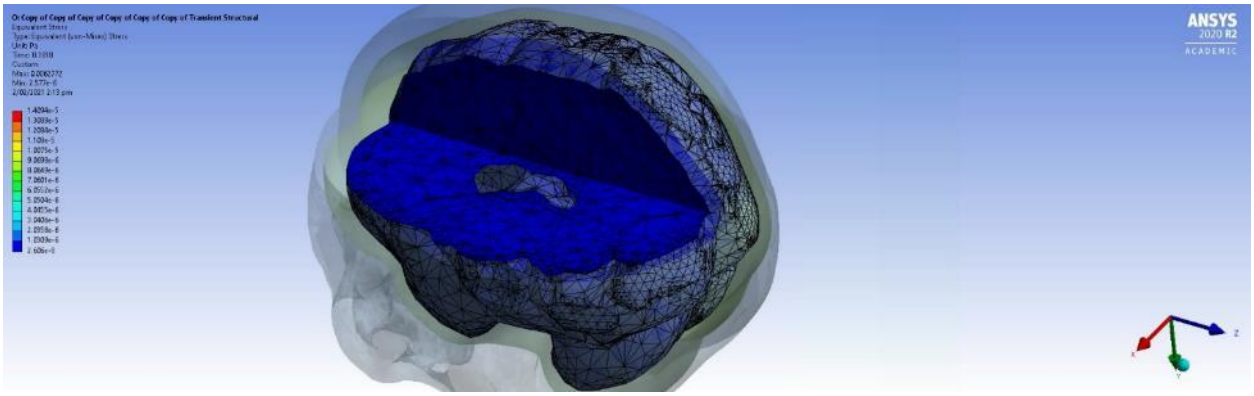
ANSYS
2020 R2
ACADEMIC

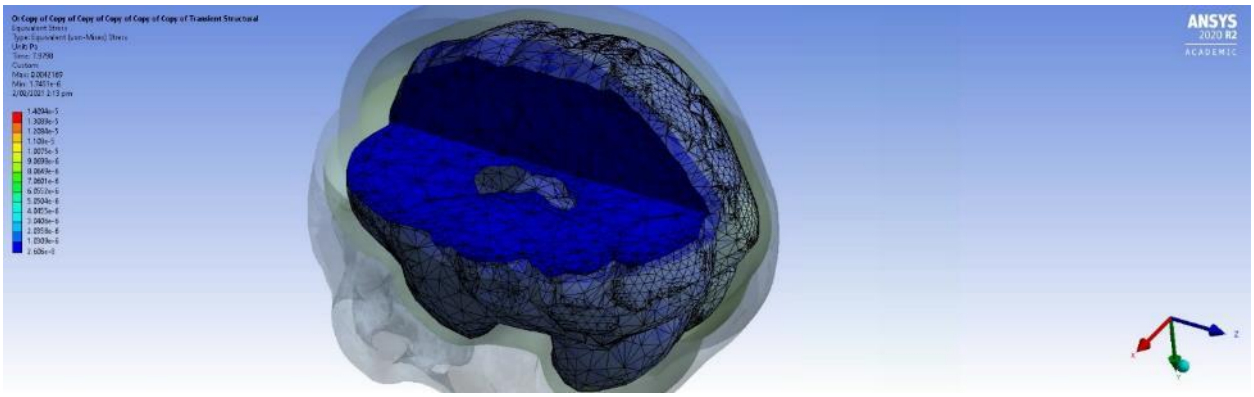
ANSYS
2020 R2
ACADEMIC

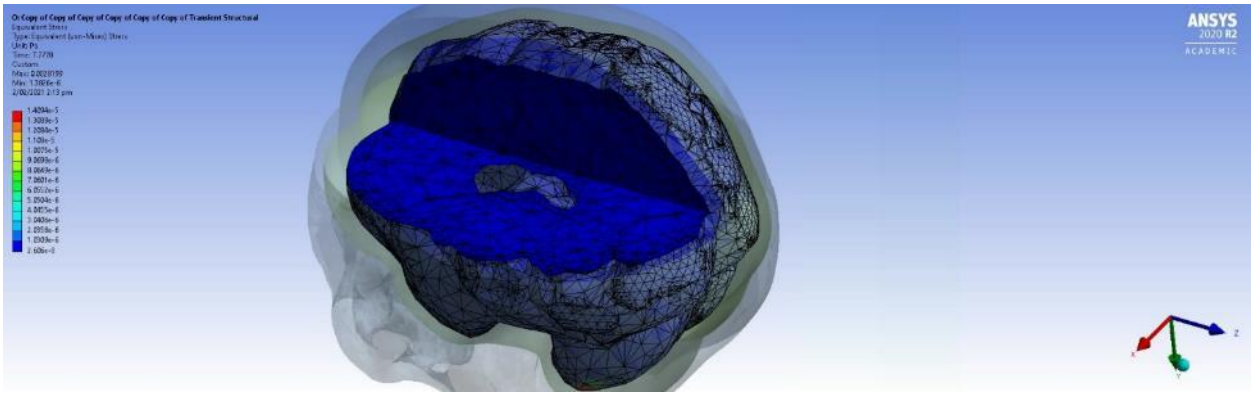
ANSYS
2020 R2
ACADEMIC

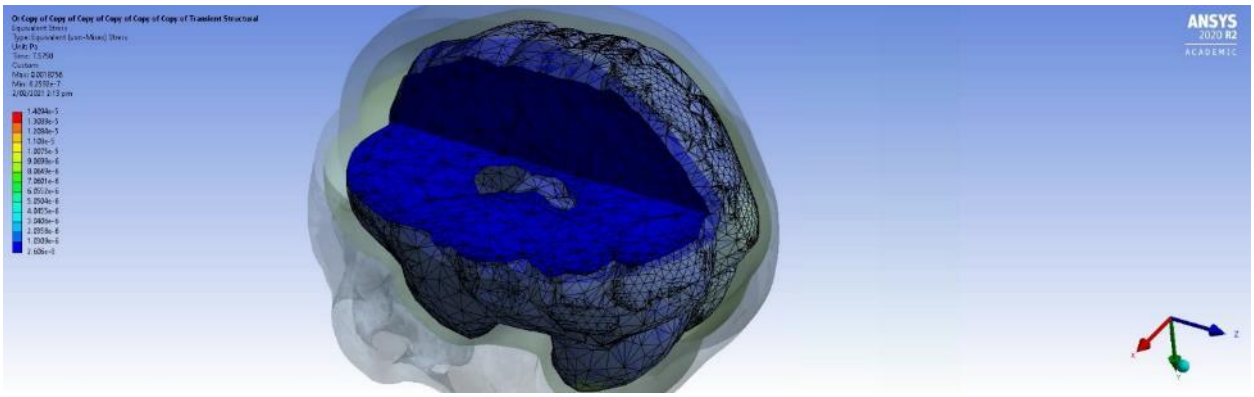
ANSYS
2020 R2
ACADEMIC

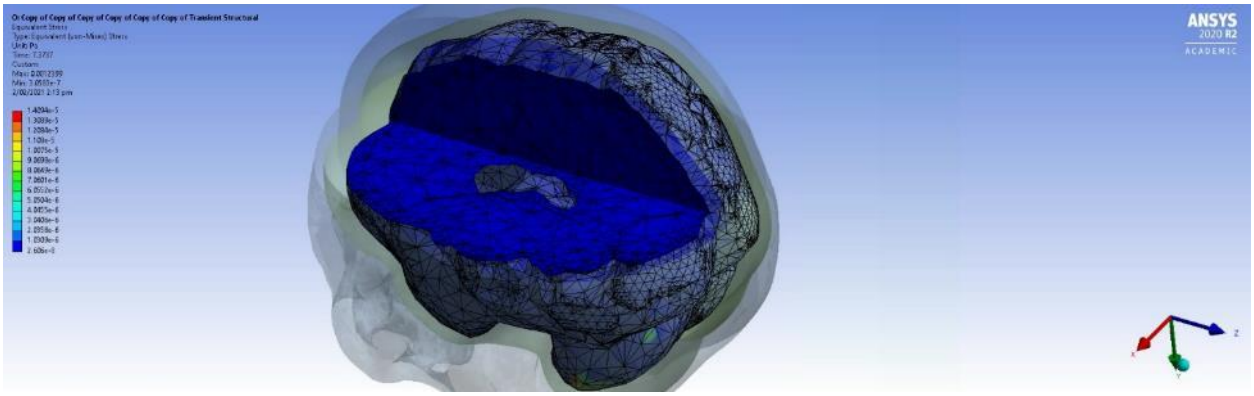
ANSYS
2020 R2
ACADEMIC

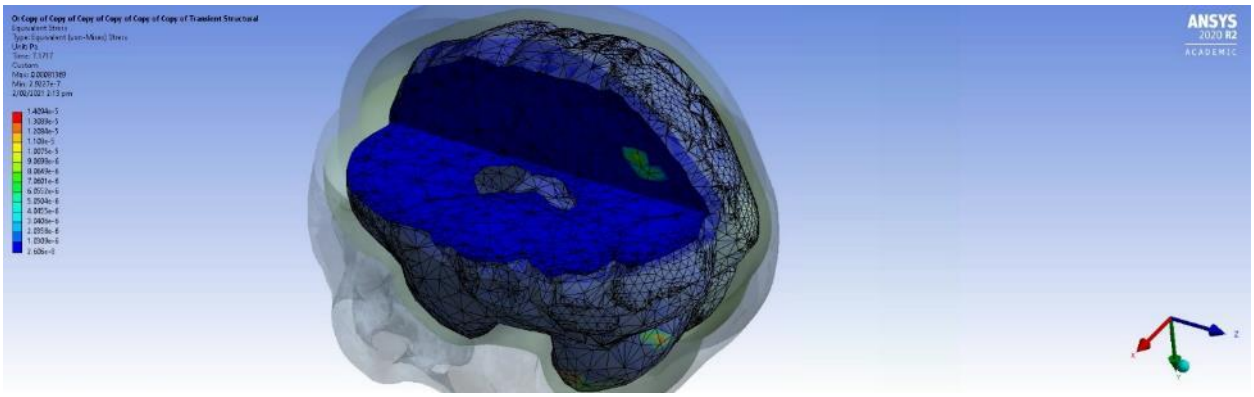
ANSYS
2020 R2
ACADEMIC

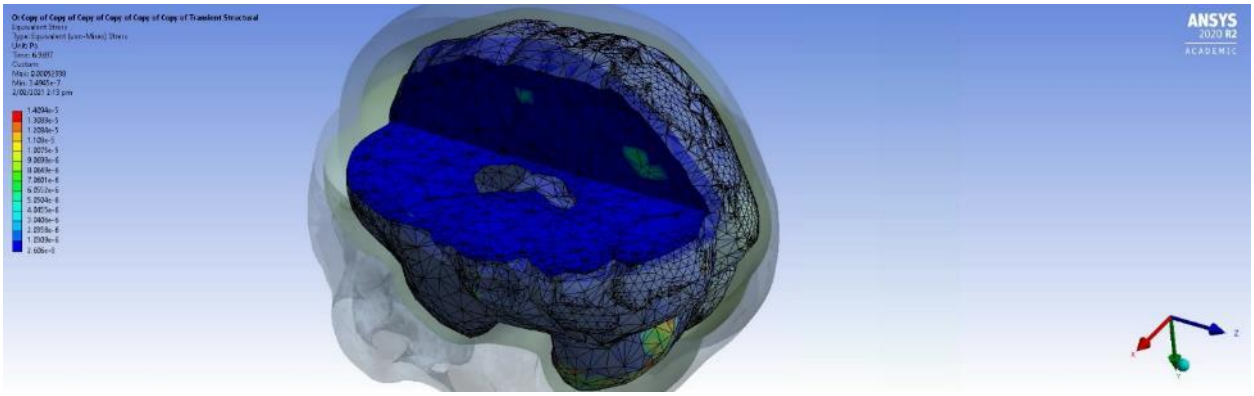
ANSYS
2020 R2
ACADEMIC

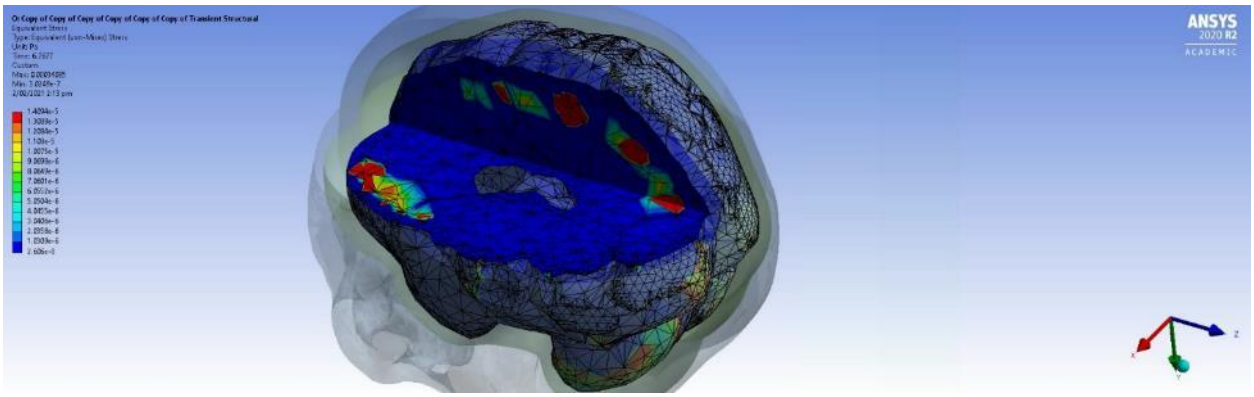
ANSYS
2020 R2
ACADEMIC

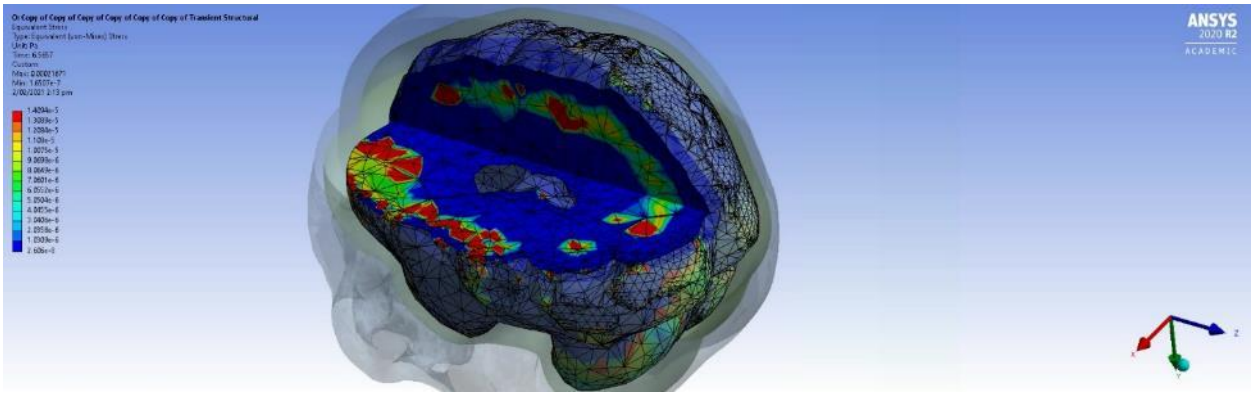
ANSYS
2020 R2
ACADEMIC

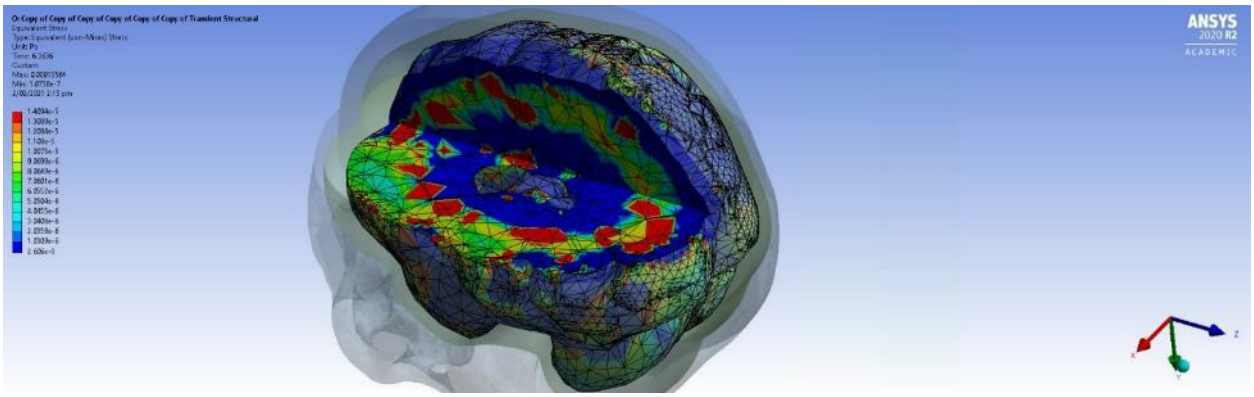
ANSYS
2020 R2
ACADEMIC

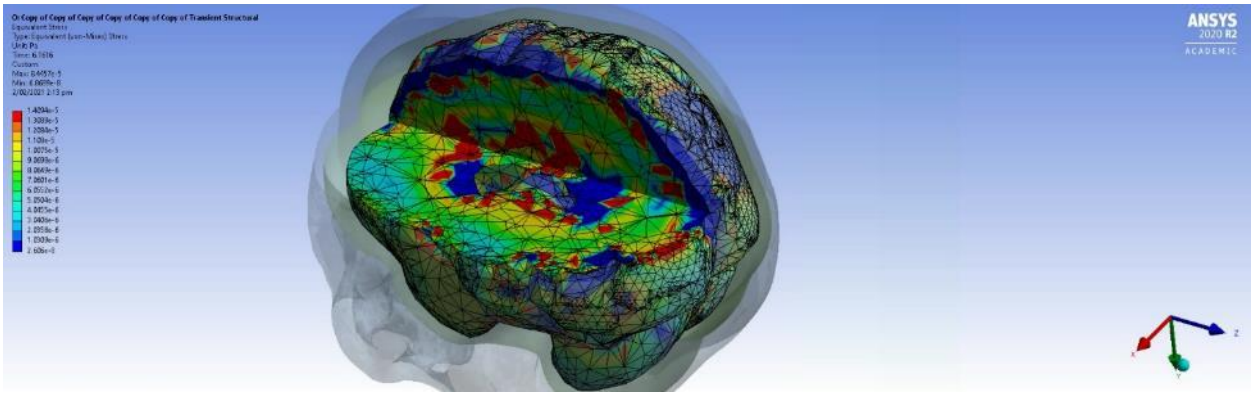
ANSYS
2020 R2
ACADEMIC

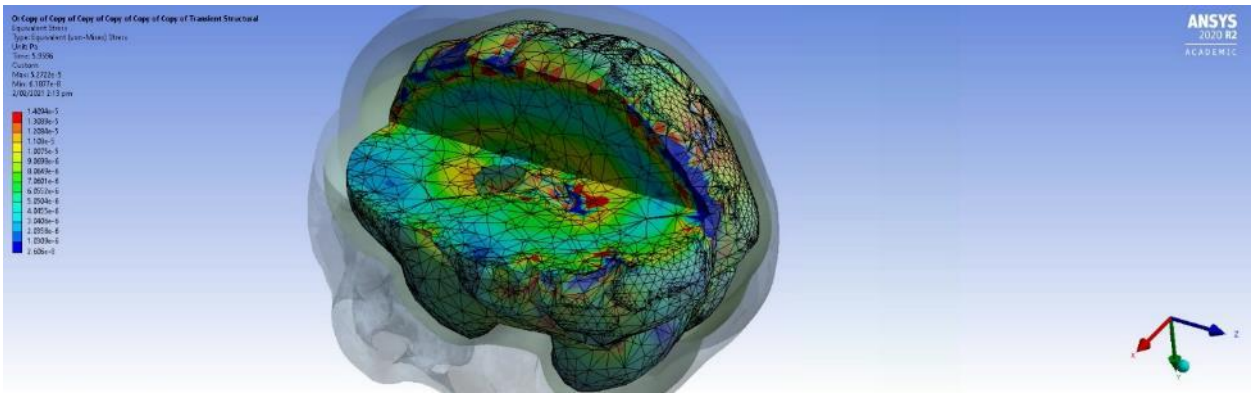
ANSYS
2020 R2
ACADEMIC

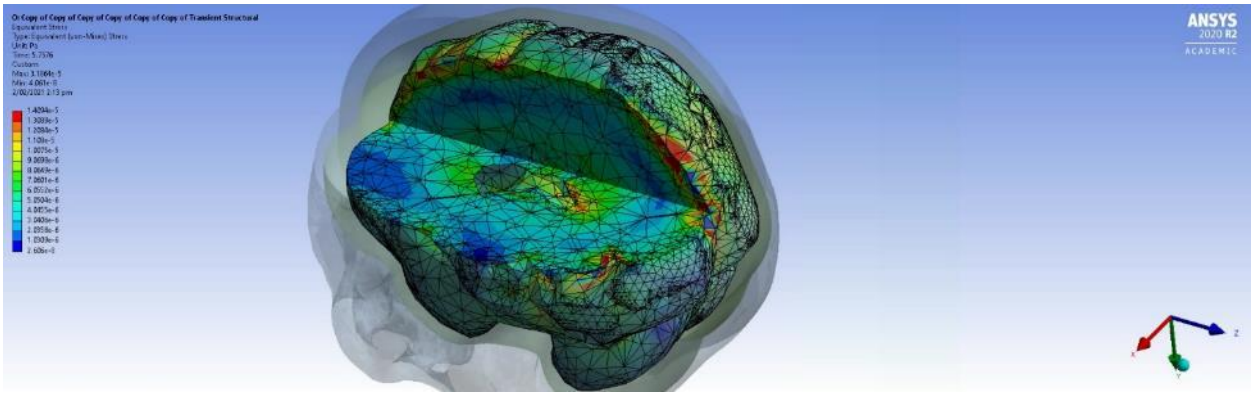
ANSYS
2020 R2
ACADEMIC

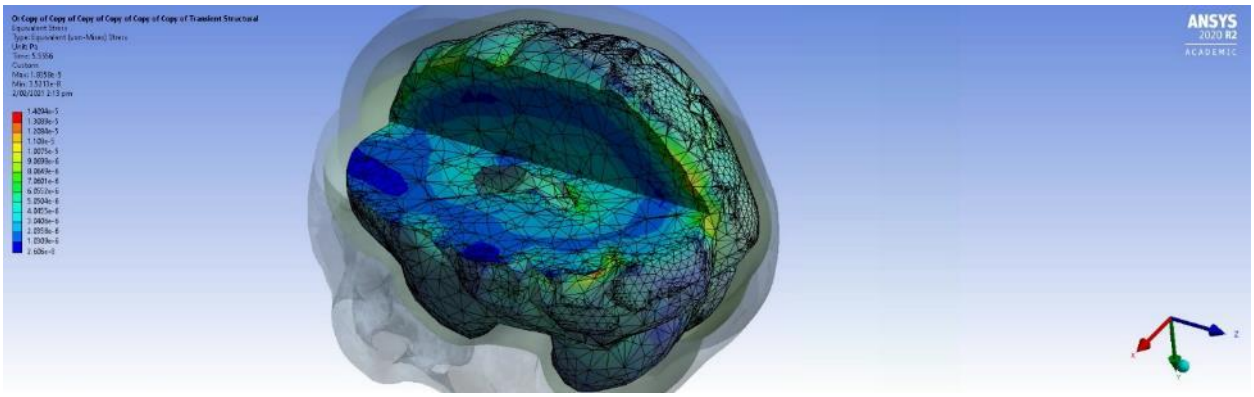
ANSYS
2020 R2
ACADEMIC

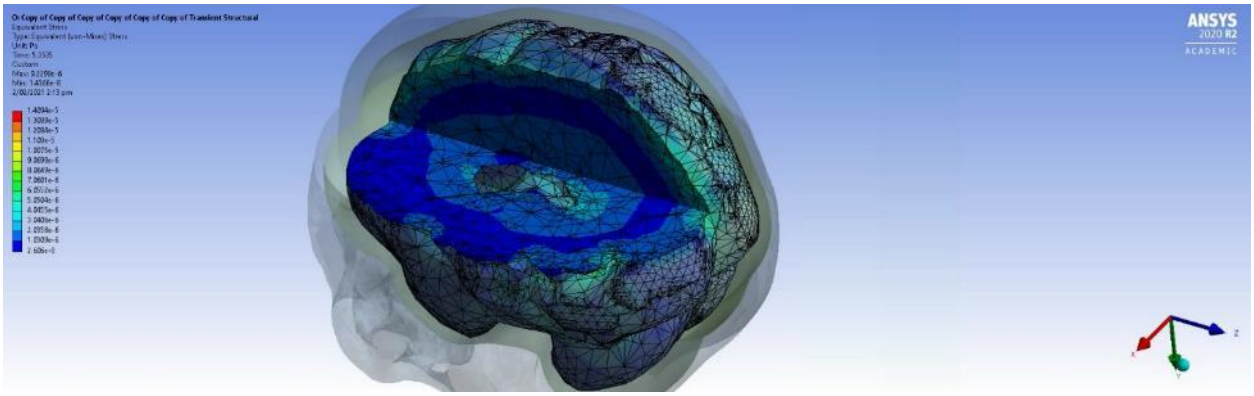
ANSYS
2020 R2
ACADEMIC

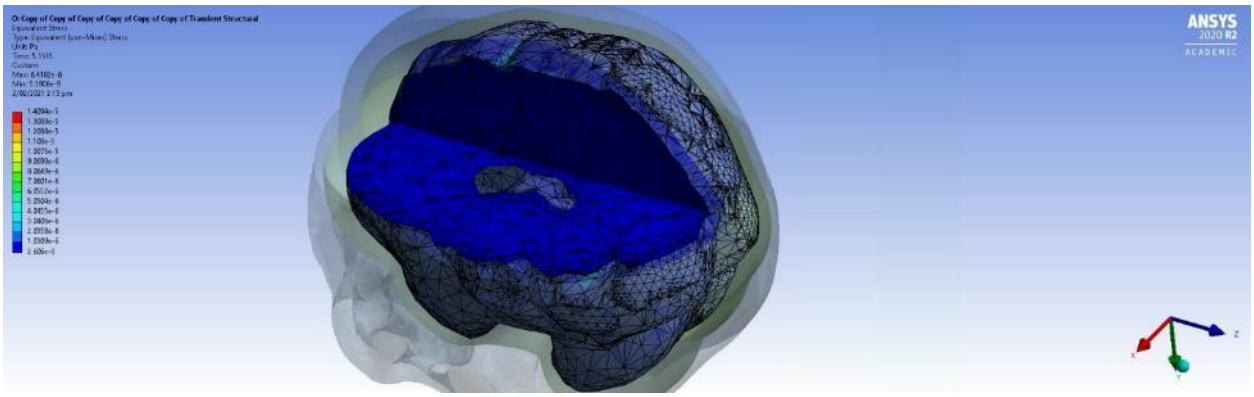
ANSYS
2020 R2
ACADEMIC

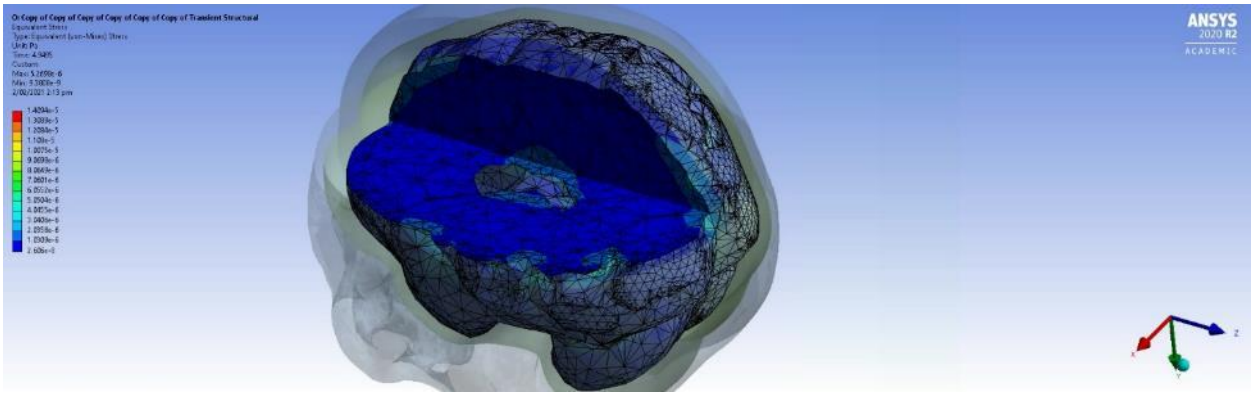
ANSYS
2020 R2
ACADEMIC

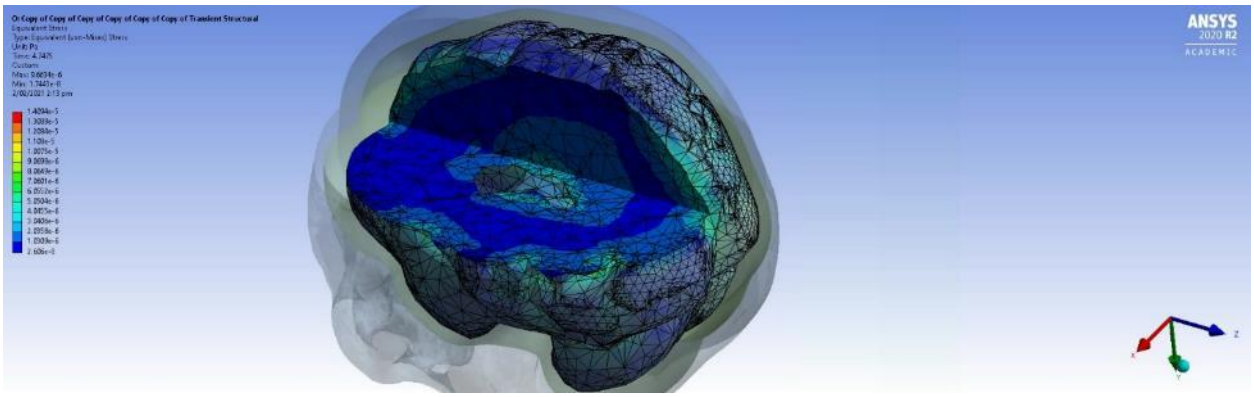
ANSYS
2020 R2
ACADEMIC

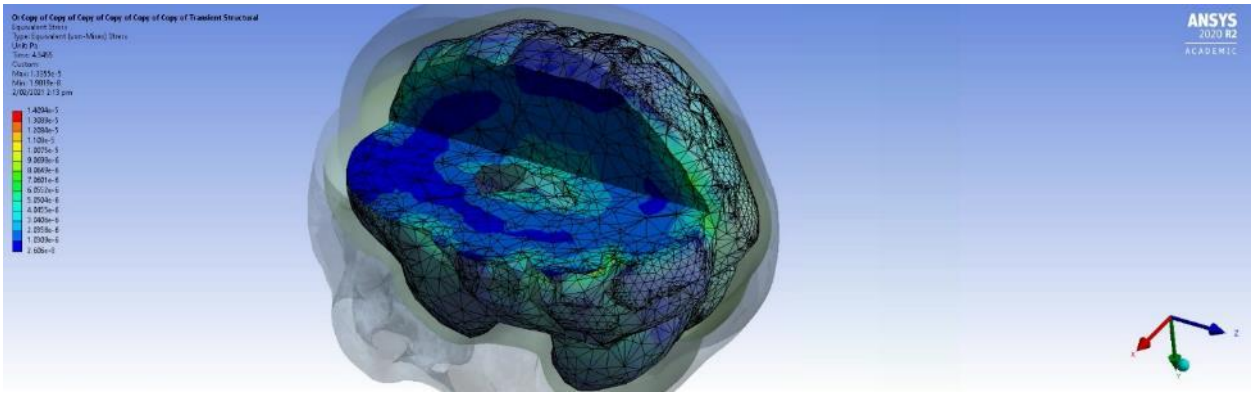
ANSYS
2020 R2
ACADEMIC

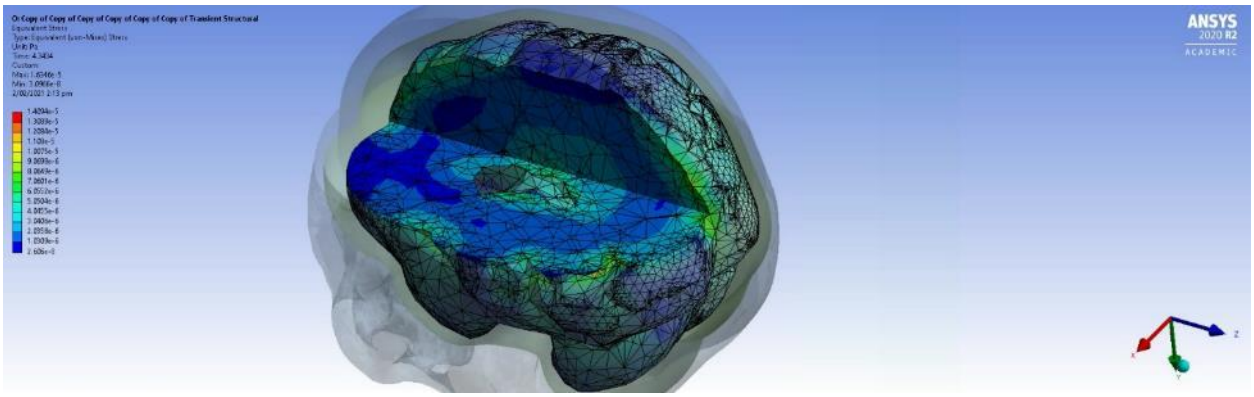
ANSYS
2020 R2
ACADEMIC

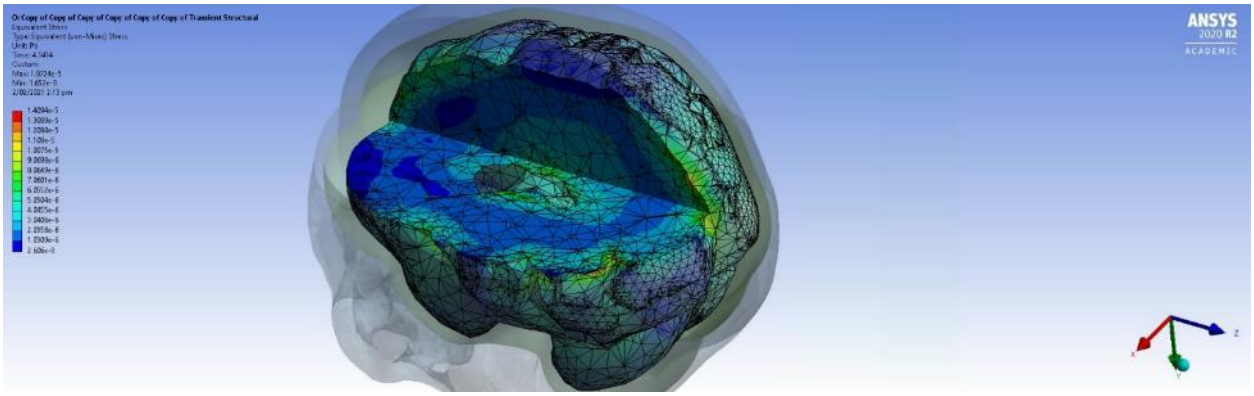
ANSYS
2020 R2
ACADEMIC

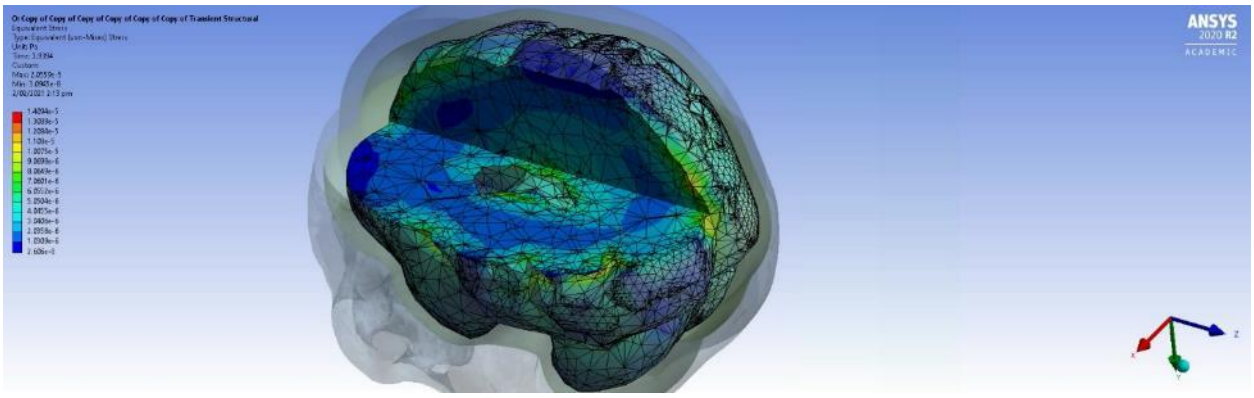
ANSYS
2020 R2
ACADEMIC

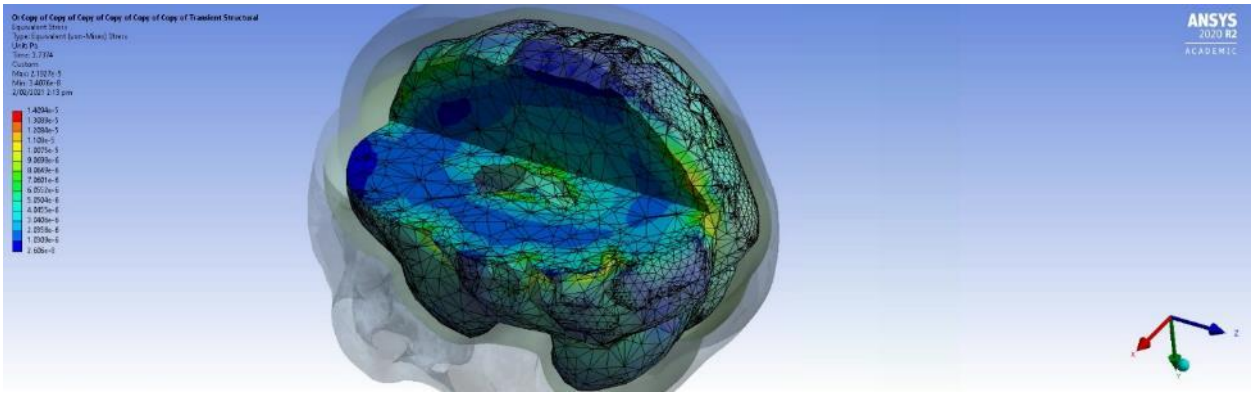
ANSYS
2020 R2
ACADEMIC

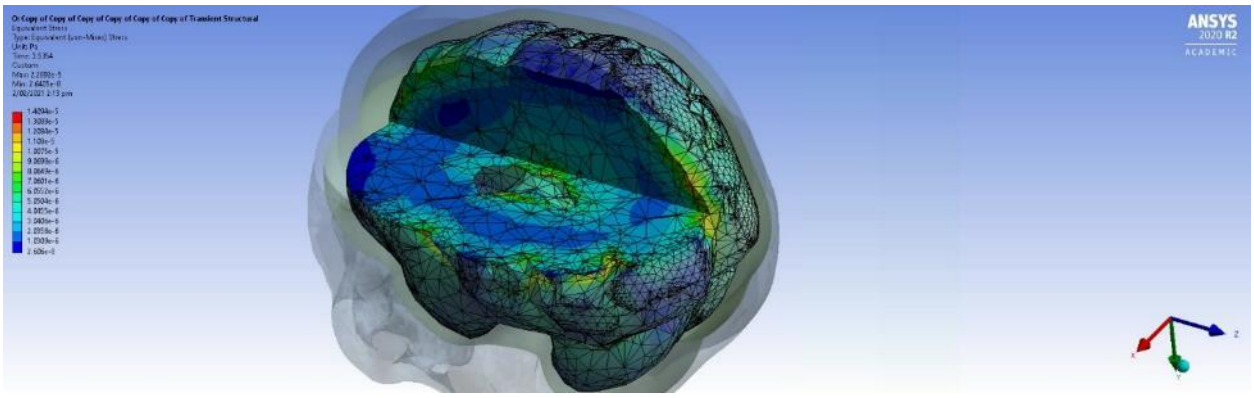
ANSYS
2020 R2
ACADEMIC

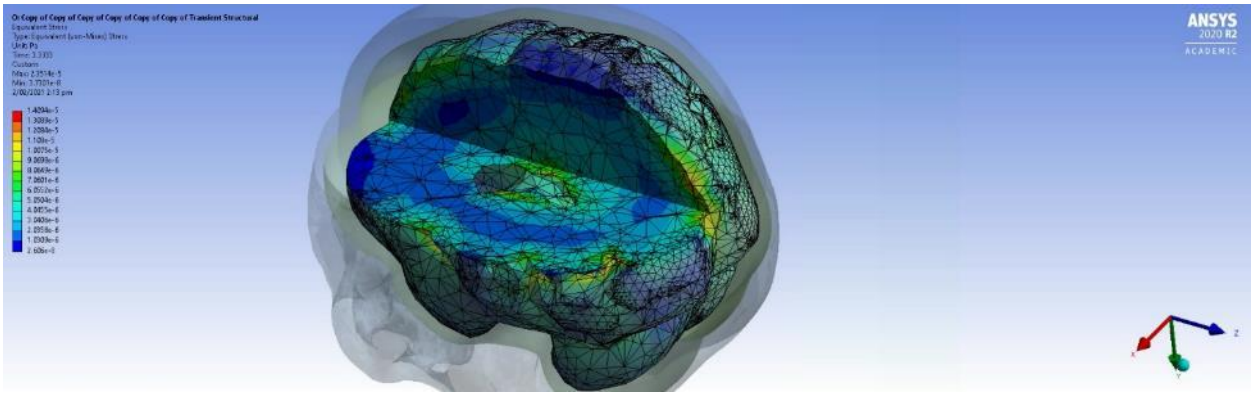
ANSYS
2020 R2
ACADEMIC

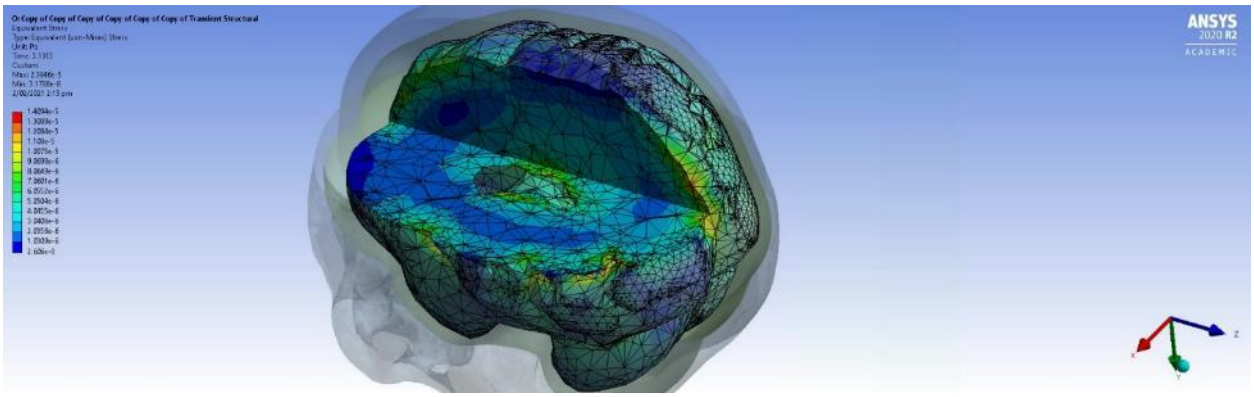
ANSYS
2020 R2
ACADEMIC

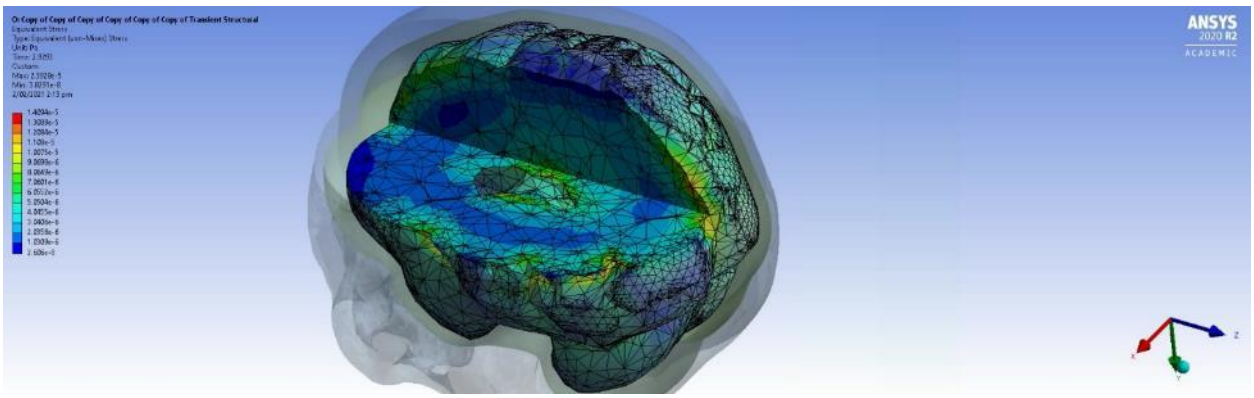
ANSYS
2020 R2
ACADEMIC

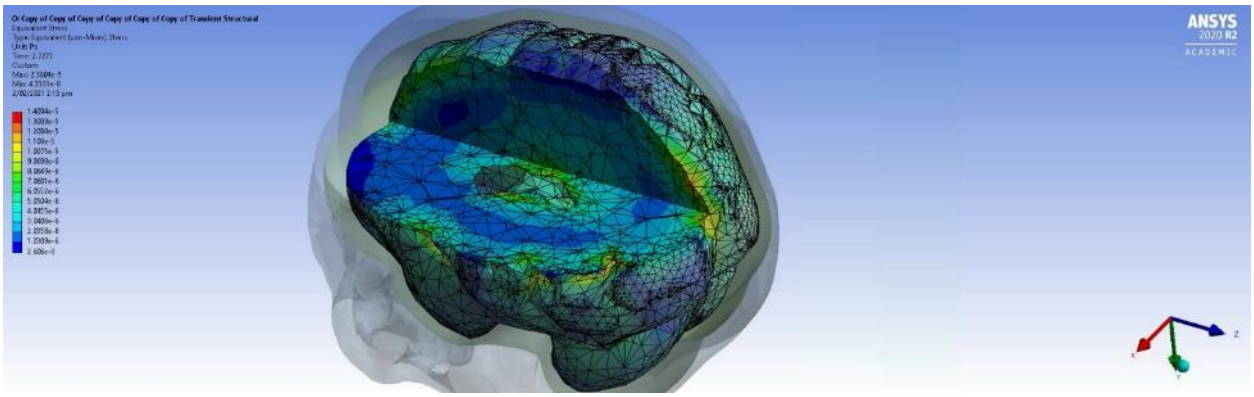
ANSYS
2020 R2
ACADEMIC

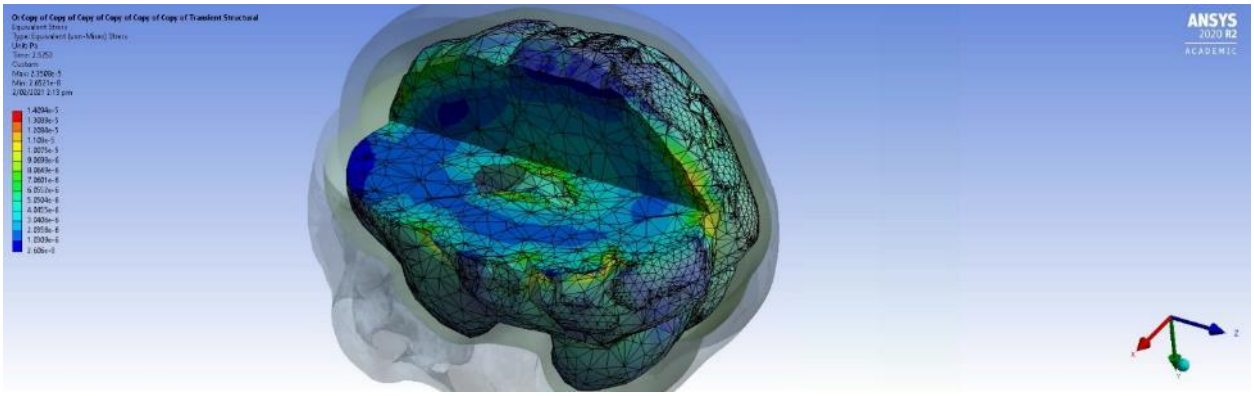
ANSYS
2020 R2
ACADEMIC

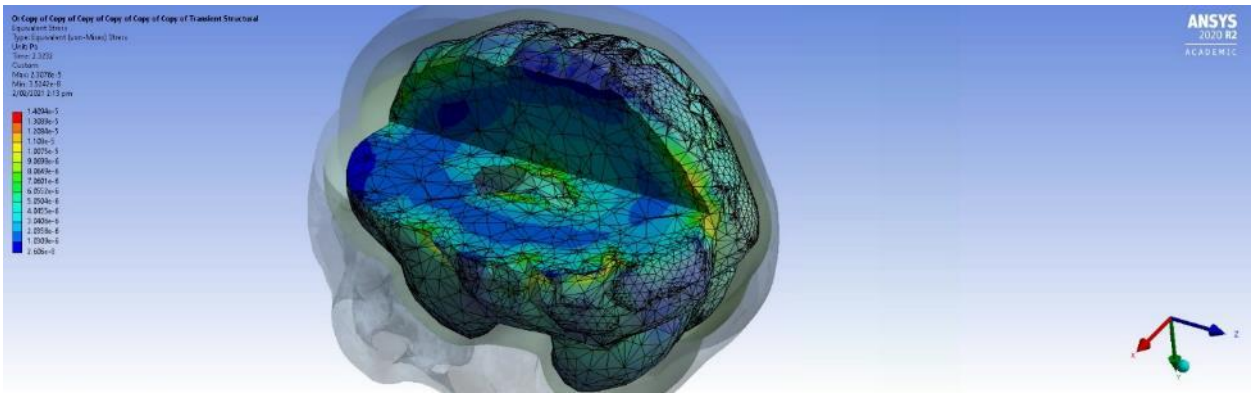
ANSYS
2020 R2
ACADEMIC

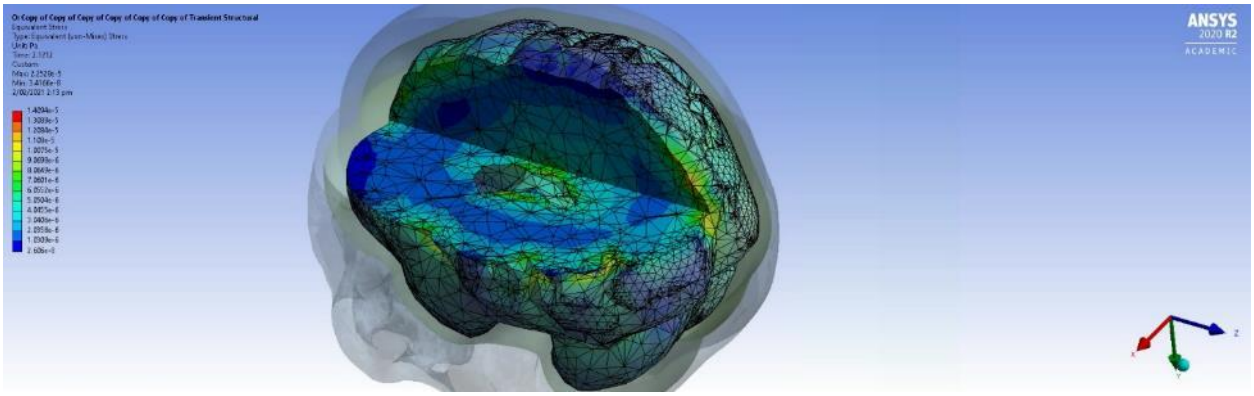
ANSYS
2020 R2
ACADEMIC

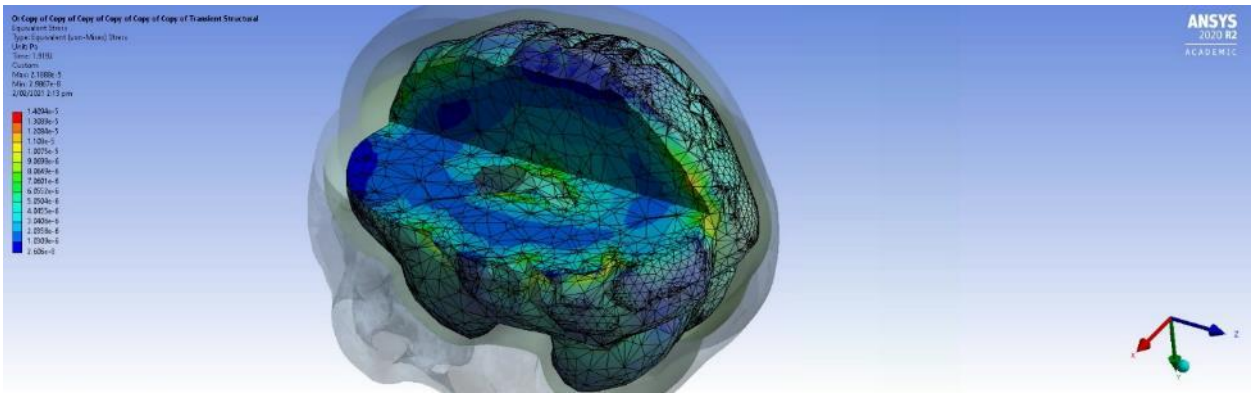
ANSYS
2020 R2
ACADEMIC

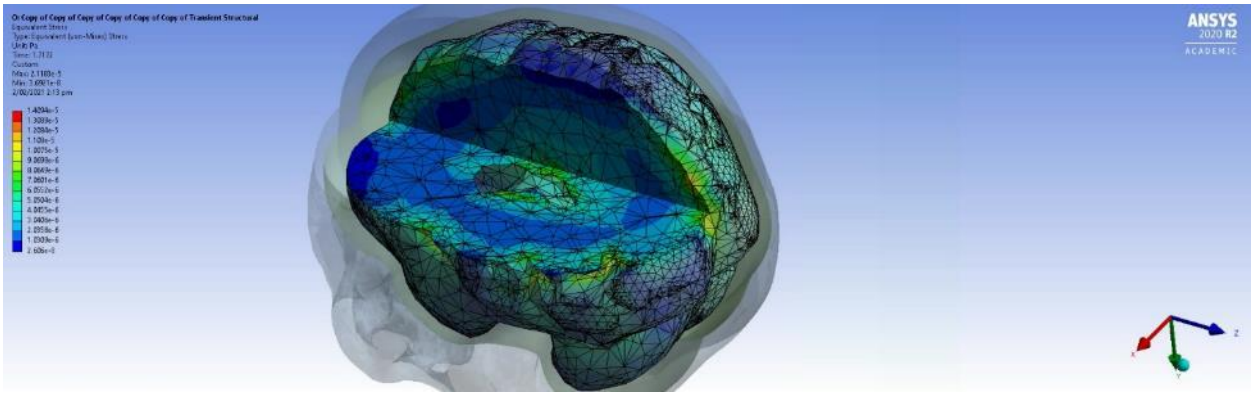
ANSYS
2020 R2
ACADEMIC

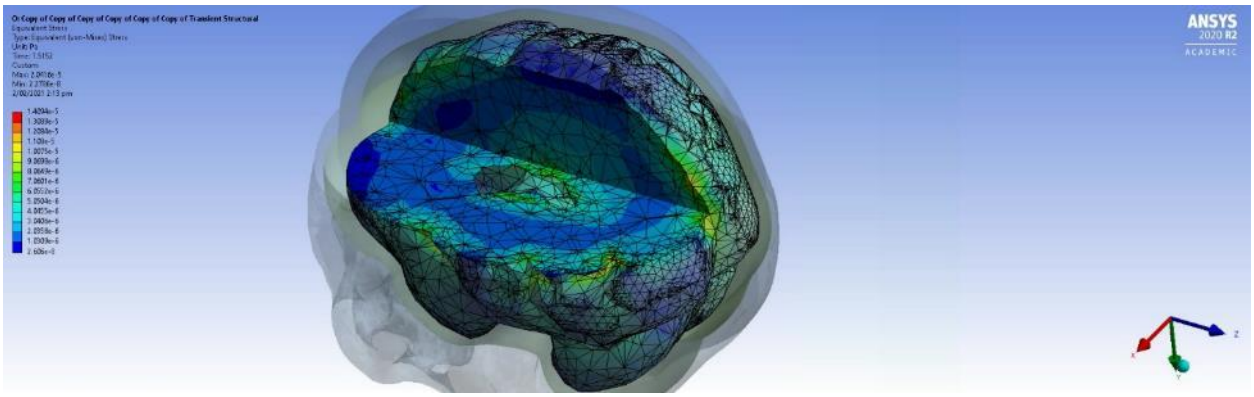
ANSYS
2020 R2
ACADEMIC

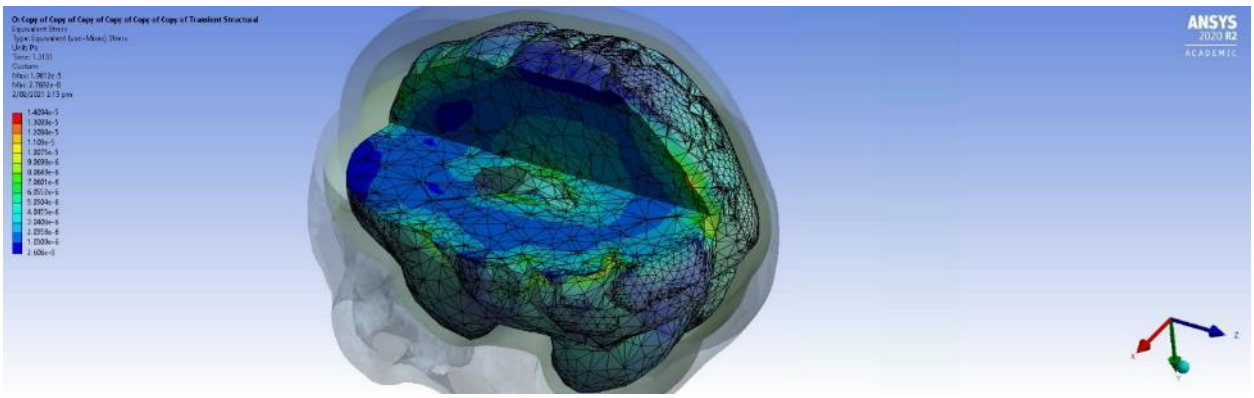
ANSYS
2020 R2
ACADEMIC

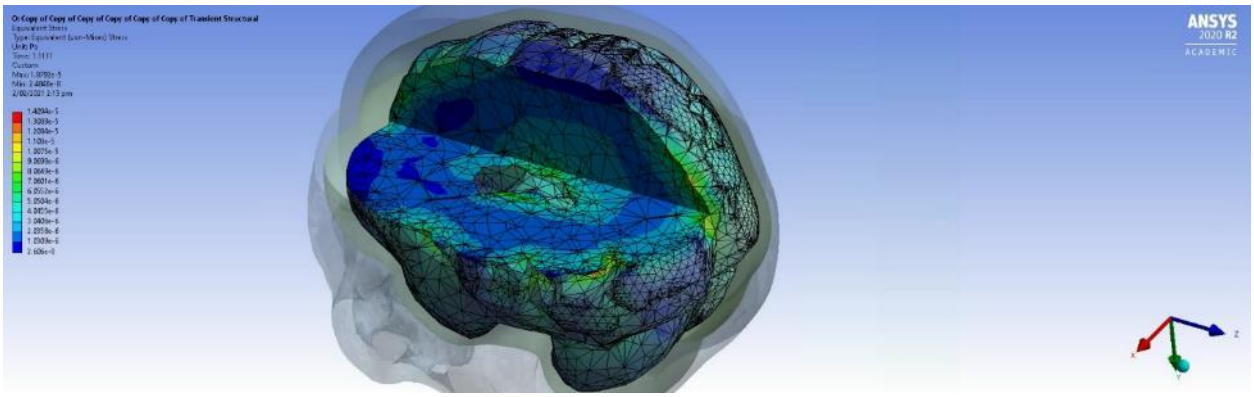
ANSYS
2020 R2
ACADEMIC

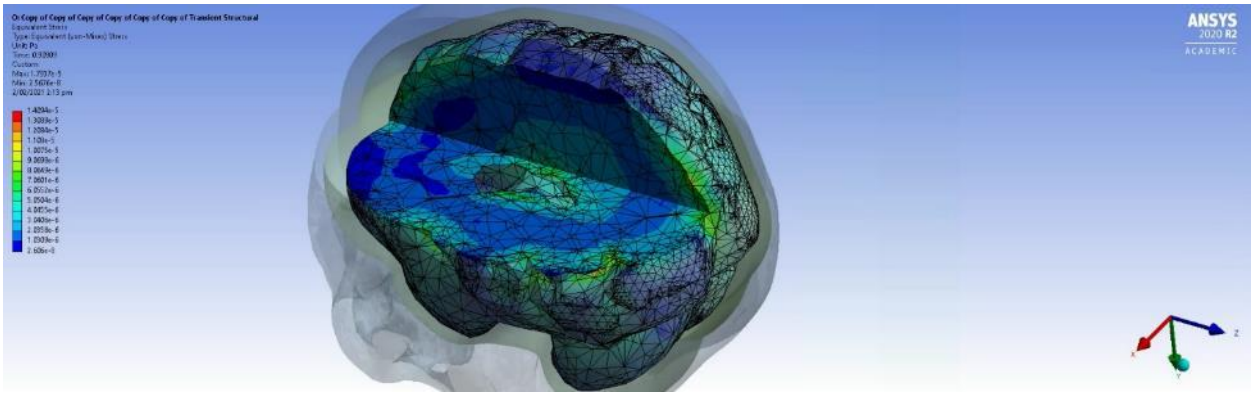
ANSYS
2020 R2
ACADEMIC

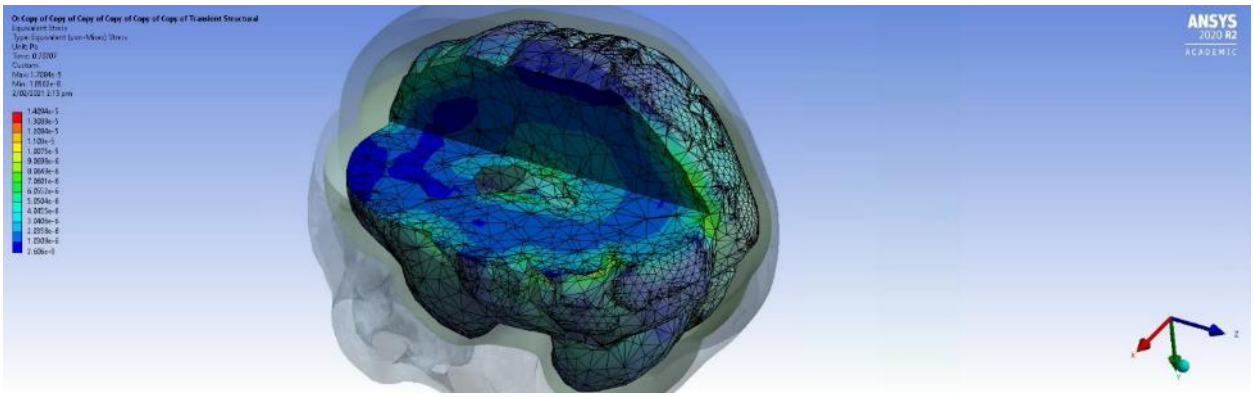
ANSYS
2020 R2
ACADEMIC

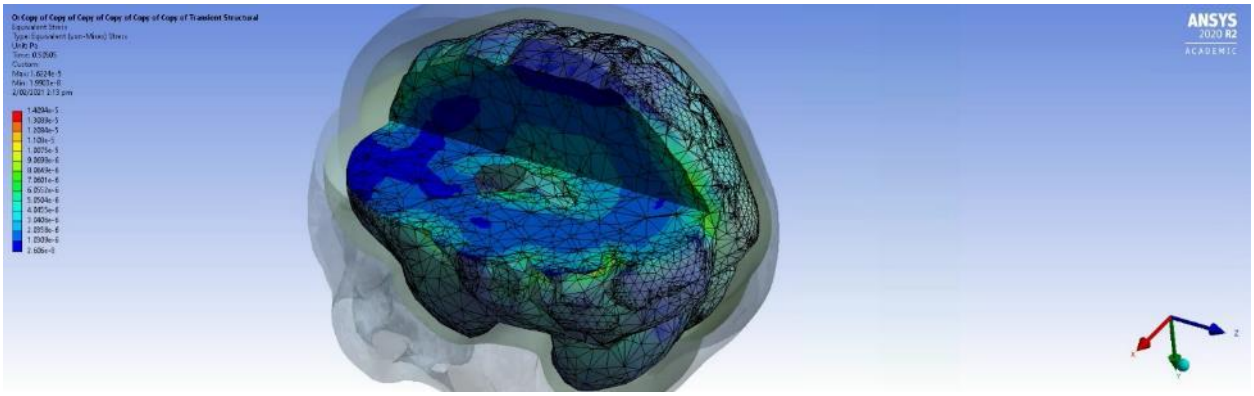
ANSYS
2020 R2
ACADEMIC

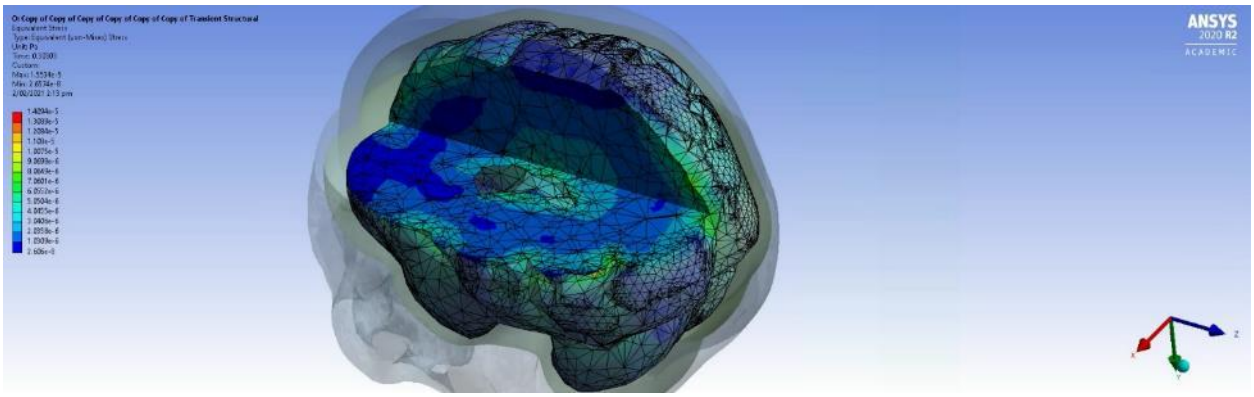
ANSYS
2020 R2
ACADEMIC

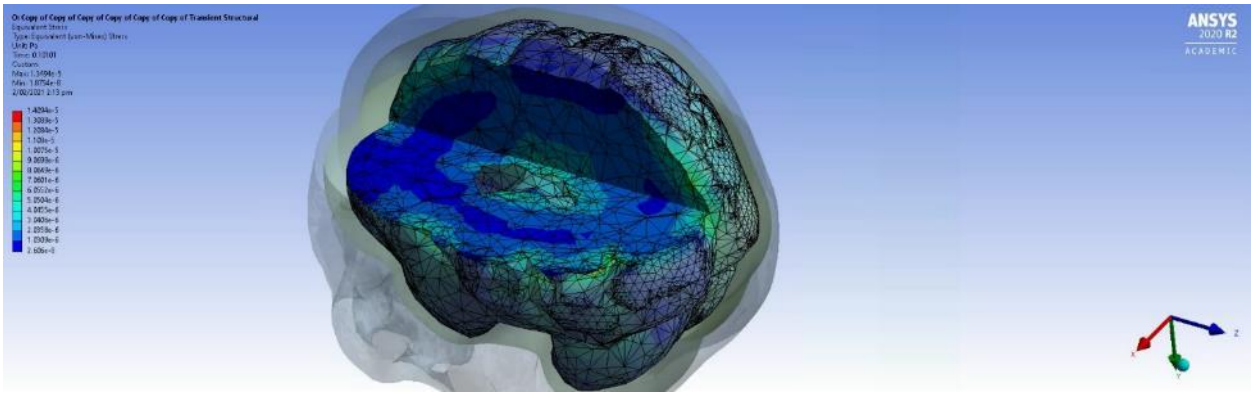

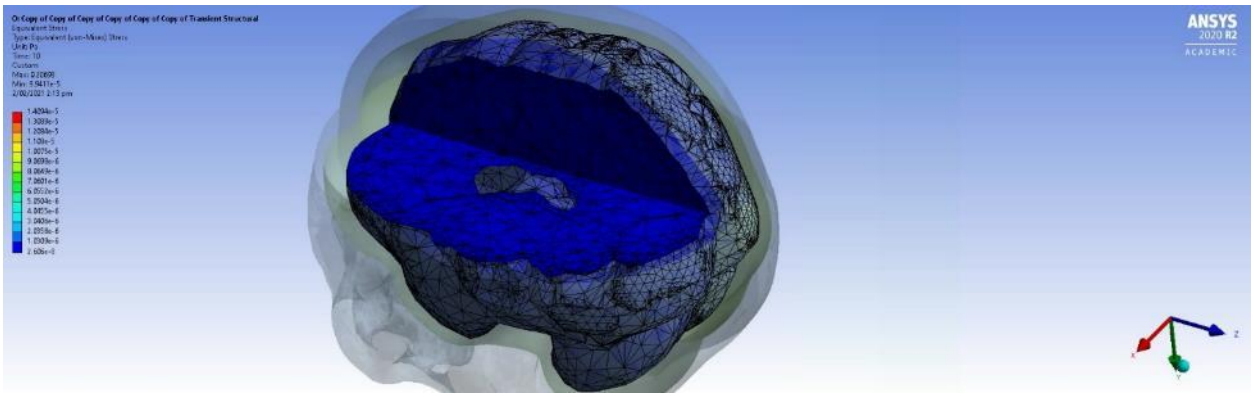

Impact Zone 6

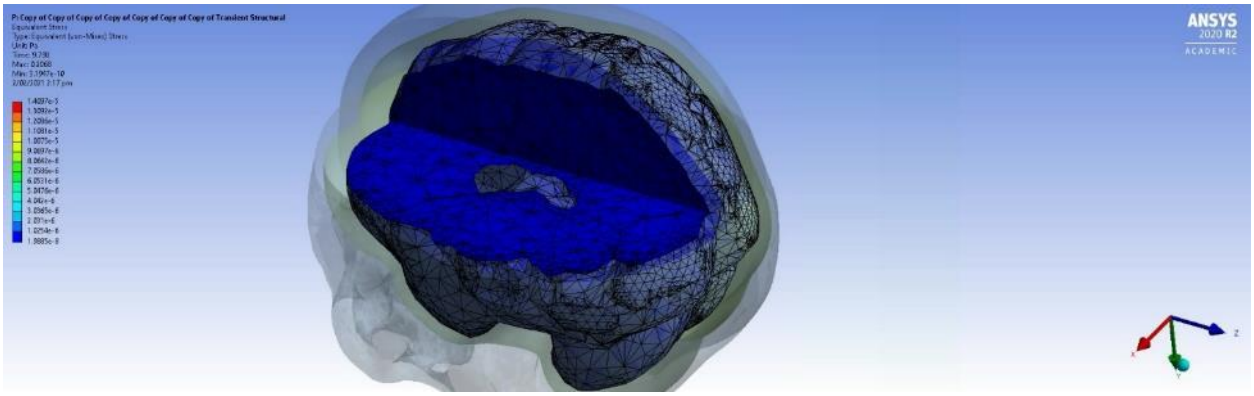

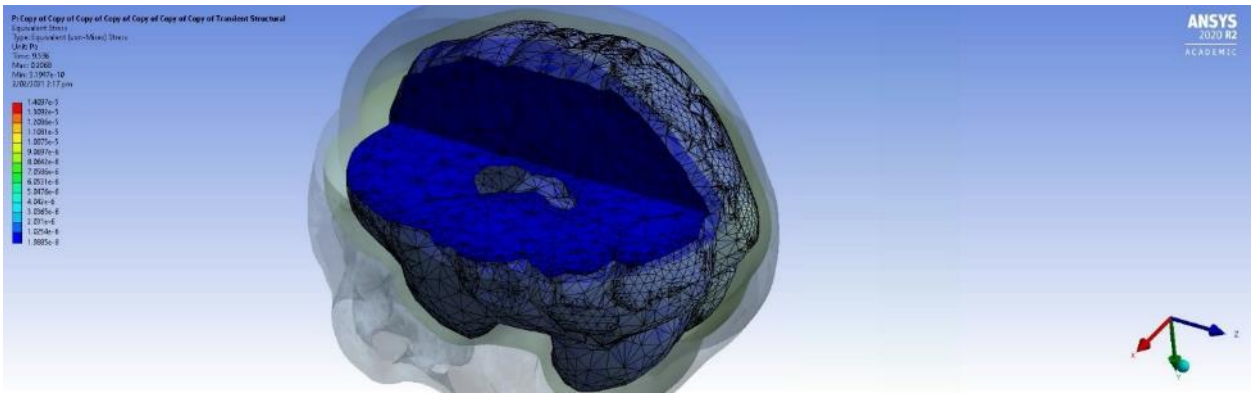

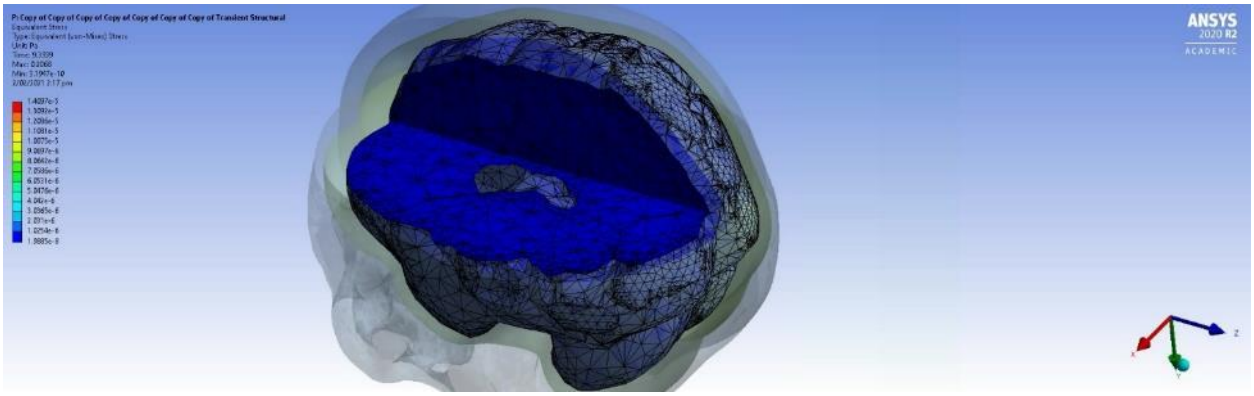
ANSYS
2020 R2
ACADEMIC

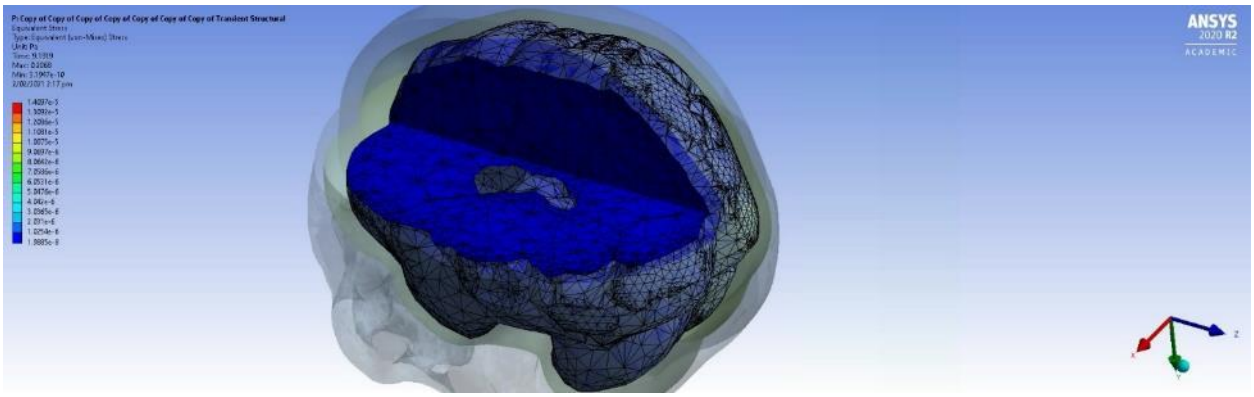
ANSYS
2020 R2
ACADEMIC

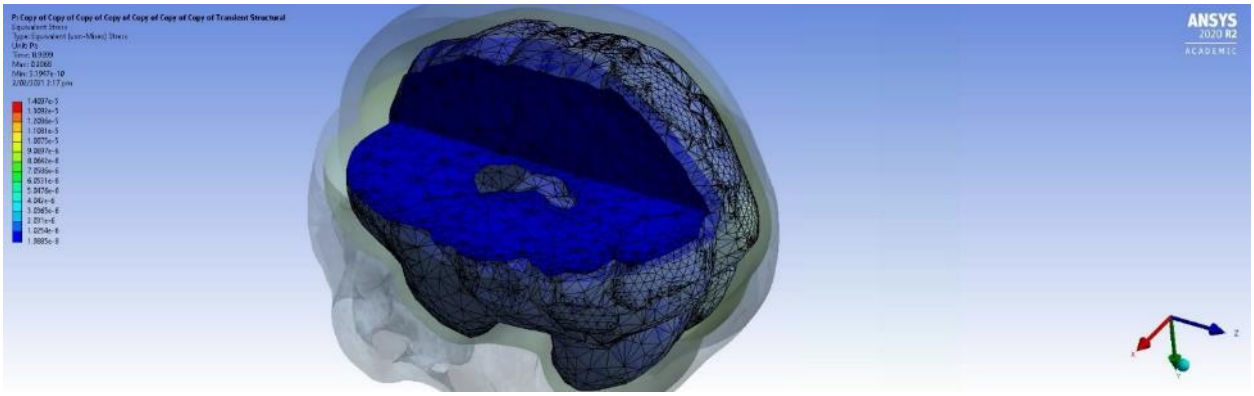
ANSYS
2020 R2
ACADEMIC

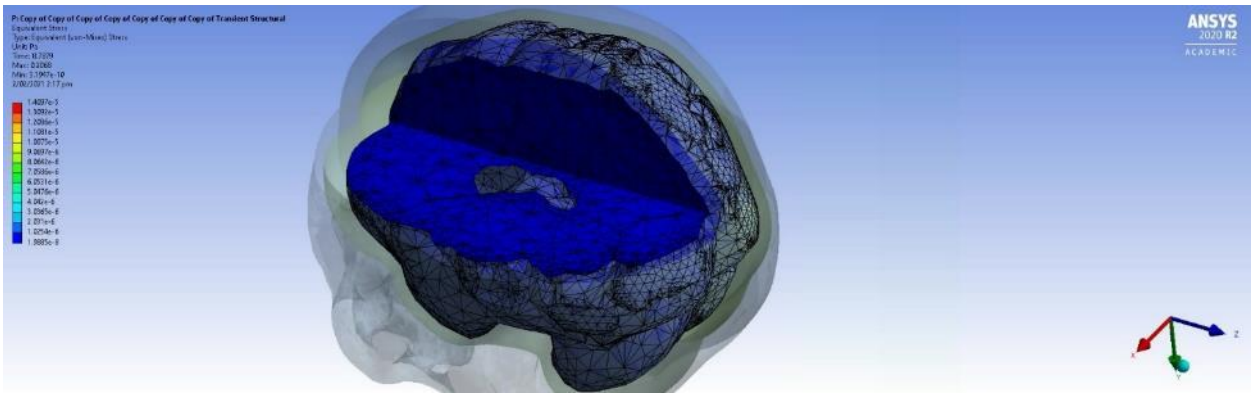
ANSYS
2020 R2
ACADEMIC

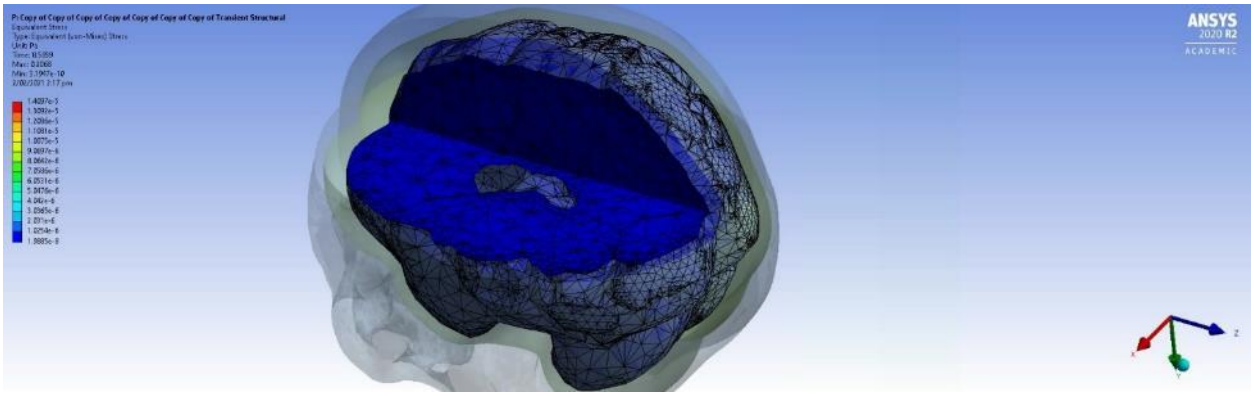
ANSYS
2020 R2
ACADEMIC

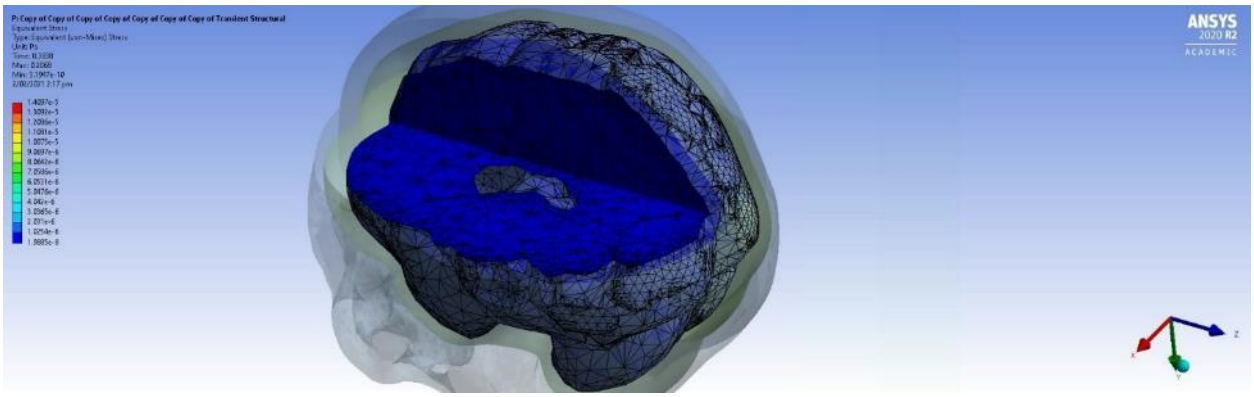
ANSYS
2020 R2
ACADEMIC

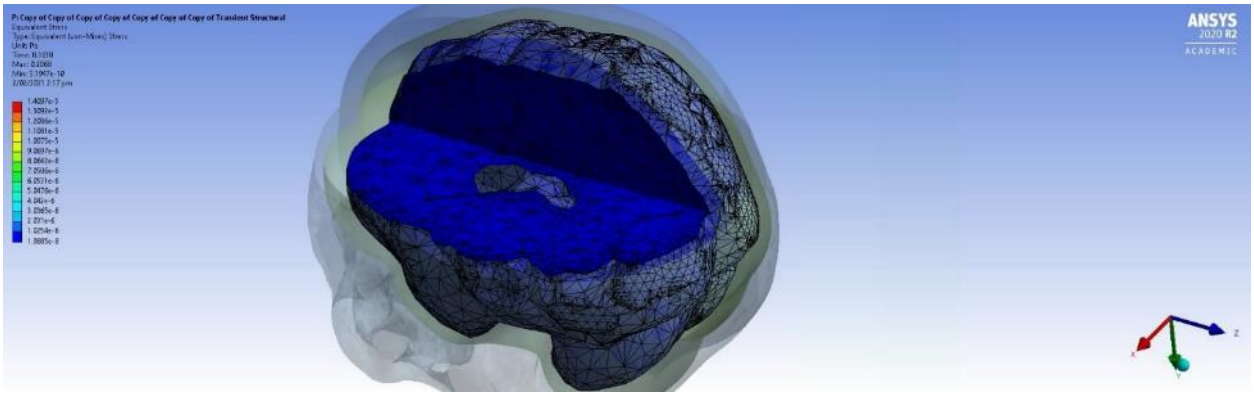
ANSYS
2020 R2
ACADEMIC

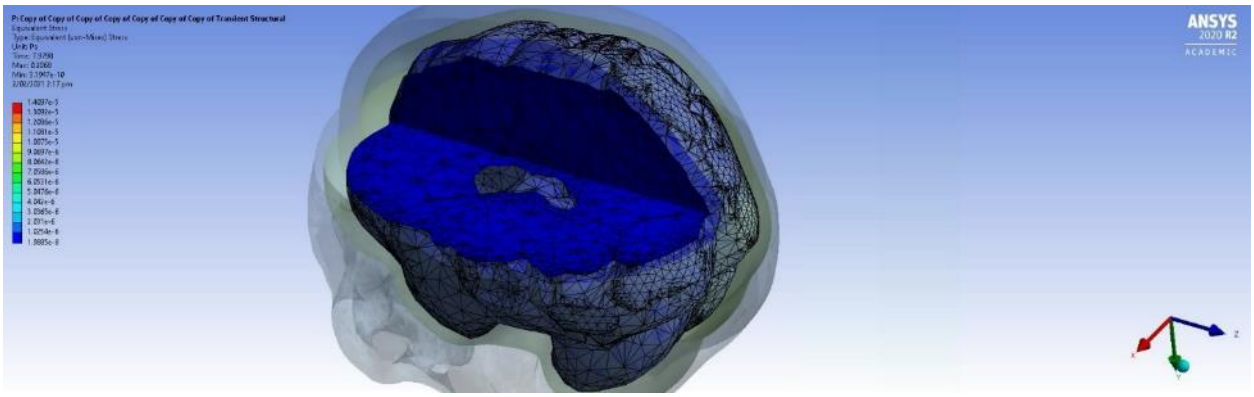
ANSYS
2020 R2
ACADEMIC

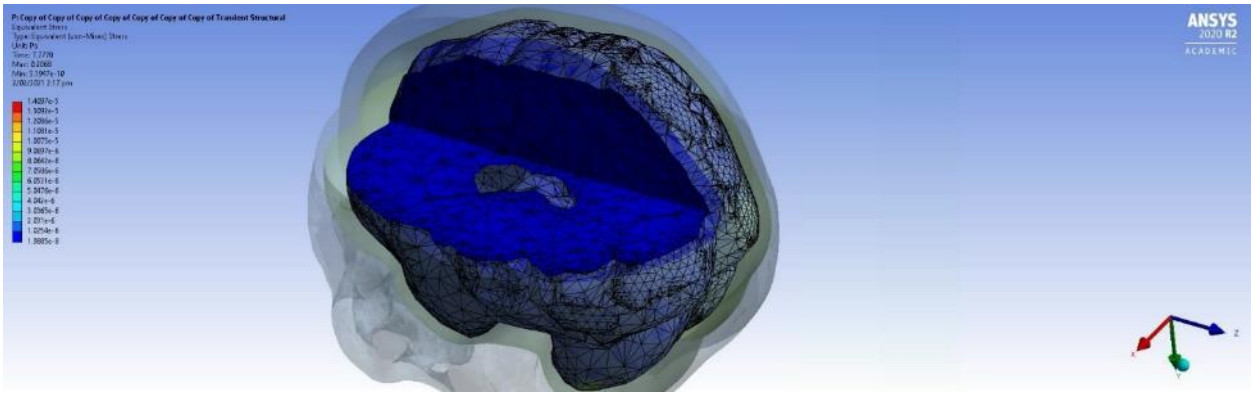
ANSYS
2020 R2
ACADEMIC

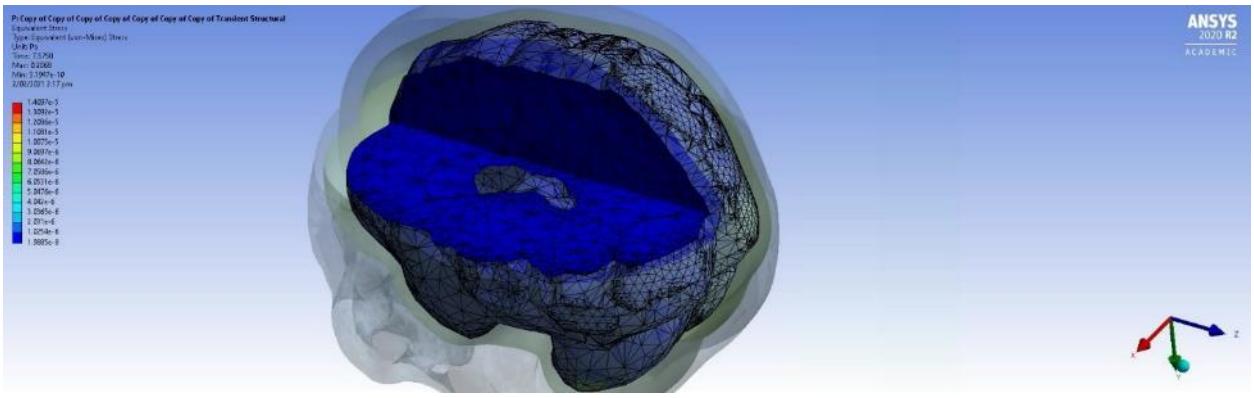
ANSYS
2020 R2
ACADEMIC

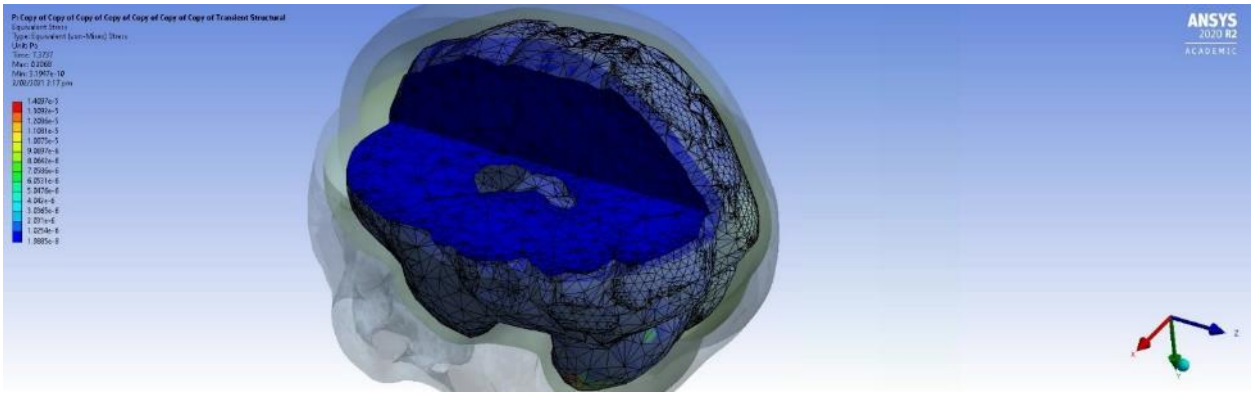
ANSYS
2020 R2
ACADEMIC

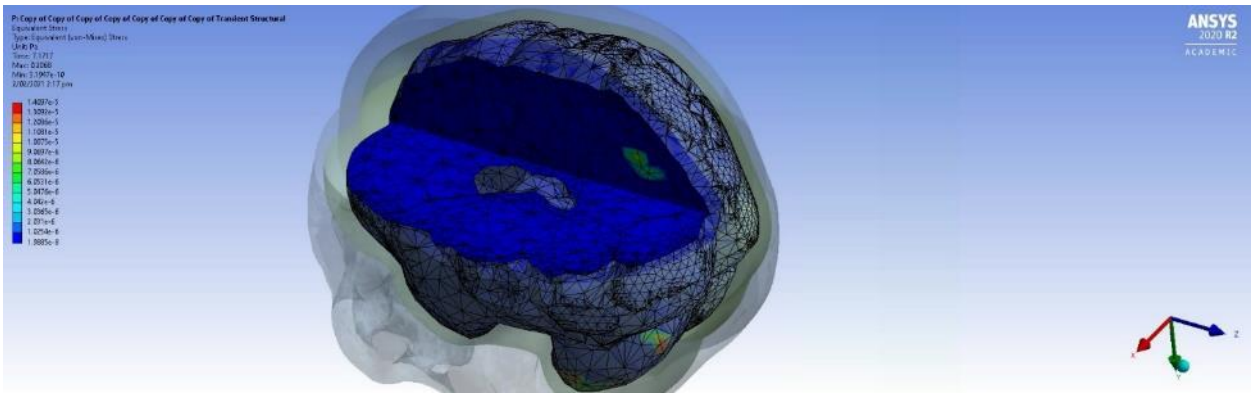
ANSYS
2020 R2
ACADEMIC

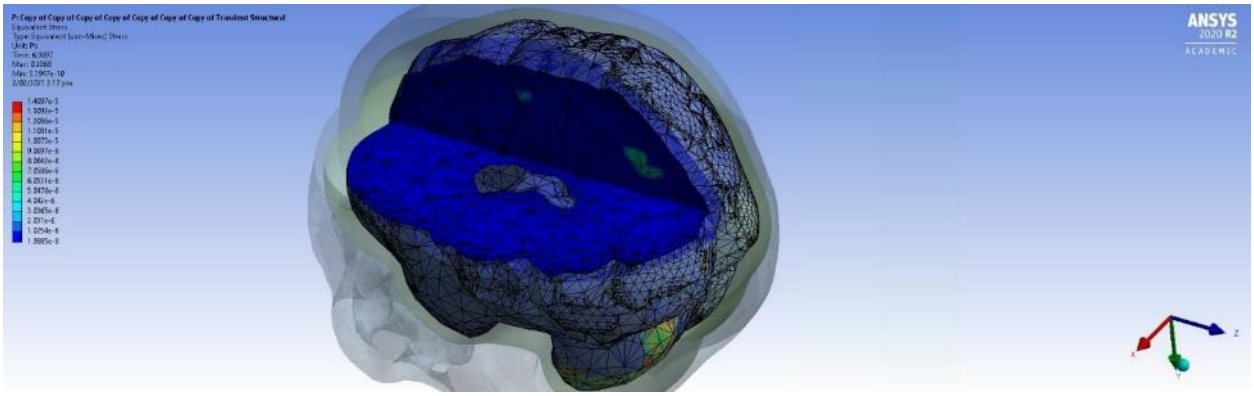
ANSYS
2020 R2
ACADEMIC

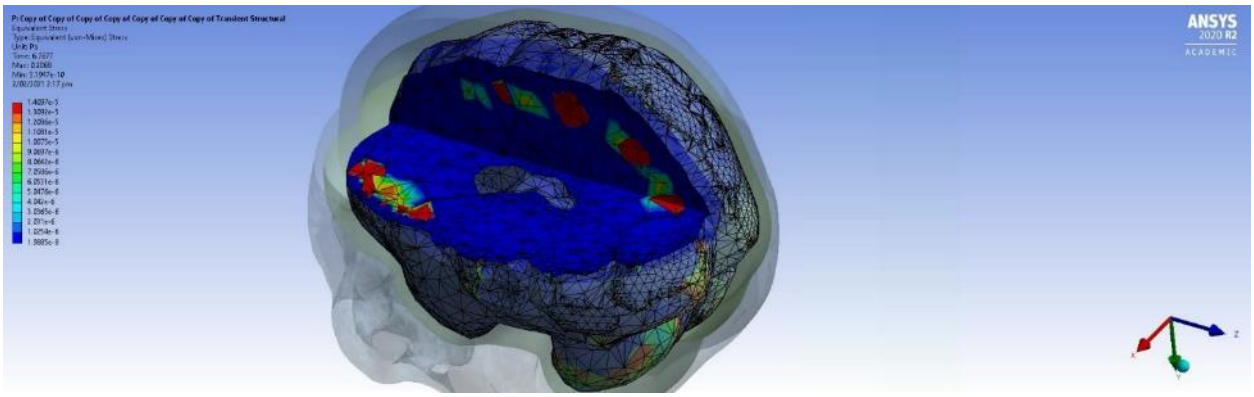
ANSYS
2020 R2
ACADEMIC

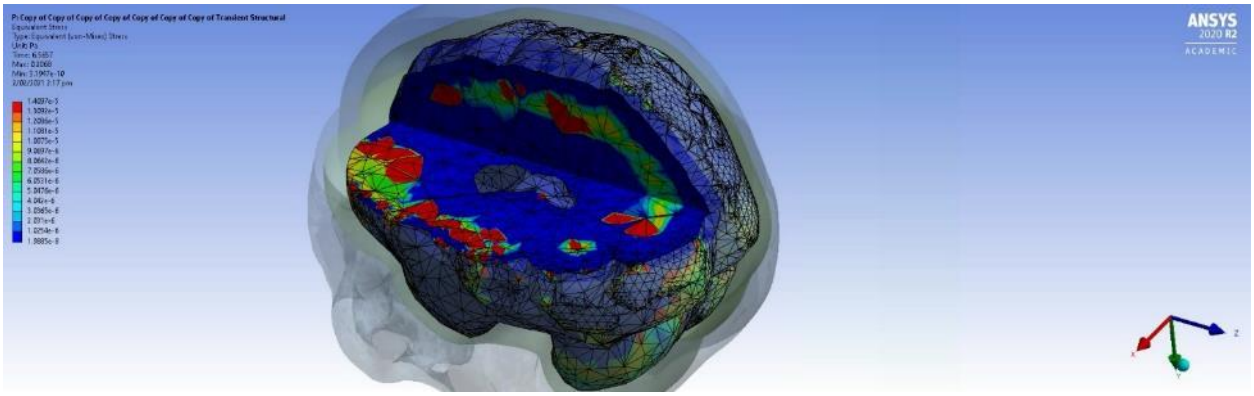
ANSYS
2020 R2
ACADEMIC

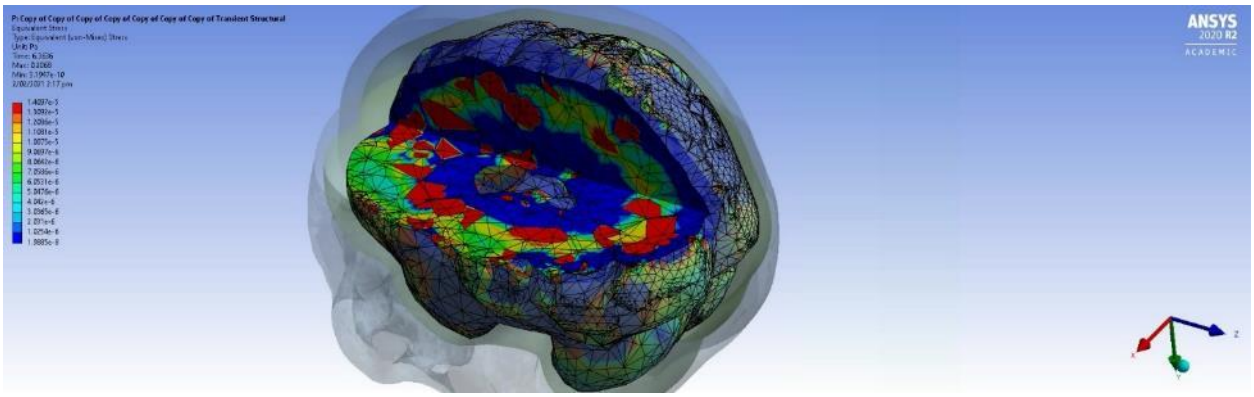
ANSYS
2020 R2
ACADEMIC

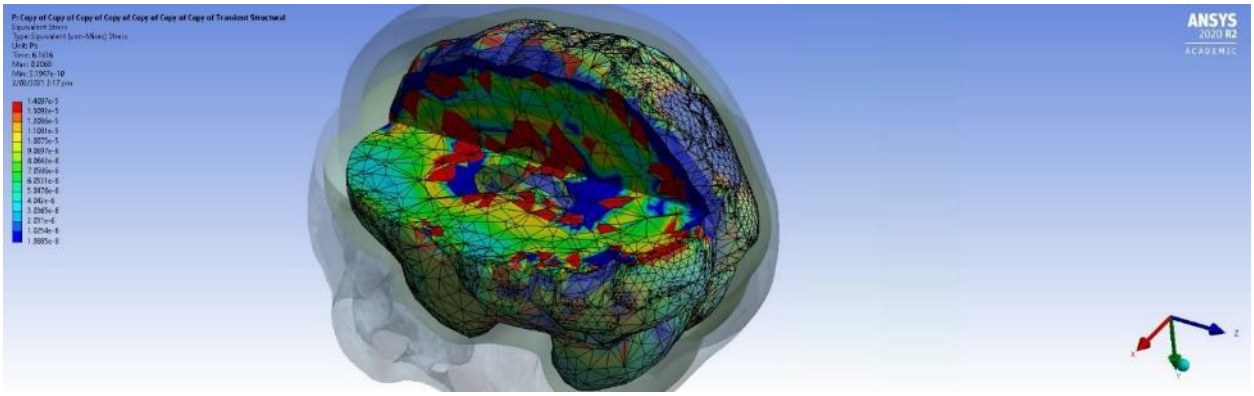
ANSYS
2020 R2
ACADEMIC

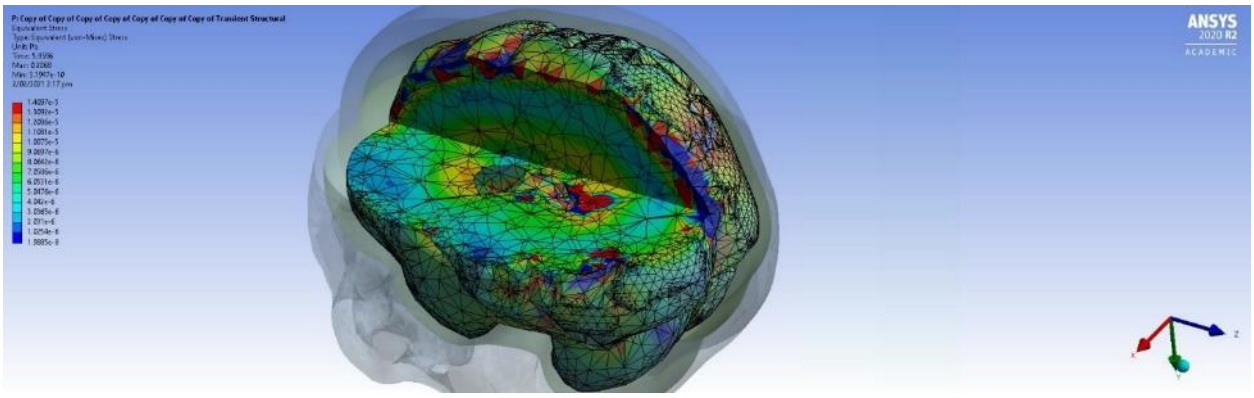
ANSYS
2020 R2
ACADEMIC

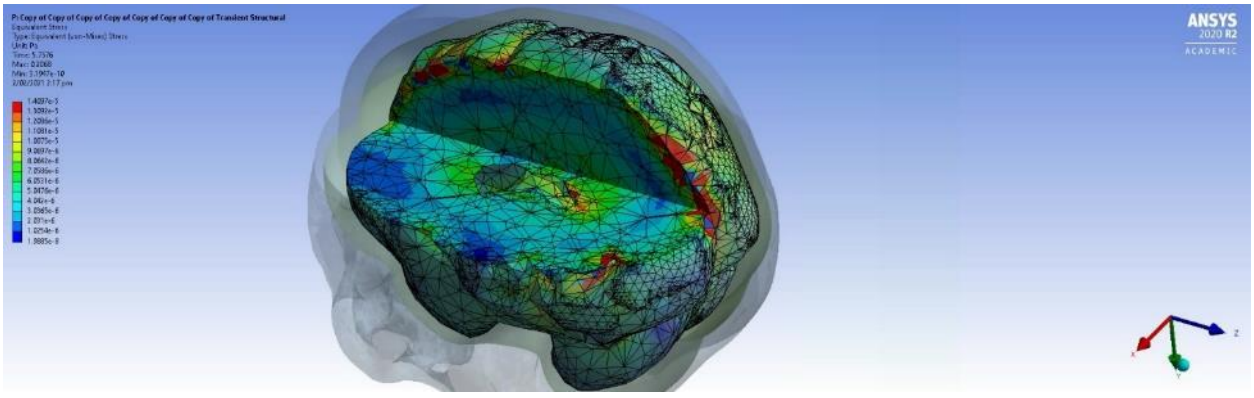
ANSYS
2020 R2
ACADEMIC

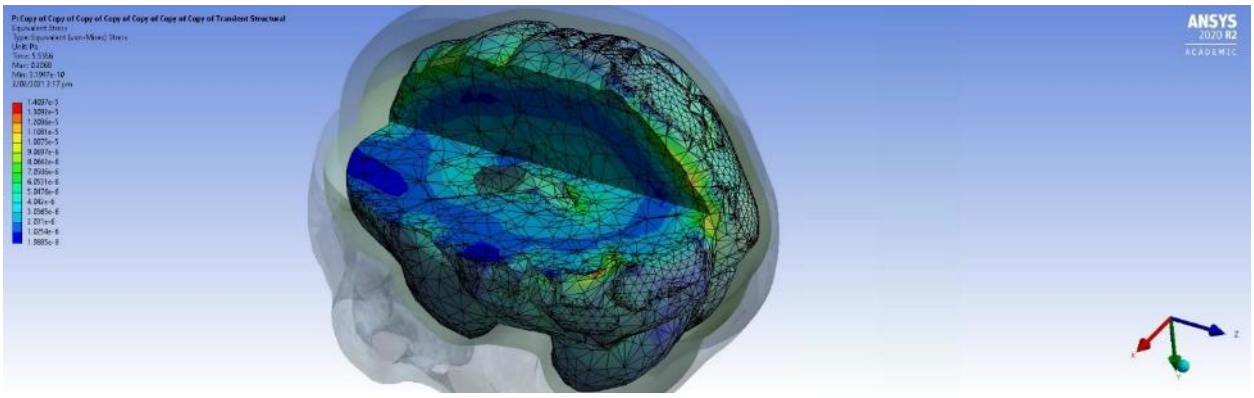
ANSYS
2020 R2
ACADEMIC

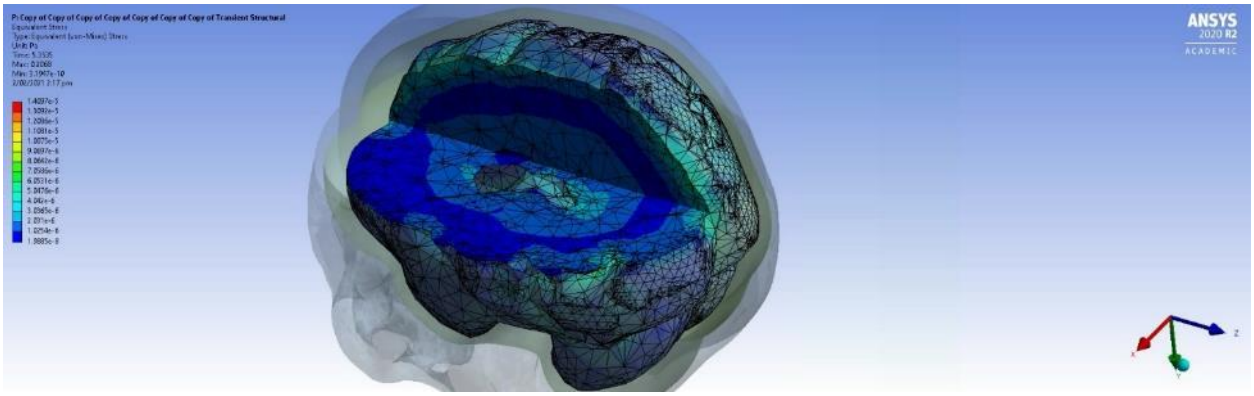
ANSYS
2020 R2
ACADEMIC

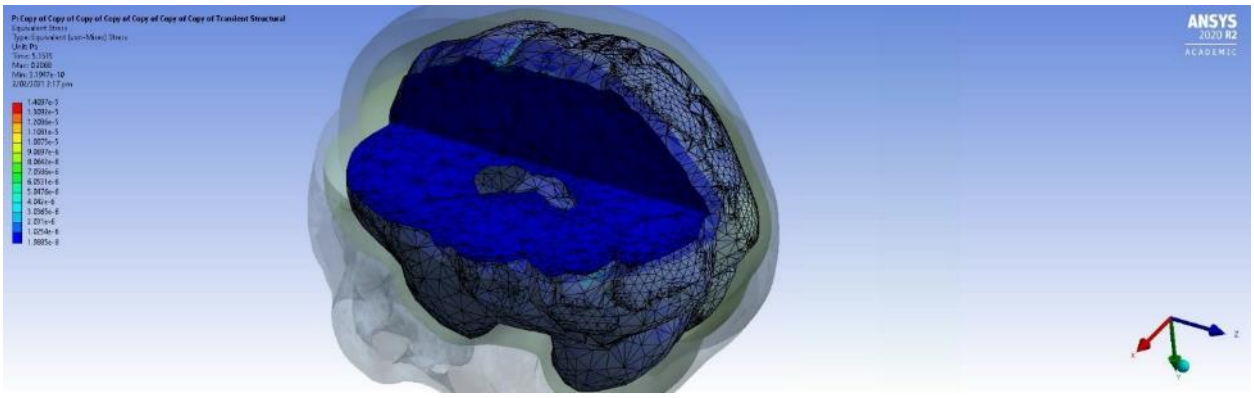
ANSYS
2020 R2
ACADEMIC

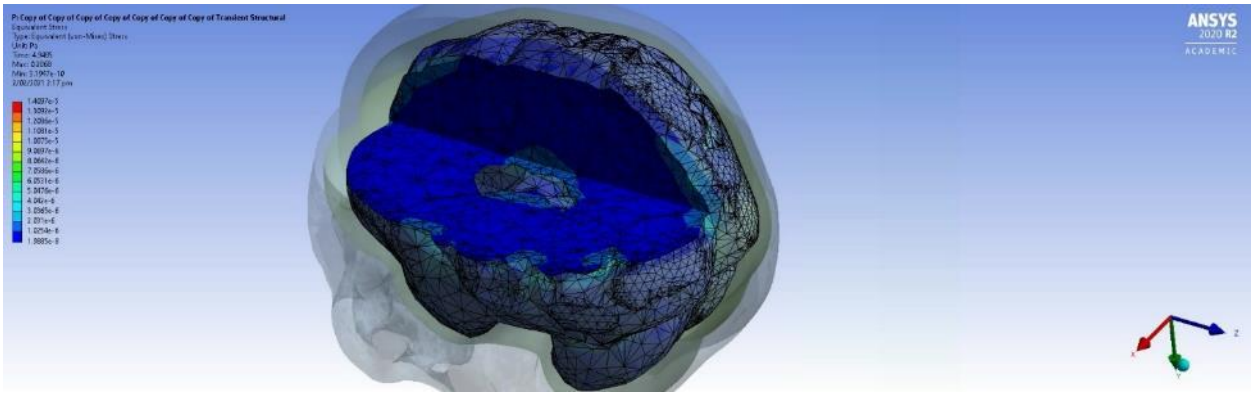
ANSYS
2020 R2
ACADEMIC

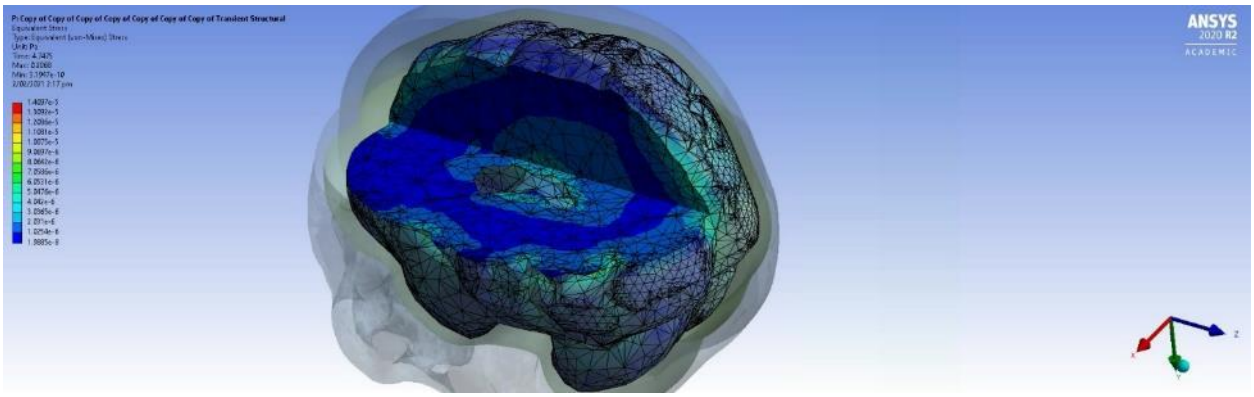
ANSYS
2020 R2
ACADEMIC

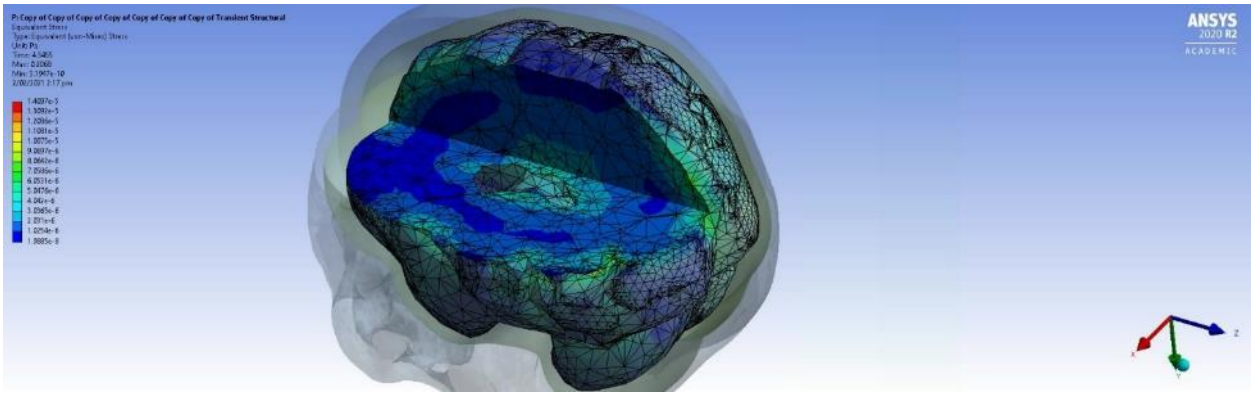
ANSYS
2020 R2
ACADEMIC

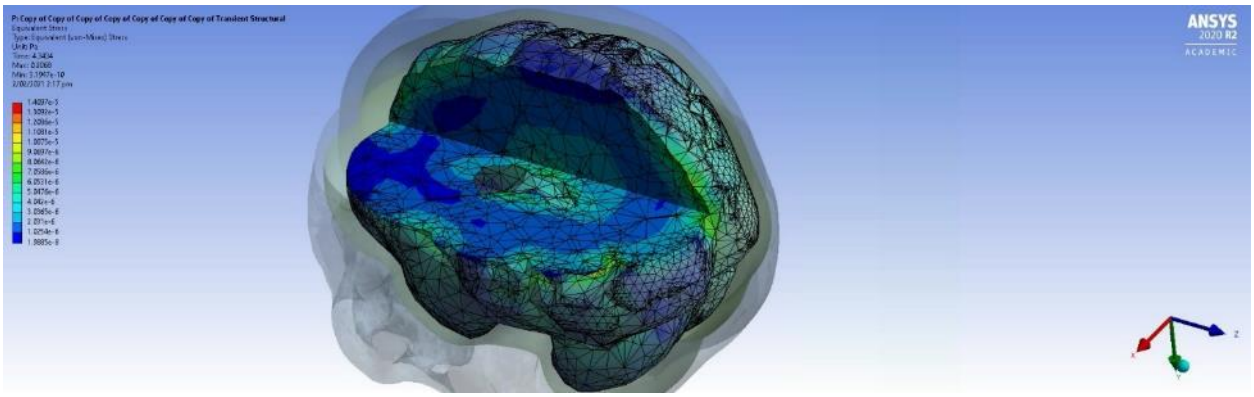
ANSYS
2020 R2
ACADEMIC

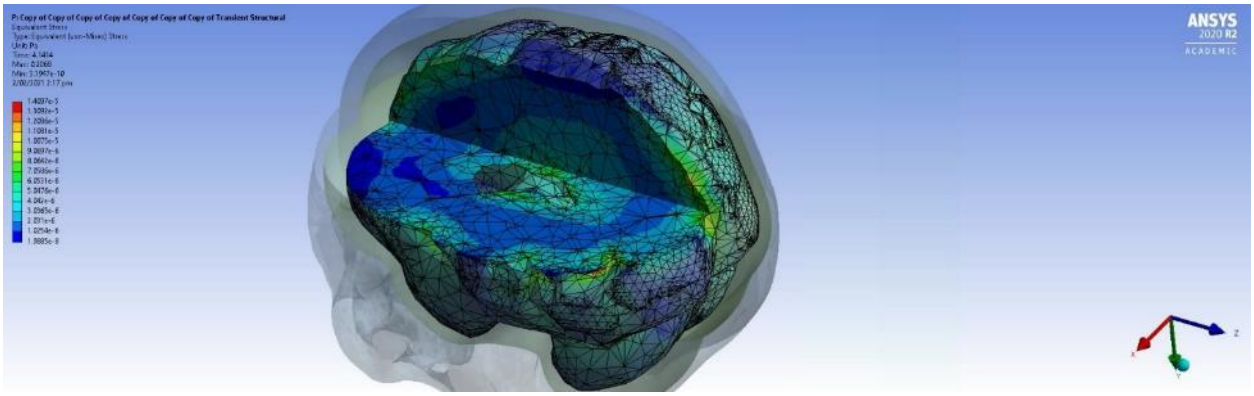
ANSYS
2020 R2
ACADEMIC

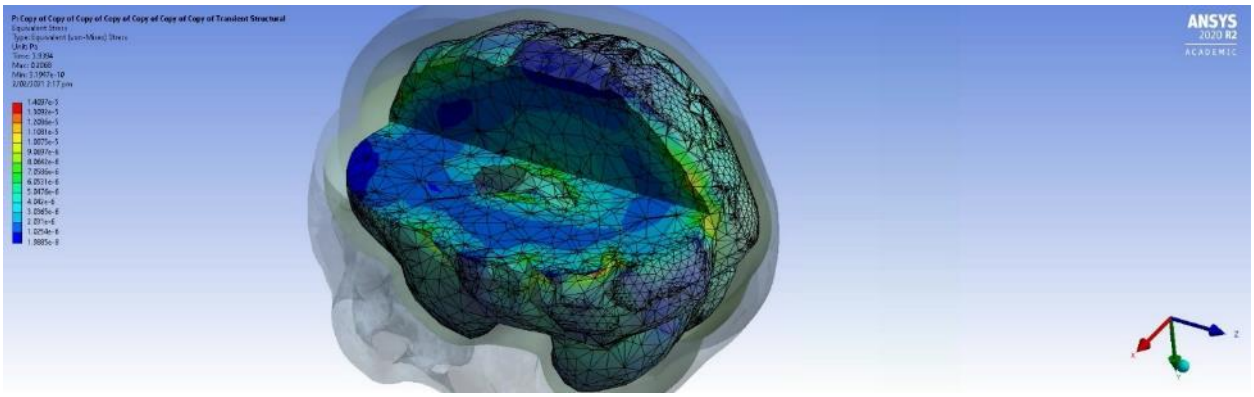
ANSYS
2020 R2
ACADEMIC

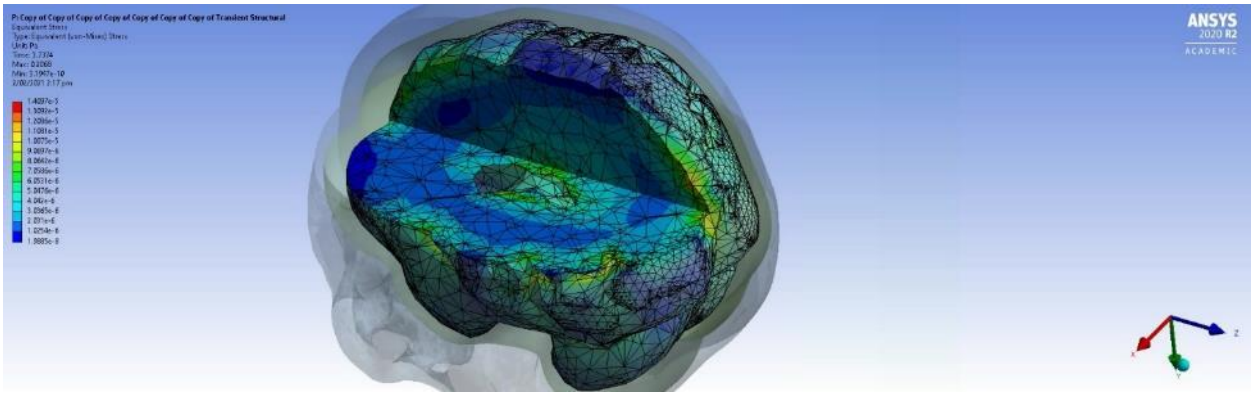
ANSYS
2020 R2
ACADEMIC

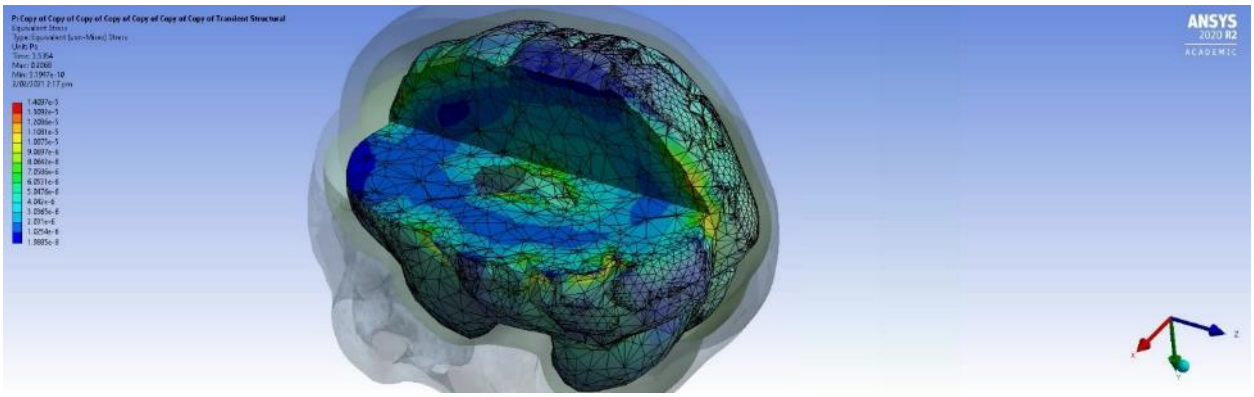
ANSYS
2020 R2
ACADEMIC

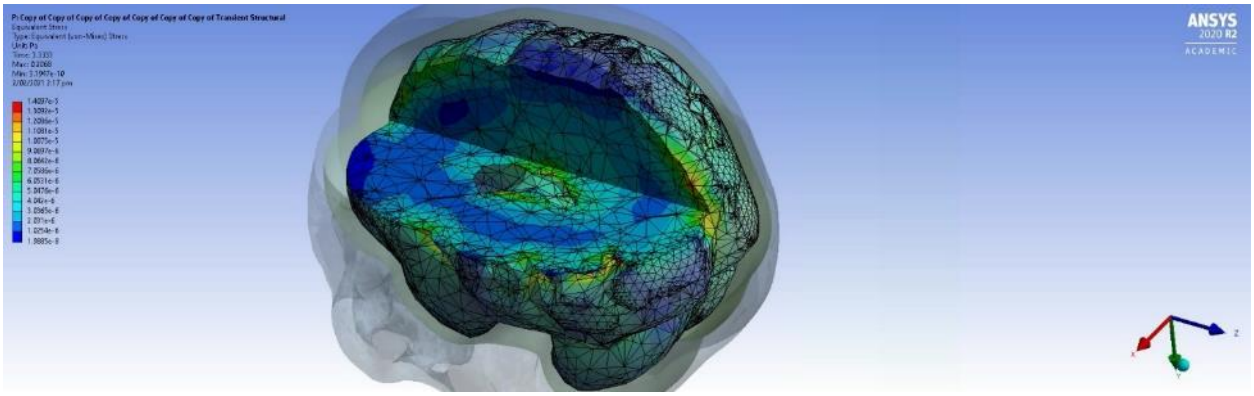
ANSYS
2020 R2
ACADEMIC

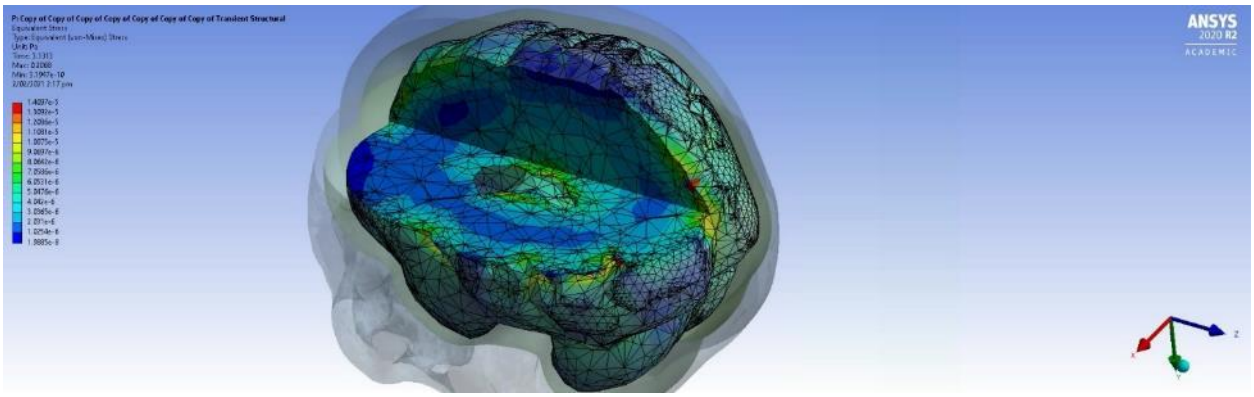
ANSYS
2020 R2
ACADEMIC

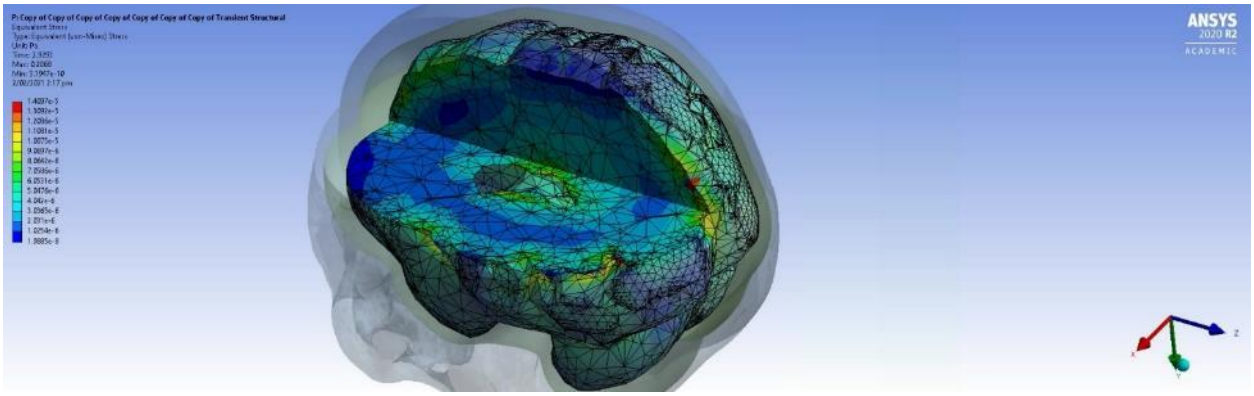
ANSYS
2020 R2
ACADEMIC

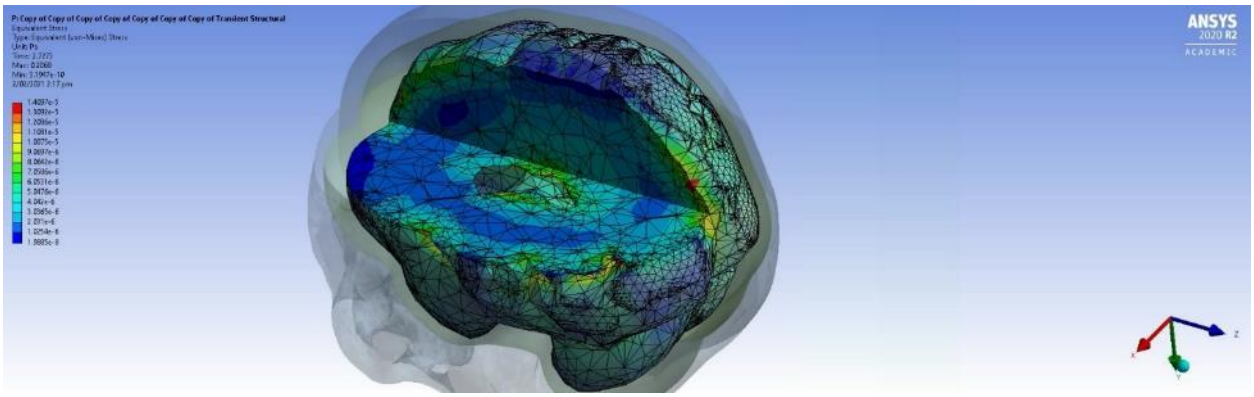
ANSYS
2020 R2
ACADEMIC

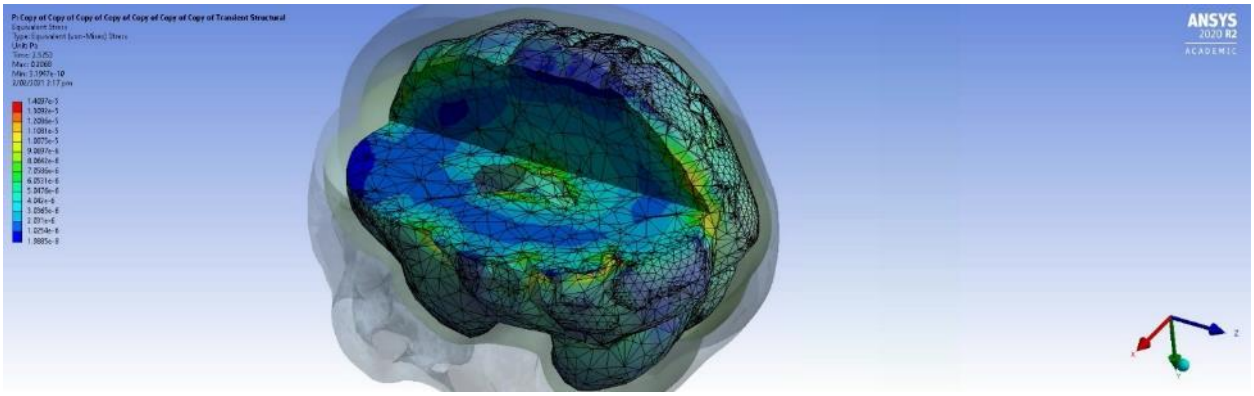
ANSYS
2020 R2
ACADEMIC

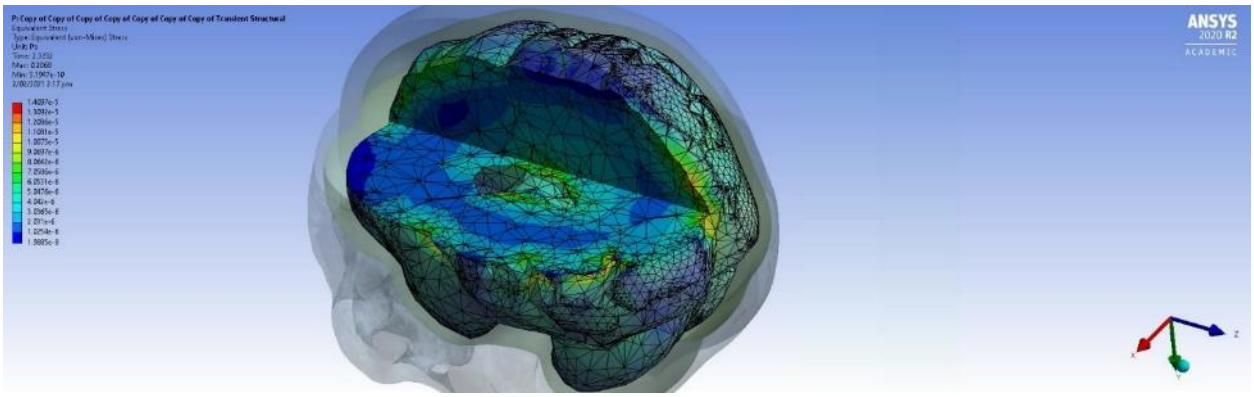
ANSYS
2020 R2
ACADEMIC

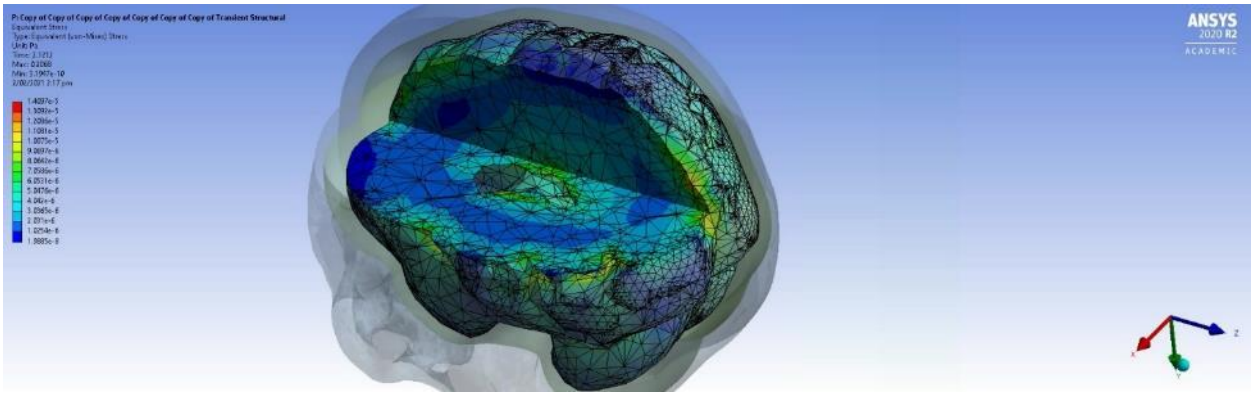
ANSYS
2020 R2
ACADEMIC

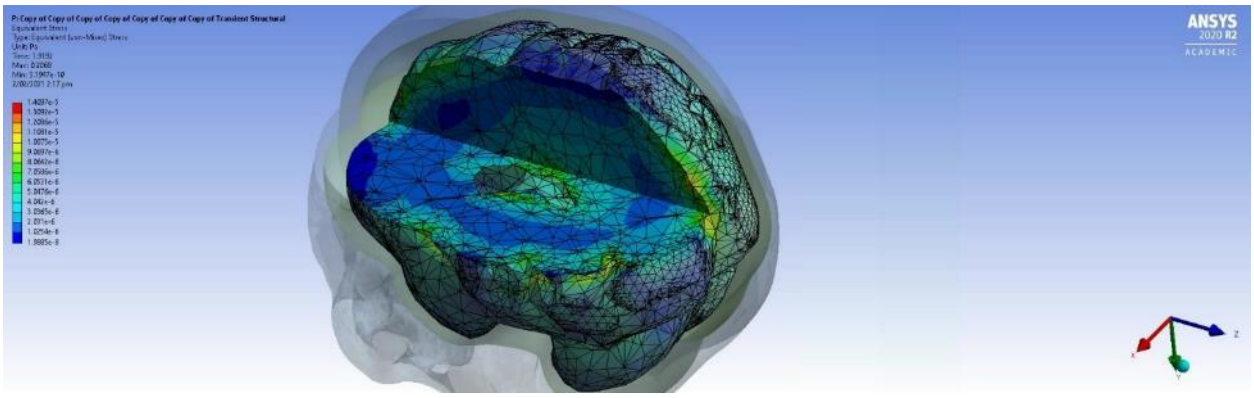
ANSYS
2020 R2
ACADEMIC

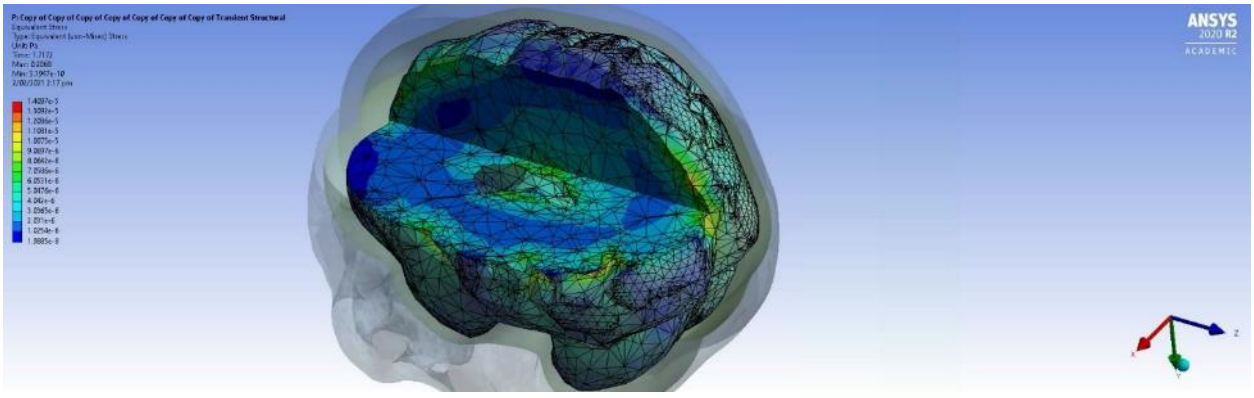
ANSYS
2020 R2
ACADEMIC

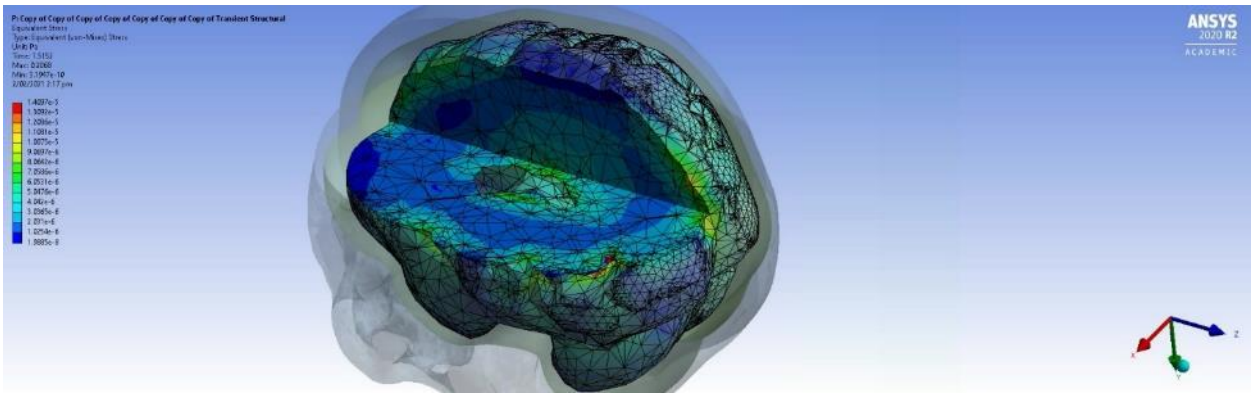
ANSYS
2020 R2
ACADEMIC

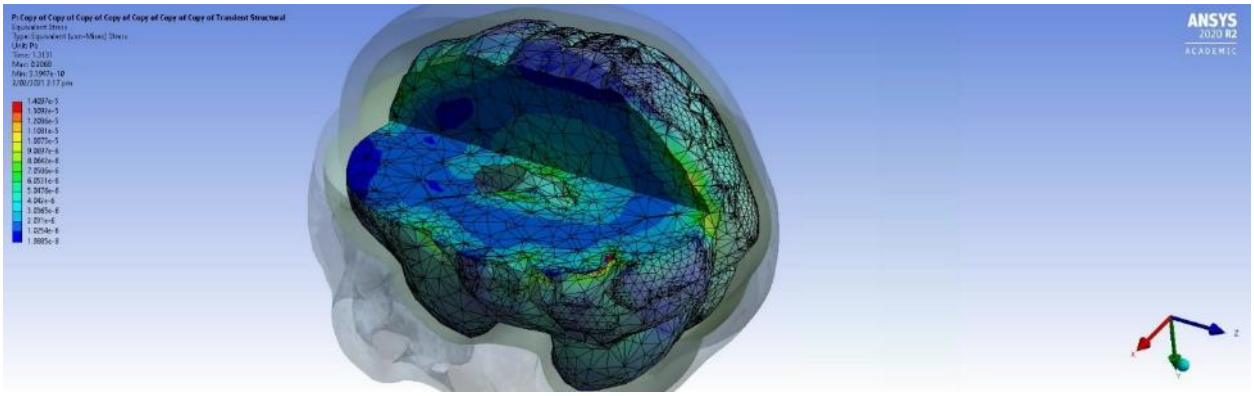
ANSYS
2020 R2
ACADEMIC

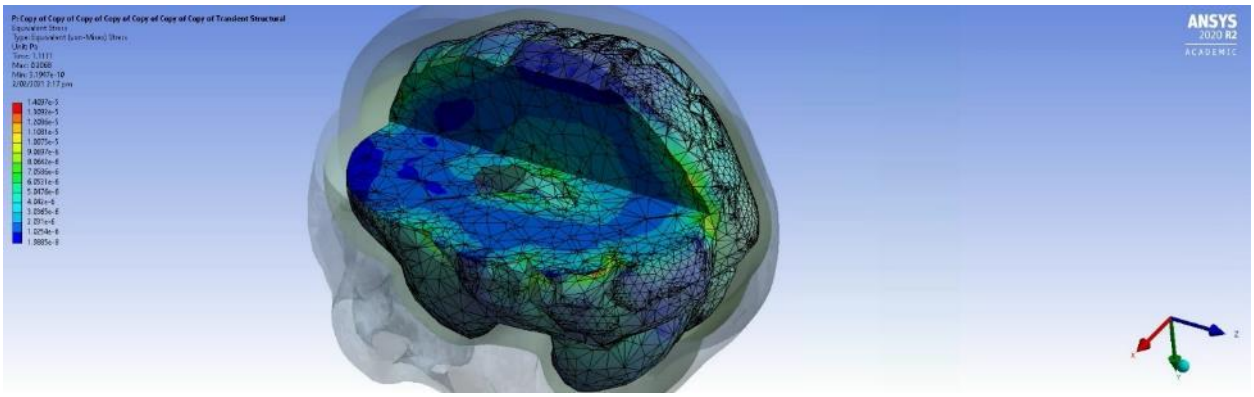
ANSYS
2020 R2
ACADEMIC

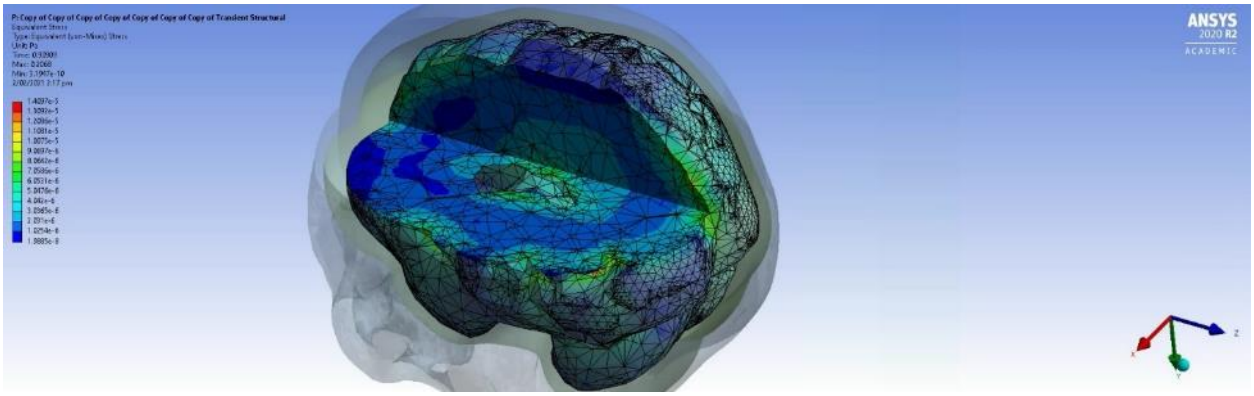
ANSYS
2020 R2
ACADEMIC

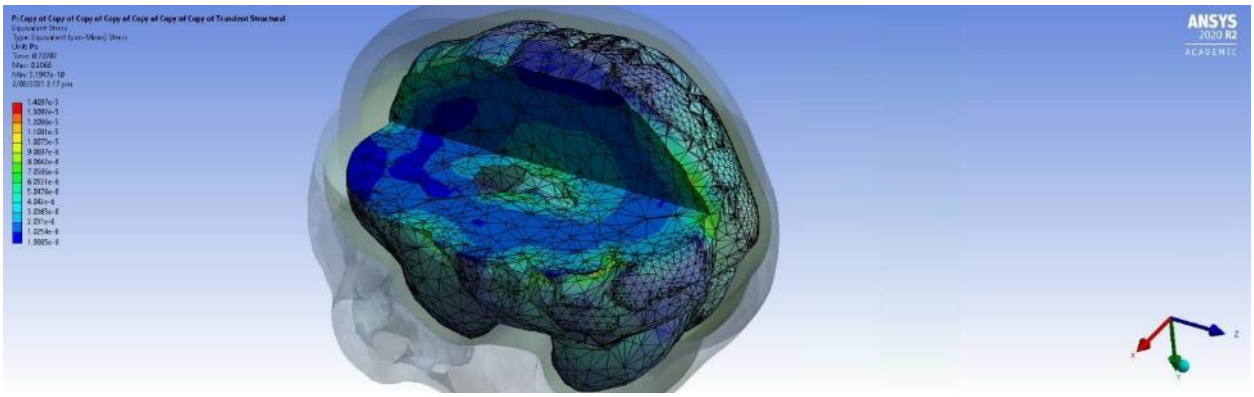
ANSYS
2020 R2
ACADEMIC

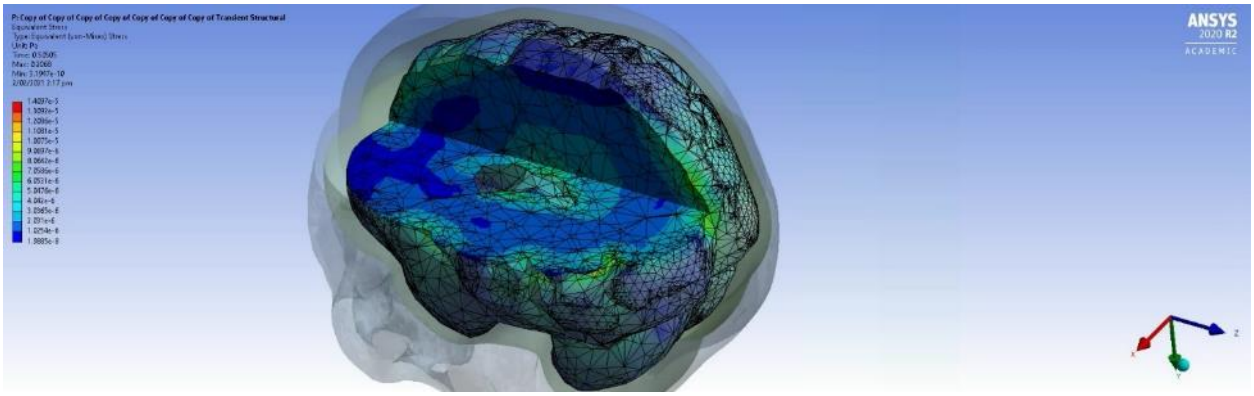
ANSYS
2020 R2
ACADEMIC

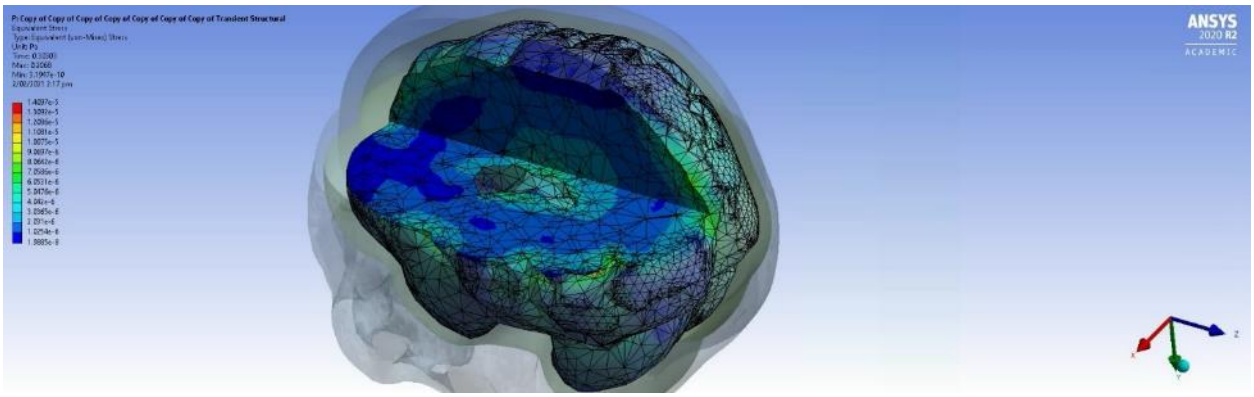
ANSYS
2020 R2
ACADEMIC

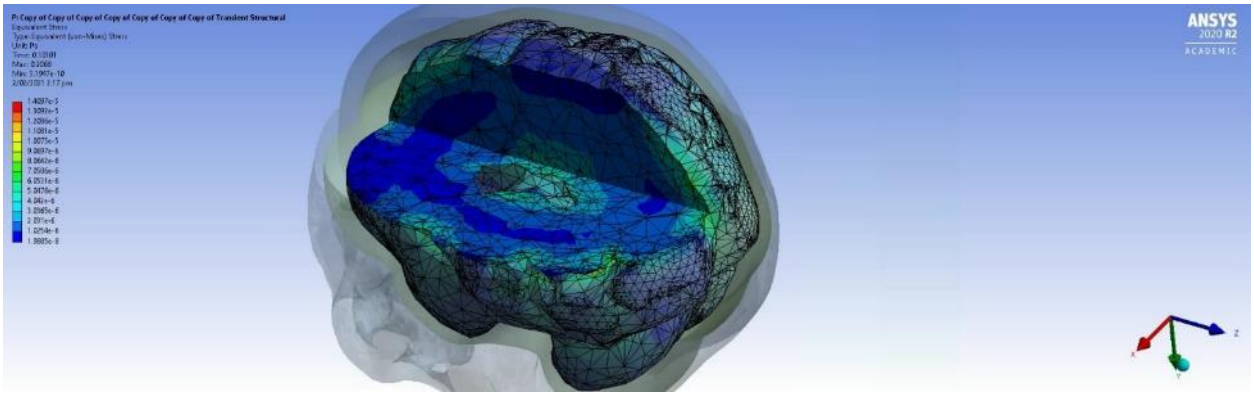
ANSYS
2020 R2
ACADEMIC

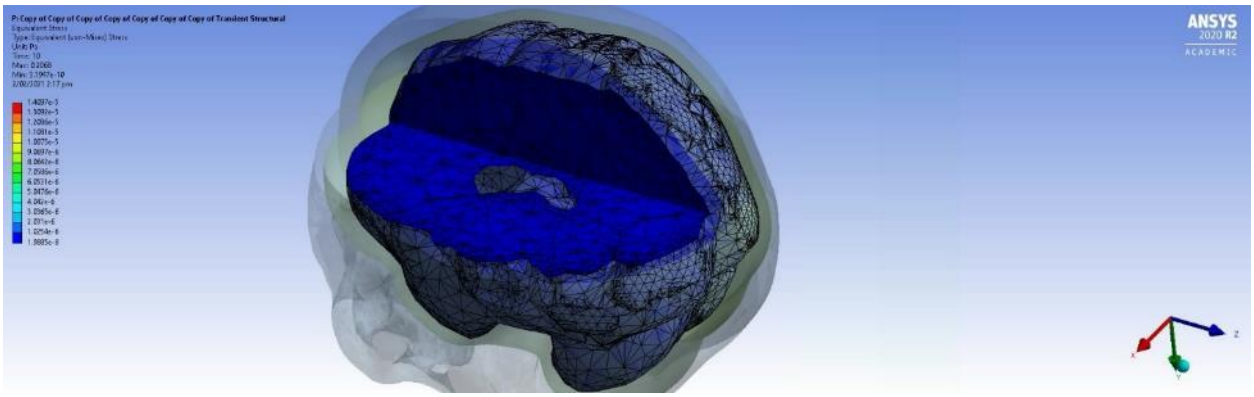
ANSYS
2020 R2
ACADEMIC

Impact Zone 7

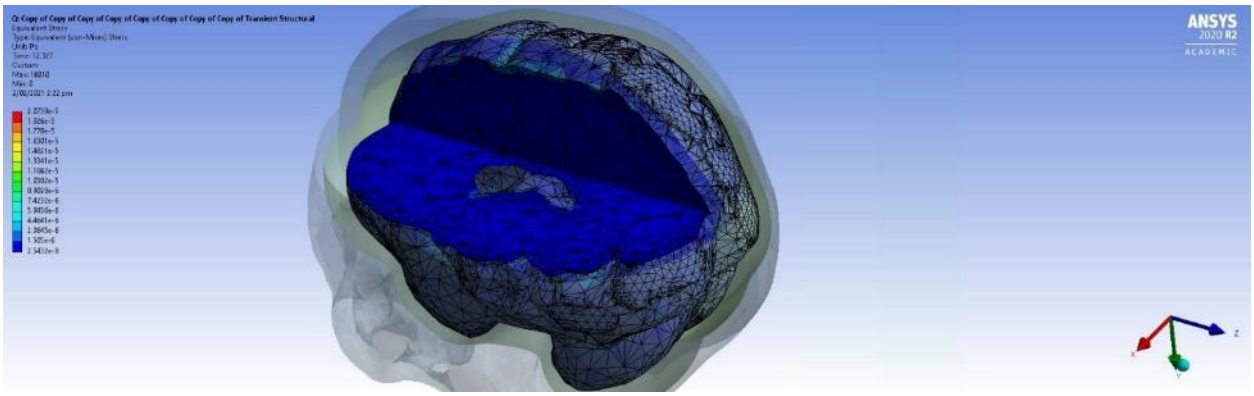

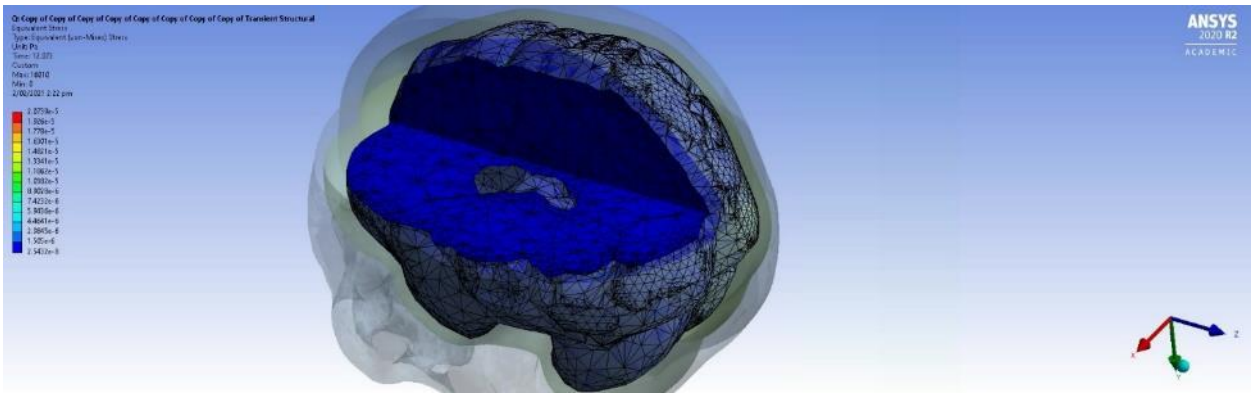

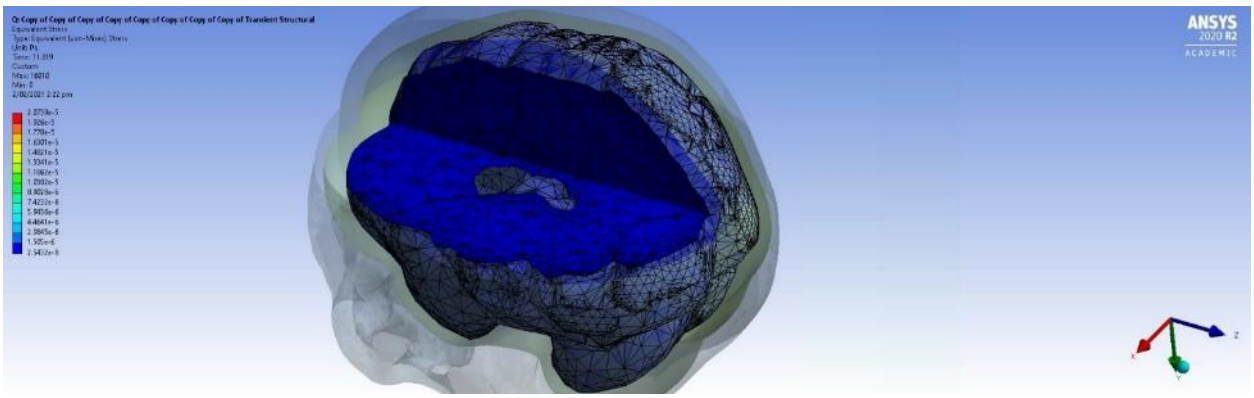

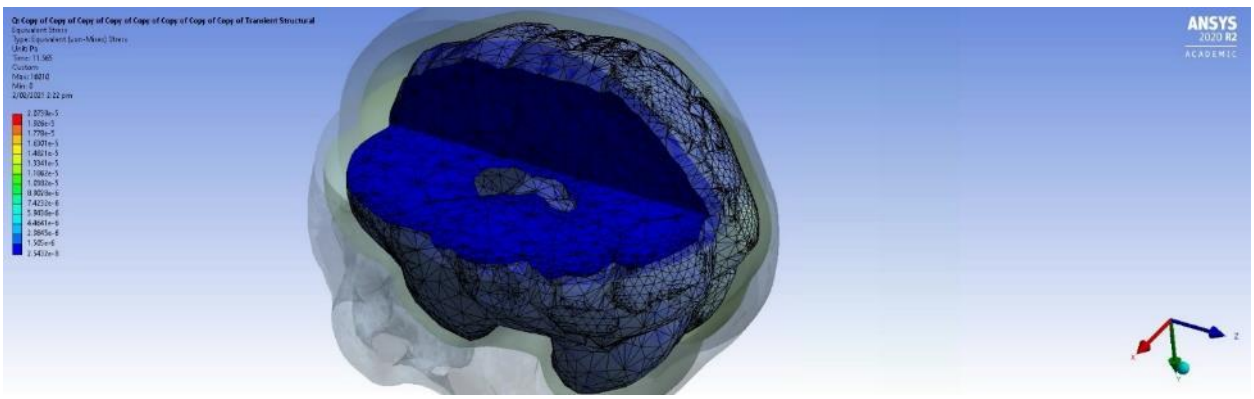

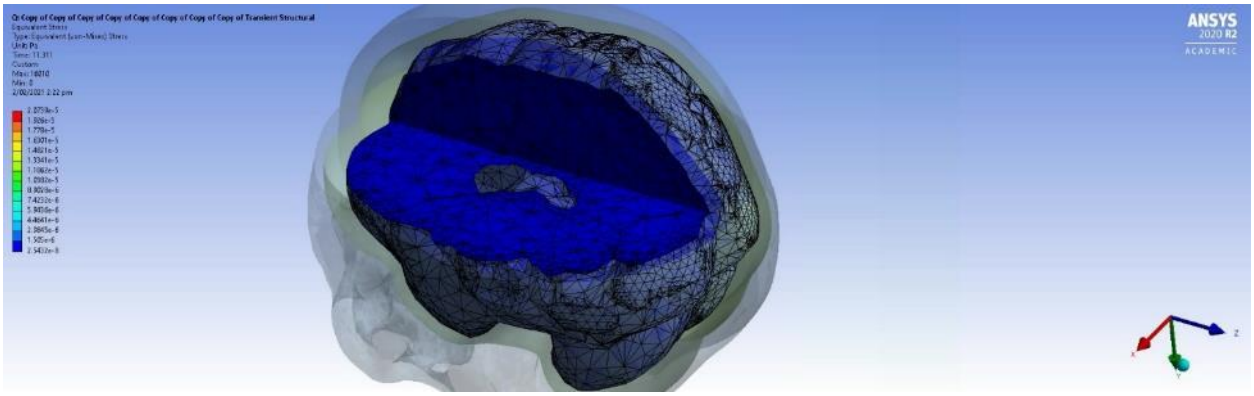
ANSYS
2020 R2
ACADEMIC

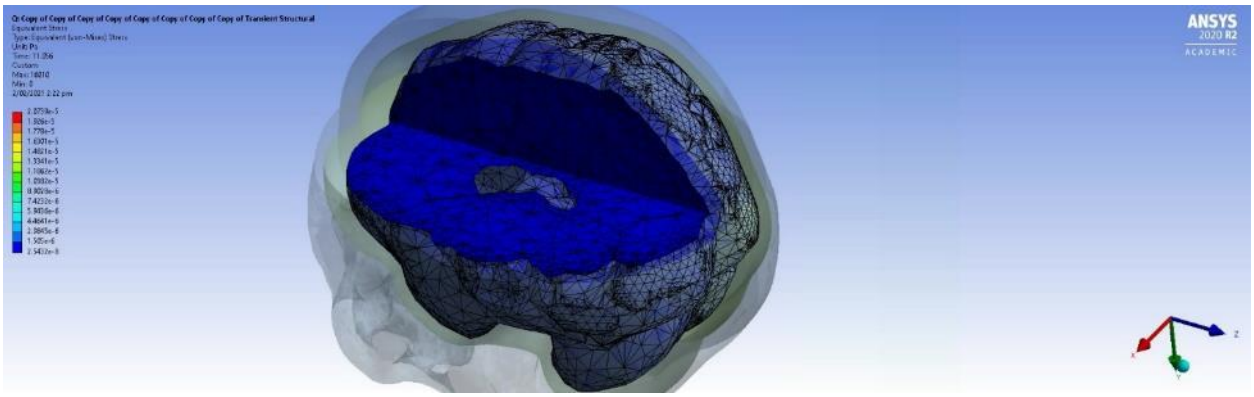
ANSYS
2020 R2
ACADEMIC

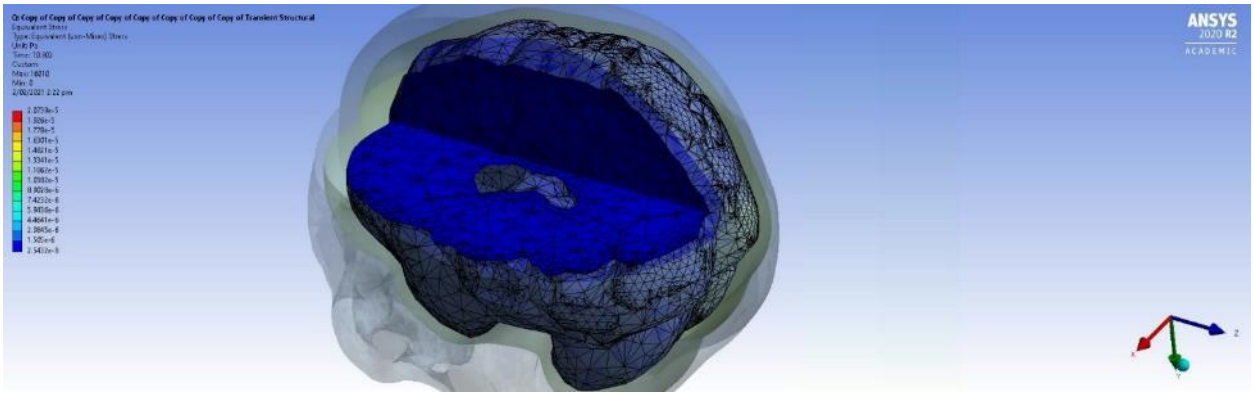
ANSYS
2020 R2
ACADEMIC

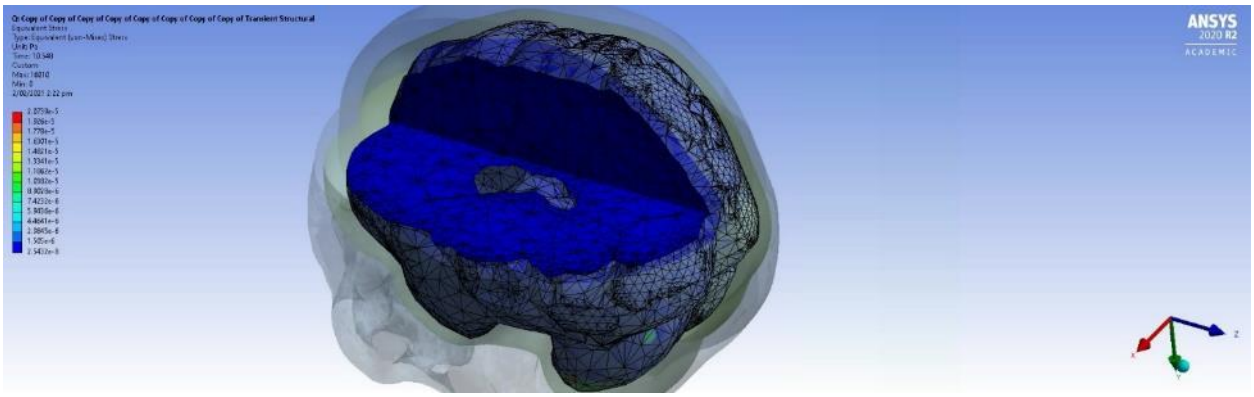
ANSYS
2020 R2
ACADEMIC

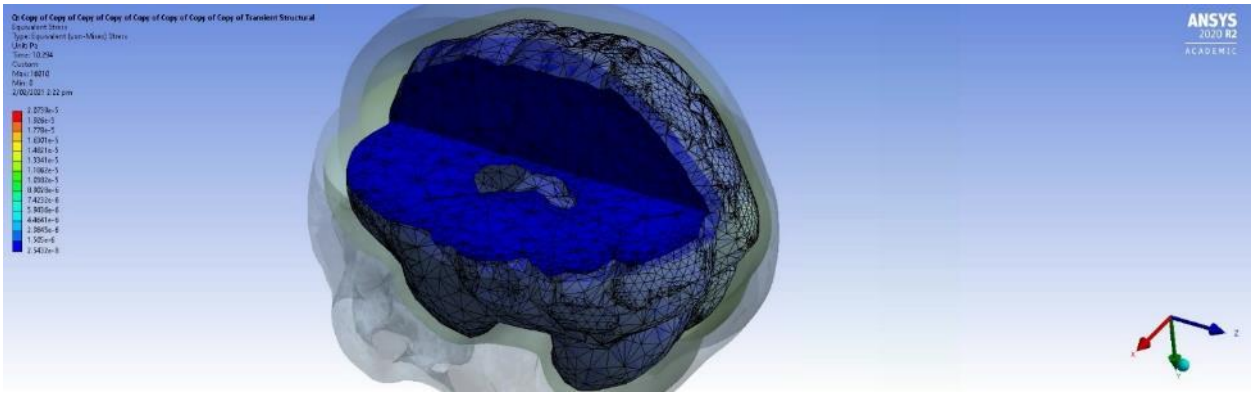
ANSYS
2020 R2
ACADEMIC

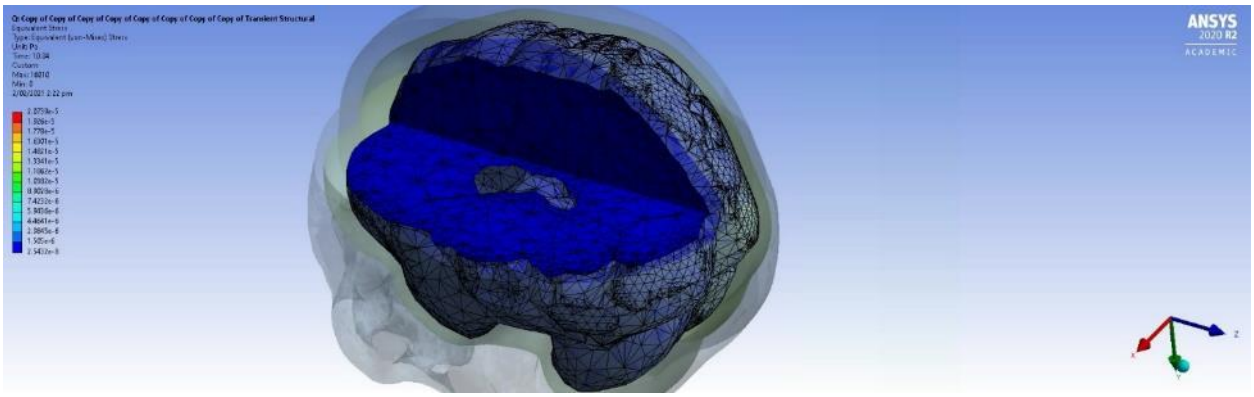
ANSYS
2020 R2
ACADEMIC

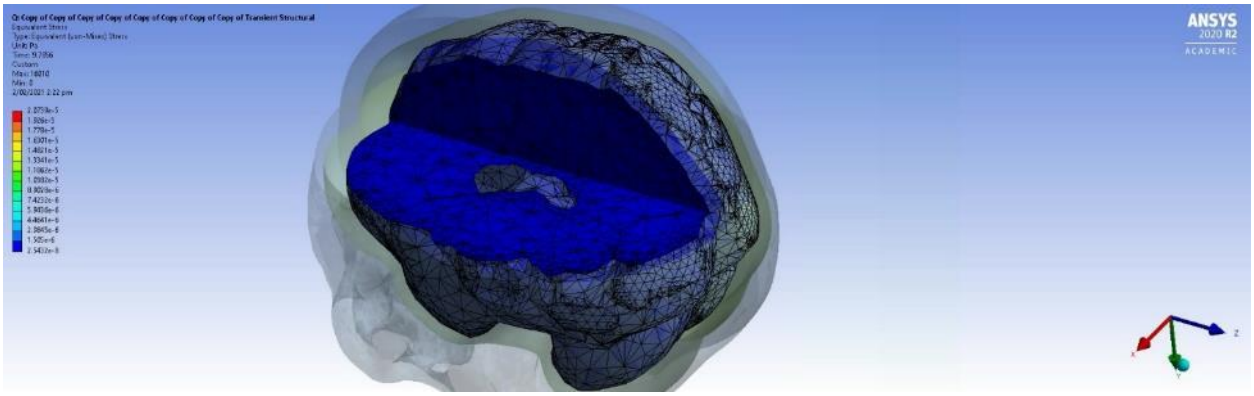
ANSYS
2020 R2
ACADEMIC

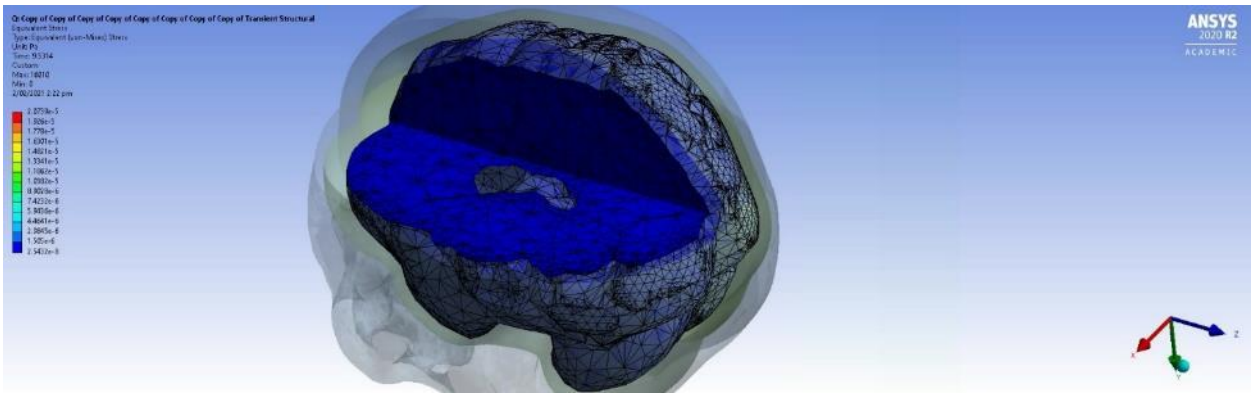
ANSYS
2020 R2
ACADEMIC

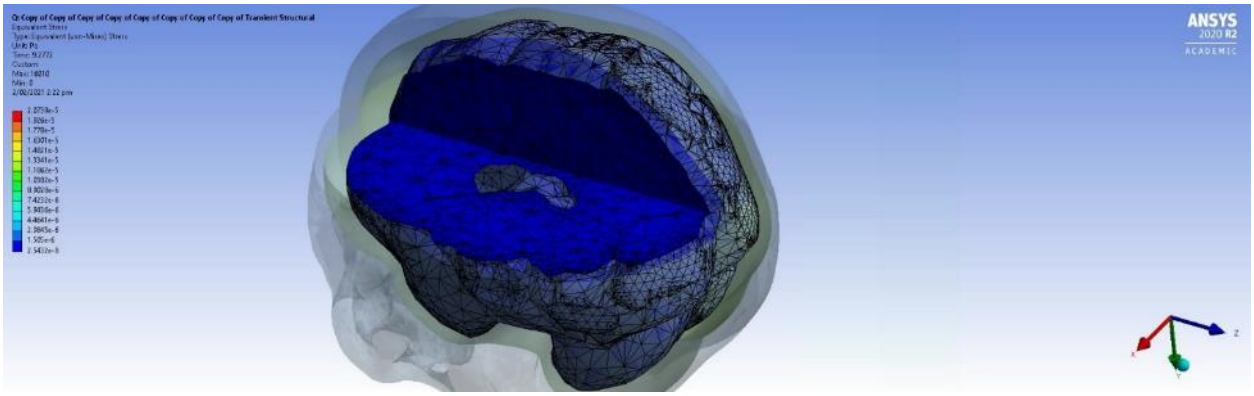
ANSYS
2020 R2
ACADEMIC

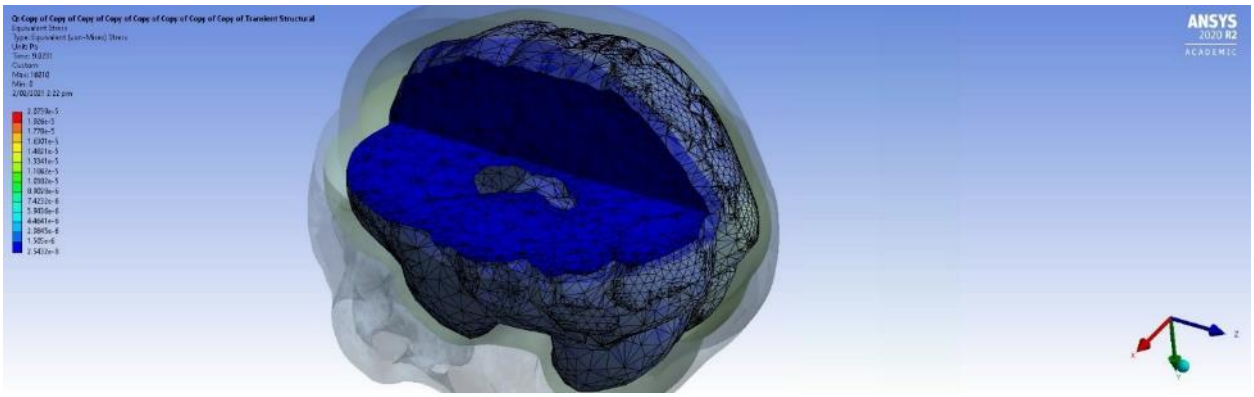
ANSYS
2020 R2
ACADEMIC

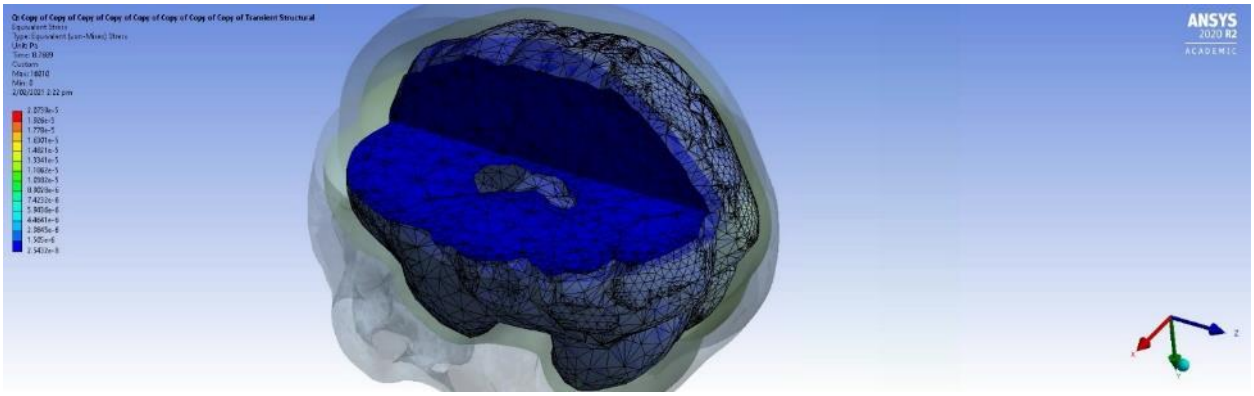
ANSYS
2020 R2
ACADEMIC

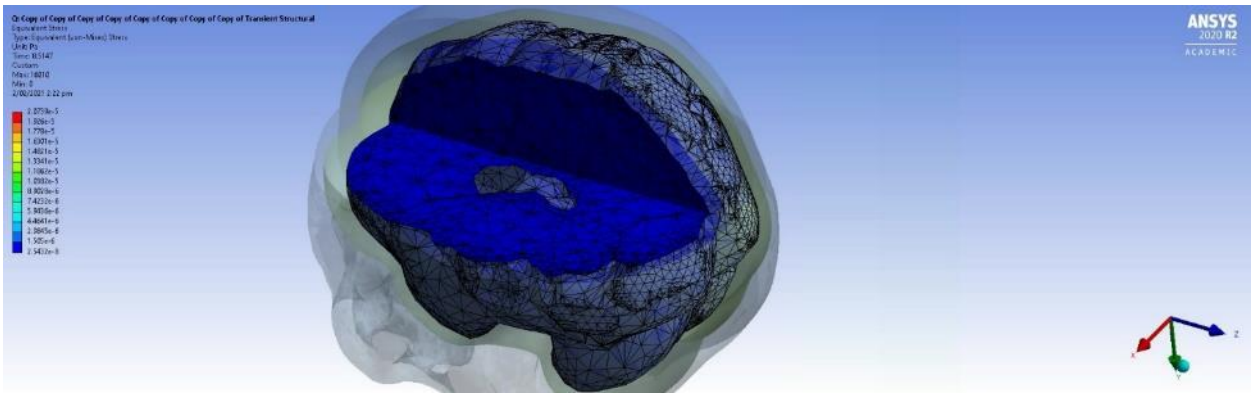
ANSYS
2020 R2
ACADEMIC

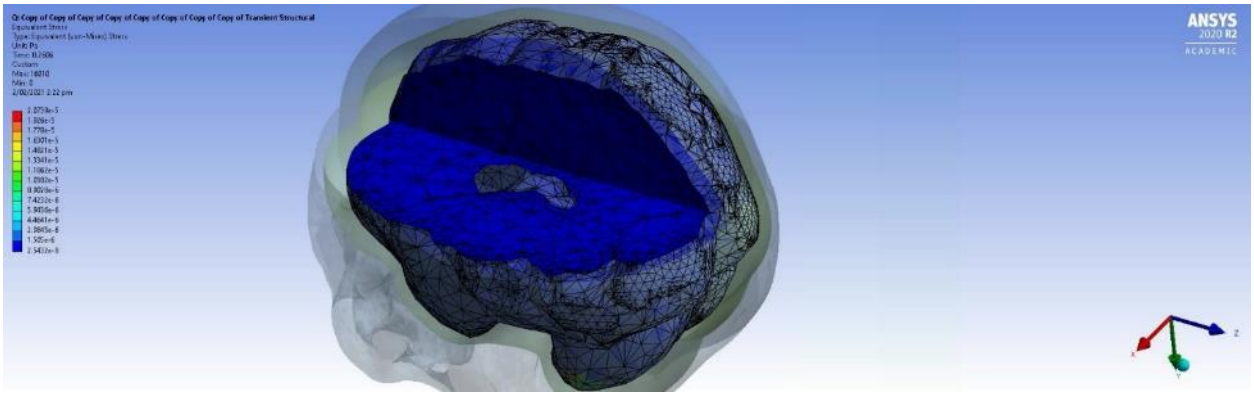
ANSYS
2020 R2
ACADEMIC

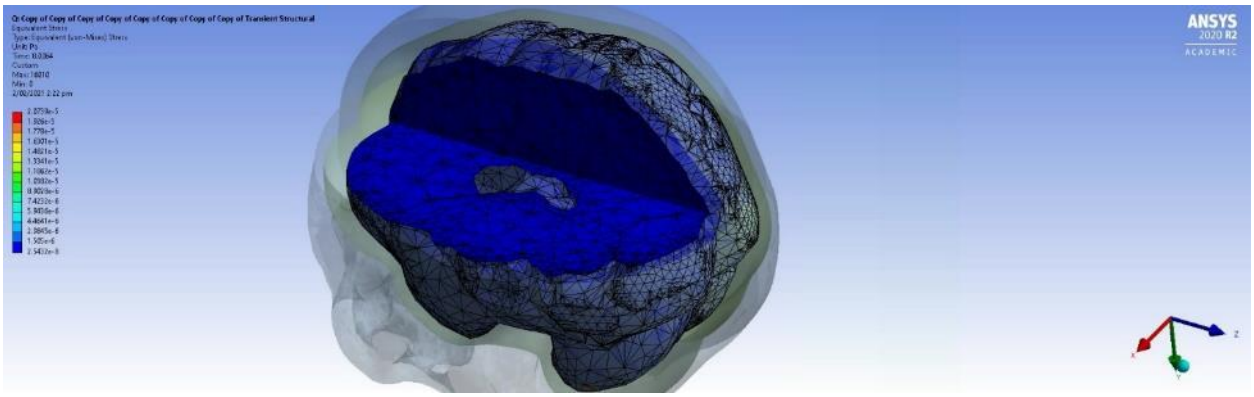
ANSYS
2020 R2
ACADEMIC

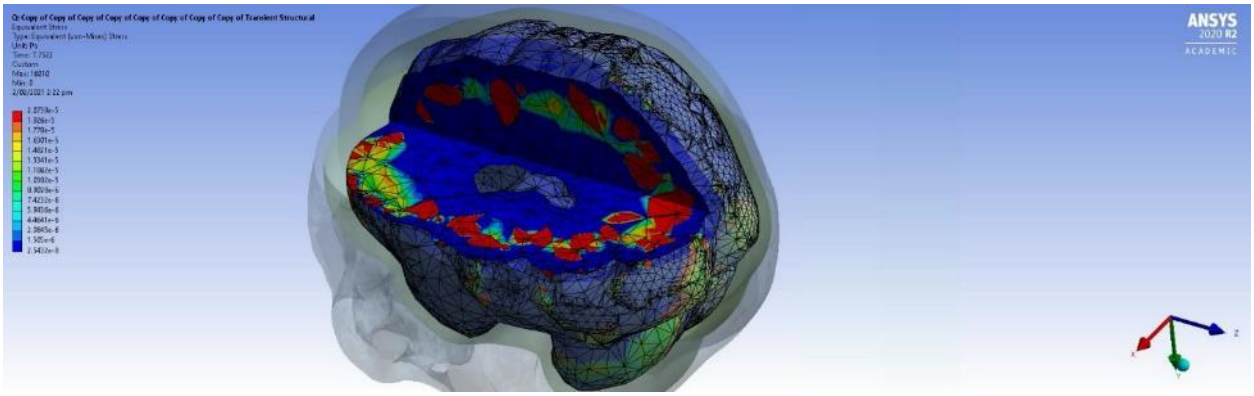
ANSYS
2020 R2
ACADEMIC

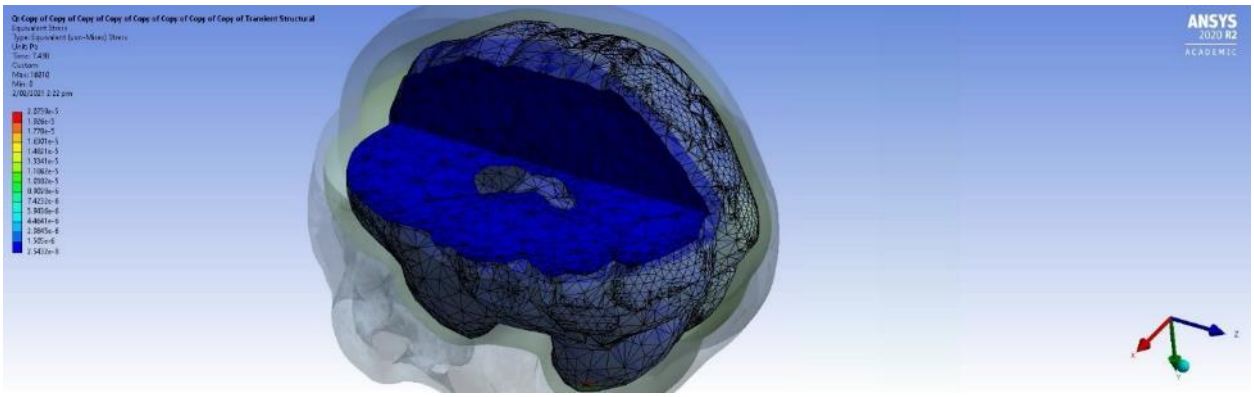
ANSYS
2020 R2
ACADEMIC

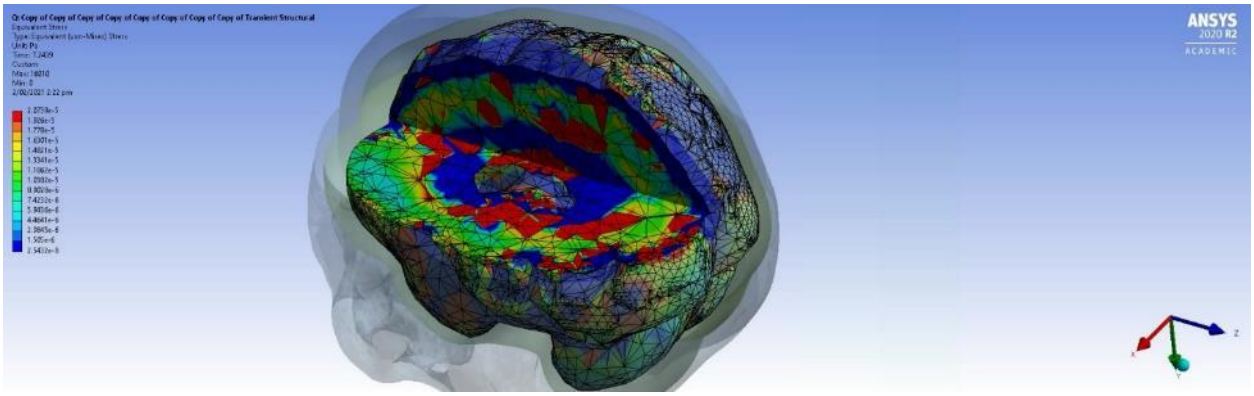
ANSYS
2020 R2
ACADEMIC

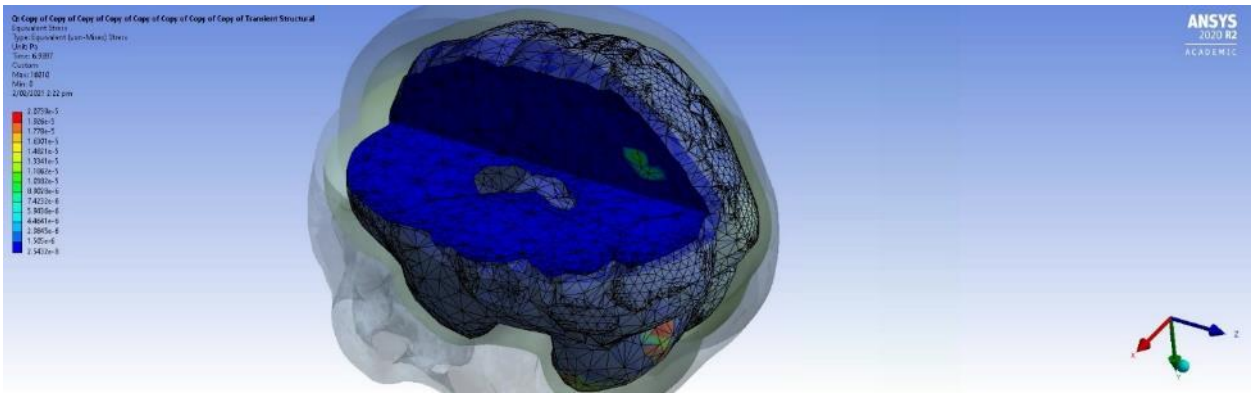
ANSYS
2020 R2
ACADEMIC

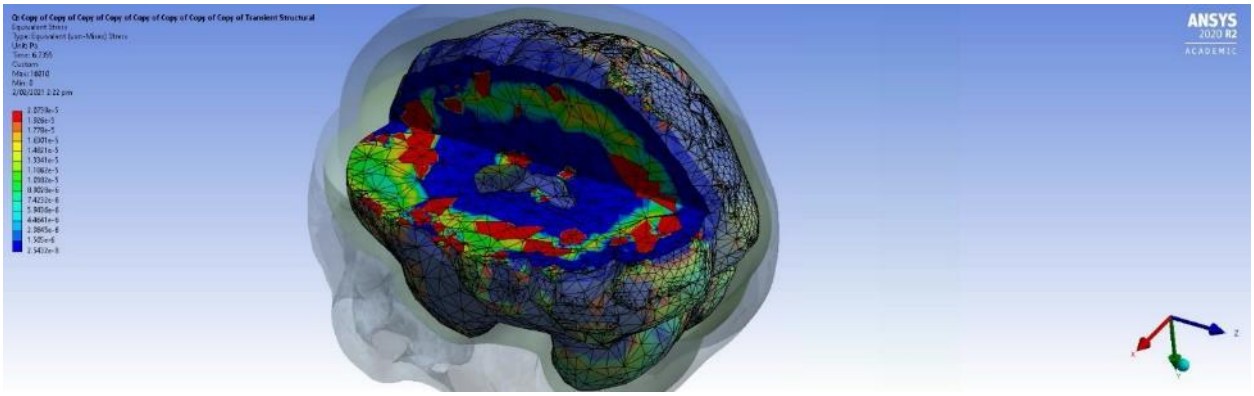
ANSYS
2020 R2
ACADEMIC

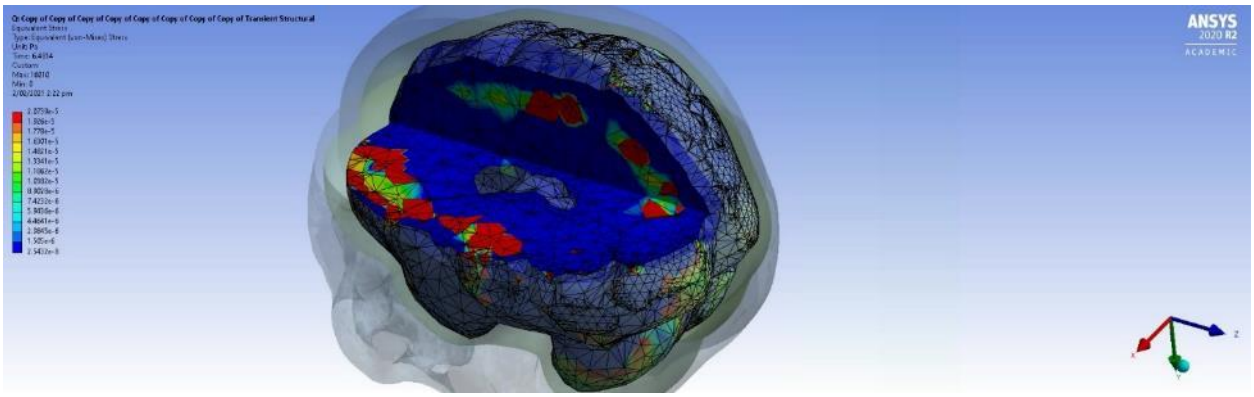
ANSYS
2020 R2
ACADEMIC

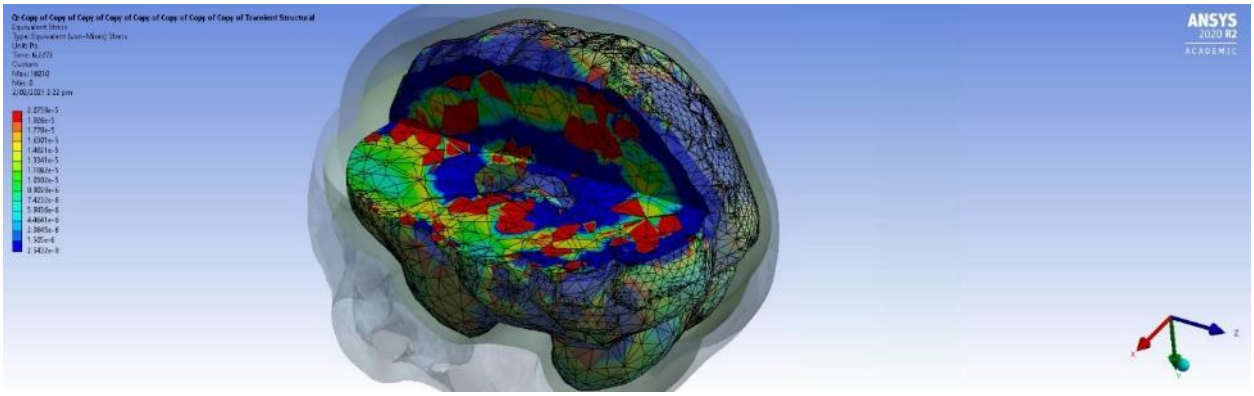
ANSYS
2020 R2
ACADEMIC

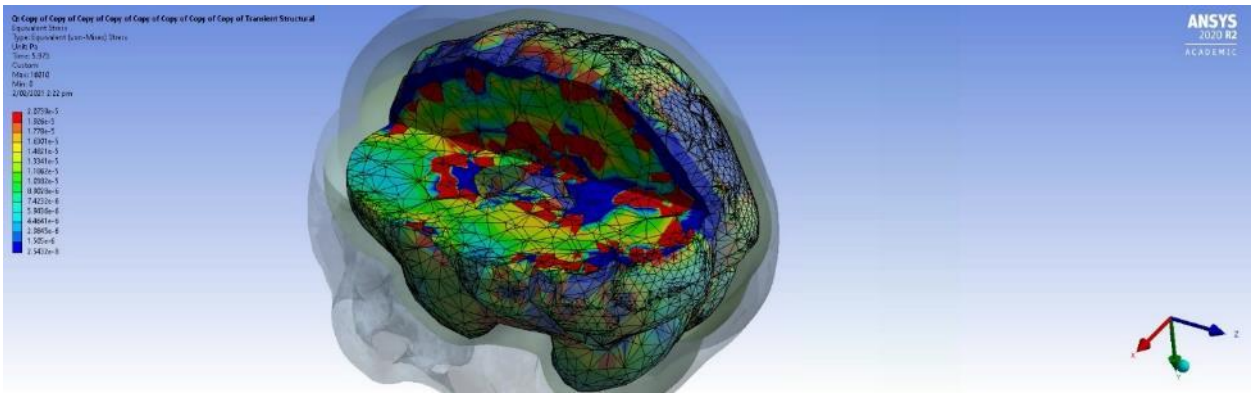
ANSYS
2020 R2
ACADEMIC

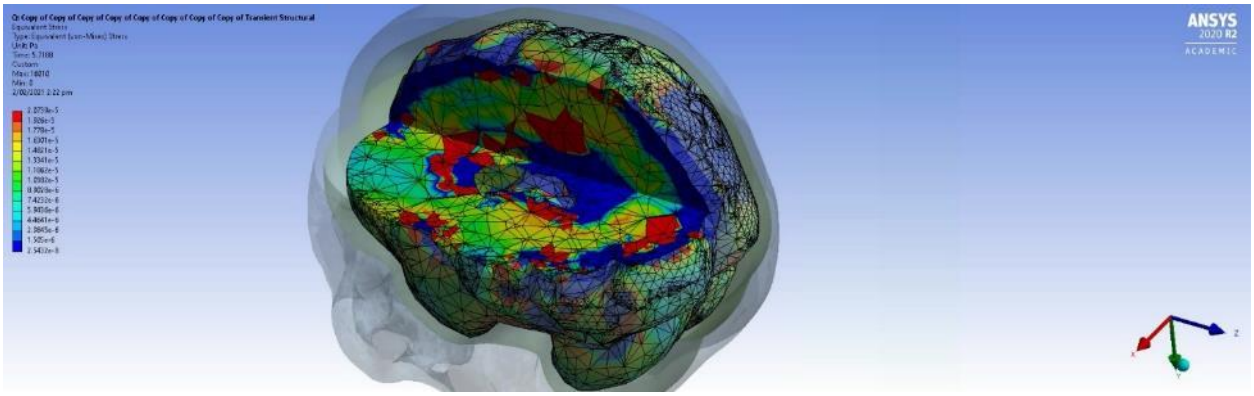
ANSYS
2020 R2
ACADEMIC

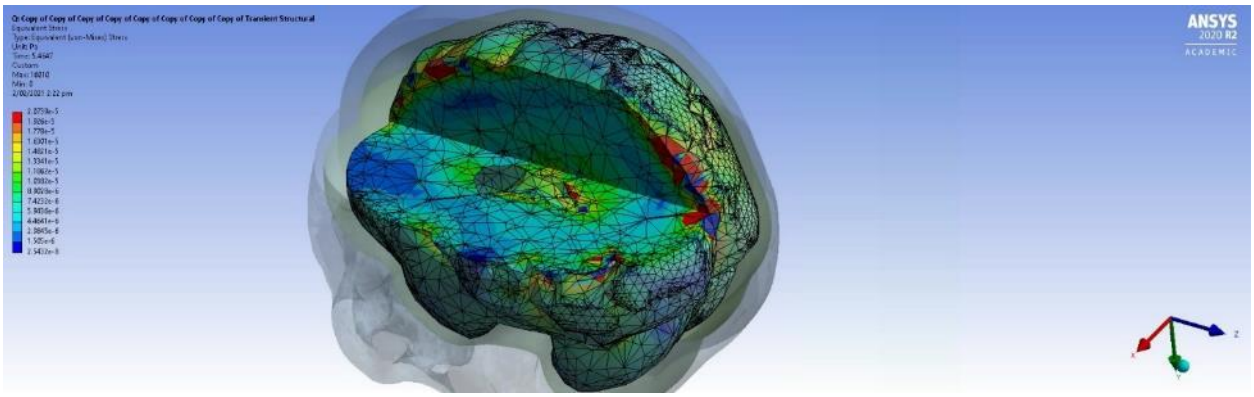
ANSYS
2020 R2
ACADEMIC

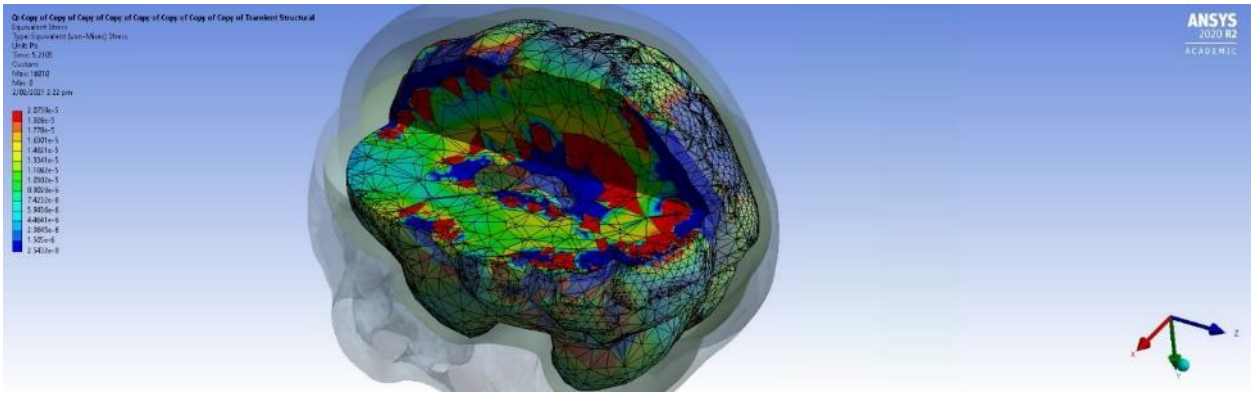
ANSYS
2020 R2
ACADEMIC

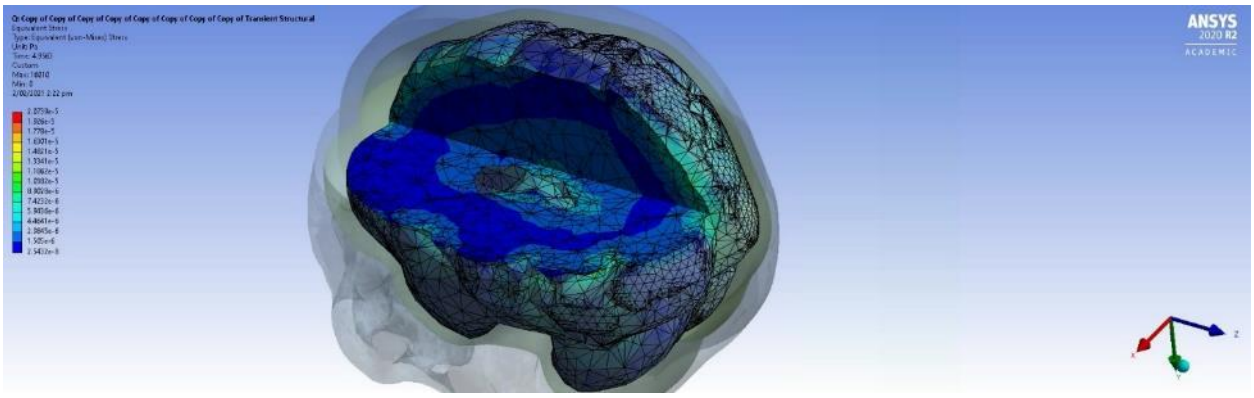
ANSYS
2020 R2
ACADEMIC

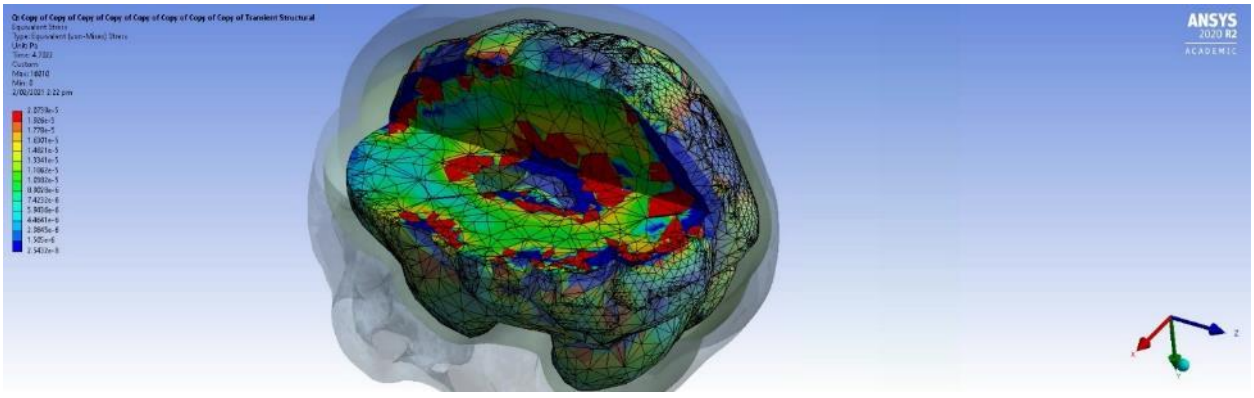
ANSYS
2020 R2
ACADEMIC

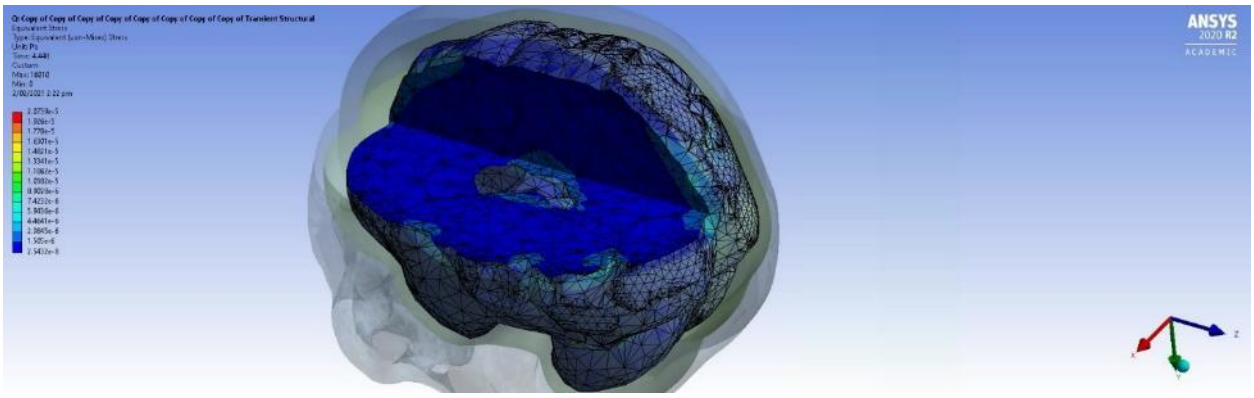
ANSYS
2020 R2
ACADEMIC

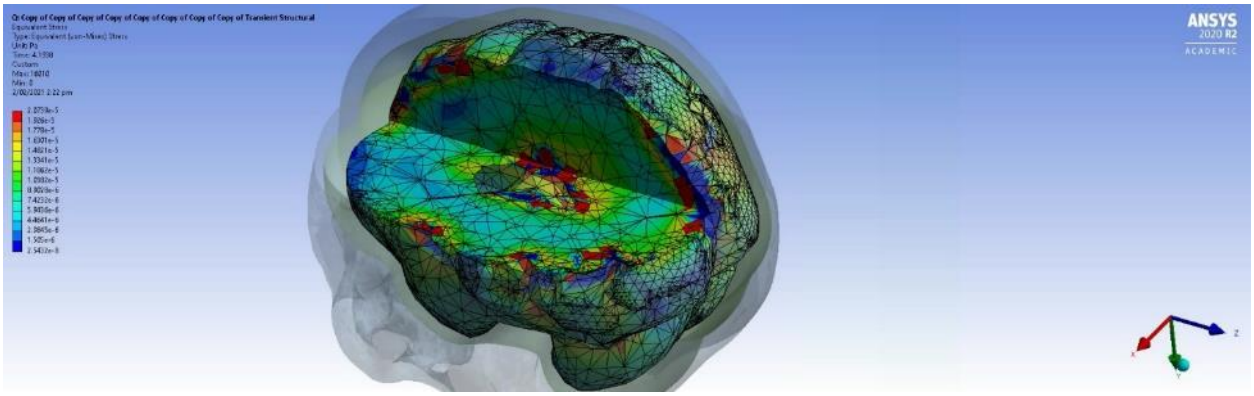
ANSYS
2020 R2
ACADEMIC

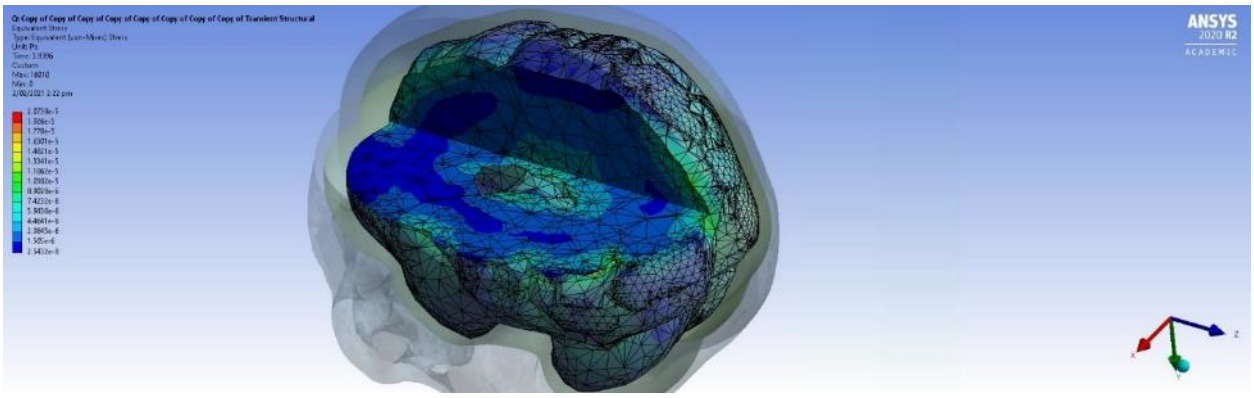
ANSYS
2020 R2
ACADEMIC

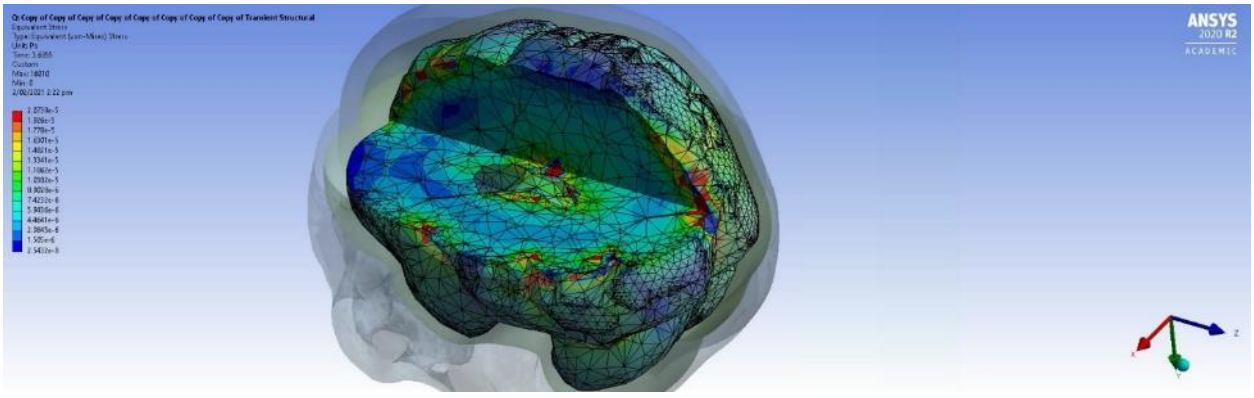
ANSYS
2020 R2
ACADEMIC

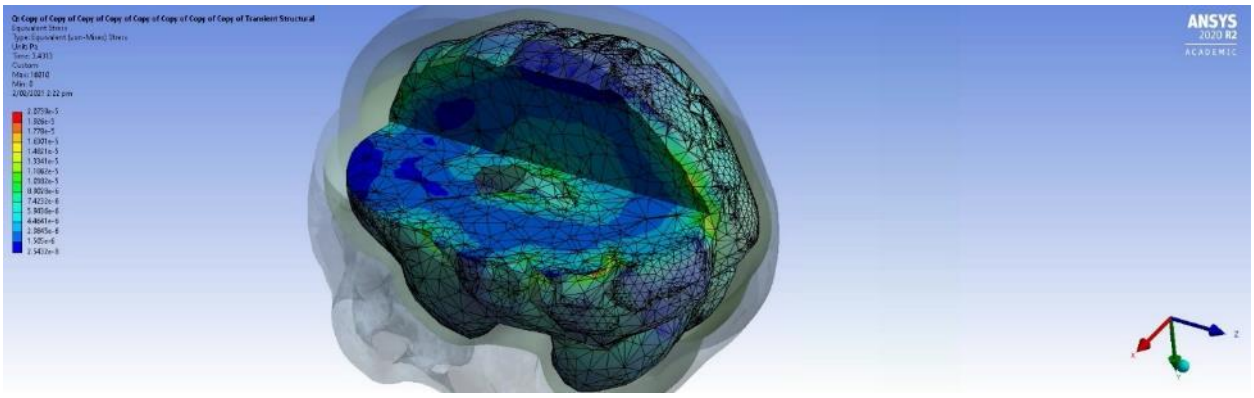
ANSYS
2020 R2
ACADEMIC

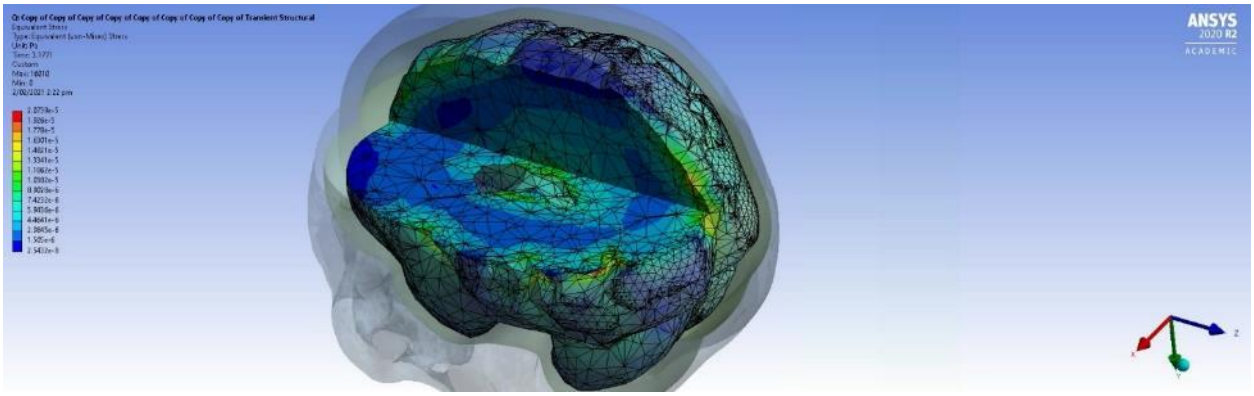
ANSYS
2020 R2
ACADEMIC

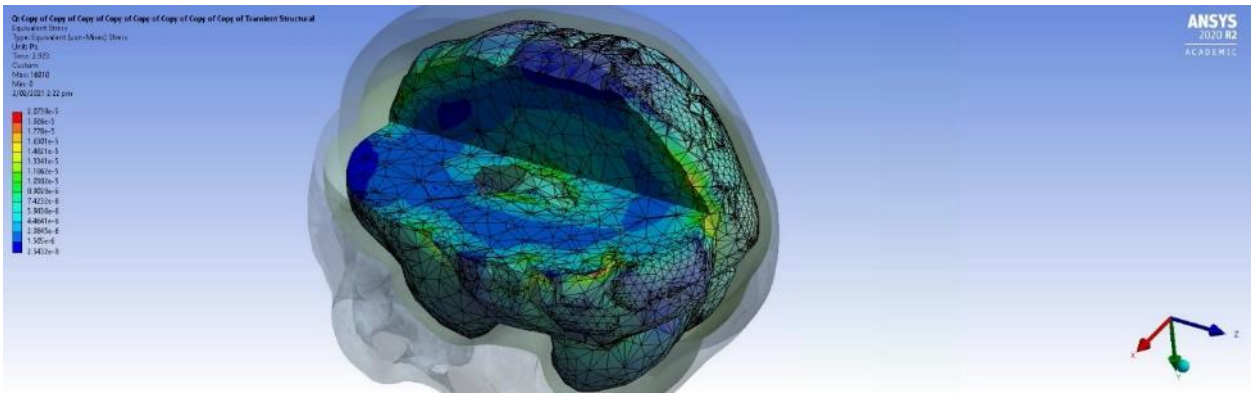
ANSYS
2020 R2
ACADEMIC

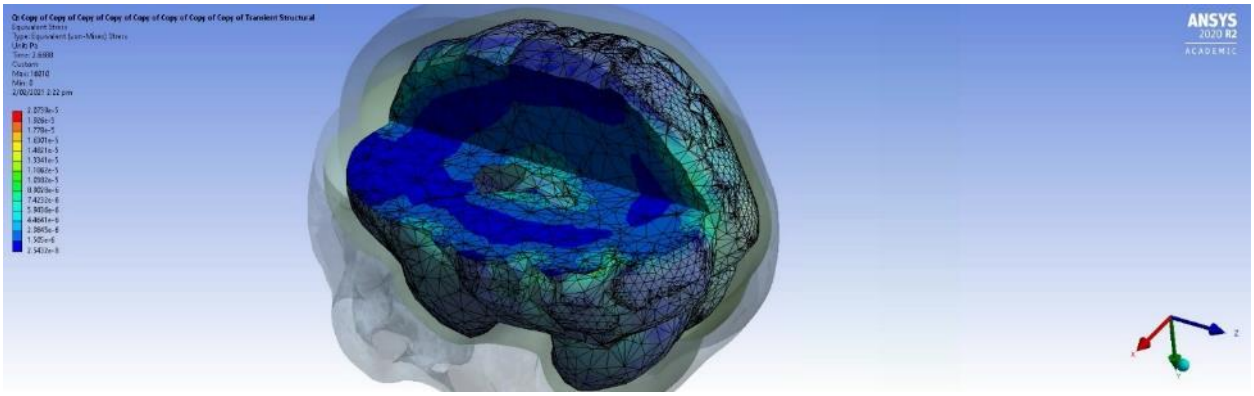
ANSYS
2020 R2
ACADEMIC

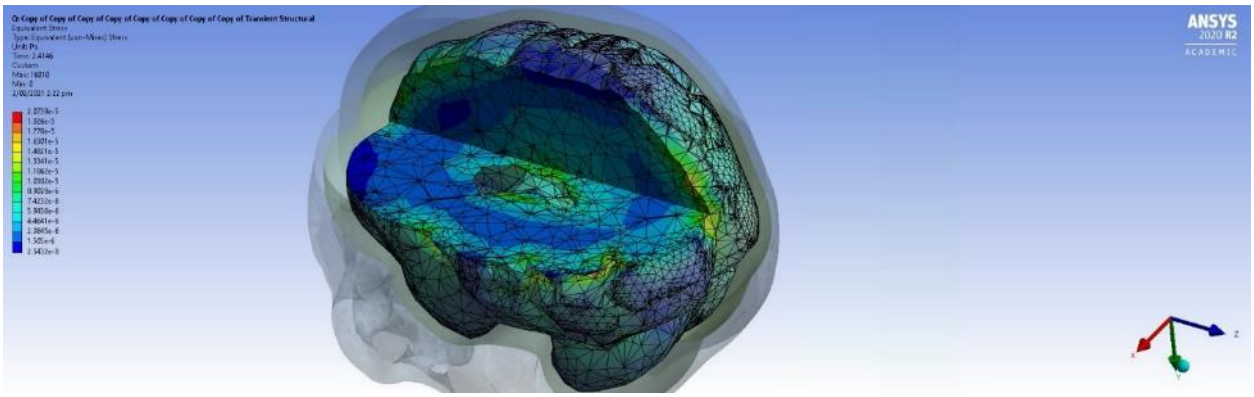
ANSYS
2020 R2
ACADEMIC

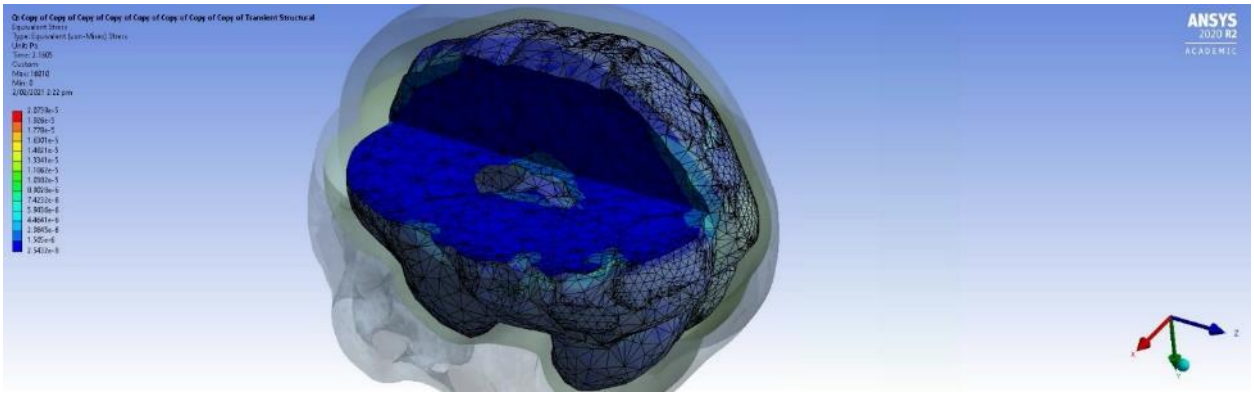
ANSYS
2020 R2
ACADEMIC

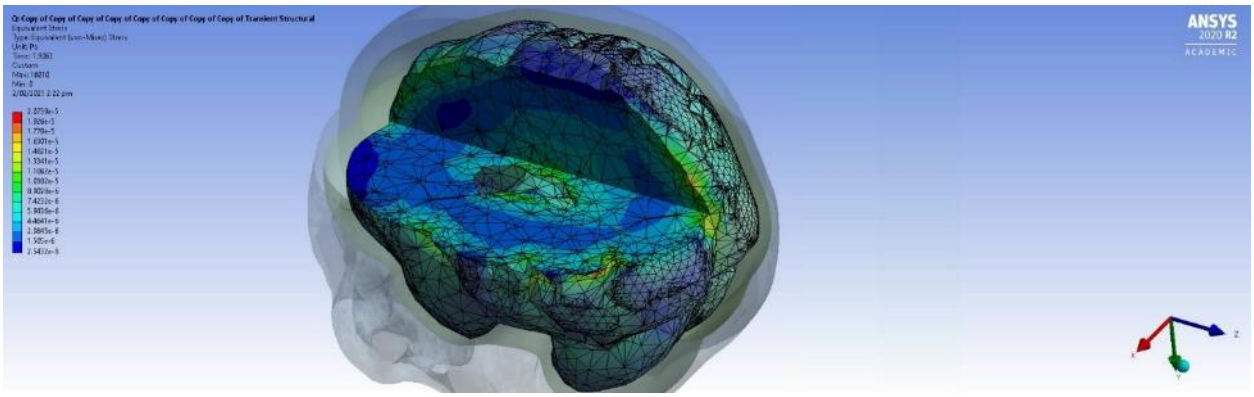
ANSYS
2020 R2
ACADEMIC

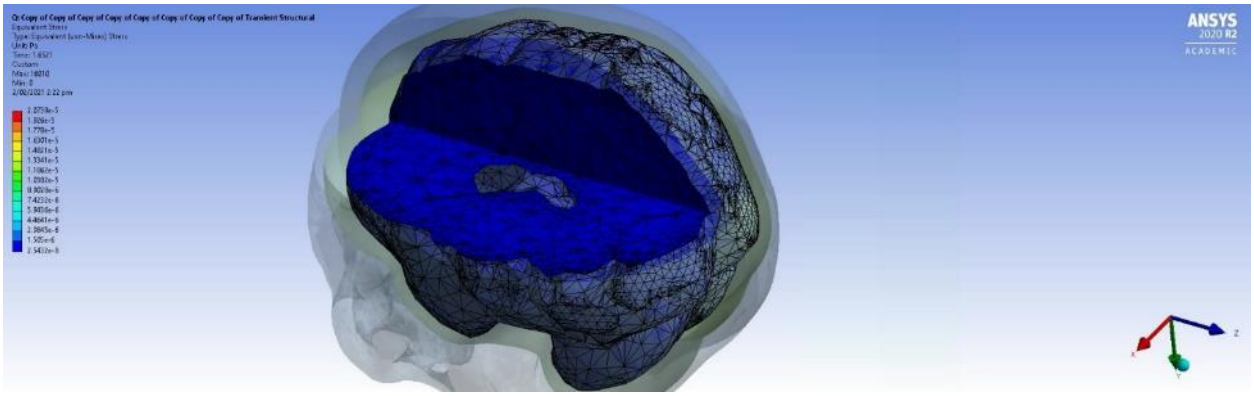
ANSYS
2020 R2
ACADEMIC

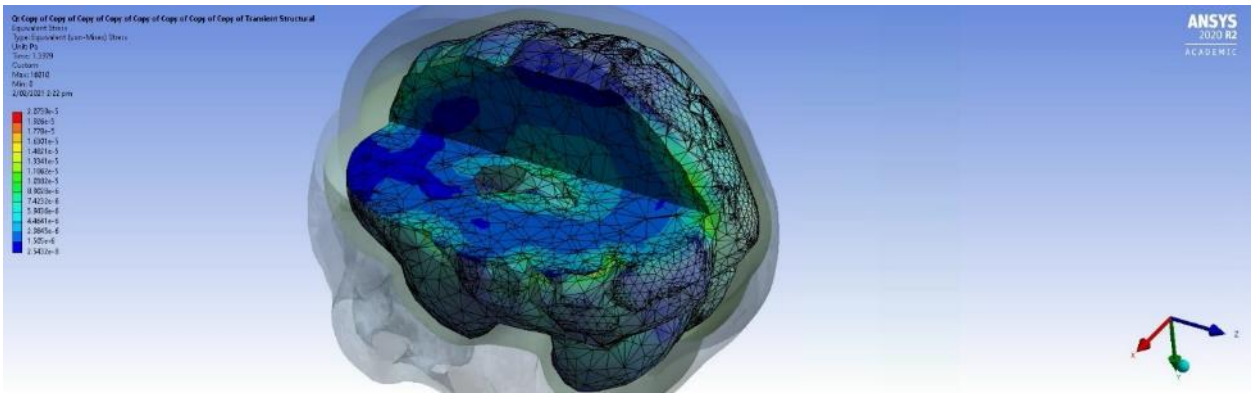
ANSYS
2020 R2
ACADEMIC

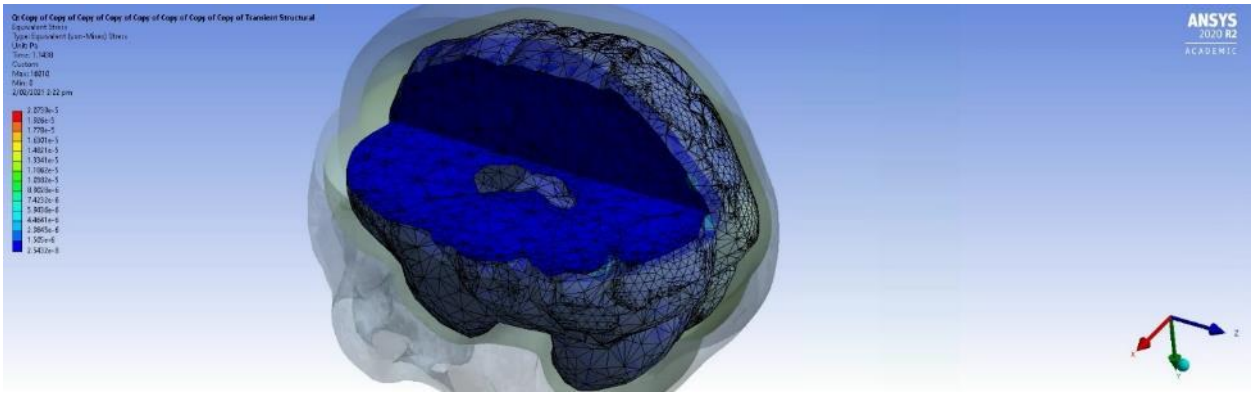
ANSYS
2020 R2
ACADEMIC

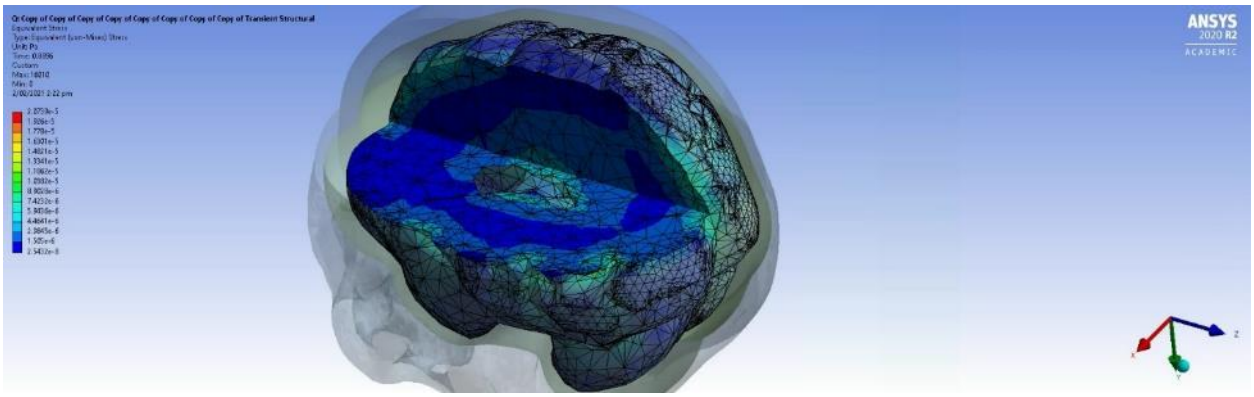
ANSYS
2020 R2
ACADEMIC

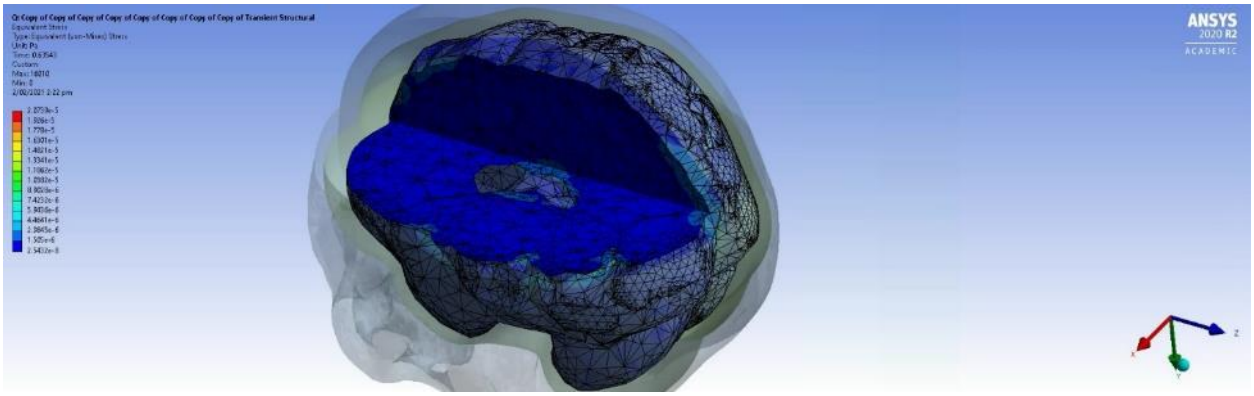
ANSYS
2020 R2
ACADEMIC

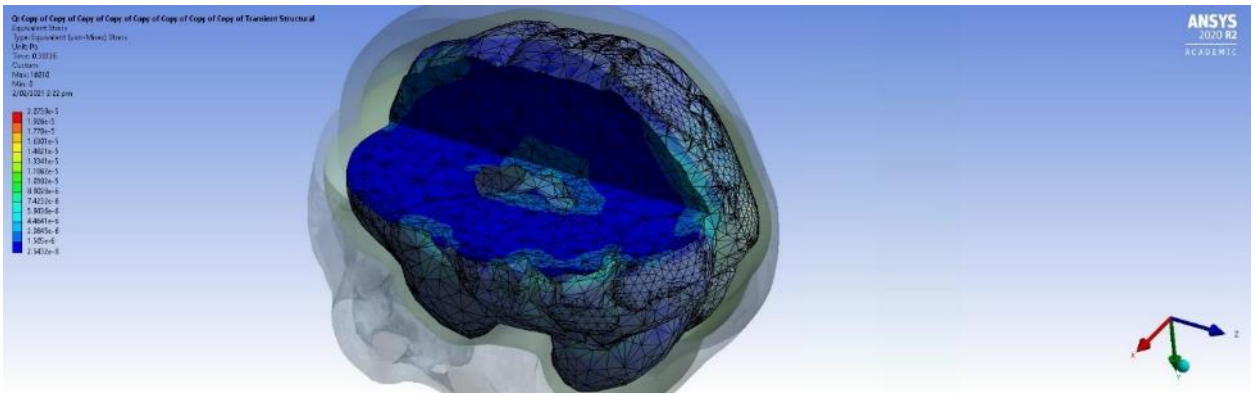
ANSYS
2020 R2
ACADEMIC

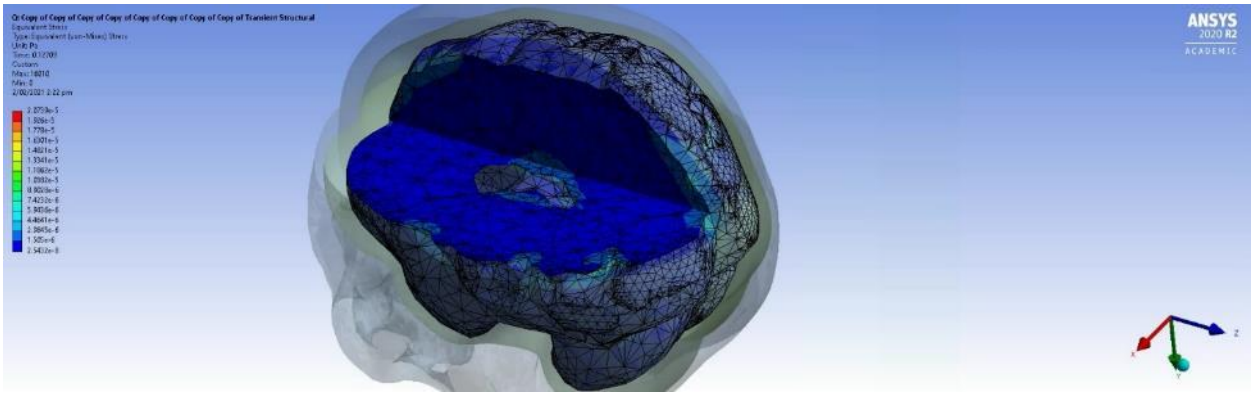

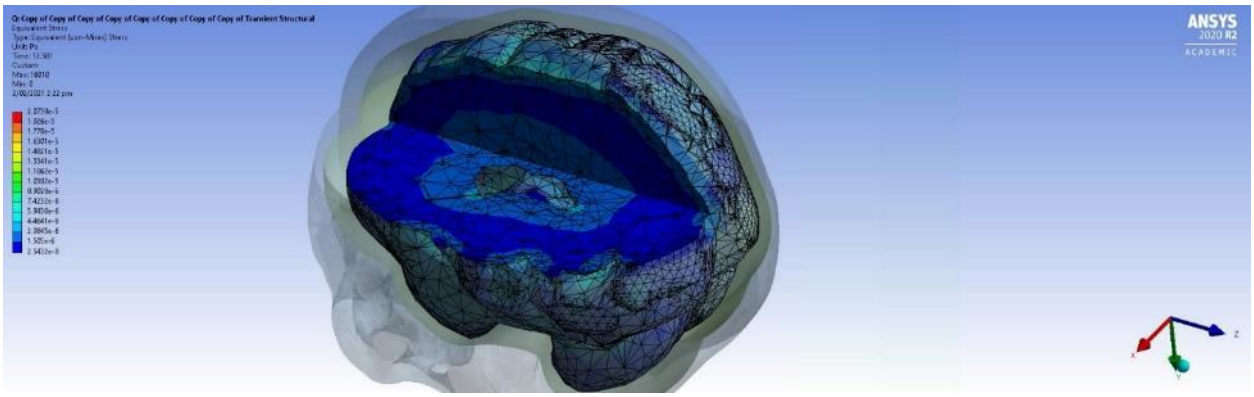

Impact Zone 8

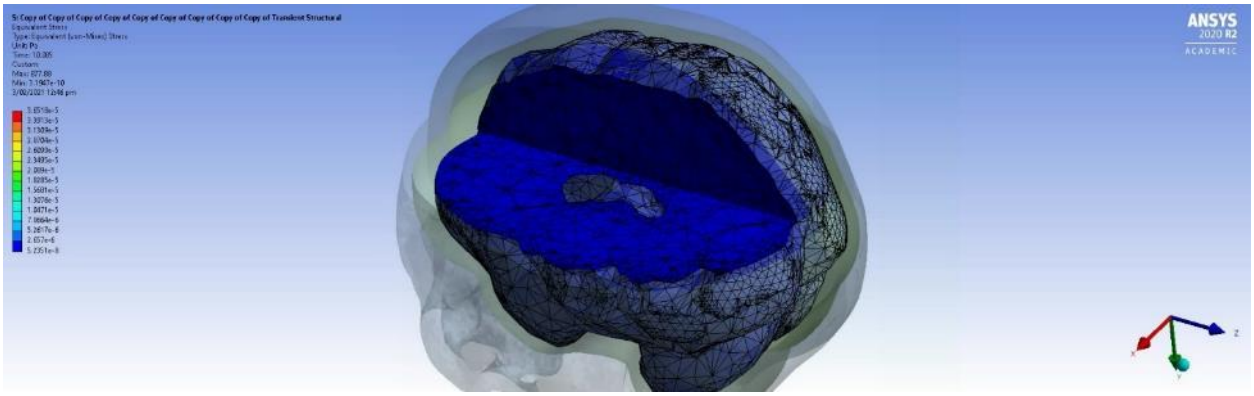

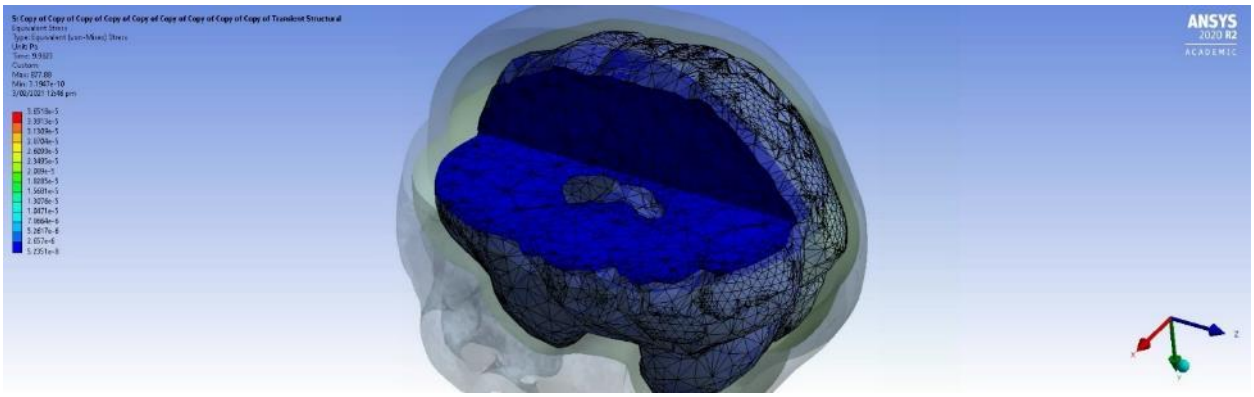

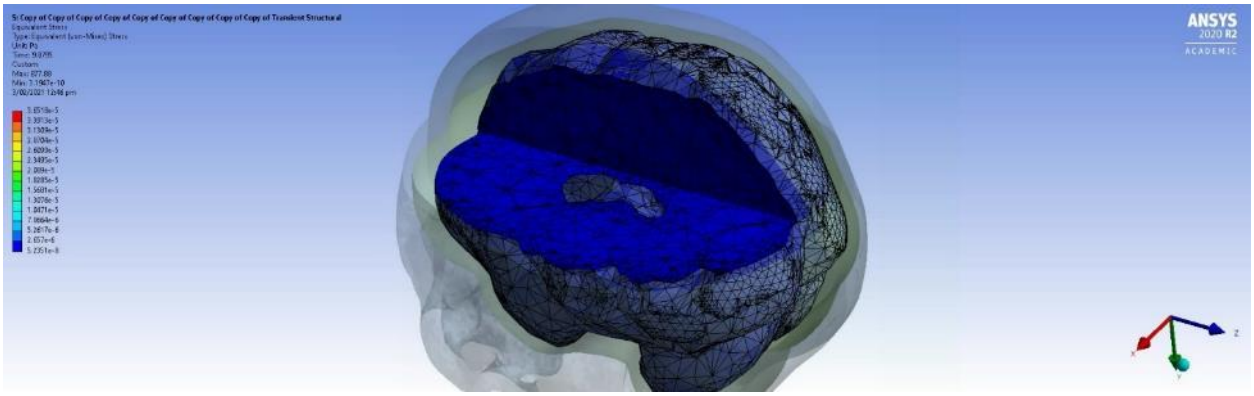
ANSYS
2020 R2
ACADEMIC

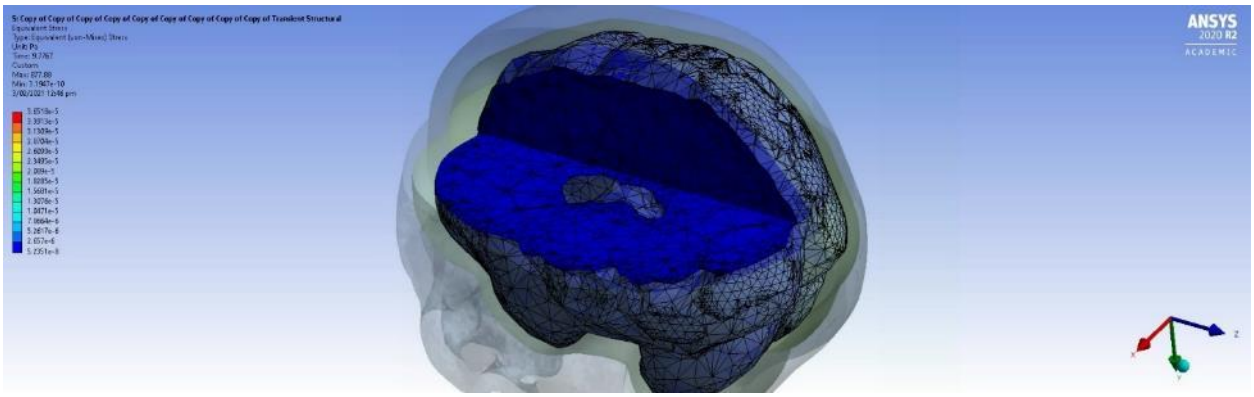
ANSYS
2020 R2
ACADEMIC

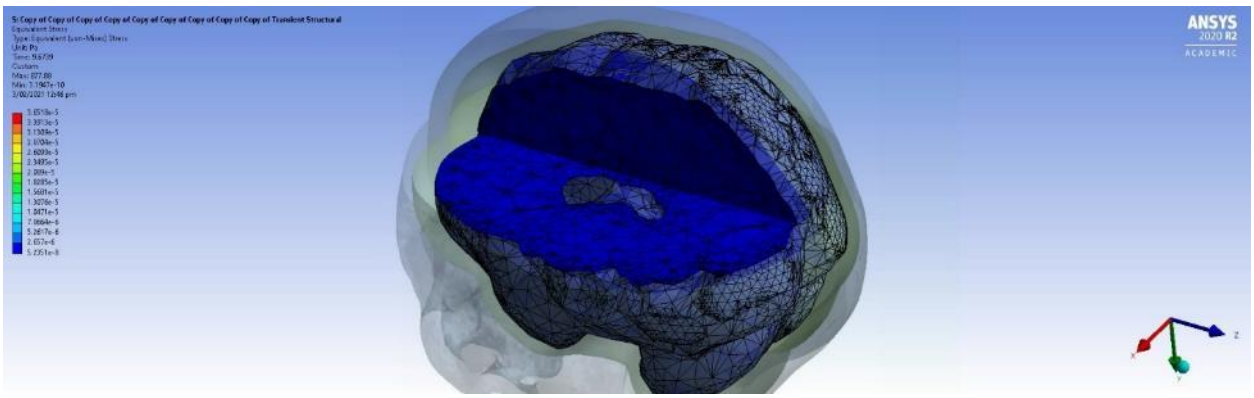
ANSYS
2020 R2
ACADEMIC

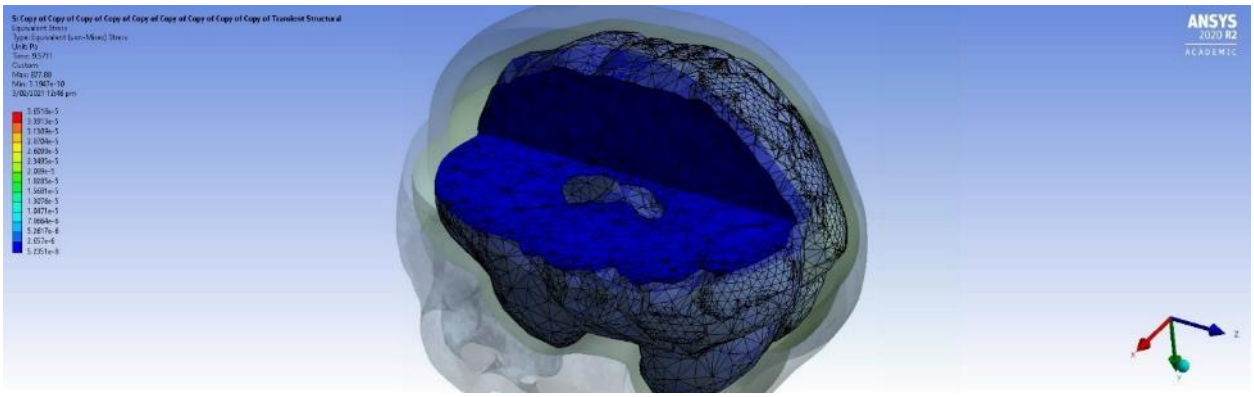
ANSYS
2020 R2
ACADEMIC

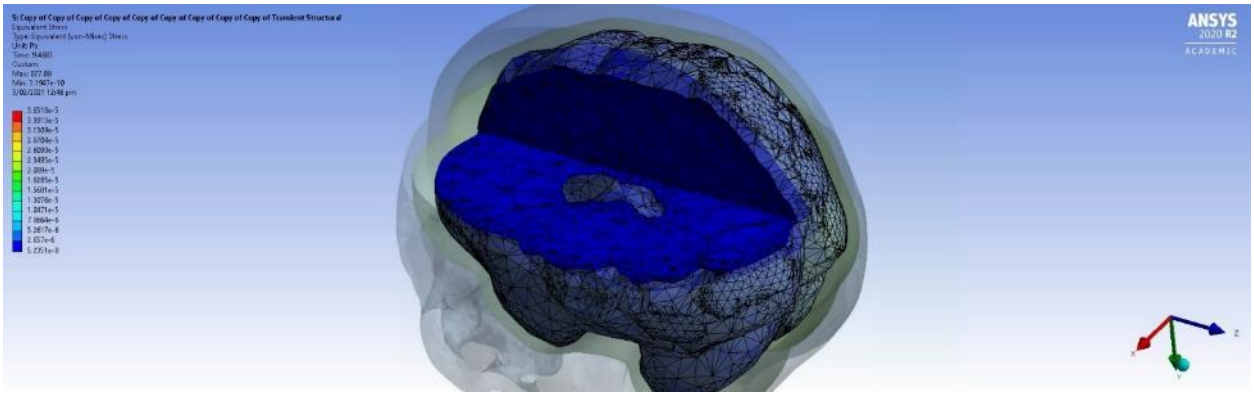
ANSYS
2020 R2
ACADEMIC

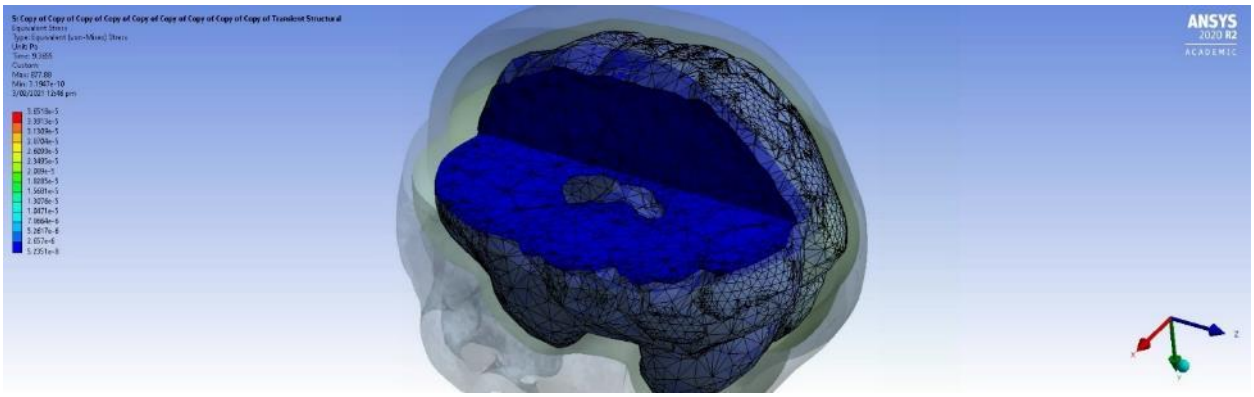
ANSYS
2020 R2
ACADEMIC

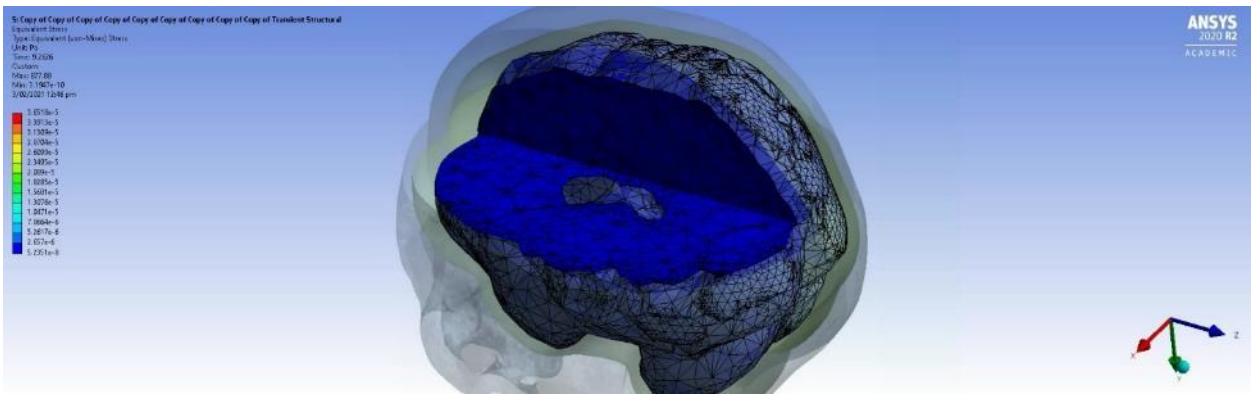
ANSYS
2020 R2
ACADEMIC

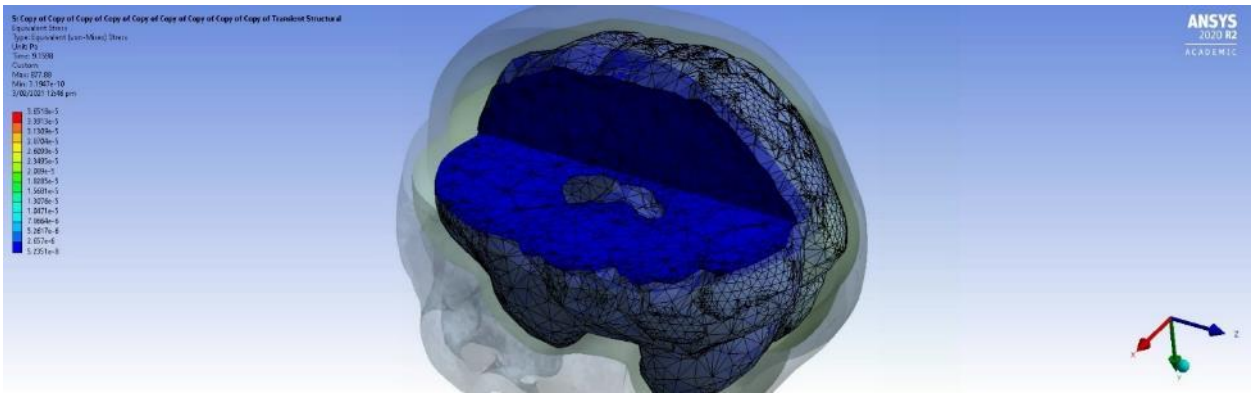
ANSYS
2020 R2
ACADEMIC

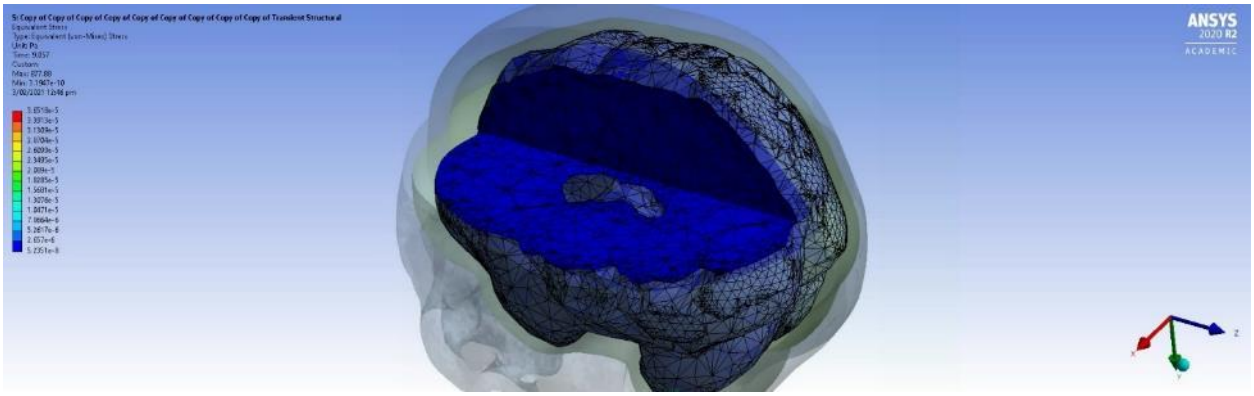
ANSYS
2020 R2
ACADEMIC

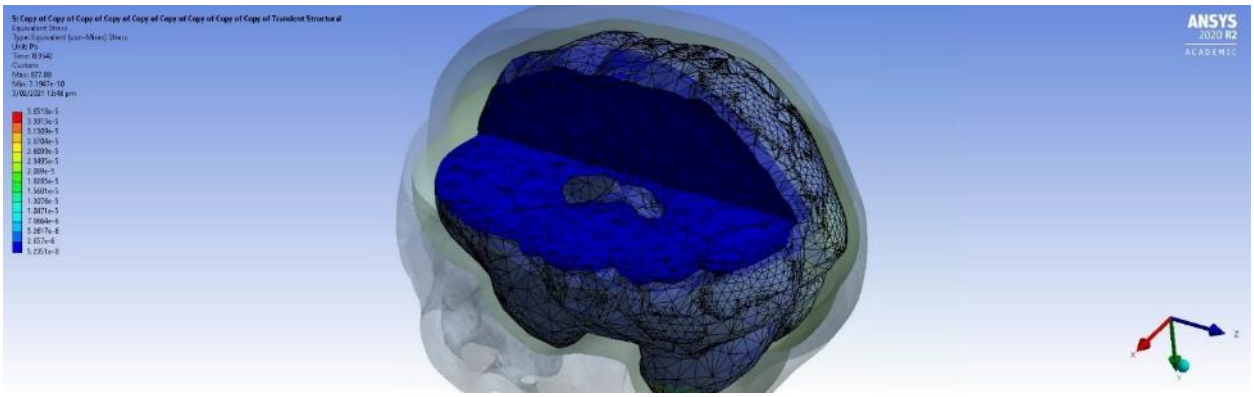
ANSYS
2020 R2
ACADEMIC

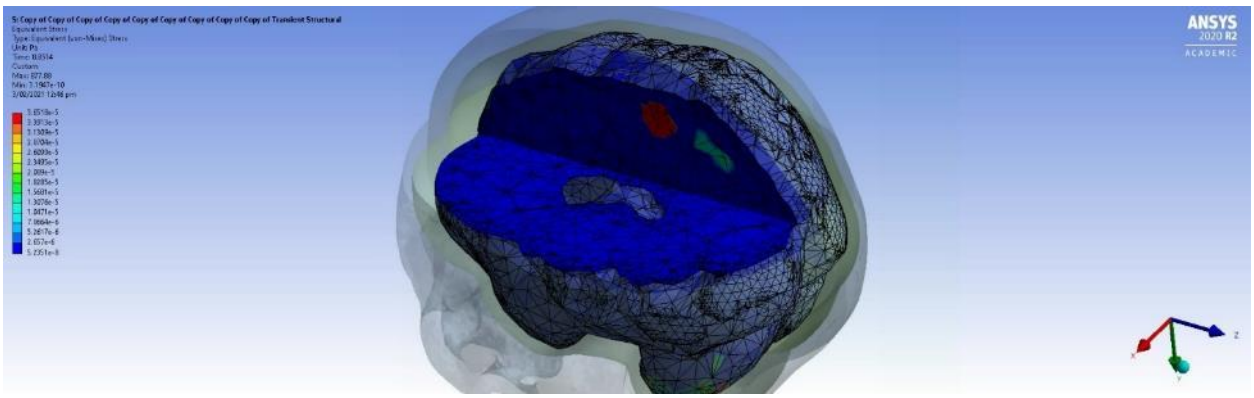
ANSYS
2020 R2
ACADEMIC

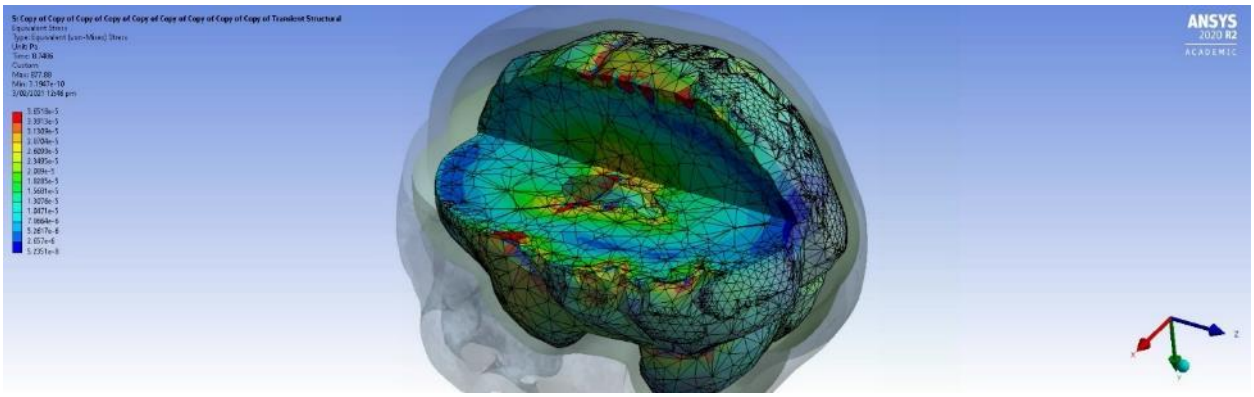
ANSYS
2020 R2
ACADEMIC

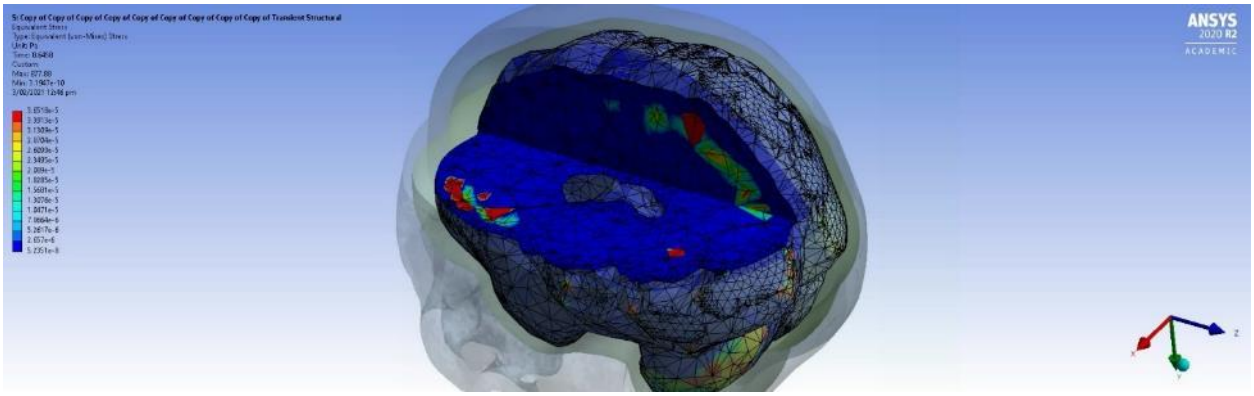
ANSYS
2020 R2
ACADEMIC

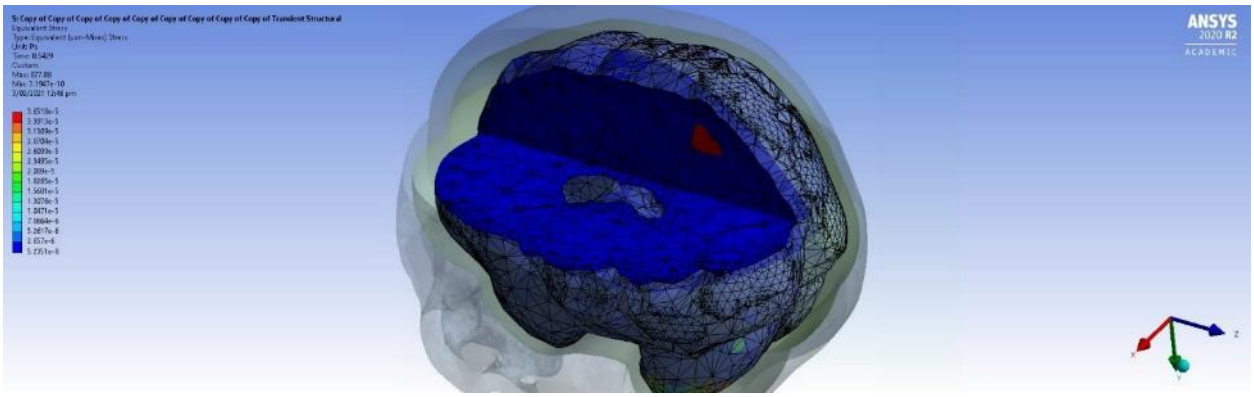
ANSYS
2020 R2
ACADEMIC

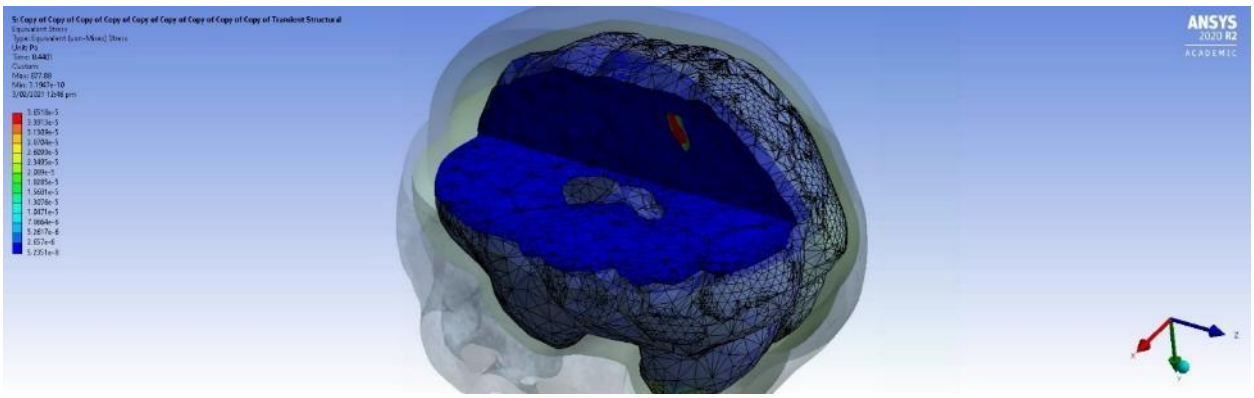
ANSYS
2020 R2
ACADEMIC

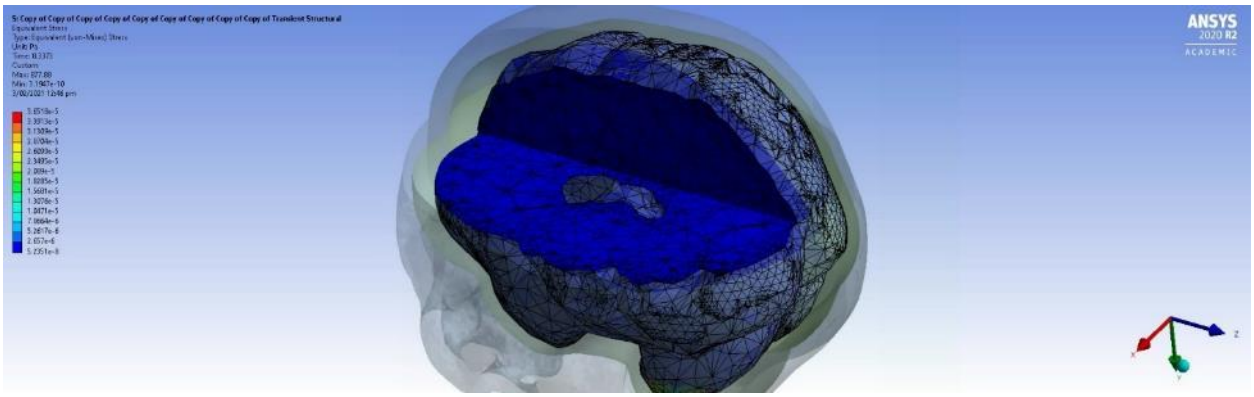
ANSYS
2020 R2
ACADEMIC

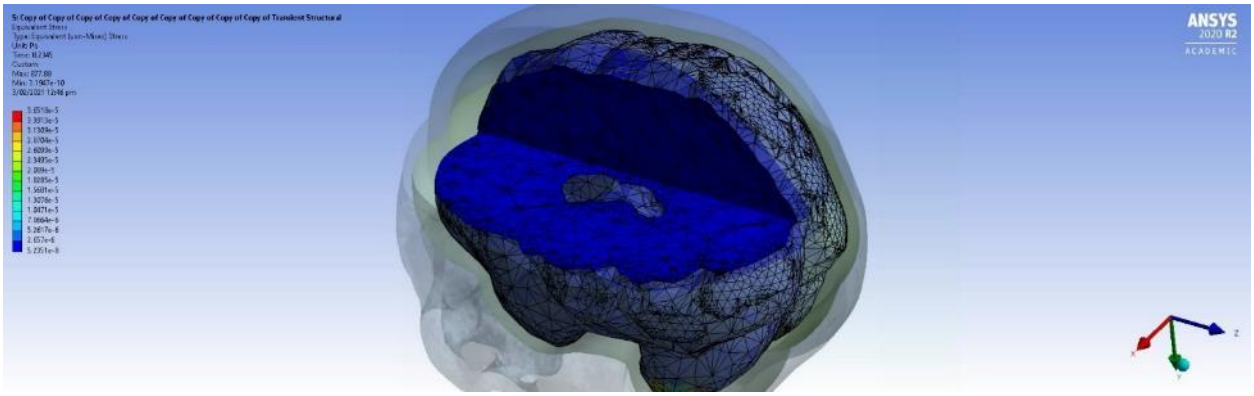
ANSYS
2020 R2
ACADEMIC

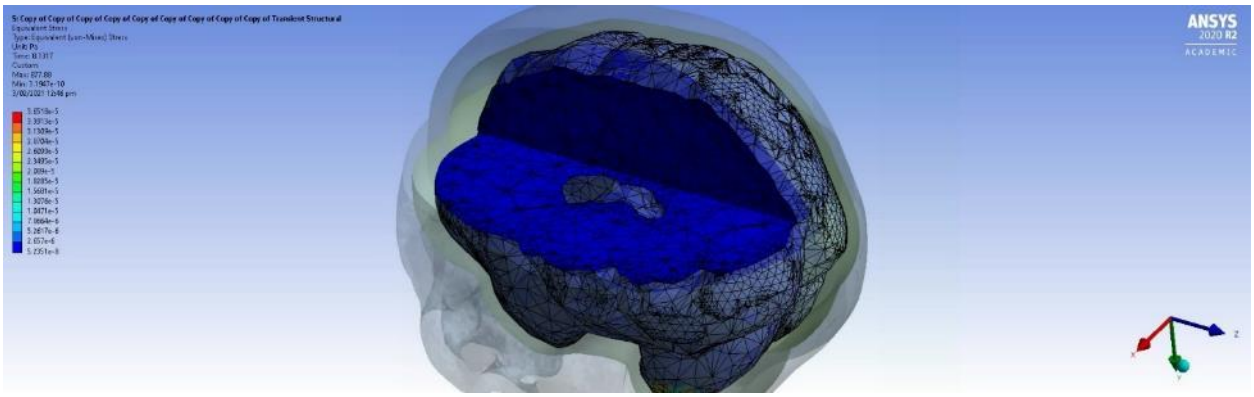
ANSYS
2020 R2
ACADEMIC

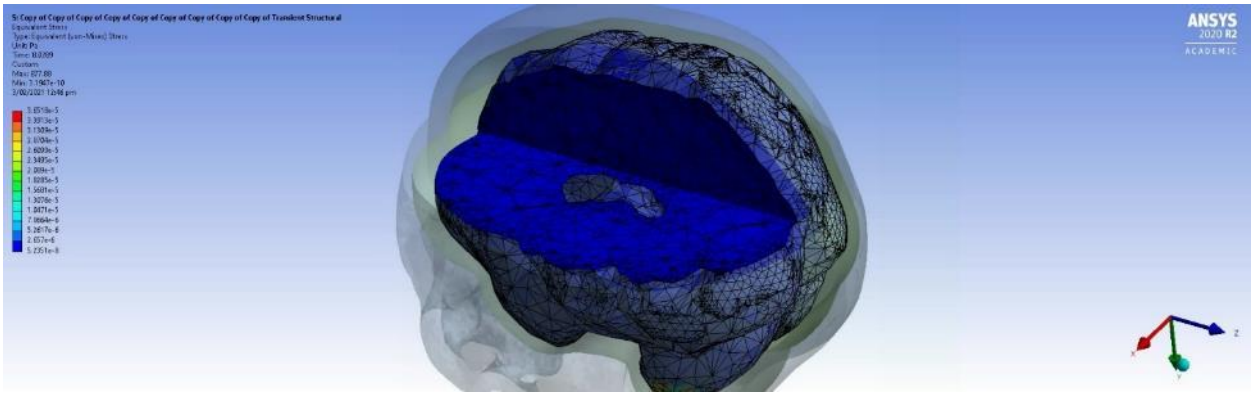
ANSYS
2020 R2
ACADEMIC

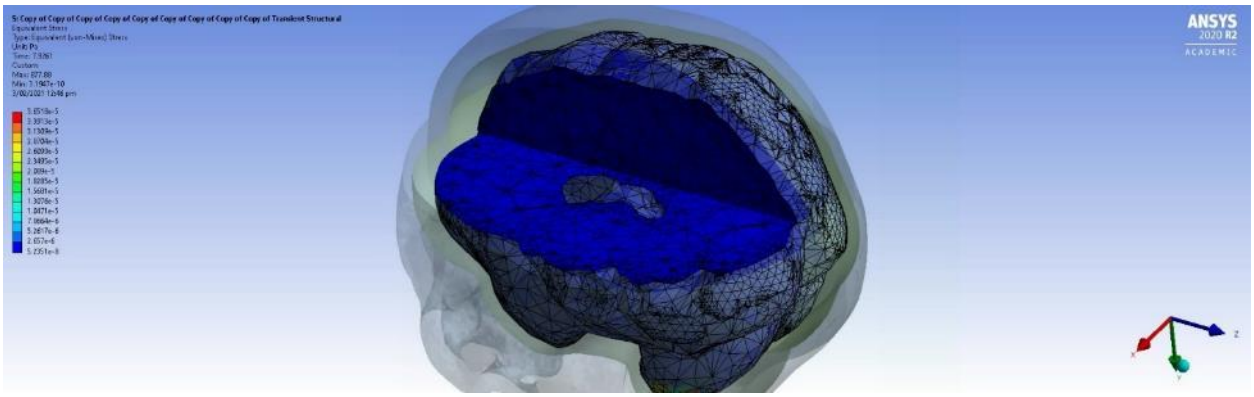
ANSYS
2020 R2
ACADEMIC

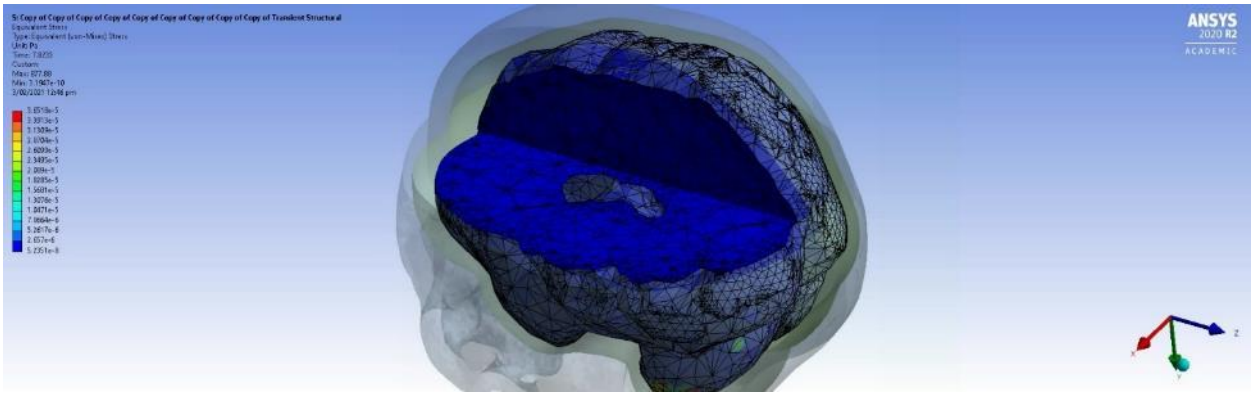
ANSYS
2020 R2
ACADEMIC

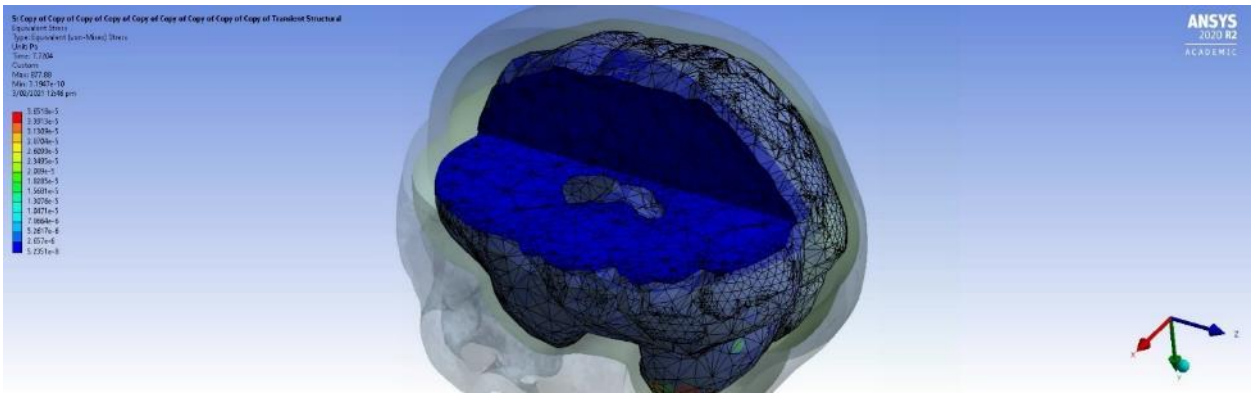
ANSYS
2020 R2
ACADEMIC

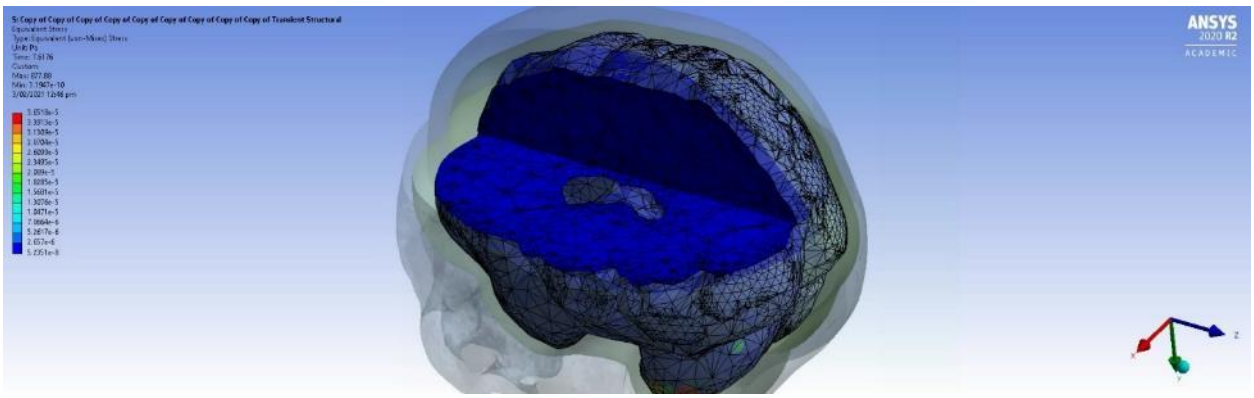
ANSYS
2020 R2
ACADEMIC

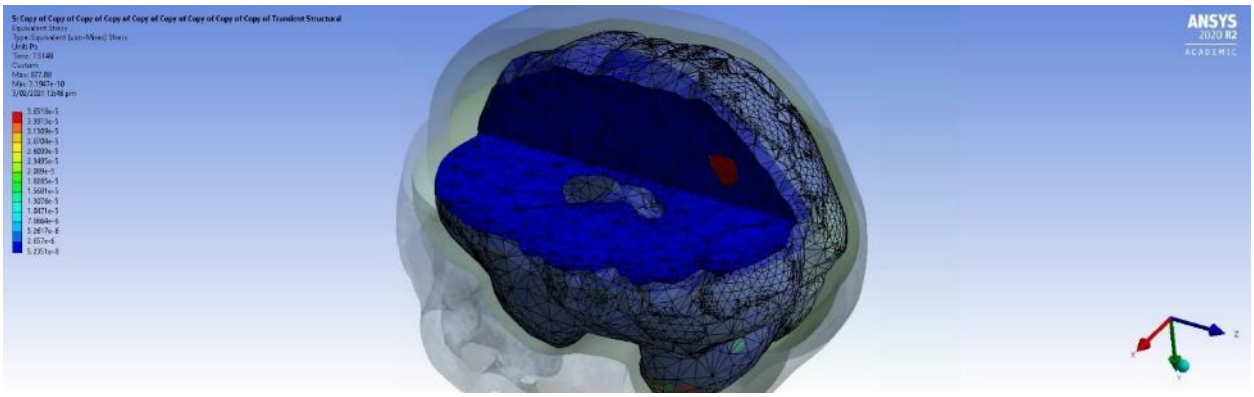
ANSYS
2020 R2
ACADEMIC

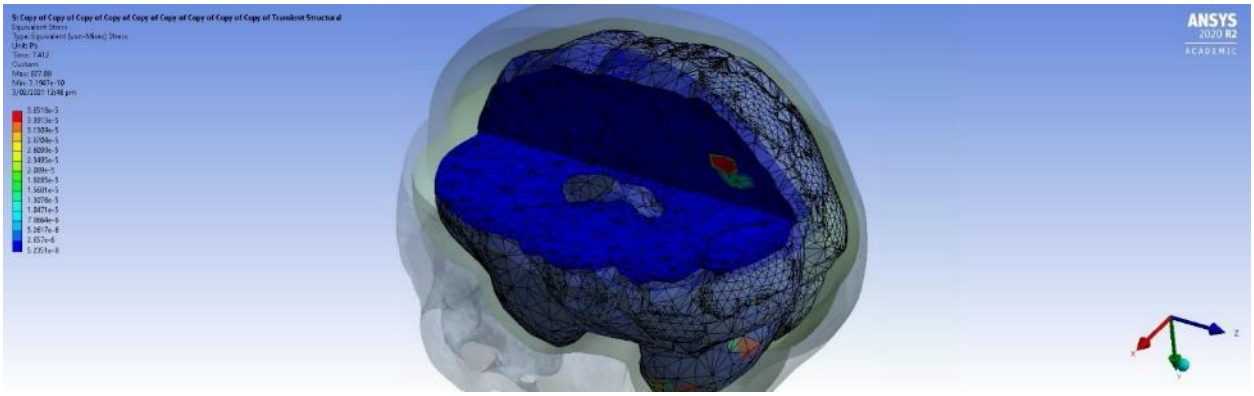
ANSYS
2020 R2
ACADEMIC

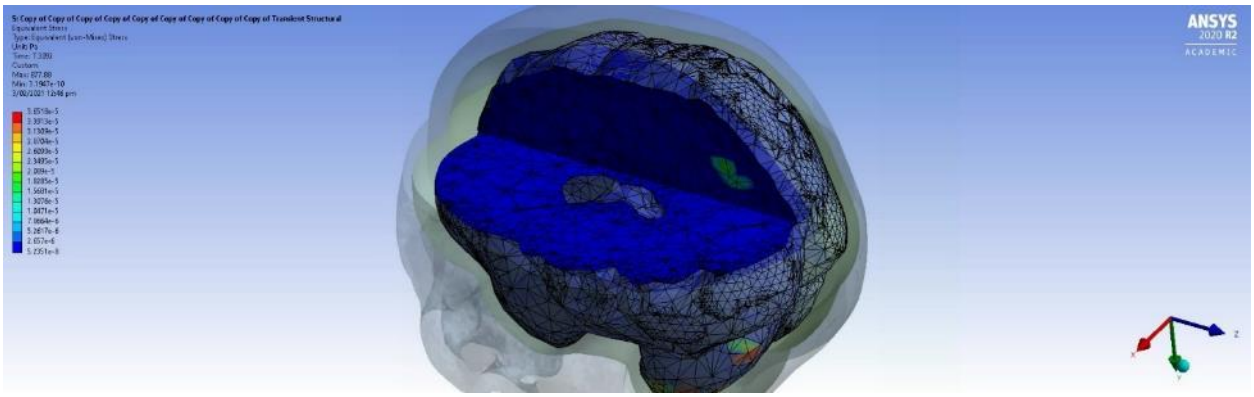
ANSYS
2020 R2
ACADEMIC

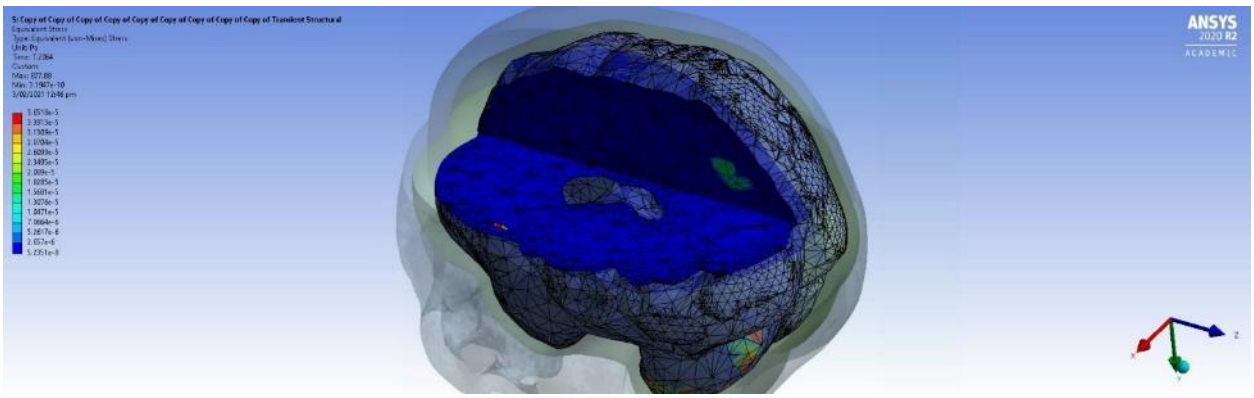
ANSYS
2020 R2
ACADEMIC

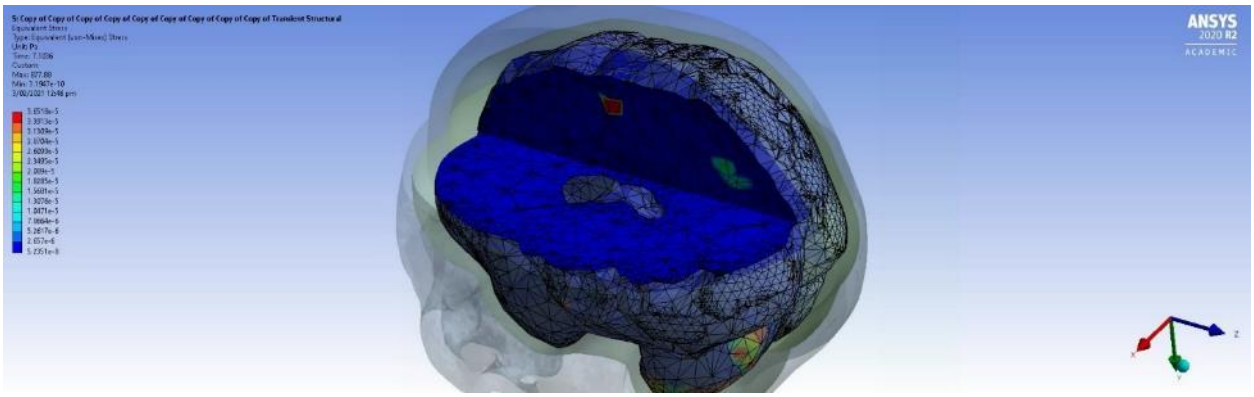
ANSYS
2020 R2
ACADEMIC

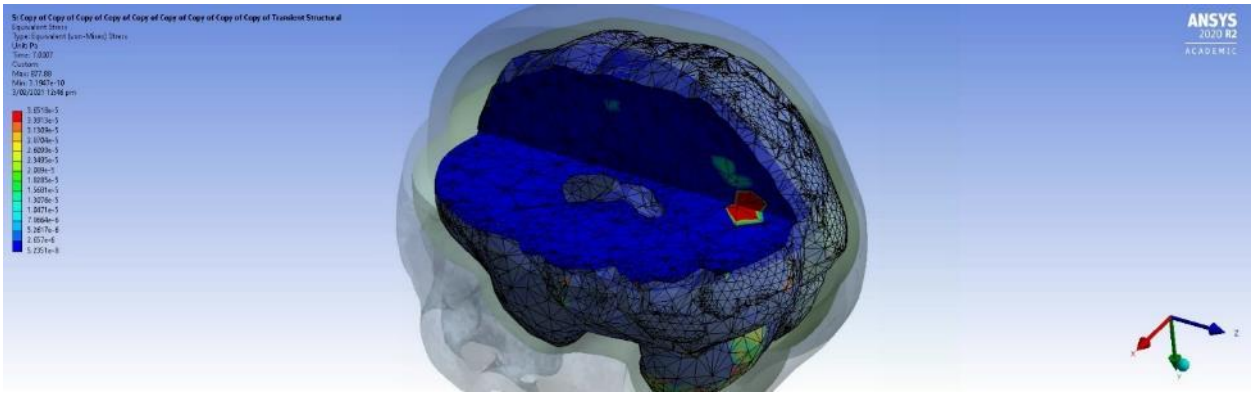
ANSYS
2020 R2
ACADEMIC

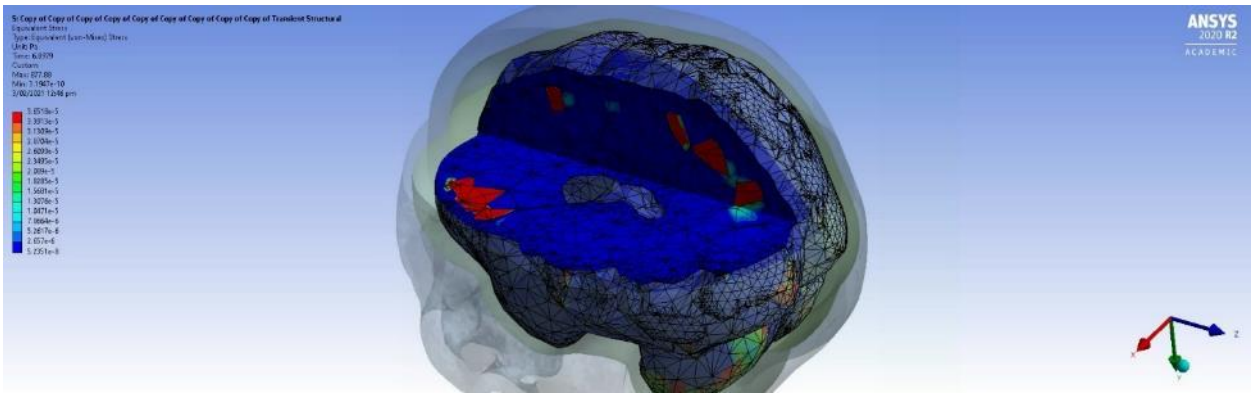
ANSYS
2020 R2
ACADEMIC

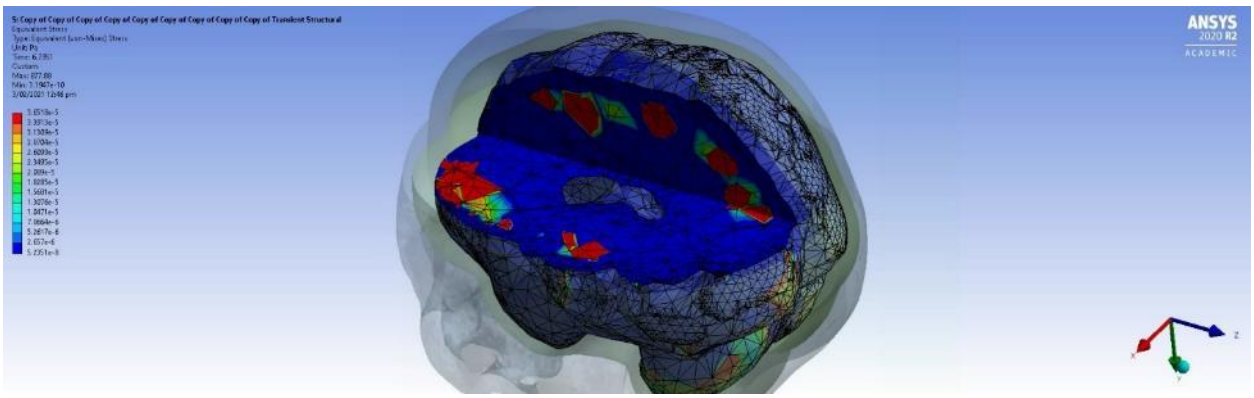
ANSYS
2020 R2
ACADEMIC

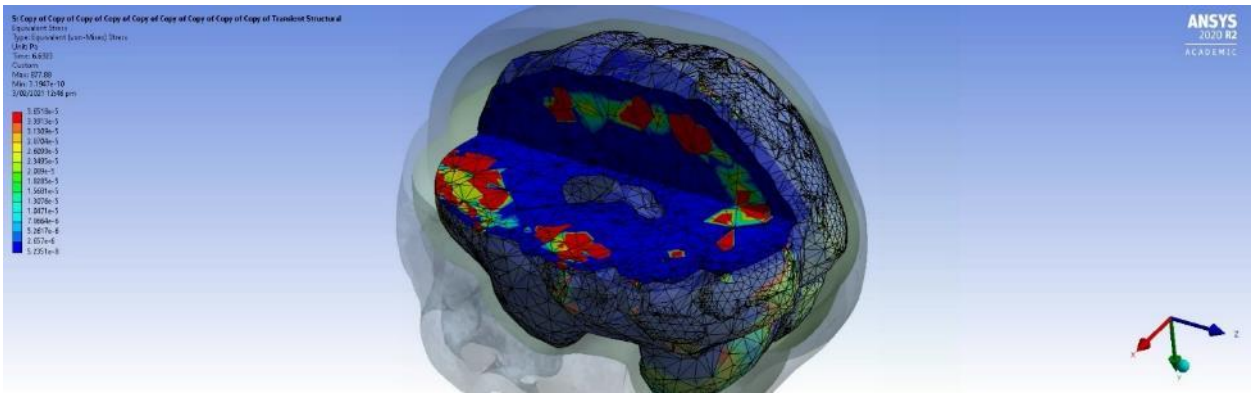
ANSYS
2020 R2
ACADEMIC

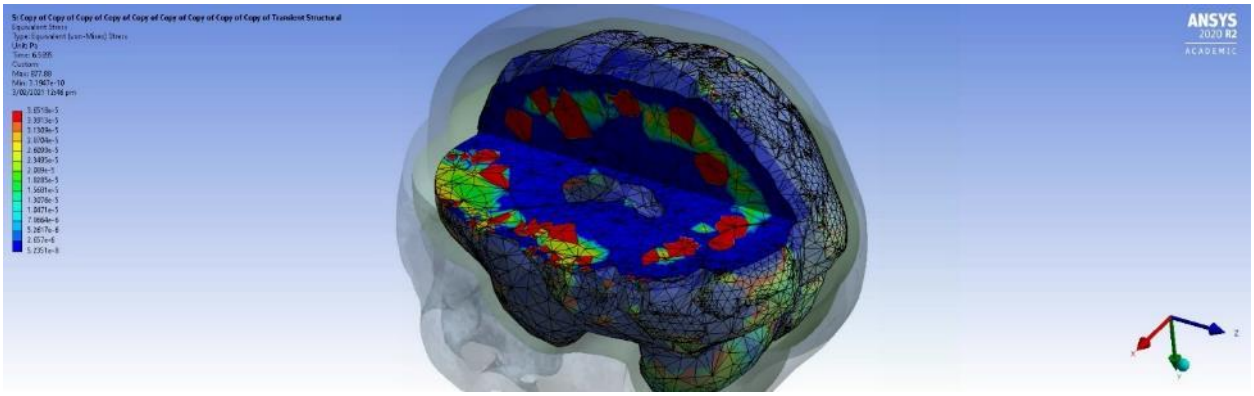
ANSYS
2020 R2
ACADEMIC

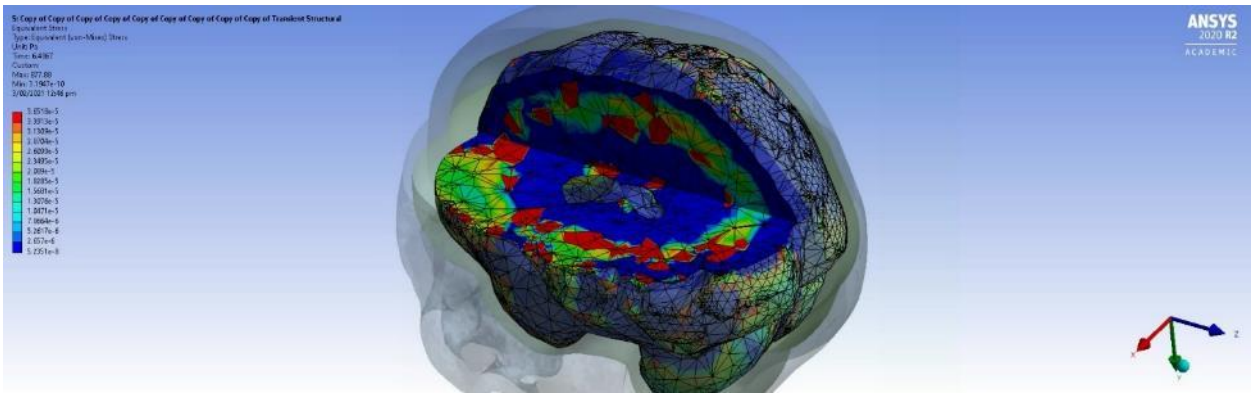
ANSYS
2020 R2
ACADEMIC

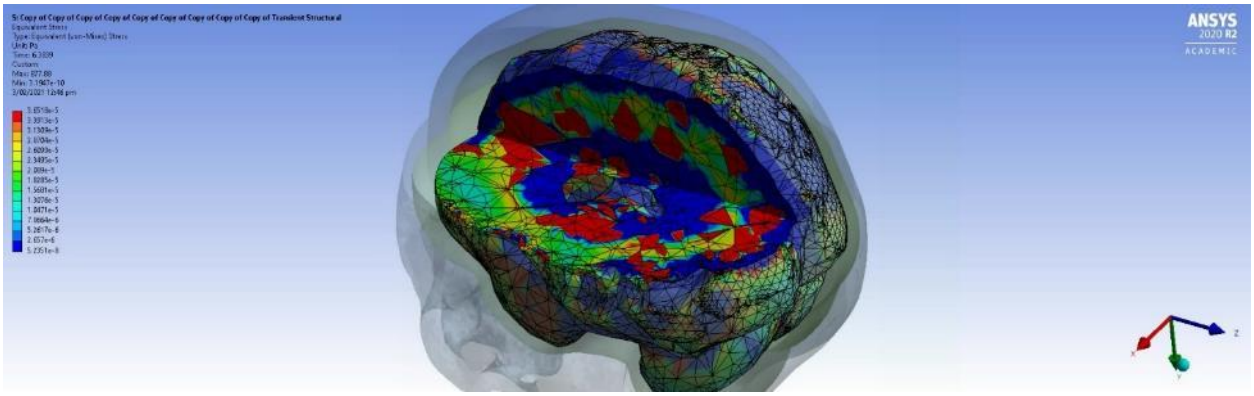
ANSYS
2020 R2
ACADEMIC

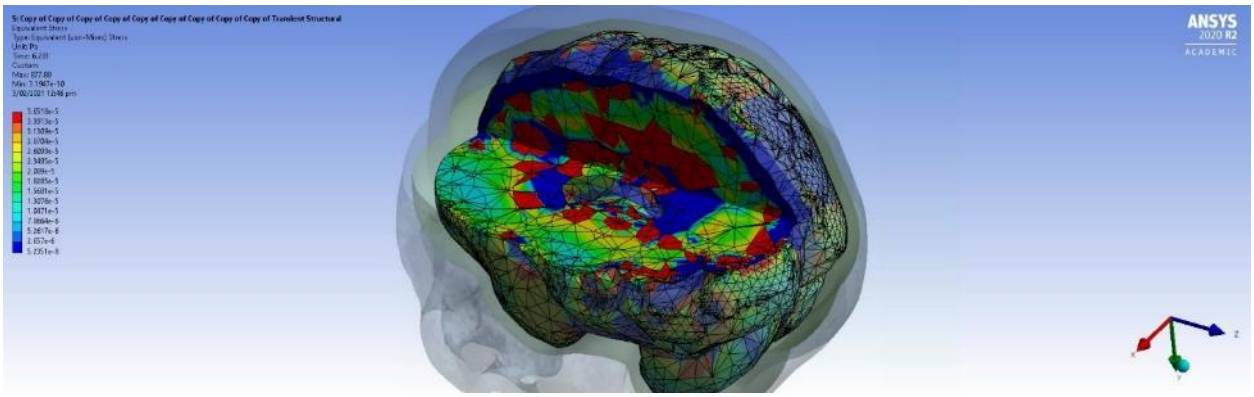
ANSYS
2020 R2
ACADEMIC

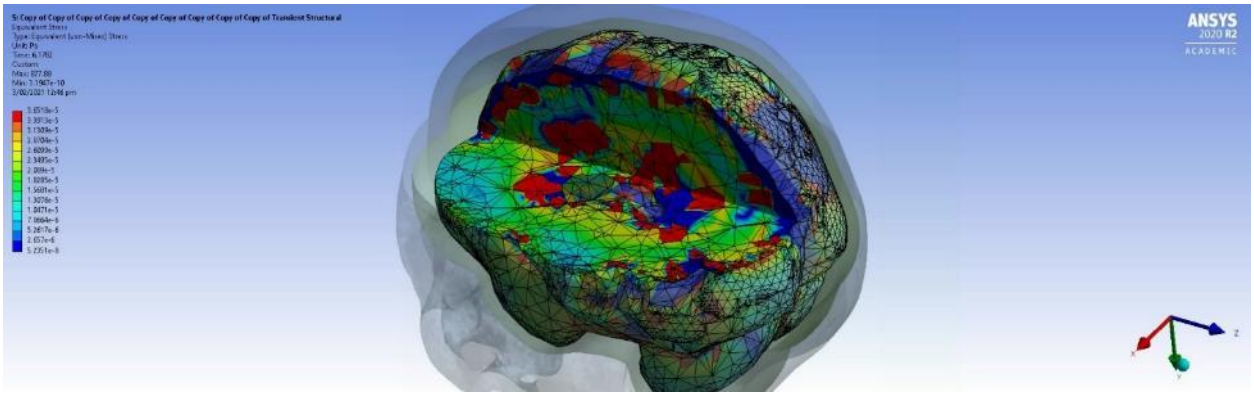
ANSYS
2020 R2
ACADEMIC

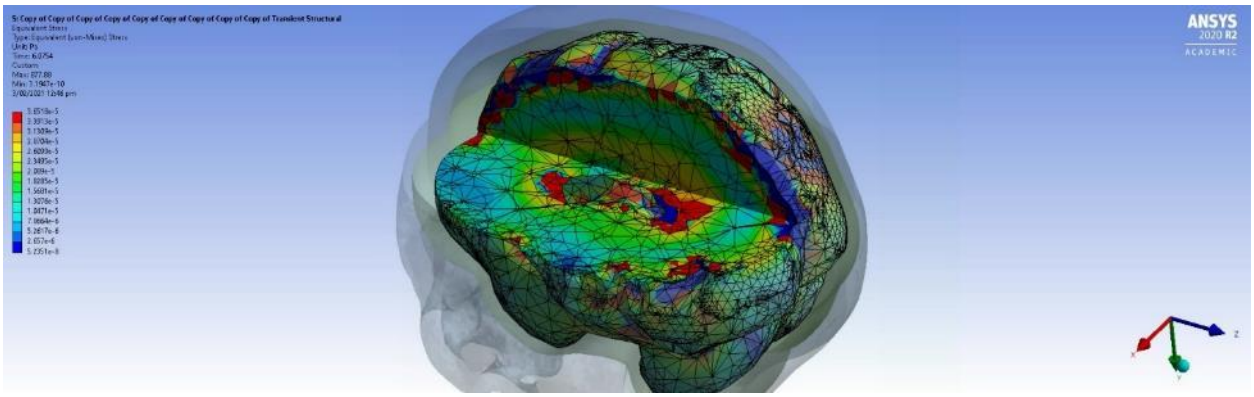
ANSYS
2020 R2
ACADEMIC

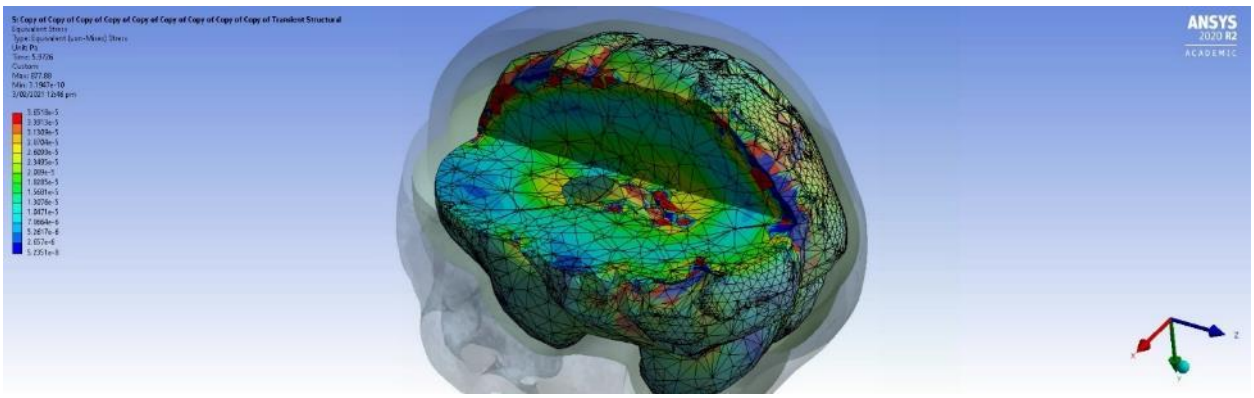
ANSYS
2020 R2
ACADEMIC

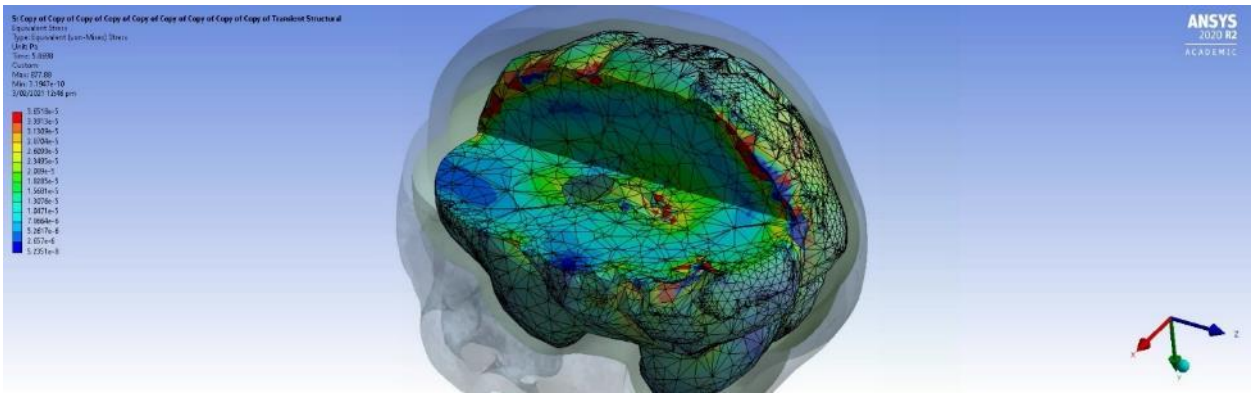
ANSYS
2020 R2
ACADEMIC

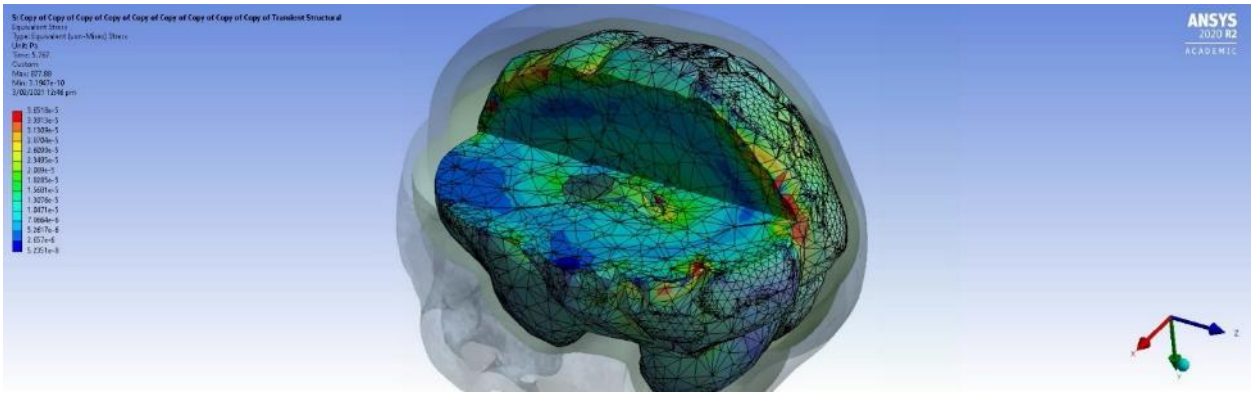
ANSYS
2020 R2
ACADEMIC

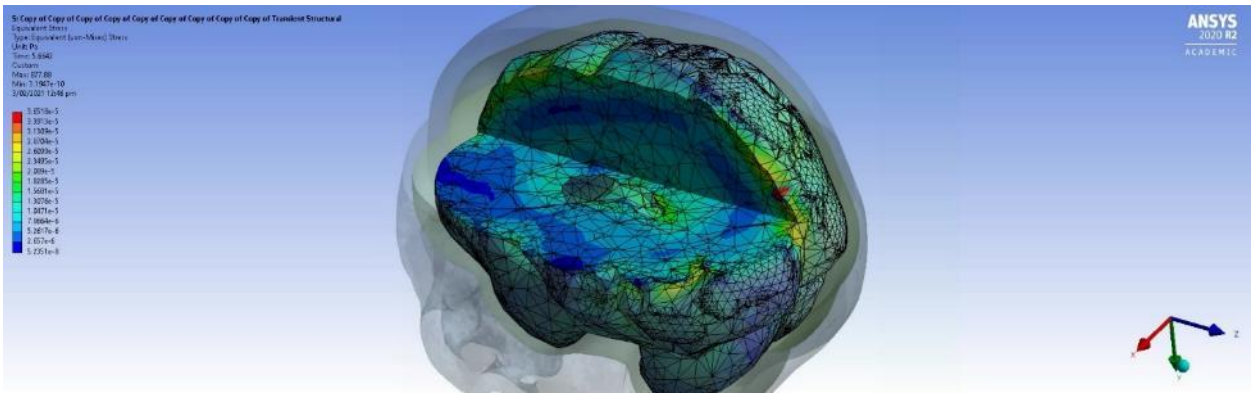
ANSYS
2020 R2
ACADEMIC

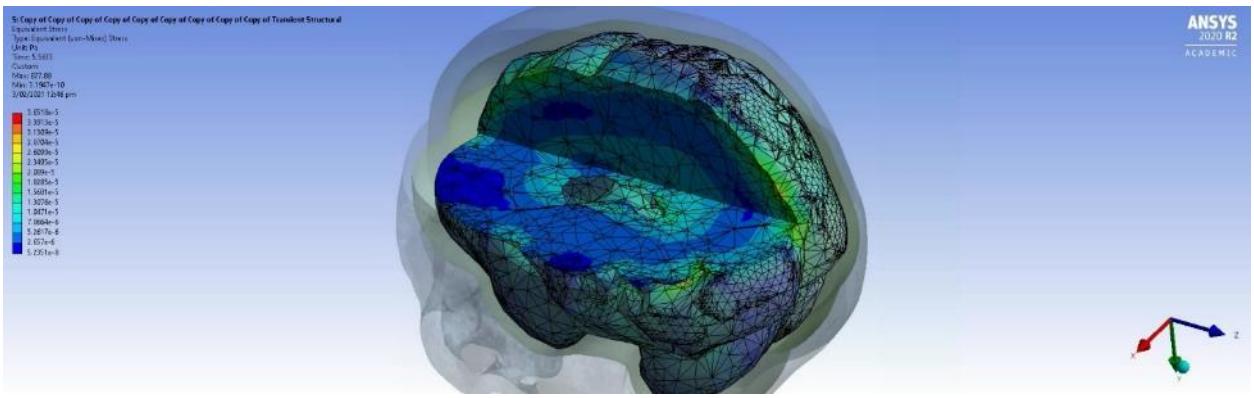
ANSYS
2020 R2
ACADEMIC

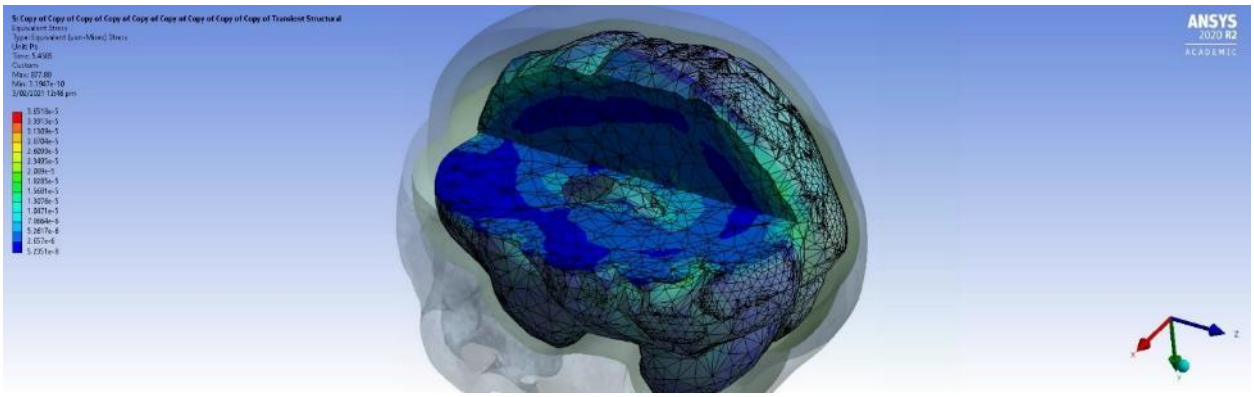
ANSYS
2020 R2
ACADEMIC

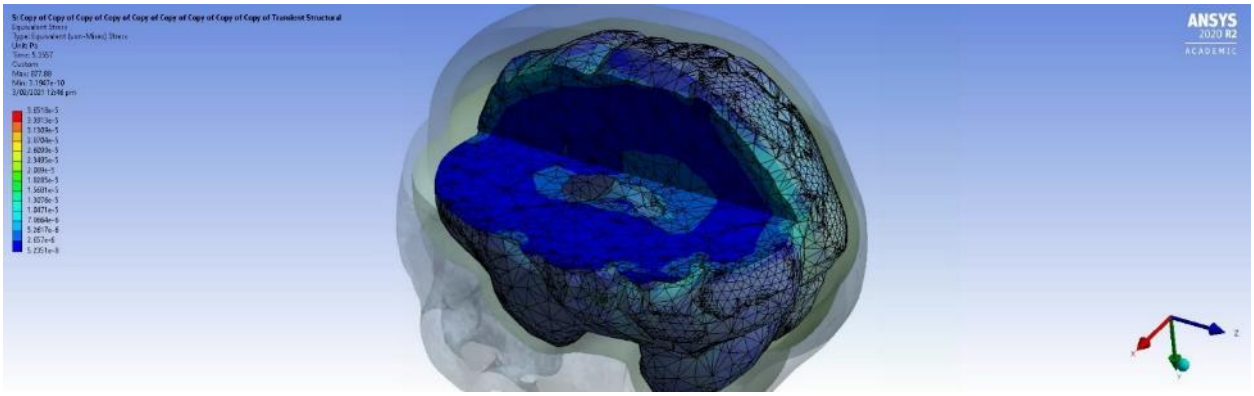
ANSYS
2020 R2
ACADEMIC

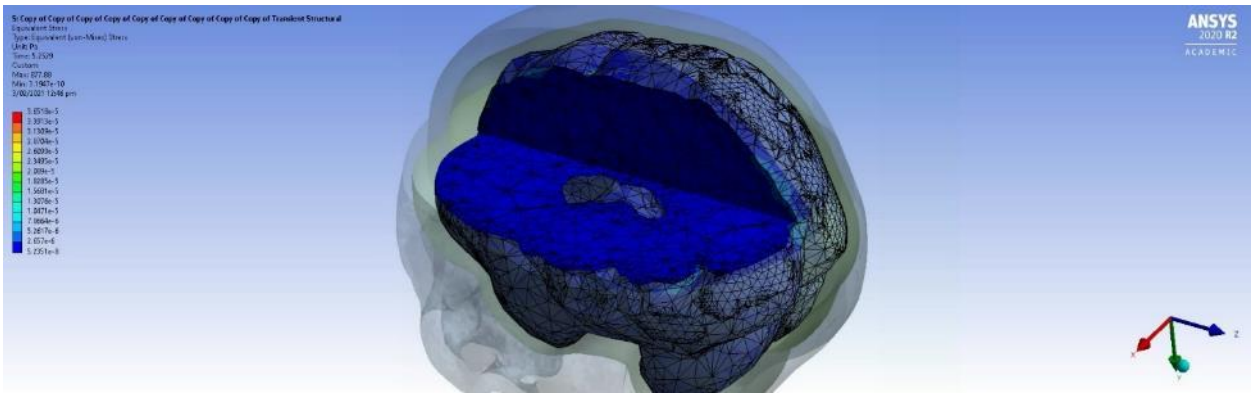
ANSYS
2020 R2
ACADEMIC

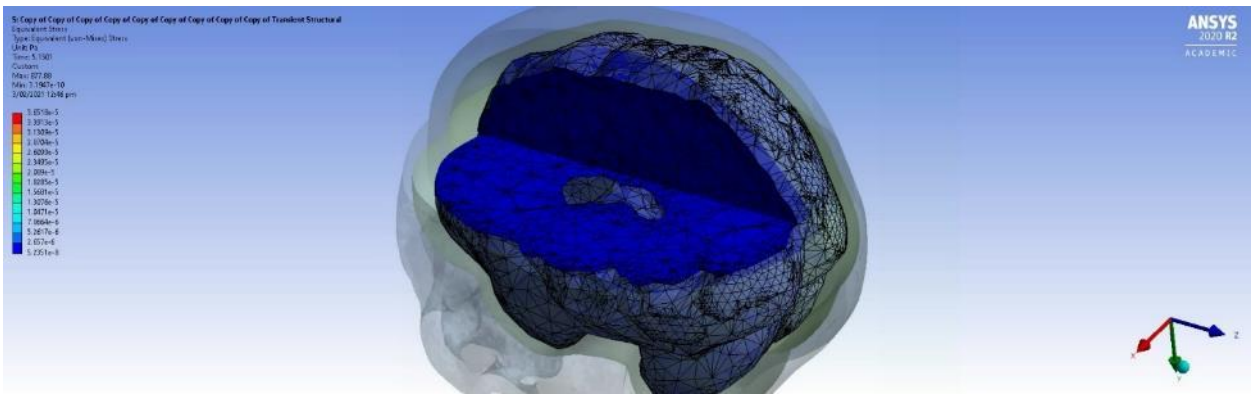
ANSYS
2020 R2
ACADEMIC

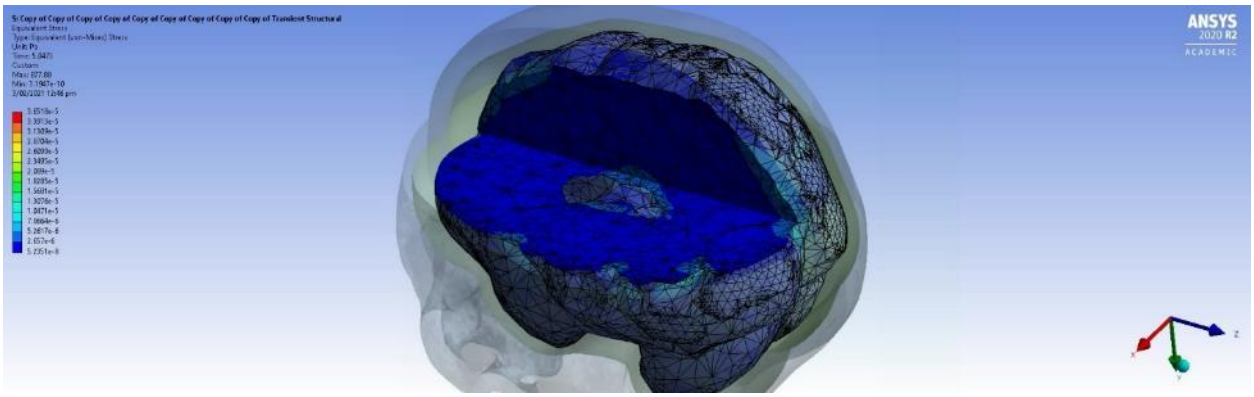
ANSYS
2020 R2
ACADEMIC

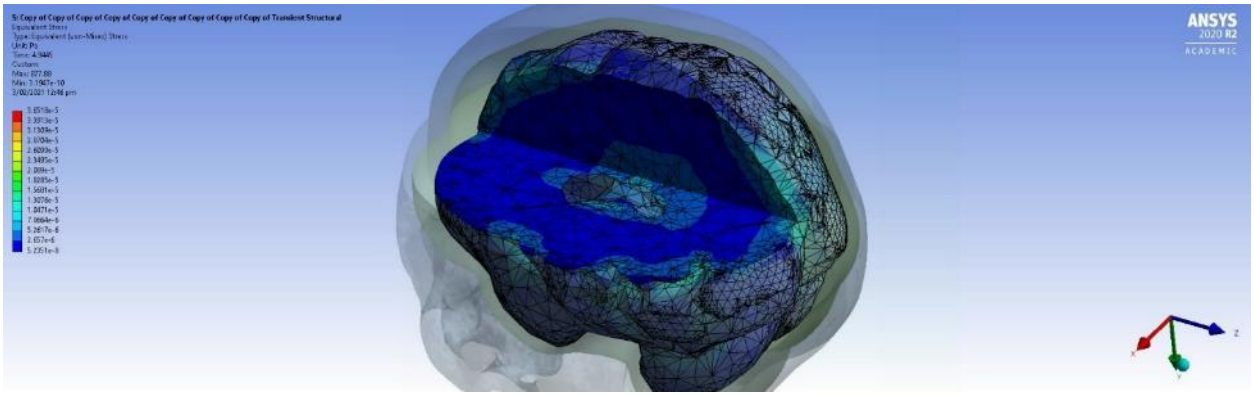
ANSYS
2020 R2
ACADEMIC

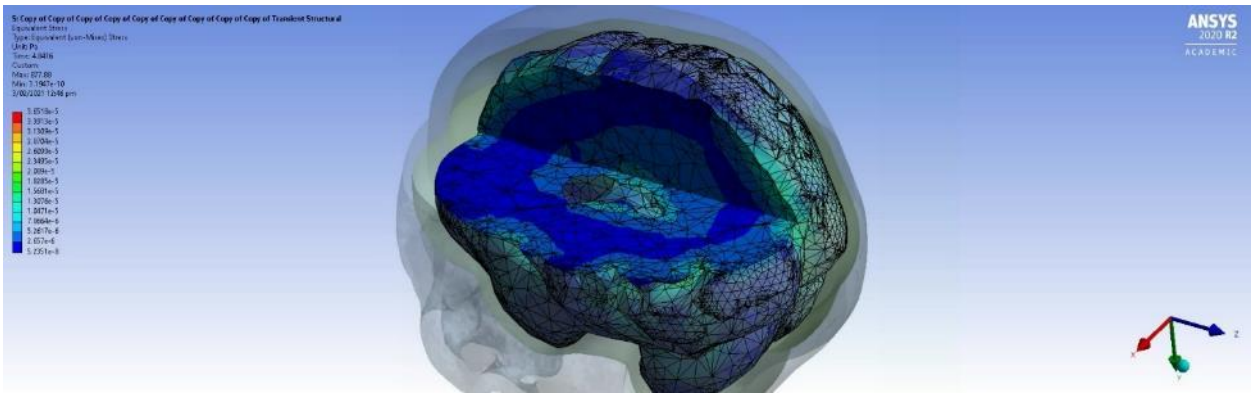
ANSYS
2020 R2
ACADEMIC

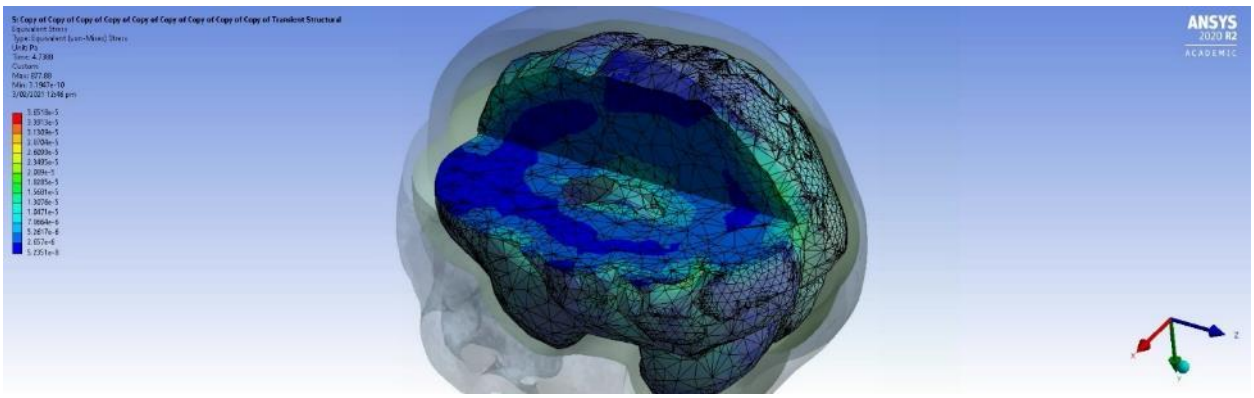
ANSYS
2020 R2
ACADEMIC

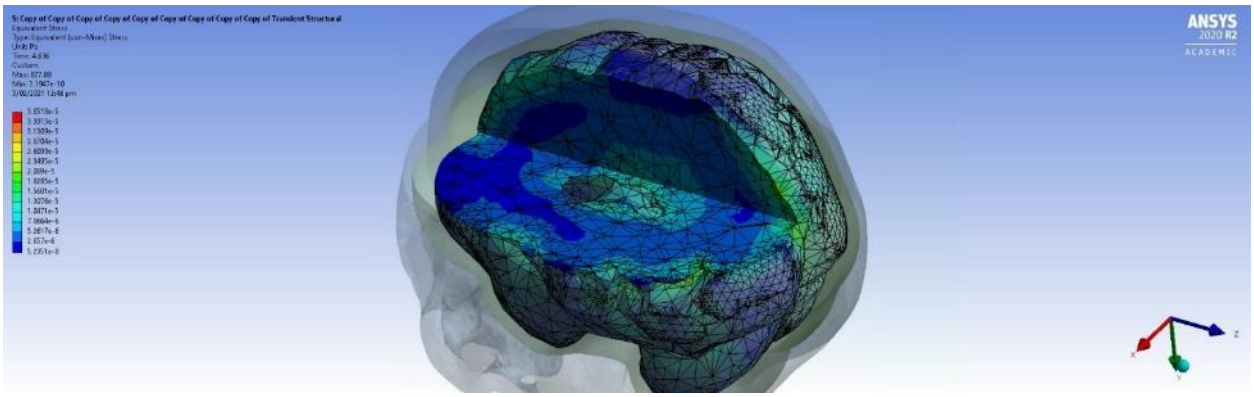
ANSYS
2020 R2
ACADEMIC

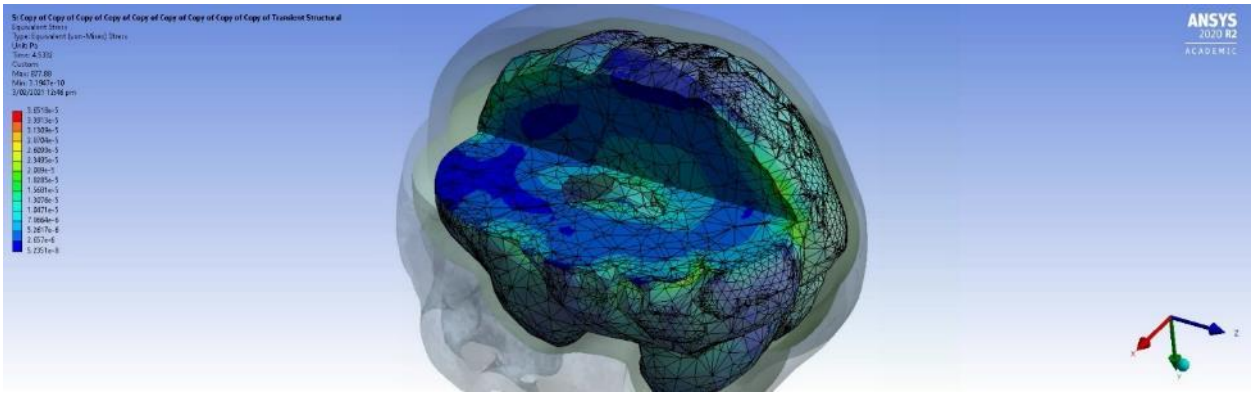
ANSYS
2020 R2
ACADEMIC

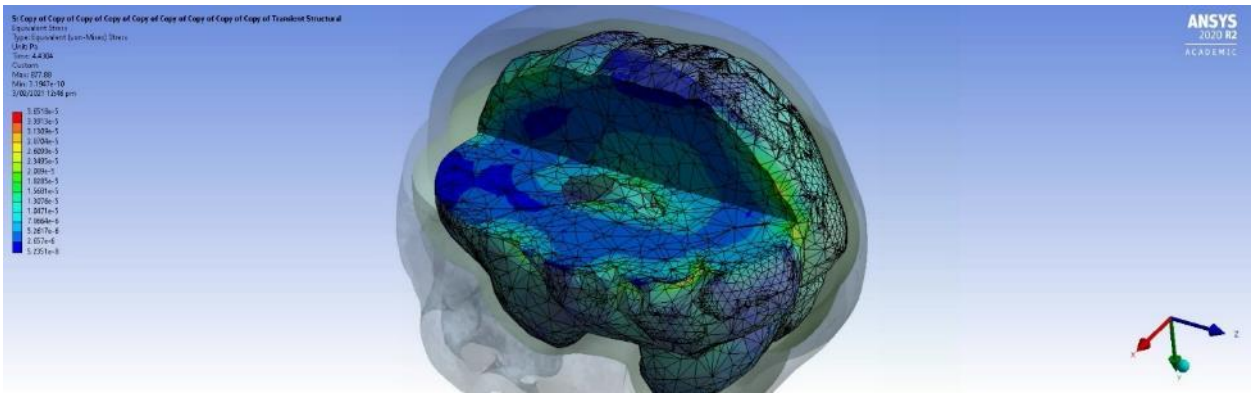
ANSYS
2020 R2
ACADEMIC

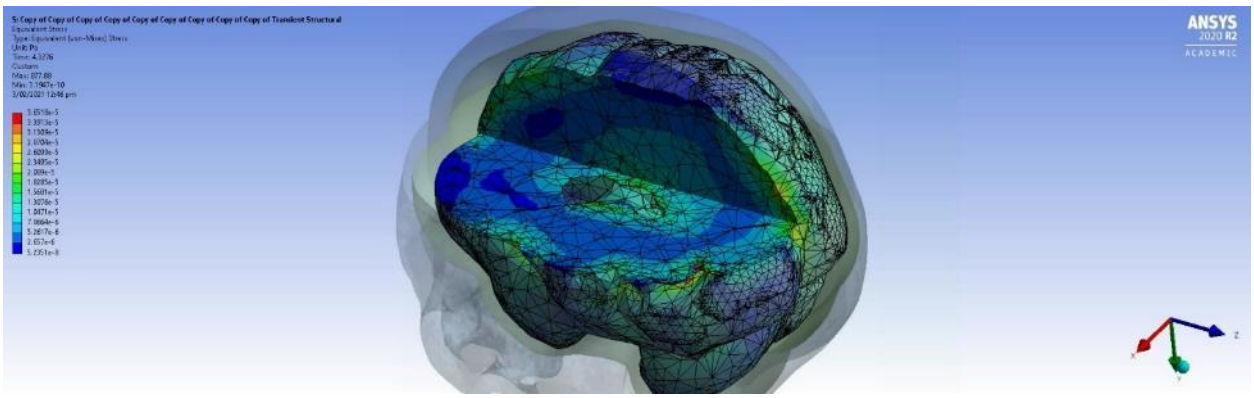
ANSYS
2020 R2
ACADEMIC

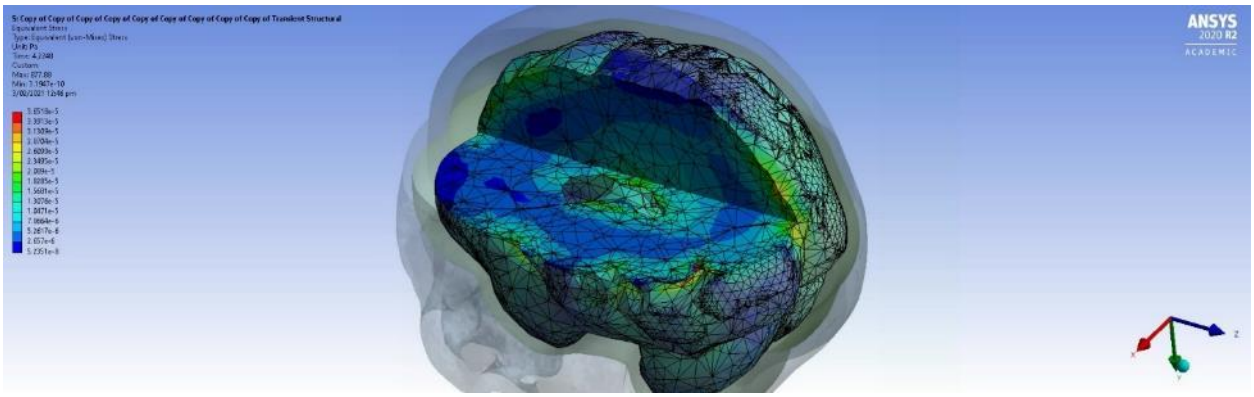
ANSYS
2020 R2
ACADEMIC

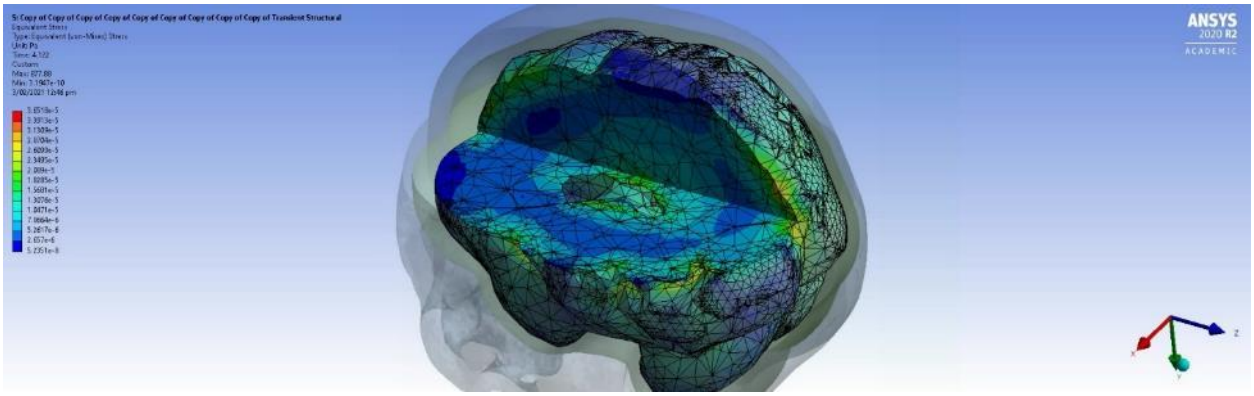
ANSYS
2020 R2
ACADEMIC

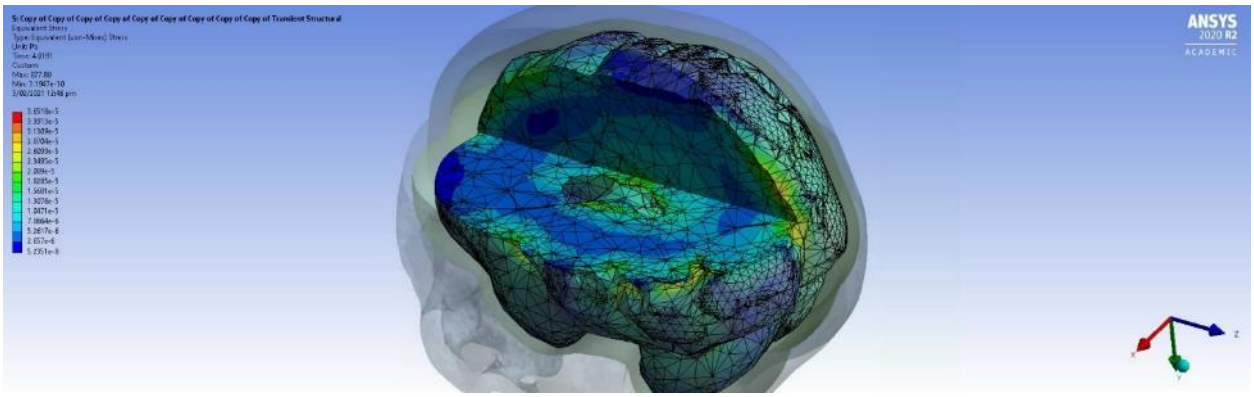
ANSYS
2020 R2
ACADEMIC

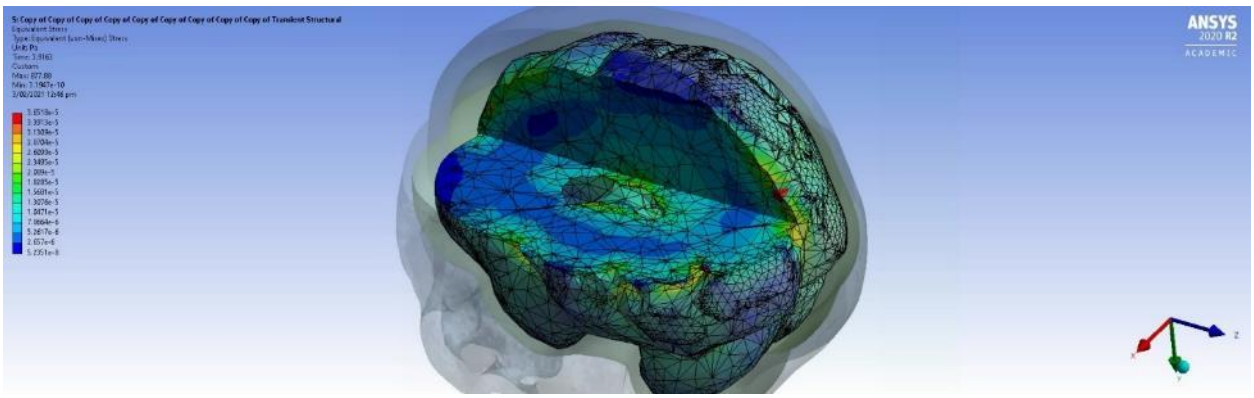
ANSYS
2020 R2
ACADEMIC

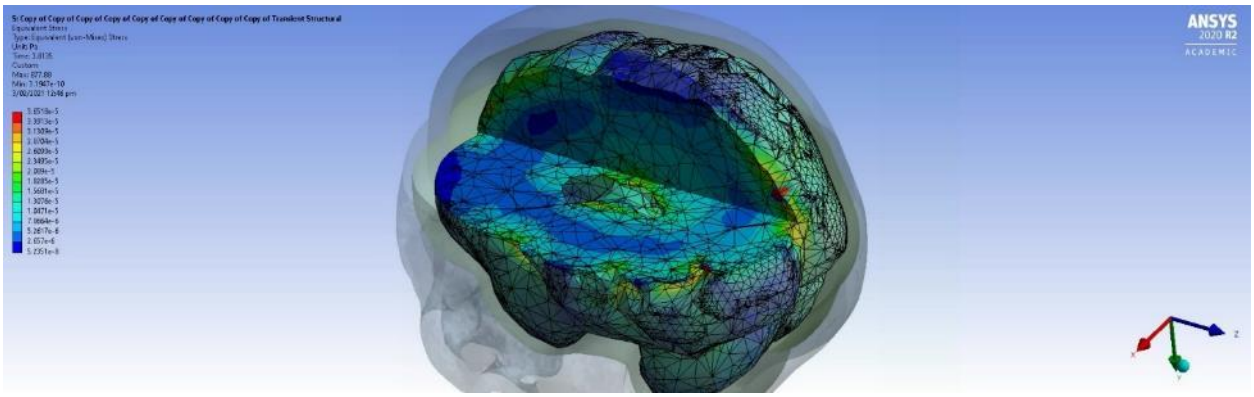
ANSYS
2020 R2
ACADEMIC

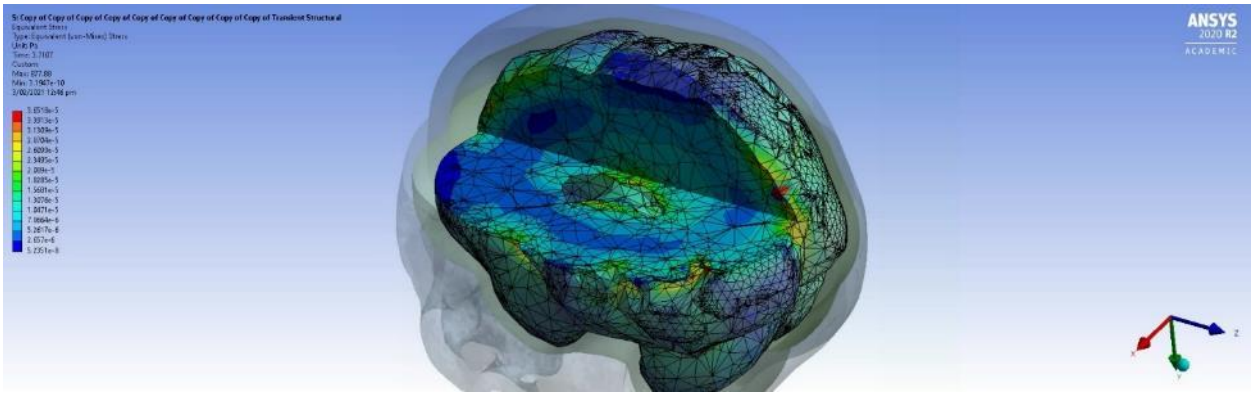
ANSYS
2020 R2
ACADEMIC

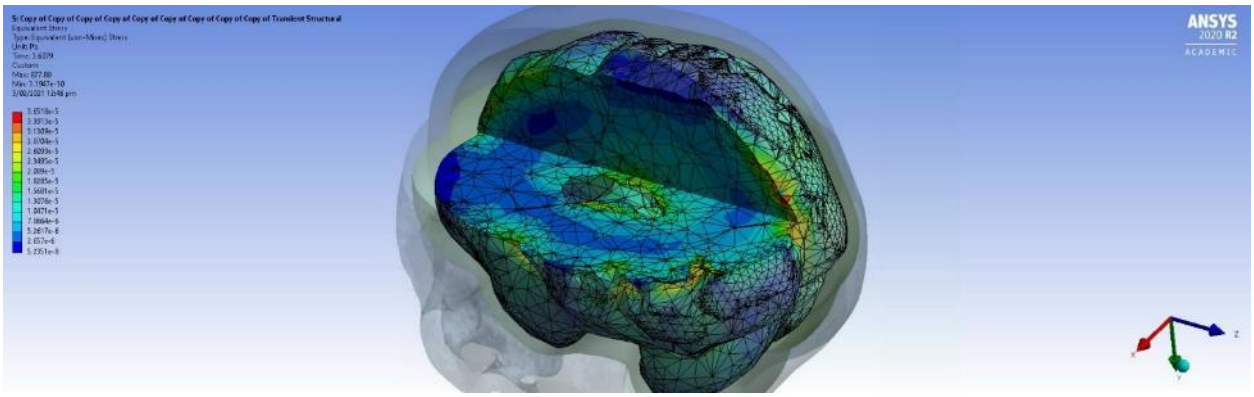
ANSYS
2020 R2
ACADEMIC

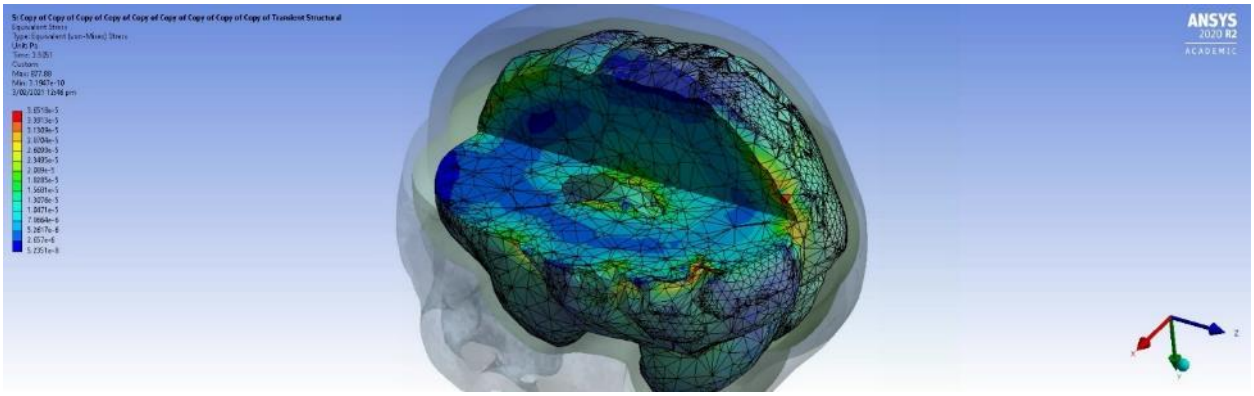
ANSYS
2020 R2
ACADEMIC

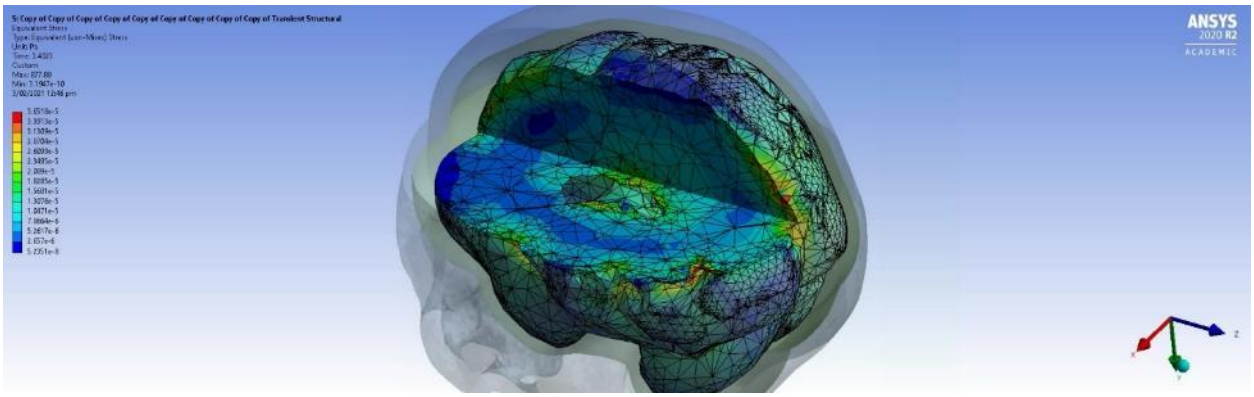
ANSYS
2020 R2
ACADEMIC

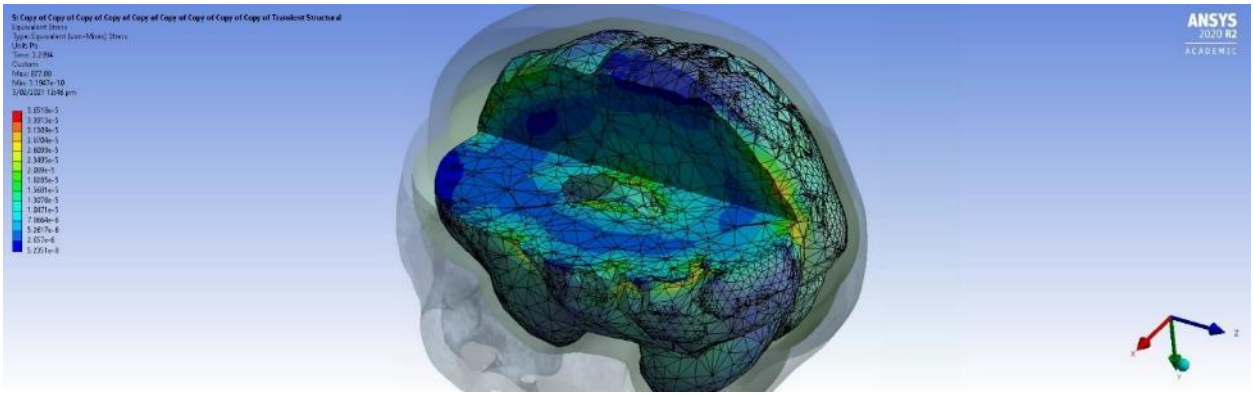
ANSYS
2020 R2
ACADEMIC

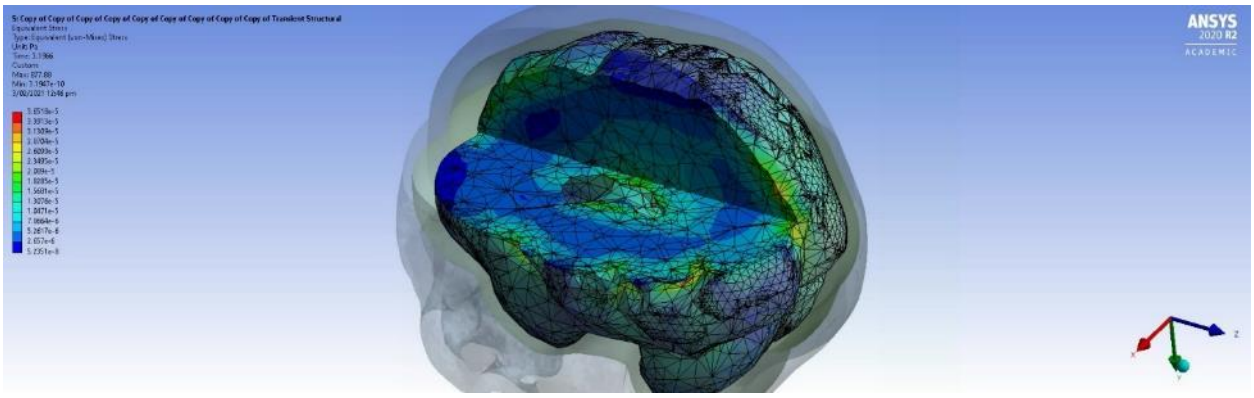
ANSYS
2020 R2
ACADEMIC

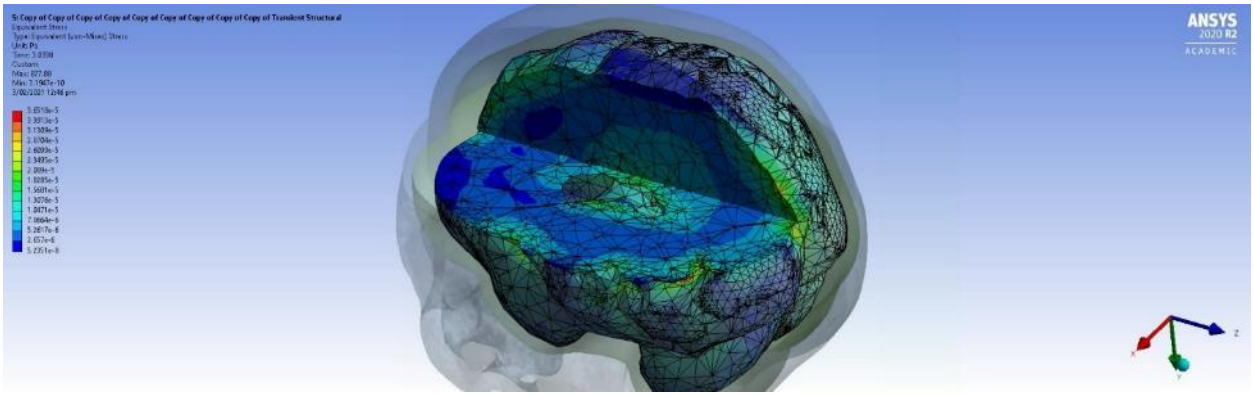
ANSYS
2020 R2
ACADEMIC

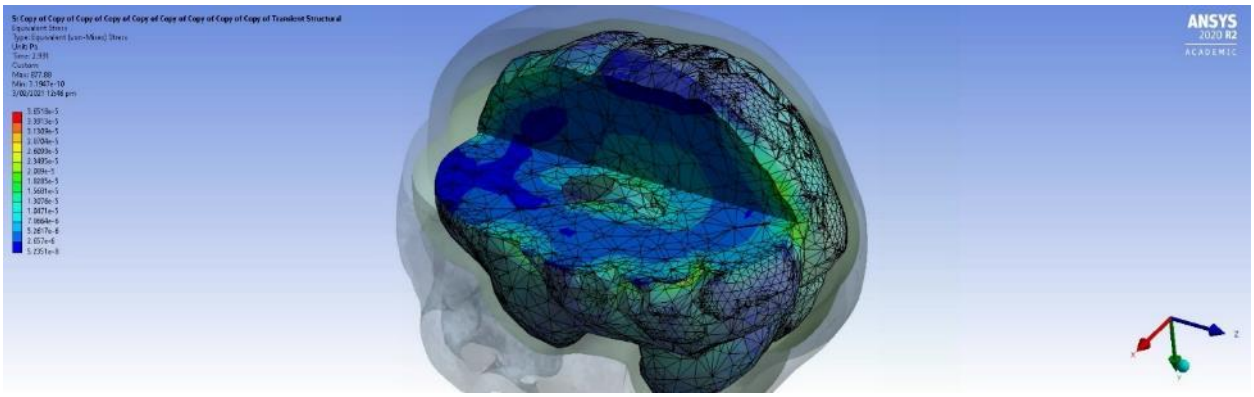
ANSYS
2020 R2
ACADEMIC

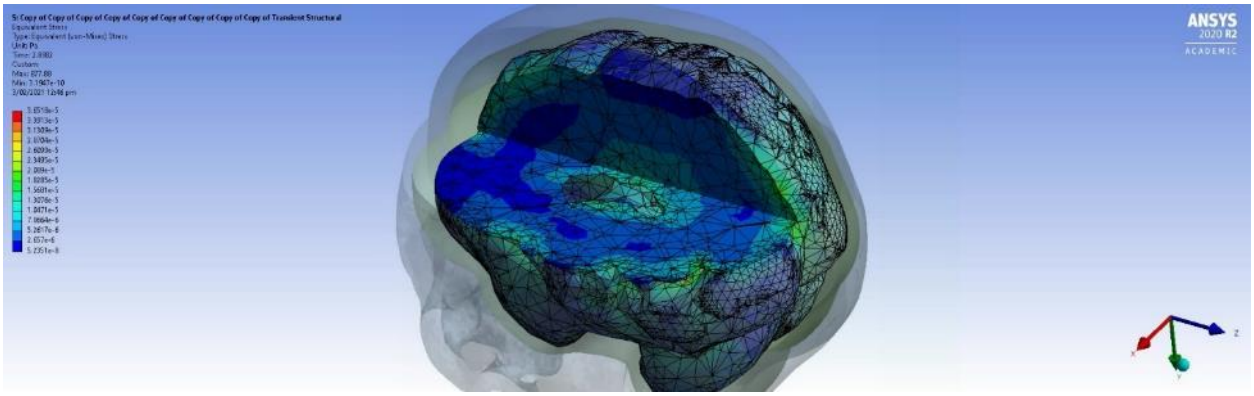
ANSYS
2020 R2
ACADEMIC

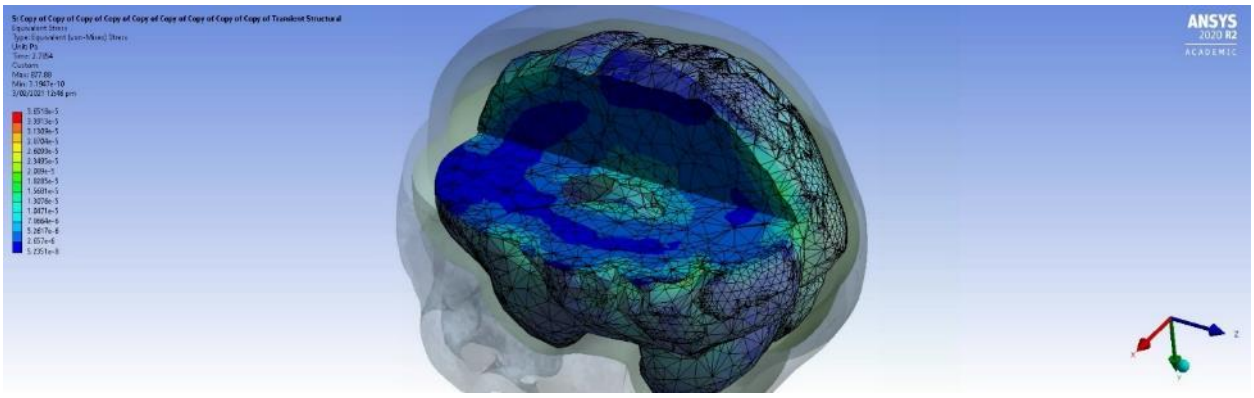
ANSYS
2020 R2
ACADEMIC

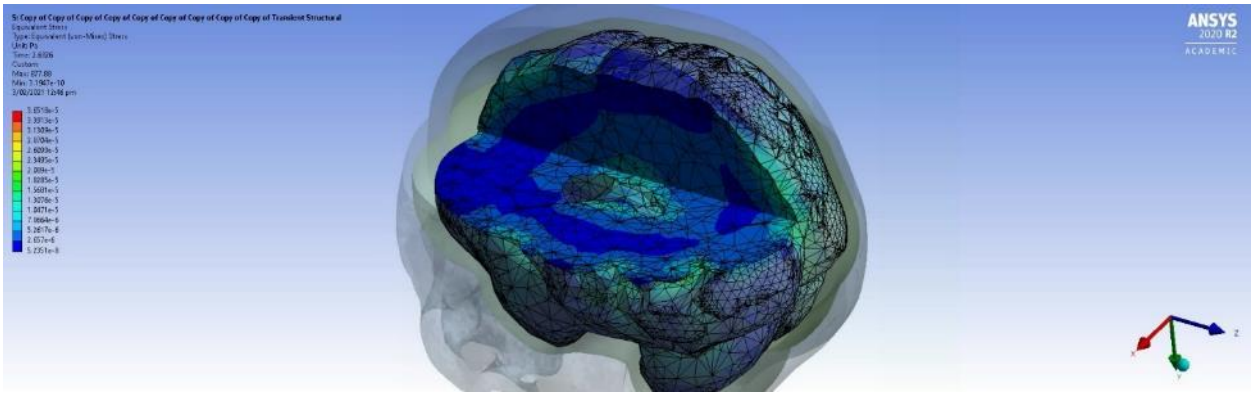
ANSYS
2020 R2
ACADEMIC

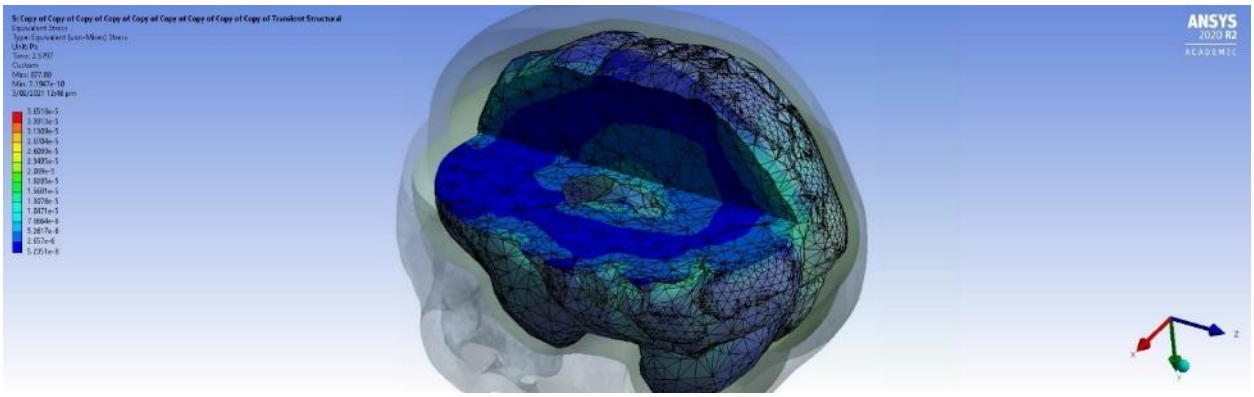
ANSYS
2020 R2
ACADEMIC

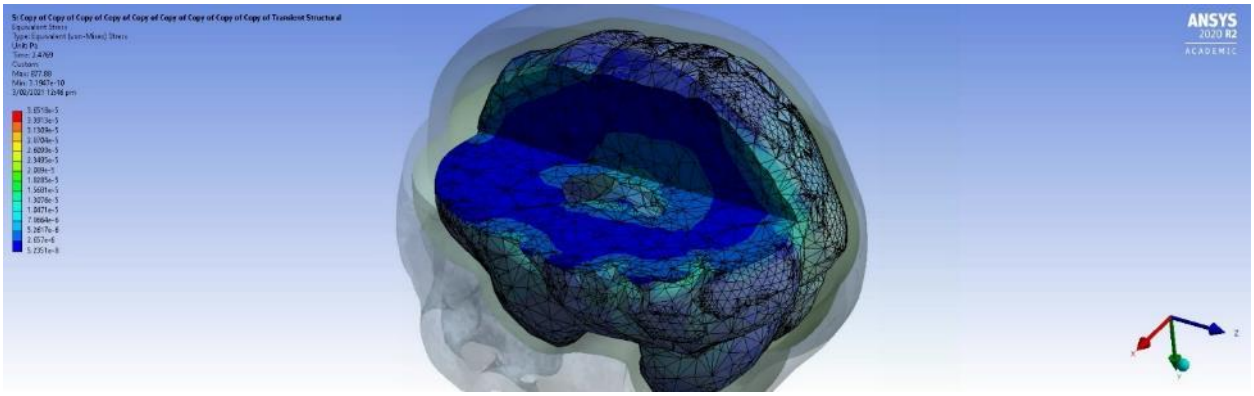
ANSYS
2020 R2
ACADEMIC

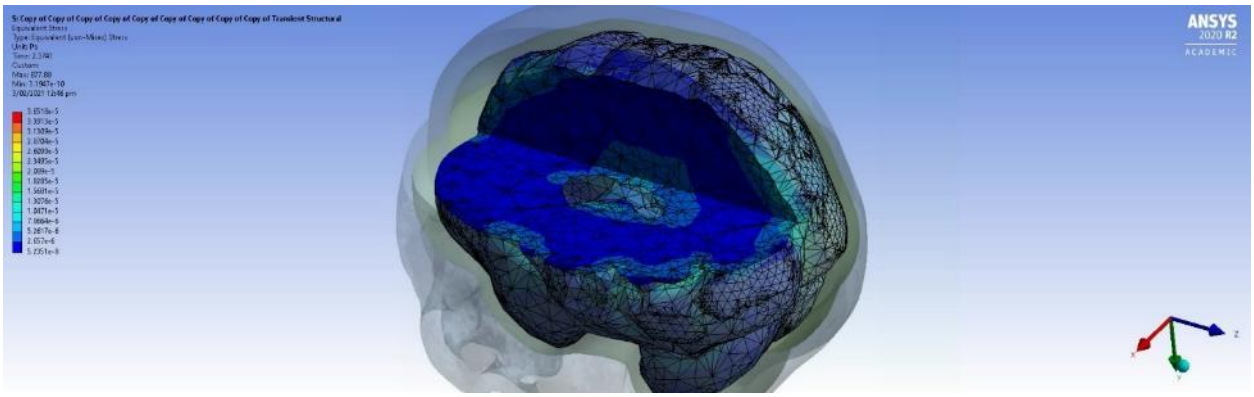
ANSYS
2020 R2
ACADEMIC

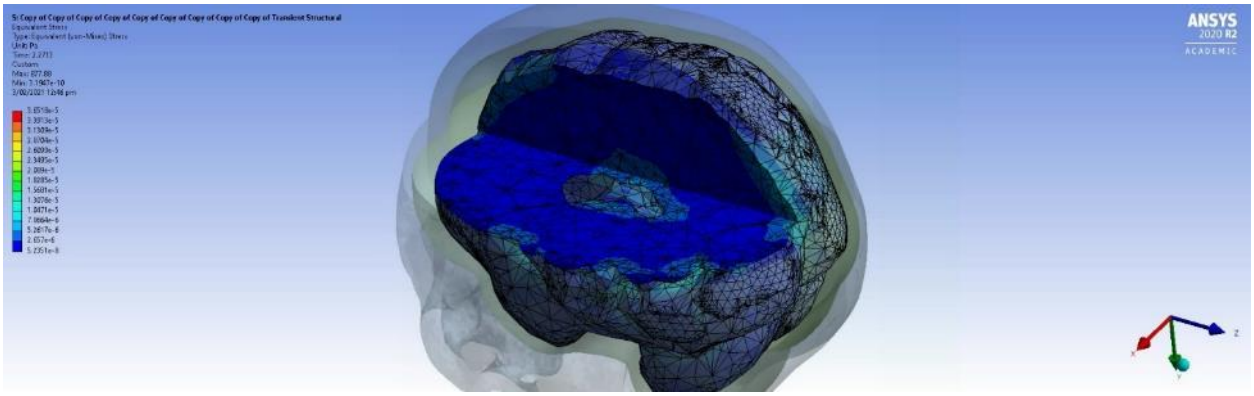
ANSYS
2020 R2
ACADEMIC

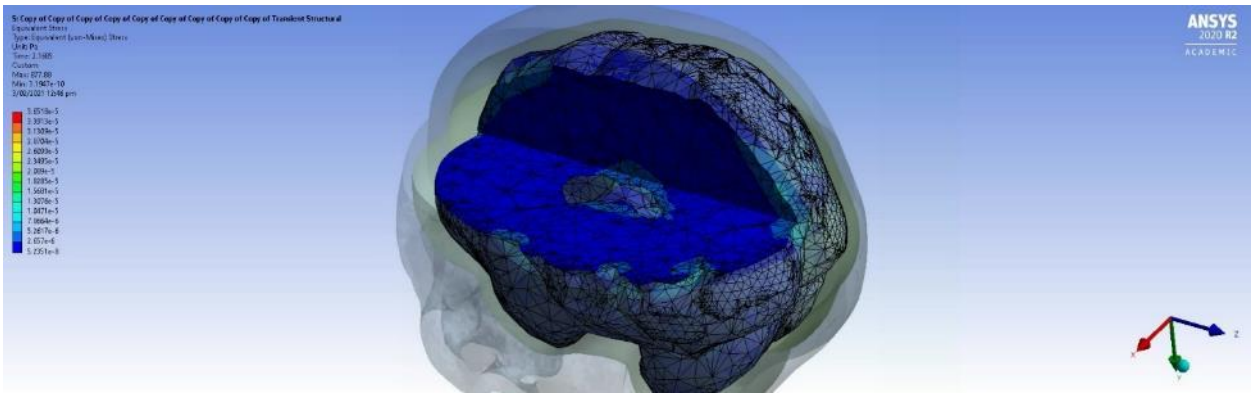
ANSYS
2020 R2
ACADEMIC

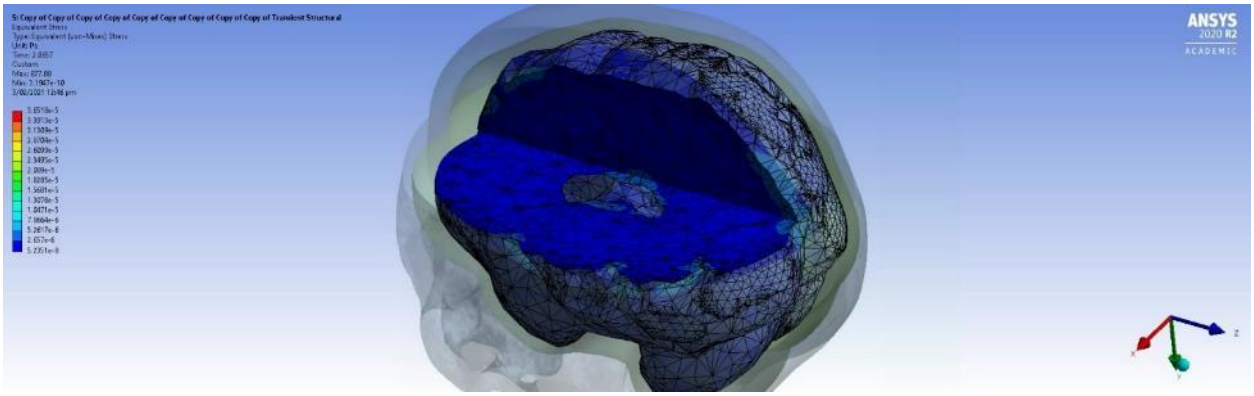
ANSYS
2020 R2
ACADEMIC

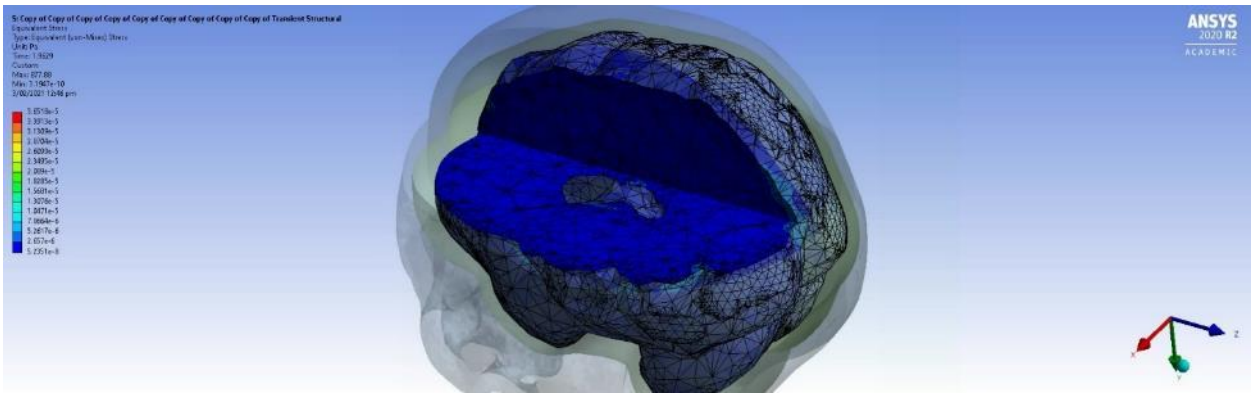
ANSYS
2020 R2
ACADEMIC

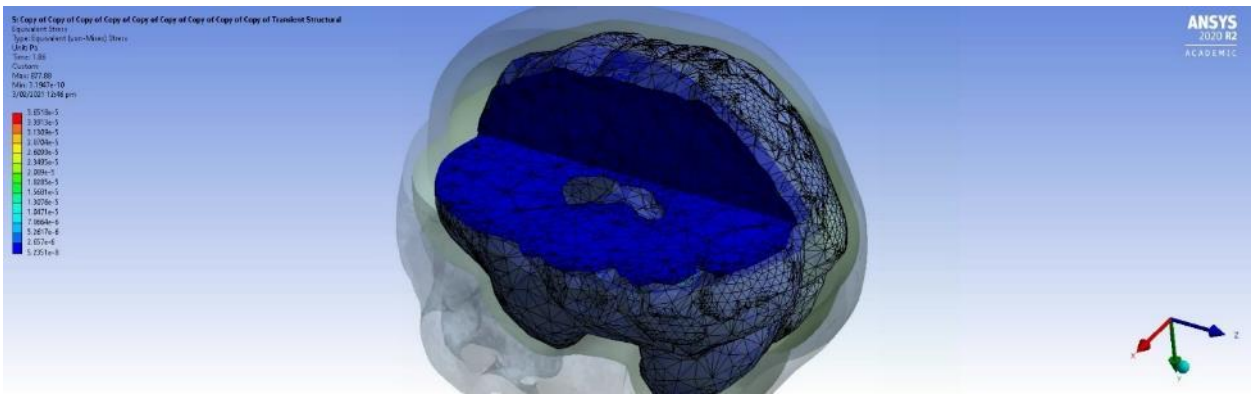
ANSYS
2020 R2
ACADEMIC

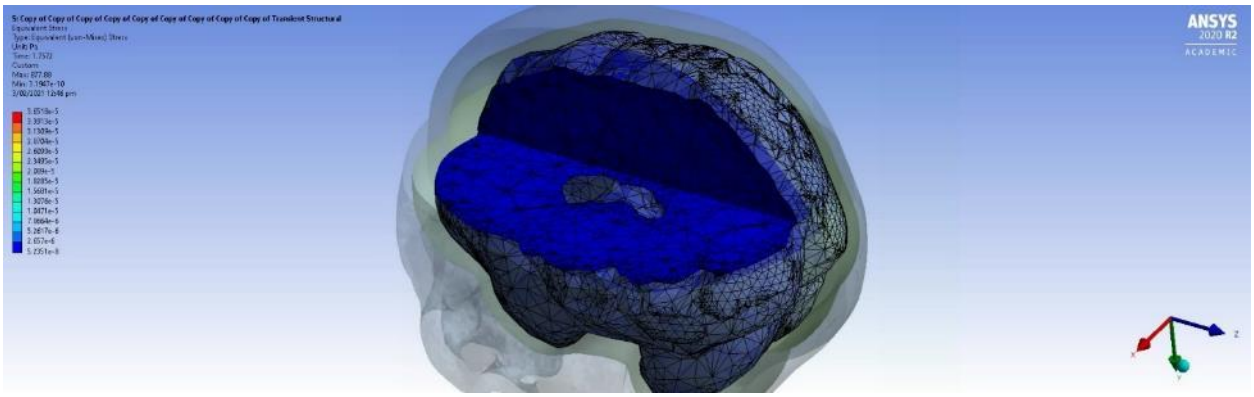
ANSYS
2020 R2
ACADEMIC

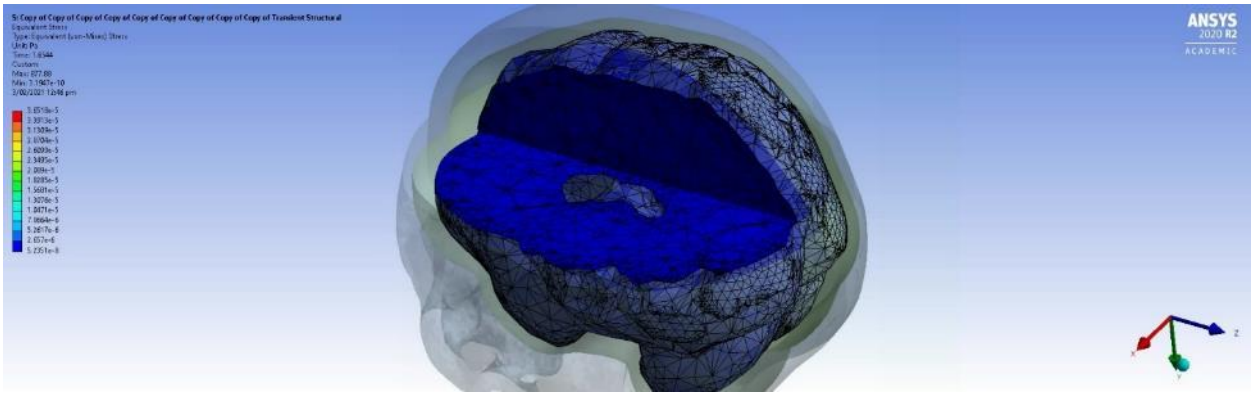
ANSYS
2020 R2
ACADEMIC

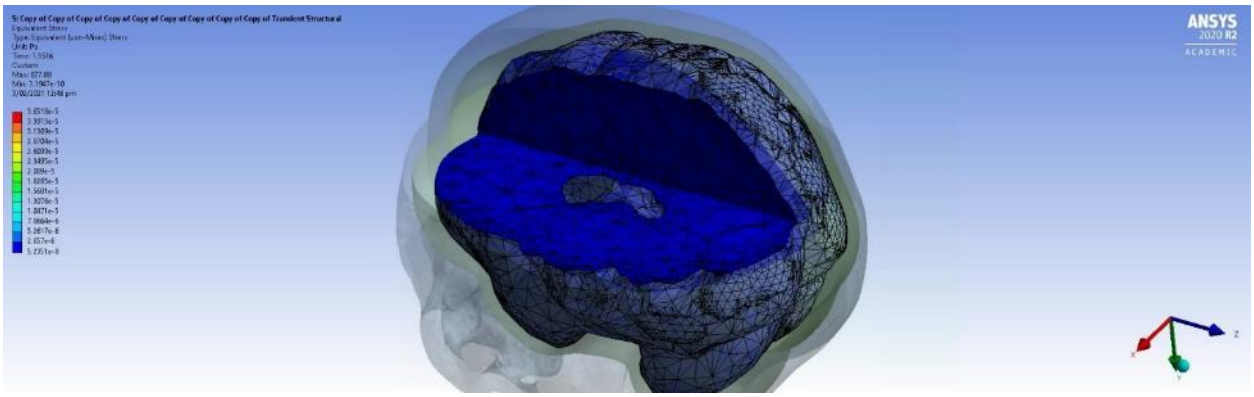
ANSYS
2020 R2
ACADEMIC

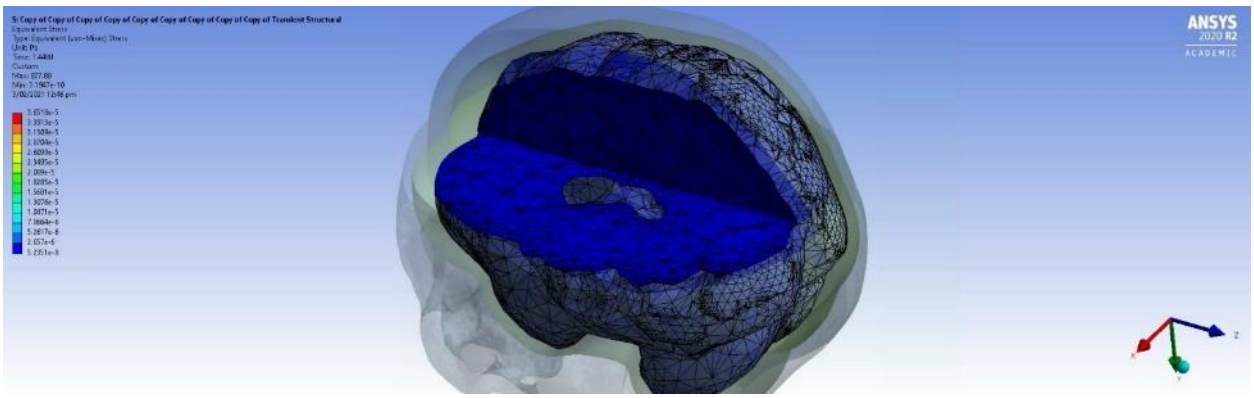
ANSYS
2020 R2
ACADEMIC

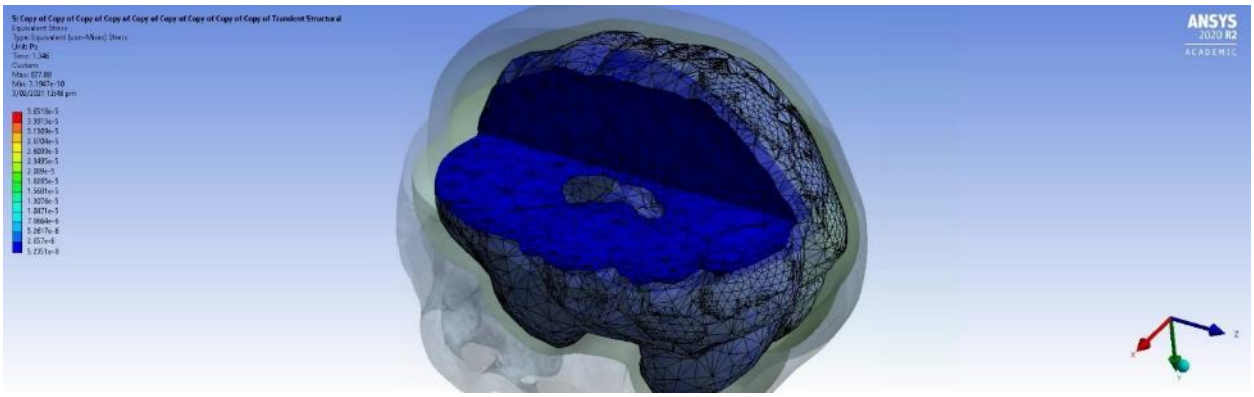
ANSYS
2020 R2
ACADEMIC

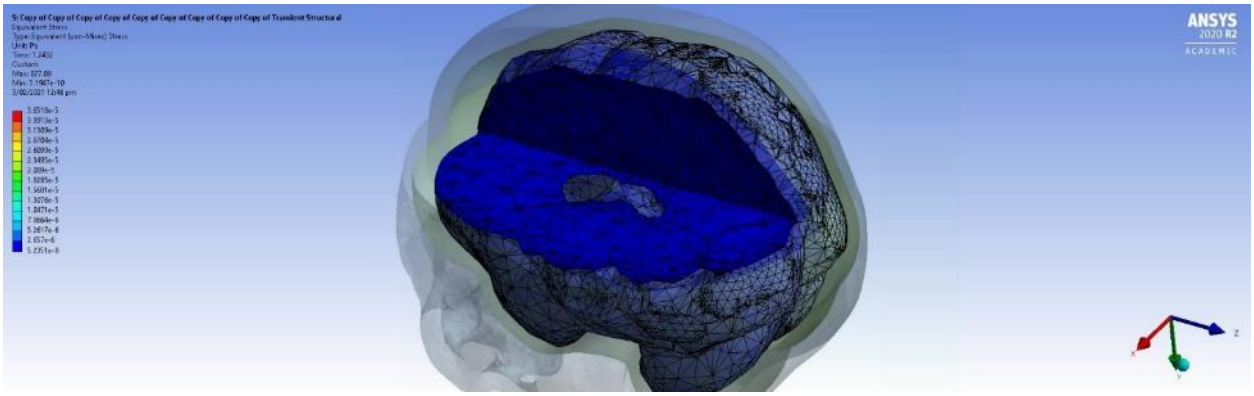
ANSYS
2020 R2
ACADEMIC

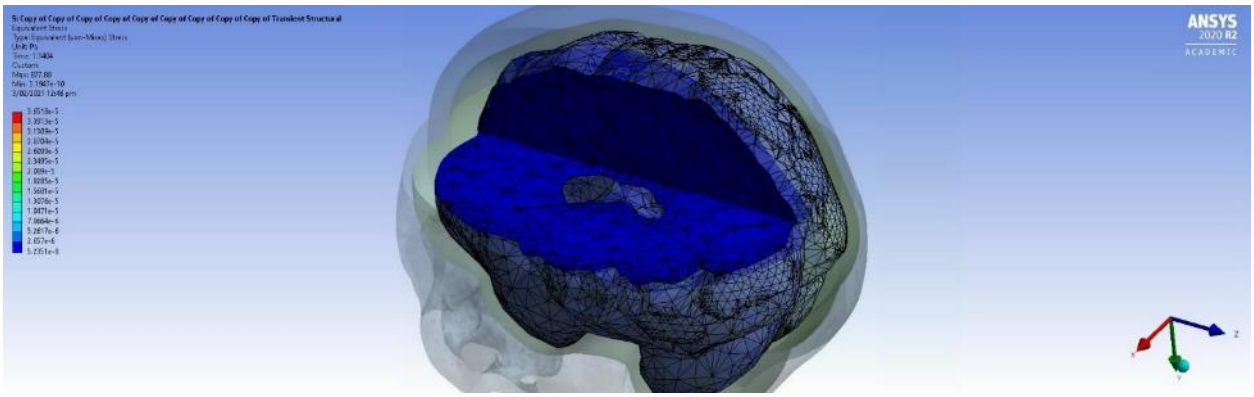
ANSYS
2020 R2
ACADEMIC

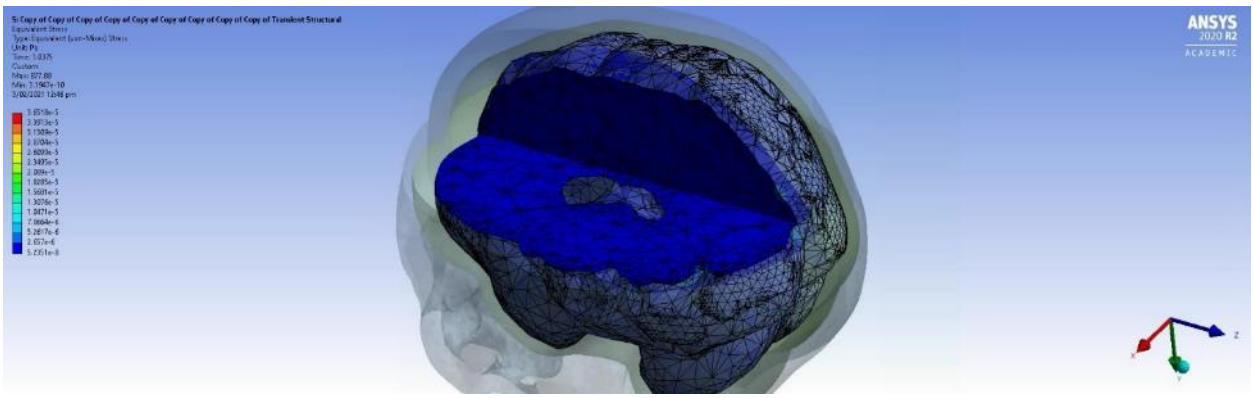
ANSYS
2020 R2
ACADEMIC

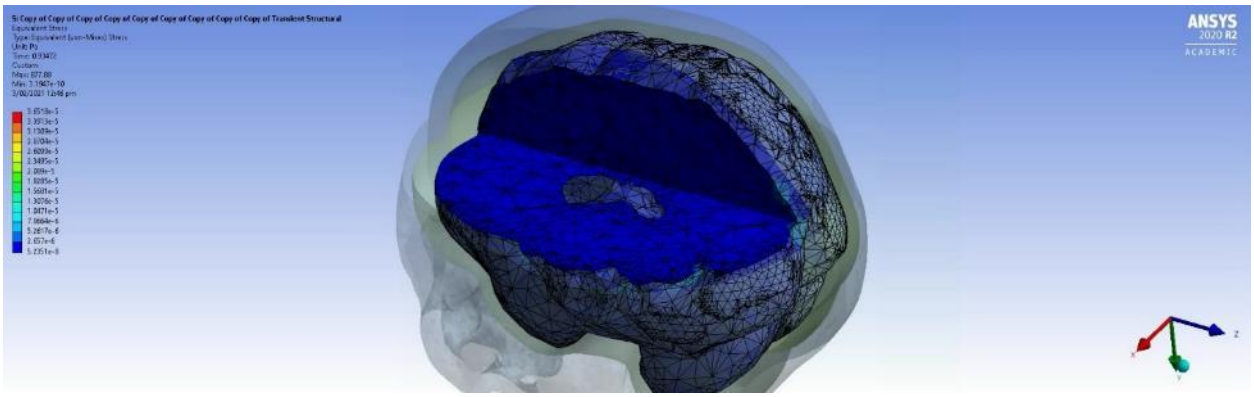
ANSYS
2020 R2
ACADEMIC

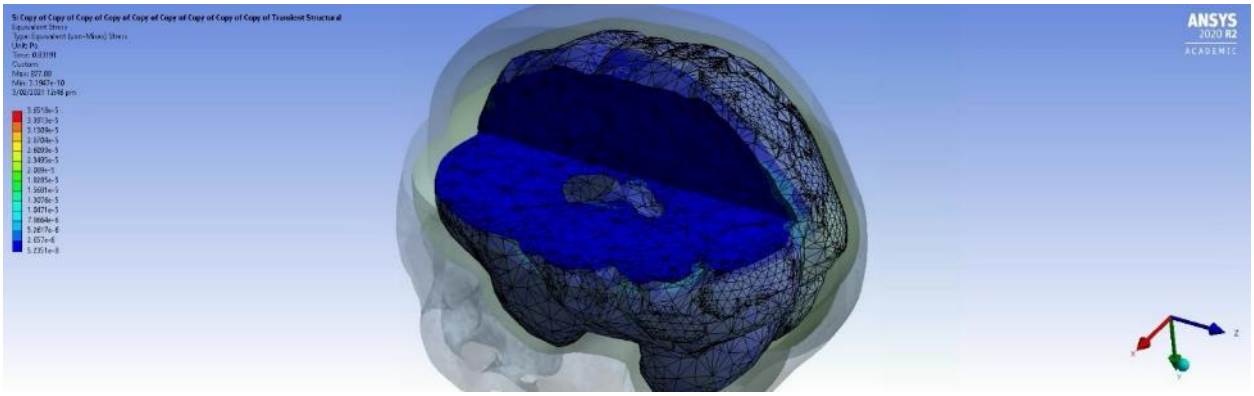
ANSYS
2020 R2
ACADEMIC

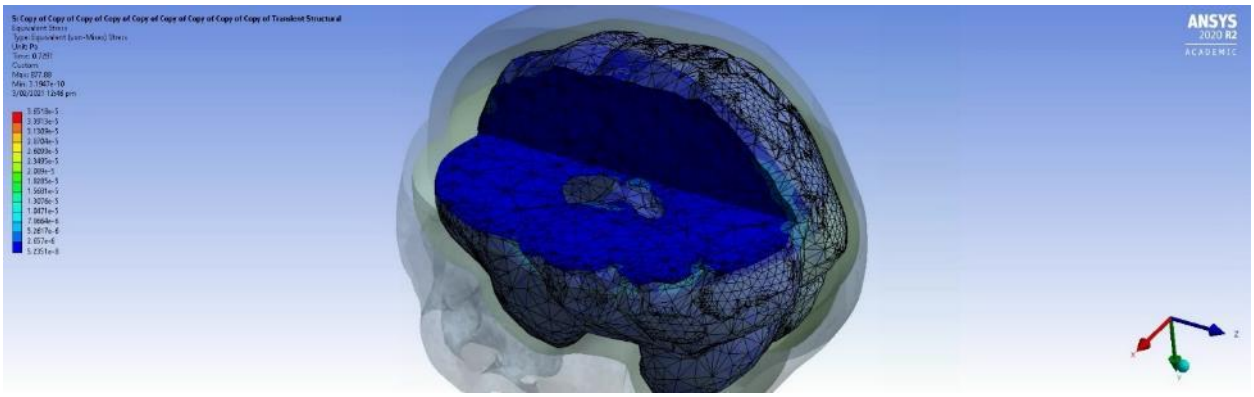
ANSYS
2020 R2
ACADEMIC

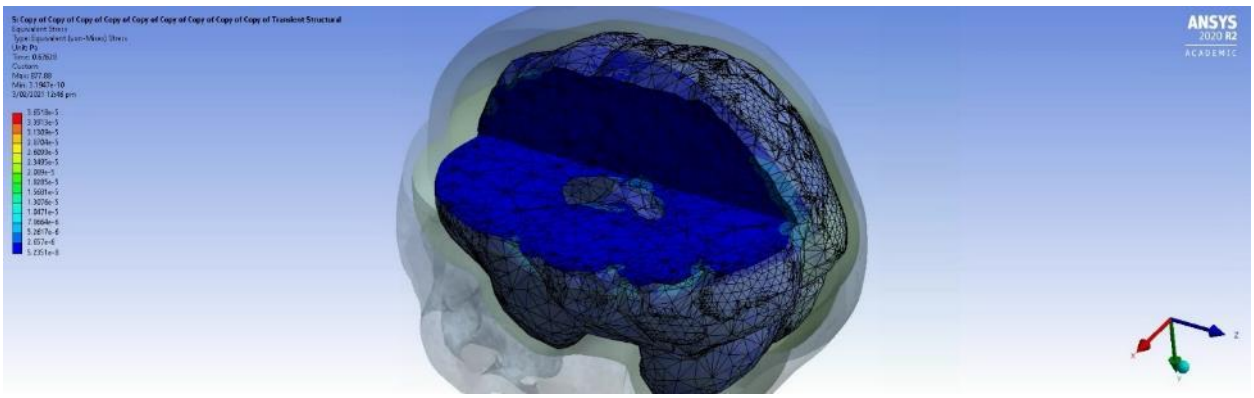
ANSYS
2020 R2
ACADEMIC

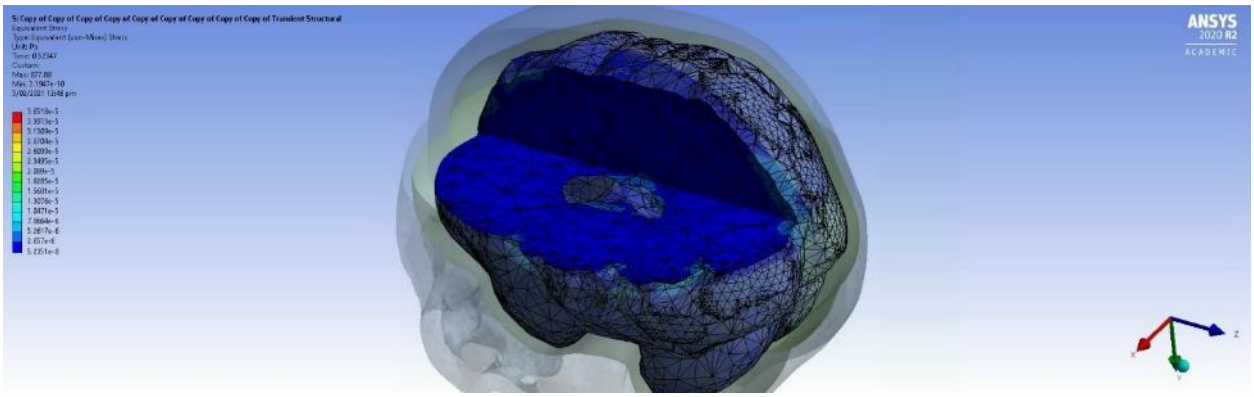
ANSYS
2020 R2
ACADEMIC

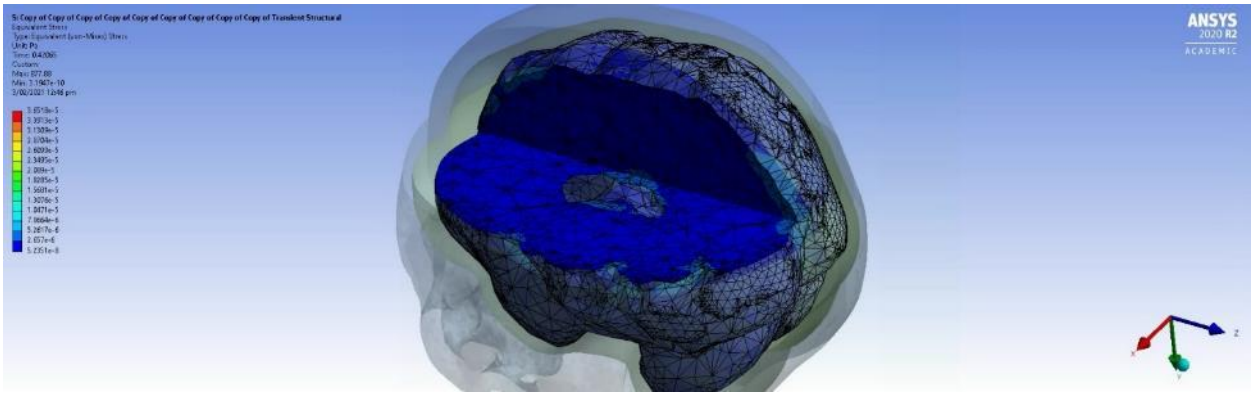
ANSYS
2020 R2
ACADEMIC

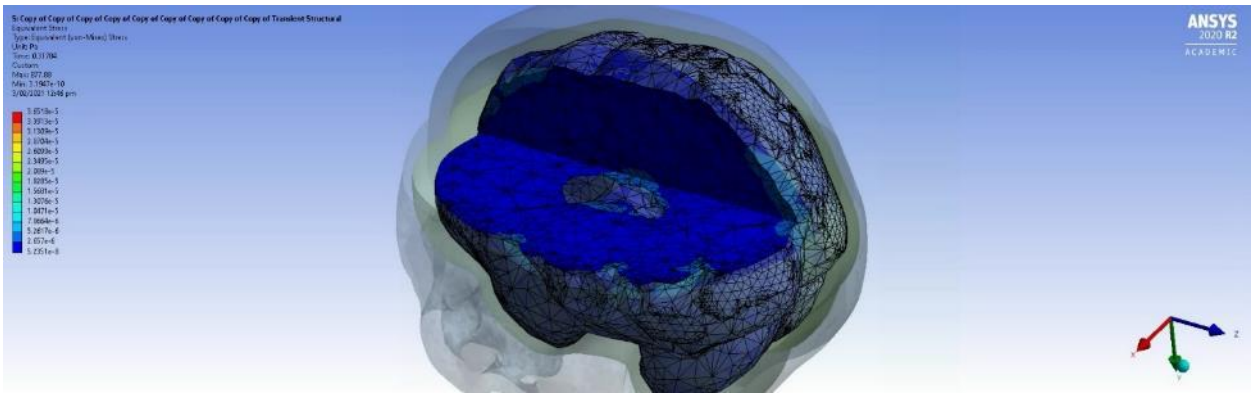
ANSYS
2020 R2
ACADEMIC

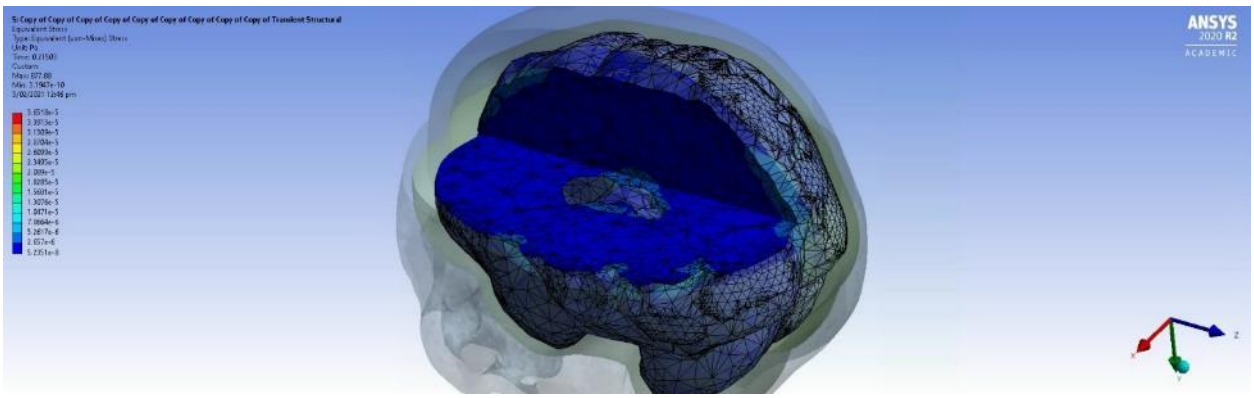
ANSYS
2020 R2
ACADEMIC

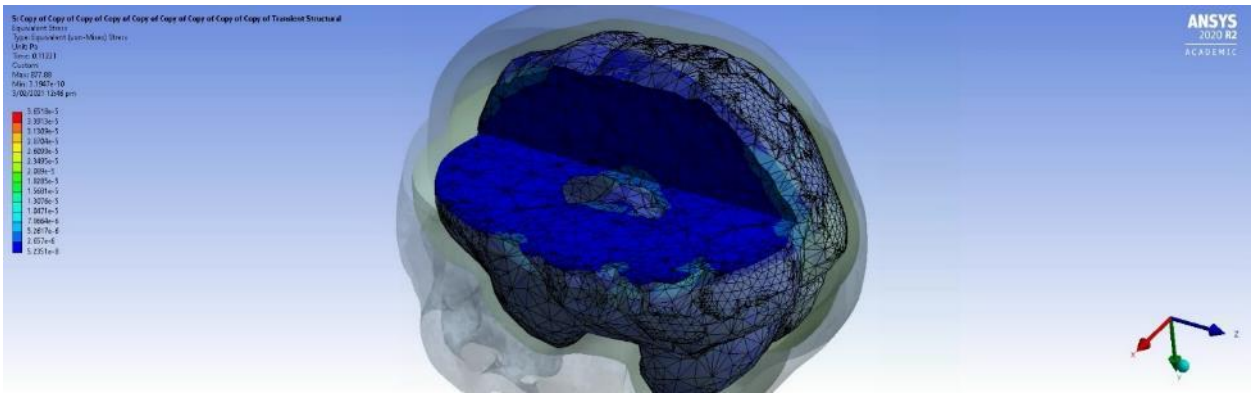
ANSYS
2020 R2
ACADEMIC

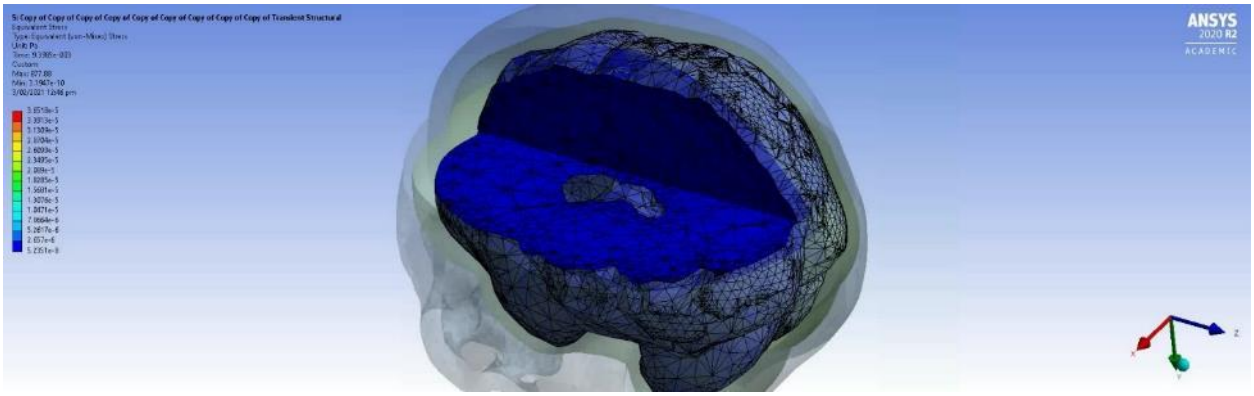

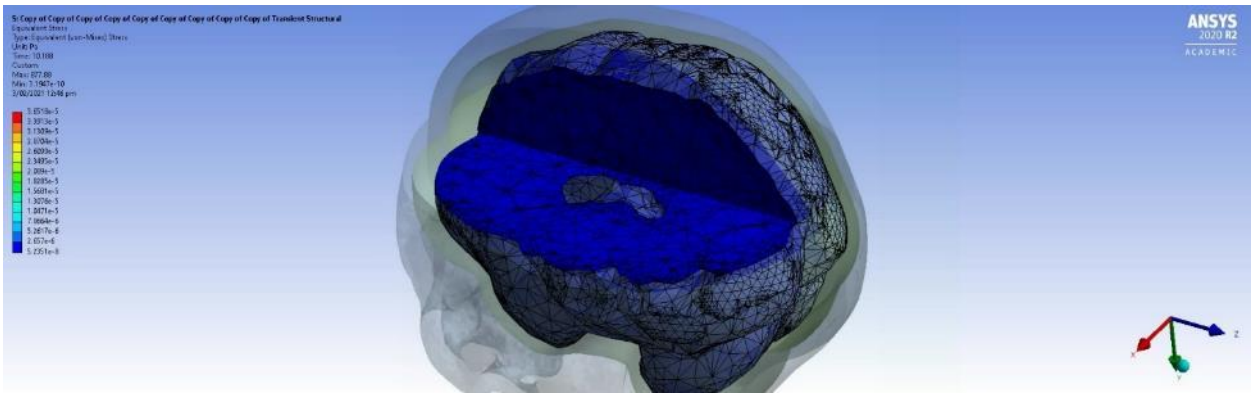

Impact Zone 9

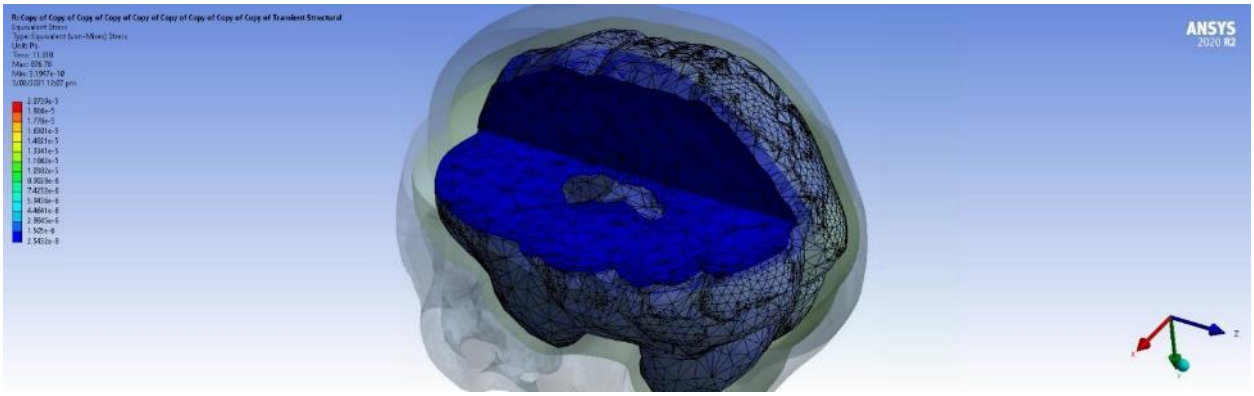

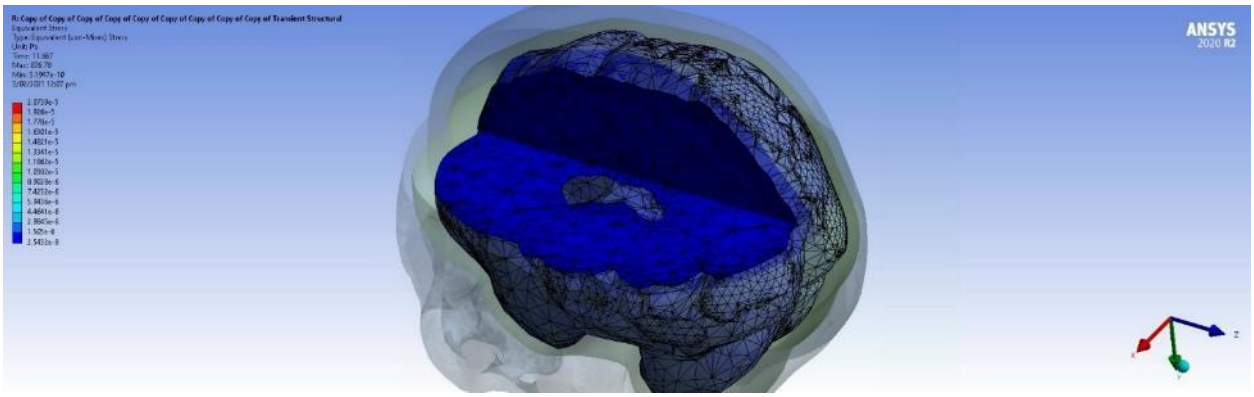

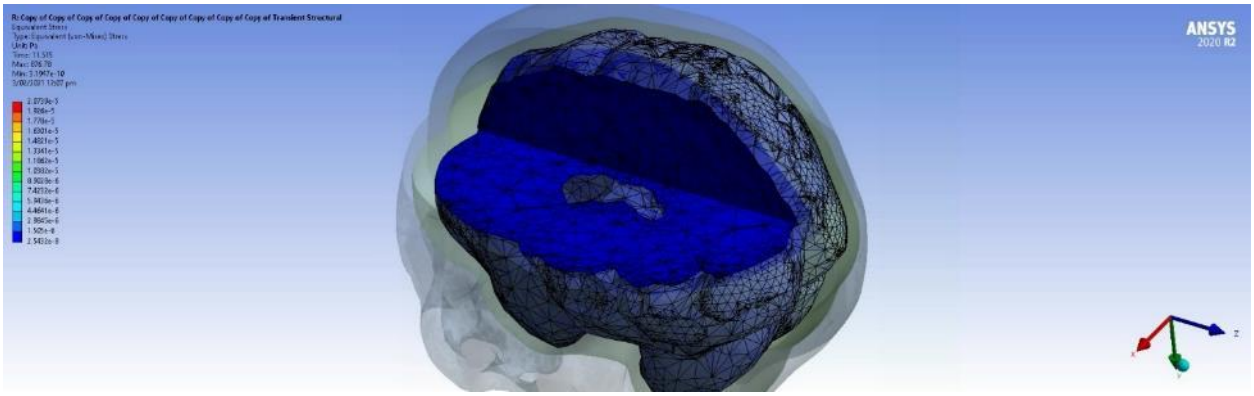
ANSYS
2020 R2

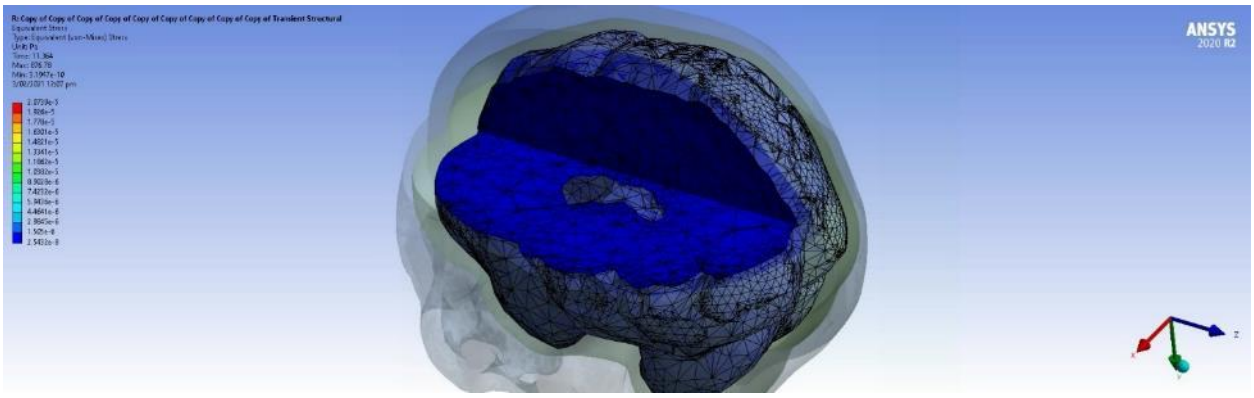
ANSYS
2020 R2

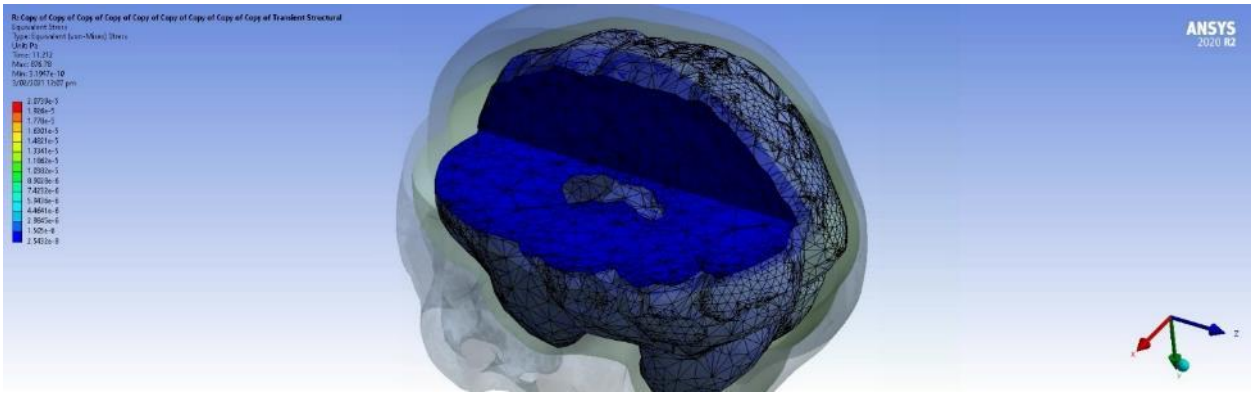
ANSYS
2020 R2

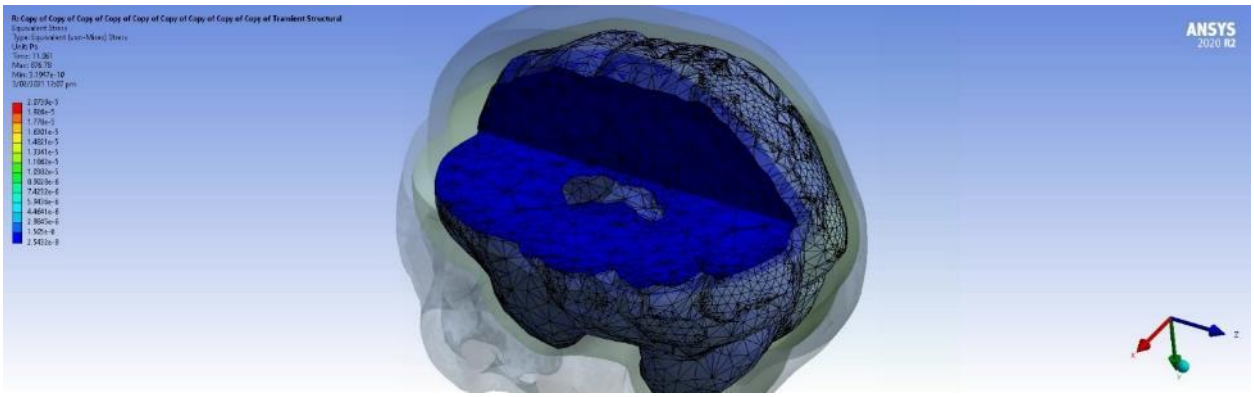
ANSYS
2020 R2

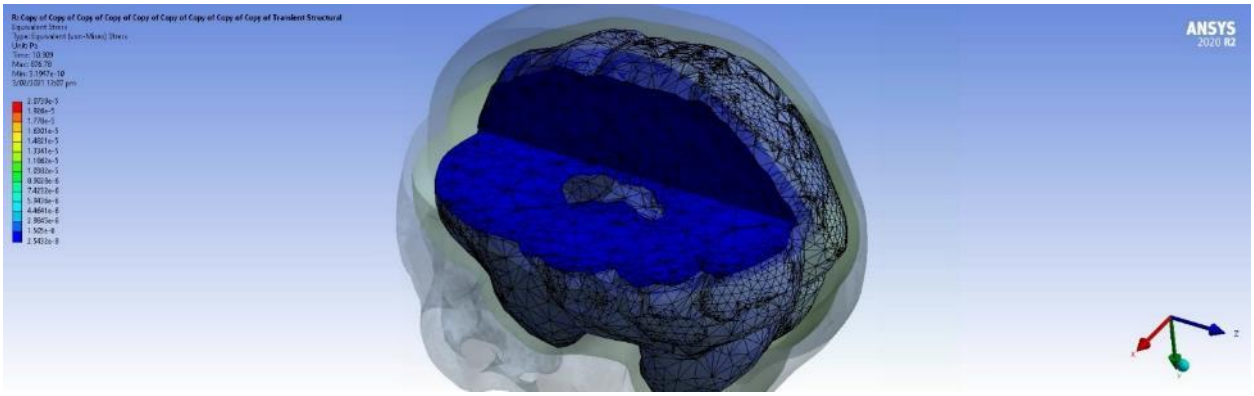
ANSYS
2020 R2

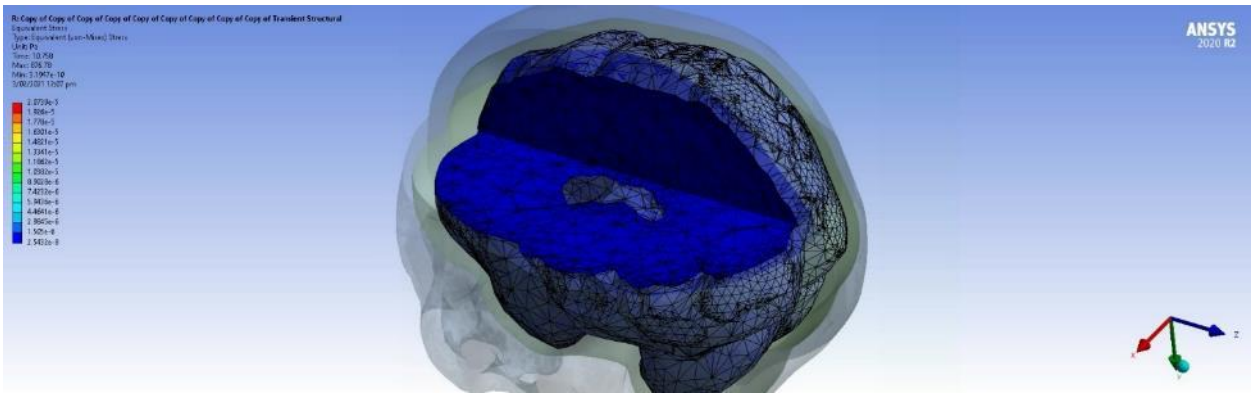
ANSYS
2020 R2

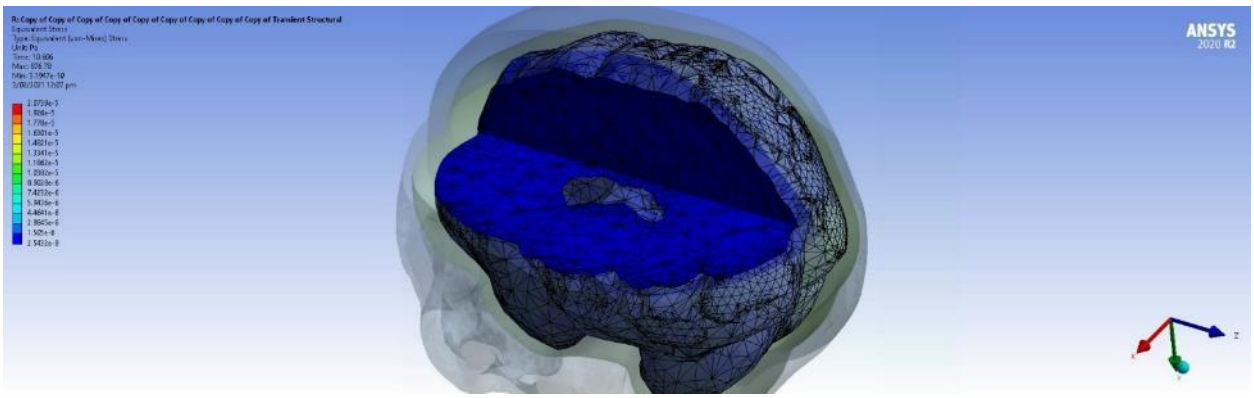
ANSYS
2020 R2

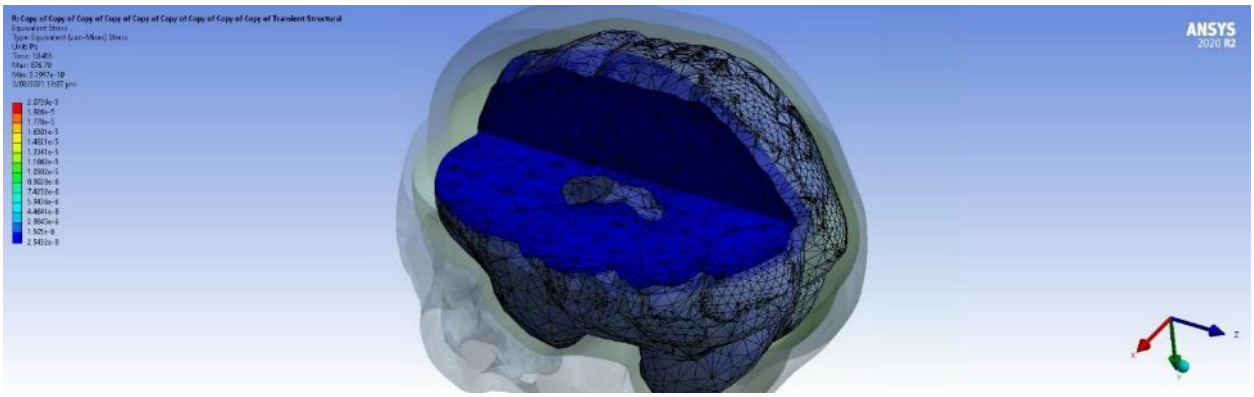
ANSYS
2020 R2

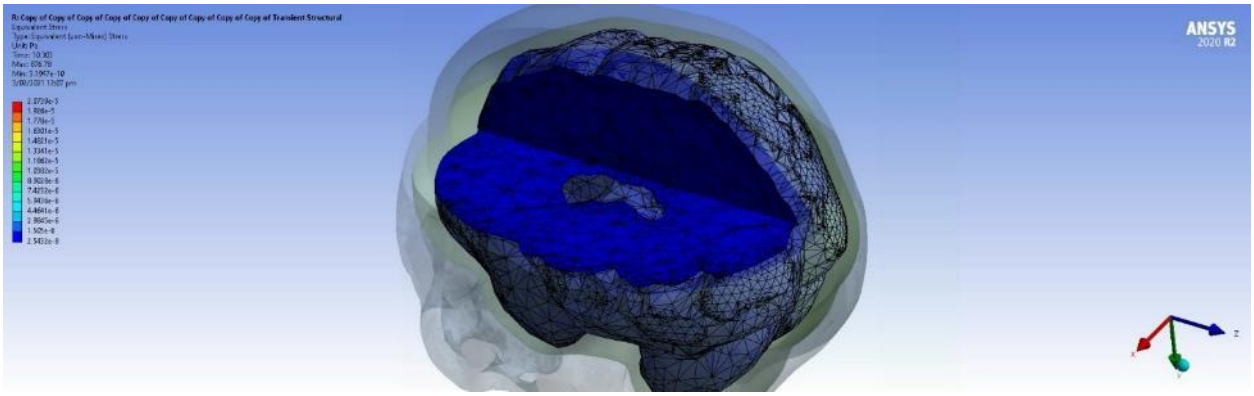
ANSYS
2020 R2

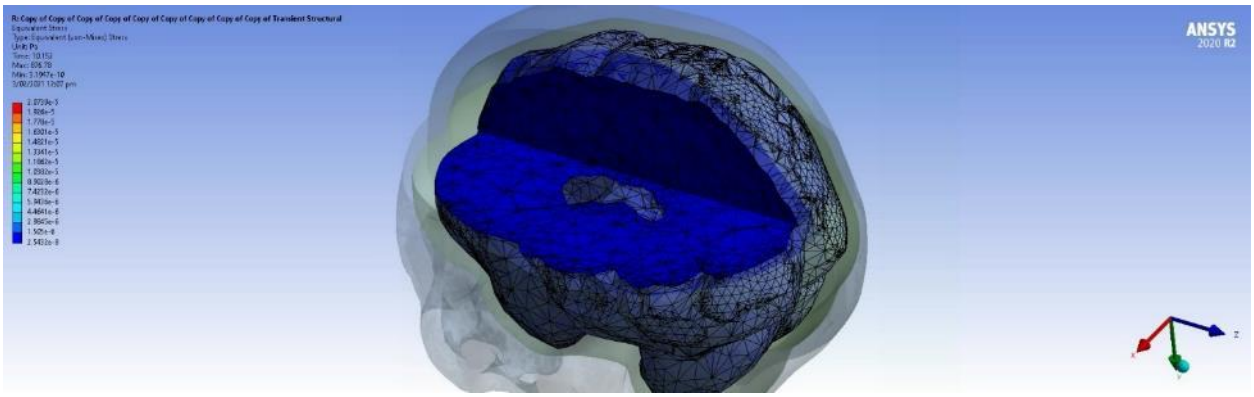
ANSYS
2020 R2

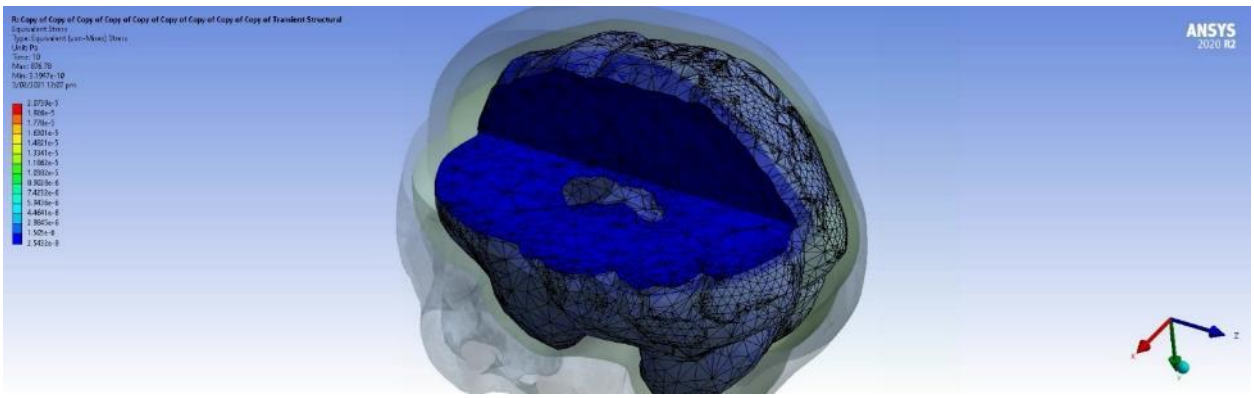
ANSYS
2020 R2

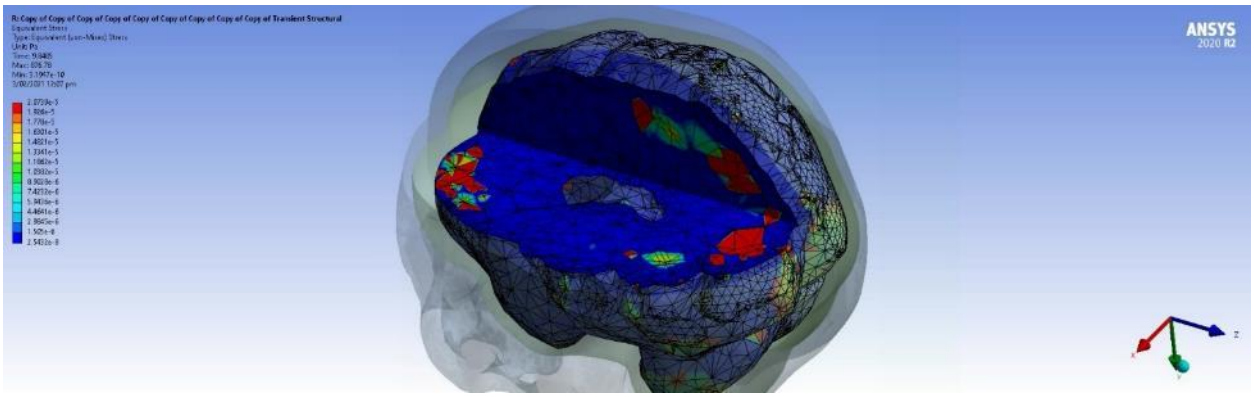
ANSYS
2020 R2

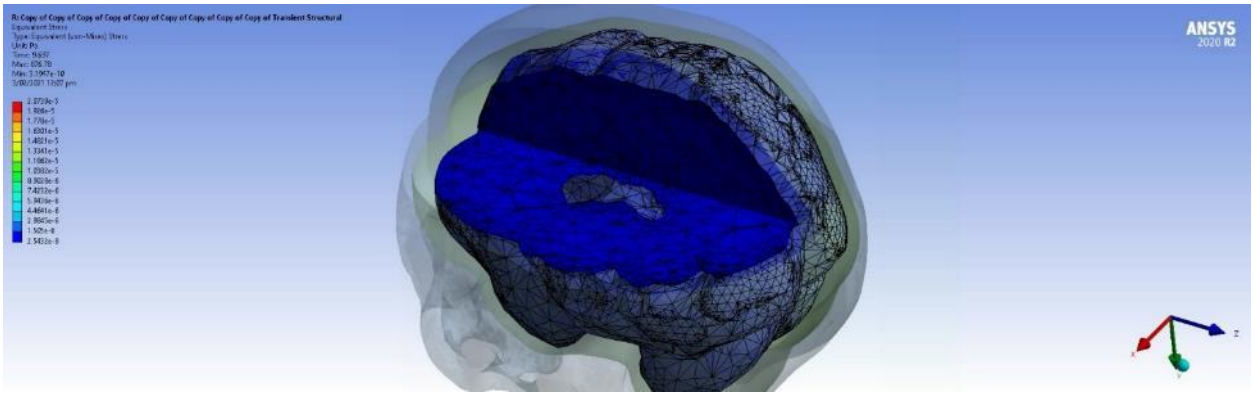
ANSYS
2020 R2

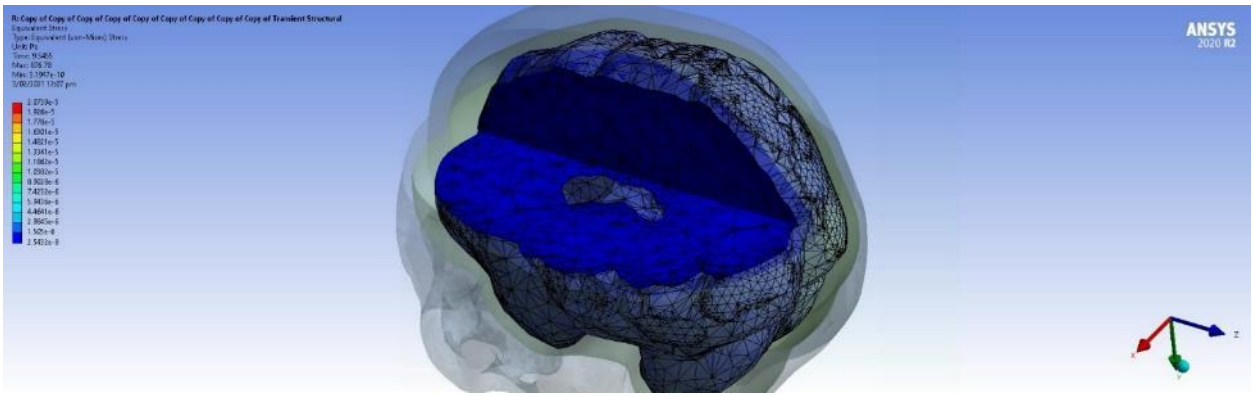
ANSYS
2020 R2

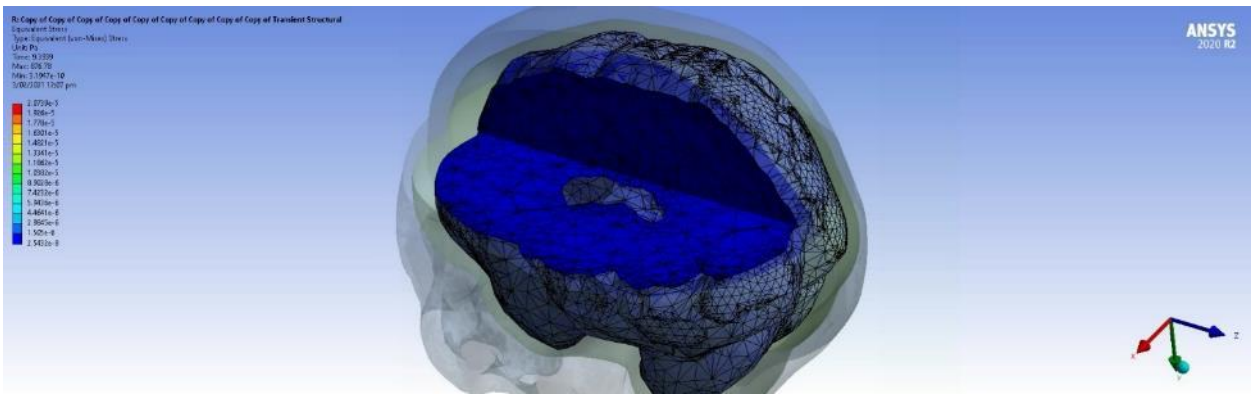
ANSYS
2020 R2

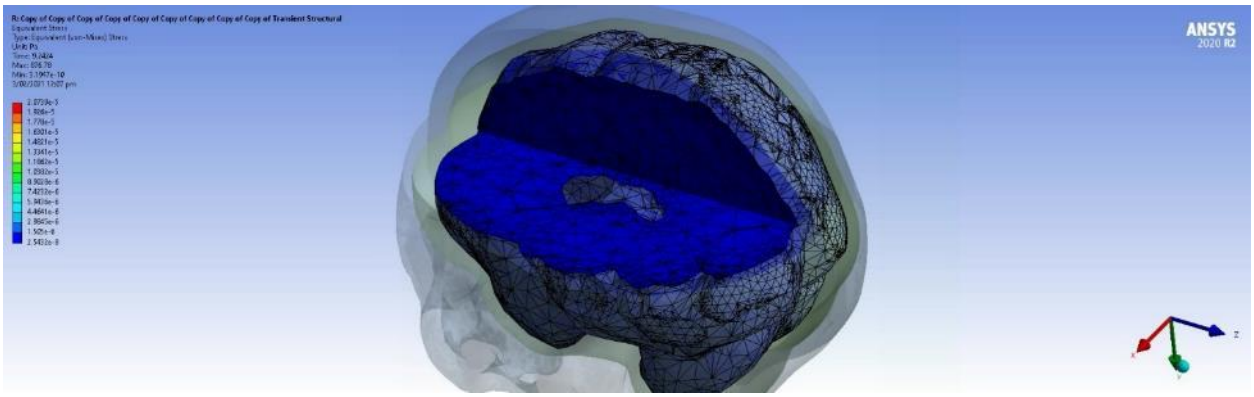
ANSYS
2020 R2

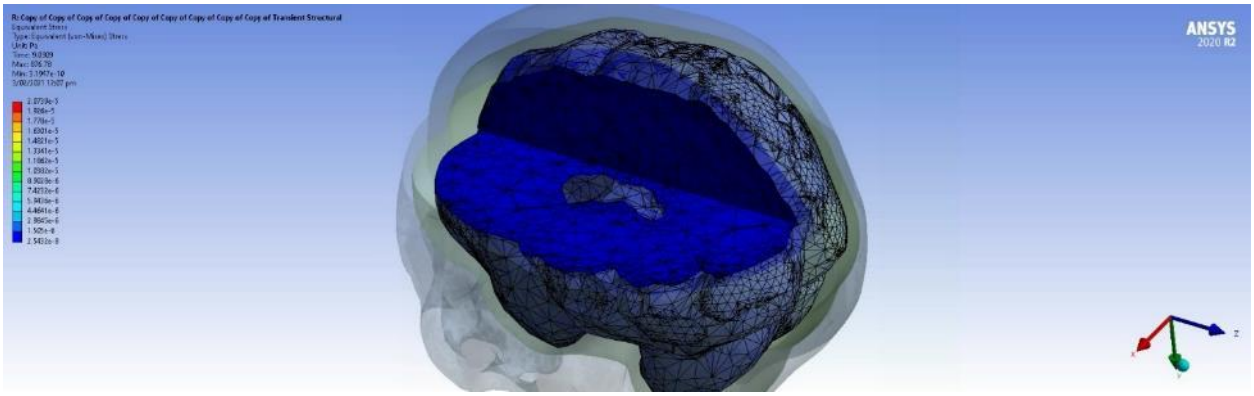
ANSYS
2020 R2

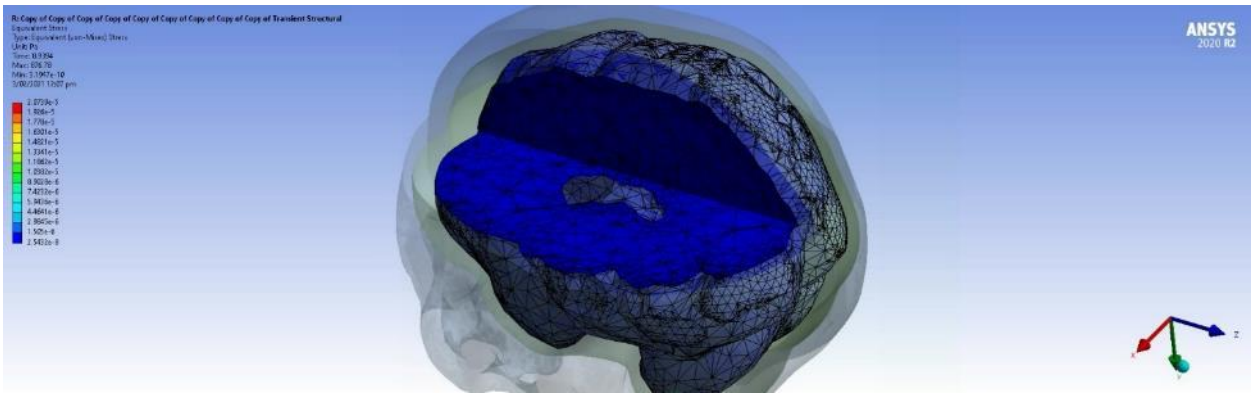
ANSYS
2020 R2

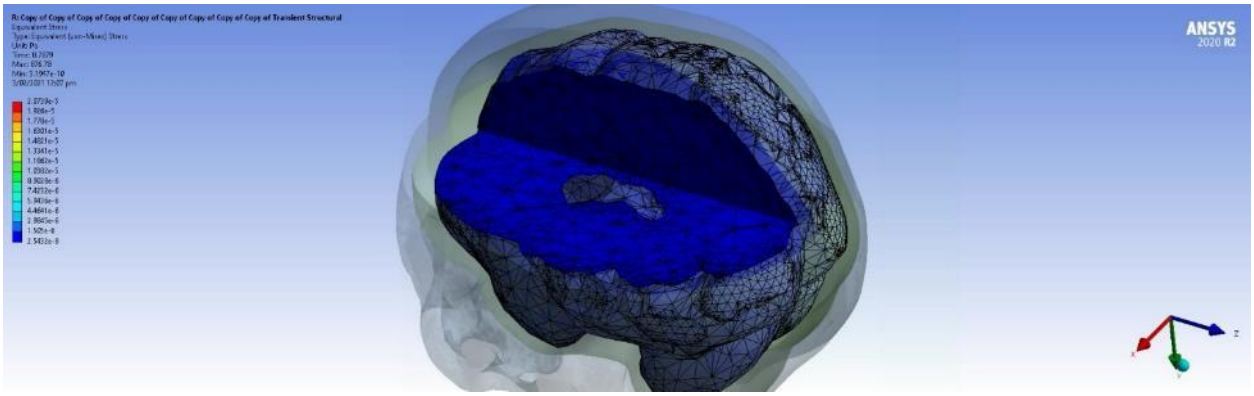
ANSYS
2020 R2

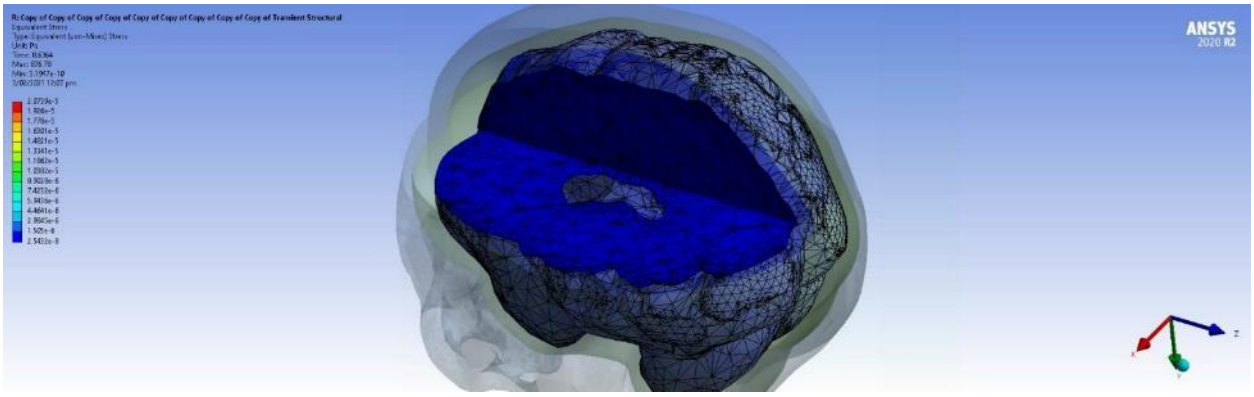
ANSYS
2020 R2

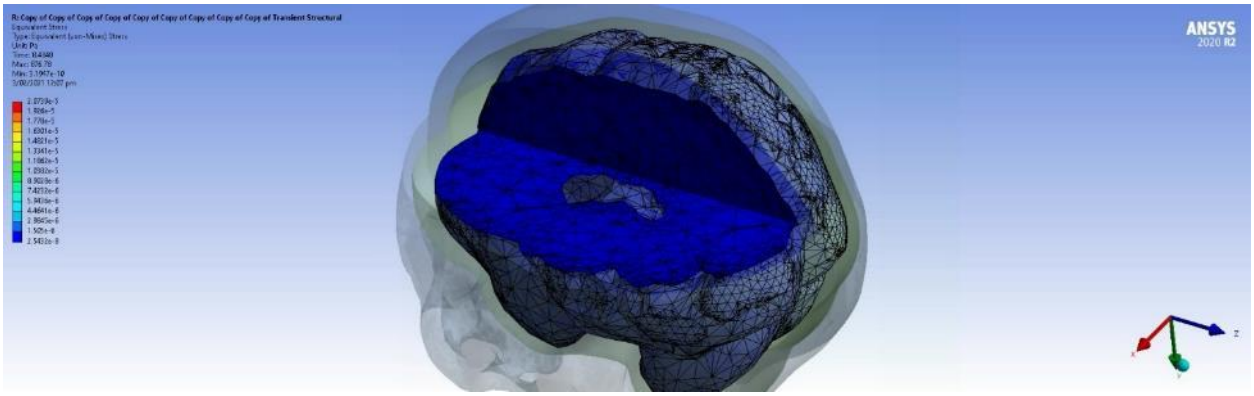
ANSYS
2020 R2

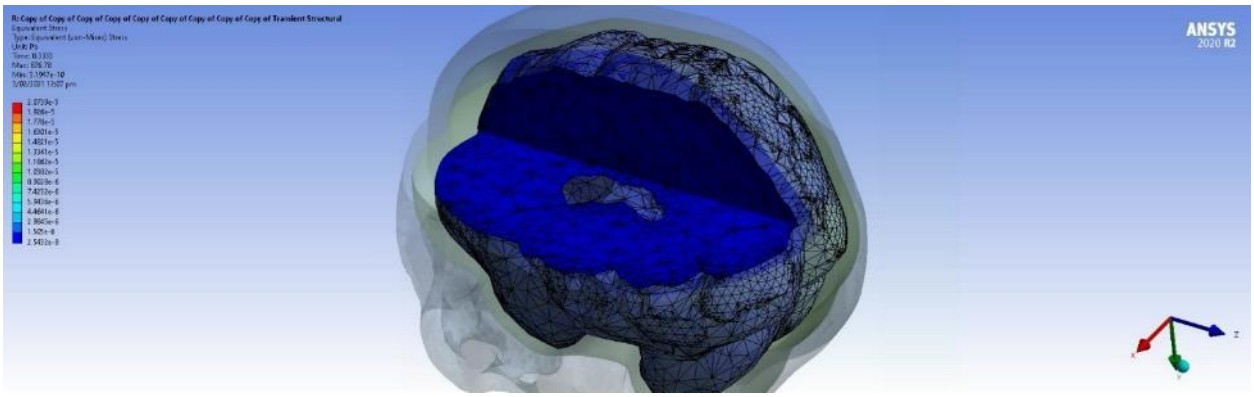
ANSYS
2020 R2

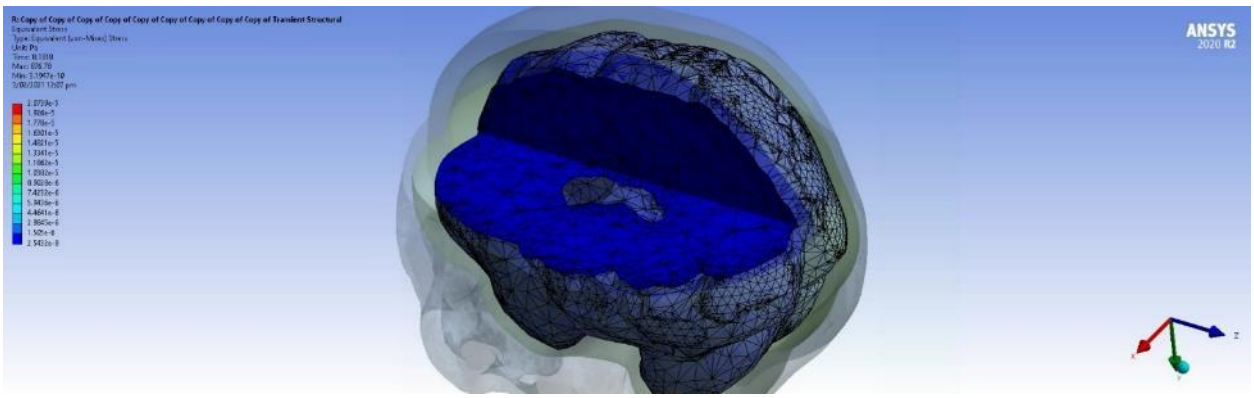
ANSYS
2020 R2

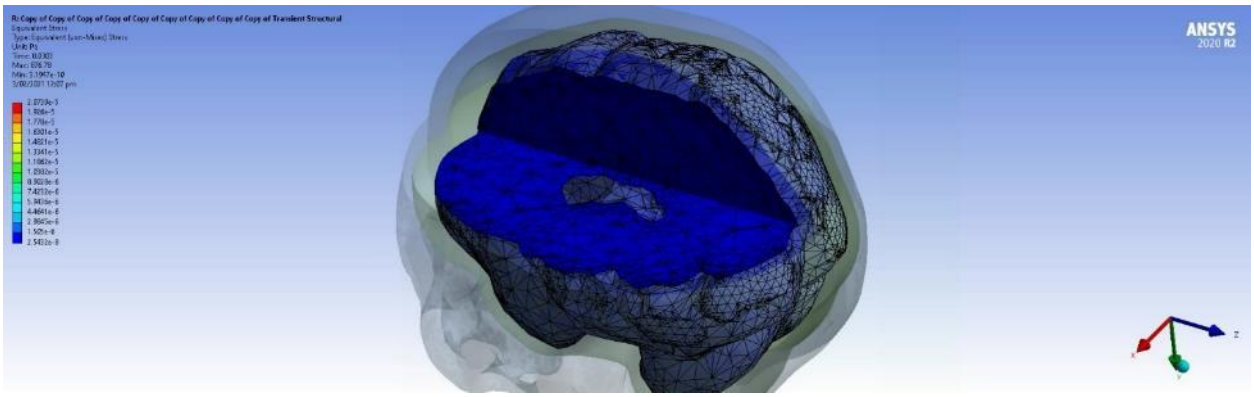
ANSYS
2020 R2

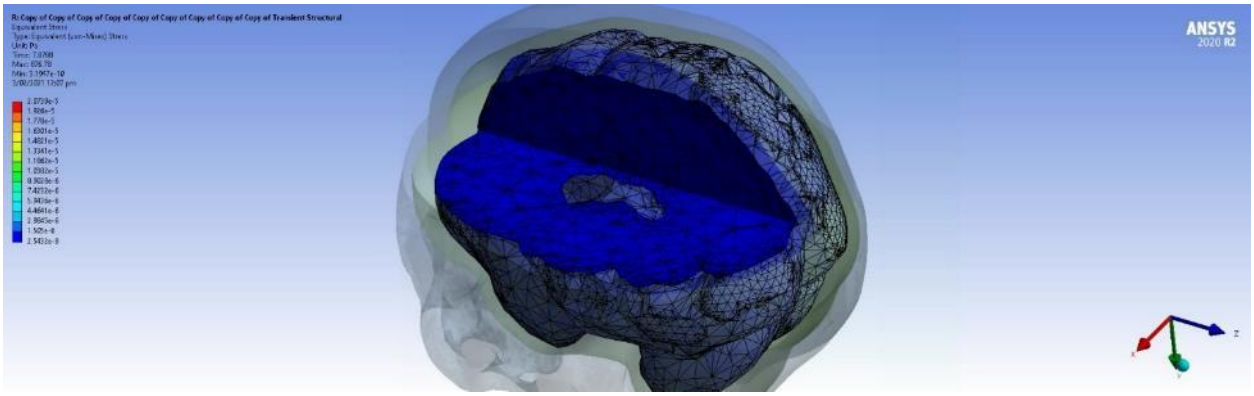
ANSYS
2020 R2

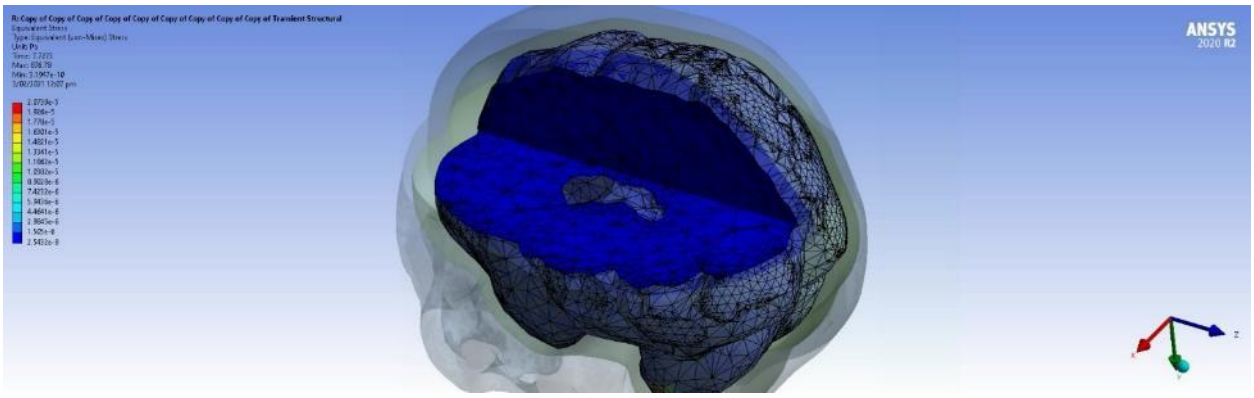
ANSYS
2020 R2

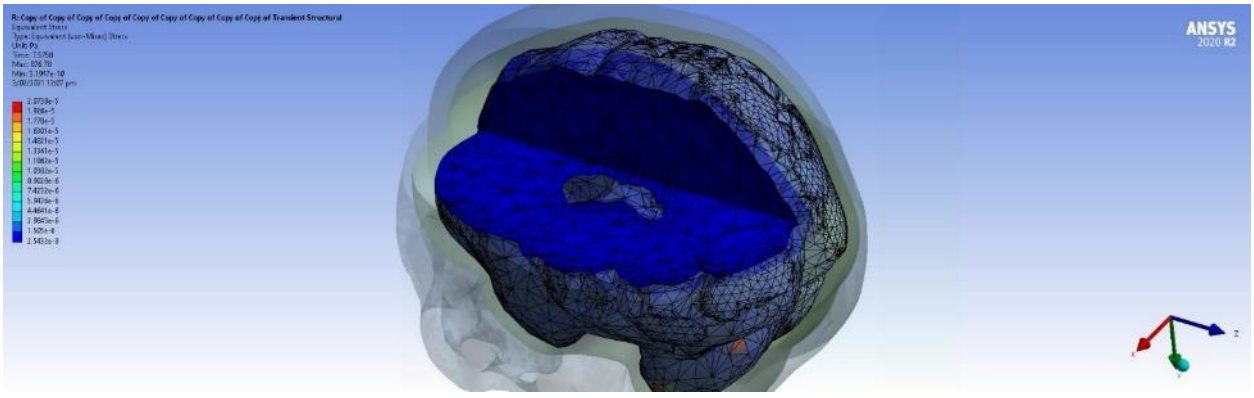
ANSYS
2020 R2

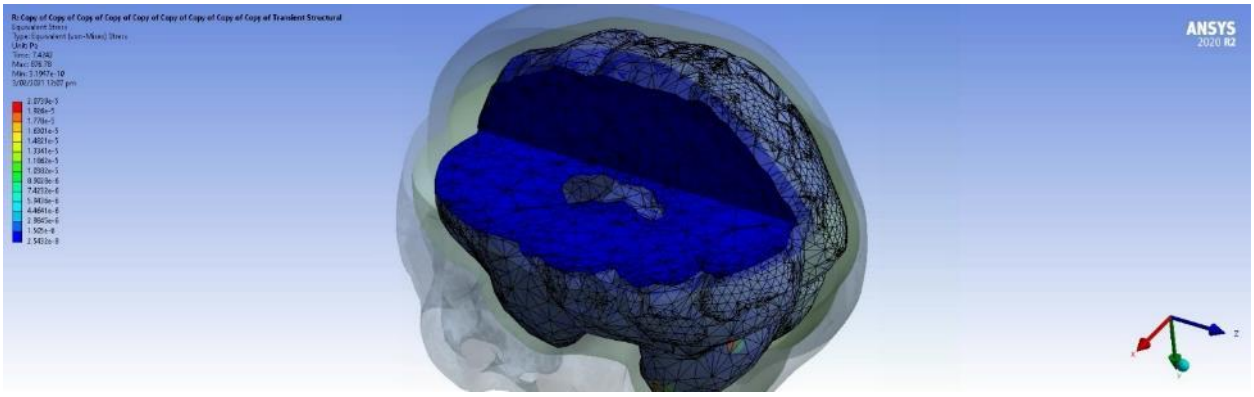
ANSYS
2020 R2

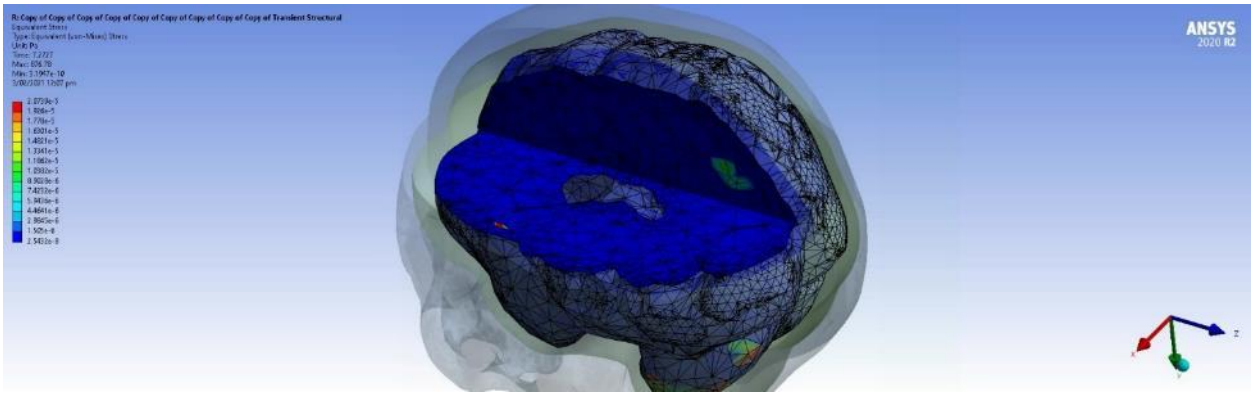
ANSYS
2020 R2

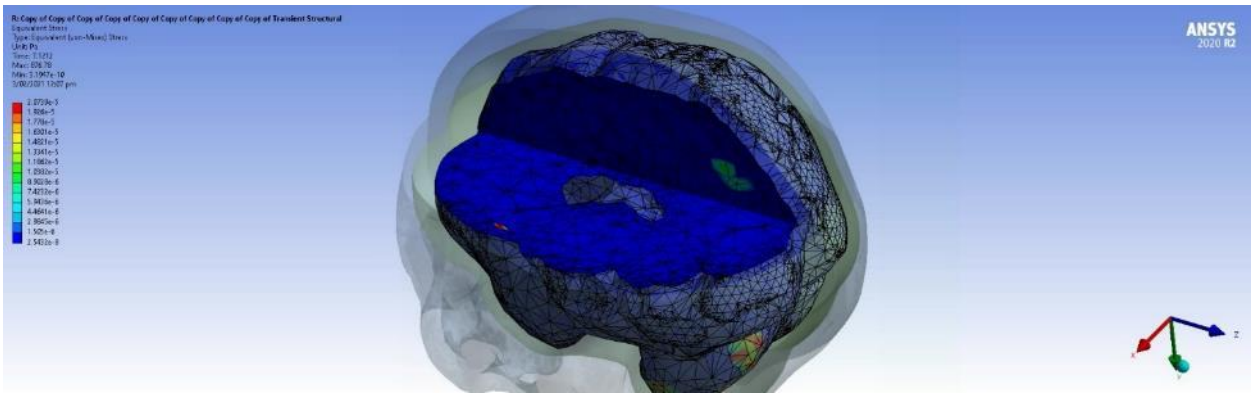
ANSYS
2020 R2

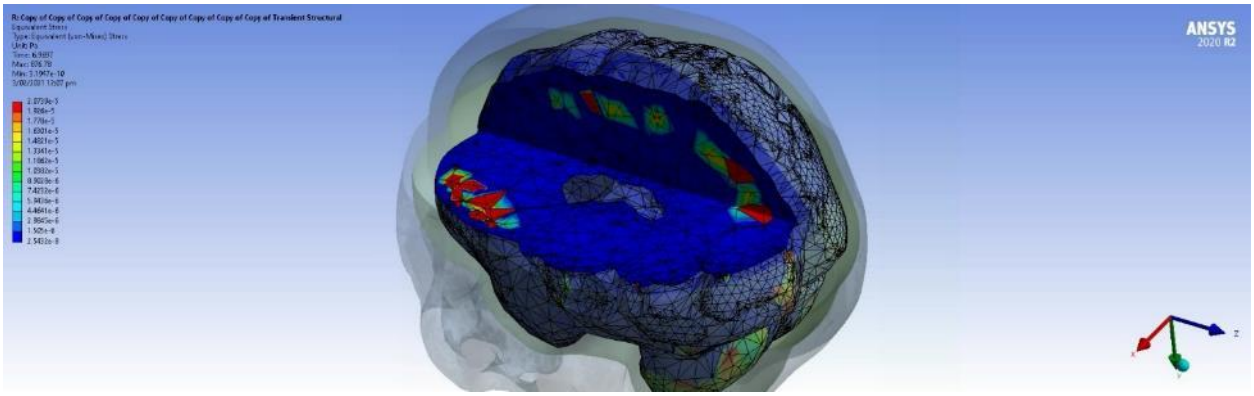
ANSYS
2020 R2

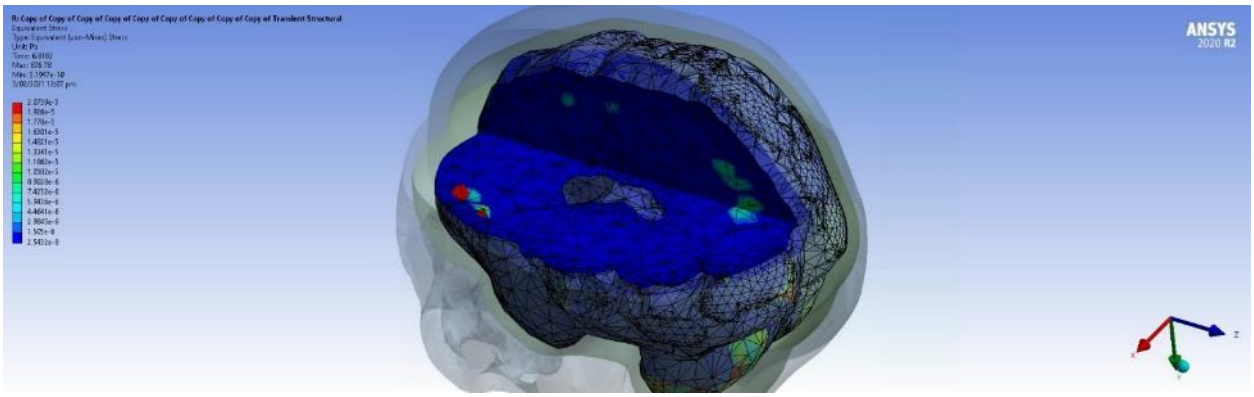
ANSYS
2020 R2

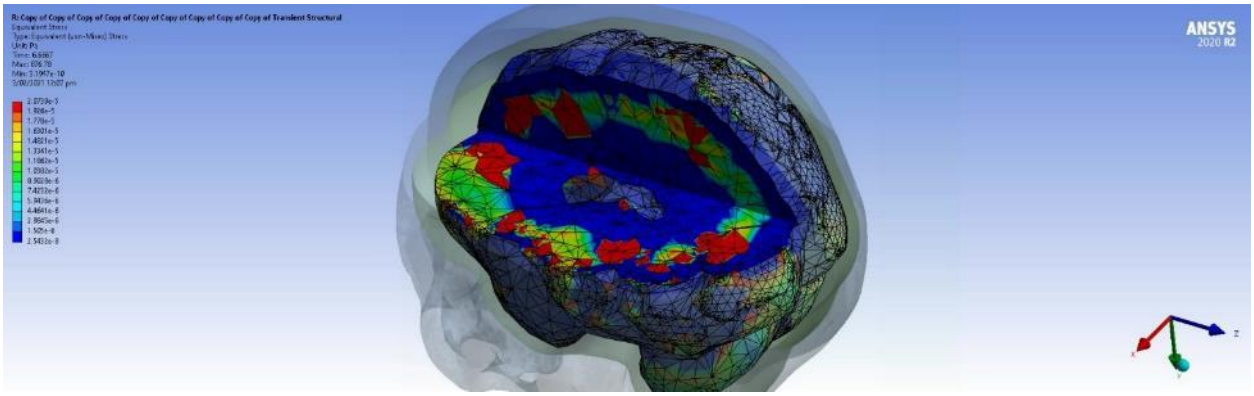
ANSYS
2020 R2

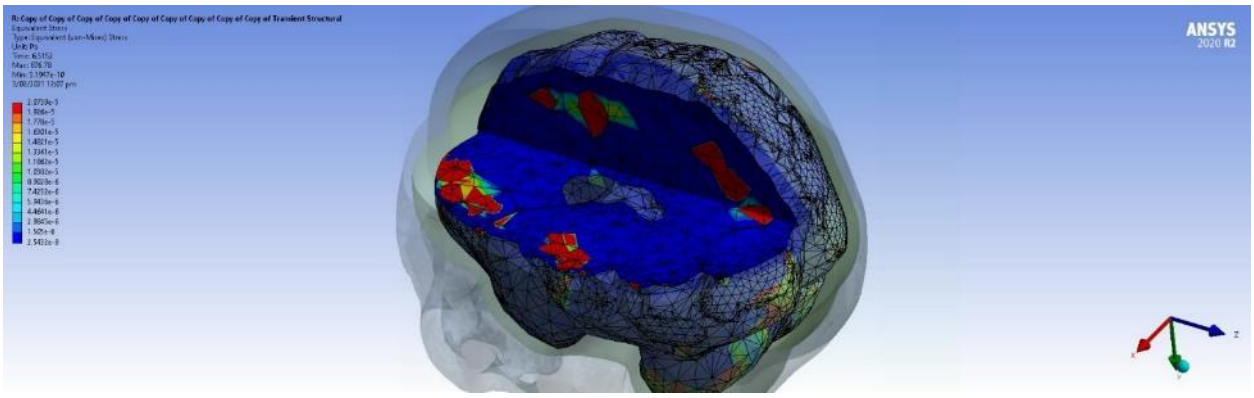
ANSYS
2020 R2

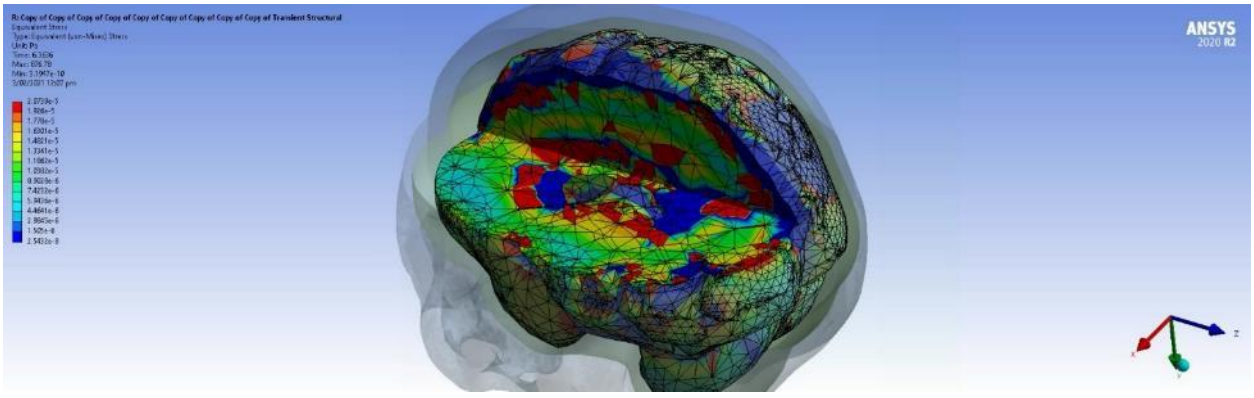
ANSYS
2020 R2

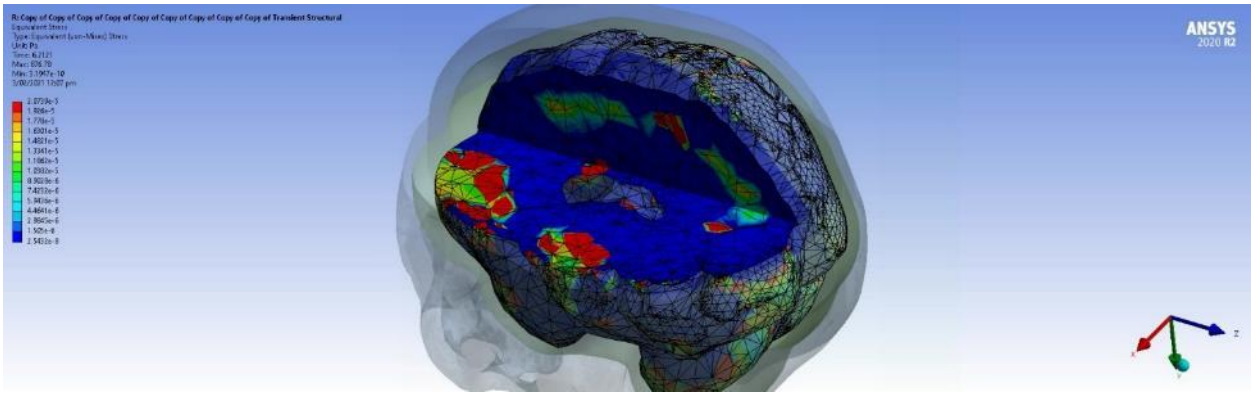
ANSYS
2020 R2

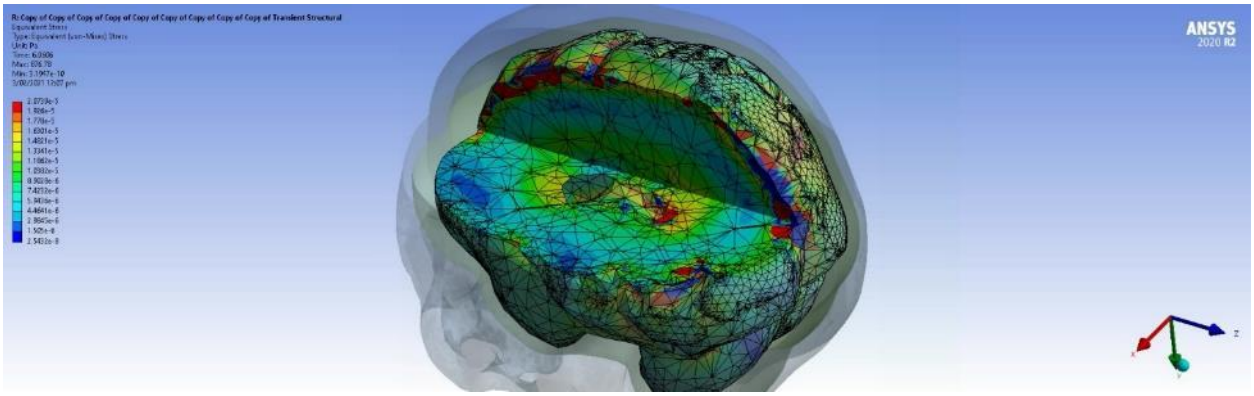
ANSYS
2020 R2

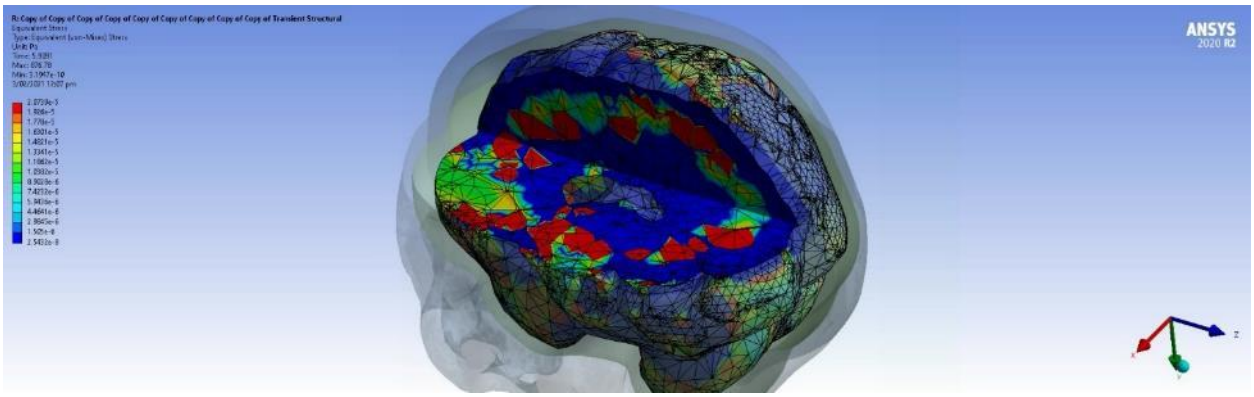
ANSYS
2020 R2

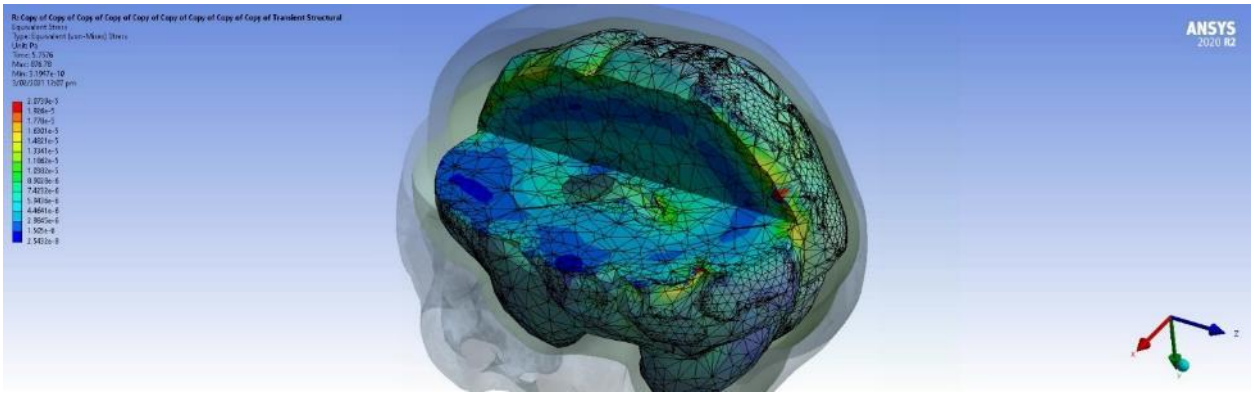
ANSYS
2020 R2

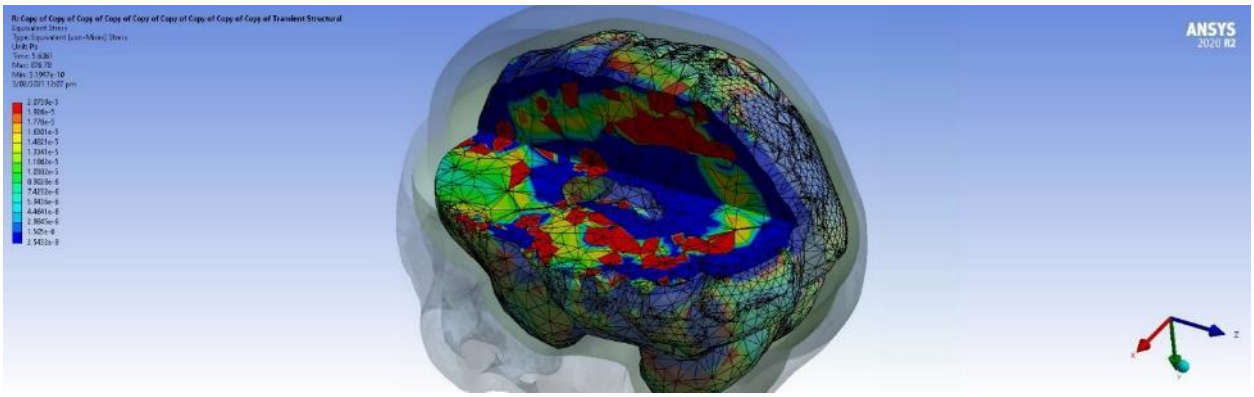
ANSYS
2020 R2

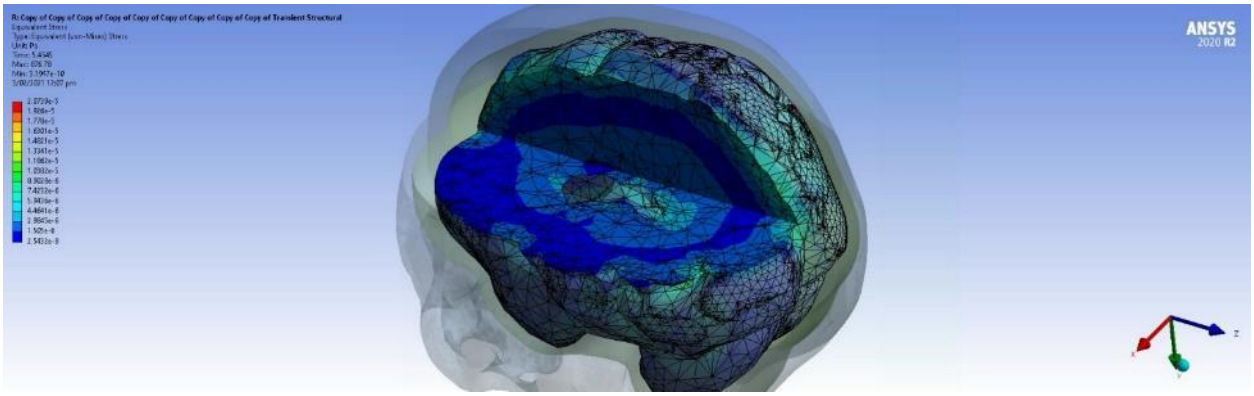
ANSYS
2020 R2

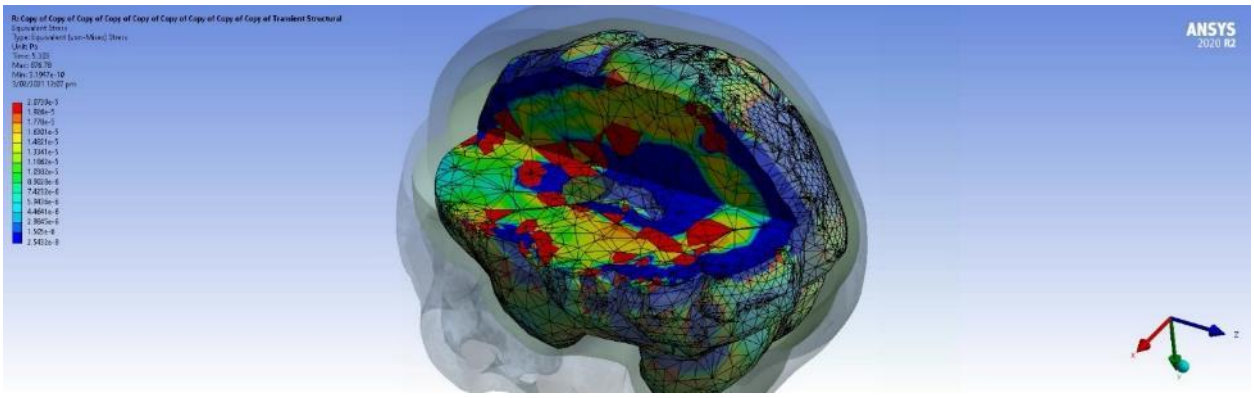
ANSYS
2020 R2

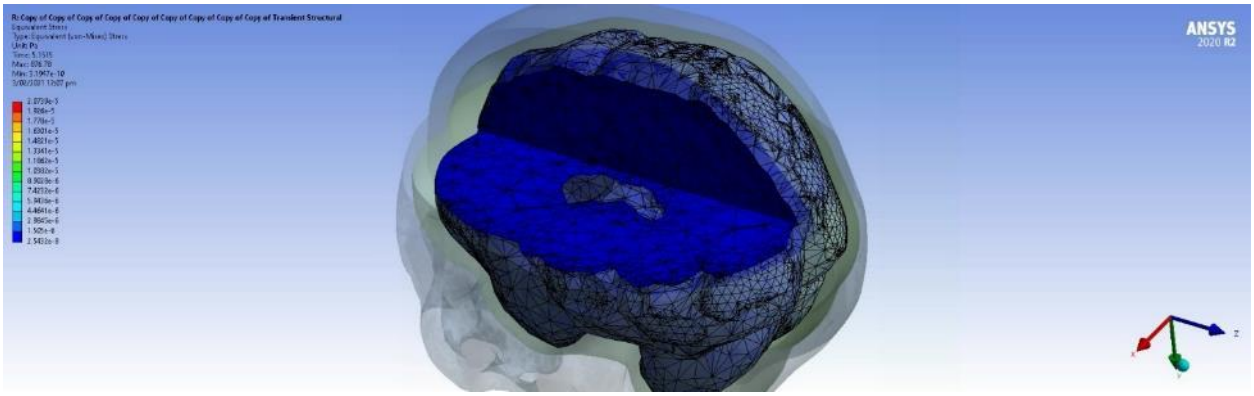
ANSYS
2020 R2

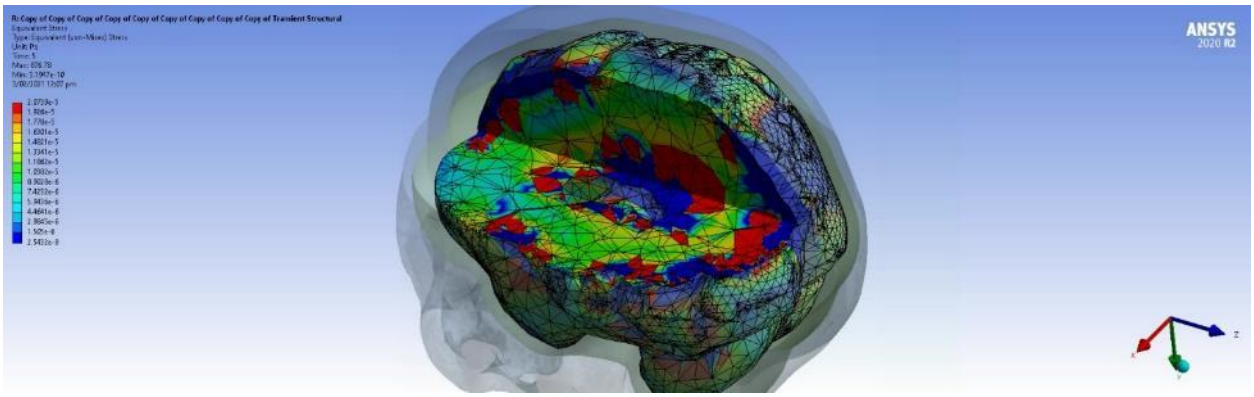
ANSYS
2020 R2

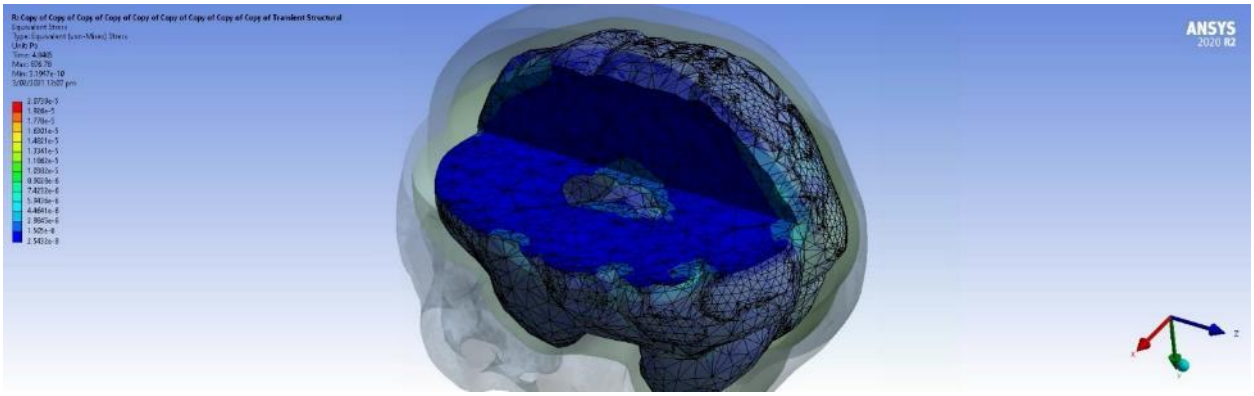
ANSYS
2020 R2

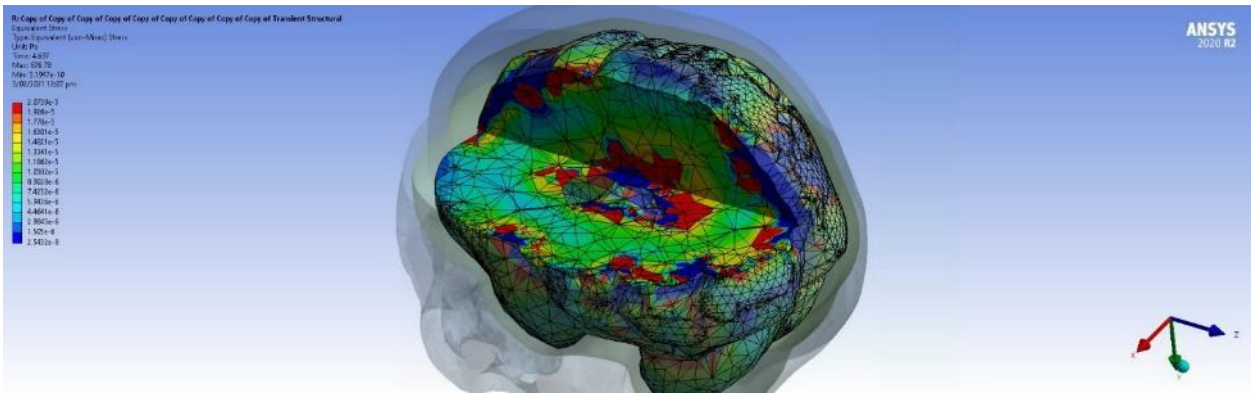
ANSYS
2020 R2

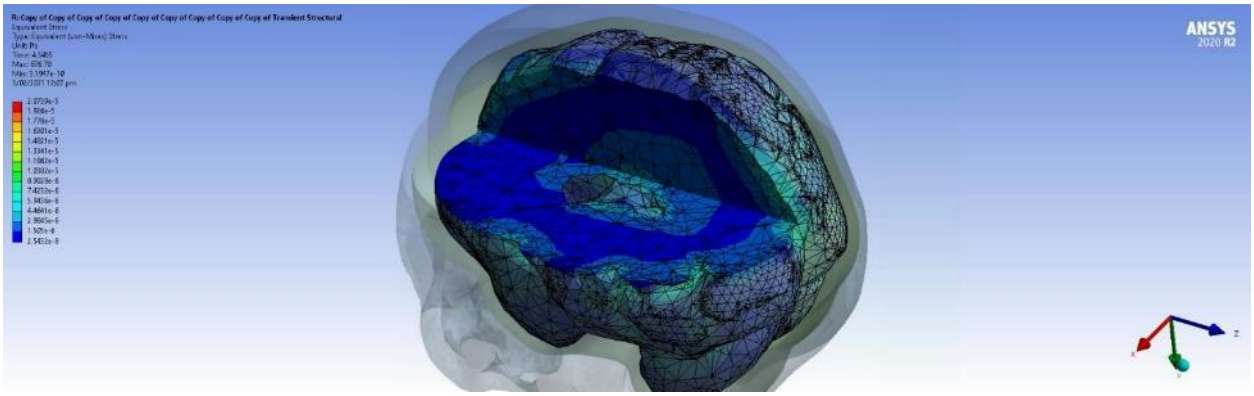
ANSYS
2020 R2

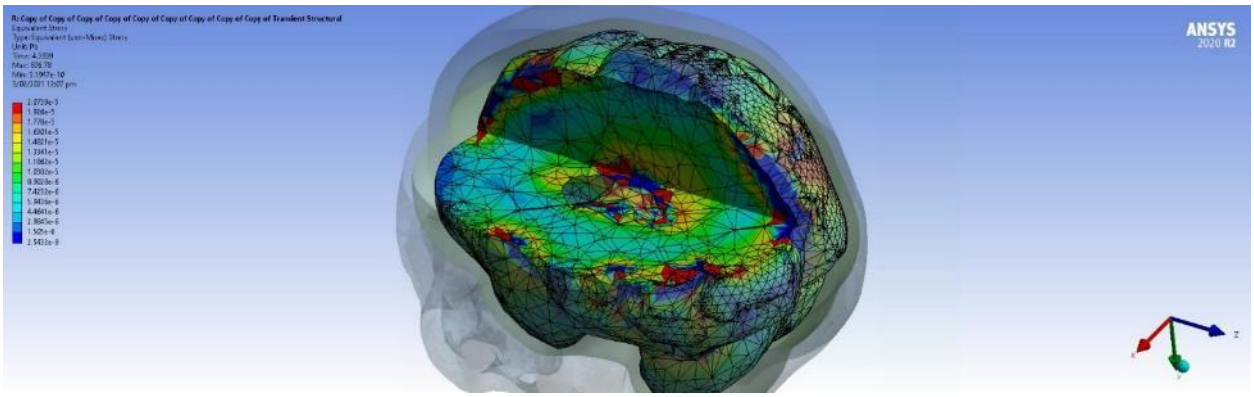
ANSYS
2020 R2

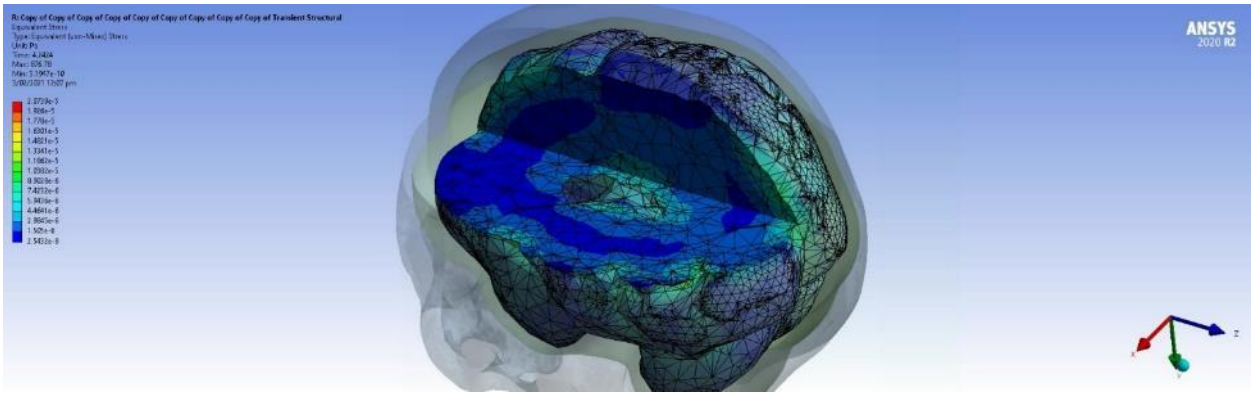
ANSYS
2020 R2

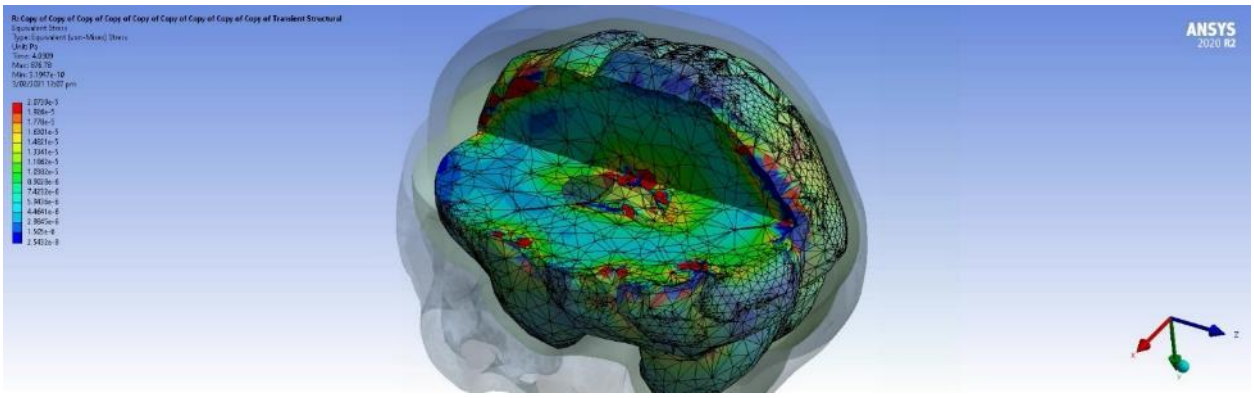
ANSYS
2020 R2

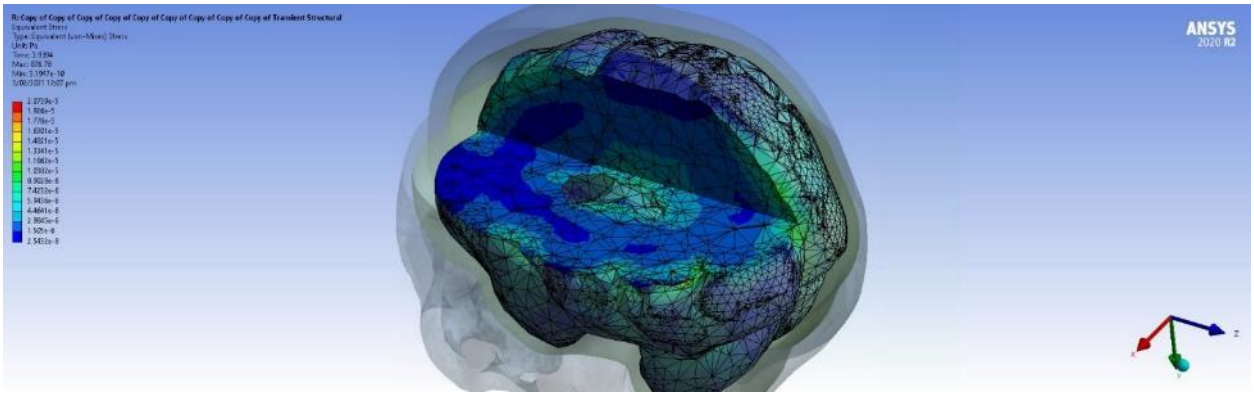
ANSYS
2020 R2

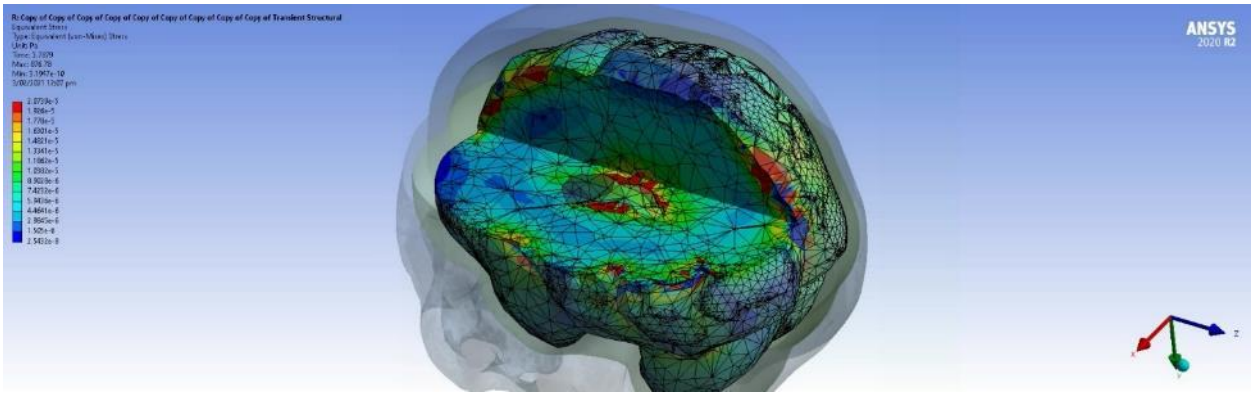
ANSYS
2020 R2

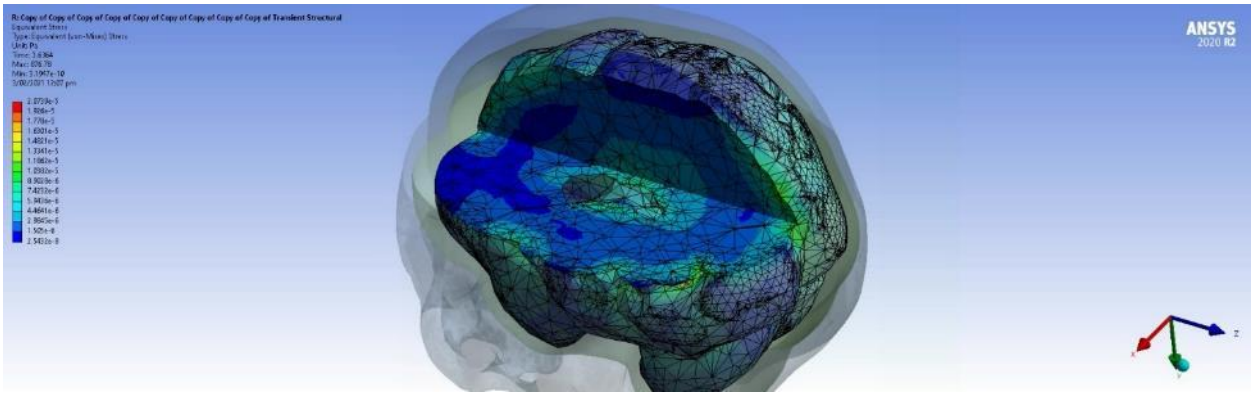
ANSYS
2020 R2

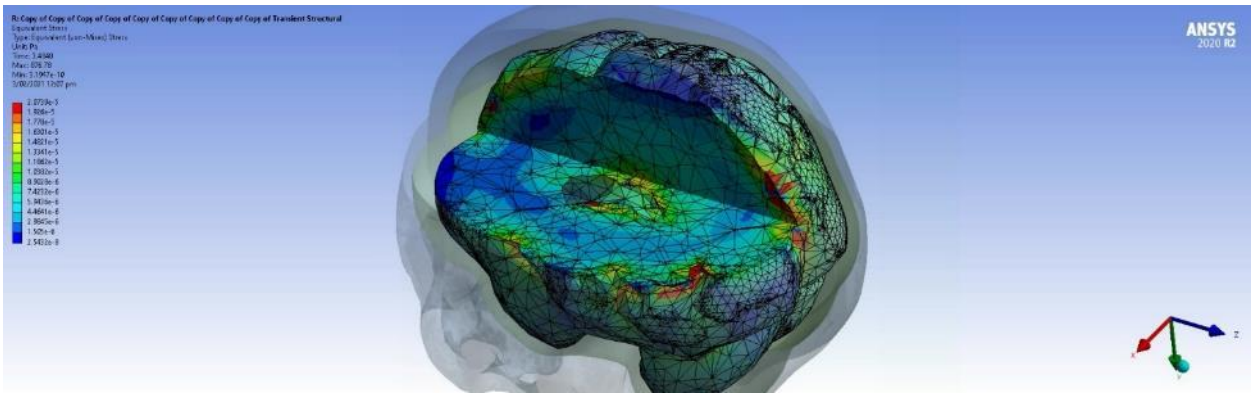
ANSYS
2020 R2

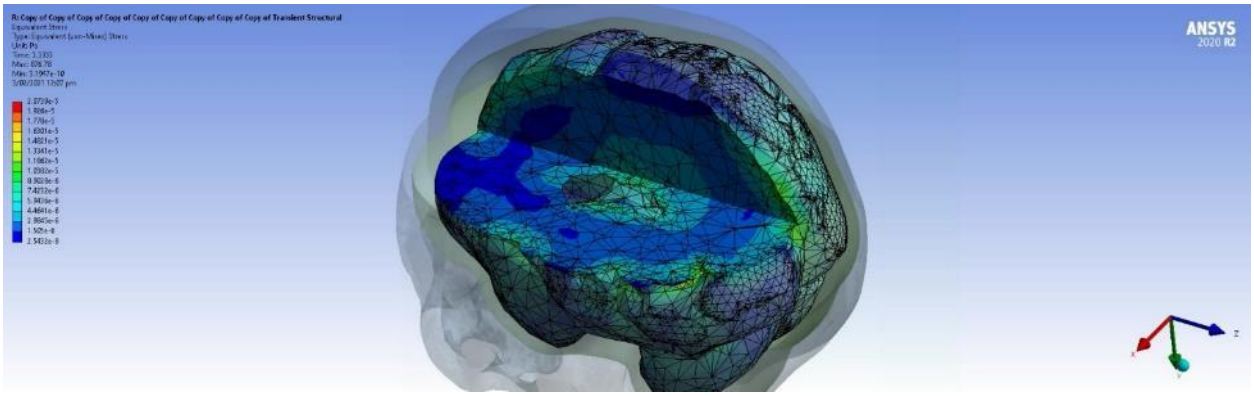
ANSYS
2020 R2

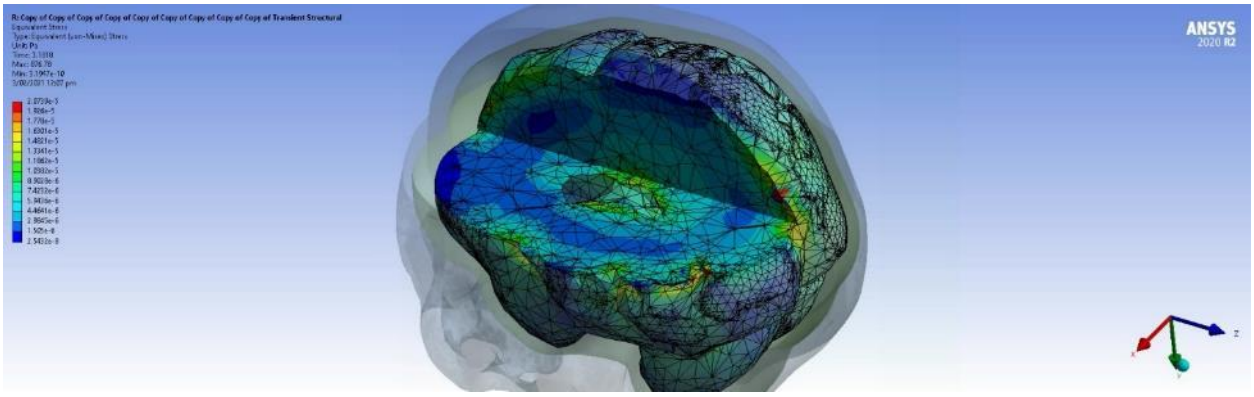
ANSYS
2020 R2

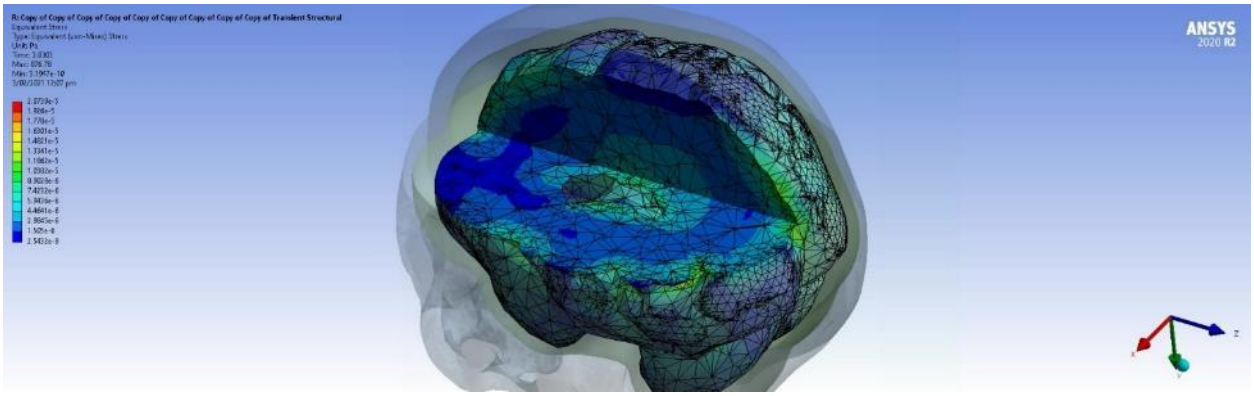
ANSYS
2020 R2

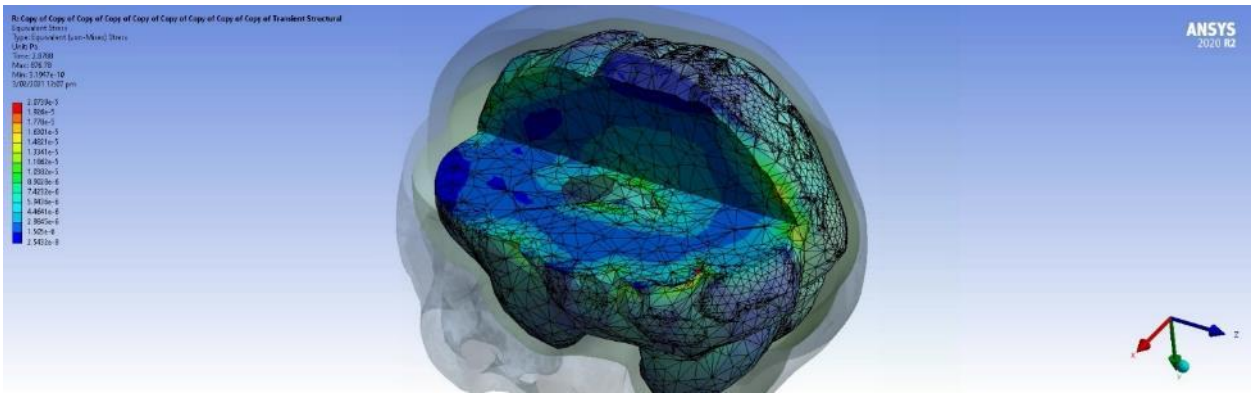
ANSYS
2020 R2

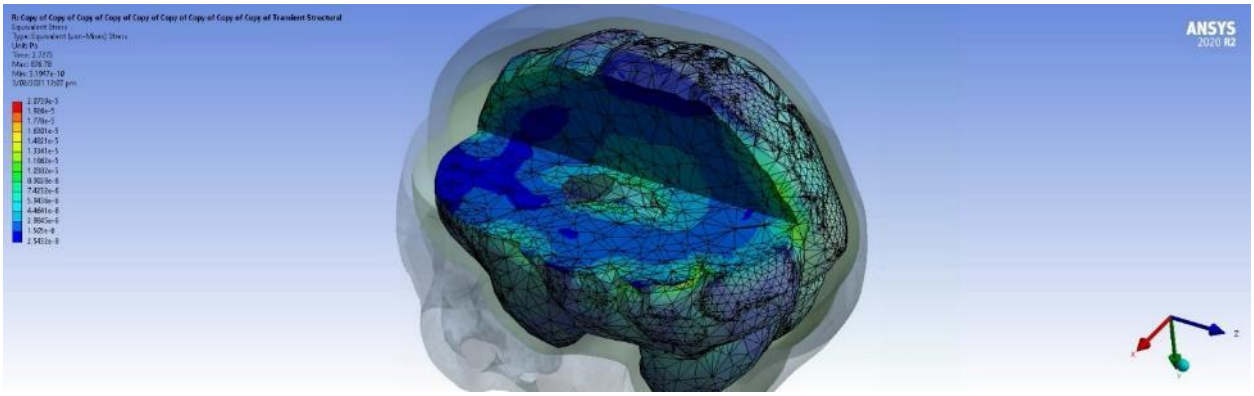
ANSYS
2020 R2

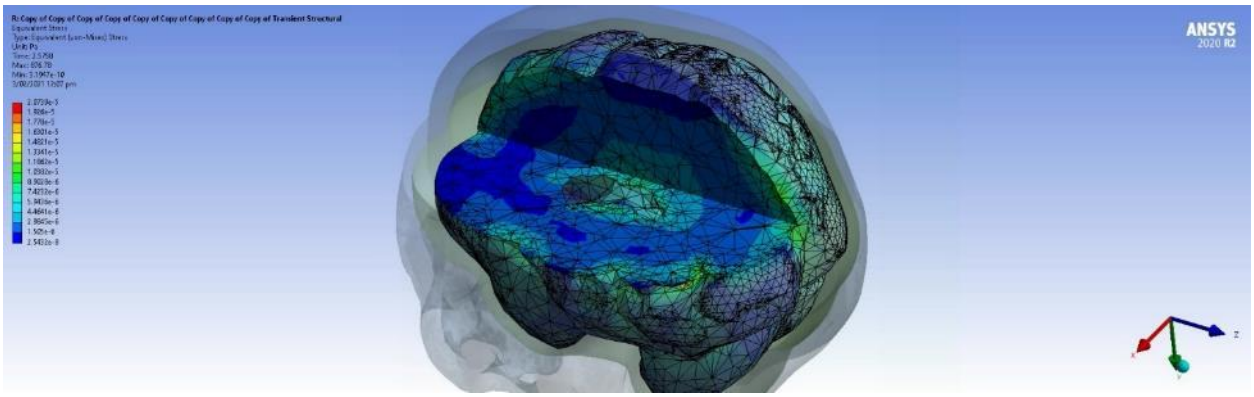
ANSYS
2020 R2

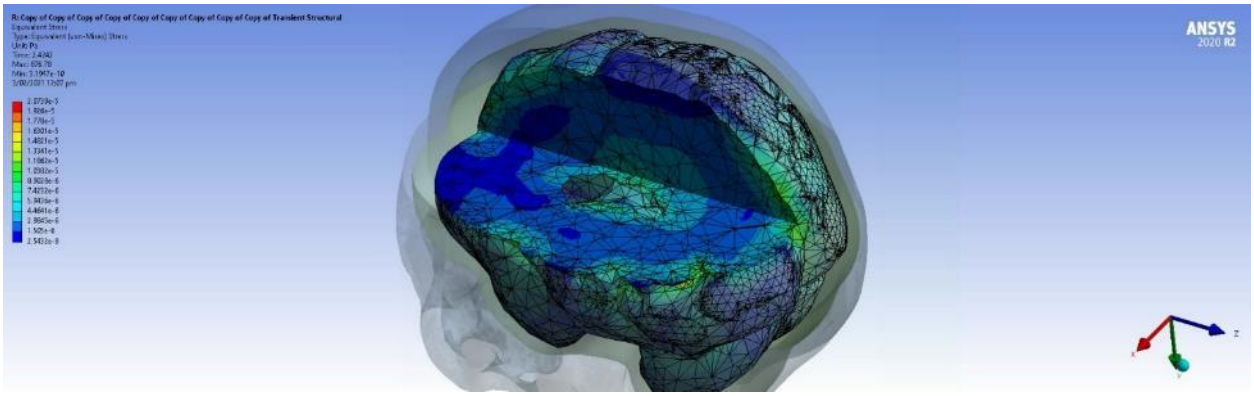
ANSYS
2020 R2

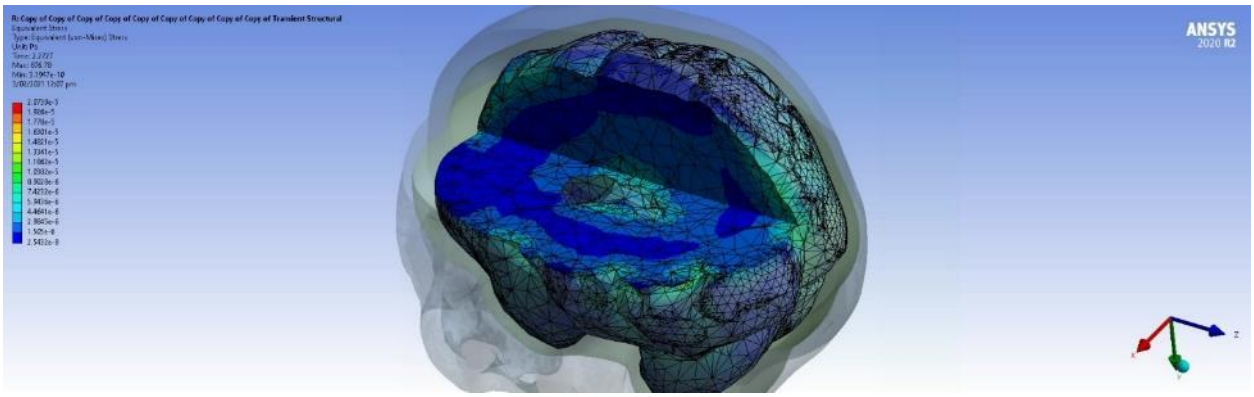
ANSYS
2020 R2

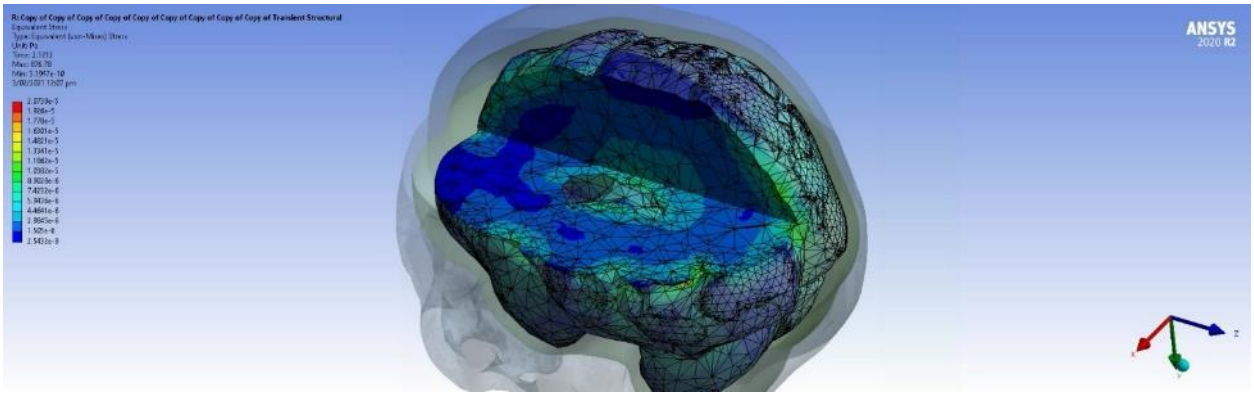
ANSYS
2020 R2

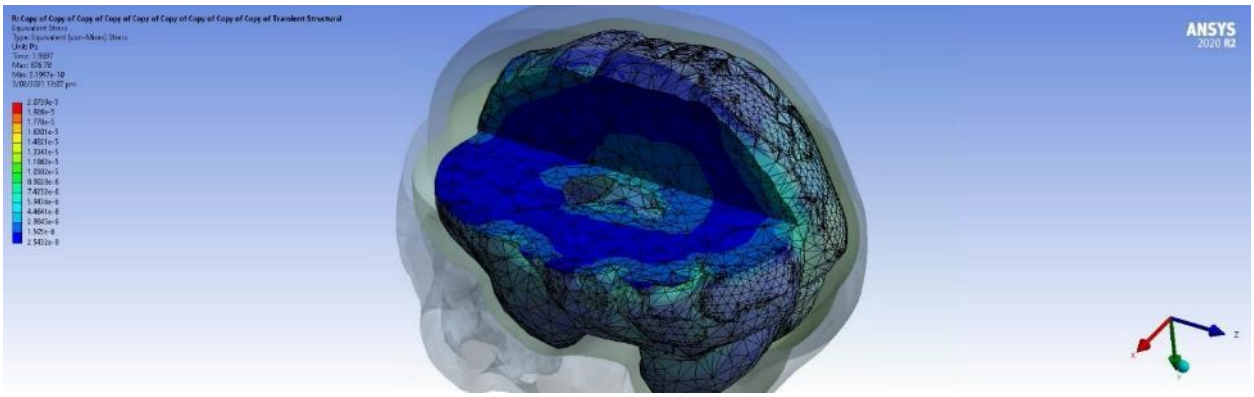
ANSYS
2020 R2

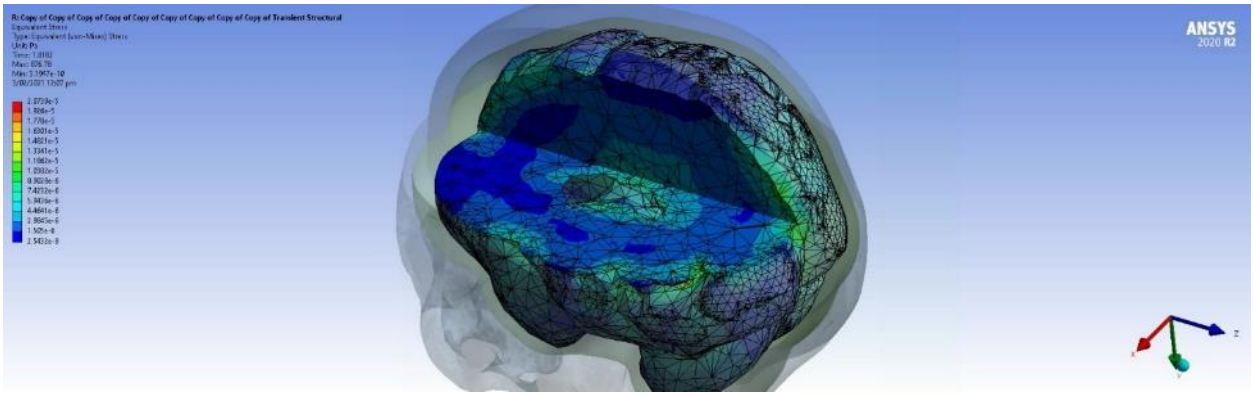
ANSYS
2020 R2

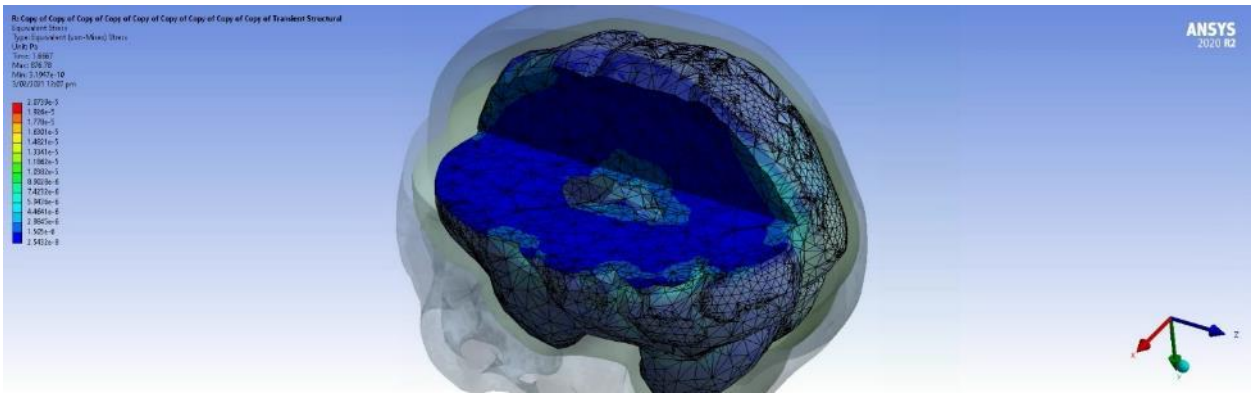
ANSYS
2020 R2

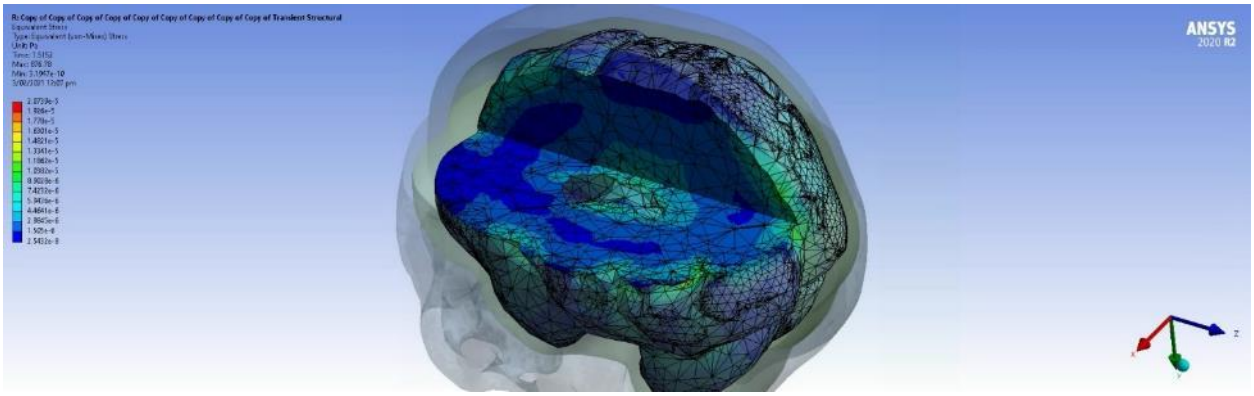
ANSYS
2020 R2

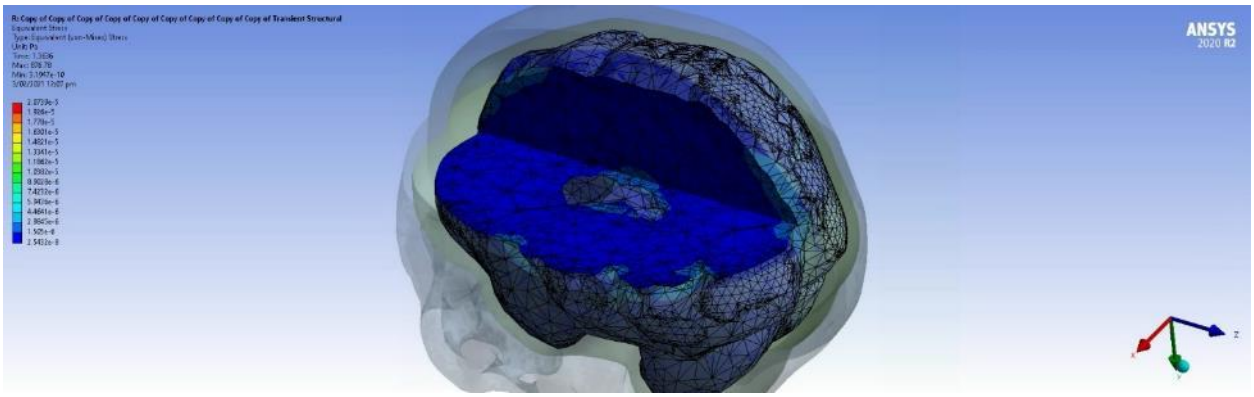
ANSYS
2020 R2

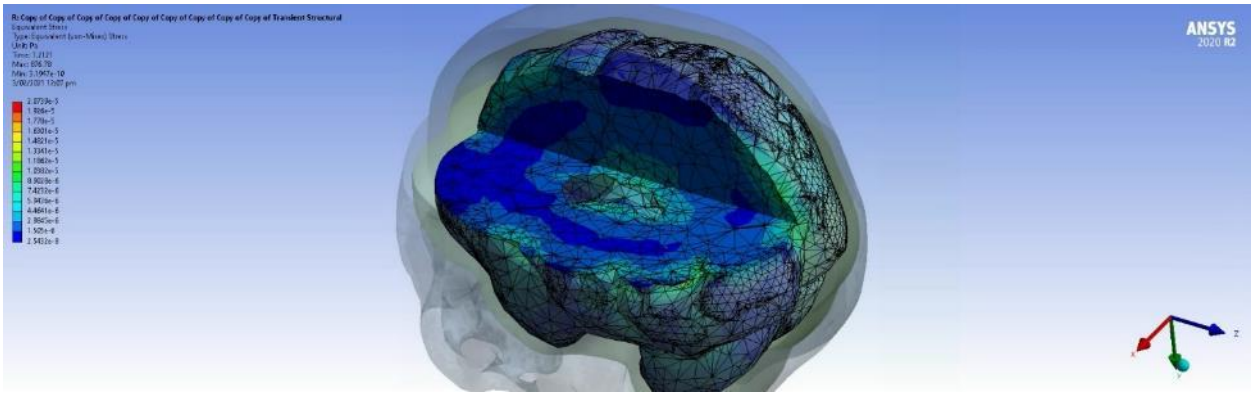
ANSYS
2020 R2

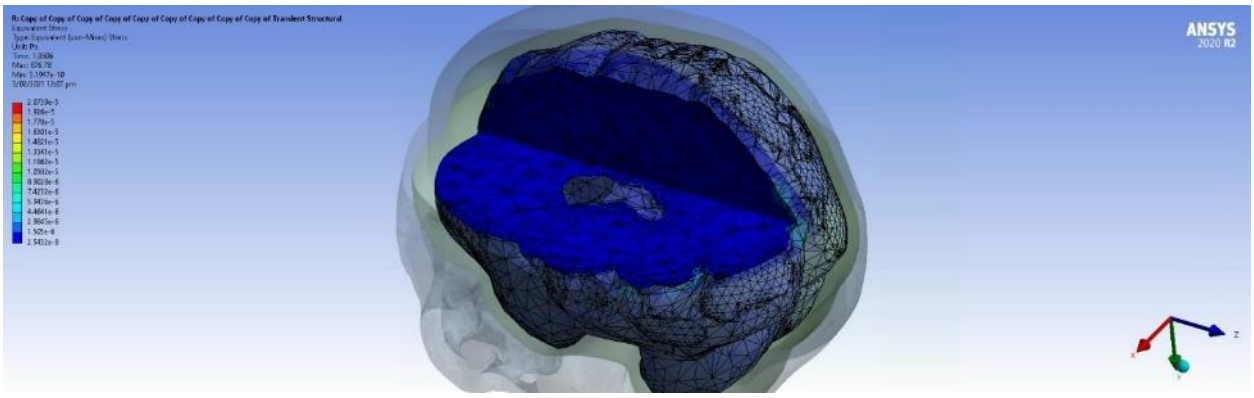
ANSYS
2020 R2

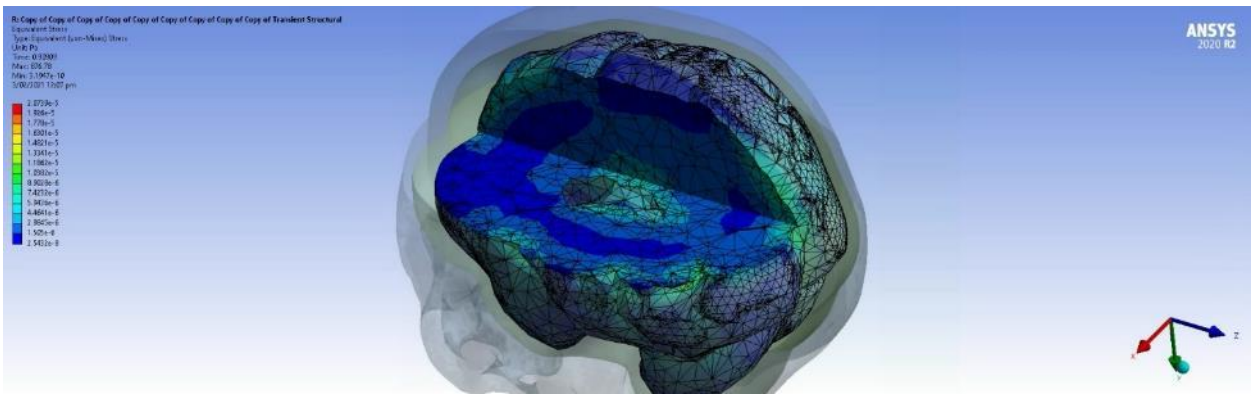
ANSYS
2020 R2

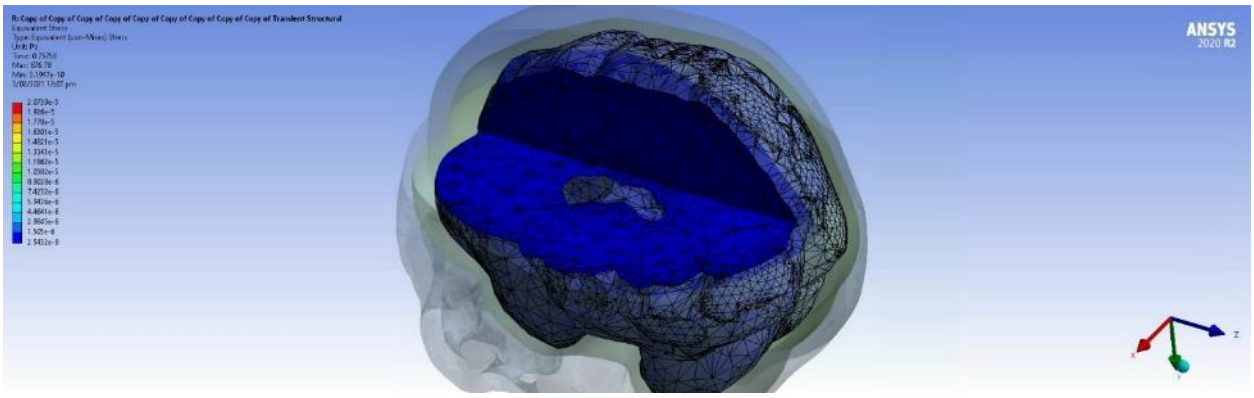
ANSYS
2020 R2

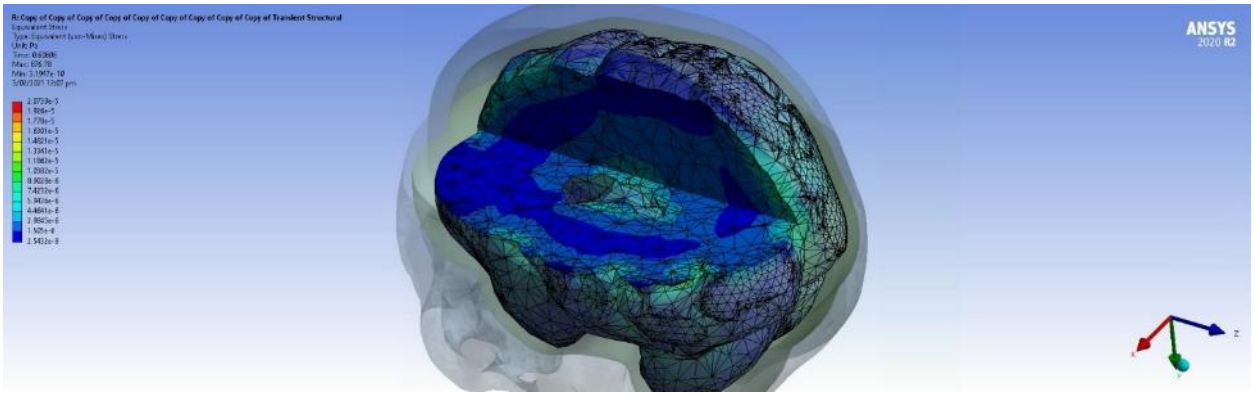
ANSYS
2020 R2

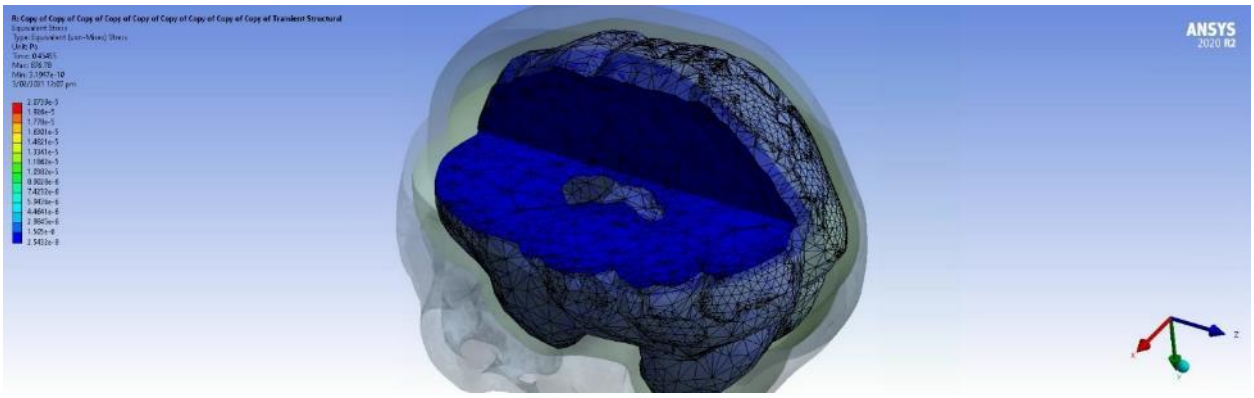
ANSYS
2020 R2

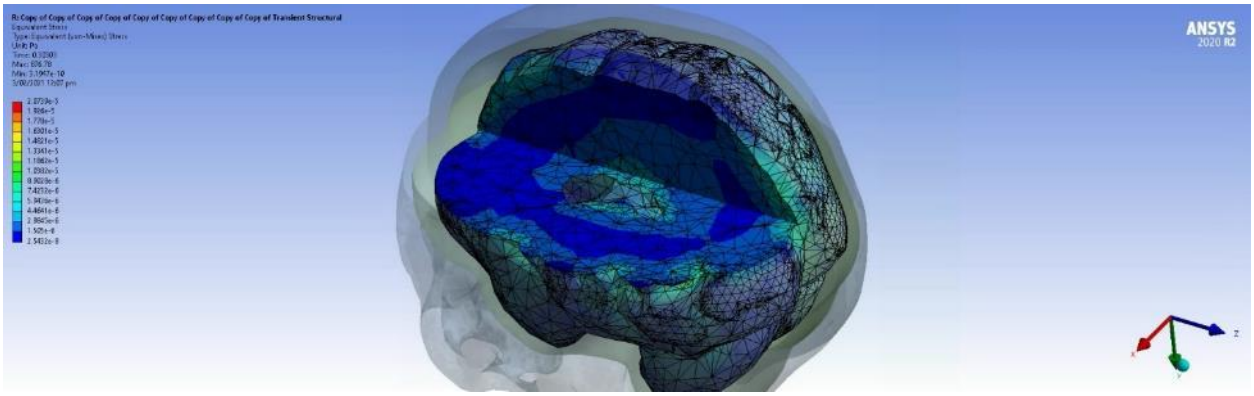
ANSYS
2020 R2

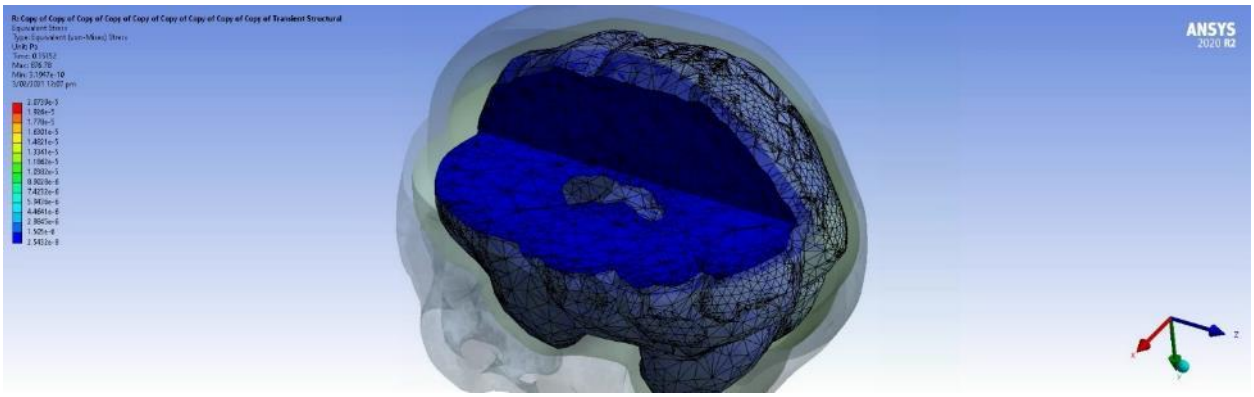
ANSYS
2020 R2

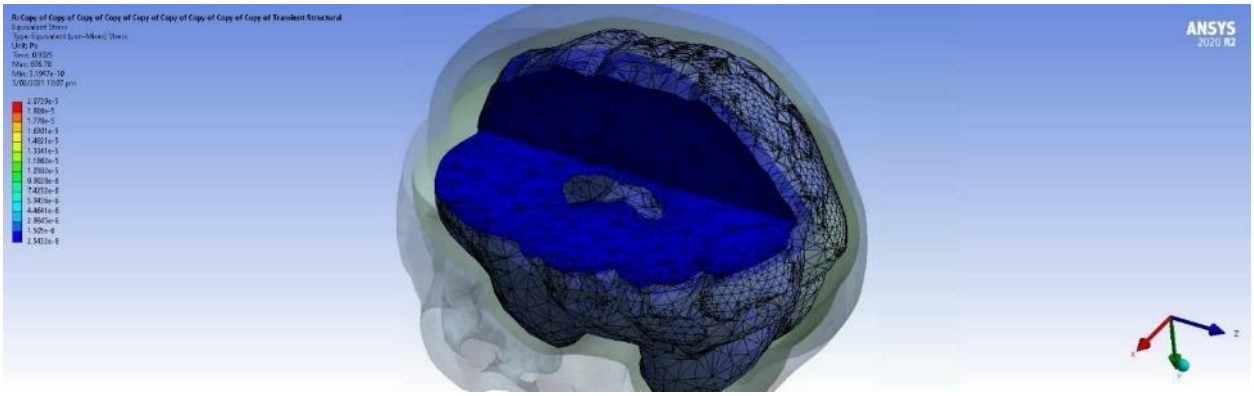
ANSYS
2020 R2

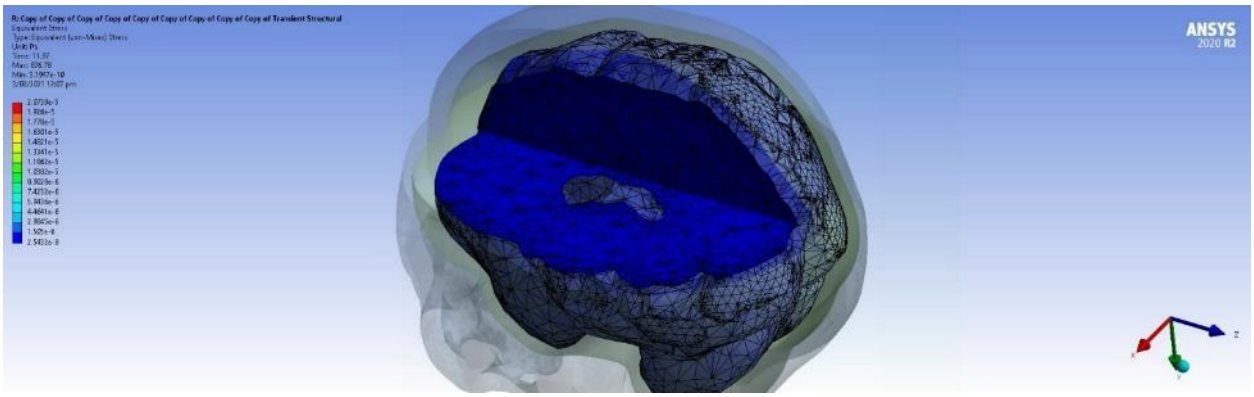
ANSYS
2020 R2